Gas Dynamics

Volume 2: Multidimensional Flow

Maurice J. Zucrow / Joe D. Hoffman

Volume II

Gas Dynamics

Multidimensional Flow

board of advisors, engineering

A. H-S. Ang University of Illinois	Civil Engineering—Systems and Probability
Donald S. Berry Northwestern University	Transportation Engineering
James Gere Stanford University	Civil Engineering and Applied Mechanics
J. Stuart Hunter Princeton University	Engineering Statistics
T. William Lambe *R. V. Whitman* Massachusetts Institute of Technology	Civil Engineering—Soil Mechanics
Perry L. McCarty Stanford University	Environmental Engineering
Don T. Phillips Texas A&M	Industrial Engineering
Dale Rudd University of Wisconsin	Chemical Engineering
Robert F. Steidel, Jr. University of California–Berkeley	Mechanical Engineering
R. N. White Cornell University	Civil Engineering—Structures

Volume II

Gas Dynamics

Multidimensional Flow

Maurice J. Zucrow
Joe D. Hoffman

School of Mechanical Engineering Purdue University

JOHN WILEY AND SONS
New York Santa Barbara London Sydney Toronto

Library of Congress Cataloging in Publication Data:

Zucrow, Maurice Joseph 1899-1975.
Gas dynamics.

Vol. 2 has title: Multidimensional flow.
Includes bibliographical references and indexes.
1. Gas dynamics. I. Hoffman, Joe D., 1934- joint author. II. Title.

QC168.Z8 1976 533'.2. 76-6855
ISBN 0-471-98440-X(v.1)
ISBN 0-471-018066-6 (v.2)

Printed in the United States of America

10 9 8 7 6 5 4 3 2 1

preface

This is Volume II of *Gas Dynamics*. The first volume introduces the science of gas dynamics. In Volume I, the concepts of steady one-dimensional flow are presented in depth, and the concepts of multidimensional flow are introduced. This book continues the material presented in Volume I, with major emphasis placed on the application of the method of characteristics to both unsteady and steady multidimensional flows.

The philosophy employed in Volume I is followed here. The subject matter is presented in sufficient detail so that the student can understand the material without the assistance of an instructor. This volume, even more than the first, deals with numerical procedures for solving gas dynamic problems. Consequently, there is a significant number of illustrative examples.

An introduction to chemical thermodynamics is presented in Chapter 14, followed by a discussion of the steady one-dimensional flow of chemically reacting gas mixtures and gas-particle mixtures. Chapter 15 extends the material presented in Chapter 11 to the problems of three-dimensional acoustic waves and steady two-dimensional transonic flow.

Chapter 12 in Volume I introduces the method of characteristics, and applies that procedure to an interior point in a steady two-dimensional irrotational supersonic flow field. Chapter 16 in this volume extends that material to include the unit processes for the boundary points of the flow and to present several engineering applications. Chapter 17 discusses the application of the method of characteristics to steady two-dimensional isentropic supersonic flow problems. Chapter 18 presents an introduction to the steady two-dimensional flow of nonequilibrium chemically reacting gas mixtures and gas-particle mixtures. Chapter 19 extends the material presented in Chapter 13 of Volume I, which is concerned with unsteady one-dimensional continuous flow. The general features of unsteady one-dimensional flow with discontinuities are discussed in Chapter 19, and the unit processes are developed for the boundary points of the flow. Several applications of practical interest are presented.

An introduction to the method of characteristics for flows having three independent variables is presented in Chapter 20.

The method of characteristics is emphasized heavily in this book in the chapters concerned with multidimensional flows (i.e., Chapters 12, 13, and 16 to 20) for two reasons. First, a thorough understanding of the physics of flows governed by hyperbolic partial differential equations is absolutely essential before numerical solutions for such flows can be obtained. The concepts of the domain of dependence, the range of influence, and the characteristics as the paths of propagation of the physical information through the flow field must be fully understood and accounted for in any solution procedure. The theoretical method of characteristics provides the necessary insight and understanding of the physics discussed above.

Second, the numerical method of characteristics provides the most accurate numerical procedure for solving flows governed by hyperbolic partial differential equations. Strict adherence to the domain of dependence and range of influence of

the governing equations can be achieved by the numerical method of characteristics. The solution is propagated numerically along the characteristics of the flow, which are also the carriers of information in the fluid itself. A full appreciation of the stability of a numerical solution procedure can be obtained only by completely understanding the concept of the domain of dependence of the differential equations.

Many finite difference procedures other than the numerical method of characteristics have been used to solve hyperbolic partial differential equations. When applying any of those procedures, it is necessary to understand fully the domain of dependence and the physical propagation paths if a valid solution is to result. Consequently, the insight into the physics of the flow afforded by the method of characteristics is fundamental to any numerical procedure for solving hyperbolic partial differential equations. Chapters 12, 13, and 16 to 20 provide that insight.

The material presented in Volume II is based on experience gained over the last 15 years in courses taught at Purdue University, graduate theses supervised, and consulting work performed for the propulsion industry. Many individuals contributed to the material presented in this volume, and I have acknowledged those contributions at the appropriate places in the text. I especially thank Miss Cynthia Hoffman for the excellent typing of the manuscript.

Joe D. Hoffman

West Lafayette, Indiana, 1977

contents

Volume II

Gas Dynamics

Multidimensional Flow

14
steady one-dimensional flow of chemically reacting gas mixtures and gas-particle mixtures

14–1 PRINCIPAL NOTATION FOR CHAPTER 14

The notation presented in Section 3-1 applies to the flows discussed in this chapter. The following additional notation is applicable.

A_i	denotes chemical symbol of species i.
$[A_i]$	molar concentration [moles/volume] of species i.
A_p	condensed particle drag function.
B_p	condensed particle heat transfer function.
c_{pi}	specific heat at constant pressure of species i.
C_D	drag coefficient of condensed particles.
$C_D^\dagger$	$= C_D / C_{D,\,\text{Stokes}}$.
C_i	$= m_i/m = \rho_i/\rho$, mass fraction of species i.
F	$= U - tS$, Helmholtz free energy.
g	$= h - ts$, specific Gibbs free energy.
G	$= H - tS$, Gibbs free energy, or mass flux $G = \dot{m}/A$.
h_p	enthalpy of condensed particle.
H_i°	absolute enthalpy of species i.
$(H^\circ - H_{298}^\circ)_i$	sensible enthalpy of species i.
$(\Delta H_{f,298}^\circ)_i$	energy of formation of species i.
K	reaction rate, in general.
K_b	backward reaction rate.
K_f	forward reaction rate.
K_P	equilibrium constant.
m	mass of a system.
m	number of chemical reactions in a chemically reacting system.
m_i	mass of species i.
$\overline{m}$	$= m/N$, molecular weight of a system.
$\overline{m}_i$	$= m_i/N_i$, molecular weight of species i.
$\dot{m}_g$	mass flow rate of gas in a gas-particle mixture.
$\dot{m}_p$	mass flow rate of particles in a gas-particle mixture.
$(\text{Mass})_p$	mass of a discrete particle.
n	number of species in a gas mixture.
n_A	number of atomic species in a gas mixture.
n_M	number of molecular species in a gas mixture.
N	moles of a system.
N_i	moles of species i.
Nu	$= \mathbf{h}\,(2r_p)/\kappa$, Nusselt number.
$\text{Nu}^\dagger$	$= \text{Nu}/\text{Nu}_{\text{Stokes}}$.
p_i	$= X_i p$, partial pressure of species i.
P_c	combustion pressure.
Pr	$= c_p \mu/\kappa$, Prandtl number.
r_p	radius of a particle.
Re	$= (2r_p)(V - V_p)\rho/\mu$, relative Reynolds number.
$\bar{s}_i^\circ$	$= \bar{\phi}_i^\circ = \int (\bar{c}_{pi}/t)\,dt$.
t_R	temperature of combustion reactants.
t_P	temperature of combustion products.
t_p	temperature of condensed particle.
t_{pm}	melting temperature of condensed particle.
V_p	velocity of condensed particle.
X_i	$= N_i/N$, mole fraction of species i.

Greek

μ_i	chemical potential of species i.
ν_i'	stoichiometric coefficient of species i in reactants.
ν_i''	stoichiometric coefficient of species i in products.
$\Delta\mu$	$= \sum_{i=1}^{n} \Delta\nu_i \mu_i$.
$\Delta\nu$	$= \sum_{i=1}^{n} \Delta\nu_i$.
$\Delta\nu_i$	$= (\nu_i'' - \nu_i')$.
$\Delta\nu_j$	$= \sum_{i=1}^{n} \Delta\nu_{ij} = \Delta\nu$ in reaction j.
$\Delta\nu_{ij}$	$= (\nu_{ij}'' - \nu_{ij}') = \Delta\nu_i$ in reaction j.
$\prod_{i=1}^{n} a_i$	denotes the product $a_1 a_2 \cdots a_n$.
ρ_i	$= m_i/m = C_i\rho$, partial density of species i.
ρ_p	density of condensed particles per unit volume of flowing medium.
ρ_{mp}	density of the particle material.
$\sum_{i=1}^{n} a_i$	denotes the sum $a_1 + a_2 + \cdots + a_n$.
σ_i	species source function of species i.
φ	oxidizer to fuel ratio in a chemical reaction.
ϕ	$= \int_{t_o}^{t} c_p \frac{dt}{t}$

Subscripts

i	denotes chemical species, $(i = 1, \ldots, n)$.
ij	denotes species i in reaction j.
j	denotes chemical reaction, $(j = 1, \ldots, \mathrm{m})$
p	denotes property of condensed particle.
P	denotes combustion products.
R	denotes combustion reactants.

Superscripts

$^\circ$	denotes thermally perfect gas property at one atmosphere pressure.
*	denotes critical (i.e., sonic) property.

Other

$(\bar{\ })$	denotes molar basis.

14–2 INTRODUCTION

The four fundamental physical laws governing fluid flow processes, discussed in Section 2–2, are independent of both the properties of the flowing fluid and the flow process under consideration. Their application in a specific case, however, requires that the equation of state for the fluid be known; the latter equation relates the thermodynamic properties p, v or ρ, t, h, u, s, and a, and as stated several times in the preceding chapters, it may be in algebraic, tabular, or graphical form.

In Chapters 3 to 9, the four fundamental physical laws are applied to the analysis of steady one-dimensional flows, and in Chapters 10 to 13 and 15 to 20, they are applied to the analysis of multidimensional flows. In the special case where the flowing fluid is a perfect gas, the equation of state has a particularly simple algebraic form (see Section 1–15), and closed form solutions to the fundamental laws may be obtained for a variety of simple flows (see Sections 4–4, 5–5, 6–5, 7–4, 7–7, and 8–4).

In many real flow situations, however, the flowing gas deviates from perfect gas behavior because of imperfect gas effects such as the following.

1. Variations in the specific heats because of the activation of vibrational and electronic modes of energy stored in the gas molecules.
2. Variations in the gas constant of a single species due to the intermolecular forces and the effects of molecular volume.
3. Variations in the molecular weight and the specific heats of a gas mixture because of chemical reactions.

Procedures for taking into account imperfect gas effects are discussed in Chapters 4 to 13, and numerical examples are presented to illustrate those procedures in Chapters 4 to 8 (see Sections 4–5, 5–6, 6–6, 7–5, 7–8, and 8–5).

Sections 14–3 to 14–6 are concerned with imperfect gas effects arising from Item 3 above, chemical reactions. The basic equations of chemical thermodynamics, as they apply to a mixture of perfect gases, are derived. Those equations are applied to the problems of adiabatic combustion, isentropic flow processes, and the flow of nonequilibrium chemically reacting gas mixtures.

The flow of gas-particle mixtures, in which extremely small condensed particles are suspended in a flowing gas, is discussed in Section 14–7. Gas-particle mixtures occur in fogs, liquid fuel sprays, combustors, aerosols of all types, and the combustion products of metalized rocket propellant fuels.

Because of the complexity of the equations describing chemically reacting flows and gas-particle flows, the solutions to their governing equations are obtainable in most cases only by applying numerical techniques. For the above flows, the general features of the relevant numerical methods of analysis are presented.

14–3 INTRODUCTION TO CHEMICAL THERMODYNAMICS[1–3]

In this section, the basic principles are developed for the steady one-dimensional flow of a compressible fluid where chemical reactions take place. For brevity, such a flow is termed a *chemically reacting flow.*

14–3(a) Thermodynamic Properties of a Mixture of Chemically Reacting Thermally Perfect Gases

The thermodynamic properties of a mixture of thermally perfect gases are discussed in Section 1–15(h). A summary of those results is presented here.

Each individual chemical species i ($i = 1, \ldots, n$) is assumed to obey the perfect gas law. Thus,

$$p_i = \rho_i R_i t \qquad (i = 1, \ldots, n) \tag{14.1}$$

where thermal equilibrium is assumed to exist so that $t_i = t$. Dalton's law is applicable; that is, the mixture pressure is the sum of the partial pressures of the

individual species, so that

$$p = \sum_{i=1}^{n} p_i \tag{14.2}$$

where p_i is the partial pressure of species i. The mass fraction C_i of species i is defined as

$$C_i = \frac{m_i}{m} = \frac{\rho_i}{\rho} \tag{14.3}$$

Combining equations 14.1 to 14.3 yields

$$p = \rho t \sum_{i=1}^{n} C_i R_i = \rho R t \tag{14.4}$$

where

$$R = \sum_{i=1}^{n} C_i R_i = \frac{\bar{R}}{\bar{m}} \tag{14.5}$$

where R is the gas constant for the gas mixture and $\bar{m}$ is the effective molecular weight.

On a molar basis, the equations pertinent to a mixture of thermally perfect gases are the following.

$$p_i \mathcal{V} = N_i \bar{R} t \tag{14.6}$$

$$N = \sum_{i=1}^{n} N_i \tag{14.7}$$

$$X_i = \frac{N_i}{N} \tag{14.8}$$

$$p \mathcal{V} = N \bar{R} t \tag{14.9}$$

$$\bar{m} = \sum_{i=1}^{n} X_i \bar{m}_i \tag{14.10}$$

Combining equations 14.6 to 14.8 gives

$$p_i = X_i p \tag{14.11}$$

From equation 1.141b

$$X_i = \frac{C_i \bar{m}}{\bar{m}_i} \tag{14.12}$$

When performing *thermochemical calculations*, the *absolute enthalpy** of each species, denoted by H_i°, must be employed. The magnitude of the absolute enthalpy H_i° is equal to the sum of the sensible enthalpy change above some reference temperature plus the chemical energy required for forming the chemical species from its naturally occurring elements at the reference temperature. The reference temperature is generally 298.15 K, and the naturally occurring elements

*In this section, H denotes the *absolute enthalpy*, not the *stagnation enthalpy*. The superscript ° denotes the standard state value, taken as a pressure of 1 atm for a perfect gas.

at that temperature are H_2(gas), O_2(gas), F_2(gas), N_2(gas), C(graphite), and so on.[4] Thus,

$$H_i^\circ = (H^\circ - H_{298}^\circ)_i + (\Delta H_{f,298}^\circ)_i \tag{14.13}$$

where $(H^\circ - H_{298}^\circ)$ denotes the sensible enthalpy change between $t = 298.15$ K and $t = t$, and $\Delta H_{f,298}^\circ$ denotes the *energy of formation* at $t = 298.15$ K. *By definition*, the energies of formation of the naturally occurring species are zero, and the energy of formation for a given chemical species is defined relative to the naturally occurring species.

Thermochemical calculations are generally performed in terms of molar properties. Consequently, that mass basis is employed in this discussion. The sensible enthalpy of a thermally perfect gas is given by equation 1.142d, where $\bar{h}_i$ in equation 1.142d is now denoted by $(\bar{H}^\circ - \bar{H}_{298}^\circ)_i$. Thus,

$$\left(\bar{H}^\circ - \bar{H}_{298}^\circ\right)_i = \int_{298.15}^{t} \bar{c}_{pi}\, dt \tag{14.14}$$

The absolute enthalpy H of the gas mixture is given by

$$H = N\bar{H} = \sum_{i=1}^{n} N_i \bar{H}_i^\circ = N \sum_{i=1}^{n} X_i \bar{H}_i^\circ \tag{14.15}$$

where $\bar{H}$ is the absolute enthalpy per mole of the gas mixture.
Values of $(\bar{H}^\circ - \bar{H}_{298}^\circ)_i$ and $(\Delta \bar{H}_{f,298}^\circ)_i$ are given in Table D.1 in Appendix D for 13 selected species, and in Reference 4 for over 1100 species.

The entropy of a mixture of thermally perfect gas is given by equation 1.156. Thus,

$$S = \sum_{i=1}^{n} N_i \bar{\phi}_i^\circ - N\bar{R} \ln p_c - N\bar{R} \sum_{i=1}^{n} X_i \ln X_i \tag{14.16}$$

where $\bar{\phi}_i^\circ$, for a given species, is defined by equation 1.150, and it is determined at a pressure of one atmosphere. Values of $\bar{\phi}_i^\circ$ are obtainable from Table D.1 for 13 selected species, and from Reference 4 for over 1100 species where $\bar{\phi}_i^\circ$ is denoted by S_i°.

The determination of thermodynamic derivatives, such as c_p, c_v, and a^2, becomes complicated for a reacting mixture of thermally perfect gases. For example, the molar specific heat at constant pressure for a gas mixture is given by

$$\bar{c}_p = \left(\frac{\partial \bar{H}}{\partial t}\right)_p = \sum_{i=1}^{n} X_i \left(\bar{c}_p^\circ\right)_i + \sum_{i=1}^{n} \bar{H}_i^\circ \left(\frac{\partial X_i}{\partial t}\right)_{p, N_{j, j \neq i}} \tag{14.17}$$

When the mixture is inert, the chemical reactions are said to be *frozen*, and the second term in equation 14.17 is zero. Equation 14.17 becomes

$$\bar{c}_{pf} = \sum_{i=1}^{n} X_i \left(\bar{c}_p^\circ\right)_i \tag{14.18}$$

where $\bar{c}_{pf}$ is the frozen specific heat at constant pressure. When the chemical reactions proceed at an infinite rate, the chemical reactions are said to be *in equilibrium*, and the second term in equation 14.17 must be determined. At chemical equilibrium, terms analogous to the second term in equation 14.17 appear in expressions for all of the thermodynamic derivatives. In particular, it must be

noted that $a^2 \neq \gamma Rt$, where $\gamma = c_p/c_v$, unless the reactions are frozen. In general, a thermodynamic property known as the *isentropic exponent* γ_S is defined as follows.[5]

$$\gamma_S \equiv \left(\frac{\partial \ln p}{\partial \ln \rho}\right)_s = \frac{\rho}{p}\left(\frac{\partial p}{\partial \rho}\right)_s = \frac{\rho a^2}{p} \tag{14.19}$$

For a frozen composition $\gamma_{Sf} = \gamma$, but for an equilibrium composition

$$\gamma_{Se} = -\frac{\gamma}{\left(\frac{\partial \ln v}{\partial \ln p}\right)_t} \tag{14.20}$$

Thus, $\gamma_{Se} \neq \gamma$. Reference 5 presents the detailed expressions for the thermodynamic derivatives of interest in gas dynamics.

One final thermodynamic property of interest in chemical thermodynamics is the equilibrium constant K_P, defined in Section 14–3(d). In that section, it is shown that K_P depends on the values of t, $\bar{h}_i^\circ$, and $\bar{s}_i^\circ$ for the chemical species participating in a given chemical reaction (see equation 14.80). Consequently, K_P may be determined when the values of $\bar{h}_i^\circ$ and $\bar{s}_i^\circ$ are known.

For a perfect gas, $\bar{h}_i^\circ$ and $\bar{s}_i^\circ$ depend only on the temperature t. The enthalpy $\bar{h}_i^\circ$ in equation 14.80 is the absolute enthalpy $\bar{H}_i^\circ$ defined by equation 14.13, expressed on a molar basis. The entropy $\bar{s}_i^\circ$, expressed on a molar basis, may be obtained from equation 1.163, Section 1–16(b), by specifying $p = p_o = 1$ atm, so that $\bar{s}_i^\circ = \bar{\phi}_i^\circ$. When $c_p(t)$ is specified by the fourth-order polynomial equation, equation 1.158, $(\bar{H}^\circ - \bar{H}_{298}^\circ)_i$ and $\bar{\phi}_i^\circ$ may be determined from equations 1.159 and 1.166, respectively. Table 1.6 presents the magnitudes of the coefficients in the polynomial equations for the specific heats for several gases; the values are taken from Reference 5, which presents the values of the coefficients for nearly 500 substances.

Subroutine THERMO, presented in Section 1–16(b), calculates h and ϕ based on the aforementioned polynomial equations for the specific heat of a substance. A modified version of subroutine THERMO, subroutine JANNAF, is presented below for the calculation of $\bar{c}_p^\circ$, $\bar{H}^\circ$, $\bar{\phi}^\circ$, and $\log_{10} K_P$, in both SI and EE units. The input variables described in Table 1.7 are applicable to subroutine JANNAF, with the following modifications. The species for which the table is to be determined must be species 1 in the data deck. The variable X(J) denotes the stoichiometric coefficients in the standard form of the reaction equation (see equation 14.45), with X(1) = 1.0, and the remaining values of X(J) being negative. The variable IUNITS is not employed. The remaining variables presented in Table 1.7 are applicable to subroutine JANNAF. Default values of TM = 1000.0, TREF = 298.15, HBASE = 0.0, and MASS = 2 are specified within the program, and need not be specified in the data deck unless different values are desired.

```
      SUBROUTINE JANNAF
C     THERMODYNAMIC PROPERTY DATA FOR A THERMALLY PERFECT GAS
      DIMENSION A(5,9,2),HI(9,2),SI(9,2),X(9),W(9),GAS(9),M(15),DT(15)
      NAMELIST /DATA/NX,X,W,MASS,TI,TM,TREF,M,DT,A,HI,SI,HBASE
      CPF(J,K)=X(J)*(A(1,J,K)+A(2,J,K)*T+A(3,J,K)*T**2+A(4,J,K)*T**3+
     1A(5,J,K)*T**4)*P
      HF(J,K)=X(J)*(HI(J,K)+A(1,J,K)*T+A(2,J,K)*T**2/2.0+A(3,J,K)*T**3/
     13.0+A(4,J,K)*T**4/4.0+A(5,J,K)*T**5/5.0)*R
      SF(J,K)=X(J)*(SI(J,K)+A(1,J,K)*ALOG(T)+A(2,J,K)*T+A(3,J,K)*T**2/
     12.0+A(4,J,K)*T**3/3.0+A(5,J,K)*T**4/4.0)*R
```

```
C     READ INPUT DATA AND INITIALIZE PARAMETERS

   10 READ (5,1000) GAS $ WRITE (6,2000) GAS $ TM=1000.0
      TREF=298.15 $ HBASE=0.0 $ MASS=2 $ GC=4.1868 $ GD=1000.0
      GH=2.325965 $ GK=0.43429448 $ GT=1.8 $ R=8.31434 $ READ (5,DATA)
      IF (MASS.EQ.1) GM=W(1) $ IF (MASS.EQ.2) GM=1.0
      TI=TI-DT(1) $K=1 $L=0 $N=1 $ T=TREF $ DELH=(HF(1,K)-HBASE)/(GD*GM)

C     CALCULATE THERMODYNAMIC PROPERTIES

   80 NT=M(N) $ DO 100 I=1,NT $ T=(TI+FLOAT(I)*DT(N)) $ H=0.0 $ S=0.0
      IF (T.GT.TM) K=2 $ DO 90 J=1,NX $ H=H+HF(J,K) $ S=S+SF(J,K)
   90 CONTINUE $ CK=CPF(1,K)/GM $ HK=HF(1,K)/(GD*GM)-DELH $SK=SF(1,K)/GM
      CR=CK/GC $ HR=HK/GH $ SR=SK/GC $ TR=T*GT $ DG=H-T*S
      Z=-GK*DG/(R*T) $ IF (NX.EQ.1) Z=0.0 $ L=L+1
      WRITE (6,2010) T,CK,HK,SK,Z,SR,HR,CR,TR $ IF (L.LT.56) GO TO 100
      WRITE (6,2000) GAS $ L=0
  100 CONTINUE $ N=N+1 $ TI=T $ IF((N.EQ.15).OR.(M(N).EQ.0)) GO TO 10
      GO TO 80

 1000 FORMAT (9A6)
 2000 FORMAT (1H1,33X,28HTHERMODYNAMIC PROPERTIES OF ,9A6//16X,4HT, K,5X
     12HCP,8X,1HH,9X,1HS,7X,6HLOG KP,6X,1HS,8X,1HH,6X,2HCP,5X4HT, R/1H )
 2010 FORMAT (F20.0,2F9.3,F10.3,F11.5,2F9.3,F8.3,F7.0)
      END
```

Table D.1 presents, in both SI and EE units, the values of $\bar{c}_p^\circ$, $\overline{H}^\circ$, $\bar{\phi}^\circ$, and $\log_{10} K_P$ for 13 substances, as calculated by subroutine JANNAF. The data deck for the determination of Table D.1h for water (H_2O) is presented in Table 14.1. Reference 4 presents the values of $\bar{c}_p^\circ$, $\overline{H}^\circ$, $\bar{\phi}^\circ$, and $\log_{10} K_P$ for over 1100 substances.

Table 14.1 Input Data Deck for the Determination of Table D.1h

```
WATER (H2O)
$DATA NX=3, TI=100.0, M(1)=2,1,1,47,0, DT(1)=100.0,98.15,1.85,100.0,
A(1,1,1)=4.07013E+00, -1.10845E-03,  4.15212E-06, -2.96374E-09,  8.07021E-13,
A(1,1,2)=2.71676E+00,  2.94514E-03, -8.02244E-07,  1.02267E-10, -4.84721E-15,
HI(1,1)=-3.02797E+04,       HI(1,2)=-2.99058E+04,
SI(1,1)=-3.22700E-01,       SI(1,2)=6.63057E+00,   X(1)=1.0,     W(1)=18.016,
A(1,2,1)=3.05745E+00,  2.67652E-03, -5.80992E-06,  5.52104E-09, -1.81227E-12,
A(1,2,2)=3.10019E+00,  5.11195E-04,  5.26442E-08, -3.49100E-11,  3.69453E-15,
HI(2,1)=-9.88905E+02,       HI(2,2)=-8.77380E+02,
SI(2,1)=-2.29971E+00,       SI(2,2)=-1.96294E+00,  X(2)=-1.0,    W(2)=2.016,
A(1,3,1)=3.62560E+00, -1.87822E-03,  7.05545E-06, -6.76351E-09,  2.15560E-12,
A(1,3,2)=3.62195E+00,  7.36188E-04, -1.96522E-07,  3.62016E-11, -2.89456E-15,
HI(3,1)=-1.04752E+03,       HI(3,2)=-1.20198E+03,
SI(3,1)= 4.30528E+00,       SI(3,2)= 3.61510E+00,  X(3)=-0.5,   W(3)=31.99935$
```

14–3(b) The Basic Equations of Chemical Thermodynamics

Figure 14.1 illustrates schematically a *closed system*; one that permits heat and work exchanges or interactions with its surroundings, but no mass transfer. Assume that the fluid comprising the system is an inert gas that is in thermodynamic equilibrium (i.e., thermal, mechanical, and chemical equilibrium), so that the fluid is a simple thermodynamic system. The first law of thermodynamics for a simple system is given by equation 1.46. Thus,

$$dE = \delta Q - \delta W \tag{14.21}$$

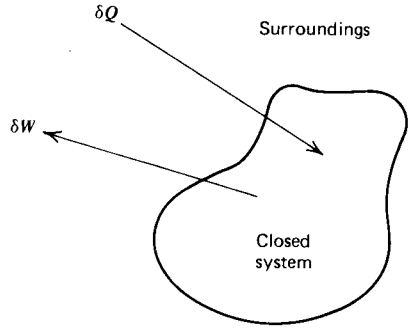

Figure 14.1 Schematic illustration of a closed system.

where E is the total stored energy of the system including the energy of formation, and δQ and δW are the heat and work interactions, respectively, with the surroundings. For a reversible process, equations 1.44 and 1.62 are applicable. Thus,

$$\delta W_R = p\, d\mathcal{V} \qquad \text{and} \qquad \delta Q_R = t\, dS \tag{14.22}$$

Substituting equations 14.22 into equation 14.21, we obtain

$$dE = t\, dS - p\, d\mathcal{V} \tag{14.23}$$

Equation 14.23 applies to both reversible and irreversible (natural) processes, because it involves only thermodynamic properties; the latter are independent of the path of integration, as shown in Section 1–7(a). Equation 14.23 is known as the *basic thermodynamic equation* for a closed system containing an inert fluid in thermodynamic equilibrium.

Figure 14.2 illustrates schematically an *open system*; one that allows energy and mass exchanges with its surroundings so that neither its size nor its chemical composition remains constant. Assume that all of the species comprising the open system are chemically inert. The aforementioned system is no longer a simple thermodynamic system, because every thermodynamic property of the system depends not only on any two of the other thermodynamic properties, such as p, t, $\mathcal{V}$, H, U, and S, but also on the mass of each chemical species involved. In such a case, the total stored energy of the system may be expressed as

$$E = E(\mathcal{V}, S, N_i) \tag{14.24}$$

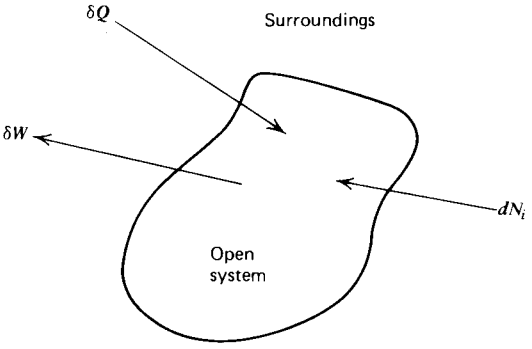

Figure 14.2 Schematic illustration of an open system.

where N_i denotes the number of moles of species i and $\mathcal{V}$ is the total volume. Differentiating equation 14.24, we obtain

$$dE = \left(\frac{\partial E}{\partial \mathcal{V}}\right)_{S,N_i} d\mathcal{V} + \left(\frac{\partial E}{\partial S}\right)_{\mathcal{V},N_i} dS + \sum_{i=1}^{n} \bar{\mu}_i dN_i \tag{14.25}$$

where, *by definition*, employing Gibb's notation, the *molar chemical potential* $\bar{\mu}_i$ of a given species is given by

$$\bar{\mu}_i \equiv \left(\frac{\partial E}{\partial N_i}\right)_{S,\mathcal{V},N_{j,j\neq i}} \tag{14.26}$$

The subscript $j, j \neq i$ in equation 14.26 denotes that the mass of all of the species except species i remains constant when calculating the derivative. Equation 14.25 may be simplified by comparing it with equation 14.23, which is applicable when $dN_i = 0$. Thus,

$$\left(\frac{\partial E}{\partial \mathcal{V}}\right)_{S,N_i} = -p \qquad \text{and} \qquad \left(\frac{\partial E}{\partial S}\right)_{\mathcal{V},N_i} = t \tag{14.27}$$

Consequently, equation 14.25 may be rewritten to read as follows.

$$dE = t\,dS - p\,d\mathcal{V} + \sum_{i=1}^{n} \bar{\mu}_i dN_i \tag{14.28}$$

Equation 14.28 is the *basic thermodynamic equation* for an open system comprising a mixture of inert gases.

Equation 14.28 may be extended to a mixture of chemically reacting gases. Consider the closed system illustrated in Fig. 14.3. Assume that each individual species is a thermally (but not calorically) perfect gas. In view of that assumption, each component gas behaves as though it occupies the entire volume of the system at its own partial pressure p_i, independent of the presence of the other species [see Section 1–15(h)]. As illustrated schematically in Fig. 14.3, each component gas may be considered to be an inert subsystem that exchanges mass with its surroundings; the latter comprise all of the remaining subsystems of the total system. Consequently, the basic thermodynamic equation for an open system, equation 14.28, is

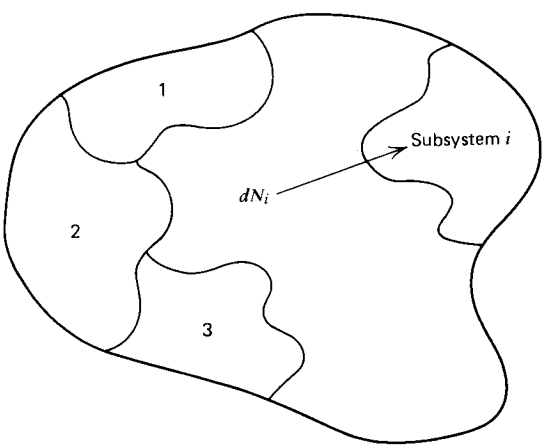

Figure 14.3 A mixture of thermally perfect gases considered as a series of independent open subsystems.

applicable to each of the inert subsystems. Hence, for species i,

$$dE_i = t\,dS_i - p_i\,d\mathcal{V} + \bar{\mu}_i\,dN_i \tag{14.29}$$

The mass transfer between the subsystems arises from chemical reactions rather than from the transfer of mass across the boundary of the total system.

The thermodynamic properties of a mixture of thermally perfect gases may be obtained by summing the properties of the individual species. Thus,

$$E = \sum_{i=1}^{n} E_i \qquad S = \sum_{i=1}^{n} S_i \qquad p = \sum_{i=1}^{n} p_i \tag{14.30}$$

Summing equation 14.29 over the n species involved, and introducing equations 14.30, we obtain

$$dE = t\,dS - p\,d\mathcal{V} + \sum_{i=1}^{n} \bar{\mu}_i\,dN_i \tag{14.31}$$

which is identical to equation 14.28.

For a system at rest, or for an observer moving at the same speed as the system, $E = U$, where U is the internal energy of the system. For the latter, the enthalpy $H = U + p\mathcal{V}$, where H is the absolute enthalpy since U includes the energies of formation of the individual species. Accordingly, equation 14.31 may be transformed to read

$$t\,dS = dH - \mathcal{V}\,dp - \sum_{i=1}^{n} \bar{\mu}_i\,dN_i \tag{14.32}$$

On a molar basis, equation 14.32 becomes

$$t\,d\bar{s} = d\bar{h} - \bar{v}\,dp - \sum_{i=1}^{n} \bar{\mu}_i\,dX_i \tag{14.33}$$

where a bar ($\bar{}$) over a property indicates that it applies to one mole of the gas. On a mass basis, equation 14.32 transforms to

$$t\,ds = dh - v\,dp - \sum_{i=1}^{n} \mu_i\,dC_i \tag{14.34}$$

where $C_i = m_i/m = \rho_i/\rho$ is the *mass fraction* of species i.

Equations 14.31 to 14.34 are alternate forms of the *basic thermodynamic equation* for a system of chemically reacting thermally perfect gases.

By definition, the *Gibbs free energy* G is given by

$$G \equiv H - tS = \sum_{i=1}^{n} N_i g_i = \sum_{i=1}^{n} N_i (h_i - t s_i) \tag{14.35}$$

The *Helmholtz free energy* F is defined by

$$F \equiv U - tS \tag{14.36}$$

It is shown in most books on chemical thermodynamics [1–3] that the *molar chemical potential* $\bar{\mu}_i$ is given by

$$\bar{\mu}_i = \left(\frac{\partial U}{\partial N_i}\right)_{S,\mathcal{V},N_{j,j\neq i}} = \left(\frac{\partial H}{\partial N_i}\right)_{S,p,N_{j,j\neq i}} = \left(\frac{\partial F}{\partial N_i}\right)_{t,\mathcal{V},N_{j,j\neq i}} = \left(\frac{\partial G}{\partial N_i}\right)_{p,t,N_{j,j\neq i}} \tag{14.37}$$

It is also shown that the *specific chemical potential* μ_i is equal to the *specific Gibbs free energy* g_i. For a pure species i

$$dg_i = dh_i - t\,ds_i - s_i\,dt \tag{14.38}$$

From equation 1.65, $dh - t\,ds = v\,dp$. Substituting the latter expression into equation 14.38, we obtain

$$dg_i = v_i\,dp_i - s_i\,dt \tag{14.39}$$

Equation 14.39 may be integrated at constant temperature from the *standard state* for a gas (denoted by the superscript °, defined as 1 atm pressure and a reference temperature that is generally equal to 298.15 K) to a final state where the pressure is equal to the partial pressure p_i of the species i in the gas mixture. Replacing the specific volume v_i by $R_i t/p_i$ in equation 14.39 and integrating at the constant temperature t between the aforementioned limits yields

$$g_i - g_i^\circ = R_i t \ln\left(\frac{p_i}{p = 1 \text{ atm}}\right) \tag{14.40}$$

Therefore, since $\mu_i = g_i$, we obtain

$$\mu_i = \mu_i^\circ + R_i t \ln p_i \tag{14.41}$$

where p_i is measured in atmospheres, and μ_i° is the specific Gibbs free energy at the *standard state*.

From equation 3.159, Table 3.1, for a steady frictionless flow in the absence of body forces, the momentum equation is

$$v\,dp + d\left(\frac{V^2}{2}\right) = 0 \tag{14.42}$$

Equation 14.42 is the Bernoulli equation, which is valid along streamlines [see Section 3–5(a)]. Substituting equation 14.42 into equation 14.34, we obtain

$$t\,ds = dh + d\left(\frac{V^2}{2}\right) - \sum_{i=1}^{n} \mu_i\,dC_i \tag{14.43}$$

For a steady adiabatic flow ($\delta Q = \delta W = 0$), the stagnation enthalpy $h + (V^2/2)$ remains constant along streamlines [where h includes both the sensible enthalpy and the energy of formation, see Section 14–3(a)]. Hence, equation 14.43 becomes

$$t\,ds = -\sum_{i=1}^{n} \mu_i\,dC_i \qquad (\textit{for steady adiabatic flow}) \tag{14.44}$$

Equation 14.44 relates the change in the specific entropy of a flowing gas to the change in its composition caused by chemical reactions.

14–3(c) The General Reaction Equation

A general chemical reaction may be represented by the following *general reaction equation*.

$$\sum_{i=1}^{n} \nu_i' A_i \underset{K_b}{\overset{K_f}{\rightleftharpoons}} \sum_{i=1}^{n} \nu_i'' A_i \tag{14.45}$$

The symbol A_i denotes the chemical species, the coefficients ν_i' and ν_i'' are the *stoichiometric coefficients* of the reactants and products, respectively, of the balanced chemical equation, and K_f and K_b denote the reaction rate constants for the forward and backward reactions, respectively.

The symbol K without a subscript denotes a general reaction rate constant when the direction of the reaction is obvious (see equation 14.103). The symbols K_f and K_b denote the reaction rate constants for the forward and backward reactions, respectively, when both directions of a reaction are considered simultaneously (see equation 14.45). In a reacting mixture where m reactions occur simultaneously (see equation 14.83), the symbols K_{fj} and K_{bj} denote the forward and backward reaction rate constants, respectively, for reaction j ($j=1,\ldots,\mathrm{m}$).

By convention, the species on the left-hand side of equation 14.45 are termed the *reactants* and those on the right-hand side are called the *products*. The positive direction of the reaction is defined as left to right, from reactants to products. Equation 14.45 specifies an elementary molecular reaction between colliding particles. Equation 14.45 may also be employed as a bookkeeping equation for an overall reaction, but in that case the reaction rates are meaningless.

For example, consider the elementary dissociation reaction where a hydrogen molecule H_2 encounters a third body M, which has sufficient relative energy to split the H_2 molecule into two H atoms by its collision with the H_2 molecule. The third body, which may be any of the other species in the mixture, remains chemically unchanged during the collision. Equation 14.45 becomes

$$\mathrm{H_2} + M \underset{K_b}{\overset{K_f}{\rightleftharpoons}} 2\mathrm{H} + M \tag{14.46}$$

Let $i=1$ denote H_2, $i=2$ denote M, and $i=3$ denote H. The stoichiometric coefficients are accordingly

$$\nu_1'=1 \quad \nu_2'=1 \quad \nu_3'=0 \quad \nu_1''=0 \quad \nu_2''=1 \quad \nu_3''=2 \tag{14.47}$$

An example where the reaction equation, equation 14.45, is employed as a bookkeeping equation is that presented below for the overall reaction between hydrogen and flourine. Thus,

$$\mathrm{H_2} + \varphi\mathrm{F_2} = a\mathrm{H_2} + b\mathrm{F_2} + c\mathrm{HF} + d\mathrm{H} + e\mathrm{F} \tag{14.48}$$

In equation 14.48, φ is the *molar oxidizer to fuel ratio*, and a, b, c, d, and e are the moles of the different species in the completed chemical reaction. In equation 14.45, let $A_1=\mathrm{H_2}$, $A_2=\mathrm{F_2}$, $A_3=\mathrm{HF}$, $A_4=\mathrm{H}$, and $A_5=\mathrm{F}$. Then,

$$\begin{array}{lllll} \nu_1'=1 & \nu_2'=\varphi & \nu_3'=0 & \nu_4'=0 & \nu_5'=0 \\ \nu_1''=a & \nu_2''=b & \nu_3''=c & \nu_4''=d & \nu_5''=e \end{array} \tag{14.49}$$

14-3(d) The Criterion for Chemical Equilibrium

The first law of thermodynamics may be expressed as

$$dE = \delta Q - \delta W = \delta Q - p\,d\mathcal{V} \tag{14.50}$$

where, for a system in mechanical equilibrium, equation 1.44 gives

$$\delta W = p\,d\mathcal{V} \tag{14.51}$$

From the second law of thermodynamics (equation 1.68)

$$t\,dS \geqslant \delta Q \tag{14.52}$$

where the equality applies to reversible (i.e., *equilibrium*) processes and the inequality applies to irreversible (i.e., *nonequilibrium*) processes. Subtracting $dE + p\,d\mathcal{V}$ from both sides of equation 14.52, we obtain

$$t\,dS - dE - p\,d\mathcal{V} \geqslant \delta Q - dE - p\,d\mathcal{V} \tag{14.53}$$

The right-hand side of equation 14.53 is identically zero, as may be seen from equation 14.50. Hence, equation 14.53 reduces to

$$t\,dS - dE - p\,d\mathcal{V} \geqslant 0 \tag{14.54}$$

Combining equations 14.31 and 14.54, we obtain

$$\sum_{i=1}^{n} \bar{\mu}_i\,dN_i \leqslant 0 \tag{14.55}$$

In equation 14.55, the equality applies to reversible processes and the inequality to irreversible (natural) processes.

From the general reaction equation, equation 14.45, when the reaction proceeds in the forward direction

$$dN_i \propto (\nu_i'' - \nu_i') \tag{14.56}$$

where ν_i' and ν_i'' are the stoichiometric coefficients of species i in the reactants and products, respectively. Substituting equation 14.56 into equation 14.55 yields

$$\sum_{i=1}^{n} (\nu_i'' - \nu_i')\,\bar{\mu}_i \leqslant 0 \tag{14.57}$$

Hence, for an equilibrium chemical reaction

$$\sum_{i=1}^{n} (\nu_i'' - \nu_i')\,\bar{\mu}_i = 0 \tag{14.58}$$

and for a nonequilibrium chemical reaction

$$\sum_{i=1}^{n} \nu_i' \bar{\mu}_i > \sum_{i=1}^{n} \nu_i'' \bar{\mu}_i \tag{14.59}$$

Equation 14.58 is the *criterion for chemical equilibrium.*

Equation 14.59 indicates that for a nonequilibrium reaction, the reaction proceeds from a state of higher chemical potential to a state of lower chemical potential.

The effect of chemical reactions on the entropy of a gas mixture may be determined from equation 14.44, which is repeated below for convenience.

$$t\,ds = -\sum_{i=1}^{n} \mu_i\,dC_i \tag{14.44}$$

For an inert mixture, that is, one having a *frozen* chemical composition, there is no change in the mass fractions C_i. Hence, $dC_i = 0$, and equation 14.44 becomes

$$ds_{\text{frozen}} = 0 \tag{14.60}$$

The flow of a gas having a frozen chemical composition ($dC_i = 0$) is termed a *frozen flow*.

For a mixture of reacting gases that is in *chemical equilibrium*, equation 14.55 shows that

$$\sum_{i=1}^{n} \bar{\mu}_i dN_i = m \sum_{i=1}^{n} \mu_i dC_i = 0 \tag{14.61}$$

where m is the mass of the reacting gas mixture. Substituting equation 14.61 into equation 14.44, we obtain

$$ds_{\text{equilibrium}} = 0 \tag{14.62}$$

The flow of a chemically reacting gas mixture that is in chemical equilibrium is termed an *equilibrium flow*.

Equations 14.60 and 14.62 show that both *frozen* and *equilibrium* flows of a gas mixture are *isentropic processes*.

When the chemical reactions in a chemically reacting gas mixture are not in equilibrium, the flow is termed a *nonequilibrium flow*, and equation 14.55 becomes

$$\sum_{i=1}^{n} \bar{\mu}_i dN_i = m \sum_{i=1}^{n} \mu_i dC_i < 0 \tag{14.63}$$

Substituting equation 14.63 into equation 14.44 gives

$$ds_{\text{nonequilibrium}} > 0 \tag{14.64}$$

Equation 14.64 shows that in a nonequilibrium chemically reacting flow the entropy of the flowing gas mixture increases.

Substituting for $\bar{\mu}_i$ from equation 14.41 into equation 14.58 yields

$$\sum_{i=1}^{n} (\nu_i'' - \nu_i')\left(\bar{\mu}_i^\circ + \bar{R}t \ln p_i\right) = 0 \tag{14.65}$$

By definition, let

$$\Delta\nu_i \equiv (\nu_i'' - \nu_i') \tag{14.66}$$

$$\Delta\nu \equiv \sum_{i=1}^{n} \Delta\nu_i \tag{14.67}$$

$$\Delta\bar{\mu} \equiv \sum_{i=1}^{n} (\nu_i'' - \nu_i')\,\bar{\mu}_i^\circ \tag{14.68}$$

Substituting those definitions into equation 14.65, we obtain

$$\Delta\bar{\mu} + \bar{R}t \sum_{i=1}^{n} \Delta\nu_i \ln p_i = 0 \tag{14.69}$$

Since the sum of the logarithms $\Sigma\Delta\nu_i \ln p_i$ is equal to the logarithm of the products $\ln \Pi p_i^{\Delta\nu_i}$, equation 14.69, therefore, becomes

$$\Delta\bar{\mu} + \bar{R}t \ln\left(\prod_{i=1}^{n} p_i^{\Delta\nu_i}\right) = 0 \tag{14.70}$$

Rearranging equation 14.70, we obtain

$$\prod_{i=1}^{n} p_i^{\Delta\nu_i} = \exp\left(-\frac{\Delta\bar{\mu}}{\bar{R}t}\right) = K_P(t) \tag{14.71}$$

where $K_P(t)$ is called the *equilibrium constant*. Recalling that the partial pressure $p_i = X_i p$, equation 14.71 may be written as

$$\prod_{i=1}^{n} X_i^{\Delta\nu_i} = K_P(t) \prod_{i=1}^{n} p^{-\Delta\nu_i} = K_P(t) p^{-\Delta\nu} \tag{14.72}$$

where X_i is the mole fraction of species i. Equation 14.72 is known as the *equilibrium equation*. From equation 14.72, it is apparent that the equilibrium constant has the units of $p^{\Delta\nu}$, where p is in atmospheres because the reference pressure for the determination of the molar chemical potential $\bar{\mu}_i^\circ$ is one atmosphere.

The equilibrium constant $K_P(t)$ for the general chemical reaction

$$\nu_1' A_1 + \nu_2' A_2 + \cdots \rightleftharpoons \nu_2'' A_1 + \nu_2'' A_2 + \cdots \tag{14.73}$$

expressed in terms of the mole fractions of the reactants and products is given by

$$K_P(t) p^{-\Delta\nu} = \frac{X_1^{\nu_1''} X_2^{\nu_2''} \cdots}{X_1^{\nu_1'} X_2^{\nu_2'} \cdots} \tag{14.74}$$

For example, for the chemical reaction

$$H_2 + \frac{1}{2} O_2 \rightleftharpoons H_2O \tag{14.75}$$

let $A_1 = H_2$, $A_2 = O_2$, and $A_3 = H_2O$. Accordingly,

$$\nu_1' = 1 \qquad \nu_2' = \frac{1}{2} \qquad \nu_3' = 0 \qquad \nu_1'' = 0 \qquad \nu_2'' = 0 \qquad \nu_3'' = 1 \tag{14.76}$$

$$\Delta\nu_1 = 0 - 1 = -1 \qquad \Delta\nu_2 = 0 - \frac{1}{2} = -\frac{1}{2} \qquad \Delta\nu_3 = 1 - 0 = 1 \tag{14.77}$$

$$\Delta\nu = -1 - \frac{1}{2} + 1 = -\frac{1}{2} \tag{14.78}$$

Hence, equation 14.72 becomes

$$\frac{X_{H_2O}}{X_{H_2} X_{O_2}^{1/2}} = K_{P,H_2O} p^{1/2} \tag{14.79}$$

The equilibrium constant K_P may be defined for any chemical reaction. Its value, however, depends on the specific reaction equation. For example, consider the following three chemical reactions.

(a) $H_2 + \frac{1}{2} O_2 = H_2O$ $\qquad K_P = \dfrac{X_{H_2O}}{X_{H_2} X_{O_2}^{1/2}} p^{-1/2}$

(b) $2H_2 + O_2 = 2H_2O$ $\qquad K_P = \dfrac{X_{H_2O}^2}{X_{H_2}^2 X_{O_2}} p^{-1}$

(c) $H_2O = H_2 + \frac{1}{2} O_2$ $\qquad K_P = \dfrac{X_{H_2} X_{O_2}^{1/2}}{X_{H_2O}} p^{1/2}$

The equilibrium constant for reaction (b) is the square of that for reaction (a), while that for reaction (c) is the reciprocal of that for reaction (a), verifying the statement that the equilibrium constant depends on the specific reaction equation, and not solely on the species involved.

It is convenient to define a standard form for the reaction equation that is to be employed in specifying equilibrium constants. The most convenient standard form is that employed in Reference 4. It assumes that one mole of a species is formed from the appropriate number of moles of the reference species, which are the naturally occurring forms of the atoms comprising the species in question. For example

$$\frac{1}{2}H_2 = H$$

$$H_2 + \frac{1}{2}O_2 = H_2O$$

$$C(s) + O_2 = CO_2$$

The equilibrium constants associated with the naturally occurring elements themselves are zero. By employing the standard form of the reaction equation, values of the equilibrium constant may be determined for a given species. Values of $K_P(t)$ for more than 1100 substances, based on the aforementioned standard form of the reaction equation, are presented in Reference 4.

The equilibrium constant $K_P(t)$ is defined in terms of the molar chemical potential $\bar{\mu}_i$ by equation 14.71. As pointed out in Section 14–3(b), the chemical potential $\bar{\mu}_i$ is equal to the Gibb's specific free energy $\bar{g}_i$. Consequently, equation 14.71, when combined with equation 14.68, becomes

$$\ln K_P = -\frac{\Delta\bar{\mu}}{\bar{R}t} = -\frac{1}{\bar{R}t}\left[\sum_{i=1}^{n}(\nu_i'' - \nu_i')\left(\bar{h}_i^\circ - t\bar{s}_i^\circ\right)\right] \tag{14.80}$$

where $\bar{h}_i^\circ$ and $\bar{s}_i^\circ$ are the molar specific enthalpy and molar specific entropy, respectively, calculated at the reference pressure (one atmosphere). Note that $\bar{h}_i^\circ$ includes the energy of formation of species i, and is thus the absolute enthalpy $\bar{H}_i^\circ$ defined by equation 14.13. Values of K_P may be determined by the subroutine JANNAF described in Section 14–3(a). Table D.1 presents values of K_P for 13 substances, as determined by subroutine JANNAF.

Example 14.1. Hydrogen was used as the working fluid for the solid core nuclear rocket engine, known as the NERVA engine, because of its low molecular weight and large specific heat. The hydrogen was heated by passing it over heating surfaces containing fissionable material. The resulting high temperature gas was then expanded through a De Laval propulsive nozzle. Due to the heat addition, the hydrogen partially dissociates and its composition and thermodynamic properties change. Calculate the *degree of dissociation*, which is *defined* as the mole fraction of atomic hydrogen produced, as a function of the temperature and the pressure.

Solution

The general bookkeeping equation is

$$H_2 = aH_2 + bH \tag{a}$$

The molecular reaction equation is

$$H_2 + M \underset{K_b}{\overset{K_f}{\rightleftharpoons}} 2H + M \tag{b}$$

where M, the third body, is either H_2 or H. The equilibrium equation appropriate to this reaction is

$$\frac{1}{2}H_2 \rightleftharpoons H \tag{c}$$

Let the chemical species $A_1 = H_2$ and $A_2 = H$. Then $X_1 = X_{H_2}$ and $X_2 = X_H$, and the stoichiometric coefficients are

$$\nu_1' = \frac{1}{2} \qquad \nu_2' = 0 \qquad \nu_1'' = 0 \qquad \nu_2'' = 1$$

Accordingly,

$$\Delta\nu_1 = \nu_1'' - \nu_1' = 0 - \frac{1}{2} = -\frac{1}{2}$$

$$\Delta\nu_2 = \nu_2'' - \nu_2' = 1 - 0 = 1$$

$$\Delta\nu = \Delta\nu_1 + \Delta\nu_2 = -\frac{1}{2} + 1 = \frac{1}{2}$$

$$\prod_{i=1}^{n} X_i^{\Delta\nu_i} = X_{H_2}^{\Delta\nu_1} X_H^{\Delta\nu_2} = \frac{X_H}{X_{H_2}^{1/2}}$$

Substituting those results into equation 14.72 gives

$$\frac{X_H}{X_{H_2}^{1/2}} = K_{P,H} p^{-1/2} \tag{d}$$

Since $X_H + X_{H_2} = 1$, eliminating X_{H_2} from equation (d) and rearranging, yields the following quadratic equation for X_H.

$$X_H^2 + X_H\left(\frac{K_{P,H}^2}{p}\right) - \left(\frac{K_{P,H}^2}{p}\right) = 0 \tag{e}$$

Solving the above equation for X_H gives

$$X_H = -\left(\frac{K_{P,H}^2}{2p}\right) + \left[\left(\frac{K_{P,H}^2}{2p}\right)^2 + \left(\frac{K_{P,H}^2}{p}\right)\right]^{1/2} \tag{f}$$

where p is in atmospheres. The values of $\log K_{P,H}$ and $K_{P,H}$ as a function of the temperature t tabulated below are taken from Table D.1f.

t, K	500	1000	1500	2000	2500	3000
$\log K_{P,H}$	-20.159	-8.646	-4.757	-2.791	-1.602	-0.804
$K_{P,H}$	$6.934 \cdot 10^{-21}$	$2.259 \cdot 10^{-8}$	$1.750 \cdot 10^{-5}$	$1.618 \cdot 10^{-3}$	0.02500	0.1570

Table 14.2 presents X_H, calculated from equation (f), as a function of the temperature t and the pressure p. Figure 14.4 presents X_H as a function of the temperature t for different constant values of the pressure p (in *atmospheres*).

Table 14.2 Degree of Dissociation X_H of Hydrogen as a Function of Pressure and Temperature

Temperature,	Pressure, atmospheres				
K	0.01	0.1	1	10	100
500	$6.934 \cdot 10^{-20}$	$2.193 \cdot 10^{-20}$	$6.934 \cdot 10^{-21}$	$2.193 \cdot 10^{-21}$	$6.934 \cdot 10^{-22}$
1000	$2.259 \cdot 10^{-7}$	$7.144 \cdot 10^{-8}$	$2.259 \cdot 10^{-8}$	$7.144 \cdot 10^{-9}$	$2.259 \cdot 10^{-9}$
1500	$1.754 \cdot 10^{-4}$	$5.546 \cdot 10^{-5}$	$1.754 \cdot 10^{-5}$	$5.546 \cdot 10^{-6}$	$1.754 \cdot 10^{-6}$
2000	$1.605 \cdot 10^{-2}$	$5.103 \cdot 10^{-3}$	$1.617 \cdot 10^{-3}$	$5.115 \cdot 10^{-4}$	$1.618 \cdot 10^{-4}$
2500	$2.207 \cdot 10^{-1}$	$7.599 \cdot 10^{-2}$	$2.469 \cdot 10^{-2}$	$7.875 \cdot 10^{-3}$	$2.497 \cdot 10^{-3}$
3000	$7.642 \cdot 10^{-1}$	$3.890 \cdot 10^{-1}$	$1.455 \cdot 10^{-1}$	$4.855 \cdot 10^{-2}$	$1.562 \cdot 10^{-2}$

Atmospheres $\times 1.01325 \cdot 10^5 = N/m^2$
Atmospheres $\times 14.696 = lbf/in^2$.

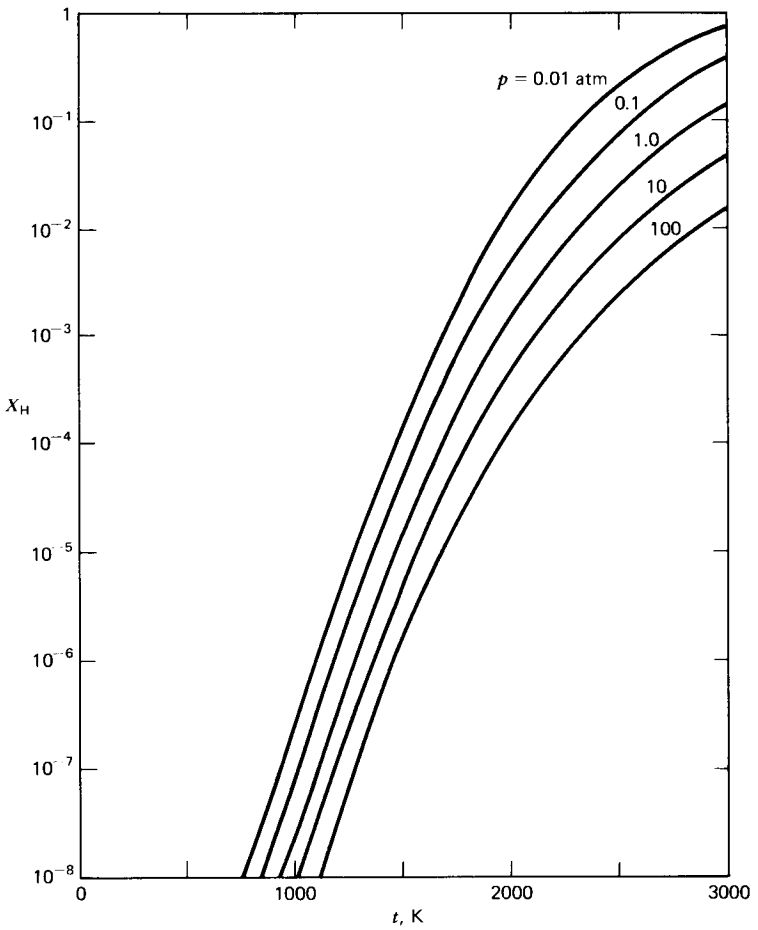

Figure 14.4 Degree of dissociation X_H of hydrogen as a function of the temperature for different pressures.

14–3(e) The Species Source Function

If a chemical reaction is not in equilibrium, there is a net rate of either generation or depletion of each species, called the *species source function*, which is denoted by σ_i. The magnitude of σ_i depends on the local thermodynamic properties of the flowing gas. We may, therefore, write

$$\sigma_i = \sigma_i(p, \rho, C_i) \tag{14.81}$$

For a chemically reacting mixture of thermally perfect gases, an explicit expression is derived for the species source function σ_i in this section.

In a mixture of chemically reacting gases, many elementary reactions may occur simultaneously. Denote the individual reactions by the subscript $j (j = 1, \ldots, \mathrm{m})$, where m denotes the total number of elementary chemical reactions involved. For a given set of initial reactants, the combination of the individual reactions that occurs is known as the *reaction mechanism*. For example, consider the reactants H_2 and F_2. The overall reaction equation is given by equation 14.48. The corresponding reaction mechanism proposed by Cherry[6] is as follows.

$$F_2 + M \rightleftharpoons 2F + M \tag{14.82a}$$

$$H_2 + M \rightleftharpoons 2H + M \tag{14.82b}$$

$$HF + M \rightleftharpoons H + F + M \tag{14.82c}$$

$$HF + F \rightleftharpoons H + F_2 \tag{14.82d}$$

$$HF + H \rightleftharpoons H_2 + F \tag{14.82e}$$

$$2HF \rightleftharpoons H_2 + F_2 \tag{14.82f}$$

The first three reactions are known as *dissociation reactions*, and the last three reactions are termed *binary exchange reactions*. For the above reaction mechanism, $\mathrm{m} = 6$.

For a mixture of gases in which several reactions occur simultaneously, the general reaction equation, equation 14.45, becomes

$$\sum_{i=1}^{n} \nu'_{ij} A_i \underset{K_{bj}}{\overset{K_{fj}}{\rightleftharpoons}} \sum_{i=1}^{n} \nu''_{ij} A_i \qquad (j = 1, \ldots, \mathrm{m}) \tag{14.83}$$

The equilibrium equation, equation 14.72, becomes

$$\prod_{i=1}^{n} X_i^{\Delta\nu_{ij}} = K_{P,j}(t) p^{-\Delta\nu_j} \qquad (j = 1, \ldots, \mathrm{m}) \tag{14.84}$$

The relationship between the species source function σ_i and the thermodynamic properties of the reacting gas mixture is based on the *law of mass action*.[1,2] That law states that "*the rate at which an elementary reaction proceeds is proportional to the product of the molar concentrations of the reactants each raised to a power equal to its stoichiometric coefficient in the reaction equation.*" Define the molar concentration by $[A_i]$ = moles/volume, where

$$[A_i] = \frac{N_i}{\forall} = \frac{\rho_i}{\bar{m}_i} = \frac{C_i \rho}{\bar{m}_i} \tag{14.85}$$

Accordingly, the law of mass action yields the following relationship for an arbitrary reaction j.

$$\{\text{Rate}\}_j \propto [A_1]^{\nu_{1j}}[A_2]^{\nu_{2j}} \cdots [A_n]^{\nu_{nj}} = \prod_{i=1}^{n} [A_i]^{\nu_{ij}} \qquad (j=1,\ldots,m) \quad (14.86)$$

Equation 14.86 may be written as the following equality.

$$\{\text{Rate}\}_j = K_j \prod_{i=1}^{n} [A_i]^{\nu_{ij}} \qquad (j=1,\ldots,m) \quad (14.87)$$

In equation 14.87, K_j is the *reaction rate constant* for the *arbitrary reaction j*; experiments show that K_j depends only on the temperature of the reactants. Hence, for the general reaction equation, equation 14.83, equation 14.87 becomes

$$\{\text{Rate left-to-right}\}_j = \{\text{Rate } L \rightarrow R\}_j = K_{fj} \prod_{i=1}^{n} [A_i]^{\nu'_{ij}} \quad (j=1,\ldots,m) \quad (14.88)$$

and

$$\{\text{Rate right-to-left}\}_j = \{\text{Rate } R \rightarrow L\}_j = K_{bj} \prod_{i=1}^{n} [A_i]^{\nu''_{ij}} \quad (j=1,\ldots,m) \quad (14.89)$$

where K_{fj} and K_{bj} denote, respectively, the pertinent forward and backward reaction rate constants for the arbitrary reaction j.

The time rate of change of the molar concentration of species i is also directly proportional to the stoichiometric coefficients of A_i in the reaction equation. For the left-to-right direction of reaction j*

$$\frac{d[A_i]_j}{dt} = \{\text{Rate } L \rightarrow R\}_j (\nu''_{ij} - \nu'_{ij}) = \{\text{Rate } L \rightarrow R\}_j \Delta\nu_{ij} \quad (14.90)$$

Combining equations 14.88 and 14.90 gives for the left-to-right reaction

$$\frac{d[A_i]_j}{dt} = \Delta\nu_{ij} K_{fj} \prod_{i=1}^{n} [A_i]^{\nu'_{ij}} \quad (14.91)$$

By analogy, we obtain for the right-to-left direction of reaction j

$$\frac{d[A_i]_j}{dt} = \{\text{Rate } R \rightarrow L\}_j (\nu'_{ij} - \nu''_{ij}) = \{\text{Rate } R \rightarrow L\}_j (-\Delta\nu_{ij}) \quad (14.92)$$

$$\frac{d[A_i]_j}{dt} = -\Delta\nu_{ij} K_{bj} \prod_{i=1}^{n} [A_i]^{\nu''_{ij}} \quad (14.93)$$

The net rate of generation of species i for reaction j is the sum of the generation rates $L \rightarrow R$ and $R \rightarrow L$. Thus,

$$\frac{d[A_i]_j}{dt} = \Delta\nu_{ij} \left[K_{fj} \prod_{i=1}^{n} [A_i]^{\nu'_{ij}} - K_{bj} \prod_{i=1}^{n} [A_i]^{\nu''_{ij}} \right] \quad (14.94)$$

*In this section, the symbol t denotes the time when it appears in the derivative operator $d()/dt$. Otherwise, t denotes the temperature.

The units of $d[A_i]_j/dt$ are moles/volume-time. On a mass basis, equation 14.94 becomes

$$\sigma_{ij} = \frac{d[A_i]_j}{dt}\bar{m}_i \quad (j=1,\ldots,\mathrm{m}) \tag{14.95}$$

Summing over all of the m reactions comprising the *reaction mechanism*, we obtain

$$\sigma_i = \sum_{j=1}^{\mathrm{m}} \sigma_{ij} = \sum_{j=1}^{\mathrm{m}} \frac{d[A_i]_j}{dt}\bar{m}_i \tag{14.96}$$

Substituting equations 14.85 and 14.94 into equation 14.96, we obtain

$$\sigma_i = \bar{m}_i \sum_{j=1}^{\mathrm{m}} \Delta\nu_{ij}\left[K_{fj}\prod_{i=1}^{n}\left(\frac{\rho C_i}{\bar{m}_i}\right)^{\nu'_{ij}} - K_{bj}\prod_{i=1}^{n}\left(\frac{\rho C_i}{\bar{m}_i}\right)^{\nu''_{ij}}\right] \tag{14.97}$$

Equation 14.97 defines the *species source function* σ_i for species i in a mixture of chemically reacting gases. Since K_{fj} and K_{bj} are functions only of the temperature, and $t = p/\rho R$, equation 14.97 may be expressed in the functional form presented earlier (see equation 14.81). Thus,

$$\sigma_i = \sigma_i(p, \rho, C_i) \tag{14.98}$$

At equilibrium $\sigma_i = 0$, and equation 14.97 yields

$$\frac{K_{fj}}{K_{bj}} = \prod_{i=1}^{n}\left(\frac{\rho C_i}{\bar{m}_i}\right)^{\Delta\nu_{ij}} \quad (j=1,\ldots,\mathrm{m}) \tag{14.99}$$

The mole fraction X_i of species i is given by equation 14.12. Thus,

$$X_i = \frac{C_i\bar{m}}{\bar{m}_i} \tag{14.100}$$

Substituting equation 14.100 and the perfect gas equation of state, $p = \rho Rt$, into the equation for the equilibrium constant, equation 14.72, we obtain the equilibrium constant $K_{P,j}$ for reaction j. Thus,

$$K_{P,j} = (\bar{R}t)^{\Delta\nu_j}\prod_{i=1}^{n}\left(\frac{\rho C_i}{\bar{m}_i}\right)^{\Delta\nu_{ij}} \quad (j=1,\ldots,\mathrm{m}) \tag{14.101}$$

Comparing equations 14.99 and 14.101, it is seen that

$$\frac{K_{fj}}{K_{bj}} = K_{P,j}(\bar{R}t)^{-\Delta\nu_j} \quad (j=1,\ldots,\mathrm{m}) \tag{14.102}$$

Equation 14.102 shows that the forward and backward reaction rates are not independent, but they are coupled through the equilibrium constant $K_{P,j}$.

According to current theories, before a molecule can enter into a chemical reaction it must be *activated*; that is, it must possess a certain minimum energy E_a, called its *activation energy*. The latter is the energy required for weakening or

breaking the chemical bonds of the molecule. The magnitude of E_a is determined experimentally.

An important characteristic of the rates of chemical reactions is their strong dependence on the reaction temperature t. Increasing the temperature t produces a rapid increase in the chemical reaction rate, and it is presumed to cause either a weakening or the destruction of the intramolecular bonds. In the case of a gas phase reaction, the random thermal motions of the reacting gas molecules cause a tremendous number of collisions. It is estimated that, at standard conditions, each molecule on the average experiences 10^{10} collisions per second. However, only the collisions of the activated molecules are sufficiently energetic for producing a chemical reaction, and such collisions are relatively few.

Arrhenius (1899) proposed the following equation for the dependence of the chemical reaction rate K on the temperature t. Thus,

$$K = A \exp\left(-E_a/\bar{R}t\right) \tag{14.103}$$

where A is known as the *frequency factor*, which is a measure of the total number of collisions. Since the latter is proportional to $\sqrt{t}$, we may write

$$A = \text{constant}\sqrt{t} \tag{14.104}$$

The exponential term $\exp(-E_a/\bar{R}t)$ is related to the fraction of the molecules having energies larger than the activation energy E_a.

Practically speaking, reaction rates must be determined experimentally, and accurate measurements are difficult to accomplish. Measurements of chemical reaction rates show that the rates predicted by equation 14.103 are much too fast. Accordingly, the experimental results are usually expressed by an equation having a form similar to that of the Arrhenius equation; for example by an equation such as

$$K = Bt^{\alpha} \exp\left(-E/\bar{R}t\right) \tag{14.105}$$

where K denotes the reaction rate, and B, α, and E are constants independent of the gas temperature. The magnitudes of the latter constants depend on the particular reaction.

Table 14.3 presents values of the backward reaction rate K_b for the reactions presented in equation 14.82.[6] Reference 7 is an excellent source of reaction rate data.

Table 14.3 Backward Reaction Rate Constants K_b for the H_2–F_2 System. $K_b = Bt^{\alpha}\exp(-E/\bar{R}t)$ in cm, mol, K, s Units.

Reaction	B	α	$(E/\bar{R})$, K
(14.82a)	$1.10 \cdot 10^{18}$	−1.5	0
(14.82b)	$7.50 \cdot 10^{18}$	−1.0	0
(14.82c)	$7.50 \cdot 10^{18}$	−1.0	0
(14.82d)	$5.28 \cdot 10^{12}$	0.5	4000
(14.82e)	$5.00 \cdot 10^{12}$	0.0	5700
(14.82f)	$1.75 \cdot 10^{10}$	0.5	19,997

(Taken from Reference 6.)

Example 14.2. Calculate the forward and backward reaction rate constants, denoted by K_f and K_b, respectively, for the dissociation of H_2 specified by equation 14.82b.

Solution

The reaction equation for the dissociation of H_2 is

$$H_2 + M \underset{K_b}{\overset{K_f}{\rightleftharpoons}} 2H + M \tag{a}$$

From Table 14.3, the constants in equation 14.105 for the backward reaction rate constant K_b are $B = 7.50 \cdot 10^{18}$, $\alpha = -1$, and $E/\bar{R} = 0$. Hence, $\exp(-E/\bar{R}t) = 1$, and equation 14.105 yields

$$K_b = 7.50 \cdot 10^{18} t^{-1.0} \frac{\text{cm}^6}{\text{mol}^2 - \text{s}} \tag{b}$$

The equilibrium equation (see equation 14.72) corresponding to equation (a) is

$$\frac{X_H^2}{X_{H_2}} = K_{P,2H} p^{-1} \tag{c}$$

The reaction equation involving H_2 and H corresponding to the data for the equilibrium constant $K_{P,H}$ in Table D.1f is

$$\frac{1}{2} H_2 \rightleftharpoons H \tag{d}$$

The corresponding equilibrium equation is [see equation (d) in Example 14.1]

$$\frac{X_H}{X_{H_2}^{1/2}} = K_{P,H} p^{-1/2} \tag{e}$$

Comparing equations (c) and (e), it is apparent that

$$K_{P,2H} = K_{P,H}^2 \tag{f}$$

From equation 14.82b the symbol j of the factor $K_{P,j}$ in equation 14.102 denotes 2H. Hence, equation 14.102 yields

$$K_f = K_b K_{P,2H} (\bar{R}t)^{-\Delta\nu} = \frac{K_b K_{P,2H}}{\bar{R}t} \tag{g}$$

At $t = 5000$ K, equation (b) gives

$$K_b = 7.50 \cdot 10^{18} (5000)^{-1} = 1.50 \cdot 10^{15} \frac{\text{cm}^6}{\text{mol}^2 - \text{s}}$$

From Table D.1f, $\log K_{P,H} = 0.806$, and $K_{P,H} = 6.40$. Thus,

$$K_{P,2H} = K_{P,H}^2 = (6.40)^2 = 41.0 \text{ atm}$$

Table 14.4 Values of $K_{P,H}$, $K_{P,2H}$, K_b, and K_f for the Reaction $H_2 + M \rightleftharpoons 2H + M$

t, K	$K_{P,H}$	$K_{P,2H}$	K_b, $\frac{cm^6}{mol^2 - s}$	K_f, $\frac{cm^3}{mol - s}$
500	$6.93 \cdot 10^{-21}$	$4.80 \cdot 10^{-41}$	$1.50 \cdot 10^{16}$	$1.73 \cdot 10^{-29}$
1000	$2.26 \cdot 10^{-9}$	$5.11 \cdot 10^{-18}$	$7.50 \cdot 10^{15}$	$4.62 \cdot 10^{-7}$
1500	$1.75 \cdot 10^{-5}$	$3.06 \cdot 10^{-10}$	$5.00 \cdot 10^{15}$	$1.23 \cdot 10^{1}$
2000	$1.62 \cdot 10^{-3}$	$2.62 \cdot 10^{-6}$	$3.75 \cdot 10^{15}$	$5.92 \cdot 10^{4}$
3000	$1.57 \cdot 10^{-1}$	$2.46 \cdot 10^{-2}$	$2.50 \cdot 10^{15}$	$2.47 \cdot 10^{8}$
4000	1.59	2.53	$1.88 \cdot 10^{15}$	$1.43 \cdot 10^{10}$
5000	6.40	$4.10 \cdot 10^{1}$	$1.50 \cdot 10^{15}$	$1.48 \cdot 10^{11}$

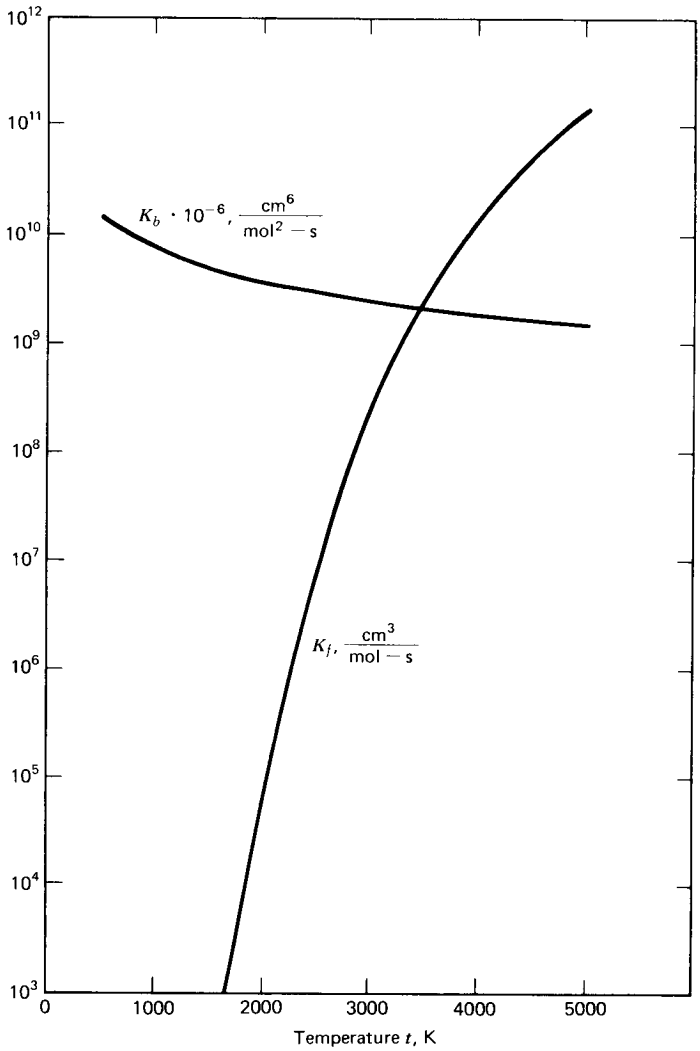

Figure 14.5 Forward reaction rate K_f and backward reaction rate K_b for the reaction $H_2 + M \rightleftharpoons 2H + M$ as a function of the temperature.

From equation (g), we obtain

$$K_f = \left[\frac{1.50 \cdot 10^{15}\,\text{cm}^6}{\text{mol}^2 - \text{s}}\right][41.0\ \text{atm}]\left[\frac{\text{mol} - \text{K}}{8.4133\,\text{N-m}}\right]\left[\frac{1}{5000\,\text{K}}\right]$$

$$\times \left[\frac{1.01325 \cdot 10^5\,\text{N}}{\text{m}^2 - \text{atm}}\right]\left[\frac{\text{m}}{100\,\text{cm}}\right]^3$$

$$K_f = 1.48 \cdot 10^{11}\,\frac{\text{cm}^3}{\text{mol} - \text{s}}$$

In general, for the units employed in Table 14.3

$$K_f = (0.012043)\frac{K_b K_{P,2\text{H}}}{t}$$

Table 14.4 presents values of $K_{P,\text{H}}$, $K_{P,2\text{H}}$, K_b, and K_f for temperatures ranging from 500 to 5000 K. Figure 14.5 presents K_b and K_f as a function of the temperature t.

14–4 ADIABATIC COMBUSTION

The general features of chemical thermodynamics as it applies to a mixture of thermally perfect gases are discussed in Section 14–3. In this section, those concepts are applied to determine the products of combustion for an adiabatic combustor (i.e., a combustor for which $\delta W = \delta Q = \delta F_{\text{f}} = g\,dz = 0$) at a specified pressure. This discussion is limited to gaseous species. When condensed species are present, the calculations become more complex, but the same general procedure is applicable. A generalized computer program for performing such calculations, including condensed species, is presented in Reference 5.

Figure 14.6 illustrates schematically an idealized adiabatic combustor. The reactants enter the combustor at the left and the products leave at the right. The composition of the reactants, denoted by $N_{i,R}$, their temperature t_R, and the combustion stagnation pressure P_c are assumed to be known. The composition of the combustion products, denoted by $N_{i,P}$, and their temperature t_P are to be determined when the chemical reactions are in equilibrium. As indicated above, the gas flow through the combustor is assumed to be adiabatic and frictionless and body forces are negligible ($\delta Q = \delta W = \delta F_{\text{f}} = g\,dz = 0$). In addition, it is assumed that the velocity of the flowing gas in the combustor is so small that its kinetic energy is negligible.

A procedure for obtaining $N_{i,P}$ and t_P for an adiabatic combustor is presented below.

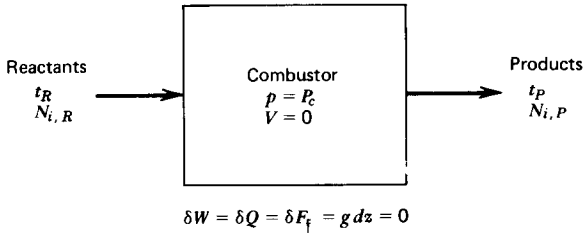

Figure 14.6 Schematic illustration of an idealized adiabatic combustor.

1. *The general reaction equation.* For determining the equilibrium composition for the gas inside of an adiabatic combustor, the molecular reaction mechanism is not needed. However, the chemical species which appear in the products must be either known or assumed. The general reaction equation, equation 14.45, repeated and renumbered below, is employed as an overall bookkeeping equation.

$$\sum_{i=1}^{n} \nu_i' A_i = \sum_{i=1}^{n} \nu_i'' A_i \tag{14.106}$$

Equation 14.48, repeated and renumbered below, illustrates the application of equation 14.45 to the H_2–F_2 reaction. Thus,

$$H_2 + \varphi F_2 = aH_2 + bF_2 + cHF + dH + eF \tag{14.107}$$

The molar oxidizer to fuel ratio φ must be specified. The composition of the products, a, b, and so on, is to be determined. The particular species assumed to be present in the products are based on past experience. If such experience is lacking, the products may be assumed to comprise all of the species that may be formed from the different atoms present in the reactants.

2. *Mass balance of atoms.* The law of the conservation of mass applies to all of the atoms participating in the reaction. Let n_A and n_M denote the number of atomic and molecular species, respectively, that are present in the combustor. Then

$$n = n_A + n_M \tag{14.108}$$

where n denotes the total number of both types of species present. As mentioned above, the products must contain all of the atoms present in the reactants. The conservation of atoms yields the following equations.

$$\sum_{\text{Reactants}} (\text{Atoms})_k = \sum_{\text{Products}} (\text{Atoms})_k \qquad (k = 1, \ldots, n_A) \tag{14.109}$$

For the H_2–F_2 reaction, equation 14.109 gives

$$\text{H:} \quad 2 = 2a + c + d \tag{14.110}$$

$$\text{F:} \quad 2\varphi = b + c + e \tag{14.111}$$

The number of moles of the combustion products is

$$N = \sum_{i=1}^{n} N_i \tag{14.112}$$

Dividing equation 14.112 by N yields

$$1 = \sum_{i=1}^{n} X_i \tag{14.113}$$

For the H_2–F_2 reaction, equations 14.112 and 14.113 yield

$$N = a + b + c + d + e \tag{14.114}$$

$$1 = X_{H_2} + X_{F_2} + X_{HF} + X_H + X_F \tag{14.115}$$

3. *Equilibrium equations.* At equilibrium, each *molecular species* must be in chemical equilibrium with the naturally occurring species that form the molecular species. The equilibrium constant K_P at the combustion pressure P_c is

$$K_{P,\ell} = P_c^{\Delta\nu_\ell} \prod_{i=1}^{n} X_{i\ell}^{\Delta\nu_{i\ell}} \qquad (\ell = 1, \ldots, n_M) \tag{14.116}$$

The equilibrium constant $K_{P,\ell}$ may be obtained from Table D.1 for a few selected species; Reference 4 presents values of $K_{P,\ell}$ for more than 1100 species. For the H_2–F_2 reaction

$$\tfrac{1}{2}H_2 \rightleftharpoons H \qquad \frac{X_H}{X_{H_2}^{1/2}} = p^{-1/2} K_{P,H} \tag{14.117}$$

$$\tfrac{1}{2}F_2 \rightleftharpoons F \qquad \frac{X_F}{X_{F_2}^{1/2}} = p^{-1/2} K_{P,F} \tag{14.118}$$

$$\tfrac{1}{2}H_2 + \tfrac{1}{2}F_2 \rightleftharpoons HF \qquad \frac{X_{HF}}{X_{H_2}^{1/2} X_{F_2}^{1/2}} = p^0 K_{P,HF} \tag{14.119}$$

4. *The energy equation.* For an adiabatic combustor with no work and negligible potential and kinetic energies, an energy balance yields

$$H_{\text{Reactants}} = H_{\text{Products}} \tag{14.120}$$

where

$$H = \sum_{i=1}^{n} N_i \bar{H}_i^\circ \tag{14.121}$$

and $\bar{H}_i^\circ$ is the absolute enthalpy of species i, defined by equation 14.13. Substituting equation 14.13 into equation 14.120, we obtain

$$\sum_{i=1}^{n} \left\{ N_i \left[\left(\bar{H}^\circ - \bar{H}_{298}^\circ \right)_i + \left(\Delta \bar{H}_{f,298}^\circ \right)_i \right] \right\}_{\text{Reactants}} = \sum_{i=1} \left\{ N_i \left[\left(\bar{H}^\circ - \bar{H}_{298}^\circ \right)_i + \left(\Delta \bar{H}_{f,298}^\circ \right)_i \right] \right\}_{\text{Products}} \tag{14.122}$$

For a given chemical reaction, H_R may be determined once $N_{i,R}$ and t_R are specified. Then

$$H_P = \sum_{i=1}^{n} \left\{ N_i \left[\left(\bar{H}^\circ - \bar{H}_{298}^\circ \right)_i + \left(\Delta \bar{H}_{f,298}^\circ \right)_i \right] \right\}_{\text{Products}} = H_R = \text{constant} \tag{14.123}$$

5. *Summary of equations.* For a given combustion problem, there are $(4+n)$ variables.

$$\varphi,\ t_R,\ P_c,\ t_P, \text{ and } N_{i,P} \quad (i = 1, \ldots, n)$$

φ, t_R, and P_c must be specified, thus leaving to be determined the $(n+1)$ variables t_P and $N_{i,P}$. For determining those $(n+1)$ variables, there are n_A atom mass

balance equations, n_M equilibrium equations, and the energy balance, for a total of $(n+1)$ equations. Consequently, there are a sufficient number of equations available for determining t_P and $N_{i,P}$. Because of the nonlinear nature of the equilibrium equations, the solution to the system of $(n+1)$ equations must be accomplished ordinarily by an iterative procedure.

6. *Numerical calculation procedure.* The following iterative numerical procedure may be employed for solving the aforementioned system of equations.

(a) Determine φ, t_R, and P_c, calculate H_R, assume the species to be present in the products, and determine the corresponding equilibrium equations.
(b) Assume t_P, and determine $K_{P,\ell}$ and $\overline{H}_i^\circ$ from either tables such as Table D.1, or from Reference 4.
(c) Solve equations 14.109 and 14.116 for $N_{i,P}$; this step generally requires an iterative procedure.
(d) Calculate the enthalpy of the products H_P, and determine if equation 14.123 is satisfied to within an acceptable tolerance. If not, repeat steps (b) and (c). The secant method [see Appendix A–4(b)] may be employed for determining subsequent trial values for t_P. When convergence is achieved, the combustion temperature t_P and the composition of the products $N_{i,P}$ are determined.
(e) Calculate the thermodynamic properties of interest.

The thermochemical calculations presented in this section are of the type where the pressure and the enthalpy are assigned, that is, of the type (p,h). Chemical equilibrium calculations may also be made for other assigned thermodynamic states, such as (t,p), (s,p), (t,v), (u,v), and (s,v). The computer program described in Reference 5 has the capability of performing chemical equilibrium calculations for any of the aforementioned six types of assigned thermodynamic states. It also performs calculations for equilibrium and frozen expansions to assigned pressures [see Sections 14–5(a) and 14–5(b)], calculates the properties of Chapman–Jouguet detonations (see Section 9–4), and determines the flow properties behind incident and reflected shock waves (see Section 7–5). The computer program is applicable to condensed species as well as gaseous species.

The equation of state for any mixture of gases may be converted into tabular form by the repetitive application of the techniques presented in the present section. Indeed, the computer program itself may be regarded as being the equation of state, because the specification of any two thermodynamic properties is sufficient for determining the remaining properties. Consequently, the methods developed in Sections 4–5, 5–6, 6–6, 7–5, 7–8, and 8–5 for taking into account imperfect gas effects may be employed in conjunction with the computer program, making it possible, therefore, to solve a wide variety of imperfect gas flow problems; provided that the gaseous mixture may be assumed to be either frozen or in chemical equilibrium.

Example 14.3. A gas-fueled rocket motor burning fluorine and hydrogen as the propellants operates at a combustion pressure of $6.895 \cdot 10^5$ N/m^2. The oxidizer to fuel ratio by mass is 12.0, and the temperature of the reactants is $t_R = 298.15$ K. Calculate the temperature, composition, and entropy of the products of combustion.

Solution

The overall bookkeeping equation for the H_2–F_2 reaction system is equation 14.107. The atomic mass balances are specified by equations 14.110 and 14.111, and equation 14.115 expresses the conservation of mole fractions. The equilibrium

equations are equations 14.117 to 14.119. The values for the equilibrium constants are presented in Table D.1.

The value of the molar oxidizer to fuel ratio φ may be determined from the mass oxidizer to fuel ratio as follows.

$$\varphi = \left(\frac{\text{mass of oxidizer } F_2}{\text{mass of fuel } H_2} \right) \frac{\bar{m}_{\text{fuel}}}{\bar{m}_{\text{oxidizer}}} = \frac{12(2.016)}{38.00} = 0.63670$$

From equation 14.122, the enthalpy of the reactants H_R is

$$H_R = (1)(0+0) + (0.63670)(0+0) = 0$$

For this special case where both of the reactants are naturally occurring elements at the reference temperature $t_R = t_{\text{ref}} = 298.15$ K, $H_R = 0$. The combustion pressure, in atmospheres, is

$$P_c = \frac{6.895 \cdot 10^5}{1.0133 \cdot 10^5} = 6.8046$$

The solution is obtained by solving the aforementioned equations for the given values of φ, H_R, and P_c. Since those equations are nonlinear, the solution is obtained by iteration.

In the present problem, the numerical work may be reduced by noting that the mole fraction of F_2 in the reaction equation, equation 14.107, is several orders of magnitude smaller than the mole fraction of F. From equation 14.118, the mole fractions X_{F_2} and X_F are related by

$$X_{F_2} = \frac{p X_F^2}{K_{P,F}^2} \tag{a}$$

From Table D.1c, $K_{P,F}$ is found to vary from 318.4 at $t = 5000$ K to 14.86 at $t = 2000$ K. Since X_F is expected to be quite small, the value of X_{F_2} will be several orders of magnitude smaller than the value of X_F. It may be assumed, therefore, that the combustion products contain no F_2. The accuracy of that approximation must be verified by calculating X_{F_2} from equation (a) after the solution for X_F is obtained.

The calculation equations. Solving equation 14.117 for X_H yields

$$X_H = \frac{K_{P,H}}{p^{1/2}} X_{H_2}^{1/2} \tag{b}$$

Equations 14.117 and 14.118 may be solved for X_{H_2} and X_{F_2}, respectively, and the results may be substituted into equation 14.119. Thus,

$$X_{HF} = \left(\frac{p K_{P,HF}}{K_{P,H} K_{P,F}} \right) X_H X_F = C X_H X_F \tag{c}$$

where C denotes the term inside the parentheses in equation (c). Substituting equation (c) into equation 14.115 yields

$$X_F = \frac{1 - X_{H_2} - X_H}{C X_H + 1} \tag{d}$$

where X_{F_2} in equation 14.115 is assumed to be negligible in view of the assumption made earlier that there is no F_2 in the combustion products. Additionally, the term b in equations 14.107 and 14.111 may be assigned the value $b=0$. Divide equations 14.110 and 14.111 (with $b=0$) by the total number of moles N, noting that $a/N=X_{H_2}$, $c/N=X_{HF}$, and so on. The following two equations are obtained.

$$\frac{2}{N}=2X_{H_2}+X_{HF}+X_H$$

$$\frac{2\varphi}{N}=0+X_{HF}+X_F$$

Eliminating N from the last two equations and solving for X_{H_2} yields

$$X_{H_2}=\frac{1-\varphi}{2\varphi}X_{HF}+\frac{1}{2\varphi}X_F-\frac{1}{2}X_H$$

Since $\varphi=0.6367$ for the present problem, the last equation becomes

$$X_{H_2}=0.2853X_{HF}+0.7853X_F-0.5X_H \tag{e}$$

Dividing equation 14.111 by N and solving for N, we obtain

$$N=\frac{2}{2X_{H_2}+X_{HF}+X_H} \tag{f}$$

Equations (b) through (e) are four equations for determining the mole fractions X_{H_2}, X_{HF}, X_H, and X_F. Those equations may be solved as follows.

1. Assume the temperature of the reaction products t_P, and determine the values of the equilibrium constants.
2. Assume a value for X_{H_2}.
3. Solve equation (b) for X_H.
4. Solve equation (d) for X_F.
5. Determine X_{HF} from equation (c).
6. Calculate X_{H_2} from equation (e), and compare the result with the value assumed in step 2. Repeat steps 2 through 6 until X_{H_2} converges.
7. Calculate H_P from equation 14.123 and compare with H_R. Repeat steps 1 through 7 until t_P converges.

Initial estimate for t_P. An initial estimate for t_P is obtained by assuming that all of the F_2 combines with H_2 to form HF, and that the excess H_2 appears as H. Equation 14.107 becomes

$$H_2+0.63670\,F_2=1.2734\,HF+0.7266\,H$$

Assuming several values of t_P, calculating the corresponding values of H_P, and interpolating for $H_P=H_R=0$, we obtain t_P approximately equal to 3600 K.

Assume $t_P=3600$ K. From Tables D.1c, D.1e, and D.1f,

$$K_{P,H}=0.73282 \qquad K_{P,F}=142.89 \qquad K_{P,HF}=12.560$$

From equation (c),

$$C=\frac{pK_{P,HF}}{K_{P,H}K_{P,F}}=\frac{(6.8046)(12.560)}{(0.73282)(142.89)}=816.21$$

1. Assume $X_{H_2}=0.1$. From equations (b), (d), (c), and (e), respectively

$$X_H=\frac{(0.73282)(0.1)^{1/2}}{2.60856}=0.08884$$

$$X_F=\frac{1-0.1-0.08884}{(816.21)(0.08884)+1}=0.01103$$

$$X_{HF}=(816.21)(0.08884)(0.01103)=0.79981$$

$$X_{H_2}=(0.2853)(0.79981)+(0.7853)(0.01103)-(0.5)(0.08884)=0.19243$$

2. Assume $X_{H_2}=0.15$. Repeating the above calculations, we obtain

$$X_H=0.10880 \qquad X_F=0.00825 \qquad X_{HF}=0.73263 \qquad X_{H_2}=0.16110$$

3. The secant method [see Appendix A–4(b)] is applied to determine the next trial value for X_{H_2}. Let X_a denote the assumed value of X_{H_2} for a given trial, and X_c denote the corresponding calculated value of X_{H_2}. Denote the various trials by the superscript i. Thus,

$$\frac{X_c^{i+1}-X_c^i}{X_a^{i+1}-X_a^i}=\frac{X_c^i-X_c^{i-1}}{X_a^i-X_a^{i-1}} \tag{g}$$

Substituting the results of the first two trials into equation (g), we obtain

$$\frac{X_c^{i+1}-0.16110}{X_a^{i+1}-0.15}=\frac{0.16110-0.19243}{0.15-0.10}=-0.62664 \tag{h}$$

Noting that $X_c=X_a$ when the iteration converges, let $X_c^{i+1}=X_a^{i+1}=X_{H_2}^{i+1}$ and solve equation (h) to obtain $X_{H_2}^{i+1}=0.15682$. Then

$$X_H=0.11125 \qquad X_F=0.00797 \qquad X_{HF}=0.72396 \qquad X_{H_2}=0.15718$$

4. X_{H_2} is sufficiently accurate to warrant determining whether or not the value of H_P is sufficiently close to zero. From equation (f)

$$N=\frac{2}{2(0.15718)+0.72396+0.11125}=1.73978$$

$$N_{H_2}=X_{H_2}N=(0.15718)(1.73978)=0.27346$$

$$N_H=0.19355 \qquad N_F=0.01387 \qquad N_{HF}=1.25953$$

Values of $(\bar{H}^\circ-\bar{H}^\circ_{298})_i$ and $(\Delta\bar{H}^\circ_{f,298})_i$ are obtained from Table D.1 at $t_P=3600$ K. Employing equation 14.123

$$H_P=(0.27346)(111.372)+(0.19355)(68.632+217.986)$$
$$+(0.01387)(69.751+78.910)+(1.25953)(110.101-272.456)$$

$$H_P=-116.530 \text{ kJ}$$

The above value of H_P is smaller than $H_R = 0$. Hence, the assumed value $t_P = 3600$ K is too low. For the next trial value assume $t_P = 4000$ K.

Assume $t_P = 4000$ K. From Table D.1,

$$K_{P,H} = 1.5849 \qquad K_{P,F} = 190.11 \qquad K_{P,HF} = 4897.8$$

From equation (c),

$$C = \frac{(6.8046)(4897.8)}{(1.5849)(190.11)} = 110.61$$

1. $X_{H_2} = 0.10$ $X_H = 0.19213$ $X_F = 0.03181$ $X_{HF} = 0.67606$ $X_{H_2} = 0.12179$
2. $X_{H_2} = 0.12$ $X_H = 0.21047$ $X_F = 0.02758$ $X_{HF} = 0.64207$ $X_{H_2} = 0.09960$
3. The next trial value of $X_{H_2} = 0.11033$ is obtained from the secant method. Then $X_{H_2} = 0.11033$ $X_H = 0.20181$ $X_F = 0.02949$ $X_{HF} = 0.65836$ $X_{H_2} = 0.11008$
4. $N = 1.85129$ $N_{H_2} = 0.20379$ $N_H = 0.37361$ $N_F = 0.05459$ $N_{HF} = 1.21881$ $H_P = -35.090$ kJ

The secant method is applied for obtaining the next trial value of t_P. Thus, for a desired value of $H_P = 0$

$$\frac{0-(-35.090)}{t_P - 4000} = \frac{-116.530-(-35.090)}{3600-4000} = 0.20360$$

Solving the above equation yields $t_P = 4172.3$ K.

Final solution. The procedure presented above is repeated four more times to achieve convergence. The final results are $t_P = 4133$ K and

$$X_{H_2} = 0.09537 \qquad X_H = 0.23468 \qquad X_F = 0.04314 \qquad X_{HF} = 0.62681$$

The assumption that X_{F_2} is negligible is checked by substituting into equation (a). At $t_P = 4133$ K, $K_{P,F} = 206.34$. Thus,

$$X_{F_2} = \frac{(6.8046)(0.04314)^2}{(206.34)^2} = 2.97 \cdot 10^{-7}$$

The above value for X_{F_2} is sufficiently close to the assumed value, zero, to justify the assumption that $X_{F_2} = 0$.

Thermodynamic properties. From equation 14.10

$$\bar{m} = \sum_{i=1}^{n} X_i \bar{m}_i = (0.09537)(2.016) + (0.23468)(1.008)$$

$$+ (0.04314)(19.00) + (0.62681)(20.008) = 13.789$$

Dividing equation 14.16 by the number of moles N gives the following value for $\bar{S}$, the entropy per mole. Thus,

$$\bar{S} = \sum_{i=1}^{n} X_i \bar{\phi}_i^\circ - \bar{R} \ln P_c - \bar{R} \sum_{i=1}^{n} X_i \ln X_i$$

Values of $\bar{\phi}_i^\circ$ are obtained from Table D.1. Thus,

$$\bar{S} = [(0.09537)(215.023) + (0.23468)(169.252) + (0.04314)(214.981) + (0.62681)(257.427)] - 8.314\ln(6.8048) - 8.314[(0.09537)\ln(0.09537) + (0.23468)\ln(0.23468) + (0.04314)\ln(0.04314) + (0.62681)\ln(0.62681)]$$

$$\bar{S} = 230.859 - 15.943 + 8.252 = 223.168 \frac{\text{J}}{\text{mol-K}}$$

$$S = \frac{\bar{S}}{\bar{m}} = \frac{223.168}{13.789} = 16.184 \frac{\text{J}}{\text{g-K}}$$

If any additional thermodynamic properties are desired, they may be calculated by the techniques presented in Reference 5.

14–5 ISENTROPIC FLOW PROCESSES

It is shown in Section 14–3(c) that when the composition of a chemically reacting gas mixture is either frozen or in chemical equilibrium, the entropy of the gas mixture remains constant. *Frozen flow* represents the limiting case where the reaction rates are zero, and *equilibrium flow* represents the limiting case where the reaction rates are infinite. In an actual flow process the reaction rates are finite, and they have values that are between the aforementioned two limiting values.

The present section considers two types of isentropic flow processes for a mixture of chemically reacting perfect gases.

1. The properties of an equilibrium expansion from an adiabatic combustor.
2. The properties of a frozen expansion from an adiabatic combustor.

Reference 5 presents a generalized computer program for performing such calculations. The present discussion is limited to gaseous species. When condensed species are present, the calculations become more complex, but the same general procedure is applicable.

14–5(a) Equilibrium Expansion

The characteristic features of adiabatic combustion are discussed in Section 14–4. This section is concerned with determining the thermodynamic properties for an equilibrium reacting gas mixture after it expands from a known initial state. Figure 14.7 illustrates schematically the general features of the expansion process. The initial properties of the gas P_c, t_P, H_P, and $N_{i,P}$ at the entrance section of a converging-diverging nozzle are assumed to be known, and the flow properties of the gas mixture are to be determined after it has expanded to the pressure $p < P_c$.

The conservation equations for atoms and the equilibrium equations presented in Section 14–4 are applicable. In Section 14–3(c), it is shown that for a gas mixture in chemical equilibrium, the entropy remains constant. Accordingly, the energy balance specified by equation 14.120, Section 14–4, may be replaced by an entropy balance.

$$S(p,t) = S(P_c, t_P) = S_P = \text{constant} \tag{14.124}$$

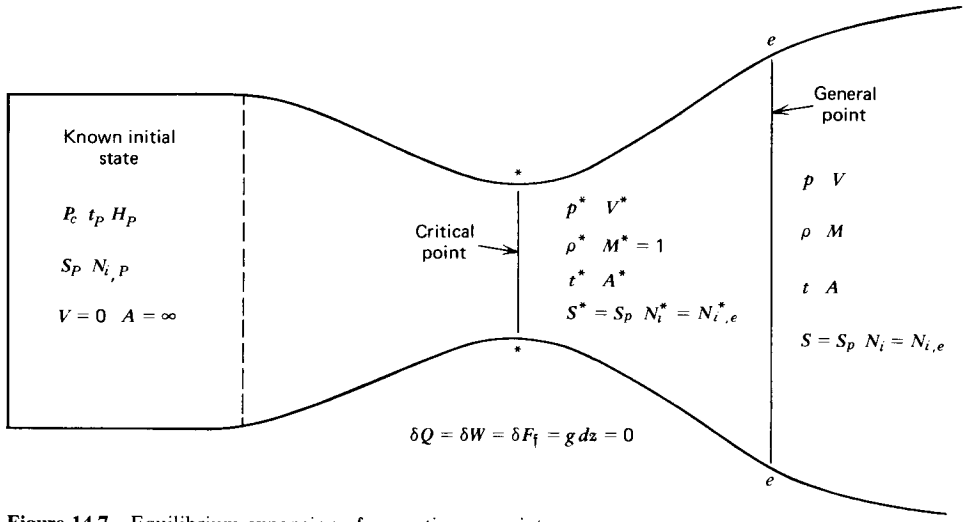

Figure 14.7 Equilibrium expansion of a reacting gas mixture.

where S is given by equation 14.16. In all other respects, the calculation procedure is identical to that discussed in Section 14–4.

The thermodynamic properties are desired at a specified final pressure p. A corresponding value of the temperature t is assumed. The equations for the mass balance of atoms and the equilibrium equations are then solved (generally by iteration) to determine the composition of the gaseous mixture N_i. The corresponding value of the entropy $S(p,t)$ is calculated and compared with that for S_P. The procedure is applied repetitively for different values of t until convergence is attained.

Once the temperature t, pressure p, and composition N_i are known, any other desired thermodynamic properties may be calculated (e.g., $\bar{m}$, R, c_p, a, etc.).

The enthalpy per mole of the gas mixture may be determined from equation 14.15, by dividing by N. Thus,

$$\bar{h}(t) = \sum_{i=1}^{n} X_i(t)\bar{H}_i^\circ(t) \qquad \left(\frac{\text{energy}}{\text{mole}}\right) \tag{14.125}$$

From Table 3.1, the energy equation for steady one-dimensional adiabatic flow in the absence of work and body forces is

$$h + \frac{V^2}{2} = \text{constant} \tag{14.126}$$

For flow with chemical reactions

$$h = \frac{\bar{h}}{\bar{m}} \qquad \left(\frac{\text{energy}}{\text{mass}}\right) \tag{14.127}$$

Substituting equation 14.127 into equation 14.126 and solving for the gas velocity V, we obtain

$$V = \left\{2\left[\frac{\bar{h}_p(t_p)}{\bar{m}_P} - \frac{\bar{h}(t)}{\bar{m}}\right]\right\}^{1/2} \tag{14.128}$$

From the continuity equation for steady one-dimentional flow

$$G = \frac{\dot{m}}{A} = \rho V \tag{14.129}$$

The thermodynamic properties at the sonic condition, denoted by the superscript *, must be determined by iteration. In Section 4–3, it is shown that for the isentropic flow of any fluid, the Mach number is unity at the minimum flow area. Hence, a trial value for p^* is assumed, and the iterative procedure described above is applied for determining the corresponding flow properties, including the Mach number. The procedure is applied repetitively for successive values of p until the value for M is within the desired tolerance for the value unity. The critical mass flux is then

$$G^* = \frac{\dot{m}^*}{A^*} = \rho^* V^* \tag{14.130}$$

The geometric area ratio ϵ corresponding to a given pressure ratio (i.e., p/P_c) may be obtained from equations 14.129 and 14.130. Thus,

$$\epsilon = \frac{A}{A^*} = \frac{G^*}{G} = \left(\frac{\dot{m}^*}{A^*}\right)\left(\frac{A}{\dot{m}}\right) = \frac{\rho^* V^*}{\rho V} \tag{14.131}$$

For a given value of the minimum area A^*, the critical mass flow rate is

$$\dot{m}^* = G^* A^* = \rho^* A^* V^* \tag{14.132}$$

Example 14.4. Consider the H_2–F_2 system described in Example 14.3. Calculate the temperature and composition for an equilibrium expansion of the combustion gases to a pressure of $0.06895 \cdot 10^5$ N/m^2. Determine the corresponding gas velocity.

Solution

The procedure for obtaining the solution is identical to that presented in steps 1 to 6 in Example 14.3, with the exception that in step 7 an entropy balance replaces the energy balance.

Initial estimate for t. For the initial estimate for t, assume that γ remains constant at the value $\gamma_{Se} = 1.1626$, which is determined from the results of Example 14.3 (see equation 14.20). For an isentropic process with γ constant

$$\frac{t}{t_P} = \left(\frac{p}{P_c}\right)^{\frac{\gamma - 1}{\gamma}} = (0.01)^{\frac{1.1626 - 1}{1.1626}} = 0.52515$$

From Example 14.3, $t_P = 4133$ K. Hence,

$$t = (4133)(0.52515) = 2170 \text{ K}$$

Assume $t = 2200$ K. From Table D.1, the equilibrium constants are

$$K_{P,\mathrm{H}} = 0.0055976 \qquad K_{P,\mathrm{F}} = 23.550 \qquad K_{P,\mathrm{HF}} = 4.7753 \cdot 10^6$$

From Example 14.3, equation (c)

$$C = \frac{p K_{P,\mathrm{HF}}}{K_{P,\mathrm{H}} K_{P,\mathrm{F}}} = 2.4648 \cdot 10^6$$

1. Assume $X_{H_2}=0.20$. The corresponding mole fractions X_H, X_F, X_{HF}, and X_{H_2} are

$$X_H=0.0095973 \qquad X_F=0.000033413 \qquad X_{HF}=0.79037 \qquad X_{H_2}=0.22072$$

2. Assume $X_{H_2}=0.21$. Then

$$X_H=0.0098343 \qquad X_F=0.000032185 \qquad X_{HF}=0.78013 \qquad X_{H_2}=0.21768$$

3. The secant method is employed for obtaining the next trial value for X_{H_2}. Thus,

$$\frac{X_{H_2}-0.21768}{X_{H_2}-0.21}=\frac{0.22072-0.21768}{0.20-0.21}=-0.30400$$

from which $X_{H_2}=0.21589$. Accordingly,

$$X_H=0.0099712 \qquad X_F=0.000031498 \qquad X_{HF}=0.77411 \qquad X_{H_2}=0.21589$$

4. X_{H_2} is sufficiently accurate for checking the value of S. From equation 14.16 and Table D.1

$$\begin{aligned}\bar{S}=&\left[(0.21589)(191.617)+(0.0099712)(156.147)+(0.000031498)(201.832)\right.\\&\left.+(0.77411)(234.592)\right]-8.314\ln(0.068045)\\&-8.314\left[(0.21589)\ln(0.21589)+(0.0099712)\ln(0.0099712)\right.\\&\left.+(0.000031498)\ln(0.000031498)+(0.77411)\ln(0.77411)\right]\end{aligned}$$

$$\bar{S}=224.532+22.345+4.784=251.661\ \frac{\text{J}}{\text{mol-K}}$$

From equation 14.10

$$\bar{m}=\sum_{i=1}^{n} X_i\bar{m}_i=15.933$$

Therefore

$$S=\frac{\bar{S}}{\bar{m}}=\frac{251.661}{15.933}=15.795\frac{\text{J}}{\text{g-K}}$$

The above value of S is smaller than the value obtained from the solution of Example 14.3; that is, $S_P=16.184$ J/g-K. A larger value for t is, therefore, required.

Assume $t=2500$ K. From Table D.1

$$K_{P,H}=0.025003 \qquad K_{P,F}=40.926 \qquad K_{P,HF}=7.6913\cdot 10^5$$

$$C=\frac{pK_{P,HF}}{K_{P,H}K_{P,F}}=5.1146\cdot 10^4$$

1. Assume $X_{H_2}=0.20$. Then

$$X_H=0.042865 \qquad X_F=0.00034519 \qquad X_{HF}=0.75679 \qquad X_{H_2}=0.19475$$

2. Assume $X_{H_2}=0.19475$. Then

$$X_H=0.042299 \qquad X_F=0.00035250 \qquad X_{HF}=0.76260 \qquad X_{H_2}=0.19670$$

3. The next trial value of $X_{H_2}=0.19617$ is obtained by applying the secant method. Then

$$X_H=0.042453 \qquad X_F=0.00035049 \qquad X_{HF}=0.76102 \qquad X_{H_2}=0.19617$$

4. From equation 14.16 and Table D.1

$$\bar{S}=227.215+22.345+5.523=255.083\ \frac{\text{J}}{\text{mol-K}}$$

$$\bar{m}=15.670$$

$$S=16.278\ \frac{\text{J}}{\text{g-K}}$$

The next trial value for t is obtained by applying the secant method. Thus, for the desired value of $S=16.184$ J/g-K

$$\frac{16.184-16.278}{t-2500}=\frac{15.795-16.278}{2200-2500}=0.0016100$$

Hence, for the third trial value of t, we obtain $t=2441.6$ K.

Final trial. The above procedure is repeated once more to achieve convergence. The results are $t=2443$ K and

$$X_H=0.03325 \qquad X_F=0.00023 \qquad X_{HF}=0.76478 \qquad X_{H_2}=0.20175$$

Thermodynamic properties and velocity. From equation 14.10

$$\bar{m}=\sum_{i=1}^{n} X_i\bar{m}_i=(0.03325)(1.008)+(0.00023)(19.00)$$
$$+(0.76478)(20.008)+(0.20175)(2.016)=15.746$$

From equation 14.125 and Table D.1

$$\bar{h}=\sum_{i=1}^{n} X_i\bar{H}_i^\circ=(0.03325)(217.986+44.578)+(0.00023)(78.910+45.621)$$
$$+(0.76478)(-272.456+68.164)+(0.20175)(68.433)=-133.672\ \frac{\text{kJ}}{\text{mol}}$$

From equation 14.128

$$V=\left\{2\left[\frac{0}{13.789}-\left(\frac{-133{,}672\ \text{J}}{\text{mol}}\right)\left(\frac{\text{mol}}{15.746\ \text{g}}\right)\right]\left(\frac{1000\ \text{g}}{\text{kg}}\right)\left(\frac{\text{m}-\text{kg}}{\text{N}-\text{s}^2}\right)\right\}^{1/2}$$

$$V=4120.5\ \text{m/s}$$

When employing equation 14.128, the mass basis for the values of $\bar{h}$ and $\bar{h}_P$ must be known. The values of $(\bar{H}^\circ-\bar{H}^\circ_{298})$ and $\Delta\bar{H}^\circ_{f,298}$ presented in Table D.1 have units of kJ/mol. The units of $\bar{m}$ may be based on any compatible set of mass units; for example, g/mol, kg/kmol, and lbm/lbmol.

14–5(b) Frozen Expansion

When the expansion process is either extremely fast or the reactions are extremely slow, the composition of the gas mixture may remain essentially unchanged; that is, at its initial composition, as illustrated schematically in Fig. 14.8. Such a process is called a *frozen flow*.

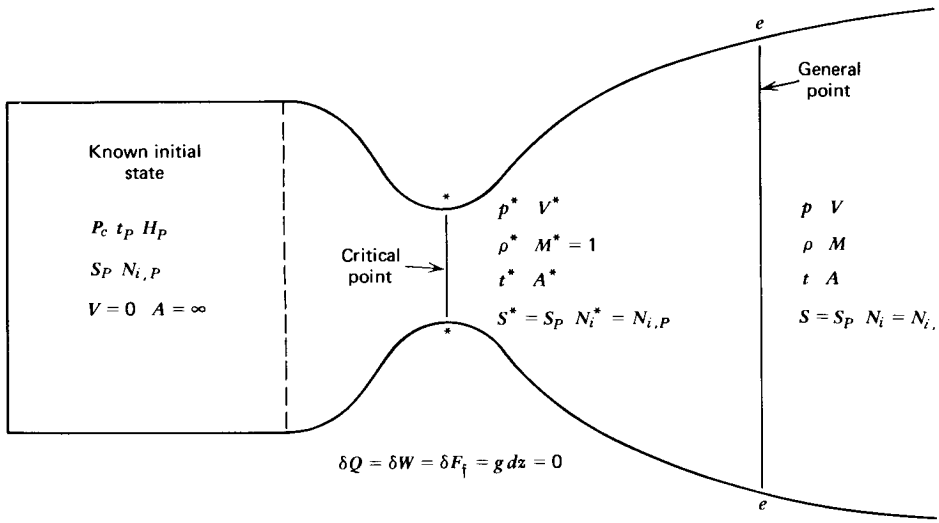

Figure 14.8 Frozen expansion of a reacting gas mixture.

For a frozen expansion

$$N_i = N_{i,P} = \text{constant} \tag{14.133}$$

As shown in Section 14–3(c), the flow of a chemically frozen mixture is isentropic. Hence,

$$S(p,t) = S(P_c,t_P) = S_P = \text{constant} \tag{14.134}$$

Consequently, the determination of the thermodynamic properties for a frozen flow is straightforward. For a specified value of the pressure p, a corresponding temperature t is assumed, and the entropy $S(p,t)$ is calculated and compared with S_P. The procedure is applied repetitively for different values of t until convergence is obtained. The remaining thermodynamic properties of interest may then be calculated.

Example 14.5. The products of the chemical reaction of the gases H_2 and F_2 in a rocket motor, operating under the conditions specified in Example 14.3, are expanded to a static pressure of $0.06895 \cdot 10^5$ N/m^2. Assume that the expansion is *frozen* and determine the properties of the expanded gas mixture.

Solution

During a frozen expansion, the composition of the gases remains unchanged. The problem, therefore, reduces to determining the temperature at which the entropy balance is satisfied.

Initial estimate of t. The initial estimate for t is obtained by assuming that γ remains constant at the value $\gamma_{Sf} = 1.3357$ determined from the results of Example

14.3. For an isentropic process

$$\frac{t}{t_P} = \left(\frac{p}{P_c}\right)^{\frac{\gamma-1}{\gamma}} = (0.01)^{\frac{1.3357-1}{1.3357}} = 0.31430$$

Hence

$$t = (4133)(0.31430) = 1299.0 \text{ K}$$

Assume $t = 1300$ K. From equation 14.16 and Table D.1

$$\bar{S} = \big[(0.09537)(174.201) + (0.23468)(145.211) + (0.04314)(190.795) + (0.62681)(217.245)\big] - 8.314\ln(0.06805) - 8.314\big[(0.09537)\ln(0.09537) + (0.23468)\ln(0.23468) + (0.04314)\ln(0.04314) + (0.62681)\ln(0.62681)\big]$$

$$\bar{S} = 195.094 + 22.344 + 8.247 = 225.685 \frac{\text{J}}{\text{mol-K}}$$

$$S = \frac{\bar{S}}{\bar{m}} = \frac{225.685}{13.789} = 16.367 \frac{\text{J}}{\text{g-K}}$$

The above value of S is larger than $S_P = 16.184$ J/g-K obtained in the solution of Example 14.3. A smaller value is, therefore, assumed for t.

Assume $t = 1200$ K. From equation 14.16 and Table D.1

$$\bar{S} = \big[(0.09537)(171.698) + (0.23468)(143.548) + (0.04314)(189.104) + (0.62681)(214.743)\big] + 22.344 + 8.247 = 223.415 \frac{\text{J}}{\text{mol-K}}$$

$$S = \frac{223.415}{13.789} = 16.202 \frac{\text{J}}{\text{g-K}}$$

The next trial value for t is obtained by the secant method [see Appendix A-4(b)]. For the desired value of $S = 16.184$ J/g-k, we obtain

$$\frac{16.184 - 16.202}{t - 1200} = \frac{16.367 - 16.202}{1300 - 1200} = 0.0016462$$

$$t = 1189.1 \text{ K}$$

Final trial. The procedure presented above is repeated once more to achieve convergence. The final result is $t = 1190$ K.

Thermodynamic properties and velocity. From Example 14.3, $\bar{m} = 13.789$, and from equation 14.125 and Table D.1

$$\bar{h} = \sum_{i=1}^{n} X_i \bar{H}_i^\circ = -91{,}919 \frac{\text{J}}{\text{mol}}$$

From equation 14.128

$$V = \left\{ \frac{2\big[0 - (-91{,}919)\big](1000)}{13.789} \right\}^{1/2} = 3651.3 \text{ m/s}$$

Example 14.6. Determine, by employing the computer program described in Reference 5, the composition, the temperature, and the Mach number for the H_2–F_2 reactant system described in Example 14.3 for (a) equilibrium expansion, and (b) frozen expansion, both from the adiabatic combustor. Assume that the converging-diverging discharge nozzle has an area ratio of 50, and that the exit velocity from the nozzle is supersonic.

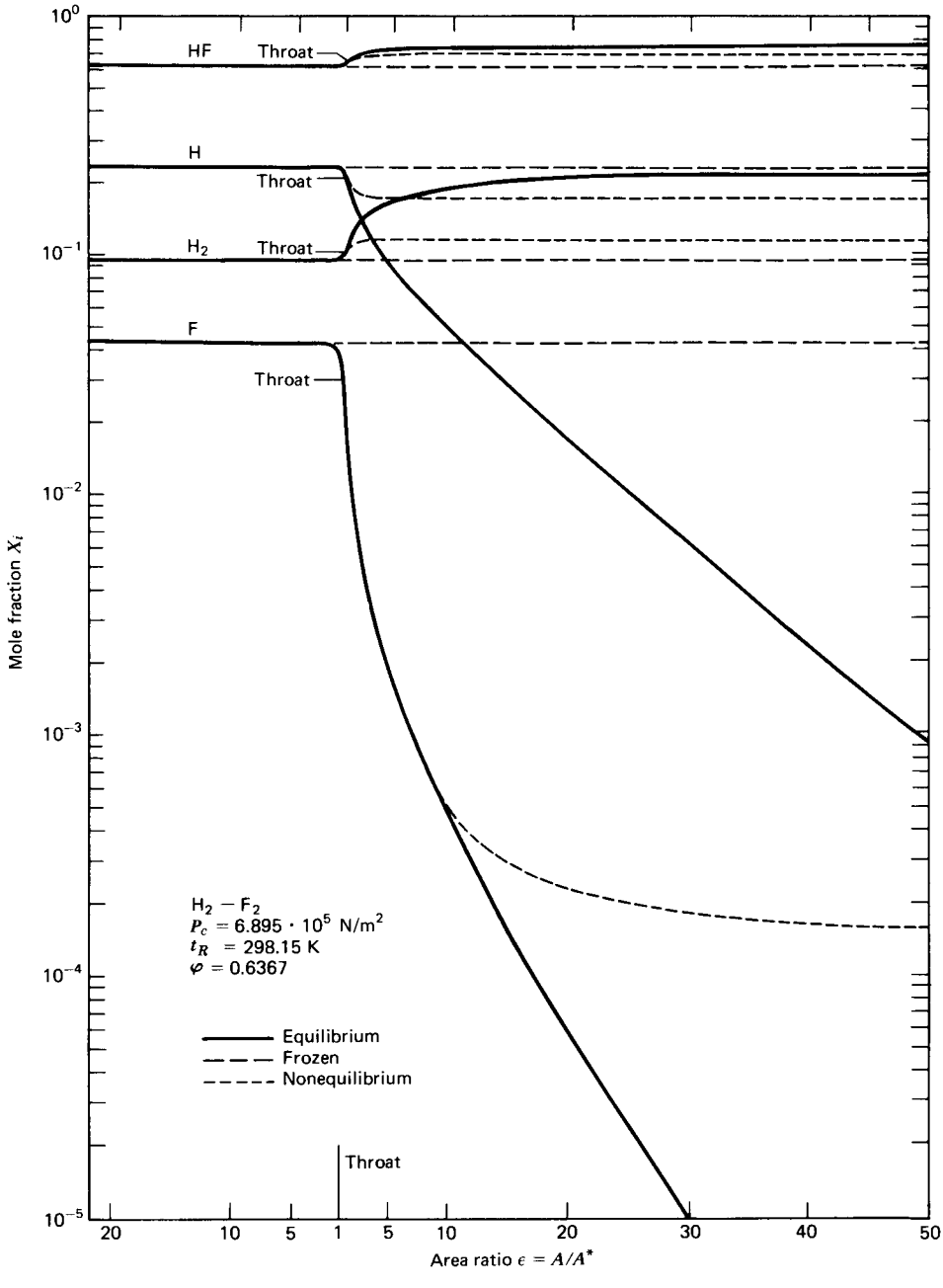

Figure 14.9 Mole fractions X_i as a function of the area ratio ϵ for the H_2–F_2 reaction from Examples 14.6 and 14.7.

Solution

Figure 14.9 presents the mole fractions X_i of the gaseous products as a function of the nozzle area ratio ϵ, from the combustor exit section through the length of the nozzle. For the frozen expansion, the mole fractions remain constant. For the equilibrium expansion, there is substantially no change in the composition of the gaseous mixture in the subsonic portion of the nozzle upstream of an area ratio of

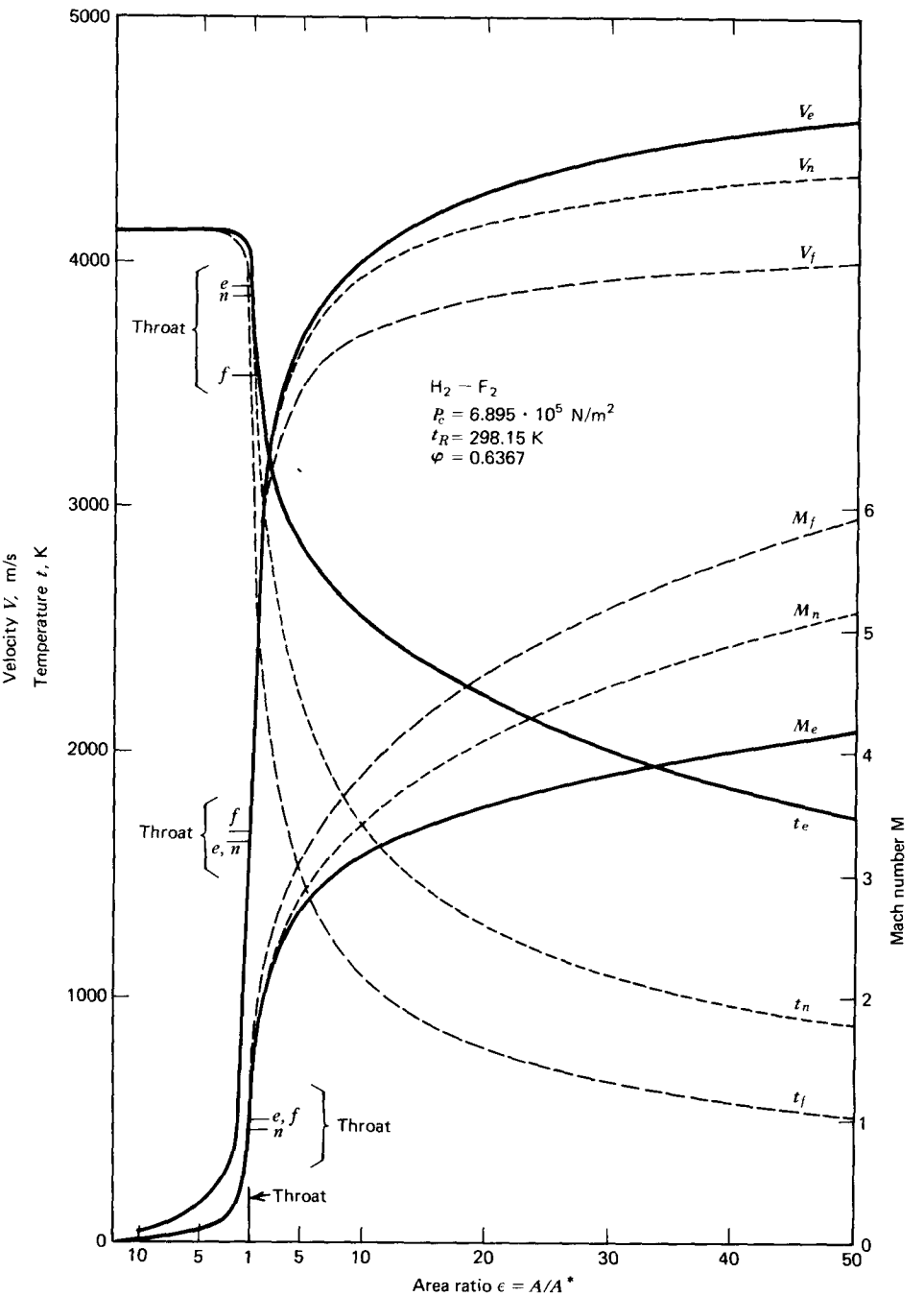

Figure 14.10 Temperature t, velocity V, and Mach number M as a function of the area ratio ϵ for the H_2–F_2 reaction from Examples 14.6 and 14.7.

two. At that value of ϵ, the dissociated species H and F begin to recombine rapidly, and their mole fractions decrease to insignificant values at the nozzle exit plane. Correspondingly, the mole fractions of H_2 and HF increase.

Figure 14.10 presents the temperature, velocity, and Mach number distributions for both equilibrium and frozen flow as functions of the nozzle area ratio ϵ. For the equilibrium expansion, the temperature decreases at a slower rate, the velocity increases at a faster rate, and the Mach number increases at a slower rate, than they do for the frozen expansion. The differences are a direct result of the chemical energy released by the recombination of H and F into H_2 and HF. For the case in hand, the differences between the corresponding flow properties for the equilibrium expansion and the frozen expansion are quite large, because the H_2–F_2 reaction is a very energetic one.

Figures 14.9 and 14.10 also present the results obtained in Example 14.7 for the corresponding nonequilibrium expansion.

14–6 FLOW OF NONEQUILIBRIUM CHEMICALLY REACTING GAS MIXTURES[8]

The basic principles of chemically reacting flow are derived in Section 14–3. In Section 14–4, those principles are applied to an adiabatic combustion chamber. Equilibrium flow expansion and frozen flow expansion are considered in Section 14–5. As stated in the preceding, equilibrium flow corresponds to the upper limit for the chemical reaction kinetics where the reaction rates are infinite, and frozen flow corresponds to the lower limit where the reaction rates are zero. For an actual gas flow having finite reaction rates, the magnitudes of those rates are between the rates for those two limiting cases. The inherent features of chemically reacting flows having finite reaction rates are discussed in this section.

14–6(a) Governing Equations for Nonequilibrium Chemically Reacting Flow

Figure 14.11 illustrates schematically an element of length dx of a one-dimensional flow passage through which flows a nonequilibrium chemically reacting mixture of

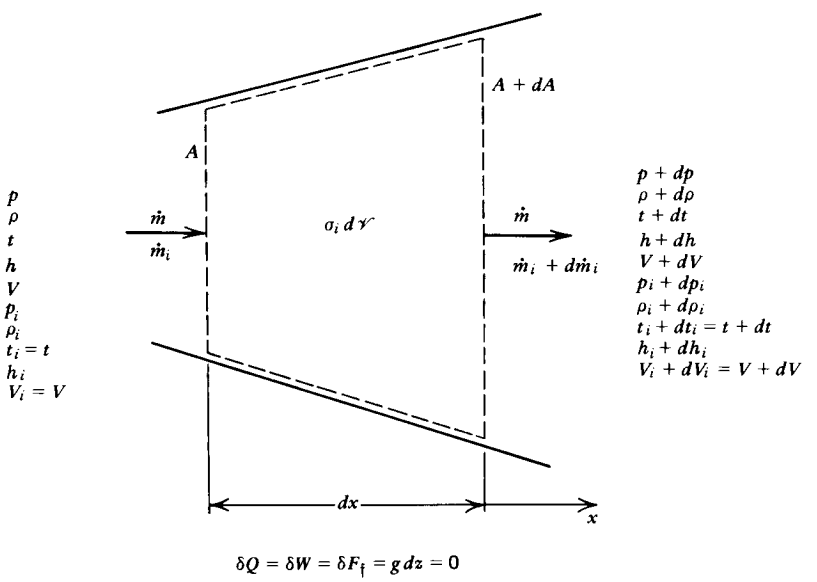

$$\delta Q = \delta W = \delta F_f = g\,dz = 0$$

Figure 14.11 Flow model for the nonequilibrium flow of a chemically reacting gas mixture.

thermally perfect gases. The flow is steady and progresses in the direction of increasing values of x. The flow takes place under the conditions $\delta Q = \delta W = \delta F_f = g\,dz = 0$. From Table 3.1, we obtain

1. *Momentum equation*

$$\rho V \frac{dV}{dx} + \frac{dp}{dx} = 0 \tag{14.135}$$

2. *Energy equation*

$$h + \frac{V^2}{2} = \text{constant} \tag{14.136}$$

where h denotes the absolute enthalpy, which comprises the sum of the sensible enthalpy plus the energy of formation. On a mass basis, it follows from equations 14.13 and 14.15 that h is given by

$$h = \sum_{i=1}^{n} C_i h_i = \sum_{i=1}^{n} C_i \left[\int_{t_o}^{t} c_{pi}\,dt + h_i^\circ \right] \tag{14.137}$$

where h_i° denotes the energy of formation per unit mass.

3. *Continuity equation*

Because of the chemical reactions, the composition of the flowing gas varies along the flow path. Consequently, to obtain the continuity equation for the flow, the law of the conservation of mass must be applied to each chemical species in the flowing gaseous mixture. Hence, for species i, assuming that there is no mass diffusion or thermal nonequilibrium so that $V_i = V$ and $t_i = t$, we may write

$$d\dot{m}_i = d(\rho_i A V) = \sigma_i (A\,dx) \qquad (i = 1, \ldots, n) \tag{14.138}$$

In equation 14.138, σ_i denotes the *species source function* defined by equation 14.97 for a mixture of thermally perfect gases.

Substituting $\rho_i = C_i \rho$ into equation 14.138 yields

$$d(C_i \rho A V) = (\rho A V)\,dC_i + C_i\,d(\rho A V) = \sigma_i (A\,dx) \qquad (i = 1, \ldots, n) \tag{14.139}$$

From Table 3.1, for a steady one-dimensional flow, the global continuity equation is

$$\dot{m} = \rho A V = \text{constant} \tag{3.158}$$

Combining equations 14.139 and 3.158 yields

$$(\rho A V)\,dC_i = \sigma_i (A\,dx)$$

or

$$\rho V \frac{dC_i}{dx} = \sigma_i \qquad (i = 1, \ldots, n) \tag{14.140}$$

Logarithmic differentiation of equation 3.158, the global continuity equation, yields the differential form of the global continuity equation. Thus,

$$\frac{1}{\rho}\frac{d\rho}{dx} + \frac{1}{A}\frac{dA}{dx} + \frac{1}{V}\frac{dV}{dx} = 0 \tag{14.141}$$

4. *Thermal equation of state*

The thermal equation of state for a mixture of thermally perfect gases is given by equation 14.4, which is renumbered and repeated below.

$$p = \rho t \sum_{i=1}^{n} C_i R_i = \rho R t \tag{14.142}$$

Equations 14.135 to 14.137 and 14.140 to 14.142 comprise a system of $(5+n)$ equations for determing the $(5+n)$ flow properties p, ρ, t, h, V, and C_i $(i=1,\ldots,n)$. Those equations may be solved numerically for a given nonequilibrium chemically reacting mixture, for specified initial and boundary conditions, to yield the flow properties for a gaseous mixture undergoing a finite rate process. The determination of the required thermodynamic properties (i.e., c_{pi}, h_i, and K_P) and the reaction rates (i.e., K_f and K_b) is discussed in Section 14.3.

Equation 14.136, the energy equation, may be expressed in a more convenient form for numerical calculation by differentiating it and combining the result with equation 14.137. The final result is

$$-V\frac{dV}{dx} = \frac{dh}{dx} = \sum_{i=1}^{n} h_i \frac{dC_i}{dx} + c_{pf}\frac{dt}{dx} \tag{14.143}$$

where c_{pf} is the *frozen specific heat*. Differentiating equation 14.142 logarithmically and dividing through by dx gives

$$\frac{dt}{dx} = \frac{t}{p}\frac{dp}{dx} - \frac{t}{\rho}\frac{d\rho}{dx} - \frac{t}{R}\sum_{i=1}^{n} R_i \frac{dC_i}{dx} \tag{14.144}$$

Rearranging equation 14.135 yields

$$-V\frac{dV}{dx} = \frac{1}{\rho}\frac{dp}{dx} \tag{14.145}$$

Combining equations 14.140 and 14.143 to 14.145, we obtain

$$\frac{dp}{dx} - a_f^2 \frac{d\rho}{dx} = \frac{\beta}{V} \tag{14.146}$$

where $a_f^2 = \gamma_f R t$ is the *frozen speed of sound*, $c_{pf} = \gamma_f R/(\gamma_f - 1)$, and

$$\beta \equiv \sum_{i=1}^{n} \left[\gamma_f R_i t - (\gamma_f - 1)h_i\right]\sigma_i \tag{14.147}$$

Equations 14.135, 14.140, 14.141, 14.143, and 14.146 comprise a set of $(4+n)$ nonlinear, first-order, ordinary differential equations that may be integrated numerically.

As discussed in Section 9–5(e), special precautions must be taken in the transonic region because the equations have a singularity at the location where $M=1$. Consequently, the *specified area method* should be employed upstream and downstream of the transonic region, and the *specified pressure method* should be employed in that region [see Section 9–5(e)]. The appropriate forms of the differential equations may be obtained by solving the aforementioned $(4+n)$ equations simultaneously for the $(4+n)$ derivatives. The following results are obtained.

1. *Specified area method.*

$$\frac{dV}{dx} = \frac{V}{M_f^2 - 1}\left[\frac{1}{A}\frac{dA}{dx} - \frac{\beta}{\rho V a_f^2}\right] \tag{14.148}$$

$$\frac{d\rho}{dx} = -\rho\left\{\frac{M_f^2}{M_f^2 - 1}\left[\frac{1}{A}\frac{dA}{dx} - \frac{\beta}{\rho V a_f^2}\right] + \frac{\beta}{\rho V a_f^2}\right\} \tag{14.149}$$

$$\frac{dt}{dx} = -t\left\{\frac{(\gamma_f - 1)M_f^2}{M_f^2 - 1}\left[\frac{1}{A}\frac{dA}{dx} - \frac{\beta}{\rho V a_f^2}\right] + \frac{(\gamma_f - 1)}{\gamma_f p V}\sum_{i=1}^{n} h_i \sigma_i\right\} \tag{14.150}$$

$$\frac{dC_i}{dx} = \frac{\sigma_i}{\rho V} \qquad (i = 1, \ldots, n) \tag{14.151}$$

$$p = \rho t \sum_{i=1}^{n} C_i R_i \tag{14.152}$$

where $M_f = V/a_f$ is the frozen Mach number.

2. *Specified pressure method.*

$$\frac{dV}{dx} = -\frac{1}{\rho V}\frac{dp}{dx} \tag{14.153}$$

$$\frac{d\rho}{dx} = \frac{1}{a_f^2}\left[\frac{dp}{dx} - \frac{\beta}{V}\right] \tag{14.154}$$

$$\frac{dt}{dx} = \frac{(\gamma_f - 1)t}{\gamma_f p}\left[\frac{dp}{dx} - \frac{1}{V}\sum_{i=1}^{n} h_i \sigma_i\right] \tag{14.155}$$

$$\frac{dC_i}{dx} = \frac{\sigma_i}{\rho V} \qquad (i = 1, \ldots, n) \tag{14.156}$$

$$A = \frac{\dot{m}}{\rho V} \tag{14.157}$$

The computer program presented in Reference 8 calculates the nonequilibrium expansion of a chemically reacting gas, as well as the corresponding frozen and equilibrium expansions. The program considers the six elements C, H_2, O_2, N_2, F_2, and Cl_2, 19 gaseous species containing those six elements, and 48 chemical reactions between the 19 species. The integration method is an implicit method having second-order accuracy. Because of problems of numerical instability, standard explicit integration methods are unsuitable. Brief discussions of the numerical integration method and the source of the numerical instability are presented in Section 14–6(b).

Example 14.7. Determine the flow properties of the expanded products of combustion of the H_2–F_2 system analyzed in Example 14.3, taking into account the finite reaction rates of the gases. Employ the reaction mechanism presented in

equation 14.82, the backward reaction rates presented in Table 14.3, and the equilibrium constants presented in Table D.1. Consider a De Laval nozzle having a conical converging section with a semiangle of 45 deg and a conical diverging section having a semiangle of 15 deg. The throat diameter is 0.0254 m and the radius of curvature of the circular arc throat is 0.0508 m. Employ the computer program presented in Reference 8 for performing the computations.

Solution

The distribution of the mole fractions X_i as a function of the area ratio ϵ is presented in Fig. 14.9. From those results, it is apparent that the composition of the gas remains substantially in equilibrium up to the throat. Shortly downstream from the throat, the composition essentially freezes with the nonequilibrium expanding mole fractions having magnitudes between the corresponding equilibrium and frozen values.

The temperature t, velocity V, and Mach number M are presented in Fig. 14.10 as a function of the area ratio ϵ. Those properties follow their equilibrium values to a location slightly downstream from the throat where the reactions begin to freeze. The remainder of the expansion yields values of t, V, and M that lie between their corresponding equilibrium and frozen expansion values.

14–6(b) Stability of Numerical Integration Methods

The numerical integration of the continuity equation for the chemical species, equation 14.140, for brevity termed the *species continuity equation*, encounters numerical instability when the flow is near equilibrium. From a physical viewpoint, those difficulties are a direct result of the extremely fast chemical reaction rates (or the corresponding small reaction times) near equilibrium. Many numerical methods have been proposed for surmounting those difficulties, including modified Runge-Kutta methods, higher-order predictor-corrector methods, linearized approaches, and implicit methods. The present section investigates the underlying cause of the numerical instability encountered in performing the numerical integration of a differential equation. In addition, a method is presented for eliminating the instability problem.

The *species continuity equation* may be classified as a *stiff* ordinary differential equation.[9] An understanding of the concept of a stiff differential equation may be obtained by considering the general differential equation

$$\frac{dy}{dx} = f(x,y) \tag{14.158}$$

For equation 14.158 to have a solution that is unique, the function $f(x,y)$ must not only be continuous but it must also satisfy a criterion known as the *Lipschitz condition*.[10] The latter condition is stated in terms of the *Lipschitz constant* L, which is *defined by*

$$L \equiv \left| \frac{\partial f(x,y)}{\partial y} \right| \tag{14.159}$$

A stiff ordinary differential equation may be defined loosely as one that has a large Lipschitz constant L while the solution to the differential equation behaves like a polynomial; that is, the solution has insignificant exponential growth or decay.

The inherent features of the species continuity equation for a single chemical species may be modeled by the following prototype rate equation

$$\frac{dC}{dx} = \frac{C_e - C}{\tau} \tag{14.160}$$

where C is the nonequilibrium mass fraction of the species, C_e is its equilibrium mass fraction corresponding to the local flow conditions, and τ has the character of a chemical *relaxation distance*. For a *frozen flow* the nonequilibrium mass fraction C remains constant and $\tau \to \infty$. As the flow approaches equilibrium, $C \to C_e$ and $\tau \to 0$. For small values of τ, equation 14.160 becomes very stiff and difficult to solve numerically. If C_e is assumed to be a function of x alone, then the Lipschitz constant L is given by

$$L = \left| \frac{\partial}{\partial C}\left(\frac{C_e - C}{\tau}\right) \right| = \frac{1}{\tau} \tag{14.161}$$

Accordingly, as $\tau \to 0$, $L \to \infty$.

The general features of both explicit and implicit numerical integration methods are discussed in Appendix A–6. An *explicit method* is one having its solution at an unknown point expressed entirely in terms of known points. An *implicit method* is one for which the solution at the unknown point is expressed in terms of both the unknown and the known points. When an explicit method is applied to a stiff differential equation, the accumulated error may become much larger than the true value of the solution itself, unless the step size employed in the numerical integration process is extremely small. An explicit numerical integration method that yields a *cumulative error* that grows exponentially so that the error dominates the true solution of the differential equation is termed an *unstable method.*

Tyson and Kliegel[11] explain the basic numerical difficulty associated with the numerical integration of equation 14.160 by means of the following analysis. Consider the simple case where C_{eo} is the initial value of C_e at the point $x = x_o$ and τ is constant. In addition, assume that C_e varies linearly with x. Thus,

$$C_e = C_{eo} + a(x - x_o) \tag{14.162}$$

In the above equation a is a constant. The exact solution of equation 14.160 for the above special case is given by

$$C(x) = C(x_o) + a(x - x_o) + \left[C_{eo} - C(x_o) - a\tau\right]\left[1 - e^{-x/\tau}\right] \tag{14.163}$$

where $C(x_o)$ is the value of C at $x = 0$. It is evident that the solution includes two parts, one term that varies linearly with x and another term that decays exponentially with the relaxation distance τ. Consequently, as x increases, the dependence of the solution on the initial condition decays and the solution approaches the equilibrium solution C_e.

The difficulties encountered in the numerical integration of equation 14.160 may be illustrated by applying the first-order Euler integration method, which consists of a Taylor series expansion that is truncated after the first-order term [see Appendix A–6(c) and Appendix A–6(f)].

For the *explicit numerical integration* of equation 14.160, we obtain

$$\frac{C(x_o + h) - C(x_o)}{h} = \frac{C_{eo} - C(x_o)}{\tau} \tag{14.164}$$

where $C(x_o)$ is the value of C at $x=0$. Solving equation 14.164 for $C(x_o+h)$ gives

$$C(x_o+h)=C(x_o)\left(1-\frac{h}{\tau}\right)+C_{eo}\frac{h}{\tau} \tag{14.165}$$

Applying equation 14.165 repetitively for n steps, we obtain

$$C(x_o+nh)=C(x_o)\left(1-\frac{h}{\tau}\right)^n+\sum_{i=1}^{n}\left[C_{eo}+(i-1)ah\right]\left(1-\frac{h}{\tau}\right)^{-(n+i)}\frac{h}{\tau} \tag{14.166}$$

Examination of equation 14.166 indicates that the dependence of the solution on the initial condition $C(x_o)$ decays only if the following condition is satisfied.

$$\left|1-\frac{h}{\tau}\right|<1 \qquad \text{or} \qquad h<2\tau \tag{14.167}$$

Otherwise, the solution oscillates with rapidly increasing amplitude; that is, the solution is unstable. The solution is stable only for numerical step sizes $h<2\tau$. Hence, the step size for achieving a stable integration is of the order of the relaxation distance, which approaches zero near equilibrium.

For the *implicit numerical integration* of equation 14.160, we obtain

$$\frac{C(x_o+h)-C(x_o)}{h}=\frac{(C_{eo}+ah)-C(x_o+h)}{\tau} \tag{14.168}$$

Solving equation 14.168 for $C(x_o+h)$ yields

$$C(x_o+h)=\frac{C(x_o)+(C_{eo}+ah)\frac{h}{\tau}}{\left(1+\frac{h}{\tau}\right)} \tag{14.169}$$

Applying equation 14.169 repetitively for n steps, we obtain

$$C(x_o+nh)=\frac{C(x_o)}{\left(1+\frac{h}{\tau}\right)^n}+\sum_{i=1}^{n}\left[\frac{C_{eo}+iah}{\left(1+\frac{h}{\tau}\right)^{n+1-i}}\right]\frac{h}{\tau} \tag{14.170}$$

Examination of equation 14.170 shows that the dependence of the solution on the initial condition $C(x_o)$ always decays, regardless of the step size h, and that the solution is stable for all values of h. As x increases, the number of steps n increases, and the solution approaches the equilibrium solution, which is in agreement with the exact solution given by equation 14.163.

Examination of equations 14.166 and 14.170 for the case where τ is large compared to h (i.e., far from equilibrium) shows that in that particular case the two algorithms are essentially equivalent. Consequently, either algorithm is suitable for flows far removed from equilibrium.

A problem arises in the application of an implicit method to a *nonlinear* differential equation. The prototype equation 14.160 discussed above is linear in the dependent variable $C(x)$, so that the implicit finite difference form of the right-hand side of equation 14.160, illustrated in equation 14.168, is linear in $C(x_o+h)$. Consequently, equation 14.168 may be solved directly for $C(x_o+h)$ as

in the case of equation 14.169. Consider now the general equation, equation 14.158, where $f(x,y)$ is nonlinear in y. The implicit Euler finite difference algorithm is [see Appendix A–6(f)]

$$y_{n+1}=y_n+hf_{n+1} \tag{14.171}$$

where n and $n+1$ denote the locations x_o and x_o+h, respectively. When the derivative f_{n+1} is nonlinear in y, nonlinear terms are obtained in y_{n+1} and equation 14.171 cannot be solved directly for y_{n+1}. One method employed for solving nonlinear difference equations is based on employing an iterative procedure where y_{n+1} is assumed, the nonlinear terms are determined, and a new value of y_{n+1} is calculated from the linear terms in the difference equation. The procedure is applied repetitively until convergence of y_{n+1} is attained.

An alternate procedure for solving nonlinear difference equations involves expressing the unknown derivative f_{n+1} in equation 14.171 in a Taylor series expansion [see Appendix A–6(a)] about the *known point* n, and truncating the series after the first-order terms. Thus,

$$f_{n+1}=f_n+\left(\frac{\partial f}{\partial x}\right)_n dx+\left(\frac{\partial f}{\partial y}\right)_n dy \tag{14.172}$$

Setting $dx=h$ and $dy=(y_{n+1}-y_n)$ and substituting equation 14.172 into equation 14.171, we obtain

$$y_{n+1}=y_n+h\left[f_n+h\left(\frac{\partial f}{\partial x}\right)_n+(y_{n+1}-y_n)\left(\frac{\partial f}{\partial y}\right)_n\right] \tag{14.173}$$

Equation 14.173 is linear in y_{n+1} and may be solved directly for y_{n+1}. The concept of linearizing the nonlinear terms in the implicit finite difference equation may be applied to higher-order algorithms. The method employed in Reference 8 is a second-order accurate implicit method which employs two known points, and that method has proven to be absolutely stable. The resulting numerical algorithm is not unduly complicated, and good accuracies are obtainable with a reasonable expenditure of computation time.

Example 14.8. Consider the ordinary differential equation

$$\frac{dy}{dx}=\frac{x^2-y}{(0.02)} \tag{a}$$

with the initial condition $y(0)=0$. Determine the solution at $x=2$ by the following three methods (a) exact closed form integration, (b) the explicit first-order Euler method, and (c) the implicit first-order Euler method.

Solution

(a) The exact solution to equation (a) is

$$y(x)=x^2-\frac{x}{25}+\frac{1}{1250}(1-e^{-50/x}) \tag{b}$$

At $x=2$, $y(2)=3.9208$.

(b) For the explicit first-order Euler method [see Appendix A–6(c)]

$$\frac{y_{n+1}-y_n}{h}=\frac{x_n^2-y_n}{(0.02)} \tag{c}$$

Solving equation (c) for y_{n+1}, we obtain

$$y_{n+1}=y_n+50h\left(x_n^2-y_n\right) \tag{d}$$

The Lipschitz constant L is

$$L=\left|\frac{\partial f(x,y)}{\partial y}\right|=\frac{1}{(0.02)}=50$$

Hence, the maximum stable step size is

$$h_{\max}=\frac{2}{L}=\frac{2}{50}=0.04$$

Choose $h=0.1$. Then equation (d) becomes

$$y_{n+1}=y_n+5\left(x_n^2-y_n\right) \tag{e}$$

Let $n=0$ denote $x=0$. Then

$$y_1=0+5\left[(0)^2-0\right]=0$$

$$y_2=0+5\left[(0.1)^2-0\right]=0.05$$

$$y_3=0.05+5\left[(0.2)^2-(0.05)\right]=0.0$$

$$y_4=0.0+5\left[(0.3)^2-(0.0)\right]=0.45$$

$$y_5=0.45+5\left[(0.4)^2-(0.45)\right]=-1.00$$

$$y_6=-1.00+5\left[(0.5)^2-(-1.0)\right]=5.25 \qquad \text{etc.}$$

The results are presented in Fig. 14.12. Clearly, the solution is unstable, as is to be expected, because $h=0.1>h_{\max}=0.04$.

(c) For the implicit first-order Euler method [see Appendix A–6(f)]

$$\frac{y_{n+1}-y_n}{h}=\frac{x_{n+1}^2-y_{n+1}}{(0.02)} \tag{f}$$

Solving equation (f) for y_{n+1} gives

$$y_{n+1}=\frac{y_n+50hx_{n+1}^2}{1+50h} \tag{g}$$

For $h=0.1$, equation (g) becomes

$$y_{n+1}=\frac{y_n+5x_{n+1}^2}{6} \tag{h}$$

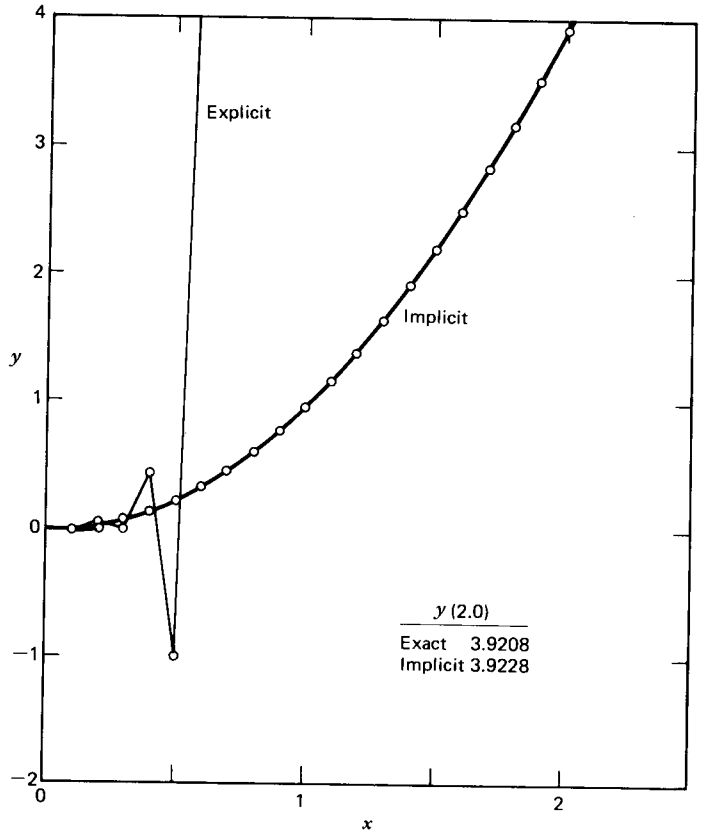

Figure 14.12 Solution to $dy/dx = 50(x^2 - y)$ with $y(0) = 0$.

Applying equation (h) repetitively, we obtain

$$y_1 = \frac{0 + 5(0.1)^2}{6} = 0.00833$$

$$y_2 = \frac{(0.00833) + 5(0.2)^2}{6} = 0.03472$$

$$y_3 = \frac{(0.03472) + 5(0.3)^2}{6} = 0.08079$$

$$y_4 = \frac{(0.08079) + 5(0.4)^2}{6} = 0.14680$$

$$y_5 = \frac{(0.14680) + 5(0.5)^2}{6} = 0.23280$$

$$y_6 = \frac{(0.23280) + 5(0.6)^2}{6} = 0.33880 \qquad \text{etc.}$$

The results are presented in Fig. 14.12. The solution is clearly stable, and it closely approximates the exact solution.

The results presented in Fig. 14.12 illustrate vividly the advantage of an implicit method over an explicit method for numerically integrating a stiff differential equation.

14–7 FLOW OF GAS-PARTICLE MIXTURES[12, 13, 14]

There are many flows involving a gas carrying suspended particles, either solid or liquid, or both. Examples are atmospheric fog, liquid fuel spray in combustors, aerosols of all types, and the combustion products of metalized rocket propellant fuels. In the latter case, the combustion products contain condensed metal oxide particles such as Al_2O_3.

Many of the solid propellant formulations for rocket motors contain very finely powdered aluminum as a principal ingredient. The addition of the aluminum powder increases the combustion temperature and the specific impulse. It also stabilizes the combustion process against the occurence of high frequency "acoustic instability" [see Section 15–4(e)]. The combustion of such a propellant results in the flow of a two-phase mixture in the propulsive nozzle of the rocket motor because of the condensation of the aluminum oxide. As a consequence of the two-phase flow, there is an inefficiency in the expansion process in the propulsive nozzle. In flowing through the nozzle, the condensed Al_2O_3 particles do not accelerate at the same rate as the gaseous combustion products. Furthermore, the temperature of the condensed Al_2O_3 particles does not decrease as rapidly as does that of the flowing combustion gas. Moreover, the condensed particles make no contribution to the combustion gas pressure.

The equations governing the steady one-dimensional flow of a *gas-particle mixture* (i.e., a gas containing suspended condensed phases) are derived in this section. Those equations are applied to the expanding flow of gas-particle mixtures in a De Laval nozzle.

14–7(a) Governing Equations for Gas-Particle Flow

Figure 14.13 illustrates the flow model for a gas carrying suspended condensed particles. The following assumptions are applicable.

1. The flow is steady and one dimensional.
2. There is no external work, no external heat transfer, no wall friction, and the effect of gravity is negligible.
3. The particles exert a body force δD on the gas, and they transfer the heat δQ to the gas.
4. The particles occupy negligible volume and are discrete; that is, they do not interact with each other. Also, they have a uniform internal temperature, are incompressible, and are spherical in shape.

In the analysis that follows, the *gas properties* are denoted by symbols without a subscript, and the *particle properties* are denoted by symbols with the subscript p.

1. *Particle continuity equation.* The mass of each particle remains constant, since by assumption the particles do not react chemically, agglomorate, or break up. Consequently, the total mass flow rate of particles $\dot{m}_p$ also remains constant. *By definition*, the *particle density* ρ_p is the *total mass of the particles per unit volume of the flow field.* Then

$$\dot{m}_p = \rho_p A V_p = \text{constant} \tag{14.174}$$

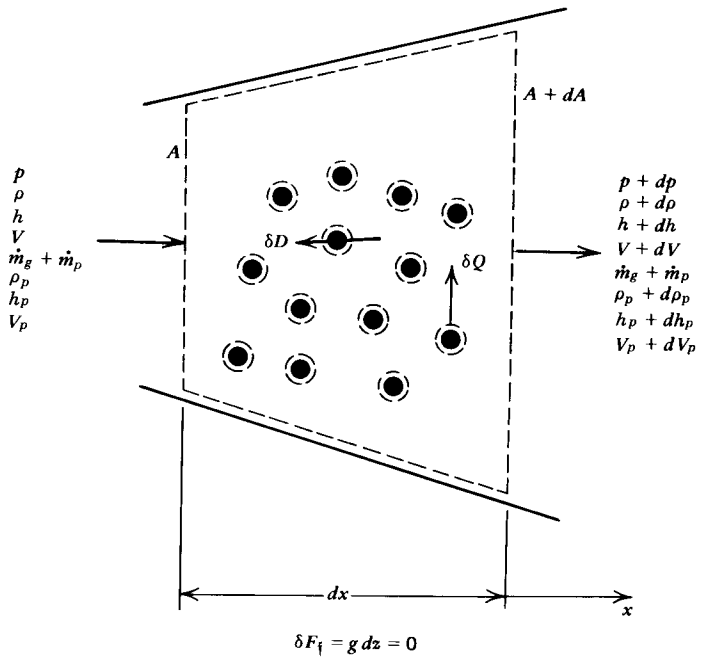

Figure 14.13 Flow model for gas-particle flow.

The definition of ρ_p is in a sense a *partial density*, which is analogous to the partial density of a gas discussed in Section 1–15(h) in connection with mixtures of gases.

2. *Particle momentum equation.* The particle drag and heat transfer model is illustrated in Fig. 14.14. For each particle, Newton's second law (equation 1.70) yields*

$$(\text{Mass})_p a_p = (\text{Mass})_p \frac{dV_p}{dt} = (\text{Mass})_p V_p \frac{dV_p}{dx} = \delta D_p \tag{14.175}$$

where δD_p is the drag on the individual particle. For a spherical particle

$$(\text{Mass})_p = \rho_{mp} \frac{4}{3} \pi r_p^3 \tag{14.176}$$

where ρ_{mp} denotes the density of the material comprising the particle and $(4/3)\pi r_p^3$ is its *volume*.

The drag force δD_p for a particle depends on its *frontal area* $A = \pi r_p^2$ and its relative velocity with respect to the flowing gas $(V - V_p)$, which is termed the *relative gas velocity*. Hence, if C_D denotes the particle drag coefficient, then

$$\delta D_p = C_D \left(\pi r_p^2\right) \frac{1}{2} \rho (V - V_p) |V - V_p| \tag{14.177}$$

It is shown in Section 5–8 that the drag coefficient C_D is a function of the Reynolds number, which is based on the relative gas velocity in the present situation.

*In this section, the symbol t denotes the time when it appears in the derivative operator $d(\ )/dt$. Otherwise, t denotes the temperature.

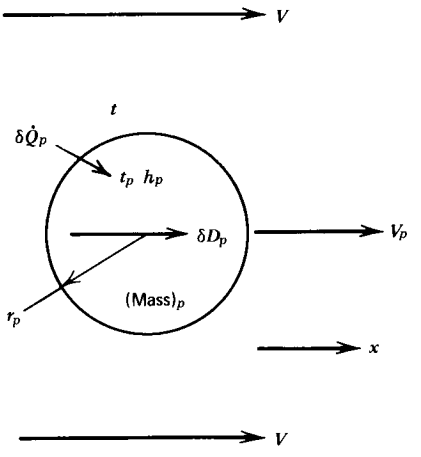

Figure 14.14 Particle drag and heat transfer model.

Combining equations 14.175 to 14.177 yields

$$V_p \frac{dV_p}{dx} = \frac{3}{8} \frac{\rho C_D}{\rho_{mp} r_p} (V - V_p)|V - V_p| \tag{14.178}$$

In the *Stokes flow regime* (i.e., $\text{Re} < 1$), the drag coefficient, denoted by $C_{D,\text{Stokes}}$, is given by

$$C_{D,\text{Stokes}} = \frac{24}{\text{Re}} = \frac{24\mu}{(2r_p)\rho|V - V_p|} \tag{14.179}$$

By definition, let

$$C_D^\dagger \equiv \frac{C_D}{C_{D,\text{Stokes}}} \tag{14.180}$$

Combining equations 14.178 to 14.180, we obtain

$$V_p \frac{dV_p}{dx} = A_p(V - V_p) \tag{14.181}$$

where

$$A_p = \frac{9}{2} \frac{\mu C_D^\dagger}{\rho_{mp} r_p^{\,2}} \tag{14.182}$$

The total drag force δD exerted by all of the particles on the gas inside of the control volume ($A\,dx$) is given by

$$\delta D = \frac{\delta D_p}{(\text{Mass})_p} \left[\rho_p (A\,dx)\right] \qquad \text{(force)} \tag{14.183}$$

Substituting equation 14.175 into equation 14.183 gives

$$\frac{\delta D}{(A\,dx)} = \rho_p V_p \frac{dV_p}{dx} \qquad \left(\frac{\text{force}}{\text{volume}}\right) \tag{14.184}$$

3. *Particle energy equation.* Since each spherical particle is assumed to be incompressible, the heat transfer δQ_p between the gas and the particle affects only the *particle enthalpy* h_p. Accordingly,

$$\delta \dot{Q}_p = (\text{Mass})_p \frac{dh_p}{dt} = (\text{Mass})_p V_p \frac{dh_p}{dx} \tag{14.185}$$

The heat transfer $\delta \dot{Q}_p$ to an individual particle having the temperature t_p is given by

$$\delta \dot{Q}_p = \mathbf{h}(4\pi r_p^2)(t - t_p) \tag{14.186}$$

where **h** is the *heat transfer film coefficient* for the particle, t is the temperature of the gas, t_p is the temperature of the particle, and $A = (4\pi r_p^2)$ is the surface area of the particle. The film coefficient **h** is defined in terms of the *Nusselt number* Nu, which is a function of the *Reynolds number*. Thus,

$$\text{Nu} \equiv \frac{\mathbf{h}(2r_p)}{\kappa} \tag{14.187}$$

where κ is the *thermal conductivity* of the gas. The *Prandtl number* Pr is defined by

$$\text{Pr} \equiv \frac{c_p \mu}{\kappa} \tag{14.188}$$

In a Stokes flow, Nu = 2. *By definition*, let

$$\text{Nu}^\dagger = \frac{\text{Nu}}{\text{Nu}_{\text{Stokes}}} = \frac{\text{Nu}}{2} \tag{14.189}$$

Combining equations 14.186 to 14.189, we obtain for the rate at which heat is transferred to a particle

$$\delta \dot{Q}_p = \frac{4\pi \mu \text{Nu}^\dagger c_p r_p (t - t_p)}{\text{Pr}} \qquad \left(\frac{\text{energy}}{\text{time}}\right) \tag{14.190}$$

Substituting equations 14.176 and 14.190 into equation 14.185, we obtain

$$V_p \frac{dh_p}{dx} = B_p (t - t_p) \tag{14.191}$$

where

$$B_p \equiv \frac{3\mu \text{Nu}^\dagger c_p}{\rho_{mp} r_p^2 \text{Pr}} \tag{14.192}$$

The total heat transfer rate $\delta \dot{Q}$ for all of the particles per unit mass of the gas inside of the control volume ($A\,dx$) is given by

$$\rho \delta \dot{Q} = \frac{\delta \dot{Q}_p}{(\text{Mass})_p} \rho_p \tag{14.193}$$

Substituting equation 14.185 into equation 14.193 yields

$$\rho \delta \dot{Q} = \rho_p V_p \frac{dh_p}{dx} \qquad \left(\frac{\text{energy}}{\text{volume-time}}\right) \tag{14.194}$$

Because the particles are incompressible, all of the work expended on them by the gas appears in the form of an increase in their kinetic energy. Hence, for each particle

$$\delta \dot{W}_p = (\text{Mass})_p \frac{d}{dt}\left(\frac{V_p^2}{2}\right) = (\text{Mass})_p V_p \frac{d}{dx}\left(\frac{V_p^2}{2}\right) \qquad \left(\frac{\text{energy}}{\text{time}}\right) \tag{14.195}$$

The total rate of work $\delta \dot{W}$ done per unit mass of gas on all of the particles inside of the control volume ($A\,dx$) is given by

$$\rho \delta \dot{W} = \frac{\delta \dot{W}_p}{(\text{Mass})_p} \rho_p \tag{14.196}$$

Substituting equation 14.195 into equation 14.196, we obtain

$$\rho \delta \dot{W} = \rho_p V_p^2 \frac{dV_p}{dx} \qquad \left(\frac{\text{energy}}{\text{volume-time}}\right) \tag{14.197}$$

4. *Particle equation of state.* For incompressible particles, only a caloric equation of state is required. Thus,

$$t_p = f(h_p) \tag{14.198}$$

If the *particle specific heat* is assumed to be constant, then

$$t_p = t_{pm} + \frac{h_p - h_{p\ell}}{c_{p\ell}} \qquad (h_p > h_{p\ell}) \tag{14.199a}$$

$$t_p = t_{pm} \qquad (h_{p\ell} > h_p > h_{ps}) \tag{14.199b}$$

$$t_p = t_{pm} + \frac{(h_p - h_{ps})}{c_{ps}} \qquad (h_{ps} > h_p) \tag{14.199c}$$

where $h_{p\ell}$ is the enthalpy of a liquid particle at its solidification temperature t_{pm}, h_{ps} is the enthalpy of a solid particle at its melting temperature t_{pm}, $c_{p\ell}$ is the specific heat of the liquid particles, and c_{ps} is the specific heat of the solid particles.

5. *Gas continuity equation.* From equation 3.158, Table 3.1,

$$\dot{m}_g = \rho A V = \text{constant} \tag{14.200}$$

6. *Gas momentum equation.* From equation 3.160, Table 3.1,

$$\frac{dp}{dx} + \rho V \frac{dV}{dx} + \frac{\delta D}{A\,dx} = 0 \tag{14.201}$$

where δD is the total drag force exerted by all of the particles on the gas. Substituting equation 14.184 into equation 14.201, we obtain

$$\rho V \frac{dV}{dx} + \rho_p V_p \frac{dV_p}{dx} + \frac{dp}{dx} = 0 \tag{14.202}$$

7. *Gas energy equation.* From equation 3.161, Table 3.1,

$$\delta W - \delta Q + dh + V\,dV = 0 \tag{14.203}$$

where δW is the work per unit mass expended by the gas on all of the particles, due to drag forces, and δQ is the heat transfer per unit mass between all of the particles and the gas. Equation 14.203 may be expressed on a rate basis by dividing by dt. Thus,

$$\delta \dot{W} - \delta \dot{Q} + \frac{dh}{dt} + V\frac{dV}{dt} = \delta \dot{W} - \delta \dot{Q} + V\frac{dh}{dx} + V^2\frac{dV}{dx} = 0 \tag{14.204}$$

Substituting equations 14.194 and 14.197 into equation 14.204 yields

$$\rho V\frac{dh}{dx} + \rho V^2\frac{dV}{dx} + \rho_p V_p\frac{dh_p}{dx} + \rho_p V_p{}^2\frac{dV_p}{dx} = 0 \tag{14.205}$$

Dividing equation 14.205 by ρV, noting that $(\rho_p V_p/\rho V) = (\dot{m}_p/\dot{m}_g)$, and integrating, we obtain

$$h + \frac{V^2}{2} + \left(\frac{\dot{m}_p}{\dot{m}_g}\right)\left(h_p + \frac{V_p{}^2}{2}\right) = H + \left(\frac{\dot{m}_p}{\dot{m}_g}\right)H_p = \text{constant} \tag{14.206}$$

where H and H_p are the respective stagnation enthalpies for the gas and the particles in the combustor.

8. *Gas equations of state*

$$h = h(p, \rho) \tag{14.207}$$

$$t = t(p, \rho) \tag{14.208}$$

For a perfect gas, equations 14.207 and 14.208 take the forms

$$h = \int_{t_0}^{t} c_p\,dt \tag{14.209}$$

$$p = \rho R t \tag{14.210}$$

Equations 14.174, 14.181, 14.191, 14.198, 14.200, 14.202, and 14.206 to 14.208 comprise a set of nine equations for determining the nine flow properties p, ρ, t, h, V, ρ_p, V_p, h_p, and t_p. Those equations may be combined into a form suitable for obtaining a numerical solution by any standard numerical integration algorithm. The equations are singular in the transonic region. Consequently, as pointed out in Section 9–5(e) and 14–6(a), the *specified area method* should be employed upstream and downstream of that region, and the *specified pressure method* should be employed in the transonic region. For particles of very small size (of the order of $r_p = 1$ micron or smaller), the equations become quite *stiff*, and the implicit numerical integration method, discussed in Section 14–6(b) and in Appendix A–6(f), should be employed.

The nine aforementioned equations may be rearranged algebraically to obtain an expression for the determination of all of the flow properties except the gas velocity

V. The following equations are obtained.

$$\frac{dV_p}{dx} = \frac{A_p(V - V_p)}{V_p} \tag{14.211}$$

$$\frac{dh_p}{dx} = \frac{B_p(t - t_p)}{V_p} \tag{14.212}$$

$$\rho_p = \frac{\dot{m}_p}{AV_p} \tag{14.213}$$

$$t_p = f(h_p) \tag{14.214}$$

$$\rho = \frac{\dot{m}_g}{AV} \tag{14.215}$$

$$h = H - \frac{V^2}{2} + \left(\frac{\dot{m}_p}{\dot{m}_g}\right)\left[H_p - \left(h_p + \frac{V_p^2}{2}\right)\right] \tag{14.216}$$

$$h = h(p, \rho) \tag{14.217}$$

$$t = t(p, \rho) \tag{14.218}$$

To complete the system of equations, an equation must be derived for determining the gas velocity V.

Specified area method. For the specified area method, an equation for determining the gas velocity V is obtained by combining the differential forms of the continuity, momentum, and energy equations for the gas (i.e., equations 14.200, 14.202, and 14.206) with the equations of state for the gas (i.e., equations 14.207 and 14.208). Differentiating equation 14.206 and solving for dV/dx yields

$$\frac{dV}{dx} = -\frac{1}{V}\left\{\frac{dh}{dx} + \left(\frac{\dot{m}_p}{\dot{m}_g}\right)\left[\frac{dh_p}{dx} + V_p\frac{dV_p}{dx}\right]\right\} \tag{14.219}$$

Substituting equations 14.211 and 14.212 into equation 14.219 gives

$$\frac{dV}{dx} = -\frac{1}{V}\left\{\frac{dh}{dx} + \left(\frac{\dot{m}_p}{\dot{m}_g}\right)\left[\frac{B_p(t - t_p)}{V_p} + A_p(V - V_p)\right]\right\} \tag{14.220}$$

Up to this point, all of the results have been applicable to both perfect gases and imperfect gases. To simplify equation 14.220 further, a specific equation of state for the *gas enthalpy* h is required. For a perfect gas, equations 14.209 and 14.210 may be combined to give

$$\frac{dh}{dx} = c_p\frac{dt}{dx} = c_p\left[\frac{t}{p}\frac{dp}{dx} - \frac{t}{\rho}\frac{d\rho}{dx}\right] \tag{14.221}$$

$$\frac{dh}{dx} = \frac{a^2}{\gamma - 1}\left[\frac{1}{p}\frac{dp}{dx} - \frac{1}{\rho}\frac{d\rho}{dx}\right] \tag{14.222}$$

The term dp/dx may be eliminated by solving equation 14.202 for dp/dx and substituting the result into equation 14.222. The term $d\rho/dx$ may be eliminated by differentiating equation 14.200, solving for $d\rho/dx$, and substituting the result into equation 14.222. Thus,

$$\frac{dh}{dx} = \frac{a^2}{\gamma - 1}\left[-\frac{1}{p}\left(\rho V \frac{dV}{dx} + \rho_p V_p \frac{dV_p}{dx}\right) + \frac{1}{V}\frac{dV}{dx} + \frac{1}{A}\frac{dA}{dx} \right] \tag{14.223}$$

The term dV_p/dx may be eliminated by introducing equation 14.211 into equation 14.223. Substituting the resulting form of equation 14.223 into equation 14.220 gives the following expression for dV/dx for the *specified area method.*

$$\frac{dV}{dx} = \frac{V}{M^2 - 1}\left\{ \frac{1}{A}\frac{dA}{dx} - \frac{1}{a^2 V_p}\left(\frac{\dot{m}_p}{\dot{m}_g}\right)\left[-(\gamma - 1)B_p(t - t_p) \right.\right.$$

$$\left.\left. + A_p \gamma (V - V_p)^2 + A V_p (V - V_p) \right] \right\} \tag{14.224}$$

Specified pressure method. For the specified pressure method, equation 14.202 may be solved directly for dV/dx, where dV_p/dx is eliminated by introducing equation 14.211. Thus,

$$\frac{dV}{dx} = -\frac{1}{\rho V}\left[\frac{dp}{dx} + A_p \rho_p (V - V_p) \right] \tag{14.225}$$

To obtain values for V_p, h_p, and V, equations 14.211, 14.212, and 14.224 or 14.225 have to be integrated numerically. The remaining flow properties may be obtained from equations 14.213 to 14.218. Reference 14 presents a computer program for implementing the numerical solution of the above system of equations.

In the actual flow of a gas-particle mixture, the particle size is nonuniform, and the particles have a continuous distribution of sizes. Figure 14.15 presents the particle size of Al_2O_3 particles as a function of the particle diameter in microns for the combustion gas produced by burning a typical aluminized solid propellant in a rocket motor. The fraction of the particles with diameters between D_p and $D_p + dD_p$ is represented by the *area* (not the ordinate) of a vertical strip having the base

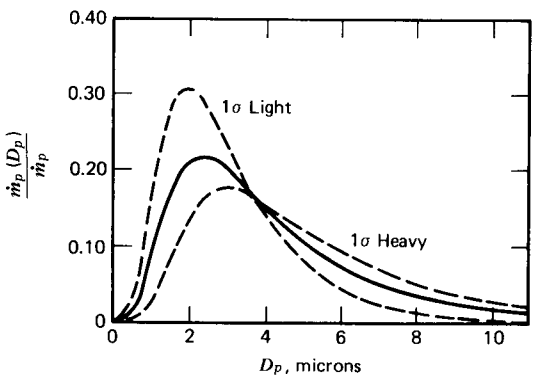

Figure 14.15 Measured particle size distribution for aluminized solid propellants (taken from Reference 13).

width dD_p. Consequently, the total area under the curve presented in Fig. 14.15 is unity.

The analysis presented in the preceding paragraphs may be extended to take into account a continuous distribution of particle sizes by replacing the actual continuous particle size distribution by a finite set of discrete particle sizes. A discrete particle size distribution, corresponding to a continuous particle size distribution such as that presented in Fig. 14.15, may be obtained by dividing the total area under the curve in Fig. 14.15 into fractional areas representing mass fractions of the total mass flow rate of particles, and determining the average particle size corresponding to each mass fraction. Table 14.5 presents a discrete Al_2O_3 particle size distribution for a typical aluminized solid propellant, where the continuous distribution is represented by five discrete sizes, each having a mass fraction of 0.20 of the total particle mass flow rate.

Table 14.5 Discrete Particle Size Distribution for Aluminized Propellants (Taken from Reference 13)

D_p, microns	$\dot{m}_{p,j} / \sum_{j=1}^{5} \dot{m}_{p,j}$
1.58	0.20
2.56	0.20
3.52	0.20
4.88	0.20
7.90	0.20

The governing equations may be extended so that they take into account a number of discrete particle sizes. If it is assumed that the particles do not interact, then each discrete particle is governed by its own set of differential equations. The effect of the drag and heat transfer on the gas due to all of the particles is obtained by summing those effects over all of the discrete particles. In the case of an aluminized solid propellant for rocket motor applications, five discrete particle sizes should yield a reasonable approximation to the actual continuous particle size distribution.

Figure 14.16 presents the properties of a steady one-dimensional gas-particle flow in a converging-diverging nozzle having the geometry illustrated in Fig. 14.16*a*. In Fig. 14.16, the results obtained by the integration of the exact equations presented in Section 14–7(a) are denoted by the solid lines, and the results of the constant lag analysis presented in Section 14–7(b) are denoted by the crosses (×) and the dashed lines. Figures 14.16*b* and 14.16*c* present the gas velocity, temperature, pressure, and density profiles. Figures 14.16*d* and 14.16*e* present the particle velocity and thermal lags, respectively, for the particle size distribution presented in Table 14.5. The lags increase rapidly as the throat is approached, peaking slightly downstream of the throat, then decrease slightly to a value which remains essentially constant for the remaining length of the nozzle. The thermal lags are larger than the velocity lags, and the lags increase as the particle diameter D_p increases. Figure 14.16*f* presents the particle-gas density ratio ρ_p/ρ, which peaks in the throat region where the particle velocity lag peaks. The results presented in Fig. 14.16 are typical of the behavior of the flow of the combustion gas from an aluminized solid propellant expanding in a converging-diverging propulsive nozzle.

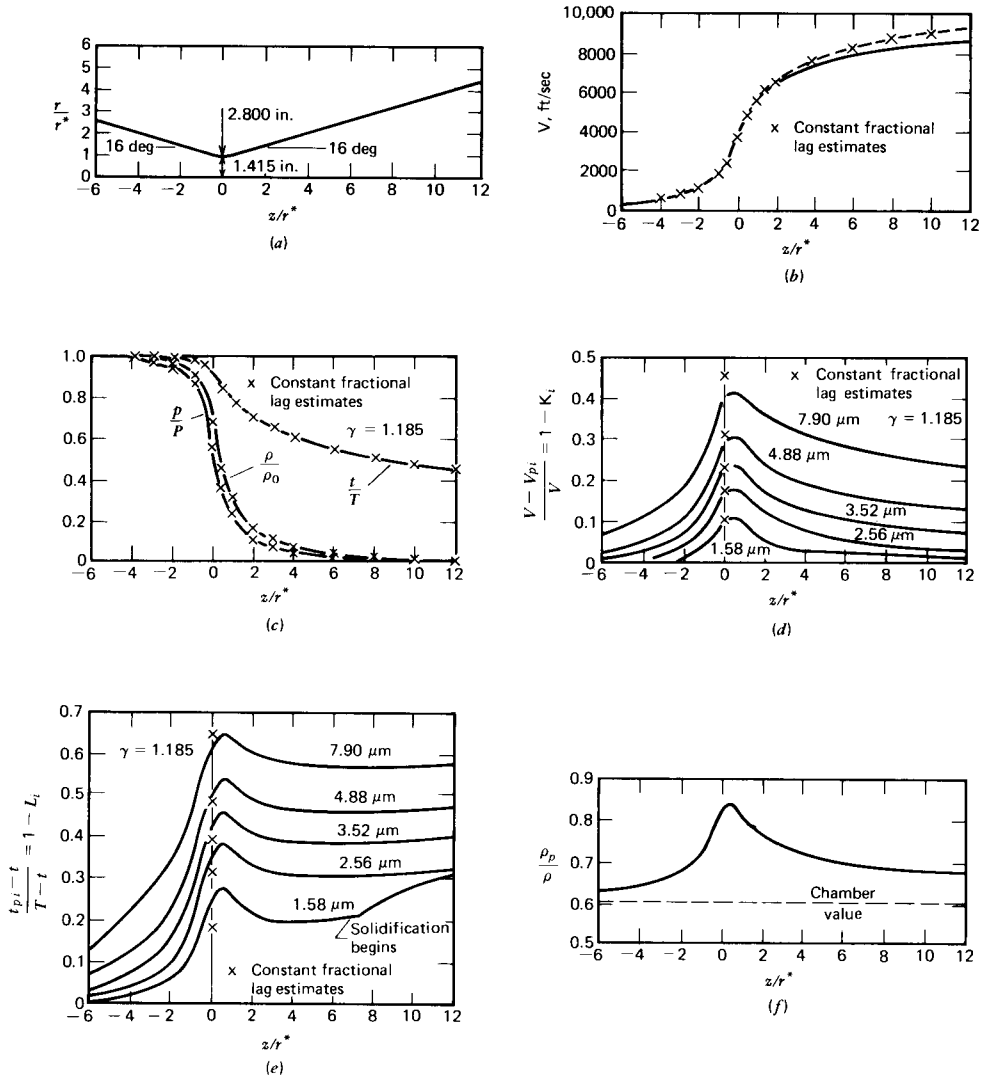

Figure 14.16 Properties of a one-dimensional gas-particle flow. (*a*) Nozzle geometry used in numerical calculations. (*b*) Gas velocity profile. (*c*) Gas temperature, pressure, and density profiles. (*d*) Particle velocity lags. (*e*) Particle temperature lags. (*f*) Particle-gas density ratio. (Taken from Reference 13.)

14–7(b) Constant Lag Flow[13]

The particle velocity V_p and temperature t_p may be related to the gas velocity V and temperature t, respectively, by the ratios K and L, which are defined by

$$K \equiv \frac{V_p}{V} \tag{14.226}$$

$$L \equiv \frac{T - t_p}{T - t} \tag{14.227}$$

where T is the stagnation temperature of the gas in the combustion chamber. The particle velocity lag and its thermal lag are related to K and L, respectively. *By*

definition, the aforementioned lags are given by

$$\textit{Velocity lag} \equiv \frac{V - V_p}{V} = (1 - K) \tag{14.228}$$

$$\textit{Thermal lag} \equiv \frac{t_p - t}{T - t} = (1 - L) \tag{14.229}$$

Kliegel[13] analyzed the case where the particles remain in the Stokes' flow regime so that $C_D^{\dagger} = \mathrm{Nu}^{\dagger} = 1.0$ (see equations 14.180 and 14.189). If it is assumed that the particles remain in the liquid phase, that the specific heats of the gas and the particles are constant, and that the velocity lag $(1 - K)$ and the thermal lag $(1 - L)$ for the particles remain constant, then it may be shown that

$$L = \left[1 + 3\mathrm{Pr} \frac{c_{p\ell}}{c_p} \frac{(1 - K)}{K} \right]^{-1} \tag{14.230}$$

Equation 14.230 shows that in the aforementioned special case the particle velocity and thermal lags are uniquely related. In most cases of engineering interest, $\mathrm{Pr} c_{p\ell}/c_p > 1/3$, and the particle thermal lag $(1 - L)$ is larger than its velocity lag $(1 - K)$. When the particle velocity and thermal lags are unity (i.e., the particle velocity $V_p = 0$ and the particle temperature $t_p = T$), the flow properties of the gas are unaffected by the presence of the particles. Consequently, in that special case, the flow behaves as a *pure gas flow*. When both the particle velocity lag and the thermal lag are zero (i.e., $V_p = V$ and $t_p = t$), the particles are said to be in *velocity* and *thermal equilibrium* with the gas.

For the case of constant lags, the equations governing gas-particle flow derived in Section 14–7(a) may be reduced to the identical form as that for the equations describing the steady one-dimensional isentropic flow of a perfect gas (see Section 4–4), except that γ and M in the isentropic flow equations are replaced by the parameters $\bar{\gamma}$ and $\bar{M}$, which are defined as follows.[13]

$$\bar{\gamma} = 1 + (\gamma - 1)\left(\frac{B}{C}\right) \tag{14.231}$$

$$\bar{M} = \sqrt{C}\, M \tag{14.232}$$

where

$$B = \frac{1 + (\dot{m}_p/\dot{m}_g) K^2}{1 + (\dot{m}_p/\dot{m}_g)(c_{p\ell}/c_p) L} \tag{14.233}$$

$$C = 1 + \left(\frac{\dot{m}_p}{\dot{m}_g}\right)\left\{ K\left[(1 - K)\gamma + K\right] + (\gamma - 1)(c_{p\ell}/c_p) BL \right\} \tag{14.234}$$

Making the above modifications, the equations for the flow property ratios of a gas-particle flow with constant lags correspond to those for an isentropic flow (see Table 4.5). Accordingly, Table C.6 may be employed for determining the flow properties for a gas-particle flow in a converging-diverging nozzle under the condition of constant lag.

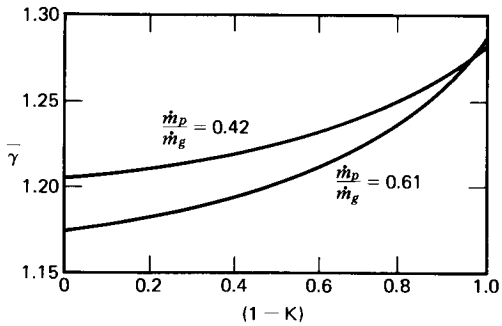

Figure 14.17 Expansion coefficient $\bar{\gamma}$ as a function of particle velocity lag $(1-K)$ in a constant lag nozzle (taken from Reference 13).

Figure 14.17 presents $\bar{\gamma}$ as a function of the particle velocity lag $(1-K)$ for the flow of a combustion gas produced by burning a typical metalized propellant. It is seen that as $(1-K)$ increases, the parameter $\bar{\gamma}$ increases and approaches the value γ for a pure gas flow. Also, as the *particle mass fraction* $\dot{m}_p/\dot{m}_g$ increases, the magnitude of $\bar{\gamma}$ decreases.

At the throat of the nozzle $\overline{M}=1$ for the equivalent isentropic flow, and from equation 14.232

$$M_t = \frac{1}{\sqrt{C}} < 1 \tag{14.235}$$

Equation 14.235 indicates that the Mach number at the nozzle throat is always less than unity. Figure 14.18*a* presents the throat Mach number, denoted by M^*, as a function of the velocity lag $(1-K)$ for the flow of combustion gas obtained by burning a typical metalized solid propellant. As the lag $(1-K)$ increases for a fixed value of the particle-to-gas mass flow rate ratio, the throat Mach number M^* also increases and approaches the value $M^*=1$. For a fixed value of the velocity lag $(1-K)$, the throat Mach number M^* decreases as the particle mass fraction $\dot{m}_p/\dot{m}_g$ increases. The total mass flow rate $\dot{m}=\dot{m}_p+\dot{m}_g$ may be determined from the properties in the nozzle throat. Because those properties depend on the magnitude of the particle velocity lag $(1-K)$, the mass flow rate for the nozzle also depends on $(1-K)$. Figure 14.18*b* presents the *normalized mass flow rate* $\dot{m}/\dot{m}_e$, where $\dot{m}$ is normalized by the equilibrium mass flow rate $\dot{m}_e$ [$\dot{m}=\dot{m}_e$ when $(1-K)=(1-L)=0$], as a function of the particle velocity lag $(1-K)$, for the combustion gas from the same solid propellant. The normalized mass flow rate for the nozzle is influenced strongly by the particle velocity lag; it increases with both $(1-K)$ and $\dot{m}_p/\dot{m}_g$.

Substituting equation 14.226 into the particle momentum equation, equation 14.181, we obtain

$$\frac{dV_p}{dx} = A_p(1-K)K^{-1} = \text{constant} \tag{14.236}$$

and

$$\frac{dV}{dx} = A_p(1-K)K^{-2} = \text{constant} \tag{14.237}$$

Equation 14.237 shows that the assumption of a constant particle velocity lag

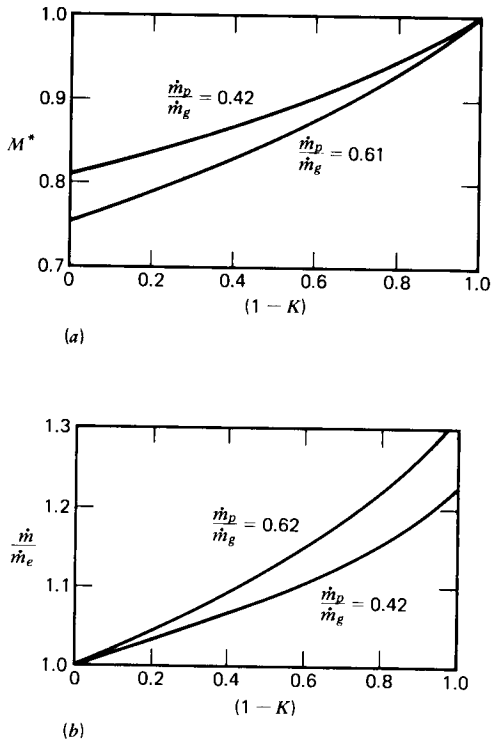

Figure 14.18 Throat Mach number and mass flow rate as a function of particle velocity lag $(1-K)$ in a constant lag nozzle. (*a*) Throat Mach number. (*b*) Mass flow rate. (Taken from Reference 13.)

imposes the restriction that the gas velocity gradient dV/dx is constant, which is a reasonable approximation in the throat region of a De Laval nozzle. For the inlet and exit portions of the nozzle, however, the aforementioned assumption is invalid. Kliegel[13] shows that a nozzle designed to give a constant lag is trumpet shaped, with the inlet and exit area increasing exponentially as one moves in either direction from the throat region; the configuration is approximately symmetrical.

The constant lag analysis presented in this section is, at best, an approximation to the actual flow process. The analysis based on the assumption of constant lag flow does, however, yield considerable insight into the general features of gas-particle flows. In fact, the results of an *equilibrium analysis* where $(1-K)=(1-L)=0$ is an upper bound for an actual flow, and the *frozen analysis* where $(1-K)=(1-L)=1$ yields a lower bound. The actual values of the flow properties must lie between the values for those two limiting cases. The results presented in Fig. 14.16 show that the analysis based on constant velocity and thermal lags is in fair agreement with the results obtained by the numerical integration of the exact equations presented in Section 14–7(a).

Example 14.9. The products of combustion of an aluminized solid propellant flow through a converging-diverging propulsive nozzle having a throat radius $y_t = 0.0762$ m and an area ratio $\epsilon = 30$. The stagnation temperature and pressure at the nozzle entrance are 3333 K and $34.47 \cdot 10^5$ N/m^2, respectively. The ratio of the Al_2O_3 particle mass flow rate $\dot{m}_p$ to the gas mass flow rate $\dot{m}_g$ is $\dot{m}_p/\dot{m}_g = 0.5$. For the gas, $\gamma = 1.30$, $\Pr = 0.50$, $c_p = 1884$ J/kg-K, and $R = 430.4$ J/kg-K. For the Al_2O_3 particles, $c_{p\ell} = 1420$ J/kg-K. For a constant lag flow with a velocity lag of 20 percent

[i.e., $(1-K)=0.20$ and $K=V_p/V=0.80$], calculate (a) the thermal lag $(1-L)$, (b) the effective specific heat ratio $\bar{\gamma}$, (c) the throat Mach number M_t, and (d) the exit Mach number M_e.

Solution

(a) From equation 14.230,

$$L=\left[1+\frac{3(0.50)(0.34)(0.20)}{(0.45)(0.8)}\right]^{-1}=0.780$$

$$(1-L)=1-0.780=0.220$$

Thus, the thermal lag is 22 percent, which is 2 percent larger than the velocity lag.

(b) From equations 14.233, 14.234, and 14.231, respectively, we obtain

$$B=\frac{1+(0.5)(0.8)^2}{1+(0.5)(0.34/0.45)(0.780)}=1.01957$$

$$C=1+(0.5)\{(0.8)[(0.2)(1.30)+(0.8)]+(0.30)(0.34/0.45)(1.01957)(0.780)\}$$

$$C=1.51413$$

$$\bar{\gamma}=1+\frac{(0.3)(1.01957)}{1.51413}=1.202$$

(c) From equation 14.232, noting that $\overline{M}_t=1.0$, we obtain

$$M_t=\frac{\overline{M}_t}{\sqrt{C}}=\frac{1.0}{\sqrt{1.51413}}=0.8127$$

(d) From Table C.6, for $\bar{\gamma}=1.20$ and $\epsilon=30$, $\overline{M}_e=4.039$. Thus,

$$M_e=\frac{\overline{M}_e}{\sqrt{C}}=\frac{4.039}{\sqrt{1.51413}}=3.2825$$

REFERENCES

1. J. F. Clarke and M. McChesney, *The Dynamics of Real Gases*, Chapter 2, Butterworths, London, 1964.
2. W. G. Vincenti and C. H. Kruger, *Introduction to Physical Gas Dynamics*, Wiley, New York, 1965.
3. K. Wark, *Thermodynamics*, Second Edition, McGraw-Hill, New York, 1971.
4. D. R. Stull, H. Prophet, et al., *JANAF Thermochemical Tables*, Second Edition, NSRDS-NBS 37, National Standard Reference Data Series, National Bureau of Standards, June 1971.
5. S. Gordon and B. J. McBride, "Computer Program for Calculation of Complex Chemical Equilibrium Compositions, Rocket Performance, Incident and Reflected Shocks, and Chapman-Jouguet Detonations," NASA SP-273, 1971.
6. S. S. Cherry, "Screening of Reaction Rates," Report No. 08832-6002-T000, TRW Systems Group, Redondo Beach, Calif., 6 December 1967.
7. "High Temperature Reaction Rate Data," a continuing series of reports by the Department of Physical Chemistry, the University of Leeds, England.

8. H. M. Frey, J. R. Kliegel, G. R. Nickerson, and T. J. Tyson, "ICRPG One-Dimensional Kinetic Nozzle Analysis Program," Dynamic Science, Monrovia, Calif., July 1968.
9. C. F. Curtiss and J. O. Hirschfelder, "Integration of Stiff Equations," Proceedings National Academy of Science, Vol. 38, 1952, pp. 235–243.
10. P. Henrici, *Discrete Variable Methods in Ordinary Differential Equations*, Wiley, New York, 1962.
11. T. J. Tyson and J. R. Kliegel, "An Implicit Integration Procedure for Chemical Kinetics," Paper No. 68-180, American Institute of Aeronautics and Astronautics, 6th Aerospace Sciences Meeting, January 1968.
12. J. D. Hoffman, "An Analysis of the Effects of Gas-Particle Mixtures on the Performance of Rocket Nozzles," Ph. D. Thesis, Purdue University, January 1963.
13. J. R. Kliegel, "Gas Particle Nozzle Flows," *Ninth International Symposium on Combustion*, Academic Press, New York, 1963, pp. 811–826.
14. J. R. Kliegel, V. Quan, S. S. Cherry, and H. M. Frey, "One-Dimensional, Two-Phase, Reacting Gas Nonequilibrium Performance Program," Report No. 02874-6005-R000, TRW Systems, Redondo Beach, Calif., August 1967.

15
three-dimensional acoustic waves and steady two-dimensional transonic flow

15–1 PRINCIPAL NOTATION FOR CHAPTER 15

The notation of Chapter 10 (Section 10–1) is applicable here. The following additional notation is employed in the present chapter.

$\tilde{a}$ dimensional local speed of sound.
a_∞ free-stream sonic speed.
a^* free-stream critical sonic speed.
C_c geometrical contraction factor of a nozzle throat.
J_n Bessel function of the first kind of order n.
M_∞ free-stream Mach number.
p perturbation pressure.

$\tilde{p}$ dimensional pressure.
u x direction perturbation velocity.
$\tilde{u}$ x direction dimensional velocity.
u' x direction nondimensional perturbation velocity.
U_∞ x direction free-stream velocity.
v y direction perturbation velocity.
$\tilde{v}$ y direction dimensional velocity.
v' y direction nondimensional perturbation velocity.
$\mathbf{V}_\infty$ free-stream velocity vector.
w z direction perturbation velocity.
$\tilde{w}$ z direction dimensional velocity.
y_t radius of a nozzle throat.

Greek Letters

α linear axial perturbation velocity gradient for a nozzle.
δ 0 for planar flow, 1 for axisymmetric flow.
ϵ axial location of the sonic point in a nozzle.
ρ perturbation density.
$\tilde{\rho}$ dimensional density.
ρ_t radius of curvature of a nozzle throat.
ϕ' nondimensional perturbation velocity potential.
Φ velocity potential.

Subscripts

∞ denotes free-stream value of a property.

Other

∇^2 Laplacian operator,

$$\text{Cartesian coordinates:} \quad \nabla^2 = \frac{\partial^2}{\partial x^2} + \frac{\partial^2}{\partial y^2} + \frac{\partial^2}{\partial z^2}$$

$$\text{Cylindrical coordinates:} \quad \nabla^2 = \frac{\partial^2}{\partial r^2} + \frac{1}{r}\frac{\partial}{\partial r} + \frac{1}{r^2}\frac{\partial^2}{\partial \theta^2} + \frac{\partial^2}{\partial z^2}$$

15–2 INTRODUCTION

For a stationary gas or a flowing gas having a velocity that deviates only slightly from parallel uniform flow, the method of *small perturbations* may be employed for linearizing the governing nonlinear partial differential equations. The method of small perturbations is introduced in Chapter 11, where it is applied to a planar acoustic wave and to the flow over a wavy wall.

In this chapter, the method of small perturbations is applied to three-dimensional acoustic wave motion and to the steady two-dimensional irrotational transonic flow in the throat region of a converging-diverging nozzle.

15–3 THE THREE-DIMENSIONAL WAVE EQUATION

The propagation of a small planar pressure disturbance in a stationary gas is governed by the *one-dimensional wave equation* that is derived in Section 11–3 (see equation 11.17). In the derivation of that equation it is assumed that the pressure

disturbance is very small, that the process is isentropic, and that the velocity and its derivatives are small compared to the speed of sound in the undisturbed gas. The same assumptions are applicable to the propagation of a small pressure disturbance in a three-dimensional region; the governing partial differential equation in that case is called the *three-dimensional wave equation.*

For the isentropic flow under consideration, the continuity, momentum, and speed of sound equations are the following.

1. *Continuity equation* (equation 10.1)

$$\tilde{\rho}_t + \nabla \cdot (\tilde{\rho}\mathbf{V}) = 0 \tag{15.1}$$

2. *Momentum equation* (equation 10.8)

$$\tilde{\rho}\frac{D\mathbf{V}}{Dt} + \nabla\tilde{p} = 0 \tag{15.2}$$

3. *Speed-of-sound equation* (equation 10.124)

$$\frac{D\tilde{p}}{Dt} - \tilde{a}^2\frac{D\tilde{\rho}}{Dt} = 0 \tag{15.3}$$

Combining equations 15.1 and 15.3, we obtain

$$\tilde{\rho}\tilde{a}^2\nabla \cdot \mathbf{V} + \frac{D\tilde{p}}{Dt} = 0 \tag{15.4}$$

In equations 15.1 to 15.4 the *tilde* over a letter denotes that it is a *dimensional* flow property ($\tilde{\rho}$, $\tilde{p}$, $\tilde{u}$, etc.). A letter without the tilde denotes a *perturbation* or *disturbance* in the pertinent flow property (ρ, p, u, etc.). *By definition*

$$\tilde{u} = u \qquad \tilde{v} = v \qquad \tilde{w} = w \tag{15.5a}$$

$$\tilde{p} = p_\infty + p \tag{15.5b}$$

$$\tilde{\rho} = \rho_\infty + \rho \tag{15.5c}$$

$$\tilde{a} = a_\infty + a \tag{15.5d}$$

where $u_\infty = v_\infty = w_\infty = 0$, u, v, and w are very small, and p, ρ, and a are much smaller than the corresponding undisturbed values p_∞, ρ_∞, and a_∞, respectively.

Following the procedure presented in Section 11–3(a), the following set of four linearized equations are obtained for the propagation of a small pressure disturbance in a stationary gas in a three-dimensional region.

$$\rho_\infty a_\infty^2(u_x + v_y + w_z) + p_t = 0 \tag{15.6}$$

$$\rho_\infty u_t + p_x = 0 \tag{15.7}$$

$$\rho_\infty v_t + p_y = 0 \tag{15.8}$$

$$\rho_\infty w_t + p_z = 0 \tag{15.9}$$

Assume that the second derivatives are continuous and differentiate equations 15.6 to 15.9 with respect to t, x, y, and z, respectively. By combining the results and

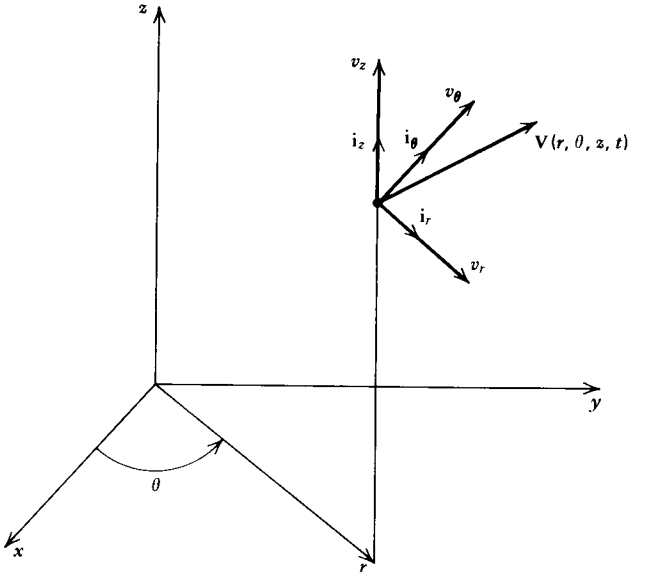

Figure 15.1 The cylindrical coordinate system.

eliminating the partial derivatives u_{xt}, v_{yt}, and w_{zt}, we obtain the following *three-dimensional wave equation.*

$$p_{tt} = a_\infty{}^2(p_{xx} + p_{yy} + p_{zz}) = a_\infty{}^2 \nabla^2 p \tag{15.10}$$

where ∇^2 denotes the *Laplacian* operator.

The three-dimensional wave equation may be expressed in any coordinate system by expressing the Laplacian operator in that coordinate system. For example, if a cylindrical coordinate system is employed with r, θ, and z as the coordinates (see Fig. 15.1), equation 15.10 becomes

$$p_{tt} = a_\infty{}^2\left(p_{rr} + \frac{1}{r}p_r + \frac{1}{r^2}p_{\theta\theta} + p_{zz}\right) \tag{15.11}$$

The three-dimensional wave equation has the same general features as the one-dimensional wave equation. Equation 15.10 (and its equivalent, equation 15.11) is linear, so that the superposition of solutions is permissible. Consequently, the waves that may be propagating in all three coordinate directions simultaneously may be superimposed for obtaining the distributions of the fluid properties in the flow field.

15–4 WAVE PROPAGATION IN A CYLINDRICAL CAVITY

The D'Alembert solution of the one-dimensional wave equation is presented in Section 11–3(b). The general solution of the three-dimensional wave equation for the acoustic oscillations in a cylindrical acoustical cavity is presented in this section.

15–4(a) General Solution of the Three-Dimensional Wave Equation

The problem of determining the modes of oscillation and their corresponding frequencies due to small pressure disturbances of a gas in a cylindrical cavity,

illustrated in Fig. 15.2, is of both theoretical and practical interest. Because the amplitudes of the pressure oscillations are assumed to be very small, comparable to those of sound waves, the cylindrical cavity where the oscillations occur is termed a *cylindrical acoustical cavity*, and the oscillations are termed *acoustical oscillations*. A cylindrical coordinate system is employed in the analysis (see Fig. 15.1) in which the z axis coincides with the longitudinal axis of the cylindrical acoustical cavity. It is assumed that all gas motions in the cavity are isentropic and that the perturbations in the fluid properties, ρ, p, u, and so on, are very small. Hence, equation 15.11 governs the motion of the gas.

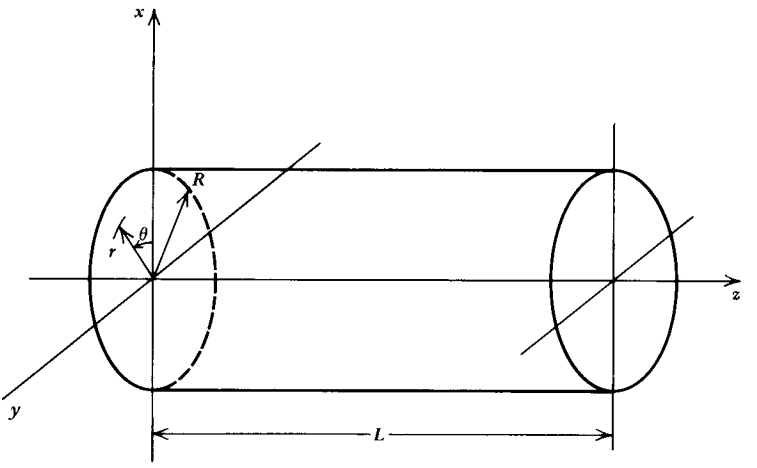

Figure 15.2 Coordinate system and geometry for a right circular cylinder.

To obtain the *general solution* of equation 15.11, the method of separation of variables is employed [see Section 11-5(a)]. It is assumed, therefore, that the general solution may be expressed as the product of four independent complex-valued functions of the variables r, θ, z, and t. Thus,

$$p(r,\theta,z,t) = R(r)\Theta(\theta)Z(z)T(t) \tag{15.12}$$

Substituting equation 15.12 into equation 15.11, dividing the result by $R\Theta ZT$, and letting the *prime* superscript $(\,)'$ denote the derivative of a function with respect to its argument (e.g., $T'' = d^2T(t)/dt^2$), we obtain

$$\frac{T''}{a_\infty{}^2 T} = \frac{Z''}{Z} + \frac{R''}{R} + \frac{1}{r}\frac{R'}{R} + \frac{1}{r^2}\frac{\Theta''}{\Theta} \tag{15.13}$$

The right-hand side of equation 15.13 is independent of the variable t, while the left-hand side is independent of the variables z, r, and θ. Since the two sides equal each other, they must be equal to the same constant, which is denoted by $-\lambda^2$. Physical considerations indicate that the solution values for the fluid properties cannot *increase* exponentially, hence, the negative sign preceding λ^2. Accordingly, the left-hand side of equation 15.13 may be written in the form

$$T'' + \lambda^2 a_\infty{}^2 T = 0 \tag{15.14}$$

In like manner the right-hand side of equation 15.13 becomes

$$-\frac{Z''}{Z}=\frac{R''}{R}+\frac{1}{r}\frac{R'}{R}+\frac{1}{r^2}\frac{\Theta''}{\Theta}+\lambda^2 \tag{15.15}$$

In equation 15.15, each side must be equal to the same constant, which is denoted by ϕ^2. Hence,

$$Z''+\phi^2 Z=0 \tag{15.16}$$

and

$$\frac{R''}{R}+\frac{1}{r}\frac{R'}{R}+\frac{1}{r^2}\frac{\Theta''}{\Theta}=\phi^2-\lambda^2=-\sigma^2 \tag{15.17}$$

Hence,

$$-\frac{\Theta''}{\Theta}=r^2\frac{R''}{R}+r\frac{R'}{R}+\sigma^2 r^2 \tag{15.18}$$

Let γ^2 denote the constant that is equal to each side of equation 15.18. Then we obtain

$$\Theta''+\gamma^2\Theta=0 \tag{15.19}$$

and

$$r^2R''+rR'+(\sigma^2r^2-\gamma^2)R=0 \tag{15.20}$$

Summarizing, four ordinary differential equations have been derived that replace the three-dimensional wave equation (equation 15.11) for a cylindrical acoustical cavity. For convenience of reference, the four ordinary differential equations are assembled in Table 15.1.

Table 15.1 Ordinary Differential Equations Obtained from the Three-Dimensional Wave Equation by the Separation of Variables

General form of the solution

$$p(r,\theta,z,t)=R(r)\Theta(\theta)Z(z)T(t) \tag{15.12}$$

Ordinary differential equations

$$T''+\lambda^2 a_\infty{}^2T=0 \tag{15.14}$$
$$Z''+\phi^2Z=0 \tag{15.16}$$
$$\Theta''+\gamma^2\Theta=0 \tag{15.19}$$
$$r^2R''+rR'+(\sigma^2r^2-\gamma^2)R=0 \tag{15.20}$$

Relationship between separation constants

$$\lambda^2=\phi^2+\sigma^2 \tag{15.21}$$

15-4(b) General Solutions of the Ordinary Differential Equations

In this section the general solutions are derived for each of the ordinary differential equations presented in Table 15.1.

1. *Solution of equation* 15.14. The general solution is

$$T(t) = G\exp(ia_\infty \lambda t) + H\exp(-ia_\infty \lambda t) \tag{15.22}$$

where $i = \sqrt{-1}$.

2. *Solution of equation* 15.16. The general solution is

$$Z(z) = E\exp(i\phi z) + F\exp(-i\phi z) \tag{15.23}$$

3. *Solution of equation* 15.19. The general solution is

$$\Theta = C\exp(i\gamma\theta) + D\exp(-i\gamma\theta) \tag{15.24}$$

4. *Solution of equation* 15.20. Equation 15.20 may be rewritten as follows.

$$r^2\frac{d^2R}{dr^2} + r\frac{dR}{dr} + (\sigma^2 r^2 - n^2)R = 0 \tag{15.25}$$

The above equation is known as *Bessel's differential equation*. To every value of the parameter n there is associated two linearly independent solutions, each of which is known as a *Bessel function of order n*. One such solution is finite at $r=0$, and is termed the *Bessel function of the first kind*; it is denoted by $J_n(r)$. The other solution is known as the *Bessel function of the second kind*, which is denoted by $Y_n(r)$. It is infinite at $r=0$. For additional information on Bessel functions, see References 1 to 3.

Accordingly, the general solution of equation 15.25 is given by

$$R(r) = AJ_n(\sigma r) + BY_n(\sigma r) \tag{15.26}$$

where A and B are constants of integration.

The general solution, equation 15.12, is subject to the restriction imposed by the following relationship between the constants λ, ϕ, and σ (see equation 15.21). Thus,

$$\lambda^2 = \phi^2 + \sigma^2 \tag{15.27}$$

There is no loss of generality for a cylindrical cavity if the parameters λ, ϕ, and σ are redefined as follows.

$$\lambda = \omega / a_\infty \tag{15.28}$$

$$\sigma = \alpha / R \tag{15.29}$$

$$\phi = \xi / L \tag{15.30}$$

where

ξ = a constant characteristic of the axial oscillations.
ω = the frequency of the oscillations in the cavity.
a_∞ = the acoustic speed in the undisturbed gas.
R = the radius of the cylinder.
L = the length of the cylinder.

Hence, the general solution equations for a cylindrical cavity of radius R and length L must satisfy at all times the following relationship, based on equation 15.27. Thus,

$$\frac{\omega^2}{a_\infty{}^2} = \frac{\alpha^2}{R^2} + \frac{\xi^2}{L^2} \tag{15.31}$$

The set of equations 15.22 to 15.24 and 15.26 constitutes the general solution of the three-dimensional wave equation, equation 15.11. Reference to Table 15.2 shows that the general solution contains eight arbitrary constants; that is, A, B, C, D, E, F G and H. To obtain the solution for a specific cylindrical configuration, the additional restrictions imposed by the initial and boundary conditions must be taken into account.

Table 15.2 General Solutions to the Differential Equations for the Flow Field of a Cylindrical Acoustical Cavity

Solutions to the differential equations

$$T(t) = G\exp(i\omega t) + H\exp(-i\omega t) \tag{15.22}$$

$$Z(z) = E\exp\left(\frac{i\xi z}{L}\right) + F\exp\left(-\frac{i\xi z}{L}\right) \tag{15.23}$$

$$\Theta(\theta) = C\exp(i\gamma\theta) + D\exp(-i\gamma\theta) \tag{15.24}$$

$$R(r) = AJ_n\left(\frac{\alpha r}{R}\right) + BY_n\left(\frac{\alpha r}{R}\right) \tag{15.26}$$

Relationships between λ, σ, *and* ϕ

$$\lambda = \omega / a_\infty \tag{15.28}$$

$$\sigma = \alpha / R \tag{15.29}$$

$$\phi = \xi / L \tag{15.30}$$

$$\frac{\omega^2}{a_\infty{}^2} = \frac{\alpha^2}{R^2} + \frac{\xi^2}{L^2} \tag{15.31}$$

15-4(c) Application of the Boundary Conditions

The cylindrical cavity having the simplest boundary conditions is a hollow rigid cylinder that is closed at each end by a rigid wall perpendicular to the z axis, as illustrated in Fig. 15.2. The pertinent boundary conditions for such a cavity are as follows.

1. The velocity of the contained gas is zero in the directions normal to each solid boundary. Hence, at the radius $r = R$, the velocity component $v_r = 0$, and at $z = 0$ and $z = L$, the velocity component $v_z = 0$.
2. The function $p(r,\theta,z,t)$ is finite for all values of r, θ, z, and t.
3. The solution is periodic in θ, with a period of 2π.

The restriction imposed by boundary condition 1 is determined by applying the momentum equation (equation 15.2) in the r and z directions, introducing the assumption of small perturbations, and applying boundary condition 1. For the r direction, we obtain

$$\tilde{\rho}\left(\frac{\partial \tilde{v}_r}{\partial t} + \tilde{v}_r\frac{\partial \tilde{v}_r}{\partial r} + \frac{\tilde{v}_\theta}{r}\frac{\partial \tilde{v}_r}{\partial \theta} - \frac{\tilde{v}_\theta{}^2}{r} + \tilde{v}_z\frac{\partial \tilde{v}_r}{\partial z}\right) = -\frac{\partial \tilde{p}}{\partial r} \tag{15.32}$$

For the z direction, we obtain

$$\tilde{\rho}\left(\frac{\partial \tilde{v}_z}{\partial t} + \tilde{v}_r\frac{\partial \tilde{v}_z}{\partial r} + \frac{\tilde{v}_\theta}{r}\frac{\partial \tilde{v}_z}{\partial \theta} + \tilde{v}_z\frac{\partial \tilde{v}_z}{\partial z}\right) = -\frac{\partial \tilde{p}}{\partial z} \tag{15.33}$$

Introducing the assumption of small perturbations (see equation 15.5) into equations 15.32 and 15.33, we obtain

$$\frac{\partial p}{\partial r} = -\rho_\infty \frac{\partial v_r}{\partial t} \tag{15.34}$$

$$\frac{\partial p}{\partial z} = -\rho_\infty \frac{\partial v_z}{\partial t} \tag{15.35}$$

Applying the boundary conditions $\partial v_r/\partial t = 0$ at $r = R$ and $\partial v_z/\partial t = 0$ at $z = 0$ and $z = L$, yields $\partial p/\partial r = \partial p/\partial z = 0$ at those locations. Hence, the derivatives of the functions $R(r)$ and $Z(z)$ are zero at those locations.

$$\frac{\partial}{\partial r}\left[R(r)\right]_{r=R} = 0 \qquad \frac{\partial}{\partial z}\left[Z(z)\right]_{z=0} = 0 \qquad \frac{\partial}{\partial z}\left[Z(z)\right]_{z=L} = 0 \tag{15.36}$$

Now consider boundary condition 2, and refer to equation 15.26, Table 15.2. At $r = 0$, the Bessel function $Y_n(\alpha r/R) = -\infty$, which does not satisfy boundary condition 2. Consequently, the coefficient B in equation 15.26 must be assigned the value zero, and equation 15.26 reduces to

$$R(r) = AJ_n\left(\frac{\alpha r}{R}\right) \tag{15.37}$$

Differentiating equation 15.37 with respect to r, and noting from equation 15.36 that $dR(r)/dr = 0$ at $r = R$, we obtain

$$J_n'(\alpha) = 0 \tag{15.38}$$

where $J_n' = \partial J_n/\partial r$. Equation 15.38 has an infinite number of possible solutions (see References 1–3) that may be designated by α'_{mn}, where α'_{mn} is the $(m+1)$ root of $J_n'(r)$. To facilitate calculations, let

$$\pi\alpha_{mn} = \alpha'_{mn} \tag{15.39}$$

Hence, α_{mn} represents the roots of the equation

$$J_n'(\pi\alpha_{mn}) = 0 \tag{15.40}$$

Equation 15.37 may be replaced by

$$R(r) = AJ_n\left(\frac{\pi\alpha_{mn} r}{R}\right) \tag{15.41}$$

The roots of equation 15.40 were obtained by Converse and Hoffman[4] by applying the *half-interval method*[5] for determining the roots of nonlinear equations. The roots of equation 15.40 for m and n ranging from 0 to 4 are presented in Table 15.3.

The values of the constants in equation 15.23 (see Table 15.3) are now determined. Differentiating equation 15.23 with respect to z yields

$$\frac{\partial}{\partial z}\left[Z(z)\right] = E\left(i\frac{\xi}{L}\right)\exp\left(i\frac{\xi z}{L}\right) + F\left(-i\frac{\xi}{L}\right)\exp\left(-i\frac{\xi z}{L}\right) \tag{15.42}$$

But, from equation 15.36, $\partial Z(z)/\partial z = 0$ at $z = 0$ and at $z = L$. Substituting that result for $z = 0$ into equation 15.42 shows that $E = F$. Substituting the result for

Table 15.3 Values of α_{mn}

n \ m	0	1	2	3	4
0	0.000	1.220	2.333	3.238	4.241
1	0.586	1.697	2.717	3.726	4.731
2	0.972	2.135	3.173	4.192	5.204
3	1.337	2.551	3.612	4.643	5.662
4	1.693	2.995	4.037	5.082	6.110

(Taken from Reference 4.)

$z = L$ into equation 15.42, we obtain

$$\exp(i\xi) - \exp(-i\xi) = 2\sinh(i\xi) = 2i\sin\xi = 0 \tag{15.43}$$

For equation 15.43 to be satisfied, it is required that

$$\xi = \pi q \qquad (q = 0, 1, 2\ldots) \tag{15.44}$$

Substituting $E = F$ and $\xi = \pi q$ into equation 15.23 (see Table 15.2) yields

$$Z(z) = E\left[\exp\left(\frac{i\pi qz}{L}\right) + \exp\left(-\frac{i\pi qz}{L}\right)\right] \tag{15.45}$$

The expression in the square brackets is equal to $2\cos(\pi qz/L)$. Hence, equation 15.45 becomes

$$Z(z) = 2E\cos\left(\frac{\pi qz}{L}\right) = E'\cos\left(\frac{\pi qz}{L}\right) \tag{15.46}$$

The *circular frequency* f (rev/time) is related to the *angular frequency* ω (rad/time) by the relationship

$$\omega = 2\pi f \qquad \text{or} \qquad f = \frac{\omega}{2\pi} \tag{15.47}$$

Boundary condition 3 requires that equation 15.24 (see Table 15.2) be periodic with a period of 2π to satisfy the physical periodicity of the gas pressure in the closed cylindrical cavity. Hence,

$$\Theta(\theta) = \Theta(\theta + 2\pi k) \qquad (\text{where } k = 0, 1, 2\ldots) \tag{15.48}$$

Another condition imposed on the solution equation is, as mentioned earlier, that equation 15.31 (see Table 15.2) be satisfied under all conditions. Substituting equations 15.39, 15.44, and 15.47 into equation 15.31 and solving for $f_{m,n,q}$, the circular frequency of the oscillation, yields

$$f_{m,n,q} = \frac{a_\infty}{2}\left[\left(\frac{\alpha_{mn}}{R}\right)^2 + \left(\frac{q}{L}\right)^2\right]^{1/2} \tag{15.49}$$

where a_∞ is the acoustic speed in the undisturbed gas, and the subscripts m, n, and q are termed *wave numbers*; the latter are related to the modes of the acoustic oscillations in the closed cylindrical cavity (see Table 15.4). The frequencies of the

particular modes of the acoustic oscillations may be computed by employing equation 15.49.

Table 15.4 Relationships Between the Wave Numbers and the Acoustical Oscillation Modes for a Closed Cylindrical Cavity

Wave Number			Mode of Oscillation
m	n	q	
m	0	0	Radial
0	n	0	Tangential
0	0	q	Longitudinal (axial)
m	n	q	Combination

15–4(d) Modes of Acoustical Oscillation for a Closed Cylindrical Cavity

Any positive integer or zero may be chosen for any of the wave numbers m, n, and q. When two of the wave numbers are zero, the oscillation mode corresponding to the remaining wave number is termed a *pure mode*. If $m=n=0$ but $q\neq 0$, the oscillation mode is termed an *axial* or *longitudinal mode*; it is also called an *organ pipe mode*. Modes for which $n=q=0$ but $m\neq 0$ are termed *radial modes*, and those for which $m=q=0$ but $n\neq 0$ are called *tangential modes*. Modes corresponding to a combination of two or three wave numbers are termed *combination modes*. Modes having a wave number of unity are termed either *fundamental modes* or *first harmonic modes*. Modes for which the wave numbers are larger than unity are termed either *overtones* or *higher harmonics*. Table 15.4 presents the relationships between the wave numbers and the acoustical oscillation modes for a closed cylindrical cavity.

In the idealized case for which equation 15.11 is applicable, all of the modes listed in Table 15.4 may exist simultaneously and independently. The acoustical behavior of the closed cylindrical cavity is then expressed as the sum of all of the possible acoustical modes.

The general solution for the pressure distribution (equation 15.12, Table 15.1) may be obtained by substituting in equation 15.12 the expressions that have been derived for each of the functions on the right-hand side of that equation; that is, equations 15.22, 15.24, 15.41, and 15.46. The result is

$$p(r,\theta,z,t)=\sum_{m,n,q} AJ_n\left(\frac{\pi\alpha_{mn}r}{R}\right)\left[C\exp(in\theta)+D\exp(-in\theta)\right]$$

$$\times\left[E'\cos\left(\frac{\pi qz}{L}\right)\right]\left[G\exp(i\omega t)+H\exp(-i\omega t)\right] \qquad (15.50)$$

The *acoustic pressure* $p(r,\theta,z,t)$ is always a real quantity and may be determined, therefore, from the real part of equation 15.50. The solution was first obtained by Rayleigh.[6] It is presented below in a slightly rearranged form. Thus,

$$p(r,\theta,z,t)=\sum_{m,n,q}\left[J_n\left(\frac{\pi\alpha_{mn}r}{R}\right)\cos\left(\frac{\pi qz}{L}\right)\right]\left(\bar{A}\cos n\theta\cos\omega t\right.$$

$$\left.+\bar{B}\cos n\theta\sin\omega t+\bar{C}\sin n\theta\cos\omega t+\bar{D}\sin n\theta\sin\omega t\right) \qquad (15.51)$$

In equation 15.51, $p(r,\theta,z,t)$ gives the difference between the unsteady local pressure and the undisturbed pressure p_∞ at any point in a closed cylindrical cavity, and $\bar{A}$, $\bar{B}$, $\bar{C}$, and $\bar{D}$ denote real independent constants that are related to the complex constants appearing in equation 15.50. To determine those constants, the following *initial condition* (at time $t=0$) is applied to the *acoustic pressure*. Thus,

$$p(r,\theta,z,0)=f(r,\theta,z) \tag{15.52}$$

The function $f(r,\theta,z)$ defines the distribution of the gas pressure in the closed cylindrical cavity at the time $t=0$.

Equation 15.51 may be rearranged in the following more convenient form. Thus,

$$p(r,\theta,z,t)=\sum_{m,n,q}\left[J_n\left(\frac{\pi\alpha_{mn}r}{R}\right)\cos\left(\frac{\pi qz}{L}\right)\right]\left[M\cos(n\theta+\omega t-\delta_1)\right.$$

$$\left.+N\cos(n\theta-\omega t-\delta_2)\right] \tag{15.53}$$

where M and N are arbitrary independent amplitude constants, and δ_1 and δ_2 are arbitrary independent phase angles. The constants in equation 15.53 are related to those in equation 15.51 by the following relationships.

$$\bar{A}=M\cos\delta_1+N\cos\delta_2 \tag{15.54a}$$

$$\bar{B}=M\sin\delta_1-N\sin\delta_2 \tag{15.54b}$$

$$\bar{C}=M\sin\delta_1+N\sin\delta_2 \tag{15.54c}$$

$$\bar{D}=-M\cos\delta_1+N\cos\delta_2 \tag{15.54d}$$

Expressions for the velocity and the displacement of the gas may be obtained by integrating the vector form of the momentum equation (equation 15.2) for the case of small perturbations. The momentum equation in terms of the perturbed quantities is

$$\rho_\infty\frac{\partial\mathbf{V}}{\partial t}=-\nabla p \tag{15.55}$$

Integrating equation 15.55 yields

$$\mathbf{V}=-\frac{1}{\rho_\infty}\int_0^t\nabla p\,dt+C_1 \tag{15.56}$$

Equation 15.56 is the expression for the vector velocity of a gas particle inside of the cavity. If the average velocity inside of the cavity is assumed to be zero, then $C_1=0$. Let $\mathbf{s}$ denote the displacement of a gas particle from its mean position. Then the instantaneous velocity of the particle is

$$\mathbf{V}=\frac{d\mathbf{s}}{dt} \tag{15.57}$$

Integrating equation 15.57 gives

$$\mathbf{s}=\int_0^t\mathbf{V}\,dt+C_2 \tag{15.58}$$

Again, the integration constant C_2 may be chosen as zero.

Equation 15.53 indicates that the general wave motion inside of a rigid closed cylindrical cavity consists of standing radial and longitudinal modes, and two tangential modes of arbitrary relative amplitudes and phase angles that rotate in opposite directions (see Table 15.4). The restriction to standing waves in the radial and longitudinal directions is caused by the rigid reflecting boundaries normal to those directions. In the tangential direction, however, there are no reflecting boundaries so that a traveling tangential mode is always a distinct possibility.

A *standing wave* may be represented by two traveling waves of equal amplitude moving in opposite directions. On the other hand, a *traveling wave* may be represented as the sum of two standing waves having identical amplitudes but the waves are displaced relative to each other by one quarter of a cycle in time and one quarter of a wavelength in space.

The pure *tangential mode* has several noteworthy features. If either M or N (in equation 15.53) equals zero, then there is a tangential wave ($n \neq 0$) traveling in the circumferential direction. The frequency of that wave is $1/n$ times the frequency computed from equation 15.49 for a pure tangential wave. Consequently, the wave rotates around the inside of the cylinder so that there are rotating regions of high and low gas pressure acting on the cylinder wall. When the amplitude constants M and N are related so that $M = N$ or $M = -N$, and the phase angles $\delta_1 = \delta_2$, a standing tangential wave is formed. In that case, there are *nodal diameters* formed along which the gas pressure is invariant with time. In general, when $M \neq N$ there is no simple relationship for describing the mode of oscillation.

Figure 15.3*a* illustrates schematically the fundamental longitudinal mode of oscillation ($q = 1$) for a closed cylindrical cavity, Fig. 15.3*b* illustrates the radial mode ($m = 1$), Fig. 15.3*c* illustrates the standing tangential mode ($n = 1$, $M = N$, and $\delta_1 = \delta_2$), and Fig. 15.3*d* illustrates the traveling tangential mode ($n = 1, N = 0$).

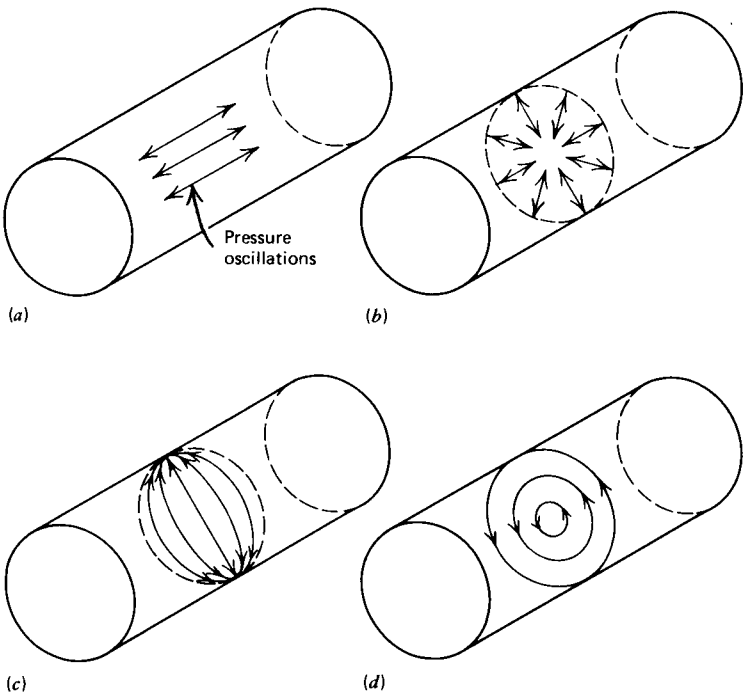

Figure 15.3 Modes of oscillation in a rigid closed cylindrical cavity. (*a*) Longitudinal mode. (*b*) Radial mode. (*c*) Standing tangential mode. (*d*) Traveling tangential mode.

Figure 15.4 illustrates schematically the envelope of the static pressures for several longitudinal modes of the acoustical oscillations in a closed cylindrical cavity: (a) the fundamental mode, $q=1$ (first harmonic), (b) the first overtone mode, $q=2$ (second harmonic), and (c) the second overtone mode, $q=3$ (third harmonic).

Figure 15.5 illustrates schematically the static pressure distributions for two different radial acoustic modes of oscillation: (a) the first radial mode, $m=1$, and (b) the second radial mode, $m=2$.

Figure 15.6 illustrates diagrammatically three different tangential modes of acoustical oscillation: (a) the first standing tangential mode ($n=1$, $M=N$, and $\delta_1=\delta_2$), (b) the second standing tangential mode ($n=2$, $M=N$, and $\delta_1=\delta_2$), and (c) the first traveling tangential mode ($n=1, N=0$).

Figure 15.7 illustrates diagrammatically the acoustic pressure distribution in the closed cylindrical cavity at different times, in terms of ωt, for the fundamental standing tangential mode of acoustic oscillation. Figure 15.8 presents the corre-

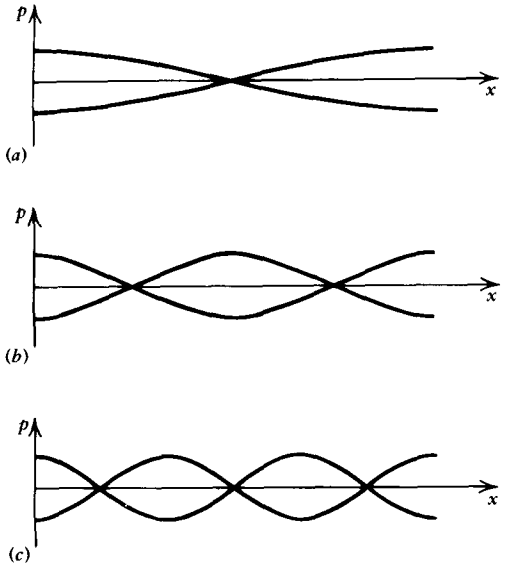

Figure 15.4 Longitudinal modes of oscillation in a closed cylindrical cavity. (*a*) Fundamental (first harmonic) mode, $q=1$. (*b*) First overtone (second harmonic) mode, $q=2$. (*c*) Second overtone (third harmonic) mode, $q=3$.

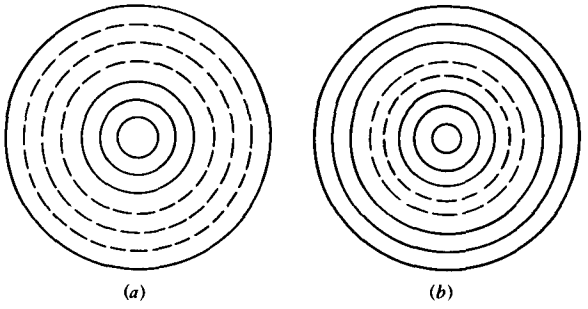

Figure 15.5 Radial modes of oscillation in a closed cylindrical cavity. (*a*) First radial mode, $m=1$. (*b*) Second radial mode, $m=2$.

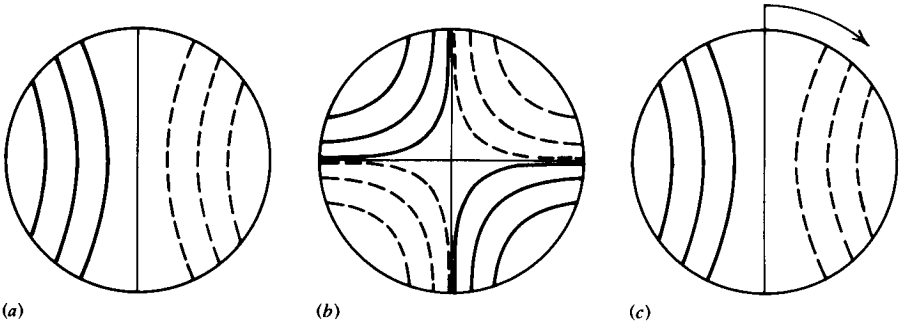

Figure 15.6 Tangential modes of oscillation in a closed cylindrical cavity. (*a*) First standing tangential mode ($n=1$, $M=N$, and $\delta_1=\delta_2$). (*b*) Second standing tangential mode ($n=2$, $M=N$, and $\delta_1=\delta_2$). (*c*) First traveling tangential mode ($n=1, N=0$).

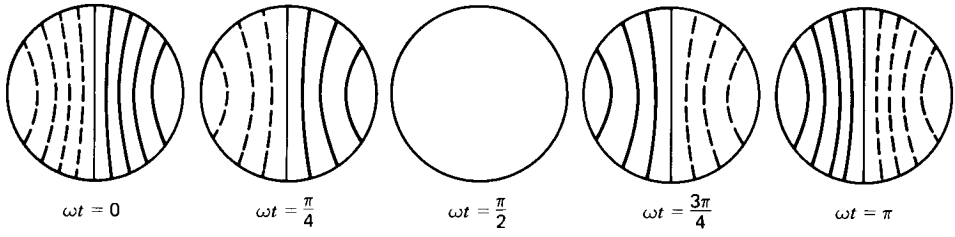

Figure 15.7 Acoustic pressure distributions at different values of ωt for the fundamental standing tangential mode of oscillation in a closed cylindrical cavity.

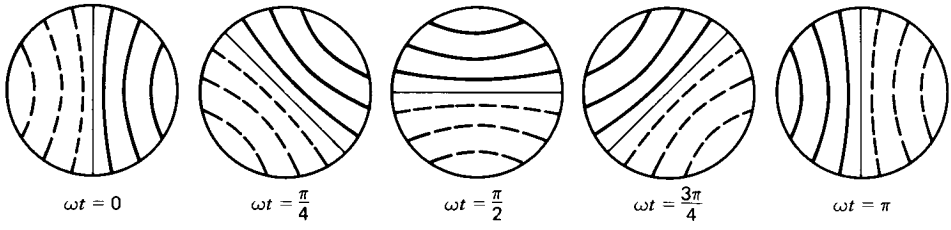

Figure 15.8 Acoustic pressure distributions at different values of ωt for the fundamental traveling tangential mode of oscillation in a closed cylindrical cavity.

sponding information for the fundamental traveling tangential mode of acoustic oscillation.

The results presented in the present section dealing with the acoustic oscillations in a closed cylindrical cavity (see Fig. 15.2) are an illustration of the application of the method of small perturbations to a gas contained in a cavity of a rather simple geometry. Analytical solutions for more complicated geometries may not be feasible so that an experimental solution of the problem may be the only practical procedure.

15–4(e) Combustion Instability in Rocket Motors[7–12]

Equation 15.53 is applicable in the case of small amplitude acoustical pressure oscillations for a gas contained in a closed cylindrical cavity, and equation 15.49 applies to the frequencies of such oscillations. Nevertheless, it has been demon-

strated experimentally that those same equations are applicable to some of the phenomena pertinent to the high frequency combustion pressure oscillations, termed *combustion instability*, *acoustic instability*, or *sonant burning*, observed in rocket motors, despite the fact that the amplitudes of those pressure oscillations may be very large; especially when compared to the amplitudes of acoustic waves.

Figure 15.9*a* illustrates schematically a longitudinal cross-section through a solid propellant rocket motor containing a cylindrical perforated propellant grain. The combustion region is between $z=0$ and $z=L$, and takes place on the inner cylindrical surface of the grain; that is, at $r=R$. Reference 7 presents the results of a large number of experimental firings with rocket motors of that general design.

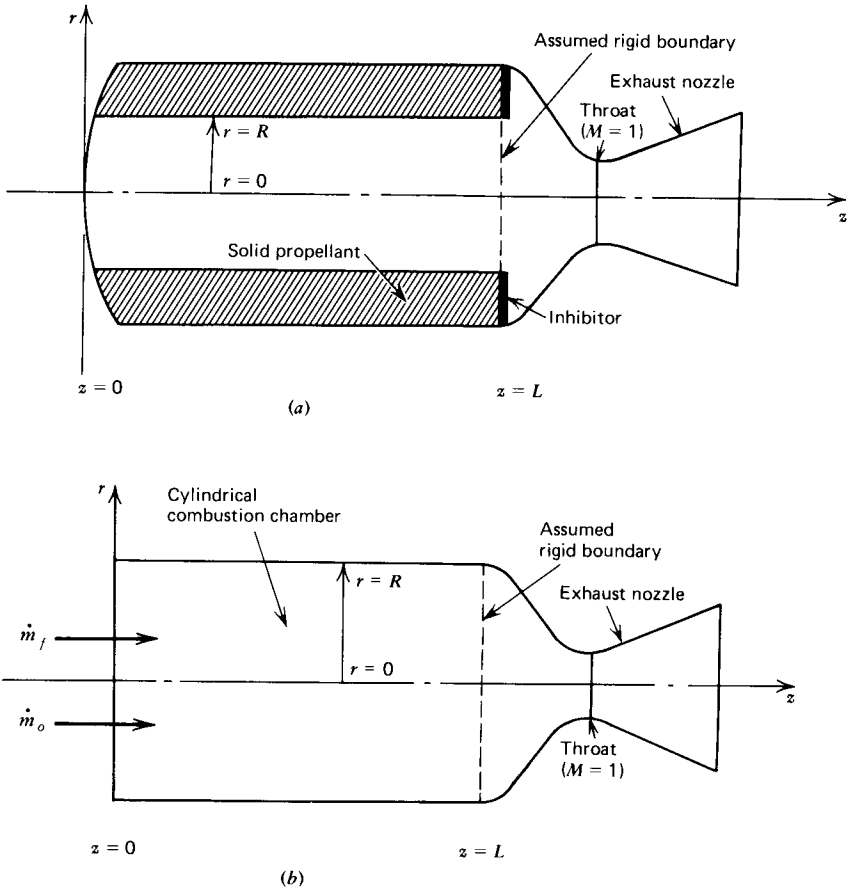

Figure 15.9 Schematic illustrations of a solid propellant and a liquid bipropellant rocket motor. (*a*) A radial burning perforated cylindrical solid propellant grain. (*b*) A liquid bipropellant rocket motor.

The rocket motors were equipped with high-frequency-response pressure measuring instruments that were arranged so that the oscillation modes inside the cylindrical cavity could be identified and their frequencies measured during sonant burning or acoustic instability conditions. Some manifestations of the occurrence of combustion instability are: (a) high-frequency large amplitude pressure oscillations, (b) high rates of heat transfer to metal parts, and (c) the relatively smooth increase in combustion pressure oscillations to very high and even destructive pressure levels. Consequently, the occurrence of combustion or acoustic instability is readily recognizable.

From an analytic standpoint, it was assumed that the cylindrical surface of the propellant grain and the nozzle end of the rocket motor behave as rigid boundaries, so that the physical model is identical with Fig. 15.2. Equation 15.11 was assumed to be the wave equation for the solid-propellant rocket motor, equation 15.53 (or its equivalent) was employed for identifying oscillation modes, and equation 15.49 was employed for computing their frequencies. The experimental results showed that during sonant burning the oscillation frequencies could be accounted for by equation 15.49; the acoustic speed for the combustion gas, calculated from thermodynamic data, was $a = 3350$ ft/sec (1021.1 m/s). Because combination modes occur, and they may have frequencies not far different from those of pure modes (tangential or longitudinal), it is not possible to identify the exact oscillation mode from frequency measurements alone, or from pressure measurements made at only one location in the cavity in the rocket motor. It is necessary to make relative phase measurements at two or more axial locations so that a pure tangential mode can be distinguished from a combination of axial and tangential modes. It was established that the acoustic oscillation theory based on small perturbations gave results that were in good agreement with the experiments as far as oscillation mode identification and oscillation frequency are concerned, for the large pressure oscillations which occurred during sonant burning.[7]

Figure 15.9*b* illustrates schematically a liquid bipropellant rocket motor burning a fuel and its oxidizer inside a cylindrical combustion chamber. In this case too, the nozzle end of the rocket motor may be assumed to be replaced by a solid boundary, and Fig. 15.2 serves as the model for combustion instability studies. High frequency oscillations, when they occur, are recognized by a loud screaming noise. Hence, the phenomena is often referred to as either *high frequency* or *screaming* combustion. Where the frequencies of the pressure oscillations with screaming combustion have been measured and the modes identified, the measurements are in satisfactory agreement with the calculated values from equations 15.49 and 15.53, respectively (see Reference 8).

Most analytical investigations concerned with the occurrence of screaming combustion or acoustic instability are based on applying the method of small perturbations to the wave equation (equation 15.11). Consequently, the solution equations presented in Table 15.2 are generally obtained. Some investigators may differ in the selection of the boundary conditions at $z = 0$ and $z = L$, but there is more or less general agreement that the combustion instability phenomena arise from the self-excitation of the acoustic oscillation modes of the gas.[9,10] Those acoustic modes and their frequencies may be calculated by the equations derived in the present section.

It is beyond the scope of this book to discuss the different mechanisms (chemical and physical, or both) that have been proposed as being the means whereby the acoustic modes are self-excited into the large amplitude oscillations observed when a rocket motor operates with combustion instability. But there is general agreement that for the mechanism to be valid it must satisfy *Rayleigh's criterion*, which because of its fundamental importance is quoted below.

"If heat be periodically communicated to, and abstraced from, a mass of air vibrating (for example) in a cylinder bounded by a piston, the effect produced will depend on the phase of the vibration at which the transfer of heat takes place. If heat be given to the air at the moment of greatest condensation, or be taken from it at the moment of greatest rarefaction, the vibration is encouraged. On the other hand, if heat be given at the moment of greatest rarefaction, or abstracted at the moment of greatest condensation, the vibration is discouraged" (Reference 6, Vol. 2, p. 226).

Example 15.1. The liquid bipropellant rocket engine illustrated schematically in Fig. 15.9*b* has a length $L = 1.50$ m and a radius $R = 0.60$ m. The combustion gases have the following properties: $\gamma = 1.30$, $R = 460.0$ J/kg-K, and $T = 3000$ K. Determine the acoustical oscillation frequencies of the first three harmonics for each of the pure modes of oscillation for the combustion chamber. Assume that the combustion gases behave as a perfect gas, and that the acoustic properties of the combustion chamber are those of a rigid right circular cylinder of length L and radius R.

Solution

For a perfect gas

$$a_\infty = (\gamma RT)^{1/2} = \left[1.3(460.0)(3000)\right]^{1/2} = 1339.4 \text{ m/s}$$

The circular frequency of oscillation is given by equation 15.49, which is repeated below for convenience.

$$f_{m,n,q} = \frac{a_\infty}{2}\left[\left(\frac{\alpha_{mn}}{R}\right)^2 + \left(\frac{q}{L}\right)^2\right]^{1/2} \tag{15.49}$$

where m, n, and q are the wave numbers defined in Table 15.4, and α_{mn} are the roots of the Bessel function $J_n'(\pi\alpha_{mn}) = 0$ tabulated in Table 15.3. For a pure acoustic mode, only one of the three wave numbers m, n, or q is nonzero.

For a pure longitudinal mode, $m = n = 0$, and

$$f_{0,0,q} = \frac{a_\infty q}{2L} = q\frac{1339.4}{2(1.50)} = 446.47q \quad \text{hertz} \tag{a}$$

where 1 hertz = 1 cycle/sec. For the fundamental mode of oscillation, $q = 1$ (i.e., the first harmonic),

$$f_{0,0,1} = 446.5 \quad \text{hertz}$$

Values of $f_{0,0,q}$ for $q = 1$ to 3 are presented in Table 15.5.

For a pure radial mode, $n = q = 0$, and

$$f_{m,0,0} = \frac{a_\infty \alpha_{m0}}{2R} = \alpha_{m0}\frac{1339.4}{2(0.6)} = 1116.2\alpha_{m0} \quad \text{hertz} \tag{b}$$

For the first harmonic mode of oscillation, $\alpha_{m0} = \alpha_{10} = 1.220$, and

$$f_{1,0,0} = (1116.2)(1.220) = 1361.8 \quad \text{hertz}$$

Values of $f_{m,0,0}$ for $m = 1$ to 3 are presented in Table 15.5.

For the pure standing tangential mode, $m = q = 0$, and

$$f_{0,n,0} = \frac{a_\infty \alpha_{0n}}{2R} = 1116.2\alpha_{0n} \quad \text{hertz} \tag{c}$$

For the first harmonic, $\alpha_{0n} = \alpha_{01} = 0.586$, and

$$f_{0,1,0} = (1116.2)(0.586) = 654.1 \quad \text{hertz}$$

Table 15.5 presents the values of $f_{0,n,0}$ for $n = 1$ to 3.

To obtain a pure traveling tangential mode, $m=q=0$, $M=N$, $\delta_1=\delta_2$, and

$$f_{0,n,0}=\frac{a_\infty \alpha_{0n}}{2Rn}=1116.2\frac{\alpha_{0n}}{n} \quad \text{hertz} \tag{d}$$

For the fundamental pure traveling tangential mode, $n=1$, and

$$f_{0,1,0}=\frac{1116.2(0.586)}{1}=654.1 \quad \text{hertz}$$

which is the same frequency as that obtained for the fundamental pure standing tangential mode. Values of $f_{0,n,0}$ for $n=1$ to 3 for the pure traveling tangential mode are presented in Table 15.5.

Table 15.5 Frequencies of Oscillation of the Pure Acoustic Modes, in Hertz, for Example 15.1

Mode	Harmonic		
	1	2	3
Longitudinal	446.5	892.9	1339.4
Radial	1361.8	2604.1	3614.3
Standing tangential	654.1	1084.9	1492.4
Traveling tangential	654.1	542.5	497.5

15–5 STEADY TWO-DIMENSIONAL TRANSONIC FLOW IN CONVERGING-DIVERGING NOZZLES

The determination of the flow pattern in the *throat region* of a two-dimensional *converging-diverging nozzle* under choked flow conditions may be accomplished by applying small perturbation techniques to the equations governing the choked flow. Small perturbation techniques are meritorious because they make it possible to obtain practical and useful results for a rather difficult flow problem, one that has been studied by a large number of investigators; a few of them are cited in References 13 to 27.

A major source of error in determining the properties of the flow field in the diverging portion of the nozzle, for brevity termed the *divergence*, may be attributed to the approximations employed for determining the properties of the flow field in the neighborhood of the *throat* of the nozzle; that is, in the throat region. The geometry of the throat region is illustrated schematically in Fig. 15.10.

Of the several methods that have been proposed for analyzing the flow field in the throat region of a two-dimensional nozzle, that due to Sauer is the simplest.[13] It is discussed here in some detail with two purposes in mind.

1. To illustrate the application of small perturbation techniques to an important practical flow problem.
2. To present a method for obtaining a reasonable approximation of the flow properties along the *sonic line* in the throat region of a nozzle, and of an initial-value line from which the method of characteristics, discussed in Chapter 16, may be initiated and applied to the supersonic flow field in the divergence.

Although Sauer's method is not the most accurate of the methods given in the references at the end of this chapter, it does have the desirable feature of being a

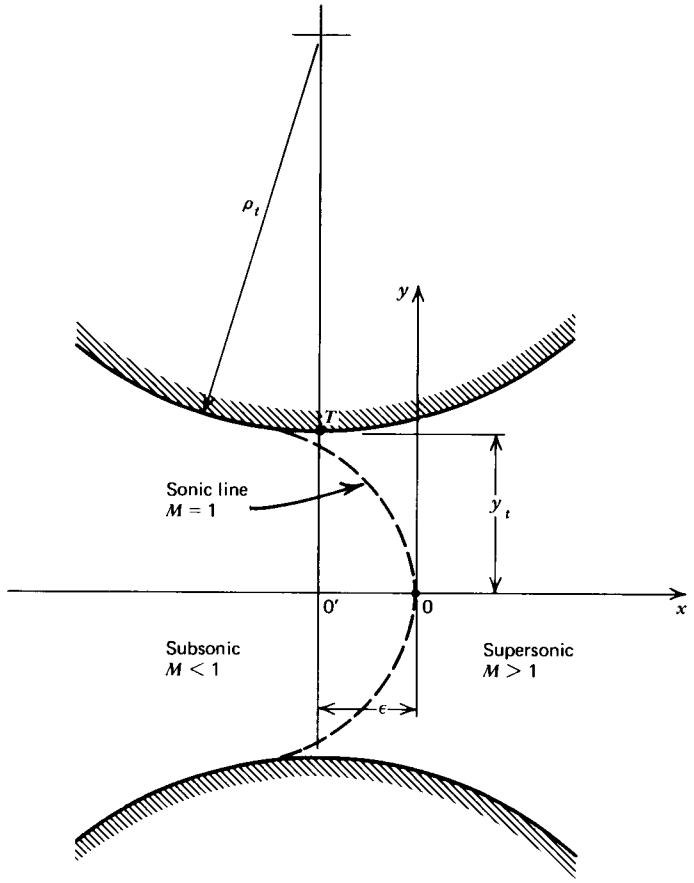

Figure 15.10 Nozzle throat geometry and coordinate system for transonic flow analysis.

closed form solution for the flow field in the nozzle throat region. Furthermore, for a nozzle with a throat having a large *radius of curvature*, denoted by ρ_t, relative to the radius of its throat, denoted by y_t, Sauer's method gives reasonably accurate results; note that the subscript t denotes *throat*, not differentiation with respect to t.

15–5(a) Determination of the Flow Field in the Throat Region

Figure 15.10 illustrates schematically the general features of the throat region of a converging-diverging nozzle. The contour of the nozzle is symmetrical with respect to the x axis, and it is assumed that the fluid flows in the positive direction of the x axis. In the figure it is anticipated that the cross-section of the sonic surface, termed the *sonic line*, is a parabola; it is the locus of all of the points in the flow field where the flow Mach number $M = 1$. It is seen in Fig. 15.10 that the sonic line starts from the wall of the nozzle at a point slightly upstream from the *throat* T, the minimum flow area, proceeds downstream, and crosses the centerline of the nozzle at point 0. Point 0 denotes the origin of the coordinate system employed in the analysis due to Sauer; it corresponds to the intersection of the sonic line with the x axis. The location of point 0, the distance ϵ downstream from the throat section T, is determined from the analysis.

For either a two-dimensional planar or axisymmetric irrotational flow, the perturbation equation is equation 11.42, which is repeated here for convenience. Thus,

$$(1-M_\infty{}^2)u_x+v_y+\delta\frac{v}{y}=M_\infty{}^2(\gamma+1)\left(\frac{u}{U_\infty}\right)u_x \tag{15.59}$$

where, as before, $\delta=0$ for a planar flow and $\delta=1$ for an axisymmetric flow.

Because the flow in the throat region is essentially one-dimensional and sonic, the undisturbed free-stream velocity U_∞ is chosen as the critical speed of sound a^*; the corresponding Mach number M_∞ is, therefore, equal to unity. Substituting $U_\infty=a^*$ and $M_\infty=1$ into equation 15.59, we obtain

$$(\gamma+1)\left(\frac{u}{a^*}\right)u_x-v_y-\delta\frac{v}{y}=0 \tag{15.60}$$

By definition, let

$$u'=\frac{u}{a^*} \qquad \text{and} \qquad v'=\frac{v}{a^*} \tag{15.61}$$

where u' and v' are termed the *nondimensional perturbation velocity components*. Introducing u' and v' into equation 15.60 transforms it to

$$(\gamma+1)u'u'_x-v'_y-\delta\frac{v'}{y}=0 \tag{15.62}$$

Since the flow in the throat region is irrotational, it is possible to define a potential function Φ for the velocity. Hence, by definition (see equation 11.45),

$$\Phi=U_\infty x+\phi=a^*(x+\phi') \tag{15.63}$$

where $\phi'(x,y)$ is the *nondimensional perturbation velocity potential*. Consequently,

$$\tilde{u}=a^*+u=a^*(1+u')=\Phi_x=a^*(1+\phi'_x) \tag{15.64}$$

$$\tilde{v}=v=a^*v'=\Phi_y=a^*\phi'_y \tag{15.65}$$

where $u'=\phi'_x$ and $v'=\phi'_y$. Substituting equations 15.64 and 15.65 into equation 15.62, we obtain

$$(\gamma+1)\phi'_x\phi'_{xx}-\phi'_{yy}-\delta\frac{\phi'_y}{y}=0 \tag{15.66}$$

Equation 15.66 is the governing equation for the nondimensional perturbation velocity potential for a transonic flow.

Equation 15.66 is still a nonlinear partial differential equation, and the methods employed in Sections 11-3 and 11-5 for linear equations are inapplicable to it. A common technique for solving nonlinear partial differential equations is to employ an approximate method where a power series solution is assumed, with the coefficients of the power series chosen in such a manner that the differential equation and the boundary conditions are satisfied. In the present case, the velocity potential $\phi'(x,y)$ may be defined by a power series in y, in which the coefficients of the y terms are functions of x. Since $u(x,y)$ is an even function of y [i.e., $u(x,y)=u(x,-y)$], $\phi'_x=u$ must be an even function of y; consequently, only even

powers of y are included in the power series. Thus,

$$\phi'(x,y)=\sum_{i=0}^{\infty} f_{2i}(x)y^{2i}=f_0(x)y^0+f_2(x)y^2+f_4(x)y^4+\cdots \tag{15.67}$$

where $y^0\equiv 1$.

The corresponding expressions for the terms ϕ'_x, ϕ'_{xx}, ϕ'_y, and ϕ'_{yy} are accordingly

$$\phi'_x=f'_0(x)+f'_2(x)y^2+f'_4(x)y^4+\cdots \tag{15.68}$$

$$\phi'_{xx}=f''_0(x)+f''_2(x)y^2+f''_4(x)y^4+\cdots \tag{15.69}$$

$$\phi'_y=2f_2(x)y+4f_4(x)y^3+\cdots \tag{15.70}$$

$$\phi'_{yy}=2f_2(x)+12f_4(x)y^2+\cdots \tag{15.71}$$

where $f'_0(x)$ denotes $df_0(x)/dx$, and so forth.

Substituting the above expressions into equation 15.66 and rearranging the result, yields the following polynomial in y. Thus,

$$y^0\left[(\gamma+1)f'_0f''_0-2f_2-2\delta f_2\right]$$

$$+y^2\left[(\gamma+1)(f'_0f''_2+f''_0f'_2)-12f_4-4\delta f_4\right]+y^4[\cdots]+\cdots=0 \tag{15.72}$$

Since the polynomial (equation 15.72) must be satisfied for all arbitrary values of x and y, the coefficients of each power of y must be identically zero.

The approximation enters by truncating the power series (equation 15.67) after a finite number of terms. Sauer[13] truncated the series after the $f_4(x)y^4$ term. Accordingly, the only complete terms of the polynomial in y contained in equation 15.72 are the first and second terms. The coefficient of y^4 and higher-order terms involve $f_6(x)$, and so on. Setting the coefficients of y^0 and y^2 equal to zero and solving for $f_2(x)$ and $f_4(x)$ yields

$$f_2(x)=\frac{(\gamma+1)f'_0f''_0}{2(1+\delta)} \tag{15.73}$$

$$f_4(x)=\frac{(\gamma+1)(f'_0f''_2+f''_0f'_2)}{4(3+\delta)} \tag{15.74}$$

Thus, $f_2(x)$ and $f_4(x)$ may be determined from the derivatives of $f_0(x)$.

When $y=0$, $u'(x,0)=f'_0(x)$, where $u'(x,0)$ defines the nondimensional perturbation velocity distribution along the x axis. Consequently, knowing $u'(x,0)$, we can determine $f_2(x)$ and $f_4(x)$ from equations 15.73 and 15.74, and, therefore, the flow field. If the axial perturbation velocity distribution is assumed to be linear, $u'(x,0)$ is given by

$$u'(x,0)=f'_0(x)=\alpha x \tag{15.75}$$

where α is a constant, termed the *coefficient of the linear nondimensional axial perturbation velocity*. Substituting equation 15.75 into equations 15.73 and 15.74

gives

$$f_2(x)=\frac{(\gamma+1)\alpha^2 x}{2(1+\delta)} \tag{15.76}$$

$$f_4(x)=\frac{(\gamma+1)^2\alpha^3}{8(1+\delta)(3+\delta)} \tag{15.77}$$

Substituting equations 15.76 and 15.77 into equation 15.67 yields

$$\phi'(x,y)=f_0(x)+\frac{(\gamma+1)\alpha^2 xy^2}{2(1+\delta)}+\frac{(\gamma+1)^2\alpha^3 y^4}{8(1+\delta)(3+\delta)} \tag{15.78}$$

Substituting equation 15.78 into equations 15.64 and 15.65 yields

$$u'(x,y)=\alpha x+\frac{(\gamma+1)\alpha^2 y^2}{2(1+\delta)} \tag{15.79}$$

$$v'(x,y)=\frac{(\gamma+1)\alpha^2 xy}{(1+\delta)}+\frac{(\gamma+1)^2\alpha^3 y^3}{2(1+\delta)(3+\delta)} \tag{15.80}$$

Equations 15.79 and 15.80 yield the nondimensional perturbation velocities for a linear axial perturbation velocity distribution.

The critical curve where $M=1$ and $(\tilde{u}^2+\tilde{v}^2)=a^{*2}$ may be determined as follows. First, substitute the definition of the *nondimensional perturbation velocities*. Thus,

$$\tilde{u}^2+\tilde{v}^2=a^{*2}=(a^*+u)^2+v^2=a^{*2}\left[(1+u')^2+v'^2\right] \tag{15.81}$$

Dividing through by a^{*2} yields

$$(1+u')^2+v'^2=1 \tag{15.82}$$

Expanding equation 15.82 and neglecting powers of u' and v' yields

$$u'=0 \tag{15.83}$$

Consequently, the critical curve where $M=1$ is established by setting $u'=0$ in equation 15.79. Thus,

$$x=-\frac{(\gamma+1)\alpha y^2}{2(1+\delta)} \tag{15.84}$$

Next, it is necessary to locate the origin of the coordinate system in the nozzle. From Fig. 15.10 it is seen that $\tilde{v}=v=v'=0$ at $x=\varepsilon$ and $y=y_t$. Substituting those values for x and y into equation 15.80 yields

$$\varepsilon=-\frac{(\gamma+1)\alpha y_t^2}{2(3+\delta)} \tag{15.85}$$

Equation 15.85 locates the origin of the coordinate system relative to the nozzle throat.

15–5(b) Determination of the Nozzle Contour

As yet, the boundary condition applicable at the inner surface of the nozzle wall has not been applied. In principle, that boundary condition will determine the wall contour required for generating the flow field specified by equations 15.79 and 15.80. The linearized (solid wall) boundary condition developed for thin bodies in Section 11-4(d) is not applicable here because the surface of the solid boundary is not located on the centerline of the flow. Consequently, the equivalent linearized boundary condition applicable to an internal flow is developed herein.

Figure 15.11 illustrates the geometric model employed for determining the curvature κ of the nozzle wall at the narrowest cross-section (the throat). The curvature κ is *defined* as the change in the direction of the tangent to a curve per unit distance along that curve. The radius of curvature at the throat ρ_t is the reciprocal of the curvature κ. From Fig. 15.11,

$$\tan\tau = \frac{v'}{(1+u')} \cong v' \tag{15.86}$$

At the point T, the *curvature* κ is given by

$$\kappa = \frac{1}{\rho_t} = \left[\frac{d(\tan\tau)}{ds}\right]_T = \left(\frac{dv'}{ds}\right)_T \tag{15.87}$$

For the derivative dv'/ds we may write

$$\frac{dv'}{ds} = v'_x\left(\frac{dx}{ds}\right) + v'_y\left(\frac{dy}{ds}\right) \tag{15.88}$$

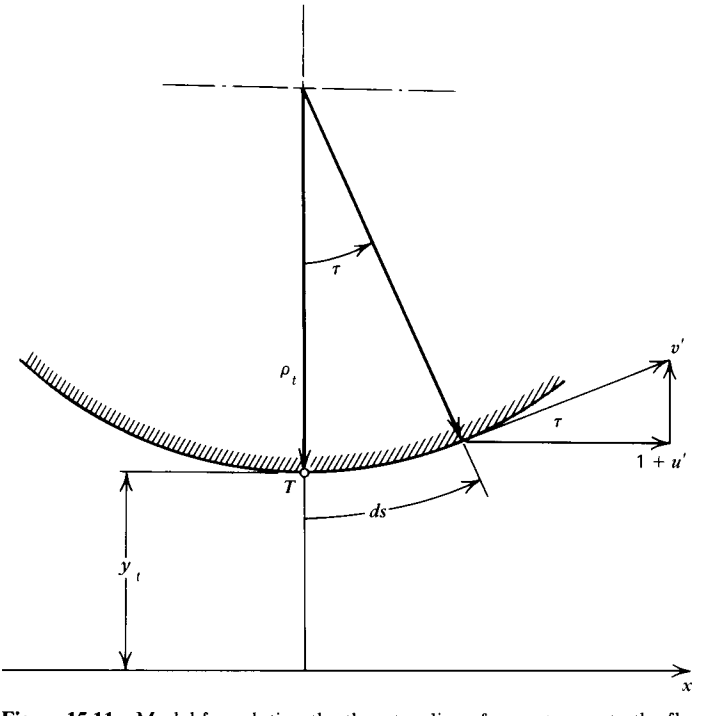

Figure 15.11 Model for relating the throat radius of curvature ρ_t to the flow field.

Consider a nozzle throat with a radius of curvature ρ_t, which is large compared to the throat radius y_t. Hence, $\rho_t \gg y_t$, $(dx/ds) \cong 1$, and $(dy/ds) \cong 0$. Accordingly, equation 15.88 reduces to

$$\frac{dv'}{ds} = v'_x \tag{15.89}$$

Substituting equation 15.89 into equation 15.87 yields

$$\rho_t = \frac{1}{\left[v'_x(x,y)\right]_T} = \frac{1}{v'_x(\varepsilon, y_t)} \tag{15.90}$$

From equation 15.80 v'_x is given by

$$v'_x = \frac{(\gamma+1)\alpha^2 y}{(1+\delta)} \tag{15.91}$$

The value of v'_x at the point T, where $x = \varepsilon$ and $y = y_t$, may be determined from equation 15.91. Substituting that result into equation 15.90, we obtain the following equation for the radius of curvature ρ_t. Thus,

$$\rho_t = \frac{(1+\delta)}{(\gamma+1)\alpha^2 y_t} \tag{15.92}$$

Up to this point it is assumed that the nondimensional axial perturbation velocity $u'(x,0)$ is known, and that a radius of curvature ρ_t for the nozzle wall, as specified by equation 15.92, is required for obtaining the correct value for $u'(x,0)$. By inverting the interpretation of the preceding results, the value of $u'(x,0)$ may be determined from the geometrical properties of the nozzle throat. Solving equation 15.92 for α yields

$$\alpha = \left[\frac{1+\delta}{(\gamma+1)\rho_t y_t}\right]^{1/2} \tag{15.93}$$

Substituting equation 15.93 for α into equation 15.85 yields the following equation for ε. Thus,

$$\varepsilon = -\frac{y_t}{2(3+\delta)}\left[\frac{(\gamma+1)(1+\delta)}{(\rho_t/y_t)}\right]^{1/2} \tag{15.94}$$

The *perturbation velocity field* near the sonic line in the throat of a nozzle is, therefore, determined by equations 15.79, 15.80, 15.93, and 15.94. The relationship between the dimensional velocities $\tilde{u}$ and $\tilde{v}$ and the nondimensional perturbation velocities u' and v' are

$$\tilde{u}(x,y) = a^*(1+u') \qquad \text{and} \qquad \tilde{v}(x,y) = a^* v' \tag{15.95}$$

15–5(c) Initial-Value Line for Supersonic Flow Field Calculations

The results presented in Sections 15-5(a) and (b) enable determining the flow field in the throat region of a nozzle. To initiate a solution for the two-dimensional supersonic flow field by the method of characteristics (see Section 16-4), a line

along which $M > 1$ across the entire throat is needed. The sonic line determined by Sauer's method is unsuitable because Mach lines from the sonic line intersect the nozzle wall upstream from the throat point T. Because point T was employed as a boundary condition in the evaluation of equation 15.92, the region of the flow field upstream from point T is within the range of influence of point T, and the method of characteristics cannot be initiated from an *initial-value line* that is in the range of influence of a downstream point. The line where $\tilde{v}=0$, illustrated in Fig. 15.12, which is only a slight distance further downstream than the sonic line, may be employed as an initial-value line for the method of characteristics. On the wall, at the throat, both the slope of the wall and $\tilde{v}$ are zero, so that the flow velocity is parallel to the wall. At every other point along the wall, there is some small difference between the wall angle and the flow angle as a consequence of the approximations introduced into the analysis. Hence, the $\tilde{v}=0$ line satisfies the solid wall boundary condition exactly.

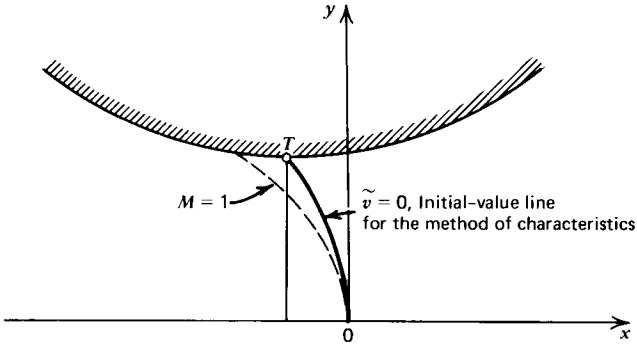

Figure 15.12 Initial-value line for the method of characteristics.

The equation of the line, which is the locus for $\tilde{v}=0$, is obtained from equation 15.80 by setting $v'=0$. Thus,

$$x = -\frac{(\gamma+1)\alpha y^2}{2(3+\delta)} \tag{15.96}$$

The dimensional velocity components $\tilde{u}$ and $\tilde{v}$ may be determined along the line $\tilde{v}=0$ at any point where x and y are specified. Since the flow is isentropic, the speed of sound a is a known function of the magnitude of the flow velocity V. Knowing V and a, the Mach number M may be calculated. The static thermodynamic properties p, ρ, and t may be computed from the stagnation values P, ρ_0, and T and the Mach number M (see Section 3-9). Hence, all of the gas dynamic properties for the flowing fluid may be determined along a line that is suitable for initiating a numerical solution by the method of characteristics for the supersonic flow field in the divergence.

The mass flow rate for the nozzle may be determined by integrating across any line generated in the throat region by applying the foregoing analysis. Because of the approximations made in the analysis, the accuracy of the results depends to some extent on the choice of the initial-value line to be employed in making the calculations. The $\tilde{v}=0$ line (see equation 15.96) is frequently employed as the initial-value line. The axial thrust developed at the throat of the nozzle may be calculated by integrating the momentum and pressure forces acting across the initial-value line.

Experimental measurements of the sonic line location in a nozzle indicate that because of the boundary layer effects, which are not included in the analytical models, the location of the experimental sonic line is slightly upstream from that obtained by analysis.[27]

A FORTRAN computer program, subroutine IVLINE, for implementing Sauer's analysis for determining the location and the flow properties along the $\tilde{v}=0$ line is presented below. The program is written in subroutine form so that it may be incorporated into other programs that require initial-value data in the throat of a converging-diverging nozzle. The control variables (DELTA, NI, IUNITS), the geometrical properties of the nozzle throat (YT, RTU), and the solution values (X, Y, U, V) are transmitted between the main program and subroutine IVLINE by COMMON statements. The subroutine is employed in Section 16-4(a) in a master logic program for calculating the supersonic flow field in the divergence of a converging-diverging nozzle of known shape. Thus, many of the variables in COMMON in subroutine IVLINE are employed in that analysis; those variables are defined in Table 16.13. The variables required for Sauer's analysis are defined in Table 15.6. FORTRAN names for all of the variables are selected to resemble the engineering names of the variables.

```
      SUBROUTINE IVLINE

C     SUBROUTINE IVLINE DETERMINES AN INITIAL-VALUE LINE, SAUERS METHOD

      COMMON /CONTRL/ DELTA,NI,NT,ICOR,E1,E2,E3,E4,E5,IUNITS,PI,RAD
      COMMON /PROPTY/ G,RG,CP,TS,PS,PA,GC,GL $ REAL M,MDOT,MDOTS
      COMMON /CONTUR/ YT,RTU,RTD,AA,AE,XE,YE
      COMMON /PERFORM/ YW,PW,MDOT,CD,F,DF,FS
      COMMON /ARRAYS/ X(99),Y(99),U(99),V(99),Q(99),A(99),P(99),R(99)

      TT(X)=TS-X*X/(2.0*GC*CP) $ AM(X)=X/SQRT(G*GC*RG*TT(X))
      PP(X)=PS*(TT(X)/TS)**(G/(G-1.0)) $ RR(X)=PP(X)/RG/TT(X)

C     CALCULATE REFERENCE PARAMETERS

      ALPHA=SQRT((1.0+DELTA)/((G+1.0)*RTU*YT)) $ DY=YT/FLOAT(NI-1)
      EPS=-(G+1.0)*ALPHA*YT**2/(2.0*(3.0+DELTA)) $ AT=PI*YT*YT/GL
      C1=-(G+1.0)*ALPHA/(2.0*(3.0+DELTA)) $ Y(21)=0.0
      C2=(G+1.0)*ALPHA**2/(2.0*(1.0+DELTA)) $ MDOT=0.0 $ F=0.0
      AS=SQRT(2.0*G*GC*RG*TS/(G+1.0)) $ MDOTS=AS*RR(AS)*AT
      FS=PP(AS)*AT+MDOTS*AS/GC $ FOD=FS-PA*AT

C     CALCULATE LOCATION AND PROPERTIES OF INITIAL-VALUE LINE POINTS,
C     AND CALCULATE MASS FLOW RATE AND THRUST AT THE INITIAL-VALUE LINE

      DO 10 I=1,NI $ J=I+20 $ IF (I.GT.1) Y(J)=Y(J-1)+DY
      X(J)=C1*Y(J)**2+0.000001 $ U(J)=AS*(1.0+ALPHA*X(J)+C2*Y(J)**2)
      X(J)=X(J)-EPS $ T=TT(U(J)) $ M=AM(U(J)) $ PZ=PP(U(J)) $RZ=RR(U(J))
      CI=3.0+(-1.0)**I $ IF ((I.EQ.1).OR.(I.EQ.NI)) CI=1.0
      MDOT=MDOT+CI*RZ*U(J)*Y(J) $ F=F+CI*((PZ-PA)+RZ*U(J)**2/GC)*Y(J)
      V(J)=0.0 $ Q(J)=U(J) $ A(J)=0.0 $ P(J)=PZ $ R(J)=RZ $ PZ=PZ/GL
      WRITE (6,2001) I,X(J),Y(J),U(J),V(J),M,Q(J),A(J),PZ,RZ,T
   10 CONTINUE $ MDOT=MDOT*2.0*PI*DY/(3.0*GL) $ F=F*2.0*PI*DY/(3.0*GL)
      CD=MDOT/MDOTS $ ETAF=F/FOD $ ETAI=ETAF/CD
      WRITE (6,2002) MDOT,MDOTS,CD,F,FOD,ETAF,ETAI $ RETURN

 2001 FORMAT (1H ,5X,I5,2F10.4,2F10.1,F10.4,F10.1,F10.4,2E13.4,F10.1)
 2002 FORMAT (1H0,9X,7HMDOT = ,F10.3,3X,8HMDOTS = ,F10.3,3X,5HCD = ,
     1F7.5//10X,4HF = ,F10.1,3X,5HFS = ,F10.1,3X,7HETAF = ,F7.5,3X,
     2 7HETAI = ,F7.5)
      END
```

The determination of the fluid properties t, M, p, and ρ for a given velocity V is accomplished by the function statements TT(X), AM(X), PP(X), and RR(X), respectively, which are based on the properties of a perfect gas (i.e., constant γ and R). The values of the thermodynamic properties (G, RG, CP, TS, PS, PA) are transmitted to the subroutine through a COMMON statement, as are the values of the fluid properties (Q, M, P, R, T, C). Those variables are defined in Table 15.7.

Table 15.6 Terminology for Subroutine IVLINE

		Control Variables
DELTA	δ,	0 planar flow, 1 axisymmetric flow
NI		odd number of equally spaced points on the $\tilde{v}=0$ line
IUNITS		1 EE units, 2 SI units
		Nozzle Throat Geometry and Performance Parameters
YT	y_t,	nozzle throat radius, m (in.)
RTU	ρ_t,	nozzle throat upstream radius of curvature, m (in.)
ALPHA	α,	coefficient of linear axial velocity perturbation, m^{-1} ($in.^{-1}$)
EPS	ϵ,	location of nozzle throat, m (in.)
ASTAR	a^*,	critical speed of sound, m/s (ft/sec)
MDOT	$\dot{m}$,	mass flow rate, kg/s (lbm/sec)
MDOTS	$\dot{m}_{1-D}$,	one-dimensional mass flow rate, kg/s (lbm/sec)
CD	C_D,	discharge coefficient, $\dot{m}/\dot{m}_{1-D}$
F	F_t,	throat thrust, N (lbf)
FS	$F_{t,1-D}$,	one-dimensional throat thrust, N (lbf)
LAMBDA	λ,	thrust ratio, $F_t/F_{t,1-D}$
		Flow Field Properties Along the $\tilde{v}=0$ Line
X	x,	axial coordinate, m (in.)
Y	y,	radial coordinate, m (in.)
U	u,	axial velocity component, m/s (ft/sec)
V	v,	radial velocity component, m/s (ft/sec)

Table 15.7 Terminology for the Thermodynamic and Gas Dynamic Properties

G	γ,	specific heat ratio
RG	R,	gas constant, J/kg-K (ft-lbf/lbm-R)
CP	c_p,	constant pressure specific heat, J/kg-K (ft-lbf/lbm-R)
TS	T,	stagnation temperature, K (R)
PS	P,	stagnation pressure, N/m^2 ($lbf/in.^2$)
PA	p_o,	ambient pressure, N/m^2 ($lbf/in.^2$)
GC		1.0 m-kg/N-s^2 in SI units, 32.174 ft-lbm/lbf-sec^2 in EE units
GL		1.0 m^2/m^2 in SI units, 144.0 $in.^2/ft^2$ in EE units
Q	V,	velocity magnitude, m/s (ft/sec)
M	M,	Mach number
P	p,	static pressure, N/m^2 ($lbf/in.^2$)
R	ρ,	density, kg/m^3 (lbm/ft^3)
T	t,	static temperature, K (R)
C	a,	speed of sound, m/s (ft/sec)

Example 15.2. The following example illustrates the application of Sauer's analysis. Consider the irrotational flow of a perfect gas with $\gamma = 1.2$ and $R = 320$ J/kg-K. The stagnation properties are $P = 70 \cdot 10^5$ N/m^2 and $T = 3000$ K. The gas flows in an axisymmetric ($\delta = 1$) converging-diverging nozzle having a throat radius $y_t = 0.025$ m and a circular arc throat contour with an upstream radius of curvature $\rho_t = 0.050$ m. Calculate (a) the location of the sonic line, (b) the location of the $\tilde{v} = 0$ line, (c) the fluid properties, $\tilde{u} = V$, M, p, ρ, and t, at 11 equally spaced points along the $\tilde{v} = 0$ line, (d) the mass flow rate and the thrust along the $\tilde{v} = 0$ line, assuming that the ambient pressure is zero, and (e) the one-dimensional sonic values of the mass flow rate and the thrust.

Solution

To determine the location of the origin for the coordinate system, the value of ε (see Fig. 15.10) must be determined. From equation 15.94

$$\varepsilon = -\frac{(0.025)}{2(3+1)}\left[\frac{(1.2+1)(1+1)}{(0.050/0.025)}\right]^{1/2} = -4.635 \text{ mm}$$

From equation 3.95 the sonic speed a^* is

$$a^* = \left[\frac{2(1.2)(320.0)(3000.0)}{(1.2+1)}\right]^{1/2} = 1023.36 \text{ m/s}$$

The coefficient of the linear axial perturbation velocity α is determined from equation 15.93. Thus,

$$\alpha = \left[\frac{1+1}{(1.2+1)(0.050)(0.025)}\right]^{1/2} = 26.968 \text{ m}^{-1}$$

(a) *Equation for the sonic line.* From equation 15.84

$$x = -\frac{(1.2+1)(26.968)}{2(1+1)} y^2 = -(14.832 \text{ m}^{-1}) y^2 \text{ m} \qquad \text{(a)}$$

where x and y are in meters. The sonic line is obtained from equation (a) by calculating the values of x corresponding to equal increments of y (see Table 15.8). Referring to Fig. 15.10, it is seen that the sonic line is referred to a coordinate system that has its origin displaced by the distance ε from the throat section. Hence, the following transformation equation must be applied to the values of x. Thus,

$$\bar{x} = x - \varepsilon = x + 4.635 \text{ mm} \qquad \text{(b)}$$

where $\bar{x}$ is measured relative to the nozzle throat location.

(b) *Equation for the $\tilde{v} = 0$ line.* From equation 15.96

$$x = -\frac{(1.2+1)(26.968)}{2(3+1)} y^2 = -(7.4162 \text{ m}^{-1}) y^2 \text{ m} \qquad \text{(c)}$$

Table 15.8 presents the values of x and $\bar{x}$ for both the sonic line and the $\tilde{v} = 0$ line as a function of y.

(c) *Determination of the fluid properties.* The expression for $\tilde{u}(x,y)$ is obtained by

Table 15.8 Solution Values for the Transonic Flow in the Nozzle Throat Region Calculated by Sauer's Method for Example 15.2

		Sonic Line		$\tilde{v}=0$ Line		Properties Along the $\tilde{v}=0$ Line				
Point	y, mm	x, mm	$\bar{x}$, mm	x, mm	$\bar{x}$, mm	$\tilde{u}=V$ m/s	M	p, N/m$^2\cdot 10^5$	ρ, kg/m^3	t, K
1	0.0	0.000	4.635	0.000	4.635	1023.4	1.0000	39.513	4.5275	2727.3
2	2.5	−0.093	4.542	−0.045	4.590	1024.6	1.0014	39.454	4.5219	2726.6
3	5.0	−0.371	4.264	−0.185	4.450	1028.5	1.0055	39.276	4.5049	2724.5
4	7.5	−0.834	3.801	−0.417	4.218	1034.9	1.0124	38.980	4.4766	2721.1
5	10.0	−1.483	3.152	−0.742	3.893	1043.8	1.0221	38.565	4.4368	2716.3
6	12.5	−2.318	2.317	−1.157	3.478	1055.3	1.0345	38.032	4.3857	2710.0
7	15.0	−3.337	1.298	−1.667	2.968	1069.4	1.0498	37.381	4.3230	2702.2
8	17.5	−4.542	0.093	−2.270	2.365	1086.0	1.0680	36.613	4.2489	2692.8
9	20.0	−5.933	−1.298	−2.967	1.668	1105.2	1.0891	35.729	4.1632	2681.9
10	22.5	−7.509	−2.874	−3.755	0.880	1127.0	1.1132	34.730	4.0660	2669.2
11	25.0	−9.270	−4.635	−4.635	0.000	1151.3	1.1402	33.619	3.9573	2654.8

applying equations 15.79 and 15.95. Thus,

$$\tilde{u}=1023.36\left[1+26.968x+\frac{(1.2+1)(26.968)^2}{2(1+1)}y^2\right] \text{ m/s}$$

$$\tilde{u}=1023.36(1+26.968x+400.00y^2) \text{ m/s} \tag{d}$$

Table 15.8 presents $\tilde{u}$ as a function of y.

Stagnation acoustic speed. From equation 3.81

$$a_o^2=\gamma RT=1.2(320.0)(3000)=1.1520\cdot 10^6 \text{ m}^2/\text{s}^2$$

Local acoustic speed. From equation 11.30, the energy equation for a perfect gas, we obtain

$$a^2=a_o^2-\frac{\gamma-1}{2}\tilde{u}^2=1.1520\cdot 10^6-0.1\tilde{u}^2 \text{ m}^2/\text{s}^2 \tag{e}$$

From the values of a and $V=\tilde{u}$, the local Mach number $M=V/a$ is readily determined.

Static temperature. From equation 3.69

$$t=\frac{T}{1+\dfrac{\gamma-1}{2}M^2}=\frac{3000}{1+0.1M^2} \quad \text{K} \tag{f}$$

Density. From equation 1.99

$$\rho=\frac{p}{Rt}=\frac{1}{320}\frac{p}{t} \quad \text{kg/m}^3 \tag{g}$$

Static pressure. From equation 3.76

$$p=\frac{P}{\left(1+\dfrac{\gamma-1}{2}M^2\right)^{\gamma/(\gamma-1)}}=\frac{70.0\cdot 10^5}{(1+0.1M^2)^{6.0}} \quad \text{N/m}^2 \tag{h}$$

By applying equations (a) to (h) all of the properties along the $\tilde{v}=0$ line may be calculated.

(d) *The mass flow rate and thrust.* Figure 15.13 presents a model for determining the differential mass flow rate $d\dot{m}$ crossing the element of area dA. Thus,

$$d\dot{m} = \rho \mathbf{V} \cdot d\mathbf{A} = \rho \tilde{u} 2\pi y \, dy \tag{i}$$

Mass flow rate across the $\tilde{v}=0$ line. Integrating equation (i) gives

$$\dot{m} = 2\pi \int_0^{y_t} \rho \tilde{u} y \, dy \tag{j}$$

The actual integration of equation (j) is accomplished by applying Simpson's rule [see Appendix A-5(b)]. Dividing the integration interval (0 to y_t) into an even number of equal subintervals (i.e., NI odd) yields the following algorithm.

$$\dot{m} = 2\pi \left(\frac{\Delta y}{3} \right) \sum_{i=1}^{11} C_i (\rho \tilde{u} y)_i = \frac{2\pi (0.0025)}{3} \sum_{i=1}^{11} C_i (\rho \tilde{u} y)_i$$

$$\dot{m} = 0.0052360 \sum_{i=1}^{11} C_i (\rho \tilde{u} y)_i \quad \text{kg/s} \tag{k}$$

where $C_i = 1, 4, 2, \ldots, 2, 4, 1$, i corresponds to the rows in Table 15.8, and ρ, $\tilde{u}$, and y have the units presented in Table 15.8. From equation (k)

$$\dot{m} = 9.0456 \quad \text{kg/s}$$

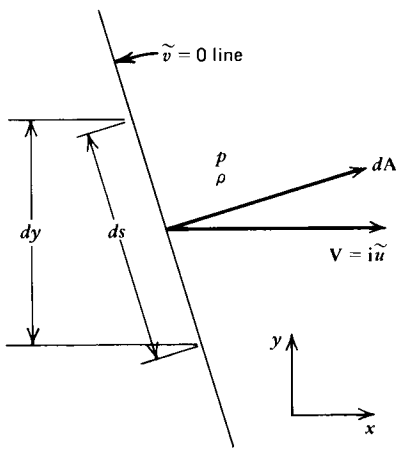

Figure 15.13 Differential model for calculating the mass flow rate and thrust across the $\tilde{v}=0$ line.

Thrust across the $\tilde{v}=0$ line. The thrust is the sum of the pressure forces and the momentum flux. Hence, from Fig. 15.13, we obtain the following expression for the differential thrust dF acting on dA.

$$dF = 2\pi y p \, dy + \tilde{u} \, d\dot{m}$$

Substituting for $d\dot{m}$ from equation (i), we obtain

$$dF = 2\pi(p + \rho\tilde{u}^2)y\,dy \tag{l}$$

Integrating equation (l) yields the thrust F. Thus,

$$F = 2\pi\int_0^{y_t}(p + \rho\tilde{u}^2)y\,dy \tag{m}$$

Equation (m) may be integrated by Simpson's rule. Thus,

$$F = 2\pi\left(\frac{\Delta y}{3}\right)\sum_{i=1}^{11} C_i\left[(p + \rho\tilde{u}^2)y\right]_i = \frac{2\pi(0.0025)}{3}\sum_{i=1}^{11} C_i\left[(p + \rho\tilde{u}^2)y\right]_i$$

$$F = 0.0052360\sum_{i=1}^{11} C_i\left[(p + \rho\tilde{u}^2)y\right]_i \quad \text{N} \tag{n}$$

The result is

$$F = 17{,}013 \quad N$$

(e) *The one-dimensional sonic mass flow rate and thrust.* From the continuity equation for steady one-dimensional choked flow

$$\dot{m}_{1-D} = \rho^* A_t a^*$$

The values of ρ^* and a^* may be obtained from point 1 in Table 15.8. Thus,

$$\dot{m}_{1-D} = 4.5275\pi(0.025)^2(1023.4) = 9.0977 \quad \text{kg/s}$$

By definition, the nozzle discharge coefficient C_D is the ratio $\dot{m}/\dot{m}_{1-D}$. Hence,

$$C_D \equiv \frac{\dot{m}}{\dot{m}_{1-D}} = \frac{9.0465}{9.0977} = 0.9944$$

The one-dimensional *sonic thrust* is given by

$$F = p^* A_t + \dot{m}_{1-D}a^* = 39.513(10^5)\pi(0.025)^2 + 9.0977(1023.4) = 17{,}069 \quad \text{N}$$

The *thrust ratio*, also termed the *thrust efficiency*, denoted by λ, is

$$\lambda \equiv \frac{F}{F_{1-D}} = \frac{17{,}013}{17{,}069} = 0.9967$$

15–5(d) Some Results Based on Sauer's Method

By following the procedure employed in Example 15.2, Sauer's method was employed for determining the sonic line and the pertinent flow field properties for the throat regions of several converging-diverging nozzles. In all cases the flowing gas is air with $\gamma = 1.4$ and $R = 287.04$ J/kg-K. The results obtained may, however, be regarded as typical for any gas.

The geometry of a nozzle throat is completely defined by specifying the value of the dimensionless ratio ρ_t/y_t. In the present study, the value selected for y_t is $y_t = 1$,

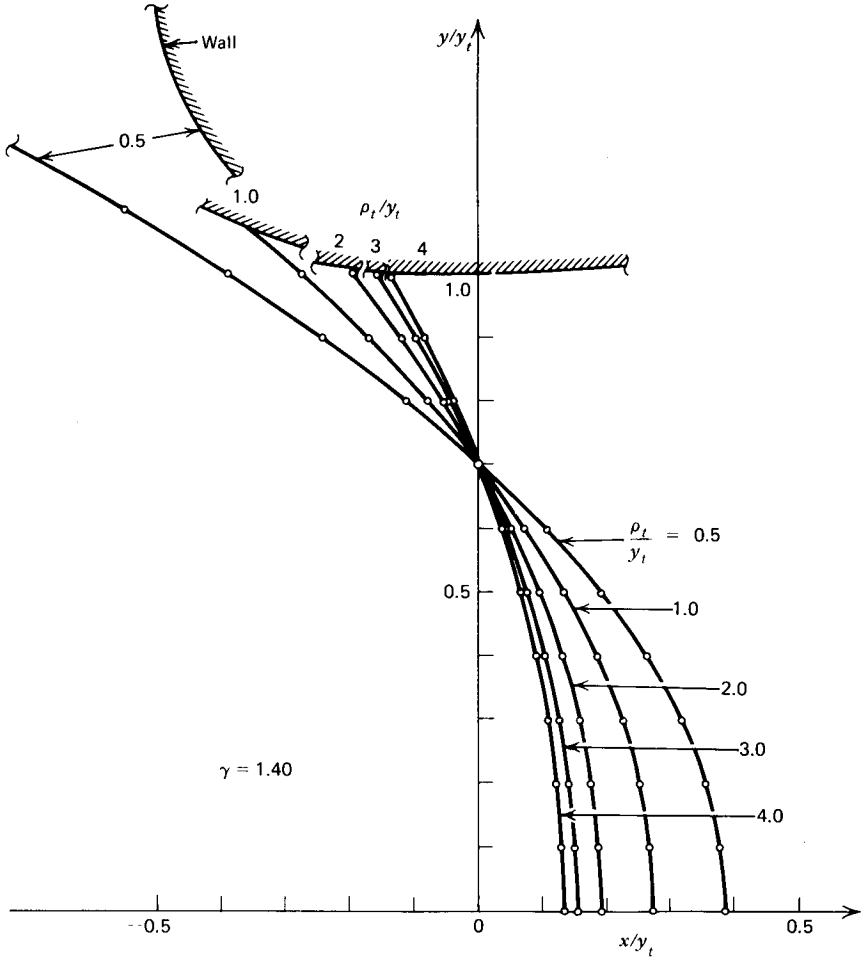

Figure 15.14 Sonic line locations in a nozzle throat (Sauer's analysis).

and the values of ρ_t are multiples or fractions of y_t. The results are presented by curves of y/y_t as a function of x/y_t for several constant values of the ratio ρ_t/y_t (see Figs. 15.14 and 15.15), and by curves of $y/y_t = f(M)$ with ρ_t/y_t as a parameter (see Fig. 15.16). The results presented in the aforementioned figures may be scaled geometrically by multiplying the pertinent geometrical values read from the curves by suitable *scale factors*. Values of ρ_t/y_t equal to 4, 3, 2, 1, and 0.5 are considered. Furthermore, the results apply to axisymmetric nozzles (i.e., $\delta = 1$) and neglect the effect of the boundary layer adjacent to the nozzle wall.[27]

Figure 15.14 presents the values of y/y_t as a function of x/y_t for the sonic lines corresponding to the aforementioned five values of ρ_t/y_t. It is evident that the sonic line location approaches the geometrical throat as the value of the ratio ρ_t/y_t increases. Moreover, the velocity profiles for the larger values of ρ_t/y_t tend to approach that for a one-dimensional flow; that is, a straight line parallel to the y-axis (see Fig. 15.16). The sonic lines for values of $\rho_t/y_t < 2$, approximately, are highly distorted, indicating that the corresponding flows deviate significantly from

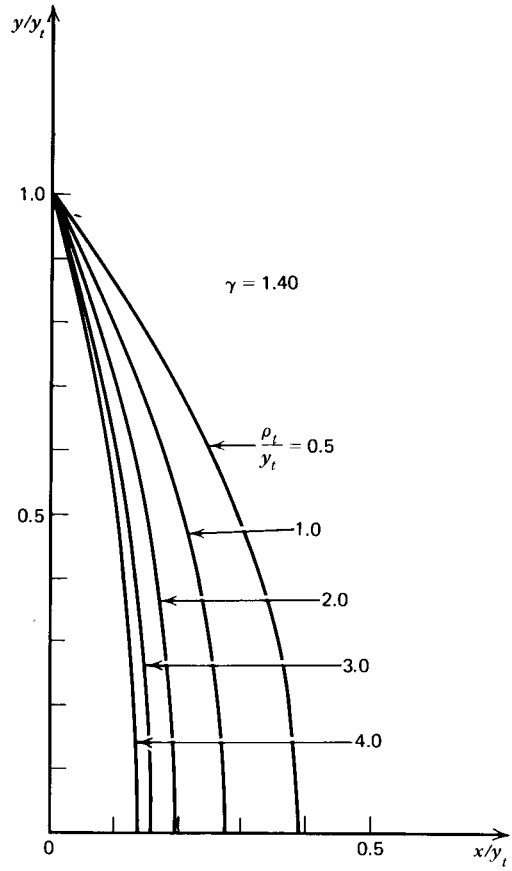

Figure 15.15 Location of $\tilde{v}=0$ lines in a nozzle throat (Sauer's analysis).

a one-dimensional flow. For example, the sonic line corresponding to $\rho_t/y_t=0.5$ actually fails to intersect the wall of the nozzle. It is apparent that Sauer's analysis gives results that deviate significantly from a uniform flow for geometries with $\rho_t/y_t<2$, approximately, and that the small perturbation model *breaks down* completely if $\rho_t/y_t<1$, approximately. Experience indicates that for nozzle geometries having $\rho_t/y_t>2$, approximately, Sauer's analysis yields results that appear reasonable. Unfortunately, there are insufficient experimental data available for establishing with definiteness the accuracy of the results predicted by any theoretical analysis for calculating the sonic line in the nozzle throat region.

Figure 15.15 presents the results obtained for the location of the $\tilde{v}=0$ line (see Fig. 15.12) for the same five values of ρ_t/y_t. The results are presented as curves of y/y_t as a function of x/y_t, with ρ_t/y_t as a parameter. It is seen that all of the lines for $\tilde{v}=0$ intersect the wall contour at the geometrical throat of the nozzle. Furthermore, comparing Figs. 15.14 and 15.15 shows that each line for $\tilde{v}=0$ passes through its sonic point on the centerline. As pointed out above, it is evident that for values of $\rho_t/y_t>2$, the flow tends to approach a uniform flow.

Figure 15.16 presents y/y_t as a function of the local Mach number M, for the same five values of ρ_t/y_t, along each of the $\tilde{v}=0$ lines presented in Fig. 15.15. As

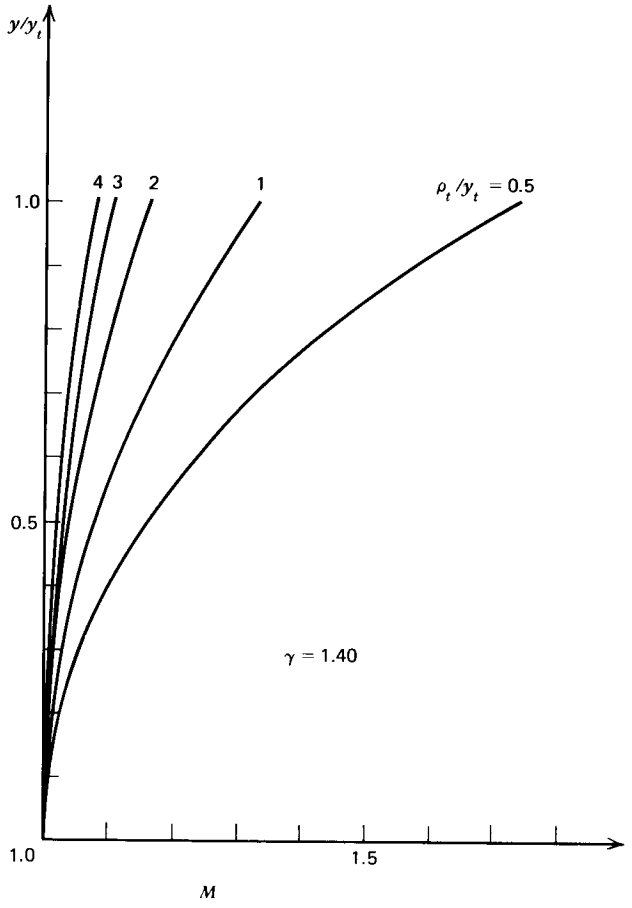

Figure 15.16 Mach number distribution along the $\tilde{v}=0$ lines (Sauer's analysis).

occurred in Figs. 15.14 and 15.15, for values of $\rho_t/y_t<2$, approximately, the curves of Fig. 15.16 also deviate substantially from that for a uniform flow; that is, $M=1=$ constant.

Figure 15.17 presents the calculated values of the *geometrical contraction factor* C_c as a function of ρ_t/y_t. *By definition* $C_c=\dot{m}/\dot{m}_{1-D}$, where $\dot{m}$ denotes the calculated value for the mass flow rate crossing the nozzle throat section, and $\dot{m}_{1-D}$ is the mass flow rate that would cross that section if the flow were one dimensional. The value of C_c measures the reduction in mass flow rate due to two-dimensional flow effects in the throat region [see Section 4-8(c)]. For comparison, the same figure presents two experimentally determined points due to Back, et al.,[22,23] and the two calculated curves based on the analyses by Hall[17] and by Kliegel;[18] the analyses due to Hall and to Kliegel are discussed briefly in Section 15-5(e). It is evident from Fig. 15.17 that the result predicted by Sauer's analysis for $\rho_t/y_t=2$ agrees satisfactorily with the experimental result. But the value predicted by Sauer's analysis for $\rho_t/y_t=0.625$ differs considerably from the value measured by Back. The figure also shows that for values of $\rho_t/y_t>2$ all three of the analytical methods predict substantially the same values.

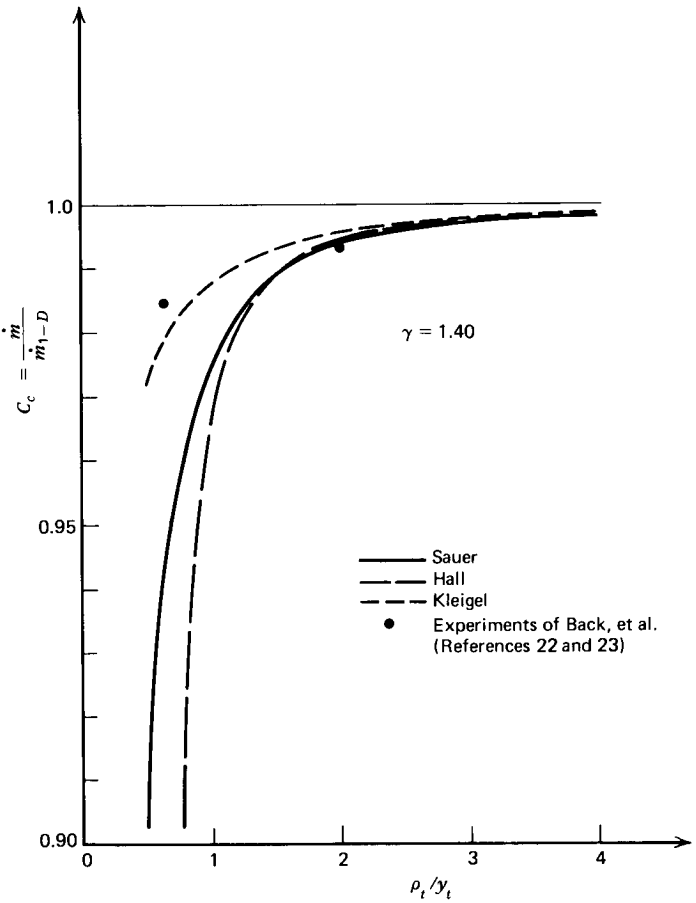

Figure 15.17 Throat contraction factor C_c.

Figure 15.18 compares the sonic lines predicted by the analyses due to Sauer and Kliegel with the experimental measurements of Back for the case where $\rho_t/y_t = 0.625$. Here again, it is evident that predictions by Sauer's analysis are considerably in error for such a small value of ρ_t/y_t.

Table 15.9 presents the calculated values, employing Sauer's analysis, for the intersection of the sonic line with the nozzle wall (in reality with the edge of the boundary layer), and also with the centerline of the nozzle, for $\rho_t/y_t = 2$ and $\rho_t/y_t = 0.625$. The table also presents the corresponding values measured by Back; the latter made no measurements on the nozzle centerline for $\rho_t/y_t = 2$. Table 15.9 shows that the agreement between theory and experiment is fairly good for $\rho_t/y_t = 2.0$. The comparison for $\rho_t/y_t = 0.625$ reinforces the statements made earlier, that Sauer's analysis is inadequate for nozzles having values of $\rho_t/y_t < 1$.

Summarizing, the small perturbation analysis for the flow in the throat region of a nozzle due to Sauer is in reasonable agreement with the available experimental data for values of $\rho_t/y_t > 2$, approximately, and is inadequate for values of $\rho_t/y_t < 1$. Section 15-5(e) presents brief descriptions of two similar methods; both include more terms in the series expansion for $\phi(x,y)$.

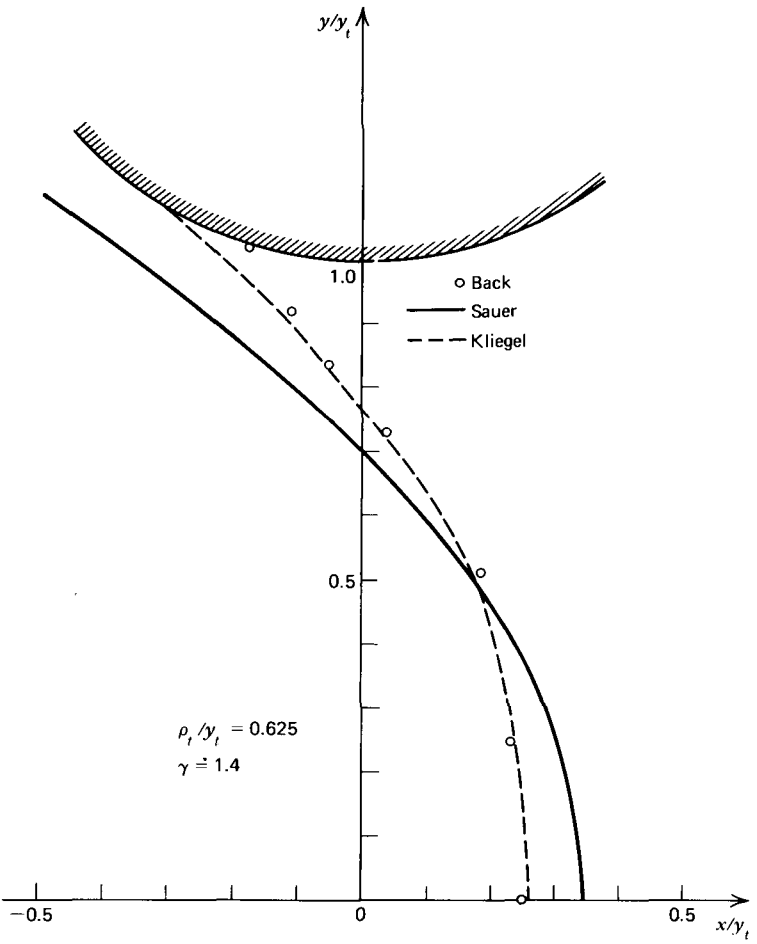

Figure 15.18 Comparison of predicted and measured sonic line locations.

Table 15.9 Location of the Sonic Line

	x/y_t			
	Wall		Centerline	
ρ_t/y_t	Back	Sauer	Back	Sauer
2.0	−0.15 to −0.16	−0.19	—	0.19
0.625	−0.13 to −0.14	−0.34	0.25	0.35

15–5(e) Other Transonic Analyses for Converging-Diverging Nozzles

The transonic analysis due to Sauer [see Sections 15-5(a) to 15-5(d)] is the most straightforward of all of those that have been proposed for solving the transonic flow problem in the throat section of a converging-diverging nozzle (see References 13 to 21). As pointed out in Section 15-5(d), that method of analysis is adequate only for values of $\rho_t/y_t > 2$, approximately. In this section, some methods that are more accurate for values of $\rho_t/y_t < 2$ are reviewed briefly, primarily for the purpose of illustrating the state of the art of the analytical methods for predicting the transonic flow in the throat region of a nozzle.

Hall's[17] method is considered first. That method is based on employing a power series expansion for the velocity components in inverse powers of the *expansion parameter* R. The following forms of series expansions are assumed, where x is measured from the throat, point 0′ in Fig. 15.10.

$$\frac{\tilde{u}(x,y)}{a^*} = 1 + \frac{u_1(r,z)}{R} + \frac{u_2(r,z)}{R^2} + \frac{u_3(r,z)}{R^3} + \cdots \tag{15.97}$$

$$\frac{\tilde{v}(x,y)}{a^*} = \left(\frac{\gamma+1}{2R}\right)^{1/2}\left[\frac{v_1(r,z)}{R} + \frac{v_2(r,z)}{R^2} + \frac{v_3(r,z)}{R^3} + \cdots\right] \tag{15.98}$$

where

$$r = \frac{y}{y_t} \qquad z = \left(\frac{2R}{\gamma+1}\right)^{1/2}\frac{x}{y_t} \qquad R = \frac{\rho_t}{y_t} \tag{15.99}$$

The functions u_1, v_1, and so on, are to be determined so that the governing equations and the boundary conditions are satisfied. The above series expansions are substituted into the full nonlinear gas dynamic equation, equation 11.29, and all of the terms involving the same power of the expansion parameter R are collected. The first approximation is obtained from the coefficient of $1/R$, the second approximation is obtained from the coefficient of $1/R^2$, and so on. The first approximation yields a solution that is identical with that obtained by employing Sauer's method. That solution is then employed for making a second approximation, and so forth. Hall obtained the solutions through the third approximation. Hall's method is limited to values of R exceeding unity; the series corresponding to equations 15.97 and 15.98 are divergent for $R < 1.0$. The following results were obtained by Hall.

$$u_1 = \frac{1}{2}r^2 - \frac{1}{4} + z \tag{15.100}$$

$$v_1 = \frac{1}{4}r^3 - \frac{1}{4}r + rz \tag{15.101}$$

$$u_2 = \frac{2\gamma+9}{24}r^4 - \frac{4\gamma+15}{24}r^2 + \frac{10\gamma+57}{288} + z\left(r^2 - \frac{5}{8}\right) - \frac{2\gamma-3}{6}z^2 \tag{15.102}$$

$$v_2 = \frac{\gamma+3}{9}r^5 - \frac{20\gamma+63}{96}r^3 + \frac{28\gamma+93}{288}r + z\left(\frac{2\gamma+9}{6}r^3 - \frac{4\gamma+15}{12}r\right) + rz^2 \tag{15.103}$$

$$\begin{aligned} u_3 = {} & \frac{556\gamma^2+1737\gamma+3069}{10368}r^6 - \frac{388\gamma^2+1161\gamma+1881}{2304}r^4 \\ & + \frac{304\gamma^2+831\gamma+1242}{1728}r^2 - \frac{2708\gamma^2+7839\gamma+14211}{82944} \\ & + z\left(\frac{52\gamma^2+51\gamma+327}{384}r^4 - \frac{52\gamma^2+75\gamma+279}{192}r^2 + \frac{92\gamma^2+180\gamma+639}{1152}\right) \\ & + z^2\left(-\frac{7\gamma-3}{8}r^2 + \frac{13\gamma-27}{48}\right) + \frac{4\gamma^2-57\gamma+27}{144}z^3 \end{aligned} \tag{15.104}$$

$$v_3 = \frac{6836\gamma^2+23031\gamma+30627}{82944} r^7 - \frac{3380\gamma^2+11391\gamma+15291}{13824} r^5$$

$$+ \frac{3424\gamma^2+11271\gamma+15228}{13824} r^3 - \frac{7100\gamma^2+22311\gamma+30249}{82944} r$$

$$+ z\left(\frac{556\gamma^2+1737\gamma+3069}{1728} r^5 - \frac{388\gamma^2+1161\gamma+1881}{576} r^3 + \frac{304\gamma^2+831\gamma+1242}{864} r \right)$$

$$+ z^2\left(\frac{52\gamma^2+51\gamma+327}{192} r^3 - \frac{52\gamma^2+75\gamma+279}{192} r \right) - z^3\left(\frac{7\gamma-3}{12} r \right) \qquad (15.105)$$

Figure 15.17 presents the calculated values obtained with Hall's analysis for the contraction factor C_c as a function of the ratio ρ_t/y_t. Near $\rho_t/y_t = 2.0$, the results obtained are in reasonable agreement with the measurements of Back, et al.[22,23] For smaller values of ρ_t/y_t, the values obtained for C_c are much too small.

The method due to Kliegel[18] is a modification of that due to Hall. It replaces the expansion parameter R in equations 15.97 and 15.98 by the expression $(R+1.0)$. A series is thus obtained that is convergent even for $R < 1.0$. Kliegel's solution takes the form

$$\frac{\tilde{u}(x,y)}{a^*} = 1 + \frac{u_1(r,z)}{(R+1)} + \frac{1}{(R+1)^2}\left[u_1(r,z) + u_2(r,z)\right]$$

$$+ \frac{1}{(R+1)^3}\left[u_1(r,z) + 2u_2(r,z) + u_3(r,z)\right] + \cdots \qquad (15.106)$$

$$\frac{\tilde{v}(x,y)}{a^*} = \left[\frac{\gamma+1}{2(R+1)}\right]^{1/2}\left\{\frac{v_1(r,z)}{(R+1)} + \frac{1}{(R+1)^2}\left[\frac{3}{2}v_1(r,z) + v_2(r,z)\right]\right.$$

$$\left. + \frac{1}{(R+1)^3}\left[\frac{15}{8}v_1(r,z) + \frac{5}{2}v_2(r,z) + v_3(r,z)\right] + \cdots\right\} \qquad (15.107)$$

where $u_1(r,z)$, and so on, are given by equations 15.100 to 15.105. Figure 15.17 presents the contraction factor C_c calculated by Kliegel's method; it is in reasonable agreement with the measurements of Back, et al.[22,23] Figure 15.18 presents the shape of the sonic line, for $\rho_t/y_t = 0.625$, as calculated by applying Kliegel's method. The agreement with the experimental measurements of Back, et al. is satisfactory everywhere except near the wall. Kliegel's method gives the velocity components in algebraic form, as do Sauer's and Hall's methods. For large values of ρ_t/y_t, the three methods of analysis are essentially equivalent. For small values of ρ_t/y_t, Kliegel's method appears to be the most accurate.

Several investigators have solved the full nonlinear governing equations by different numerical procedures. For example, Prozan and Kooker[19] solved the steady two-dimensional flow problem by a relaxation method employing an error minimization technique. Serra[20] solved the unsteady two-dimensional flow problem by the Lax-Wendroff fixed grid finite difference method. Both of the aforementioned techniques are potentially more accurate than the methods of either Sauer, Hall, or Kliegel. The increased accuracy is obtained, however, at the expense of a

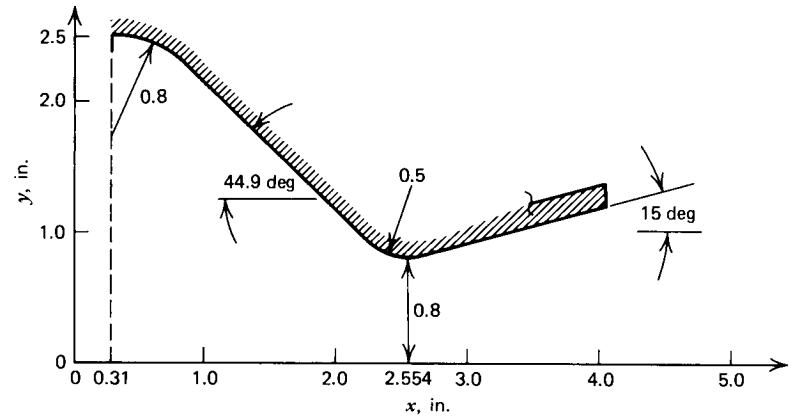

(a)

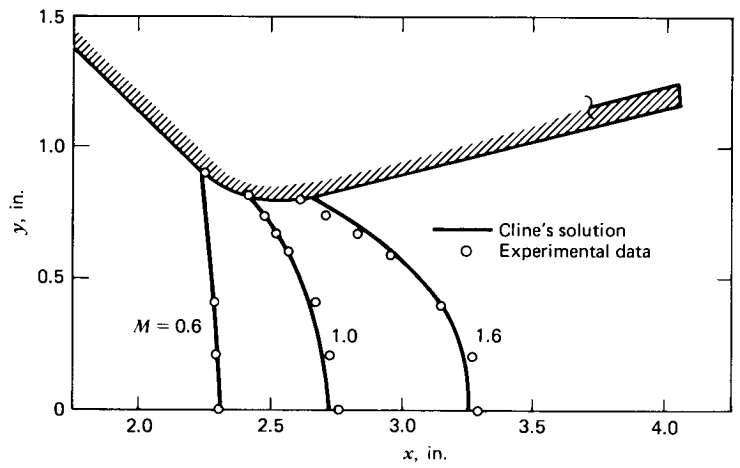

(b)

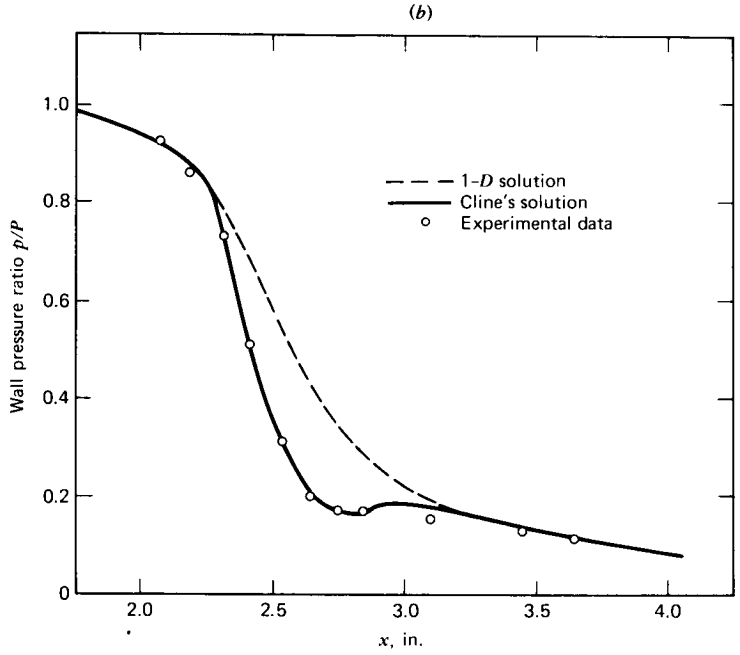

(c)

Figure 15.19 Transonic flow in a 45 deg-15-deg converging-diverging conical nozzle. (*a*) Nozzle geometry. (*b*) Mach number contours, (*c*) Wall pressure ratio. (Taken from Reference 21.)

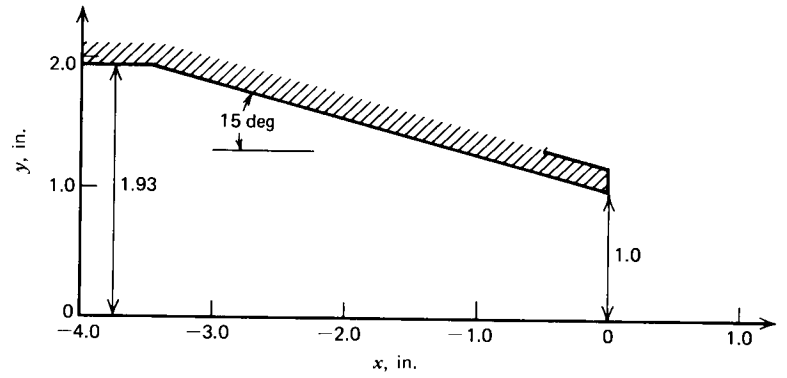

(*a*)

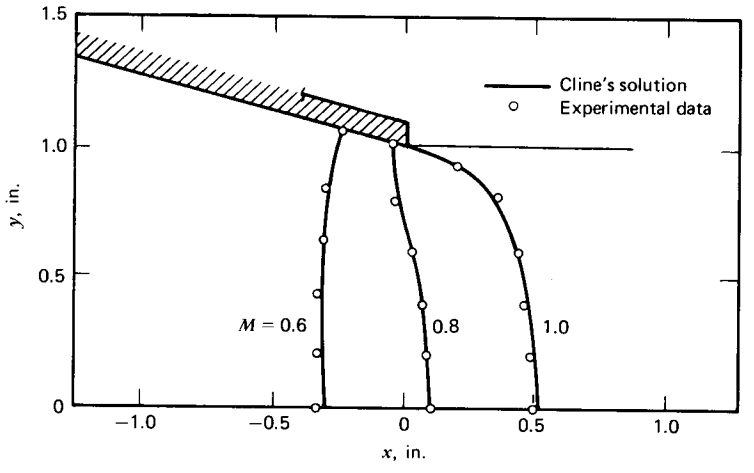

(*b*)

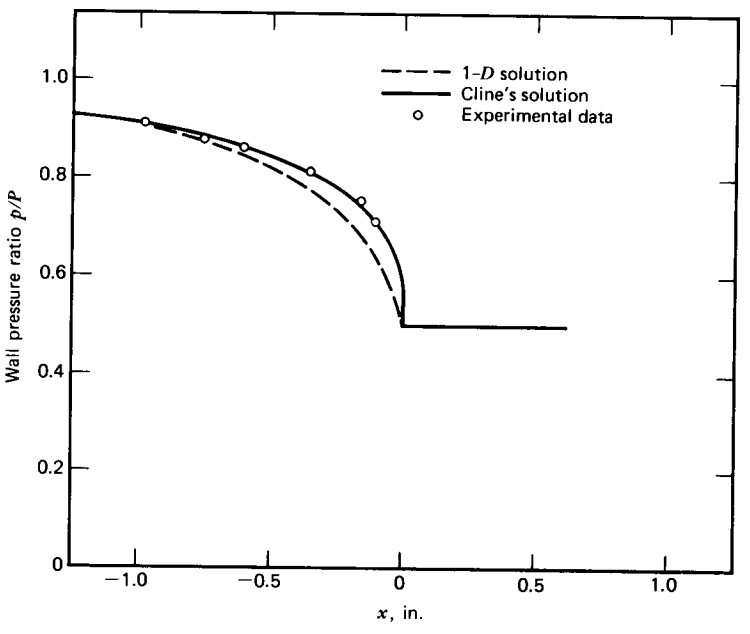

(*c*)

Figure 15.20 Transonic flow in a 15-deg converging conical nozzle. (*a*) Nozzle geometry. (*b*) Mach number contours. (*c*) Wall pressure ratio. (Taken from Reference 21.)

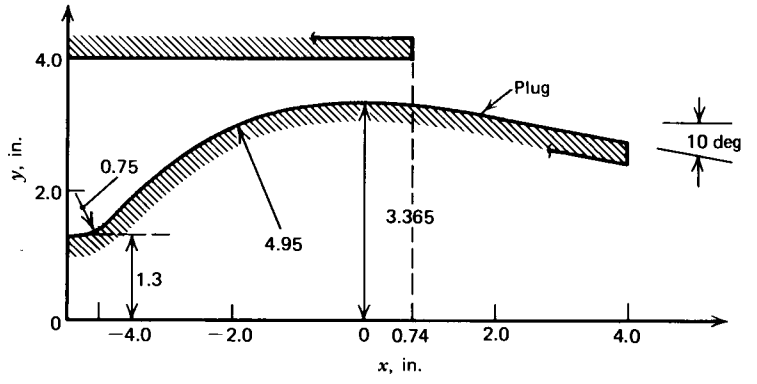

(*a*)

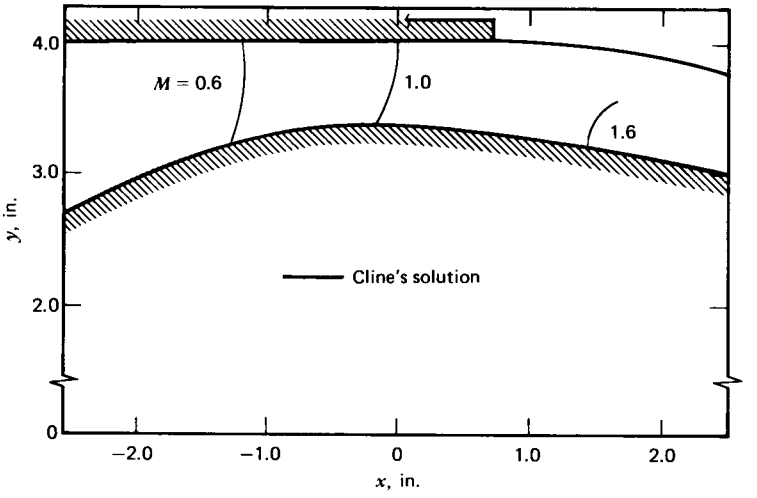

(*b*)

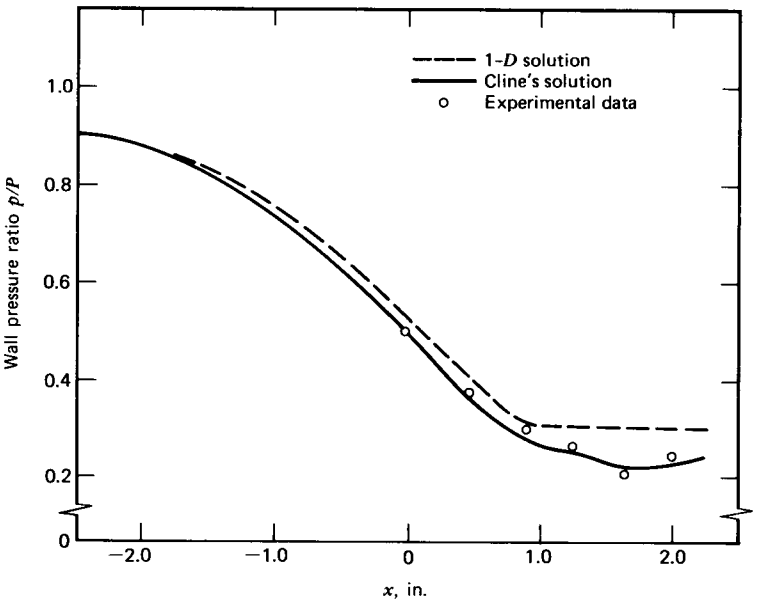

(*c*)

Figure 15.21 Transonic flow in a 10-deg conical plug nozzle. (*a*) Nozzle geometry. (*b*) Mach number contours. (*c*) Plug wall pressure ratio. (Taken from Reference 21.)

large expenditure of time for developing the computer program, and rather long computing times. Liddle and Archer[26] applied the *method of integral relations*, which has been employed for studying the transonic flow around a blunt body, to the problem of the flow in nozzles of arbitrary shape.

The method developed by Cline[21] is probably the most accurate and versatile of all of the methods discussed. Cline solved numerically the full set of nonlinear equations for unsteady flow. The MacCormack finite difference method[28] is employed for calculating the fluid properties at interior points of the flow field. The unsteady two-dimensional method of characteristics is employed for calculating the fluid properties at points on the boundaries. The steady-state solution is obtained as the asymptotic solution at large times. Cline's method requires only a modest expenditure of computer time. Figure 15.19 presents the solution for a conical converging-diverging nozzle; the semiangle of the inlet cone is 45 deg and that for the exit cone is 15 deg. The Mach number contours are shown in Fig. 15.19*b* and the wall pressure ratio is shown in Fig. 15.19*c*. The experimental data are those of Back, et al.[22,23] The computed discharge coefficient is 0.983 as compared with the experimental value of 0.985. In general, there is good agreement with the experimental data. Figure 15.20 presents the solution for a conical converging nozzle having a 15 deg semiangle. The experimental data are those of Thornock.[24] The computed discharge coefficient is 0.964 as compared with the experimental value of 0.960. In general, there is good agreement with the experimental data. Finally, Cline obtained the solution for the flow in the 10-deg conical plug nozzle shown in Fig. 15.21*a*. The experimental data are those of Bresnahan and Johns.[25] Again, there is good agreement with the experimental data. Cline's method is, therefore, capable of solving a wide variety of nozzle flow problems.

REFERENCES

1. A. Gray, G. B. Matthews, and J. M. McRobert, *A Treastise on Bessel Functions and Their Applications to Physics*, MacMillan, London, 1931.
2. J. J. Tuma, *Engineering Mathematics Handbook*, McGraw-Hill, New York, 1970, pp. 176–182.
3. L. A. Pipes and L. R. Harvill, *Applied Mathematics for Engineers and Physicists*, Third Edition, McGraw-Hill, New York, 1970, pp. 784–789
4. J. W. Converse and J. D. Hoffman, "Acoustic Standing Waves in a Rocket Combustion Chamber with Ring and Spoke Baffles," Report No. TM-67-5, JPC 436, Jet Propulsion Center, Purdue University, August 1967.
5. B. Carnahan, H. A. Luther, and J. O. Wilkes, *Applied Numerical Methods*, Wiley, New York, 1969, pp. 178–179.
6. Lord Rayleigh, *The Theory of Sound*, Vol. 2, Dover Publications, 1945.
7. R. P. Smith and D. F. Sprenger, "Combustion Instability in Solid-Propellant Rocket Motors," *Fourth Symposium (International) on Combustion*, Williams and Wilkins Company, 1953, pp. 893–906.
8. C. C. Ross and P. Datner, "Combustion Instability in Liquid-Propellant Rocket Motors —A Survey," *Selected Combustion Problems*, Butterworths Publications Ltd., 1954, pp. 352–380.
9. R. D. Geckler, "Unsolved Problems in Solid-Propellant Combustion," *Fifth Symposium (International) on Combustion*, Reinhold Publishing Company, 1955, pp. 29–40.
10. R. W. Hart and F. T. McClure, "Theory of Acoustic Instability in Solid-Propellant Combustion," *Tenth Symposium (International) on Combustion*, The Combustion Institute, Pittsburgh, Pa., 1965, pp. 1047–1065.
11. A. L. Karnesky and S. E. Colucci, "Recent Occurrences of Combustion Instability in Solid Rocket Motors—An Overview," *Journal of the American Institute of Aeronautics and Astronautics*, Vol. 12, No. 1, January 1975, pp. 33–38.

12. H. B. Mathes and E. W. Price, "Methods for Determining Characteristics of Acoustic Waves in Rocket Motors," *Journal of the American Institute of Aeronautics and Astronautics*, Vol. 12, No. 1, January 1975, pp. 39–43.
13. R. Sauer, "General Characteristics of the Flow through Nozzles at Near Critical Speeds," NACA TM No. 1147, 1947.
14. K. Oswatitsch and W. Rothstein, "Flow Pattern in a Converging-Diverging Nozzle," NACA TM No. 1215, 1949.
15. H. W. Emmons, "The Theoretical Flow of a Frictionless, Adiabatic, Perfect Gas Inside of a Two-Dimensional Hyperbolic Nozzle," NACA TN No. 1003, 1946.
16. D. F. Hopkins and D. E. Hill, "Effect of Small Radius of Curvature on Transonic Flow in Axisymmetric Nozzles," *Journal of the American Institute of Aeronautics and Astronautics*, Vol. 4, No. 8, August 1968, pp. 1337–1343.
17. I. M. Hall, "Transonic Flow in Two-Dimensional and Axially-Symmetric Nozzles," *Quarterly Journal of Mechanics and Applied Mathematics*, Vol. XV, Pt. 4, 1962, pp. 487–508.
18. J. R. Kliegel and J. N. Levine, "Transonic Flow in Small Throat Radius of Curvature Nozzles," *Journal of the American Institute of Aeronautics and Astronautics*, Vol. 7, No. 7, July 1969, pp. 1375–1378.
19. R. J. Prozan and D. E. Kooker, "The Error Minimization Technique with Application to a Transonic Nozzle Solution," *Journal of Fluid Mechanics*, Vol. 43, Part 2, 1970, pp. 269–277.
20. R. A. Serra, "The Determination of Internal Gas Flows by a Transient Numerical Technique," *Journal of the American Institute of Aeronautics and Astronautics*, Vol. 10, No. 5, May 1972, pp. 603–611.
21. M. C. Cline, "The Computation of Steady, Two-Dimensional Transonic Nozzle Flow by a Time Dependent Method," *Journal of the American Institute of Aeronautics and Astronautics*, Vol. 12, No. 4, April 1974, pp. 419–420.
22. L. H. Back, P. F. Massier, and H. L. Grier, "Comparison of Measured and Predicted Flows through Conical Supersonic Nozzles, with Emphasis on the Transonic Region," *Journal of the American Institute of Aeronautics and Astronautics*, Vol. 3, No. 9, September 1965, pp. 1606–1614.
23. R. F. Cuffel, L. H. Back, and P. F. Massier, "The Transonic Flowfield in a Supersonic Nozzle with Small Throat Radius of Curvature," *Journal of the American Institute of Aeronautics and Astronautics*, Vol. 7, No. 7, July 1969, pp. 1364–1366.
24. R. L. Thornock, "Experimental Investigation of the Flow Through Convergent-Conical Nozzles," Document No. D6-20375, The Boeing Co., September 1968.
25. D. L. Bresnahan and A. L. Johns, "Cold Flow Investigation of a Low Angle Turbojet Plug Nozzle with Fixed Throat and Translating Shroud at Mach Numbers from 0 to 2.0," NASA TM X-1619, August 1968.
26. S. G. Liddle and R. D. Archer, "Transonic Flow in Nozzles Using the Method of Integral Relations," *Journal of Spacecraft and Rockets*, Vol. 8, No. 7, July 1971, pp. 722–728.
27. R. D. Flack and H. D. Thompson, "Comparison of Pressure and LDV Velocity Measurements with Predictions in Transonic Flow," *Journal of the American Institute of Aeronautics and Astronautics*, Vol. 13, No. 1, January 1975, pp. 53–59.
28. R. W. MacCormack, "The Effect of Viscosity in Hypervelocity Impact Cratering," Paper No. 69-354, American Institute of Aeronautics and Astronautics, 1969.

16
the method of characteristics applied to steady two-dimensional irrotational supersonic flow

16–1 PRINCIPAL NOTATION FOR CHAPTERS 16 TO 20

a	speed of sound.
$C_{\pm}$	denotes characteristic curve C_+ or C_- (i.e., Mach lines).
C_D	$= \dot{m}_{2-D}/\dot{m}_{1-D}$, nozzle discharge coefficient.
F	thrust of a propulsive nozzle.
h	specific enthalpy.

$\dot{m}$	mass flow rate.
M	$= V/a$, Mach number.
p	static pressure.
p_o	ambient pressure.
P	stagnation pressure.
Q, R, S, T	coefficients in finite difference equations.
R	$= \bar{R}/\bar{m}$, gas constant.
s	specific entropy.
t	static temperature.
T	stagnation temperature.
u, v	velocity components in x,y direction, respectively.
V	$= (u^2 + v^2)^{1/2}$, magnitude of velocity.
$\mathbf{V}$	velocity vector.
x,y	two-dimensional independent coordinates.
x_e	nozzle length.
y_t	nozzle throat radius.

Greek Letters

α	$= \sin^{-1}(1/M)$, Mach angle or conical nozzle semidivergence angle.
γ	$= c_p/c_v$, specific heat ratio.
δ	$= 0$ for planar flow, $= 1$ for axisymmetric flow.
ε	$= A/A_t$, nozzle area ratio.
η_I	$= I_{sp}/I_{sp,1\text{-}D}$, specific impulse efficiency.
η_F	$= F/F_{1\text{-}D}$, thrust efficiency.
θ	$= \tan^{-1}(v/u)$, flow or streamline angle.
λ	$= (1 + \cos\alpha)/2$, nozzle divergence factor.
λ	$= \rho_t/y_t$, nondimensional nozzle throat radius of curvature.
$\lambda_\pm$	$= \tan(\theta \pm \alpha)$, slope of $C_\pm$ characteristics.
ρ	static density.
ρ_t	nozzle throat radius of curvature.
σ_i	arbitrary parameters in the method of characteristics.

Subscripts

a	nozzle throat attachment point.
e	nozzle exit lip point.
t	nozzle throat.
x,y	partial derivative with respect to x,y.
1-D	one-dimensional.
2-D	two-dimensional.
1,2,3,4	points in the finite difference networks.
+	positive, or left-running, characteristic (Mach line).
−	negative, or right-running, characteristic (Mach line).
o	streamline.

16–2 INTRODUCTION

The general theory of the method of characteristics is presented in Section 12–3. That theory is applied in Section 12–4 to develop a procedure for analyzing steady two-dimensional, planar and axisymmetric, irrotational supersonic flow. The numerical implementation of the method of characteristics is discussed in Section 12–5, where a complete numerical algorithm is developed for the unit process for an interior point in a supersonic flow field.

In this chapter, the mathematical results obtained in Chapter 12 by applying the method of characteristics to steady two-dimensional, planar and axisymmetric, irrotational supersonic flow are reviewed. Numerical algorithms for the boundary points of a flow are developed in Section 16–3.

The following types of boundary points are considered.

1. A point on a solid boundary, termed a *direct wall point*.
2. A prespecified point on a solid boundary, termed an *inverse wall point*.
3. A point on an axis of symmetry, called an *axis point*.
4. A point on a free pressure boundary, called a *free pressure boundary point*.

Numerical examples illustrating those units processes are presented, and FORTRAN computer programs for implementing all of the unit processes are given.

Applications of the numerical method of characteristics are presented for the following problems of engineering interest.

1. Analysis of the flow field in a nozzle of known shape.
2. Design of supersonic wind tunnel nozzles for parallel uniform flow.
3. Design of propulsive nozzles for maximum thrust.

An analysis is presented for the steady irrotational supersonic flow around an infinite axisymmetric cone aligned with the free stream. That type of flow is commonly called *Taylor–Maccoll flow* [see Section 7–10(b)]. A numerical example illustrating the solution of the governing equations is presented, and a FORTRAN computer program implementing the procedure is given.

16–3 UNIT PROCESSES

In this section, the mathematical results obtained in Chapter 12 are reviewed, and numerical algorithms are developed for the unit processes for the boundary points of a steady two-dimensional, planar and axisymmetric, irrotational supersonic flow field.

16–3(a) Review of Mathematical Background

The governing equations and the corresponding characteristic and compatibility equations for steady two-dimensional irrotational supersonic flow are derived in Section 12–4. The corresponding finite difference equations are determined in Section 12–5. Those results are reviewed in this section.

The equations governing the steady two-dimensional irrotational flow of a compressible fluid are the *gas dynamic equation* (equation 10.193), the *irrotationality condition* (equation 10.189), and the *speed of sound relationship* (equation 10.121). Those equations are summarized in Table 16.1.

Table 16.1 Governing Equations for Steady Two-Dimensional Irrotational Flow

$(u^2-a^2)u_x+(v^2-a^2)v_y+2uvu_y-\delta\frac{a^2v}{y}=0$	(10.193)
$u_y-v_x=0$	(10.189)
$a=a(V)=a(u,v)$ *(throughout the flow field)*	(10.121)

In equation 10.193, $\delta=0$ for planar flow and $\delta=1$ for axisymmetric flow.

Equation 10.121 is obtained from the thermodynamic properties of the fluid. It places no restrictions on the thermal and caloric equations of state for the fluid. All that is needed is that the functional relationship $a = a(V)$ be known. It may be algebraic, as in equation 3.186 for a thermally and calorically perfect gas, or in tabular form as in the case of either a frozen gas mixture having variable specific heats or an equilibrium gas mixture having a variable composition and variable specific heats (see Section 14–5).

The characteristic and compatibility equations corresponding to equations 10.193 and 10.189 are derived in Sections 12–4(b) and 12–4(c). The results are summarized in Table 16.2. The C_+ and C_- characteristics, corresponding to the + and − sign, respectively, in equation 16.1, are the Mach lines of the flow. They are illustrated in Fig. 16.1. The subscript $\pm$ in equation 16.2 indicates that the

Table 16.2 Characteristic and Compatibility Equations for Steady Two-Dimensional Irrotational Supersonic Flow

Characteristic equation

$$\left(\frac{dy}{dx}\right)_{\pm} = \lambda_{\pm} = \tan(\theta \pm \alpha) \qquad (\textit{Mach lines}) \tag{16.1}$$

Compatibility equation

$$(u^2 - a^2)\,du_{\pm} + [2uv - (u^2 - a^2)\lambda_{\pm}]\,dv_{\pm} - (\delta a^2 v/y)\,dx_{\pm} = 0 \qquad (\textit{along Mach lines}) \tag{16.2}$$

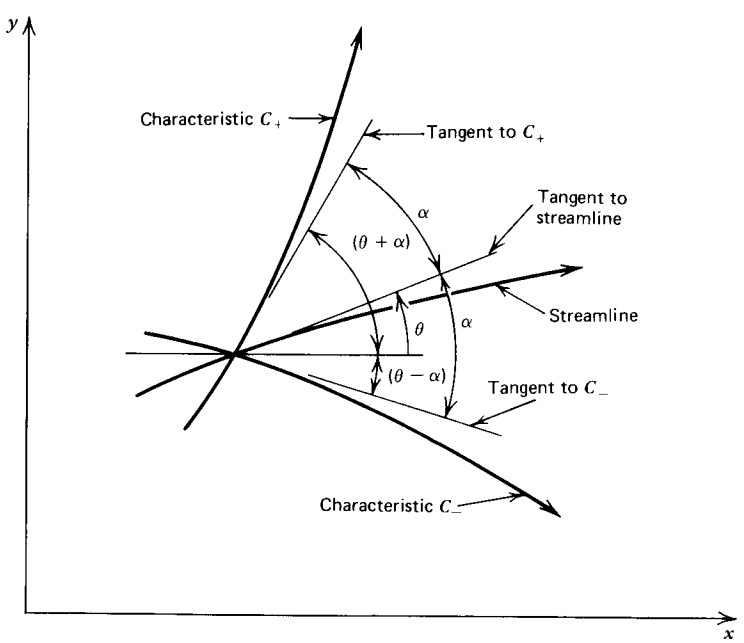

Figure 16.1 Schematic illustration of the characteristics (i.e., Mach lines) of a steady two-dimensional irrotational supersonic flow.

differentials du, dv, and dx are to be determined along the C_+ or C_- characteristic, respectively.

In Sections 12–5(c) and 12–5(d), the characteristic and compatibility equations presented in Table 16.2 are placed in finite difference form by applying the *modified Euler predictor-corrector method* [see Appendix A–6(e)] to the finite difference network illustrated in Fig. 16.2. The resulting finite difference equations are presented in Table 16.3. The corresponding computational equations based on the *average property method* for determining the coefficients of the finite differences are summarized in Table 16.4.

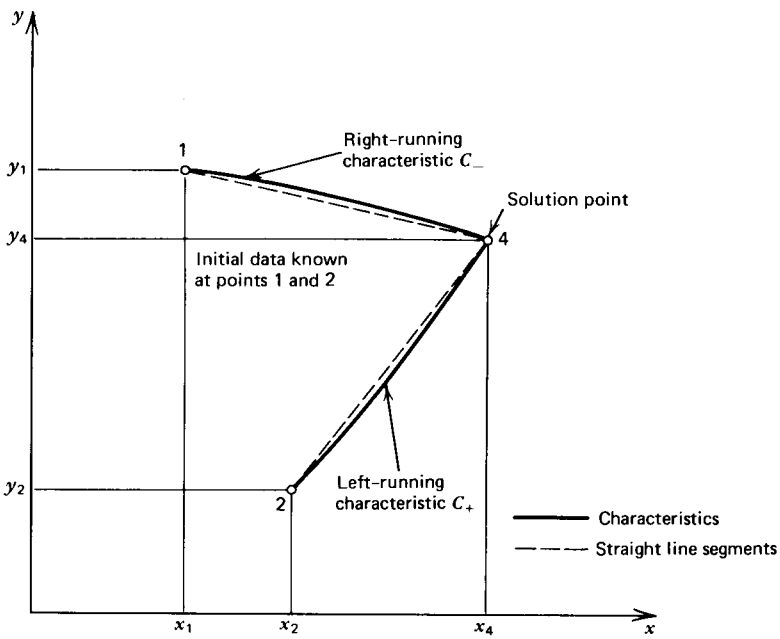

Figure 16.2 Finite difference network for applying the method of characteristics to a steady two-dimensional irrotational supersonic flow.

Table 16.3 Finite Difference Equations for Steady Two-Dimensional Irrotational Supersonic Flow

$$\Delta y_{\pm} = \lambda_{\pm} \Delta x_{\pm} \tag{16.3}$$

$$Q_{\pm} \Delta u_{\pm} + R_{\pm} \Delta v_{\pm} - S_{\pm} \Delta x_{\pm} = 0 \tag{16.4}$$

$$\lambda_{\pm} = \tan(\theta \pm \alpha) \tag{16.5}$$

$$Q = u^2 - a^2 \tag{16.6}$$

$$R = 2uv - (u^2 - a^2)\lambda \tag{16.7}$$

$$S = \delta \frac{a^2 v}{y} \tag{16.8}$$

+ or − denotes C_+ or C_- characteristic, respectively

Table 16.4 Computational Equations for Steady Two-Dimensional Irrotational Supersonic Flow

$$y_4-\lambda_+x_4=y_2-\lambda_+x_2 \tag{16.9}$$

$$y_4-\lambda_-x_4=y_1-\lambda_-x_1 \tag{16.10}$$

$$Q_+u_4+R_+v_4=T_+ \tag{16.11}$$

$$Q_-u_4+R_-v_4=T_- \tag{16.12}$$

$$T_+=S_+(x_4-x_2)+Q_+u_2+R_+v_2 \tag{16.13}$$

$$T_-=S_-(x_4-x_1)+Q_-u_1+R_-v_1 \tag{16.14}$$

$$V_\pm=\sqrt{u_\pm{}^2+v_\pm{}^2} \tag{16.15}$$

$$\theta_\pm=\tan^{-1}\left(\frac{v_\pm}{u_\pm}\right) \tag{16.16}$$

$$a_\pm=a(V_\pm) \tag{16.17}$$

$$M_\pm=\frac{V_\pm}{a_\pm} \tag{16.18}$$

$$\alpha_\pm=\sin^{-1}\left(\frac{1}{M_\pm}\right) \tag{16.19}$$

$$u_+=u_2,\quad v_+=v_2,\quad y_+=y_2 \qquad (predictor) \tag{16.20}$$

$$u_-=u_1,\quad v_-=v_1,\quad y_-=y_1 \qquad (predictor) \tag{16.21}$$

$$u_+=\frac{u_2+u_4}{2},\quad v_+=\frac{v_2+v_4}{2},\quad y_+=\frac{y_2+y_4}{2} \qquad (corrector) \tag{16.22}$$

$$u_-=\frac{u_1+u_4}{2},\quad v_-=\frac{v_1+v_4}{2},\quad y_-=\frac{y_1+y_4}{2} \qquad (corrector) \tag{16.23}$$

16–3(b) Interior Point

The unit process for a point interior to a supersonic flow field, termed an *interior point*, is described in detail in Section 12–5(d). The procedure consists of applying the computational equations presented in Table 16.4 to the finite difference grid illustrated in Fig. 16.2. Example 16.1 illustrates the calculation procedure for an interior point in its entirety.

A FORTRAN *computer program*, subroutine INTER, for implementing the calculations for an interior point employing the numerical method developed in Section 12–5(d) is described below. The program is written in subroutine form, which is suitable for direct application in a master logic program capable of determining an entire flow field. All of the control variables, the initial data (i.e., x_1, y_1, u_1, v_1, x_2, y_2, u_2, and v_2), and the solution values (i.e., x_4, y_4, u_4, and v_4) are transmitted between the main program and the subroutine through COMMON statements. The terminology employed in the program is defined in Tables 16.5 and 16.6. FORTRAN names for each variable are chosen to resemble the names employed in the modifier Euler predictor-corrector numerical method described in Section 12–5(d). The major portions of the program are identified by COMMENT cards. Figure 12.13 is a block diagram that serves as a flow diagram for the computer program.

```
      SUBROUTINE INTER

C     SUBROUTINE INTER CALCULATES THE SOLUTION AT AN INTERIOR POINT

      COMMON /CONTRL/ DELTA,NI,NT,ICOR,E1,E2,E3,E4,E5,IUNITS,PI,RAD
      COMMON /PROPTY/ G,RG,CP,TS,PS,PA,GC,GL $ REAL M
      COMMON /DATA/ X1,Y1,U1,V1,Q1,A1,P1,R1,T1,M1,X2,Y2,U2,V2,Q2,A2,P2,
     1R2,T2,M2,X3,Y3,U3,V3,Q3,A3,P3,R3,T3,M3,X4,Y4,U4,V4,Q4,A4,P4,R4,T4,
     2M4,LP,LM,LE,L12,L0 $ REAL M1,M2,M3,M4,LP,LM,LE,L12,L0

C     CALCULATE THE COEFFICIENTS FOR THE PREDICTOR

      Q=SQRT(U1**2+V1**2) $ A=ATAN(V1/U1) $ CALL THERMO (Q,P,R,T,C,M)
      LM=TAN(A-ASIN(1.0/M)) $ QM=U1**2-C**2 $ RM=2.0*U1*V1-QM*LM
      SM=DELTA*C**2*V1/Y1 $ Q=SQRT(U2**2+V2**2) $ A=ATAN(V2/U2)
      CALL THERMO (Q,P,R,T,C,M) $ LP=TAN(A+ASIN(1.0/M))
      QP=U2**2-C**2 $ RP=2.0*U2*V2-QP*LP $ SP=DELTA*C**2
      IF (Y2.EQ.0.0) SP=SP*V1/Y1 $ IF (Y2.GT.0.0) SP=SP*V2/Y2 $ ITER=0

C     SOLUTION OF THE FINITE DIFFERENCE EQUATIONS

   10 X4=(Y1-Y2-LM*X1+LP*X2)/(LP-LM) $ Y4=Y1+LM*(X4-X1)
      IF (Y4.LT.0.0) RETURN
      TM=SM*(X4-X1)+QM*U1+RM*V1 $ TP=SP*(X4-X2)+QP*U2+RP*V2
      DEN=QM*RP-QP*RM $ U4=(TM*RP-TP*RM)/DEN $ V4=(QM*TP-QP*TM)/DEN

C     CHECK FOR CONVERGENCE OR COMPLETION OF SPECIFIED ITERATIONS

      IF (ITER.EQ.ICOR) RETURN $ IF (ITER.EQ.0) GO TO 20
      IF ((ABS(X4-XC).GT.E1).OR.(ABS(Y4-YC).GT.E1)) GO TO 20
      IF ((ABS(U4-UC).LT.E2*UC).AND.(ABS(V4-VC).LT.E2*VC)) RETURN

C     CALCULATE THE COEFFICIENTS FOR THE CORRECTOR

   20 ITER=ITER+1 $ XC=X4 $ YC=Y4 $ UC=U4 $ VC=V4 $ Y=0.5*(Y1+Y4)
      U=0.5*(U1+U4) $ V=0.5*(V1+V4) $ Q=SQRT(U**2+V**2)
      A=ATAN(V/U) $ CALL THERMO (Q,P,R,T,C,M) $ LM=TAN(A-ASIN(1.0/M))
      QM=U**2-C**2 $ RM=2.0*U*V-QM*LM $ SM=DELTA*C**2*V/Y
      U=0.5*(U2+U4) $ V=0.5*(V2+V4) $ A=ATAN(V/U) $ Y=0.5*(Y2+Y4)
      Q=SQRT(U**2+V**2) $CALL THERMO(Q,P,R,T,C,M) $LP=TAN(A+ASIN(1.0/M))
      QP=U**2-C**2 $ RP=2.0*U*V-QP*LP $ SP=DELTA*C**2*V/Y $ GO TO 10
      END
```

Table 16.5 Terminology for the Supersonic Flow Method of Characteristics Programs

		Control Variables
DELTA	δ,	0 planar flow, 1 axisymmetric flow
ICOR		number of applications of the corrector desired
E1		convergence tolerance for location, m (in.)
E2		convergence tolerance for velocity, m/s (ft/sec)
GC	g_c,	1.0 m-kg/N-s^2 in SI units, 32.174 ft-lbm/lbf-sec^2 in EE units
GL		1.0 m^2/m^2 in SI units, 144.0 in.^{2}/ft^2 in EE units

		Gas Thermodynamic Properties and Stagnation Properties
G	γ,	specific heat ratio
RG	R,	gas constant, J/kg-K (ft-lbf/lbm-R)
TS	T,	stagnation temperature, K (R)
PS	P,	stagnation pressure, N/m^2 (lbf/in.^{2})
PA	p_o	ambient pressure, N/m^2 (lbf/in.^{2})

Table 16.5 Terminology for the Supersonic Flow Method of Characteristics Programs (Continued)

		Flow Field Properties
X	x,	axial coordinate, m (in.)
Y	y,	radial coordinate, m (in.)
U	u,	axial velocity, m/s (ft/sec)
V	v,	radial velocity, m/s (ft/sec)
Q	V,	velocity magnitude, m/s (ft/sec)
A	θ,	flow angle, rad
P	p,	static pressure, N/m^2 ($lbf/in.^2$)
R	ρ,	static density, kg/m^3 (lbm/ft^3)
T	t,	static temperature, K (R)
C	a,	speed of sound, m/s (ft/sec)
M	M,	Mach number
1,2,3,4		denotes properties at points in finite difference networks

Table 16.6 Terminology Employed in the Finite Difference Equations

L	$\lambda = \tan(\theta \pm \alpha)$
Q	$Q = (u^2 - a^2)$, m^2/s^2 (ft^2/sec^2)
R	$R = 2uv - \lambda(u^2 - a^2)$, m^2/s^2 (ft^2/sec^2)
S	$S = \delta a^2 v/y$, m^2/s^3 (ft^3/sec^3-in.)
T	$T = S\Delta x + Qu + Rv$, m^3/s^3 (ft^3/sec^3)
+ or −	denotes C_+ or C_- characteristic curve

The Mach number M, pressure p, density ρ, temperature t, and speed of sound a for the fluid are determined from the velocity magnitude V by calling subroutine THERMO. In this manner, the method of characteristics calculations are independent of the thermodynamic model employed for the fluid. That model may be modified by simply changing subroutine THERMO. The subroutine THERMO presented below calculates the properties of a perfect gas (i.e., constant γ and R). Other analytical equations of state may be employed, or the equation of state may be specified in tabular form.

```
      SUBROUTINE THERMO (Q,P,R,T,C,M)
C     SUBROUTINE THERMO CALCULATES M, P, R, T, AND C CORRESPONDING TO Q
      COMMON /PROPTY/ G,RG,CP,TS,PS,PA,GC,GL $ REAL M
      T=TS-Q**2/(2.0*GC*CP) $ C=SQRT(G*GC*RG*T) $ M=Q/C
      P=PS*(T/TS)**(G/(G-1.0)) $ R=P/(RG*T) $ RETURN
      END
```

The calculations may be terminated after a specified number of applications of the corrector through the input variable ICOR. ICOR = 0 gives the *Euler predictor algorithm*, ICOR = 1 yields the *modified Euler predictor-corrector algorithm*, and ICOR = 2 or more results in the *modified Euler algorithm with iteration*, where the number of applications of the corrector is equal to ICOR. Alternatively, the calculations may be terminated by convergence to a tolerance specified by the

input variables E1 and E2. When a fixed number of applications of the corrector are desired (i.e., ICOR given), E1 and E2 must be set equal to zero. When a specified tolerance is desired (i.e., E1 and E2 given), ICOR should be set equal to a large number; for example, 100.

In many situations, a combination of the two control methods is desirable. For example, in regions of the flow field where there are large gradients, convergence to a specified tolerance may be desirable. In regions of the flow field having small gradients, however, a single application of the corrector should be sufficient. Both types of control may be employed simultaneously in flow fields that have regions of both large and small gradients. For example, setting ICOR = 3, E1 = 0.001 m and E2 = 1.0 m/s would in all cases limit the number of applications of the corrector to three. In regions having small gradients, however, the convergence tolerance would generally be satisfied after only one application of the corrector. For flows that do not satisfy a reasonable convergence tolerance after three iterations, the point spacing should be reduced rather than continuing with more iterations.

Two special cases that are not accounted for in subroutine INTER may occur in the calculations for an actual flow field. The first case occurs when the slope of the right-runnning characteristic C_- is infinite; that is, $\lambda_- = \infty$. In that case, $x_4 = x_1$, and y_4 may be obtained from equation 16.9 for the line 24 in Fig. 16.2. The second case occurs when $\lambda_+ = \infty$. In that case, $x_4 = x_2$, and y_4 may be obtained from equation 16.10 for the line 14. There are several techniques that may be employed for checking the aforementioned two possibilities. The choice of technique depends on the type of computer being employed. Thus, no specific method is included in subroutine INTER. However, those two possibilities must be taken into account before the flow field computations are initiated, especially in computers having only 7 or 8 significant digits.

The interior point subroutine presented here, together with the direct wall point, inverse wall point, axis point, and free pressure boundary point subroutines presented in the remainder of this section, may be combined with a master logic program for solving a variety of steady two-dimensional irrotational supersonic flow fields.

Example 16.1 A perfect gas with $\gamma = 1.2$ and $R = 320.0$ J/kg-K is flowing in an axisymmetric propulsive nozzle having a stagnation pressure $P = 70.0 \cdot 10^5$ N/m^2 and a stagnation temperature $T = 3000$ K. The location and properties at two neighboring points in the flow field (points 1 and 2 in Fig. 16.2) are given in Table 16.7. Employing the unit process for an interior point, calculate the location of and the flow properties at the downstream intersection of the characteristics through points 1 and 2 (point 4 of Fig. 16.2) for three applications of the corrector.

Table 16.7 Initial-Value Data for an Interior Point (Example 16.1)

	Point 1	Point 2
x, m	0.131460	0.135683
y, m	0.040118	0.037123
u, m/s	2473.4	2502.8
v, m/s	812.8	737.6

Solution

The computations for the predictor and the first application of the corrector are presented below, and the results are presented in Table 16.8.

Table 16.8 Values of the Solution, for Successive Trials, for an Interior Point (Example 16.1)

	(0)	(1)	(2)	(3)
λ_+	0.61698	0.62385	0.62384	0.62384
λ_-	0.04987	0.04524	0.04492	0.04492
$Q_+ \cdot 10^{-6}$, m^2/s^2	5.7928	5.8188	5.8161	5.8162
$R_+ \cdot 10^{-6}$, m^2/s^2	0.11809	0.17786	0.17592	0.17592
$S_+ \cdot 10^{-9}$, m^2/s^3	9.3622	9.1031	9.1085	9.1088
$T_+ \cdot 10^{-9}$, m^3/s^3	14.638	14.745	14.737	14.737
$Q_- \cdot 10^{-6}$, m^2/s^2	5.6435	5.7438	5.7412	5.7412
$R_- \cdot 10^{-6}$, m^2/s^2	3.7393	3.7131	3.7114	3.7114
$S_- \cdot 10^{-9}$, m^2/s^3	9.6067	9.2288	9.2345	9.2347
$T_- \cdot 10^{-9}$, m^3/s^3	17.093	17.305	17.307	17.307
x_4, m	0.14134	0.14119	0.14118	0.14118
y_4, m	0.04061	0.04056	0.04056	0.04056
u_4, m/s	2511.0	2510.1	2510.1	2510.1
v_4, m/s	781.4	780.2	780.2	780.2

Column (0)—predictor values. Column (2)—first iteration of the corrector.
Column (1)—corrector values. Column (3)—second iteration of the corrector.

(a) *The speed of sound equation.* For a perfect gas, the speed of sound is given by equation 3.186, which is repeated below.

$$a^2 = a_o^2 - \frac{\gamma - 1}{2} V^2 = \gamma RT - \frac{\gamma - 1}{2} V^2 \tag{3.186}$$

For the present problem,

$$a = \left[1.2(320.0)(3000) - \frac{1.2-1}{2} V^2 \right]^{1/2} = (1.152 \cdot 10^6 - 0.1 V^2)^{1/2} \text{ m/s} \tag{a}$$

(b) *Calculate the coefficients for the predictor.* For the predictor, set the values of the flow properties $u_\pm$, $v_\pm$, and $y_\pm$ equal to their values at points 2 and 1, respectively. Thus,

$$u_+ = 2502.8 \text{ m/s} \qquad v_+ = 737.6 \text{ m/s} \qquad y_+ = 37.123 \text{ mm}$$

$$u_- = 2473.4 \text{ m/s} \qquad v_- = 812.8 \text{ m/s} \qquad y_- = 40.118 \text{ mm}$$

From equations 16.15 to 16.19, we obtain

$$V_+ = (u_+^2 + v_+^2)^{1/2} = [(2502.8)^2 + (737.6)^2]^{1/2} = 2609.2 \text{ m/s}$$

$$\theta_+ = \tan^{-1}\left(\frac{v_+}{u_+}\right) = \tan^{-1}\left(\frac{737.6}{2502.8}\right) = 16.421 \text{ deg}$$

$$a_+ = [1.1520 \cdot 10^6 - 0.1(2609.2)^2]^{1/2} = 686.45 \text{ m/s}$$

$$\alpha_+ = \sin^{-1}\left(\frac{a_+}{V_+}\right) = \sin^{-1}\left(\frac{686.45}{2609.2}\right) = 15.253 \text{ deg}$$

$$V_- = (u_-^2 + v_-^2)^{1/2} = [(2473.4)^2 + (812.8)^2]^{1/2} = 2603.5 \text{ m/s}$$

$$\theta_- = \tan^{-1}\left(\frac{v_-}{u_-}\right) = \tan^{-1}\left(\frac{812.8}{2473.4}\right) = 18.191 \text{ deg}$$

$$a_- = [1.1520 \cdot 10^6 - 0.1(2603.5)^2]^{1/2} = 688.61 \text{ m/s}$$

$$\alpha_- = \sin^{-1}\left(\frac{a_-}{V_-}\right) = \sin^{-1}\left(\frac{688.61}{2603.5}\right) = 15.337 \text{ deg}$$

Substituting the above values into equations 16.5 to 16.8, we obtain

$$\lambda_+ = \tan(\theta_+ + \alpha_+) = \tan(16.421 + 15.253) = 0.61698$$

$$Q_+ = u_+{}^2 - a_+{}^2 = (2502.8)^2 - (686.45)^2 = 5.7928 \cdot 10^6 \text{ m}^2/\text{s}^2$$

$$R_+ = 2u_+ v_+ - Q_+ \lambda_+ = 2.0(2502.8)(737.6) - (5.7928 \cdot 10^6)(0.61698)$$

$$R_+ = 0.11809 \cdot 10^6 \text{ m}^2/\text{s}^2$$

$$S_+ = a_+{}^2 v_+ / y_+ = (686.45)^2(737.6)/(0.037123) = 9.3622 \cdot 10^9 \text{ m}^2/\text{s}^3$$

$$\lambda_- = \tan(\theta_- - \alpha_-) = \tan(18.191 - 15.337) = 0.04987$$

$$Q_- = u_-{}^2 - a_-{}^2 = (2473.4)^2 - (688.61)^2 = 5.6435 \cdot 10^6 \text{ m}^2/\text{s}^2$$

$$R_- = 2u_- v_- - Q_- \lambda_- = 2.0(2473.4)(812.8) - (5.6435 \cdot 10^6)(0.04987)$$

$$R_- = 3.7393 \cdot 10^6 \text{ m}^2/\text{s}^2$$

$$S_- = a_-{}^2 v_- / y_- = (688.61)^2(812.8)/(0.040118) = 9.6067 \cdot 10^9 \text{ m}^2/\text{s}^3$$

(c) *Determination of* x_4, y_4, u_4, *and* v_4 *for the predictor.* Two equations for the determination of x_4 and y_4 are obtained by substituting the values of the coefficients calculated in part (b) into equations 16.9 and 16.10. Thus,

$$y_4 - 0.61698x_4 = 0.037123 - (0.61698)(0.135683) \quad \text{(b)}$$

$$y_4 - 0.04987x_4 = 0.040118 - (0.04987)(0.131460) \quad \text{(c)}$$

Solving equations (b) and (c) simultaneously, we obtain

$$x_4 = 0.141335 \text{ m} \qquad \text{and} \qquad y_4 = 0.040610 \text{ m}$$

From equations 16.13 and 16.14, the values of T_+ and T_- for the predictor are obtained. Thus,

$$T_+ = (9.3622 \cdot 10^9)(0.141335 - 0.135683) + (5.7928 \cdot 10^6)(2502.8)$$
$$+ (0.11809 \cdot 10^6)(737.6) = 14.638 \cdot 10^9 \text{ m}^3/\text{s}^3$$

$$T_- = (9.6067 \cdot 10^9)(0.141335 - 0.131460) + (5.6435 \cdot 10^6)(2473.4)$$
$$+ (3.7393 \cdot 10^6)(812.8) = 17.093 \cdot 10^9 \text{ m}^3/\text{s}^3$$

Substituting the values of $Q_{\pm}$, $R_{\pm}$, and $T_{\pm}$ into equations 16.11 and 16.12 yields the following two equations for the determination of u_4 and v_4.

$$(5.7928 \cdot 10^6)u_4 + (0.11809 \cdot 10^6)v_4 = 14.638 \cdot 10^9 \tag{d}$$

$$(5.6435 \cdot 10^6)u_4 + (3.7393 \cdot 10^6)v_4 = 17.093 \cdot 10^9 \tag{e}$$

Solving equations (d) and (e) simultaneously yields

$$u_4 = 2511.0 \text{ m/s} \qquad \text{and} \qquad v_4 = 781.4 \text{ m/s}$$

The application of the Euler predictor algorithm is complete. The column in Table 16.8 labeled (0) presents the predictor values for the terms $\lambda_{\pm}$, x_4, y_4, $Q_{\pm}$, etc.; that is, the terms that are calculated by the predictor portion of the numerical algorithm.

(d) *Calculation of the coefficients for the corrector.* One application of the corrector algorithm is presented in detail below. Before the corrector algorithm may be applied, the average values of the flow properties must be calculated (see equations 16.22 and 16.23), employing the initial and predictor values of u, v, and y. Thus,

$$u_+ = \frac{u_2 + u_4}{2} = \frac{2502.8 + 2511.0}{2} = 2506.9 \text{ m/s}$$

$$v_+ = \frac{v_2 + v_4}{2} = \frac{737.6 + 781.4}{2} = 759.5 \text{ m/s}$$

$$y_+ = \frac{y_2 + y_4}{2} = \frac{0.037123 + 0.040610}{2} = 0.038867 \text{ m}$$

$$u_- = \frac{u_1 + u_4}{2} = \frac{2473.4 + 2511.0}{2} = 2492.2 \text{ m/s}$$

$$v_- = \frac{v_1 + v_4}{2} = \frac{812.8 + 781.4}{2} = 797.1 \text{ m/s}$$

$$y_- = \frac{y_1 + y_4}{2} = \frac{0.040118 + 0.040610}{2} = 0.040360 \text{ m}$$

From equations 16.15 to 16.19

$$V_+ = \left[(2506.9)^2 + (759.5)^2\right]^{1/2} = 2619.4 \text{ m/s}$$

$$\theta_+ = \tan^{-1}\left(\frac{759.5}{2506.9}\right) = 16.855 \text{ deg}$$

$$a_+ = \left[1.1520 \cdot 10^6 - 0.1(2619.4)^2\right]^{1/2} = 682.55 \text{ m/s}$$

$$\alpha_+ = \sin^{-1}\left(\frac{682.55}{2619.4}\right) = 15.104 \text{ deg}$$

$$V_- = \left[(2492.2)^2 + (797.1)^2\right]^{1/2} = 2616.6 \text{ m/s}$$

$$\theta_- = \tan^{-1}\left(\frac{797.1}{2492.2}\right) = 17.736 \text{ deg}$$

$$a_- = \left[1.1520 \cdot 10^6 - 0.1(2616.6)^2\right]^{1/2} = 683.62 \text{ m/s}$$

$$\alpha_- = \sin^{-1}\left(\frac{683.62}{2616.6}\right) = 15.145 \text{ deg}$$

Substituting the above values into equations 16.5 to 16.8 yields

$$\lambda_+ = \tan(16.855 + 15.104) = 0.62385$$

$$Q_+ = (2506.9)^2 - (682.55)^2 = 5.8188 \cdot 10^6 \text{ m}^2/\text{s}^2$$

$$R_+ = 2.0(2506.9)(759.5) - (5.8188 \cdot 10^6)(0.62385) = 0.17786 \cdot 10^6 \text{ m}^2/\text{s}^2$$

$$S_+ = (682.55)^2(759.5)/(0.038867) = 9.1031 \cdot 10^9 \text{ m}^2/\text{s}^3$$

$$\lambda_- = \tan(17.736 - 15.145) = 0.04524$$

$$Q_- = (2492.2)^2 - (683.62)^2 = 5.7438 \cdot 10^6 \text{ m}^2/\text{s}^2$$

$$R_- = 2.0(2492.2)(797.1) - (5.7438 \cdot 10^6)(0.04524) = 3.7131 \cdot 10^6 \text{ m}^2/\text{s}^2$$

$$S_- = (683.62)^2(797.1)/(0.040360) = 9.2288 \cdot 10^9 \text{ m}^2/\text{s}^3$$

(e) *Determination of* x_4, y_4, u_4, *and* v_4 *for the corrector.* From equations 16.9 and 16.10, respectively,

$$y_4 - 0.62385x_4 = 0.037123 - (0.62385)(0.135683) \tag{f}$$

$$y_4 - 0.04524x_4 = 0.040118 - (0.04524)(0.131460) \tag{g}$$

Solving equations (f) and (g) simultaneously for x_4 and y_4, we obtain

$$x_4 = 0.141189 \text{ m} \qquad \text{and} \qquad y_4 = 0.040558 \text{ m}$$

From equations 16.13 and 16.14, respectively, we obtain

$$T_+ = (9.1031 \cdot 10^9)(0.141189 - 0.135683) + (5.8188 \cdot 10^6)(2502.8)$$
$$+ (0.17786 \cdot 10^6)(737.6) = 14.745 \cdot 10^9 \text{ m}^3/\text{s}^3$$

$$T_- = (9.2288 \cdot 10^9)(0.141189 - 0.131460) + (5.7438 \cdot 10^6)(2473.4)$$
$$+ (3.7131 \cdot 10^6)(812.8) = 17.315 \cdot 10^9 \text{ m}^3/\text{s}^3$$

Substituting for $Q_\pm$, $R_\pm$, and $T_\pm$ into equations 16.11 and 16.12, we obtain

$$(5.8188 \cdot 10^6)u_4 + (0.17786 \cdot 10^6)v_4 = 14.745 \cdot 10^9 \tag{h}$$

$$(5.7438 \cdot 10^6)u_4 + (3.7131 \cdot 10^6)v_4 = 17.315 \cdot 10^9 \tag{i}$$

Solving equations (h) and (i) simultaneously for u_4 and v_4 yields

$$u_4 = 2510.1 \text{ m/s} \qquad \text{and} \qquad v_4 = 780.2 \text{ m/s}$$

The application of the Euler corrector algorithm is complete. The column labeled (1) in Table 16.8 presents the results of applying the corrector algorithm.

(f) *Iteration of the corrector.* The results of two iterations of the corrector algorithm are presented in columns (2) and (3) in Table 16.8. Those results are obtained by twice repeatings steps (d) and (e), each with a new set of corrector values for x_4, y_4, u_4, and v_4. It is evident from columns (1), (2), and (3) of Table 16.8 that successive applications of the corrector have only a small effect on the final results.

The thermodynamic properties of the flowing fluid, such as p, ρ, and t, may be calculated from the flow velocity V and the stagnation properties of the fluid.

16–3(c) Direct Wall Point

At a solid boundary, the direction of the flow velocity vector must be identical to the slope of the wall. Because of that boundary condition, some changes are required in the numerical method presented in Section 12–5(d) for an interior point. Figure 16.3 illustrates schematically the conditions at a typical *direct wall point*, so called because the left-running characteristic C_+ is extended *directly* from a known interior point (point 2) until it intersects the wall (point 4). Point 1 does not exist physically because it is external to the flow field; the C_- characteristic connecting points 1 and 4 is, therefore, shown as a broken line. Consequently, only one characteristic and one compatibility equation are available for determining the location of the direct wall point (point 4) and the flow properties at that point. On the wall, however,

$$y = y(x) \qquad (specified) \tag{16.24}$$

$$\frac{dy}{dx} = \tan\theta = \frac{v}{u} \qquad (specified) \tag{16.25}$$

Equations 16.24 and 16.25, therefore, constitute two additional conditions for determining the location and the flow properties at point 4.

Figure 16.3 illustrates the case where the solid boundary is in the upper half of the xy plane. If the wall point is located on such a solid boundary, then equations 16.24 and 16.25 may be solved simultaneously with equations 16.9 and 16.11, which

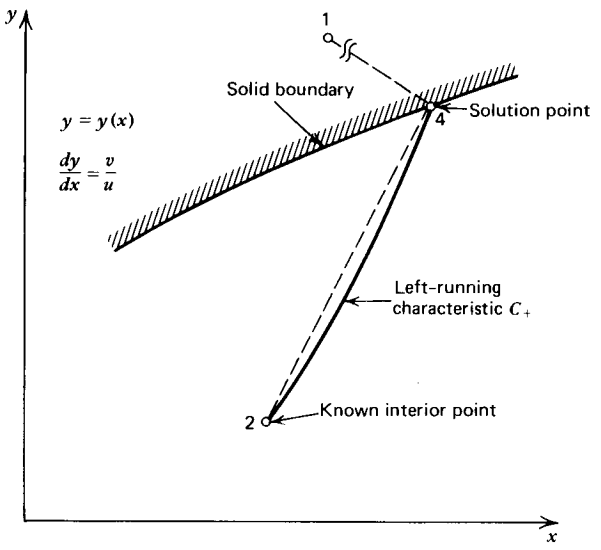

Figure 16.3 Unit process for a direct wall point.

are valid on a left-running or C_+ characteristic. If the solid boundary is in the lower half of the xy plane, then equations 16.10 and 16.12 are employed, because they are valid on a right-running or C_- characteristic.

A FORTRAN computer program, subroutine DRWALL, for implementing the numerical calculation procedure for the unit process for a direct wall point is discussed below. The computer program, like that for determining the solution for an interior point [see Section 16–3(b)], is in subroutine form. The terminology employed in the subject program is the same as that described in Tables 16.5 and 16.6. The general features of subroutine DRWALL are the same as those for subroutine INTER. The only major difference is the use of the subroutine BOUNDY for representing equations 16.24 and 16.25.

```
      SUBROUTINE DRWALL
C     SUBROUTINE WALL CALCULATES THE SOLUTION AT A DIRECT WALL POINT
      COMMON /CONTRL/ DELTA,NI,NT,ICOR,E1,E2,E3,E4,E5,IUNITS,PI,RAD
      COMMON /PROPTY/ G,RG,CP,TS,PS,PA,GC,GL $ REAL M
      COMMON /DATA/ X1,Y1,U1,V1,Q1,A1,P1,R1,T1,M1,X2,Y2,U2,V2,Q2,A2,P2,
     1R2,T2,M2,X3,Y3,U3,V3,Q3,A3,P3,R3,T3,M3,X4,Y4,U4,V4,Q4,A4,P4,R4,T4,
     2M4,LP,LM,LE,L12,L0 $ REAL M1,M2,M3,M4,LP,LM,LE,L12,L0
C     CALCULATE THE COEFFICIENTS FOR THE PREDICTOR
      ITER=0 $ Q=SQRT(U2**2+V2**2) $ A=ATAN(V2/U2)
      CALL THERMO (Q,P,R,T,C,M) $ LP=TAN(A+ASIN(1.0/M))
      QP=U2**2-C**2 $ RP=2.0*U2*V2-QP*LP $ SP=DELTA*C**2*V2/Y2
C     SOLUTION OF THE FINITE DIFFERENCE EQUATIONS
   10 CALL BOUNDY (2) $ TP=SP*(X4-X2)+QP*U2+RP*V2 $ L0=TAN(A4)
      U4=TP/(QP+L0*RP) $ V4=U4*L0 $ Q4=SQRT(U4**2+V4**2)
      CALL THERMO (Q4,P4,R4,T4,C,M4)
C     CHECK FOR CONVERGENCE OR COMPLETION OF SPECIFIED ITERATIONS
      IF (ITER.EQ.ICOR) RETURN $ IF (ITER.EQ.0) GO TO 20
      IF ((ABS(X4-XC).GT.E1).OR.(ABS(Y4-YC).GT.E1)) GO TO 20
      IF ((ABS(U4-UC).LT.E2*UC).AND.(ABS(V4-VC).LT.E2*VC)) RETURN
C     CALCULATE THE COEFFICIENTS FOR THE CORRECTOR
   20 ITER=ITER+1 $ XC=X4 $ YC=Y4 $ UC=U4 $ VC=V4 $ Y=0.5*(Y2+Y4)
      U=0.5*(U2+U4) $ V=0.5*(V2+V4) $ Q=SQRT(U**2+V**2)
      A=ATAN(V/U) $ CALL THERMO (Q,P,R,T,C,M) $ LP=TAN(A+ASIN(1.0/M))
      QP=U**2-C**2 $ RP=2.0*U*V-QP*LP $ SP=DELTA*C**2*V/Y $ GO TO 10
      END
```

The application of subroutine BOUNDY is illustrated in Example 16.2 for a nozzle having a circular arc throat joined tangentially to a wall having a contour described by second-order polynomial; that is, equation 16.24 is of the form $y = a + bx + cx^2$. The nozzle geometry is illustrated in Fig. 16.4. The determination of the coefficients a, b, and c is accomplished by an initial call of subroutine BOUNDY from the main program with the variable INITAL equal to 1. Subsequent calls from subroutine DRWALL with INITAL equal to 2 determine the point of intersection of the *left-running* characteristic 24 with the wall contour (x_4 and y_4) and the value of the wall slope $[(dy/dx)_4 = v_4/u_4]$ at the point of intersection (see

Fig. 16.3). Other types of wall contours, including tables, may be studied by replacing the subroutine BOUNDY presented here with one that specifies the particular wall contour of interest.

For a solid boundary in the lower half of the xy plane, an analogous program may be developed by employing the equations for *right-running* characteristics (equations 16.10 and 16.12). Subroutine BOUNDY must be altered also to account for the wall being in the lower half of the xy plane. The changes required are simple and straightforward; they are, therefore, not illustrated here.

As in subroutine INTER, a technique should be incorporated into subroutine DRWALL to handle the case where $\lambda_+ = \infty$. In that case, $x_4 = x_2$, and y_4 is found from the equation for the wall contour.

```
      SUBROUTINE BOUNDY (INITAL)

C     SUBROUTINE BOUNDY LOCATES THE INTERSECTION OF A LEFT-RUNNING
C     CHARACTERISTIC WITH A SECOND-ORDER QUADRATIC WALL CONTOUR

      COMMON /CONTRL/ DELTA,NI,NT,ICOR,E1,E2,E3,E4,E5,IUNITS,PI,RAD
      COMMON /CONTUR/ YT,RTU,RTD,AA,AE,XE,YE
      COMMON /DATA/ X1,Y1,U1,V1,Q1,A1,P1,R1,T1,M1,X2,Y2,U2,V2,Q2,A2,P2,
     1R2,T2,M2,X3,Y3,U3,V3,Q3,A3,P3,R3,T3,M3,X4,Y4,U4,V4,Q4,A4,P4,R4,T4,
     2M4,LP,LM,LE,L12,L0 $ REAL M1,M2,M3,M4,LP,LM,LE,L12,L0

      GO TO (10,20), INITAL

C     CALCULATE THE COEFFICIENTS A, B, AND C

   10 TA=AA/RAD $ TE=AE/RAD $ XA=RTD*SIN(TA) $ YA=YT+RTD*(1.0-COS(TA))
      C=(TAN(TE)-TAN(TA))/(2.0*(XE-XA)) $ B=TAN(TA)-2.0*C*XA
      A=YA-B*XA-C*XA**2 $ YE=A+B*XE+C*XE**2 $ LE=B+2.0*C*XE $ RETURN

C     LOCATE THE INTERSECTION OF A CHARACTERISTIC AND THE WALL

   20 IF (AA.NE.AE) GO TO 30 $ X4=(A-Y2+LP*X2)/(LP-B) $ GO TO 40
   30 X4=((LP-B)-SQRT((LP-B)**2-4.0*C*(A-Y2+LP*X2)))/(2.0*C)
   40 Y4=A+B*X4+C*X4**2 $ A4=ATAN(B+2.0*C*X4) $ RETURN
      END
```

Example 16.2. A perfect gas having $\gamma = 1.20$ and $R = 320.0$ J/kg-K is flowing in the axisymmetric converging-diverging nozzle illustrated in Fig. 16.4. The stagnation pressure $P = 70 \cdot 10^5$ N/m^2 and the stagnation temperature $T = 3000$ K. The radius of the nozzle throat $y_t = 25.0$ mm. The throat contour comprises two circular arcs. The radius of curvature of the upstream circular arc $\rho_{tu} = 50.0$ mm, and the radius of curvature of the downstream circular arc $\rho_{td} = 12.5$ mm. The throat contour is joined tangentially to a downstream contour that is specified by a second-order polynomial. The attachment angle $\theta_a = 35$ deg, and the nozzle exit lip angle $\theta_e = 10$ deg. The nozzle length is $x_e = 250.0$ mm. The location of a point near the wall and the corresponding flow properties are $x_2 = 60.480$ mm, $y_2 = 59.625$ mm, $u_2 = 1967.1$ m/s, and $v_2 = 1141.3$ m/s.

Employing the unit process for a direct wall point, calculate the location of the intersection of the wall and the left-running characteristic through point 2 (i.e., point 4), and determine the properties of the fluid at the wall point. Make three applications of the corrector.

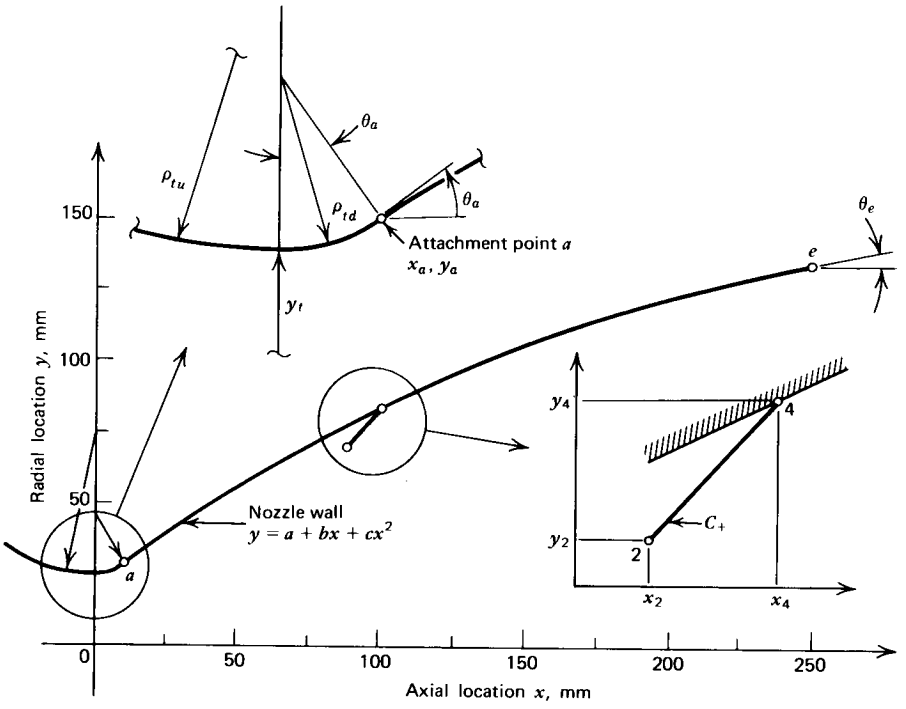

Figure 16.4 Nozzle geometry employed in subroutine BOUNDY.

Solution

The computations are presented below. The results are summarized in Table 16.9.

Table 16.9 Values of the Solution, for Successive Trials, for a Direct Wall Point (Example 16.2)

	(0)	(1)	(2)	(3)
λ_+	1.2187	1.2134	1.2135	1.2135
x_4, mm	63.460	63.488	63.485	63.485
y_4, mm	63.258	63.273	63.273	63.273
$Q_+ \cdot 10^{-6}$, m^2/s^2	3.3247	3.2581	3.2574	3.2574
$R_+ \cdot 10^{-5}$, m^2/s^2	5.4793	5.5553	5.5514	5.5514
$S_+ \cdot 10^{-10}$, m^3/s^3-m	1.2151	1.1763	1.1762	1.1762
$T_+ \cdot 10^{-9}$, m^3/s^3	7.0245	7.0784	7.0766	7.0766
u_4, m/s	1977.7	1977.4	1977.4	1977.4
v_4, m/s	1144.6	1144.4	1144.4	1144.4

Column (0)—predictor values. Column (2)—first iteration of the corrector.
Column (1)—corrector values. Column (3)—second iteration of the corrector.

(a) *Determination of the downstream wall contour.* The equation for the downstream wall contour is

$$y = a + bx + cx^2 \tag{a}$$

and

$$\frac{dy}{dx} = \tan\theta = b + 2cx \tag{b}$$

The determination of the values of the coefficients a, b, and c requires three conditions: the location of the attachment point a (x_a, y_a), the attachment angle θ_a, and the exit lip angle θ_e. The attachment point location (x_a, y_a) is determined from the following equations (see Fig. 16.4).

$$x_a = \rho_{td} \sin\theta_a \tag{c}$$

$$y_a = y_t + (1 - \cos\theta_a)\rho_{td} \tag{d}$$

where $\theta_a = 35$ deg, $\rho_{td} = 12.5$ mm, and $y_t = 25.0$ mm. Hence,

$$x_a = 12.5 \sin(35) = 7.1697 \text{ mm}$$

$$y_a = 25.0 + [1 - \cos(35)](12.5) = 27.261 \text{ mm}$$

Substituting (x_a, y_a) into equation (a) and (x_a, θ_a) and (x_e, θ_e) into equation (b) gives

$$27.261 = a + 7.1697b + (7.1697)^2 c \tag{e}$$

$$\tan(35) = 0.70021 = b + 2(7.1697)c \tag{f}$$

$$\tan(10) = 0.17633 = b + 2(250.0)c \tag{g}$$

Solving equations (e), (f), and (g) simultaneously for a, b, and c, and substituting the results into equations (a) and (b) gives

$$y = 22.1852 + 0.71568x - 0.0010787x^2 \tag{h}$$

$$\tan\theta = \frac{v}{u} = 0.71568 - 0.0021574x \tag{i}$$

where x and y are specified in mm. Equations (h) and (i) are the specific forms of equations 16.24 and 16.25 for the contour of the nozzle wall illustrated in Fig. 16.4.

(b) *The speed of sound equation.* From equation (a) of Example 16.1,

$$a = (1.1520 \cdot 10^6 - 0.1\ V^2)^{1/2} \text{ m/s} \tag{j}$$

(c) *Flow properties at the initial point.* Applying equations 16.15 to 16.19 to the given data at point 2, the initial point, yields

$$V_2 = [(1967.1)^2 + (1141.3)^2]^{1/2} = 2274.2 \text{ m/s}$$

$$\theta_2 = \tan^{-1}\left(\frac{1141.3}{1967.1}\right) = 30.122 \text{ deg}$$

$$a_2 = [1.1520 \cdot 10^6 - 0.1(2274.2)^2]^{1/2} = 796.74 \text{ m/s}$$

$$\alpha_2 = \sin^{-1}\left(\frac{796.74}{2274.2}\right) = 20.508 \text{ deg}$$

(d) *Calculation of the coefficients for the predictor.* The results from part (c) and equations 16.5 to 16.8 may be employed to obtain the predictor values for the coefficients along the C_+ characteristic connecting points 2 and 4 (see Fig. 16.4). Thus,

$$\lambda_+ = \tan(30.122 + 20.508) = 1.2187$$

$$Q_+ = (1967.1)^2 - (796.74)^2 = 3.2347 \cdot 10^6 \text{ m}^2/\text{s}^2$$

$$R_+ = 2.0(1967.1)(1141.3) - (3.2347 \cdot 10^6)(1.2187) = 5.4793 \cdot 10^5 \text{ m}^2/\text{s}^2$$

$$S_+ = (796.74)^2(1141.3)/(0.059625) = 1.2151 \cdot 10^{10} \text{ m}^2/\text{s}^3$$

(e) *Determination of x_4, y_4, u_4, and v_4 for the predictor.* From equation 16.9 and equation (h) of part (a), the following two equations relating x_4 and y_4 are obtained.

$$y_4 - 1.2187x_4 = 59.625 - 1.2187(60.480) \tag{k}$$

$$y_4 = 22.1852 + 0.71568x_4 - 0.0010787x_4^2 \tag{l}$$

Solving equations (k) and (l) gives the following predictor values for x_4 and y_4.

$$x_4 = 63.460 \text{ mm} \qquad \text{and} \qquad y_4 = 63.258 \text{ mm}$$

From equation 16.13, the predictor value for T_+ is

$$T_+ = (1.2151 \cdot 10^{10})(0.063460 - 0.060480) + (3.2347 \cdot 10^6)(1967.1) + (5.4793 \cdot 10^5)(1141.3)$$

$$T_+ = 7.0245 \cdot 10^9 \text{ m}^3/\text{s}^3$$

Equation 16.11 and equation (i) of part (a) furnish two relationships between the predictor values of u_4 and v_4. Thus,

$$(3.2347 \cdot 10^6)u_4 + (5.4793 \cdot 10^5)v_4 = 7.0245 \cdot 10^9 \tag{m}$$

$$\left[0.71568 - (0.0021574)(63.460)\right]u_4 - v_4 = 0 \tag{n}$$

Solving equations (m) and (n) gives the predictor values for u_4 and v_4.

$$u_4 = 1977.7 \text{ m/s} \qquad \text{and} \qquad v_4 = 1144.6 \text{ m/s}$$

Column (0) in Table 16.9 presents the values obtained by applying the predictor.

(f) *Application of the corrector.* The modified Euler corrector is applied by repeating steps (c) to (e) employing the average values of the flow properties, as illustrated in Example 16.1. The results are presented in column (1) of Table 16.9. Two additional iterations of the corrector are presented in columns (2) and (3) of Table 16.9. From those results it is apparent that iteration of the corrector has only a very minor effect on the final results.

16–3(d) Inverse Wall Point

The direct wall point unit process presented in Section 16–3(c) (see Fig. 16.3) is a *direct method* where the left-running characteristic C_+ from a known point within the flow (point 2) is extended to the wall, thus determining the location of the

solution point (point 4). In regions of a flow field where the property gradients are extremely large, the direct method may result in too large a spacing of the solution points along the wall. In that case, an *inverse method* may be employed that is based on spacing beforehand the solution points along the wall and employing the method of characteristics for determining the flow properties at the prespecified wall points.

Figure 16.5 illustrates schematically the situation where the initial-value points 1 and 3 are known from previous calculations, point 4 is the prespecified solution point, and point 2 is the intersection of the rearward left-running characteristic C_+ through point 4 with the right-running characteristic 13. Because the location of point 4 (x_4,y_4) is specified, only the flow properties at point 4 must be determined by the method of characteristics. Thus, the compatibility equation (equation 16.11) which is valid along the left-running characteristic 14, together with equation 16.25, may be employed for calculating u_4 and v_4 if the location and flow properties at point 2 are known. The location of point 2 is established by determining the intersection of the rearward left-running characteristic 24 (equation 16.9) with the right-running characteristic 13 (equation 16.10). The flow properties at point 2 are determined by linear interpolation between points 1 and 3.

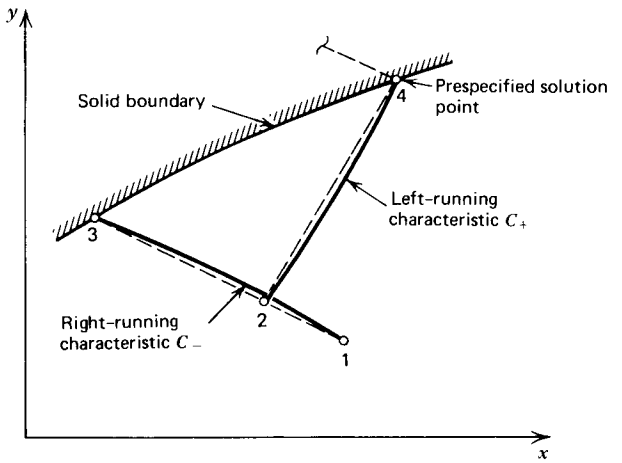

Figure 16.5 Unit process for an inverse wall point.

Since the slope of the characteristic 24 depends on the unknown flow properties at points 2 and 4, a predictor-corrector numerical method is employed to locate point 2 during each pass through the modifier Euler predictor-corrector algorithm. During the primary predictor step for determining the flow properties at point 4, the following secondary predictor-corrector method is applied for determining the location of point 2. First, the flow properties at point 2 are set equal to those at point 3, and the slope λ_+ of the characteristic 24 is determined. Second, employing that value of the slope λ_+, the location of point 2 on the rearward left-running characteristic 24 through the prespecified point 4 is calculated. Third, the flow properties at point 2 are determined by linear interpolation between points 1 and 3. A corrector step is then employed using the values of u_2 and v_2 from the third step, and point 2 is relocated. That corrector step is repeated iteratively until the location of point 2 converges to the desired tolerance. After the location of point 2 is established, the *primary predictor step* for determining the flow properties at point 4 is completed. The *primary corrector step* is then performed by relocating point 2 by

the secondary predictor-corrector technique discussed above, where now the slope of the characteristic 24 is based on the average values for u and v between the points 2 and 4. The primary corrector step may be iterated if desired.

A computer program, subroutine INWALL, for implementing the *inverse wall point unit process* is presented below. The program is in subroutine form. The terminology employed in the program is the same as that described in Tables 16.5 and 16.6. An *inverse interior point unit process* may be developed in an analogous manner.

```
      SUBROUTINE INWALL
C     SUBROUTINE INWALL CALCULATES THE SOLUTION AT AN INVERSE WALL POINT
      COMMON /CONTRL/ DELTA,NI,NT,ICOR,E1,E2,E3,E4,E5,IUNITS,PI,RAD
      COMMON /PROPTY/ G,RG,CP,TS,PS,PA,GC,GL $ REAL M
      COMMON /DATA/ X1,Y1,U1,V1,Q1,A1,P1,R1,T1,M1,X2,Y2,U2,V2,Q2,A2,P2,
     1R2,T2,M2,X3,Y3,U3,V3,Q3,A3,P3,R3,T3,M3,X4,Y4,U4,V4,Q4,A4,P4,R4,T4,
     2M4,LP,LM,LE,L12,LO $ REAL M1,M2,M3,M4,LP,LM,LE,L12,LO
C     CALCULATE PROPERTIES FOR THE PREDICTOR
      ITER=0 $ LM=(Y3-Y1)/(X3-X1) $ U4=U3 $ V4=V3 $ U2=U3 $ V2=V3 $XA=X3
C     DETERMINE THE LOCATION AND PROPERTIES AT POINT 2
   10 U=0.5*(U2+U4) $ V=0.5*(V2+V4) $ Q=SQRT(U**2+V**2)
      A=ATAN(V/U) $ CALL THERMO (Q,P,R,T,C,M) $ LP=TAN(A+ASIN(1.0/M))
      X2=(Y4-Y1+LM*X1-LP*X4)/(LM-LP) $ Y2=Y4+LP*(X2-X4)
      D=(X2-X1)/(X3-X1) $ U2=U1+D*(U3-U1) $ V2=V1+D*(V3-V1)
      IF (ITER.GT.0) GO TO 15 $ U4=U2 $ V4=V2
   15 IF (ABS(X2-XA).LT.0.000001) GO TO 20 $ XA=X2 $ GO TO 10
C     CALCULATE COEFFICIENTS AND SOLVE THE FINITE DIFFERENCE EQUATIONS
   20 U=0.5*(U2+U4) $ V=0.5*(V2+V4) $ Y=0.5*(Y2+Y4)
      Q=SQRT(U**2+V**2) $ A=ATAN(V/U) $ CALL THERMO (Q,P,R,T,C,M)
      QP=U**2-C**2 $ RP=2.0*U*V-QP*LP $ SP=DELTA*C**2*V/Y
      TP=SP*(X4-X2)+QP*U2+RP*V2 $ U4=TP/(QP+LO*RP) $ V4=U4*LO
      Q4=SQRT(U4**2+V4**2) $ CALL THERMO (Q4,P4,R4,T4,C,M4)
C     CHECK FOR CONVERGENCE OR COMPLETION OF SPECIFIED ITERATIONS
      IF (ITER.EQ.ICOR) RETURN $ IF (ITER.EQ.0) GO TO 30
      IF ((ABS(U4-UC).LT.E2*UC).AND.(ABS(V4-VC).LT.E2*VC)) RETURN
   30 ITER=ITER+1 $ UC=U4 $ VC=V4 $ GO TO 10
      END
```

Example 16.3. The perfect gas considered in Example 16.1 is flowing adjacent to the wall of a nozzle in the throat region where the inverse wall point unit process is to be employed. The unit process is illustrated in Fig. 16.5. The properties at points 1 and 3, and the location and wall angle at point 4 are specified in Table 16.10.

Table 16.10 Initial-Value Data for an Inverse Wall Point (Example 16.3)

	Point 1	Point 3	Point 4
x, mm	5.495	5.085	5.283
y, mm	26.020	26.080	26.170
u, m/s	1578.3	1577.5	—
v, m/s	705.7	702.3	—
θ, deg	—	—	25.000

Employing the unit process for an inverse wall point, calculate the flow properties at point 4 for three applications of the corrector.

Solution

The computations for the predictor are presented below. The results for three applications of the corrector are presented in Table 16.11.

Table 16.11 Values of the Solution, for Successive Trials, for an Inverse Wall Point (Example 16.3)

	(0)	(1)	(2)	(3)
λ_+	1.5029	1.5147	1.5151	1.5151
x_2, mm	5.211	5.211	5.211	5.211
y_2, mm	26.063	26.063	26.063	26.063
$Q_+ \cdot 10^{-6}$, m^2/s^2	1.6357	1.6489	1.6480	1.6480
$R_+ \cdot 10^{-6}$, m^2/s^2	−0.23882	−0.21812	−0.21823	−0.21823
$S_+ \cdot 10^{-10}$, m^3/s^3-m	2.2988	2.3468	2.3467	2.3467
$T_+ \cdot 10^{-10}$, m^3/s^3	0.24144	0.24498	0.24483	0.24483
u_4, m/s	1583.9	1583.4	1583.4	1583.4
v_4, m/s	738.5	738.3	738.3	738.3

Column (0)—predictor values. Column (2)—first iteration of the corrector.
Column (1)—corrector values. Column (3)—second iteration of the corrector.

(a) *The speed of sound equation.* From equation (a) of Example 16.1

$$a = (1.1520 \cdot 10^6 - 0.1 V^2)^{1/2} \text{ m/s} \tag{a}$$

(b) *Location of point 2 for the predictor.* The location of point 2 is determined iteratively. For the first pass, assume $u_2 = u_3$ and $v_2 = v_3$. Then,

$$\theta_2 = \tan^{-1}\left(\frac{v_2}{u_2}\right) = \tan^{-1}\left(\frac{702.3}{1577.5}\right) = 24.000 \text{ deg}$$

$$V_2 = \left[(1577.5)^2 + (702.3)^2\right]^{1/2} = 1726.8 \text{ m/s}$$

$$a_2 = \left[1.1520 \cdot 10^6 - 0.1(1726.8)^2\right]^{1/2} = 924.02 \text{ m/s}$$

$$\alpha_2 = \sin^{-1}\left(\frac{924.02}{1726.8}\right) = 32.351 \text{ deg}$$

$$\lambda_+ = \tan(24.000 + 32.351) = 1.5023$$

The equation of line 13 is

$$\frac{y - y_1}{x - x_1} = \frac{y_3 - y_1}{x_3 - x_1} = \frac{26.080 - 26.020}{5.085 - 5.495} = -0.14634$$

Thus, at point 2 on line 13

$$y_2 - 26.020 = (-0.14634)(x_2 - 5.495) \tag{b}$$

The equation of line 24 is (see equation 16.9)

$$y_2 - y_4 = \lambda_+ (x_2 - x_4)$$

$$y_2 - 26.170 = 1.5023(x_2 - 5.283) \tag{c}$$

Solving equations (b) and (c) simultaneously, we obtain

$$x_2 = 5.211 \text{ mm} \quad \text{and} \quad y_2 = 26.063 \text{ mm}$$

Interpolating along line 13 for u_2 and v_2 gives

$$u_2 = u_1 + \left(\frac{x_2 - x_1}{x_3 - x_1}\right)(u_3 - u_1) = 1578.3 + (0.69268)(1577.5 - 1578.3)$$

$$u_2 = 1577.7 \text{ m/s}$$

$$v_2 = 705.7 + (0.69268)(702.3 - 705.7) = 703.34 \text{ m/s}$$

Repeating the entire procedure with the predicted values of u_2 and v_2 yields

$$x_2 = 5.211 \text{ mm} \quad \text{and} \quad y_2 = 26.063 \text{ mm}$$

$$u_2 = 1577.7 \text{ m/s} \quad \text{and} \quad v_2 = 703.34 \text{ m/s}$$

Thus, no further iterations are required.

(c) *Calculation of the coefficients for the predictor.* Determine the flow properties at point 2. From equations 16.15 to 16.19, we obtain

$$\theta_2 = \tan^{-1}\left(\frac{703.34}{1577.7}\right) = 24.027 \text{ deg}$$

$$V_2 = \left[(1577.7)^2 + (703.34)^2\right]^{1/2} = 1727.4 \text{ m/s}$$

$$a_2 = \left[1.1520 \cdot 10^6 - 0.1(1727.4)^2\right]^{1/2} = 923.91 \text{ m/s}$$

$$\alpha_2 = \sin^{-1}\left(\frac{923.91}{1727.4}\right) = 32.334 \text{ deg}$$

From equations 16.5 to 16.8

$$\lambda_+ = \tan(24.027 + 32.334) = 1.5029$$

$$Q_+ = (1577.7)^2 - (923.91)^2 = 1.6357 \cdot 10^6 \text{ m}^2/\text{s}^2$$

$$R_+ = 2.0(1577.7)(703.34) - (1.6357 \cdot 10^6)(1.5029) = -0.23882 \cdot 10^6 \text{ m}^2/\text{s}^2$$

$$S_+ = (923.91)^2(703.34)/(0.026063) = 2.2988 \cdot 10^{10} \text{ m}^3/\text{s}^3 - \text{m}$$

(d) *Determination of u_4 and v_4 for the predictor.* From equation 16.13

$$T_+ = (2.2988 \cdot 10^{10})(0.005283 - 0.005211)$$
$$+ (1.6357 \cdot 10^6)(1577.7) + (-0.23882 \cdot 10^6)(703.34)$$

$$T_+ = 0.24144 \cdot 10^{10} \text{ m}^3/\text{s}^3$$

At point 4, $\tan\theta_4 = \tan(25.000) = 0.46631$. Thus,

$$u_4 \tan\theta_4 - v_4 = u_4(0.46631) - v_4 = 0 \tag{d}$$

From equation 16.11

$$(1.6357 \cdot 10^6)u_4 + (-0.23882 \cdot 10^6)v_4 = 0.24144 \cdot 10^{10} \tag{e}$$

Solving equations (d) and (e) for u_4 and v_4, we obtain

$$u_4 = 1583.9 \text{ m/s} \qquad \text{and} \qquad v_4 = 738.53 \text{ m/s}$$

This completes the application of the predictor. The column labeled (0) in Table 16.11 summarizes the predictor calculations.

(e) *Application of the corrector.* The modified Euler corrector is applied by repeating steps (b) to (d) employing the average values of the flow properties, as illustrated in Example 16.1. Column (1) of Table 16.11 presents the results. Columns (2) and (3) of Table 16.11 present the results of two iterations of the corrector. Iteration of the corrector has only a very small effect on the final results.

16–3(e) Axis of Symmetry Point

For a two-dimensional axisymmetric flow, the x axis is a line of symmetry. Figure 16.6 illustrates schematically a typical *axis point*, that is, point 4, located on the axis of symmetry. If point 1 is a point on the C_ characteristic through point 4, then, as illustrated in Fig. 16.6, a point 2 below the axis of symmetry may be defined that is the *mirror image* of point 1. As a result, point 4 is then analogous to the interior point illustrated in Fig. 16.2. Consequently, the procedure discussed in Section 12–5(d) may be applied for determining the location and the flow properties at the axis point, point 4 of Fig. 12.6. It should be noted, however, that in this case $y_4 = v_4 = \theta_4 = 0$, and those results simplify the unit process for an axis of symmetry point. For the latter only the right-running characteristic 14 is employed, and

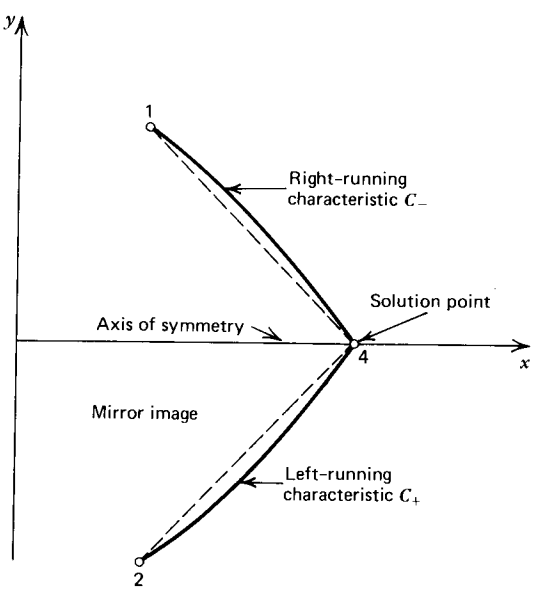

Figure 16.6 Unit process for a point on the axis of symmetry.

equations 16.10 and 16.12 are solved simultaneously with the data $y_4 = v_4 = \theta_4 = 0$ to determine x_4 and u_4. The details of the numerical calculations are illustrated in Example 16.4.

For an axisymmetric flow, the coefficient S given by equation 16.8 is indeterminate on the axis of symmetry (i.e., the x axis). However, no problem arises during the predictor calculations because the predictor calculates the value of S at point 1. Moreover, the corrector calculation of S is based on the average values of y_+ and v_+, each of which is nonzero.

A computer program, subroutine AXIS, for determining an axis point for an axisymmetric flow is presented below. The terminology and procedures employed in that program are in every way compatible with subroutines INTER, DRWALL, and INWALL.

The problem encountered in subroutines INTER, DRWALL, and INWALL when the slope of one of the Mach lines becomes infinite does not occur for an axis point. The slope of the C_- characteristic is $\lambda_- = \tan(\theta - \alpha)$, which is approximately equal to $\tan(-\alpha)$ near the axis where θ approaches zero. Since $\tan(-\alpha)$ is given by $-1/\sqrt{M^2-1}$, λ_- cannot be infinite for a *supersonic flow*, because $M > 1$.

```
      SUBROUTINE AXIS

C     SUBROUTINE AXIS CALCULATES THE SOLUTION AT AN AXIS POINT

      COMMON /CONTRL/ DELTA,NI,NT,ICOR,E1,E2,E3,E4,E5,IUNITS,PI,RAD
      COMMON /PROPTY/ G,RG,CP,TS,PS,PA,GC,GL $ REAL M
      COMMON /DATA/ X1,Y1,U1,V1,Q1,A1,P1,R1,T1,M1,X2,Y2,U2,V2,Q2,A2,P2,
     1R2,T2,M2,X3,Y3,U3,V3,Q3,A3,P3,R3,T3,M3,X4,Y4,U4,V4,Q4,A4,P4,R4,T4,
     2M4,LP,LM,LE,L12,L0 $ REAL M1,M2,M3,M4,LP,LM,LE,L12,L0

C     CALCULATE THE COEFFICIENTS FOR THE PREDICTOR

      ITER=0 $ Y4=0.0 $ V4=0.0 $ Q=SQRT(U1**2+V1**2)
      A=ATAN(V1/U1) $ CALL THERMO (Q,P,R,T,C,M) $ LM=TAN(A-ASIN(1.0/M))
      QM=U1**2-C**2 $ RM=2.0*U1*V1-QM*LM $ SM=DELTA*C**2*V1/Y1

C     SOLUTION OF THE FINITE DIFFERENCE EQUATIONS

   10 X4=X1-Y1/LM $ TM=SM*(X4-X1)+QM*U1+RM*V1 $ U4=TM/QM

C     CHECK FOR CONVERGENCE OR COMPLETION OF SPECIFIED ITERATIONS

      IF (ITER.EQ.ICOR) RETURN $ IF (ITER.EQ.0) GO TO 20
      IF ((ABS(X4-XC).LT.E1).AND.(ABS(U4-UC).LT.E2*UC)) RETURN

C     CALCULATE THE COEFFICIENTS FOR THE CORRECTOR

   20 ITER=ITER+1 $ XC=X4 $ UC=U4 $ Y=0.5*(Y1+Y4)
      U=0.5*(U1+U4) $ V=0.5*(V1+V4) $ Q=SQRT(U**2+V**2)
      A=ATAN(V/U) $ CALL THERMO (Q,P,R,T,C,M) $ LM=TAN(A-ASIN(1.0/M))
      QM=U**2-C**2 $ RM=2.0*U*V-QM*LM $ SM=DELTA*C**2*V/Y $ GO TO 10
      END
```

Example 16.4. The gas described in Example 16.1 flows through the axisymmetric nozzle illustrated in Fig. 16.4. The location of a point near the axis of symmetry (point 1 in Fig. 16.6) and the flow properties at that point are $x_1 = 79.625$ mm, $y_1 = 1.290$ mm, $u_1 = 2306.1$ m/s, and $v_1 = 35.7$ m/s. Determine the point of intersection of the C_- characteristic through point 1 with the axis of symmetry (point 4) and calculate the flow properties at point 4.

Solution

The calculations for determining the desired information at the axis of symmetry point are presented below. The results are summarized in Table 16.12.

(a) *The speed of sound equation.* From equation (a) of Example 16.1

$$a = (1.1520 \cdot 10^6 - 0.1 V^2)^{1/2} \text{ m/s} \tag{a}$$

(b) *Flow properties at the initial-value point.* From equations 16.15 to 16.19, we obtain the following values for the flow properties at the initial-value point.

$$V_1 = \left[(2306.1)^2 + (35.7)^2 \right]^{1/2} = 2306.4 \text{ m/s}$$

$$\theta_1 = \tan^{-1}\left(\frac{35.7}{2306.1} \right) = 0.887 \text{ deg}$$

$$a_1 = \left[1.1520 \cdot 10^6 - 0.1(2306.4)^2 \right]^{1/2} = 787.43 \text{ m/s}$$

$$\alpha_1 = \sin^{-1}\left(\frac{787.43}{2306.4} \right) = 19.963 \text{ deg}$$

(c) *Calculation of the coefficients for the predictor.* From part (b) and equations 16.5 to 16.8, the coefficients along the C_- characteristic are (see Fig. 16.6)

$$\lambda_- = \tan(0.887 - 19.963) = -0.34582$$

$$Q_- = (2306.1)^2 - (787.43)^2 = 4.6980 \cdot 10^6 \text{ m}^2/\text{s}^2$$

$$R_- = 2.0(2306.1)(35.7) - (4.6980 \cdot 10^6)(-0.34582) = 1.7893 \cdot 10^6 \text{ m}^2/\text{s}^2$$

$$S_- = (787.43)^2(35.7)/(0.001290) = 1.7159 \cdot 10^{10} \text{ m}^3/\text{s}^3 - \text{m}$$

(d) *Determination of x_4 and u_4 for the predictor.* From equation 16.10, noting that $y_4 = 0.0$, we obtain

$$-(-0.34582)x_4 = 1.290 - (-0.34582)(79.625) \tag{b}$$

Hence, the value of x_4 for the predictor is

$$x_4 = 83.355 \text{ mm}$$

Table 16.12 Values of the Solution, for Successive Trials, for an Axis Point (Example 16.4)

r	(0)	(1)	(2)	(3)
λ_-	−0.34582	−0.35017	−0.35033	−0.35032
x_4, mm	83.355	83.309	83.308	83.308
$Q_- \cdot 10^{-6}$, m²/s²	4.6980	4.7672	4.7647	4.7647
$R_- \cdot 10^{-6}$, m²/s²	1.7893	1.7521	1.7520	1.7520
$S_- \cdot 10^{-10}$, m³/s³ − m	1.7159	1.6988	1.6994	1.6944
$T_- \cdot 10^{-10}$, m³/s³	1.0962	1.1119	1.1113	1.1113
$u_4 = V_4$, m/s	2333.3	2332.3	2332.4	2332.4

Column (0)—predictor values. Column (2)—first iteration of the corrector.
Column (1)—corrector values. Column (3)—second iteration of the corrector.

From equation 16.14, the value of T_- for the predictor is

$$T_- = (1.7159 \cdot 10^{10})(0.083355 - 0.079625) + (4.6980 \cdot 10^6)(2306.1) + (1.7893 \cdot 10^6)(35.7)$$

$$T_- = 1.0962 \cdot 10^{10} \text{ m}^3/\text{s}^3$$

From equation 16.12, noting that $v_4 = 0.0$,

$$(4.6980 \cdot 10^6)u_4 = 1.0962 \cdot 10^{10} \tag{c}$$

Hence, the value of u_4 for the predictor is

$$u_4 = 2333.3 \text{ m/s}$$

The column labeled (0) in Table 16.12 presents the values of the properties obtained by the predictor.

(e) *Application of the corrector.* The modified Euler corrector is applied by repeating steps (b) to (d) employing the average values of the flow properties, as illustrated in Example 16.1. The results are presented in column (1) of Table 16.12. Table 16.12 also presents the results of two additional applications of the corrector in the columns labeled (2) and (3). It is seen that the effect of iteration of the corrector is very small.

16–3(f) Free Pressure Boundary Point

Figure 16.7 illustrates schematically the upper portion of the region where a jet of compressible fluid discharges into an ambient atmosphere having the static pressure p_o At a point on the outer boundary of the jet, denoted as point 4, the static pressure of the flowing fluid is $p_4 = p_o$ Such a point is termed a *free pressure boundary point*. Accordingly, the numerical procedure for analyzing a free pressure boundary point must take into account the condition $p_4 = p_o$

As in the case of a wall point (see Fig. 16.3), the C_- characteristic 14 lies outside of the flow field. Consequently, only one compatibility equation (i.e., equation 16.11) is applicable, and it is valid along the C_+ characteristic denoted by 24 in Fig. 16.7. As stated above, the static pressure at point 4 is a known quantity, that is, $p_4 = p_o$ Furthermore, the fluid velocity V and the static pressure p in the jet are related uniquely by the relationship for isentropic flow. Consequently, the velocity

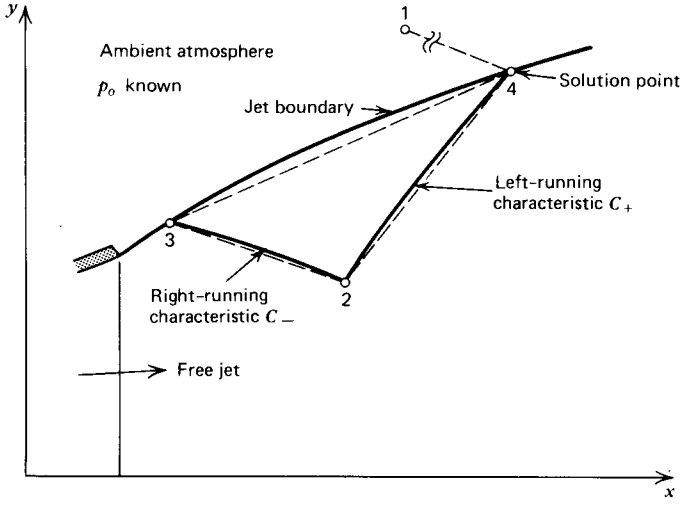

Figure 16.7 Unit process for a free pressure boundary point.

V_4 is given by

$$V_4=(u_4^2+v_4^2)^{1/2}=f(p_4)=f(p_o)=known\ value \tag{16.26}$$

Equations 16.11 and 16.26 furnish two relationships between u_4 and v_4. Solving those two equations simultaneously for u_4 and v_4 yields

$$u_4=\frac{Q_+T_+-R_+\left[V_4^2(Q_+^2+R_+^2)-T_+^2\right]^{1/2}}{Q_+^2+R_+^2} \tag{16.27}$$

$$v_4=(V_4^2-u_4^2)^{1/2} \tag{16.28}$$

An additional relationship is required for determining the location of point 4. That relationship is provided by the condition that the jet boundary is a streamline. Along the jet boundary 34 (see Fig. 16.7), the slope λ_o is

$$\frac{dy}{dx}=\frac{v}{u}=\lambda_o \tag{16.29}$$

Writing equation 16.29 in finite difference form yields

$$y_4-\lambda_o x_4=y_3-\lambda_o x_3 \tag{16.30}$$

Equations 16.9 and 16.30 may be solved simultaneously for the location of point 4.

A computer program, subroutine JET, for the determination of a point on a free pressure boundary is presented below. The terminology and procedures in subroutine JET are compatible with subroutines INTER, DRWALL, INWALL, and AXIS.

```
      SUBROUTINE JET
C     SUBROUTINE JET CALCULATES THE SOLUTION AT A JET BOUNDARY POINT
      COMMON /CONTRL/ DELTA,NI,NT,ICOR,E1,E2,E3,E4,E5,IUNITS,PI,RAD
      COMMON /PROPTY/ G,RG,CP,TS,PS,PA,GC,GL $ REAL M
      COMMON /DATA/ X1,Y1,U1,V1,Q1,A1,P1,R1,T1,M1,X2,Y2,U2,V2,Q2,A2,P2,
     1R2,T2,M2,X3,Y3,U3,V3,Q3,A3,P3,R3,T3,M3,X4,Y4,U4,V4,Q4,A4,P4,R4,T4,
     2M4,LP,LM,LE,L12,L0 $ REAL M1,M2,M3,M4,LP,LM,LE,L12,L0
C     CALCULATE THE COEFFICIENTS FOR THE PREDICTOR
      Q4=SQRT(2.0*GC*CP*T0*(1.0-(PA/P0)**((G-1.0)/G)))
      ITER=0 $ Q=SQRT(U2**2+V2**2) $ A=ATAN(V2/U2)
      CALL THERMO (Q,P,R,T,C,M) $ LP=TAN(A+ASIN(1.0/M)) $ L0=V3/U3
      QP=L2**2-C**2 $ RP=2.0*U2*V2-QP*LP $ SP=DELTA*C**2*V2/Y2
C     SOLUTION OF THE FINITE DIFFERENCE EQUATIONS
   10 X4=(Y3-Y2-L0*X3+LP*X2)/(LP-L0) $ Y4=Y3+L0*(X4-X3)
      TP=SP*(X4-X2)+QP*U2+RP*V2
      U4=(QP*TP-RP*SQRT(Q4**2*(QP**2+RP**2)-TP**2))/(QP**2+RP**2)
      V4=(TP-QP*U4)/RP
C     CHECK FOR CONVERGENCE OR COMPLETION OF SPECIFIED ITERATIONS
      IF (ITER.EQ.ICOR) RETURN $ IF (ITER.EQ.0) GO TO 20
      IF ((ABS(X4-XC).GT.E1).OR.(ABS(Y4-YC).GT.E1)) GO TO 20
      IF ((ABS(U4-UC).LT.E2*UC).AND.(ABS(V4-VC).LT.E2*VC)) RETURN
C     CALCULATE THE COEFFICIENTS FOR THE CORRECTOR
   20 ITER=ITER+1 $ XC=X4 $ YC=Y4 $ UC=U4 $ VC=V4 $ Y=0.5*(Y2+Y4)
      U=0.5*(U2+U4) $ V=0.5*(V2+V4) $ Q=SQRT(U**2+V**2)
      A=ATAN(V/U) $ CALL THERMO (Q,P,R,T,C,M) $ LP=TAN(A+ASIN(1.0/M))
      QP=L**2-C**2 $ RP=2.0*U*V-QP*LP $ SP=DELTA*C**2*V/Y
      U=0.5*(U3+U4) $ V=0.5*(V3+V4) $ L0=V/U $ GO TO 10
      END
```

Example 16.5. The gas described in Example 16.1 flows as a free jet where the ambient pressure $p_o = 60{,}000\ \text{N/m}^2$. The location and flow properties at two points in that flow field are given in Table 16.13 (see Fig. 16.7). Determine the point of intersection of the free jet boundary and the C_+ characteristic through point 2 (i.e., point 4 in Fig. 16.7), and the flow properties at point 4.

Table 16.13 Initial-Value Data for a Free Pressure Boundary Point (Example 16.5)

	Point 2	Point 3
x, m	0.34226	0.32979
y, m	0.12312	0.12351
u, m/s	2455.3	2422.5
v, m/s	619.7	663.5

Solution

The calculations for the free pressure boundary point are presented below, and the results are summarized in Table 16.14.

(a) *The speed of sound equation.* From equation (a) of Example 16.1

$$a = (1.1520 \cdot 10^6 - 0.1\ V^2)^{1/2}\ \text{m/s} \tag{a}$$

(b) *Velocity at the solution point.* Because the flow is isentropic, the fluid velocity V_4 at point 4 is given by equation 3.184, Table 3.4. Thus,

$$V_4 = \left\{ \frac{2\gamma RT}{\gamma - 1} \left[1 - \left(\frac{p_4}{P} \right)^{(\gamma-1)/\gamma} \right] \right\}^{1/2}$$

$$V_4 = \left\{ \frac{2(1.2)(320.0)(3000)}{(1.2-1)} \left[1 - \left(\frac{0.60}{70.0} \right)^{(1.2-1)/1.2} \right] \right\}^{1/2}$$

$$V_4 = 2511.7\ \text{m/s}$$

(c) *Flow properties at the initial-value point.* Applying equations 16.15 to 16.19 at the initial point (point 2, Table 16.13) yields

$$V_2 = \left[(2455.3)^2 + (619.7)^2 \right]^{1/2} = 2532.3\ \text{m/s}$$

$$\theta_2 = \tan^{-1}\left(\frac{619.7}{2455.3} \right) = 14.165\ \text{deg}$$

$$a_2 = \left[1.1520 \cdot 10^6 - 0.1(2532.3)^2 \right]^{1/2} = 714.67\ \text{m/s}$$

$$\alpha_2 = \sin^{-1}\left(\frac{714.67}{2532.3} \right) = 16.393\ \text{deg}$$

Table 16.14 Values of the Solution, for Successive Trials, for a Free Pressure Boundary Point (Example 16.5)

	(0)	(1)	(2)	(3)
λ_+	0.59041	0.56870	0.57193	0.57162
λ_o	0.27389	0.24273	0.24536	0.24510
x_4, m	0.35430	0.35275	0.35283	0.35283
y_4, m	0.13022	0.12909	0.12917	0.12916
$Q_+ \cdot 10^{-6}$, m^2/s^2	5.5178	5.5166	5.5103	5.5109
$R_+ \cdot 10^{-6}$, m^2/s^2	−0.21463	−0.33576	−0.32154	−0.32292
$S_+ \cdot 10^{-10}$, $m^3/s^3 - m$	0.25078	0.23241	0.23592	0.23561
$T_+ \cdot 10^{-10}$, m^3/s^3	1.3446	1.3361	1.3355	1.3356
u_4, m/s	2457.1	2454.5	2454.7	2454.7
v_4, m/s	520.9	533.1	531.9	532.0

Column (0)—predictor values. Column (2)—first iteration of the corrector.
Column (1)—corrector values. Column (3)—second iteration of the corrector.

(d) *Calculation of the coefficients for the predictor.* From part (c) and equations 16.5 to 16.8

$$\lambda_+ = \tan(14.165 + 16.393) = 0.59041$$

$$Q_+ = (2455.3)^2 - (714.67)^2 = 5.5178 \cdot 10^6 \text{ m}^2/\text{s}^2$$

$$R_+ = 2.0(2455.3)(619.7) - (5.5178 \cdot 10^6)(0.59041) = -0.21463 \cdot 10^6 \text{ m}^2/\text{s}^2$$

$$S_+ = (714.67)^2(619.7)/(0.12312) = 0.25708 \cdot 10^{10} \text{ m}^3/\text{s}^3 - \text{m}$$

The slope λ_o of the jet boundary 34 (see Fig. 16.7) at point 3 is given by

$$\lambda_o = \frac{v_3}{u_3} = \frac{663.5}{2422.5} = 0.27389$$

(e) *Determination of x_4, y_4, u_4, and v_4 for the predictor.* From part (d), Table 16.13, and equations 16.9 and 16.30, we obtain the predictor values for x_4 and y_4. Thus,

$$y_4 - (0.59041)x_4 = 0.12312 - (0.59041)(0.34226) \quad \text{(b)}$$

$$y_4 - (0.27389)x_4 = 0.12351 - (0.27389)(0.32979) \quad \text{(c)}$$

Solving equations (b) and (c) for x_4 and y_4 yields

$$x_4 = 0.35430 \text{ m} \quad \text{and} \quad y_4 = 0.13022 \text{ m}$$

From part (d), Table 16.13, and equation 16.13, we obtain

$$T_+ = (0.25708 \cdot 10^{10})(0.35430 - 0.34226) + (5.5178 \cdot 10^6)(2455.3) + (-0.21463 \cdot 10^6)(619.7)$$

$$T_+ = 1.3446 \cdot 10^{10} \text{ m}^3/\text{s}^3$$

From part (d), the above value for T_+, and equations 16.27 and 16.28, we obtain

the predictor values for u_4 and v_4. Thus,

$$u_4 = \frac{(5.5178 \cdot 10^6)(1.3446 \cdot 10^{10})}{(5.5178 \cdot 10^6)^2 + (-0.21463 \cdot 10^6)^2}$$

$$- \frac{(-0.21463 \cdot 10^6)\left\{(2511.7)^2\left[(5.5178 \cdot 10^6)^2 + (-0.21463 \cdot 10^6)^2\right] - (1.3446 \cdot 10^{10})^2\right\}^{1/2}}{(5.5178 \cdot 10^6)^2 + (-0.21463 \cdot 10^6)^2}$$

$$u_4 = 2457.1 \text{ m/s}$$

$$v_4 = \left[(2511.7)^2 - (2457.1)^2\right]^{1/2} = 520.9 \text{ m/s}$$

The column labeled (0) in Table 16.14 presents the values obtained by applying the predictor.

(f) *Application of the corrector.* The modified Euler corrector is applied by repeating steps (c) to (e) employing the average values of the flow properties, as illustrated in Example 16.1. Column (1) in Table 16.14 presents the results. Columns (2) and (3) of Table 16.14 present the results for two iterations of the corrector. By comparing columns (1), (2), and (3), it is seen that iteration of the corrector has only a very slight effect on the final results.

16–3(g) Scaling of Flow Fields

The steady irrotational flows discussed in this chapter have several important scaling features. From the original governing partial differential equations presented in Table 16.1, Section 16.3(a), it is seen that any linear scaling of the independent variables leaves the form of those equations unchanged. Let the scaled variables $\bar{x}$ and $\bar{y}$ be defined by

$$\bar{x} = Kx \quad \text{and} \quad \bar{y} = Ky \tag{16.31}$$

where K is a *scale factor*. Rewriting equations 10.193 and 10.189 in terms of the scaled variables $\bar{x}$ and $\bar{y}$, we obtain

$$(u^2 - a^2)u_{\bar{x}} + (v^2 - a^2)v_{\bar{y}} + 2uvu_{\bar{y}} - \delta\frac{a^2 v}{\bar{y}} = 0 \tag{16.32}$$

$$u_{\bar{y}} - v_{\bar{x}} = 0 \tag{16.33}$$

Thus, $u(\bar{x},\bar{y}) = u(Kx,Ky)$ and $v(\bar{x},\bar{y}) = v(Kx,Ky)$. Hence, once u and v have been determined for a specific flow field, the solution may be extended to any geometrically similar flow field having the *geometrical scale factor K*.

The system of governing equations includes the equation of state $a = a(V)$; the latter equation is unaffected by geometrical scaling. The equation of state does, however, depend on the properties of the fluid. In general, it is not possible to scale a functional relationship such as the equation of state. For a perfect gas, the relationship $a = a(V)$ is given by equation 3.186. Thus,

$$a^2 = a_o^2 - \frac{\gamma - 1}{2}V^2 \tag{3.186}$$

which may be rewritten in the form

$$\frac{a^2}{RT} = \left(\gamma - \frac{\gamma - 1}{2}\frac{V^2}{RT}\right) \tag{16.34}$$

For a given value of γ, it follows that a and V scale with $(RT)^{-1/2}$. It is not possible, however, to scale for different values of γ.

Since the stagnation pressure P does not enter into any of the governing flow equations, the resulting pressure field scales directly with the stagnation pressure.

The scaling rules for an irrotational flow are summarized below.

1. The velocity field, in terms of scaled dimensions, is unchanged by a linear geometrical scaling.
2. For a perfect gas, the velocity field scales directly with $(RT)^{-1/2}$.
3. The pressure field scales directly with the stagnation pressure.
4. For flows having different specific heat ratios, no scaling is possible.

The above scaling rules enable obtaining the solutions for a large number of flow fields from the computed results for a limited number of flow fields, provided, of course, that the scaling criteria are satisfield.

16–4 APPLICATIONS

In Section 16–3, numerical algorithms based on the method of characteristics are developed for steady two-dimensional, planar and axisymmetric, irrotational supersonic flow. In this section, those algorithms are applied to the following problems.

1. The analysis of the flow field inside of a nozzle of known shape.
2. The design of a nozzle contour for producing a parallel uniform flow at its *exit plane* (i.e., wind tunnel nozzle design).
3. The design of contours for propulsive nozzles that develop maximum thrust.

16–4(a) Analysis of the Flow Field for a Nozzle of Known Shape

Figure 16.8 illustrates schematically the configuration of a converging-diverging nozzle having a specified geometry. In view of the geometrical scaling rules discussed in Section 16–3(g), all of the x and y coordinates may be scaled by a geometrical scaling factor. It is convenient to scale all dimensions by the throat radius y_t. In this manner, the resulting flow field is applicable to all geometrically similar nozzles having the same throat geometry and specific heat ratio. Consequently, in Fig. 16.8, the nozzle coordinates are specified by x/y_t and y/y_t. Scaling all dimensions by the throat radius y_t may be accomplished in the computer programs presented in this chapter by specifying all dimensions as scaled dimensions in the input data. Since all of the programs compute with dimensional values, scaling by the throat radius is equivalent to analyzing a nozzle having a throat radius of 1.0 m (or 1.0 in.).

The nozzle illustrated in Fig. 16.8 has a 15-deg conical diverging section and a scaled throat radius $y_t = 1.0$. The converging portion of the nozzle, upstream from the throat, has a radius of curvature ratio $\lambda_u = \rho_{tu}/y_t = 2.0$, and the radius of curvature ratio of the downstream portion of the nozzle throat is $\lambda_d = \rho_{td}/y_t = 0.5$.

It is necessary to specify the equation of state for the gas flowing through the nozzle. That specification may take the form of equations, tables, or graphs. For a perfect gas, the equation of state is completely specified by the specific heat ratio γ,

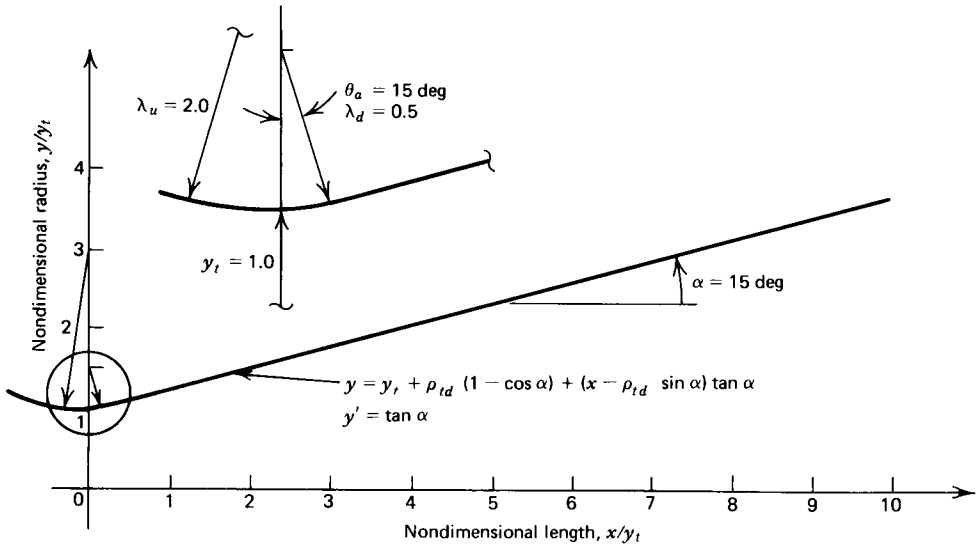

Figure 16.8 Converging-diverging nozzle with a conical diverging portion.

the gas constant R, the stagnation pressure P, and the stagnation temperature T. For illustrative purposes, assume that $\gamma = 1.2$, $R = 320.0$ J/kg-K, $P = 70.0 \cdot 10^5$ N/m^2, and $T = 3000.0$ K. Those properties are typical for the propulsive nozzle of either a liquid or a solid propellant rocket motor.

From the flow field in the throat region, an *initial-value line* must be established that is everywhere supersonic. The unit processes of the method of characteristics may then be applied to the flow field downstream from that initial-value line. In the throat region the flow is transonic, and the techniques for analyzing transonic flow discussed in Section 15–5 are applicable. By applying any of those methods, a suitable initial-value line may be established for initiating the calculation of the downstream supersonic flow field. The information required for the application of the transonic flow analyses are the throat radius y_t, the upstream throat radius of curvature ρ_{tu}, and the thermodynamic properties of the gas. For the nozzle illustrated in Fig. 16.8, Sauer's analysis[1] yields the results obtained in Example 15.2; they are summarized in Table 15.8.

An additional consideration enters when the direct marching method [see Section 12–5(b)] is applied to wall points. In the throat region where the flow property

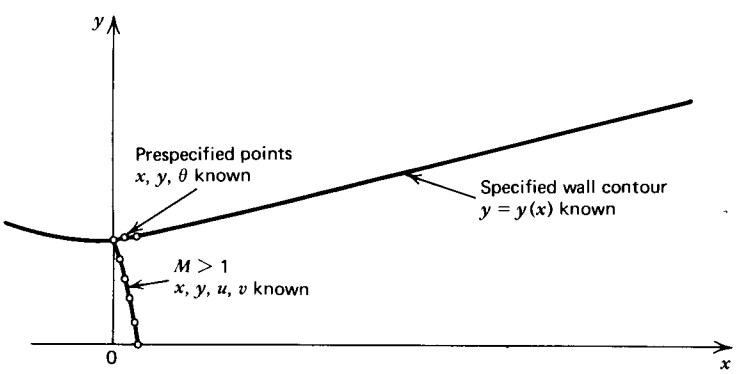

Figure 16.9 Complete initial- and boundary-value problem.

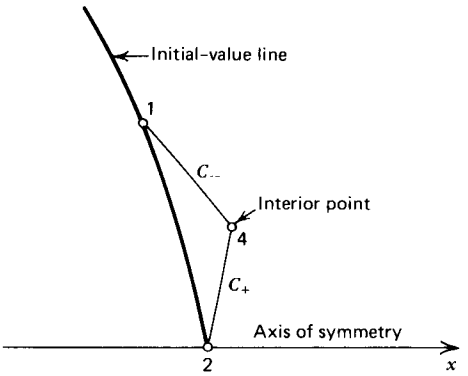

Figure 16.10 Application of the unit process for an interior point from the first two points on the initial-value line.

gradients are large, the spacing between successive intersections of left-running characteristics and the wall may be too large for obtaining the desired accuracy The inverse method discussed in Section 16–3(d) may, therefore, be employed for obtaining solutions at prespecified wall points. For example, the inverse method may be applied at each 1.0 deg turning angle along the circular arc joining the converging and diverging portions of the nozzle. Then, the direct marching method may be applied along the wall downstream from the circular arc contour.

From the above considerations, a completely determined initial-value and boundary-value problem is specified. Figure 16.9 illustrates schematically the initial-value line and selected points thereon, the prespecified wall points along the circular arc (throat) contour, and the specified contour of the diverging wall.

Figure 16.10 illustrates schematically the application of the *unit process for an interior point* [see Section 16–3(b)] at points 1 and 2, located on the lower portion of the initial-value line, for determining the location and flow properties at the interior point, point 4. Figure 16.11 illustrates schematically the application of the unit process for an *axis point* [see Section 16–3(e)] for determining the location and flow properties at the point (point 4) on the axis of symmetry of the nozzle. The foregoing procedure is repeated from the next two points on the initial-value line, thus extending the corresponding right-running characteristic to the centerline. The procedure is repeated until the complete region determined by the initial-value line

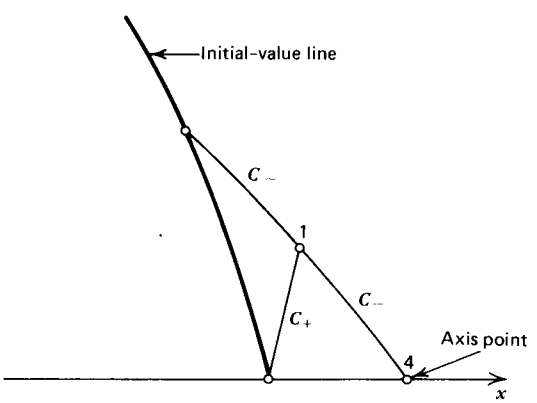

Figure 16.11 Application of the unit process for an axis point.

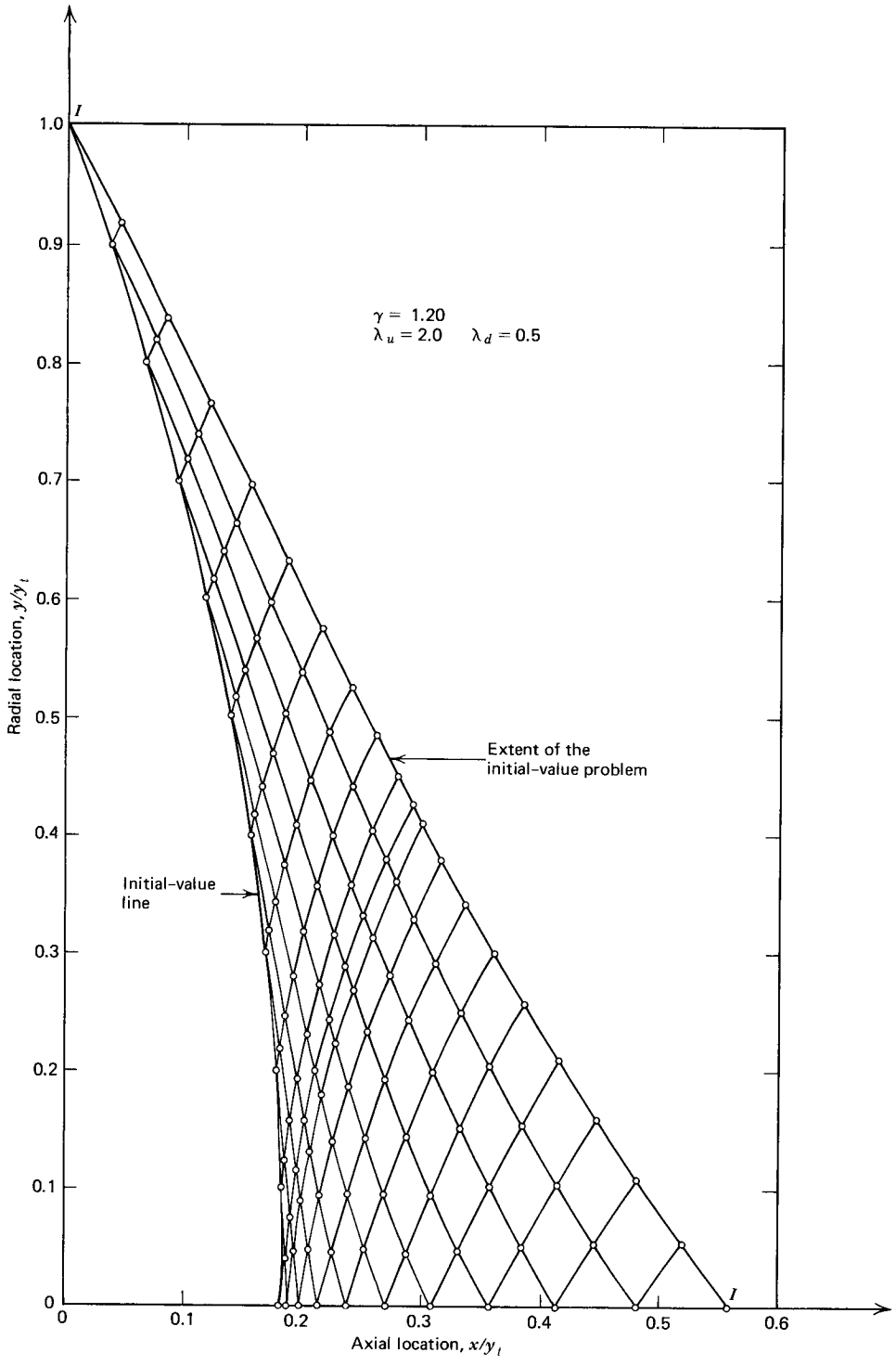

Figure 16.12 Extent of the initial-value problem.

has been developed. Figure 16.12 presents the resulting network of characteristics developed from the given initial-value line for the nozzle throat illustrated in Fig. 16.8. The initial-value problem is now complete. To continue the solution further, the wall boundary conditions must be employed.

Figure 16.13 illustrates schematically the application of the inverse wall point unit process [see Section 16–3(d)] for the first prespecified wall point on the circular arc throat contour. Once the solution for the wall point (point 4) is obtained, a right-running characteristic is originated from the wall point and continued until it intersects the centerline, as described above for the points on the initial-value line. That procedure is repeated at each successive prespecified wall point on the circular arc throat contour until the region determined by it has been developed, as illustrated in Fig. 16.14.

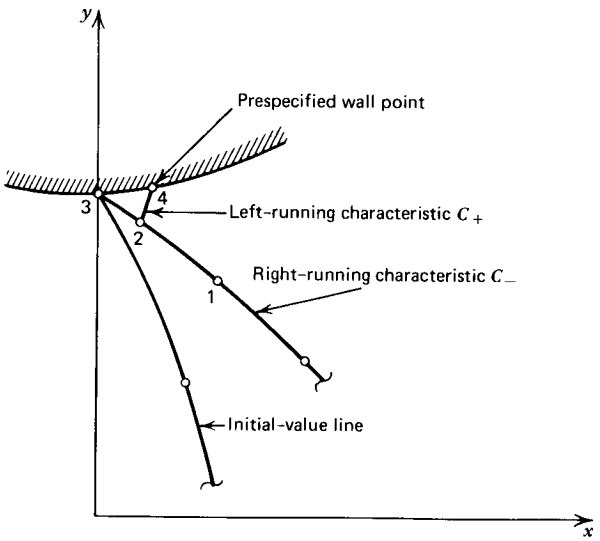

Figure 16.13 Application of the inverse wall point unit process.

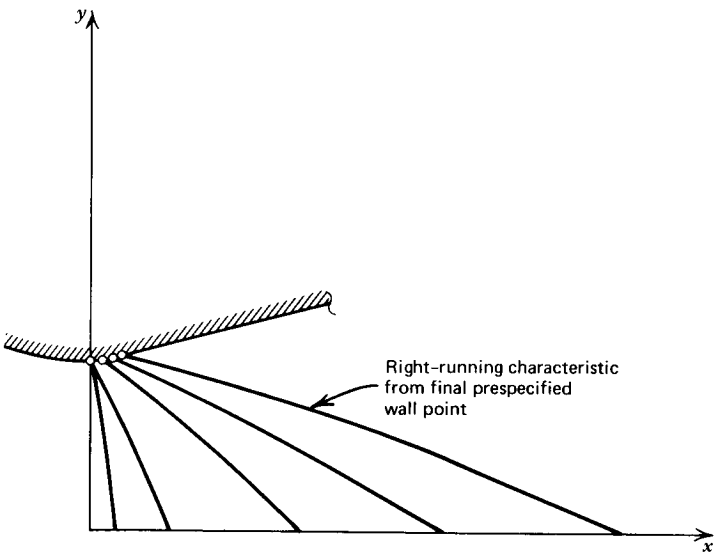

Figure 16.14 Extent of the flow field determined by the initial-expansion contour.

The wall points along the remainder of the nozzle wall downstream from the throat are determined by the direct wall point unit process described in Section 16–3(c). Figure 16.15 illustrates schematically the first such wall point (point 4) downstream from the circular arc throat contour. After point 4 is determined, a right-running characteristic C_- is extended from the wall point to the axis of symmetry, and the procedure is repeated from successive direct wall points until the entire flow field in the nozzle is determined. The extent of the flow field for the nozzle is determined by the wall point corresponding to the end of the diverging portion of the nozzle; for brevity that point is called the *nozzle exit lip point*. The nozzle exit lip point may be determined by the inverse wall point unit process. Hence, the internal flow field pertinent to the diverging wall of the nozzle may be determined up to the right-running characteristic C_- originating at the *nozzle exit lip point*, as illustrated schematically in Fig. 16.16.

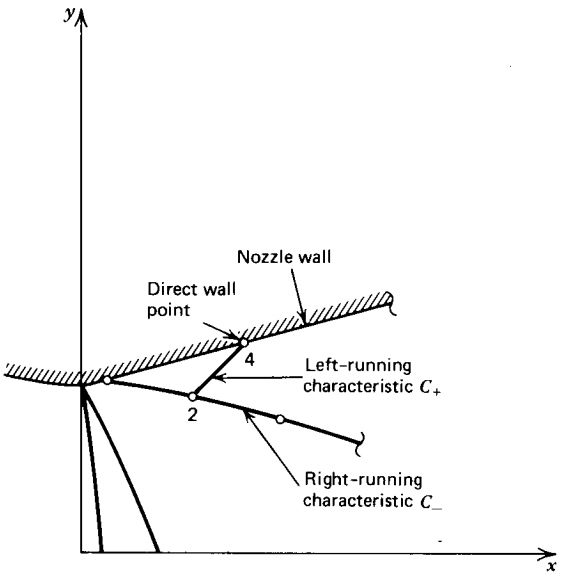

Figure 16.15 Application of the direct wall point unit process.

Selected characteristics for the conical nozzle illustrated in Fig. 16.8 are presented in Fig. 16.17. Figure 16.17*a* illustrates the entire flow field, and Fig. 16.17*b* illustrates in greater detail the characteristics in Region *ABCD* where there is overlapping of crossing characteristics in the shaded region. As discussed in Section 8–6, coalescing characteristics are compression waves that may steepen and form an oblique shock wave. When that occurs, the method of characteristics is no longer applicable because the flow properties are not continuous. Compression waves are always generated by a concave surface turning into a supersonic flow. Compression waves may also be formed at discrete points on a solid boundary where there is a discontinuity in the derivatives of the wall contour. That is the case for the nozzle illustrated in Fig. 16.8 at the attachment point where the circular arc throat contour is joined tangentially to the conical divergence. At that point, the wall contour and the wall slope are both continuous, but the wall curvature (i.e.,

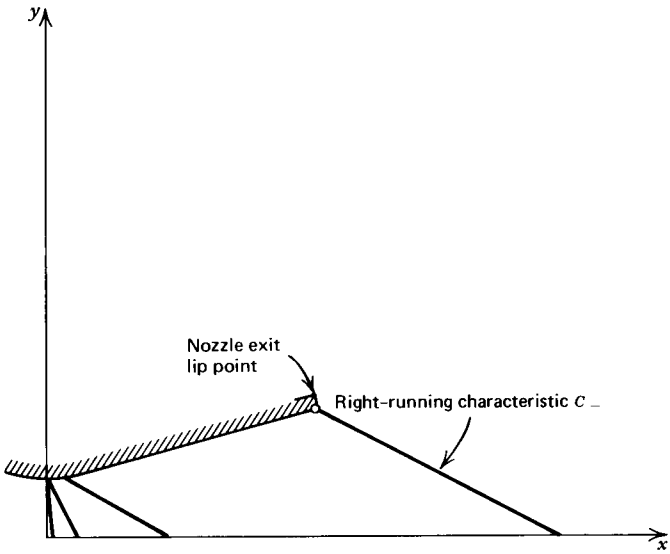

Figure 16.16 Complete flow field determined by the nozzle contour.

the rate of change of the wall slope) is discontinuous. That discontinuity in wall curvature generates the weak compression wave observed in Fig. 16.17.

When characteristics coalesce, an oblique shock wave is formed. However, if that oblique shock wave is relatively weak, it may be ignored without a serious error in the flow field calculations, since weak oblique shock waves yield an almost isentropic compression [see Section 7–4(e)]. However, if the resulting oblique shock wave is very strong, the only recourse is to treat the oblique shock wave as a discrete finite discontinuity by the methods presented in Chapter 7, as illustrated in Fig. 16.18.

Even when the oblique shock wave is weak enough to be ignored, a problem still arises in the computational logic because the direct marching logic follows discrete characteristics. When the characteristics cross, the marching logic must be modified.

Several alternatives for modifying the marching logic so that the solution may be continued when characteristics coalesce are listed below.

1. Allow the characteristics to cross, as illustrated in Fig. 16.19*a*. Eventually, succeeding characteristics will cease to cross the preceding characteristics, and the solution will once again march downstream. The intersection of the characteristics generates a *fold* in the solution surface, as illustrated in Fig. 16.19*a*, and a triple-valued solution for the flow properties in that region.
2. Terminate the crossing characteristic at the point of intersection, as illustrated in Fig. 16.19*b*, and initiate the next characteristic from the upper boundary.
3. Delete the portion of the previous characteristic that is crossed, and continue the solution characteristic from a characteristic upstream of the deleted characteristic. Figure 16.19*c* illustrates the latter procedure.

The three procedures discussed above all yield reasonable results, even for a relatively strong oblique shock wave, provided that the pressure ratio of the shock wave is less then approximately four to five. The results presented in Fig. 16.17 employ procedure 1 above.

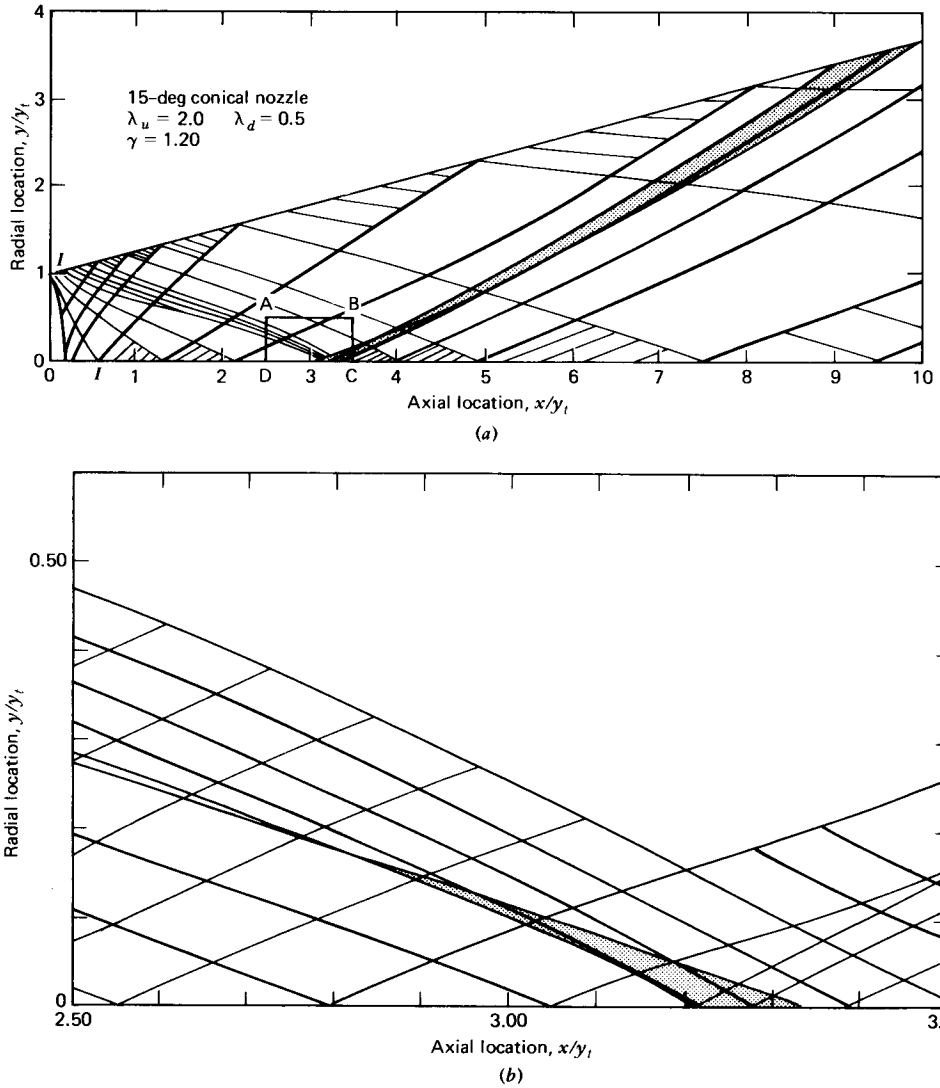

Figure 16.17 Selected characteristics for the conical nozzle illustrated in Fig. 16.8. (*a*) The entire flow field. (*b*) Region *ABCD* illustrating the overlapping of crossing characteristics.

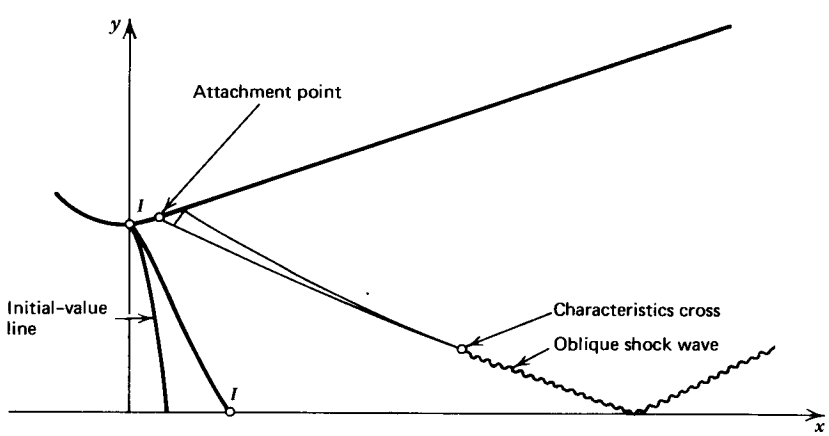

Figure 16.18 Coalescence of characteristics to form an oblique shock wave.

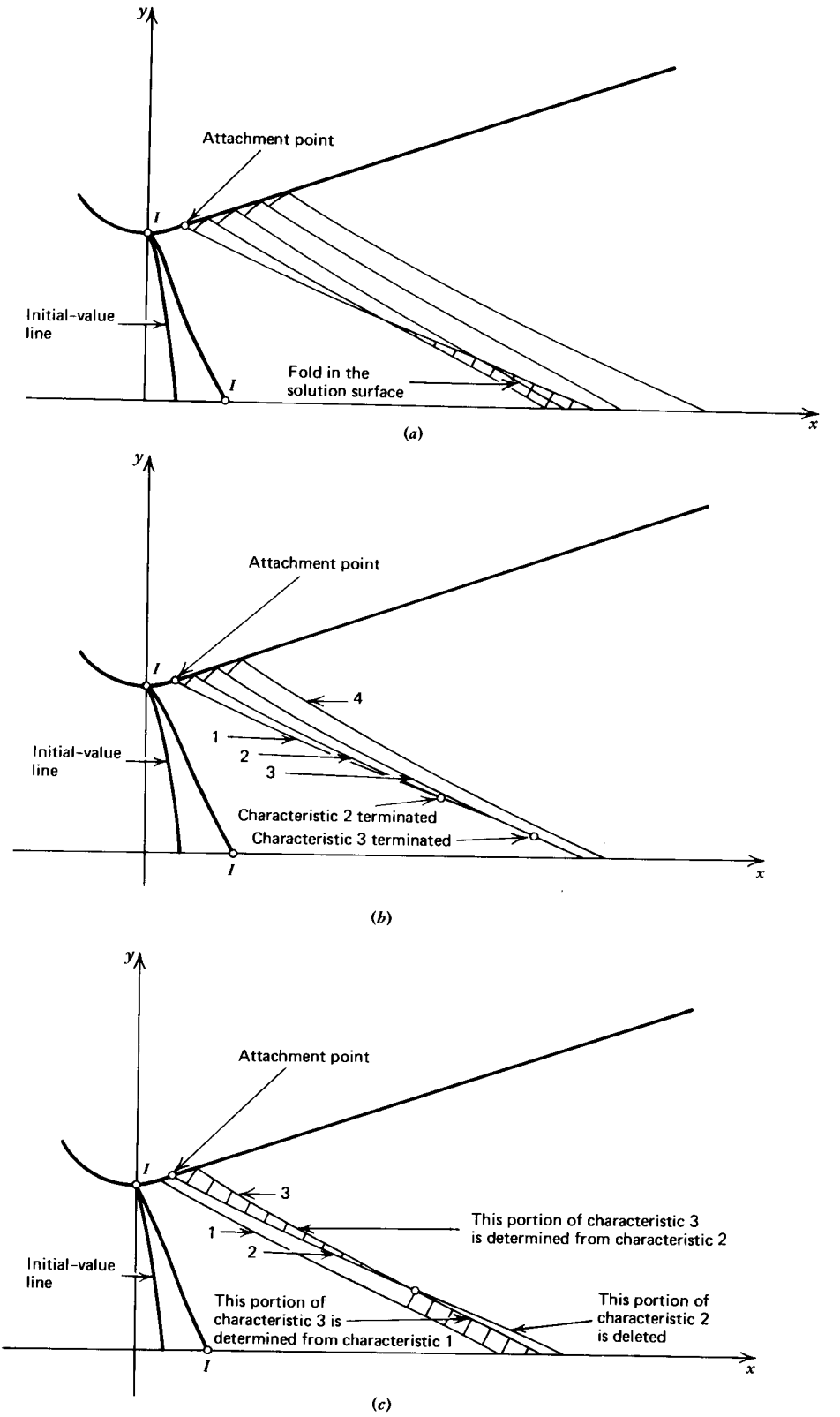

Figure 16.19 Methods for taking into account the crossing of characteristics of the same family. (*a*) Fold in solution surface. (*b*) Termination of the crossing characteristic. (*c*) Deletion of the crossed characteristic.

Figure 16.20 is a logarithmic plot of the calculated values of the pressure ratio p/P as a function of the nozzle length, downstream from the throat, for the conical nozzle illustrated in Fig. 16.8. Three curves are presented; the pressure ratio at the wall, the one-dimensional pressure ratio, and the pressure ratio along the centerline. The curves indicate that during the initial expansion near the throat, the static pressure along the wall is considerably smaller than the corresponding one-dimensional value, whereas the static pressure along the centerline is considerably higher.

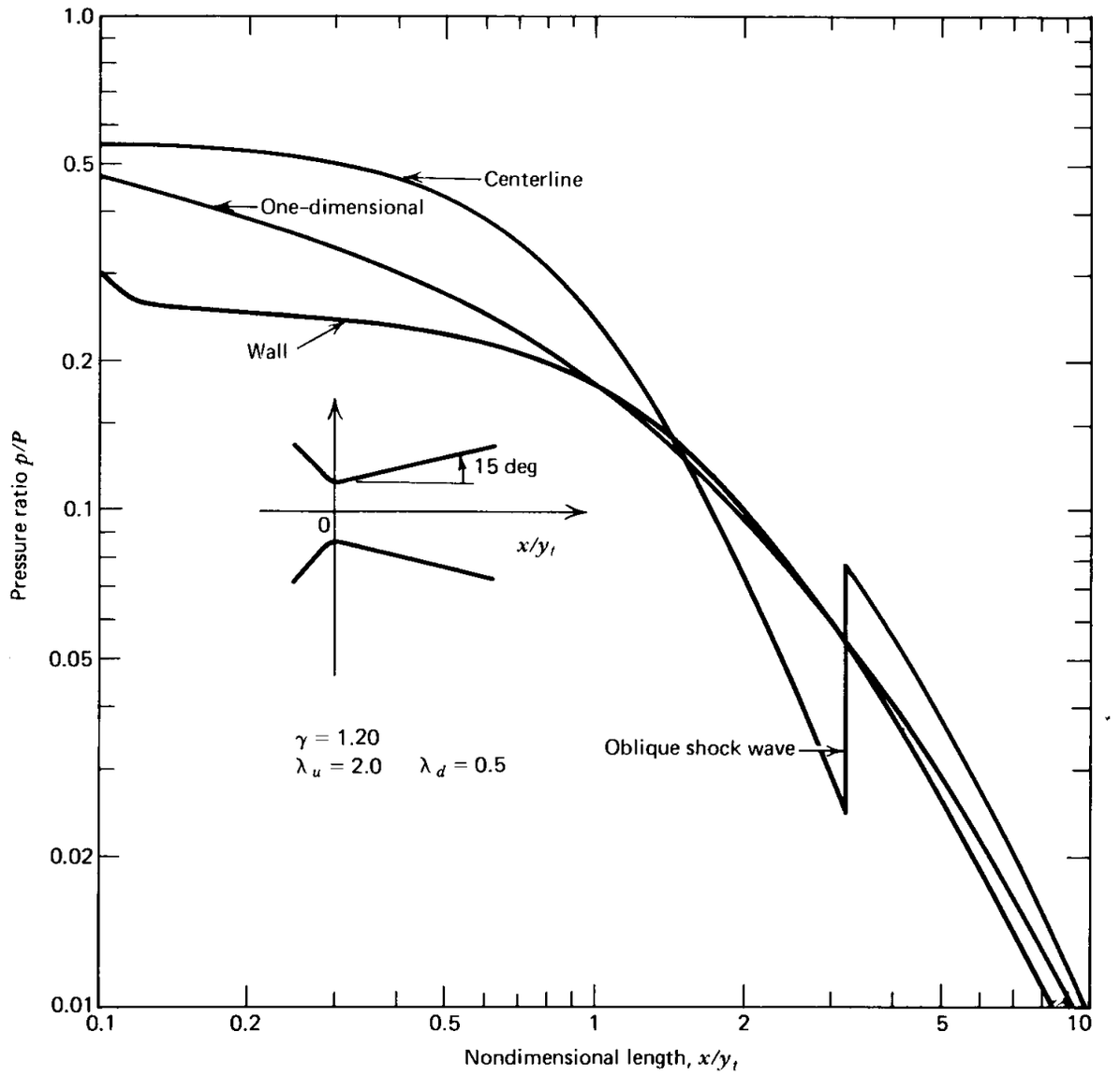

Figure 16.20 Pressure distribution in a 15-deg conical nozzle.

The three curves intersect at a location approximately $x/y_t = 1.5$ downstream from the throat, and the centerline static pressure then decreases rapidly. An oblique shock wave is formed by the coalescence of the characteristics emanating from the junction of the circular arc throat and the conical diverging section. That oblique shock wave reaches the centerline at a location $x/y_t = 3.2$ downstream from the throat and causes a sudden increase in the static pressure. Further discussion of the oblique shock wave phenomenon in supersonic nozzles is presented in References 2 to 4.

After the flow field within the nozzle has been determined, the solution then may be extended into the exhaust jet, or plume, discharged by the nozzle by applying the unit process for the *free pressure boundary* point [see Section 16–3(f)]. If the

static pressure of the gas at the nozzle exit lip exceeds that of the surrounding atmosphere, a Prandtl-Meyer, or centered, expansion wave occurs at the nozzle exit lip point. Figure 16.21 illustrates the unit process for determining the right-running characteristics emanating at specified turning angles from the nozzle exit lip point.

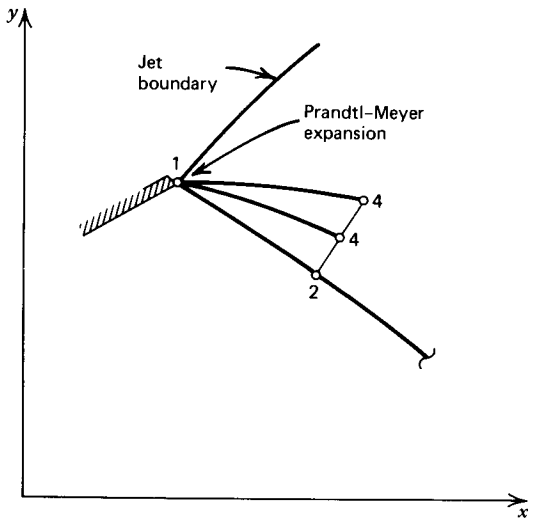

Figure 16.21 Prandtl-Meyer expansion unit process.

The flow properties at point 1 are determined by applying the Prandtl-Meyer expansion wave analysis discussed in Chapter 8. The interior point unit process [see Section 16–3(b)] may then be employed for determining the location and the flow properties at point 4, and the right-running characteristic may be extended from the nozzle exit lip to the axis. The latter process is repeated until the flow at the nozzle exit lip is turned through the angle required for equalizing the static pressures of the gas in the plume and the surrounding atmosphere. Figure 16.22 illustrates the portion of the flow field determined from the expansion fan at the nozzle exit lip.

If the gas pressure at the nozzle exit lip is less than that of the surrounding atmosphere, an oblique shock wave emanates from the nozzle exit lip and propa-

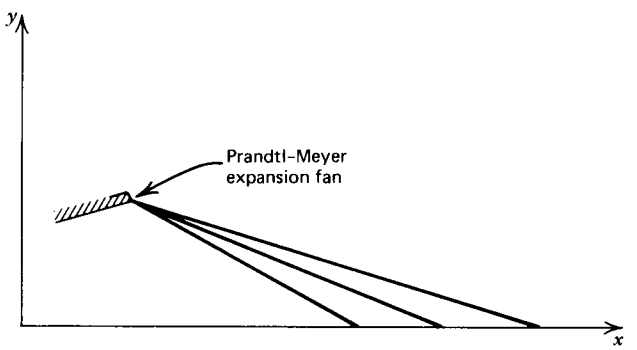

Figure 16.22 Extent of the flow field determined by the Prandtl-Meyer expansion fan at the nozzle exit lip.

gates into the flow field, as illustrated in Fig. 16.23. Since an oblique shock wave is stronger than a Mach line, the *lip shock wave* is steeper than the last right-running characteristic from the nozzle exit lip, and the oblique shock wave propagates upstream from that characteristic. Consequently, the flow field in that region must be recalculated to take into account the presence of the oblique shock wave.

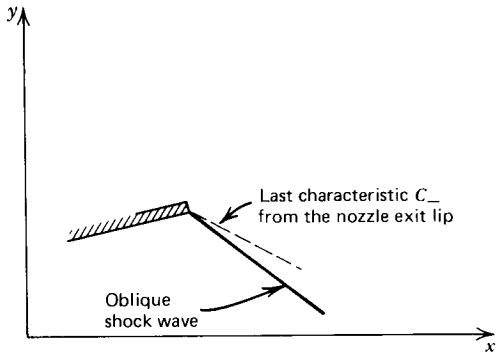

Figure 16.23 Oblique shock wave in an overexpanded nozzle flow.

Although that procedure is fairly straightforward, it is rather complex; it is not discussed any further here. Suffice it to say that the location of the oblique shock wave and the flow properties in front and in back of it are determinable. Hence, the flow field in the plume may be determined from the data pertinent to the downstream side of the oblique shock wave.

To obtain points on the boundary of the jet, the unit process for a free pressure boundary point is applied [see Section 16−3(f)]. Figure 16.24 illustrates the procedure schematically. From each point on the *jet boundary*, a right-running characteristic is extended to the axis of symmetry. Eventually, oblique, and later normal, shock waves appear embedded within the plume. Obviously the solution can only be extended into that region of the plume where the flow remains continuous and supersonic, which is not very far. It will be recalled that a basic limitation of the method of characteristics is that the dependent variables must be continuous (see Section 12–3), and the flow must be supersonic.

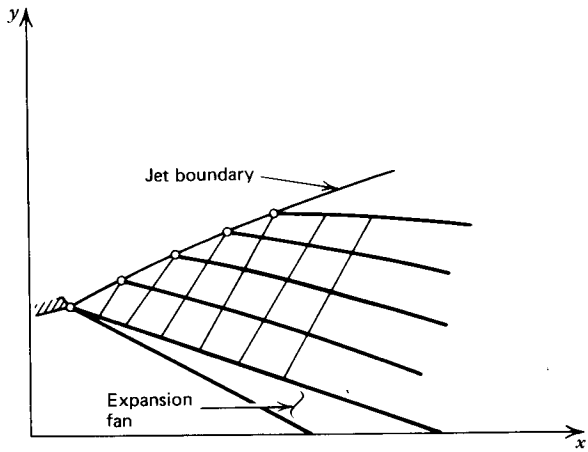

Figure 16.24 Determination of the flow field in the plume.

It is evident that the entire supersonic flow field in the diverging portion of a converging-diverging nozzle and also in the initial part of the plume leaving the nozzle exit section may be determined at a set of discrete points. The flow properties at any point in that flow field may be established by interpolating between the locations where the solution is determined.

The interaction force between the nozzle and the fluid (i.e., the nozzle thrust) may be obtained by integrating the static pressure forces and the momentum flux crossing the initial-value line, and adding the static pressure forces acting along the nozzle wall. Accordingly, all of the information that is ordinarily of interest for a converging-diverging nozzle may be determined by applying the methods developed in this chapter.

A master logic program, program NOZZLE, for implementing the solution procedure developed in the preceding discussion is presented below, along with subroutine THRUST, which determines the nozzle thrust, and subroutine MOVE, which transfers data to and from grid points and arrays. Those three computer programs, together with those presented in Section 16–3 for the unit processes and the transonic flow program (subroutine IVLINE) presented in Section 15–5(c), may be employed for calculating the flow field in a converging-diverging nozzle. Input to the program is accomplished through the NAMELIST INFO. Table 16.15 presents the input data required by the program, along with the default values defined

Table 16.15 Input Parameters for the Nozzle Flow Field Analysis Program

Parameter	Symbol	Description and Units	Default Value
DELTA	δ	0 denotes planar flow, 1 denotes axisymmetric flow	1.0
NI		number of points on the initial-value line	11
NT		number of indirect wall points on the circular arc throat contour	15
ICOR		number of applications of the corrector	2
EI		length convergence tolerance, m (in.)	0.0
E2		velocity convergence tolerance, m/s (ft/sec)	0.0
IUNITS		2 denotes SI units, 1 denotes EE units	2
G	γ	specific heat ratio	1.2
RG	R	gas constant, J/kg-K (ft-lbf/lbm-R)	320.0
TS	T	stagnation temperature, K (R)	3000.0
PS	P	stagnation pressure, N/m^2 ($lbf/in.^2$)	$70.0 \cdot 10^5$
PA	p_o	ambient pressure, N/m^2 ($lbf/in.^2$)	0.0
YT	y_t	throat radius, m (in.)	1.0
RTU	ρ_{tu}	throat upstream radius of curvature, m (in.)	2.0
RTD	ρ_{td}	throat downstream radius of curvature, m (in.)	0.5
AA	θ_a	attachment point angle, deg	15.0
AE	θ_e	exit lip point angle, deg	15.0
XE	x_e	nozzle length, m (in.)	10.0
KWRITE		0 write out solution at wall and axis points only, 1 write out the solution at all of the points	1

within the program for each parameter. The default values specify the initial-value line determined in Example 15.2 and the conical nozzle considered in Example 16.6. Crossing characteristics in this program are treated by the first of the three procedures discussed above. The input data may be specified in either EE or SI units, and the results are presented in the same units.

```
      PROGRAM NOZZLE (INPUT,OUTPUT,TAPE5=INPUT,TAPE6=OUTPUT)

C     LOGIC PROGRAM FOR ANALYSIS OF SUPERSONIC NOZZLE FLOW

      COMMON /CONTRL/ DELTA,NI,NT,ICOR,E1,E2,E3,E4,E5,IUNITS,PI,RAD
      COMMON /PROPTY/ G,RG,CP,TS,PS,PA,GC,GL $ REAL M
      COMMON /CONTUR/ YT,RTU,RTD,AA,AE,XE,YE
      COMMON /PERFORM/ YW,PW,MDCT,CD,F,DF,FS
      COMMON /ARRAYS/ X(99),Y(99),U(99),V(99),Q(99),A(99),P(99),R(99)
      COMMON /DATA/ X1,Y1,U1,V1,Q1,A1,P1,R1,T1,M1,X2,Y2,U2,V2,Q2,A2,P2,
     1R2,T2,M2,X3,Y3,U3,V3,Q3,A3,P3,R3,T3,M3,X4,Y4,U4,V4,Q4,A4,P4,R4,T4,
     2M4,LP,LM,LE,L12,L0 $ REAL M1,M2,M3,M4,LP,LM,LE,L12,L0

      NAMELIST /INFO/ DELTA,NI,NT,ICOR,E1,E2,E3,E4,E5,IUNITS,G,RG,TS,PS,
     1PA,YT,RTU,RTD,AA,AE,XE,KWRITE

C     READ INPUT DATA, WRITE IT OUT, AND INITIALIZE PARAMETERS

   10 DELTA=1.0 $ NI=11 $ NT=15 $ ICOR=2 $ E1=0.0 $ E2=0.0 $ E3=0.0
      E4=0.0 $ E5=0.0 $ IUNITS=2 $ G=1.2 $ RG=320.0 $ TS=3000.0
      PS=70.0E5 $ PA=0.0 $ YT=1.0 $RTU=2.0 $ RTD=0.5 $ AA=15.0 $ AE=15.0
      XE=10.0 $ KWRITE=1 $ READ (5,INFO) $ IF (EOF,5) 20,30
   20 CALL EXIT
   30 WRITE (6,INFO) $ PI=3.1415926 $ RAD=57.29578 $ CP=G*RG/(G-1.0)
      CALL BOUNDY(1) $ DA=AA/(FLOAT(NT)*RAD) $ WRITE (6,1000)
      GC=32.174 $ GL=144.0 $ IF (IUNITS.EQ.1) GO TO 40 $ GC=1.0 $ GL=1.0

C     CALCULATE THE FLOW FIELD FROM THE INITIAL-VALUE LINE

   40 PS=PS*GL $ PA=PA*GL $ WRITE (6,1010) $ CALL IVLINE $ WRITE(6,1000)
      DO 80 I=1,NI $ J1=NI-I+1 $ J2=J1+2*(I-1) $ WRITE (6,1010)
      DO 80 J=J1,J2 $ KW=1 $ IF (J.GT.J1) GO TO 50
      K=20+I $ CALL MOVE (4,K) $ GO TO 70
   50 CALL MOVE (1,J-1) $ IF (J.LT.J2) GO TO 60 $ CALL AXIS $ GO TO 70
   60 CALL MOVE (2,J) $ CALL INTER $ KW=KWRITE
   70 CALL MOVE (5,J) $ AP=A4*RAD $ PP=P4/GL
      IF (KW.EQ.1) WRITE (6,1020) I,J,X4,Y4,U4,V4,M4,Q4,AP,PP,R4,T4
   80 CONTINUE

C     CALCULATE THE FLOW FIELD FROM THE CIRCULAR ARC THROAT CONTOUR

      II=NI+1 $ III=NI+NT $ J2=2*NI-1 $ L=0 $ IEND=0
      DO 160 J=1,J2 $ J3=J $ KW=1 $ IF (J.EQ.J2) GO TO 130
      IF (J.GT.1) GO TO 120 $ J2=J2+1 $ A4=DA*FLOAT(I-NI)
      X4=RTD*SIN(A4) $ Y4=YT+RTD*(1.0-COS(A4)) $ L0=-X4/(Y4-(RTD+YT))
  100 N=N+1 $ CALL MOVE (3,N) $ CALL MOVE (1,N+1) $ CALL INWALL
      IF(X2.GT.X1)GO TO 110 $ CALL THRUST(I) $ WRITE(6,1010) $ GO TO 140
  110 L=L+1 $ J2=J2-1 $ GO TO 100
  120 CALL MOVE (1,J-1) $ CALL MOVE (2,J+N-1) $ CALL INTER
      KW=KWRITE $ GO TO 140
  130 CALL MOVE (1,J-1) $ CALL MOVE (6,0) $ CALL AXIS
  140 CALL MOVE (5,J) $ AP=A4*RAD $ PP=P4/GL $ LJ=L+J
      IF (KW.EQ.1) WRITE (6,1020) I,LJ,X4,Y4,U4,V4,M4,Q4,AP,PP,R4,T4
      IF (X4.GT.XE) GO TO 170
  160 CONTINUE $ IF (IEND.EQ.1) J2=J2-1 $ GO TO 180
  170 J2=J-1 $ IEND=1
  180 CONTINUE

C     CALCULATE THE FLOW FIELD FROM THE SECOND-ORDER QUADRATIC WALL

      II=III+1 $ III=1000 $ J2=J3-IEND
      DO 290 I=II,III $ IF(X(1).EQ.XE) GO TO 10 $L=L+1 $YW=Y(1) $PW=P(1)
  190 DO 270 J=1,J2 $ KW=1 $ IF ((J.EQ.J2).AND.(IEND.EQ.0)) GO TO 240
      IF (J.GT.1) GO TO 210 $ CALL MOVE (2,2) $ CALL MOVE (3,1)
      CALL DRWALL $ IF (X4.GT.XE) GO TO 200 $ CALL THRUST (I)
      WRITE (6,1010) $ GO TO 250
  200 X4=XE $Y4=YE $A4=ATAN(LE) $L=L-1 $CALL MOVE (3,1) $CALL MOVE (1,2)
      L0=LE $CALL INWALL $CALL THRUST(I) $WRITE(6,1010) $J2=J $GO TO 250
  210 CALL MOVE (1,J-1) $ CALL MOVE (2,J+1) $ CALL INTER $ KW=KWRITE
```

```
      IF (Y4.GT.0.0) GO TO 220 $ J2=J $ GO TO 240
  220 IF (X4.GT.X(1)) GO TO 250 $ J2=J2-J+1+IEND $ L=L+J-1 $ F=F-DF
      DO 230 K=2,J2 $ N=J-1+K $ CALL MOVE (4,N) $ CALL MOVE (5,K)
  230 CONTINUE $ GO TO 190
  240 CALL MOVE (1,J-1) $ CALL MOVE (6,0) $ CALL AXIS $ KW=1
  250 CALL MOVE (5,J) $ AP=A4*RAD $ PP=P4/GL $ LJ=L+J
      IF (KW.EQ.1) WRITE (6,1020) I,LJ,X4,Y4,U4,V4,M4,Q4,AP,PP,R4,T4
      IF (X4.GT.XE) GO TO 280
  270 CONTINUE $ IF (IEND.EQ.1) J2=J2-1 $ GO TO 290
  280 J2=J-1 $ IEND=1
  290 CONTINUE

 1000 FORMAT (1H1)
 1010 FORMAT (1H0,4X,1HI,4X,1HJ,6X,1HX,9X,1HY,9X,1HU,9X,1HV,9X,1HM,9X,
     11HQ,9X,1HA,9X,1HP,12X,1HR,12X,1HT/1H )
 1020 FORMAT (1H ,2I5,2F10.4,2F10.1,F10.4,F10.1,F10.4,2E13.4,F10.1)
      END

      SUBROUTINE MOVE (I,J)

C     SUBROUTINE MOVE TRANSFERS DATA TO AND FROM GRID POINTS AND ARRAYS

      COMMON /ARRAYS/ X(99),Y(99),U(99),V(99),Q(99),A(99),P(99),R(99)
      COMMON /DATA/ X1,Y1,U1,V1,Q1,A1,P1,R1,T1,M1,X2,Y2,U2,V2,Q2,A2,P2,
     1R2,T2,M2,X3,Y3,U3,V3,Q3,A3,P3,R3,T3,M3,X4,Y4,U4,V4,Q4,A4,P4,R4,T4,
     2M4,LP,LM,LE,L12,L0 $ REAL M1,M2,M3,M4,LP,LM,LE,L12,L0

      GO TO (10,20,30,40,50,60), I

   10 X1=X(J) $ Y1=Y(J) $ U1=U(J) $ V1=V(J) $ RETURN
   20 X2=X(J) $ Y2=Y(J) $ U2=U(J) $ V2=V(J) $ RETURN
   30 X3=X(J) $ Y3=Y(J) $ U3=U(J) $ V3=V(J) $ RETURN
   40 X4=X(J) $ Y4=Y(J) $ U4=U(J) $ V4=V(J) $ RETURN
   50 X(J)=X4 $ Y(J)=Y4 $ U(J)=U4 $ V(J)=V4 $ Q4=SQRT(U4**2+V4**2)
      A4=ATAN(V4/U4) $ CALL THERMO (Q4,P4,R4,T4,C,M4)
      Q(J)=Q4 $ A(J)=A4 $ P(J)=P4 $ R(J)=R4 $ RETURN
   60 X3=X2 $ Y3=Y2 $ U3=U2 $ V3=V2 $ RETURN
      END

      SUBROUTINE THRUST (I)

C     SUBROUTINE THRUST CALCULATES THE THRUST ALONG THE NOZZLE WALL

      COMMON /CONTRL/ DELTA,NI,NT,ICOR,E1,E2,E3,E4,E5,IUNITS,PI,RAD
      COMMON /PROPTY/ G,RG,CP,TS,PS,PA,GC,GL $ REAL M,MP,MDOT
      COMMON /CONTUR/ YT,RTU,RTD,AA,AE,XE,YE
      COMMON /PERFORM/ YW,PW,MDOT,CD,F,DF,FS
      COMMON /ARRAYS/ X(99),Y(99),U(99),V(99),Q(99),A(99),P(99),R(99)
      COMMON /DATA/ X1,Y1,U1,V1,Q1,A1,P1,R1,T1,M1,X2,Y2,U2,V2,Q2,A2,P2,
     1R2,T2,M2,X3,Y3,U3,V3,Q3,A3,P3,R3,T3,M3,X4,Y4,U4,V4,Q4,A4,P4,R4,T4,
     2M4,LP,LM,LE,L12,L0 $ REAL M1,M2,M3,M4,LP,LM,LE,L12,L0

C     CALCULATE THE ONE-DIMENSIONAL THRUST

      CALL THERMO (Q4,P4,R4,T,C,M) $ EE=(Y4/YT)**2 $ FAMB=PA*PI*Y4**2/GL
      C1=(G-1.0)/2.0 $ C2=(G+1.0)/2.0 $ EX=C2/(G-1.0) $ CG=(1.0/C2)**EX
   10 FM=M*EE-CG*(1.0+C1*M**2)**EX$FP=EE-CG*C2*M*(1.0+C1*M**2)**(EX-1.0)
      MP=M-FM/FP $ IF (ABS(MP-M).LT.0.000001) GO TO 20 $ M=MP $ GO TO 10
   20 FOD=FS*(1.0+G*MP**2)/SQRT(2.0*(G+1.0)*MP**2*(1.0+C1*MP**2))-FAMB

C     CALCULATE THE TWO-DIMENSIONAL THRUST

      F1=PI*(PW-PA)*YW $ F2=PI*(P4-PA)*Y4 $DF=(F1+F2)*(Y4-YW)/GL $F=F+DF
      ETAF=F/FOD $ETAI=ETAF/CD $ SPI=F/MDOT $ SPICD=FCD*CD/MDOT
      WRITE (6,2000) I,F,FOD,ETAF,SPI,SPICD,ETAI $ RETURN

 2000 FORMAT (1H0,I5,4X,4HF = ,F10.1,3X,6HFOD = ,F10.1,3X,7HETAF = ,
     1 F7.5,3X,6HISP = ,F8.3,3X,8HISPOD = ,F8.3,3X,7HETAI = ,F7.5)
      END
```

The method presented here may be applied to a nozzle of any contour wherein there is a steady two-dimensional supersonic irrotational flow for which there is a known (or determinable) initial-value line. Similar techniques are developed for rotational flows in Chapter 17. The basic computational logic is identical in both cases. Changes are required in the unit processes for rotational flow, however, because of the differences in the equations governing irrotational and rotational flow fields.

Example 16.6. Consider the conical converging-diverging nozzle discussed in Section 16–4(a) and illustrated in Fig. 16.8. Compare the mass flow rate and the thrust of the nozzle based on (a) one-dimensional planar flow, (b) one-dimensional source flow, and (c) two-dimensional axisymmetric flow. The scaled length of the nozzle is 10.0, which yields $y_e/y_t = 3.66185$ (see the equation on Fig. 16.8). Assume that the ambient pressure is zero (see Example 4.13).

Solution

The planar flow solution and the source flow solution for the above nozzle are presented in Examples 4.10 and 4.13. Those results are summarized in Table 16.16. In that table, $\dot{m}$ denotes the mass flow rate, C_D the discharge coefficient, F_t the thrust developed at the nozzle throat, F_e the thrust developed at the nozzle exit, M_e the nozzle exit lip Mach number, η_F the thrust efficiency, and η_I the specific impulse efficiency.

Table 16.16 Comparison of One- and Two-Dimensional Results for a Conical Converging-Diverging Nozzle (Example 16.6)

	$\dot{m}$, kg/s	C_D	F_t, N	F_e, N	M_e	η_F	η_I
Planar	9.09745	1.0000	17,068	24,429	3.48216	1.0000	1.0000
Source	9.09745	1.0000	—	24,039	3.49406	0.9841	0.9841
2-*D*	9.04650	0.9944	17,013	23,874	3.43680	0.9773	0.9828

The equation defining the correction factors C_D, η_I, and η_F and their interrelationship, equation 4.127, is repeated below for convenience.

$$C_D = \frac{\dot{m}}{\dot{m}_{1\text{-}D,\,\text{isentropic}}} \tag{4.127a}$$

$$\eta_I = \frac{I_{sp}}{I_{sp,\,1\text{-}D,\,\text{isentropic}}} \tag{4.127b}$$

$$\eta_F = \frac{F}{F_{1\text{-}D,\,\text{isentropic}}} \tag{4.127c}$$

$$\eta_F = C_D \eta_I \tag{4.127d}$$

The two-dimensional values for the mass flow rate $\dot{m}_{2\text{-}D}$, discharge coefficient C_D, and throat thrust F_t, calculated in Example 15.2, are presented in Table 16.16. The two-dimensional thrust F_e and the exit lip Mach number M_e, calculated with the computer program discussed in Section 16–4(a), are also presented in Table 16.16. The values of C_D, η_I, and η_F are calculated from equation 4.127.

From Table 16.16 it is seen that the thrust based on two-dimensional flow is 2.27

percent less than that for planar flow, which is a significant reduction in thrust, and must be considered in the design of a large propulsive nozzle. The source flow analysis predicts a thrust loss of 1.59 percent, which is reasonably close to the two-dimensional value of 2.27 percent.

A portion of the thrust loss due to two-dimensional flow effects results from the decreased mass flow rate corresponding to $C_D = 0.9944$. That portion of the thrust loss may be recovered by increasing the nozzle throat area by the factor $1/C_D = (1/0.9944) = 1.0056$. The specific impulse efficiency is a better measure of the true loss resulting from the two-dimensional flow effects, because the reduction in the mass flow rate is taken into account in that efficiency. From Table 16.16, it is seen that $\eta_I = 0.9828$ for the two-dimensional flow analysis, which is a reduction of 1.72 percent. The source flow analysis predicts a specific impulse loss of 1.59 percent which is quite close to the two-dimensional value of 1.72 percent.

Figure 16.25 presents η_I for conical nozzles having $\lambda_u = \rho_{tu}/y_t = 2.0$ and $\lambda_d = \rho_{td}/y_t = 0.5$, for $\gamma = 1.20$, as a function of the nozzle length for different cone angles. The source flow approximation $\eta_{I,S} = \eta_{F,S}/C_D = \lambda/C_D$, where $\lambda = (1 + \cos\alpha)/2$, is shown for comparison.

It is shown in Section 4–10(e) that, on a one-dimensional basis, the maximum thrust for a propulsive nozzle is attained when $p_e = p_o$. Accordingly, the nozzle area ratio must be chosen so that the pressure ratio $p_e/P = p_o/P$. From equation 4.102,

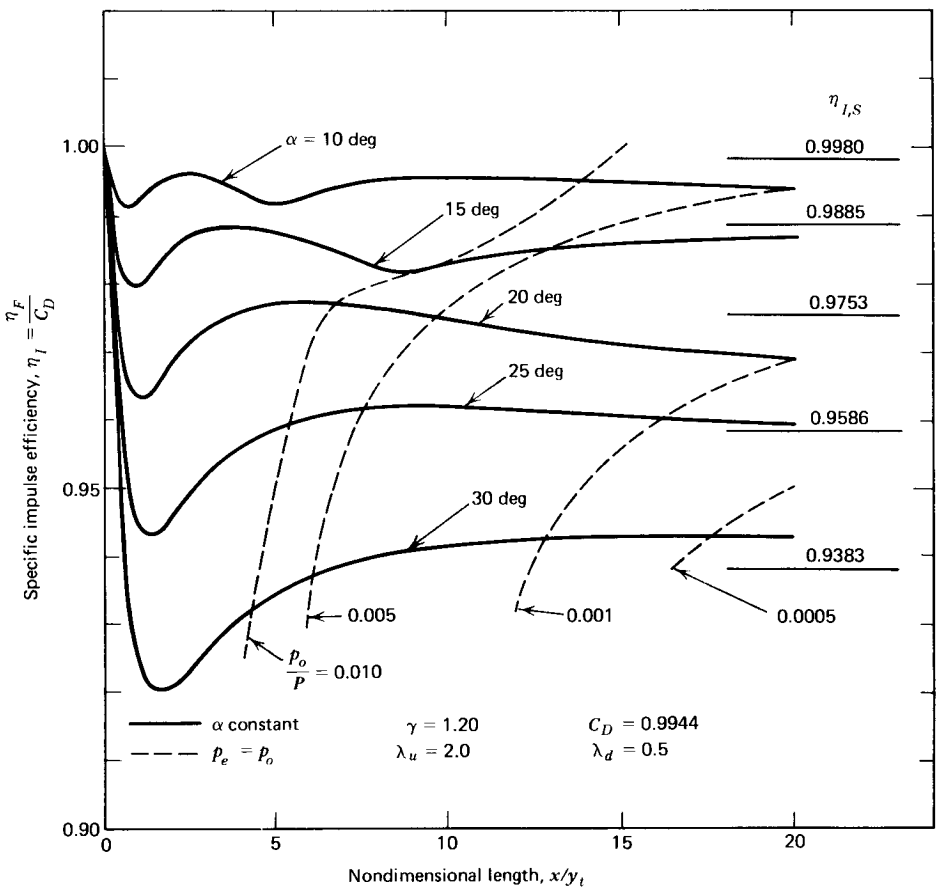

Figure 16.25 Specific impulse efficiency η_I for conical propulsive nozzles.

for $p_e/P = p_o/P$, we obtain

$$\varepsilon = \frac{A_e}{A_t} = \frac{\left(\frac{2}{\gamma+1}\right)^{1/(\gamma-1)}\left(\frac{\gamma-1}{\gamma+1}\right)^{1/2}}{\left(\frac{p_o}{P}\right)^{1/\gamma}\left[1-\left(\frac{p_o}{P}\right)^{(\gamma-1)/\gamma}\right]^{1/2}} \tag{a}$$

The equation specifying the contour of a conical nozzle is given by the equation on Fig. 16.8. Dividing that equation by y_t, we obtain

$$\frac{y}{y_t} = \varepsilon^{1/2} = 1 + \lambda_d(1-\cos\alpha) + \left(\frac{x}{y_t} - \lambda_d \sin\alpha\right)\tan\alpha \tag{b}$$

For a given pressure ratio p_o/P, equation (a) may be solved for the corresponding area ratio ε that yields a maximum thrust nozzle. The nozzle length x/y_t required to obtain that area ratio for a given cone angle α may then be determined from equation (b). For example, for $p_o/P = 0.005$, equation (a) gives $\varepsilon = 20.218$. For a 15-deg conical nozzle with $\lambda_d = 0.5$ and $\varepsilon = 20.218$, equation (b) gives $x/y_t = 13.115$. From Fig. 16.25, for $x/y_t = 13.115$ and $\alpha = 15$ deg, $\eta = 0.985$.

The dashed lines in Fig. 16.25 are determined by applying equations (a) and (b) for pressure ratios $p_o/P = 0.010$, 0.005, 0.001, and 0.0005, for maximum thrust nozzles for which $p_e = p_o$. For a given pressure ratio, the specific impulse efficiency η_I increases as the nozzle length increases because of the corresponding smaller cone angle α required to obtain the fixed area ratio ε corresponding to the given pressure ratio.

The dashed lines presented in Fig. 16.25 are based on the one-dimensional design criterion $p_e = p_o$. Consequently, that criterion may not yield maximum thrust when two-dimensional flow effects are accounted for. For example, consider a 15-deg conical nozzle operating with $p_o/P = 0.005$. From Fig. 16.25, to obtain $p_e = p_o$, $x/y_t = 13.115$. At that value of x/y_t, $\eta_I = 0.985$. A small increase in x/y_t increases η_I slightly, which may more than compensate for the corresponding small decrease in pressure p_e. That effect is quite small, however, and the dashed lines presented in Fig. 16.25 are a good approximation for the design of maximum thrust conical nozzles.

16–4(b) Supersonic Wind Tunnel Nozzle Design

The general features of supersonic wind tunnels are discussed in Section 7–12, and illustrated schematically in Fig. 7.40. Regardless of the means for furnishing the flow of gas through the wind tunnel, the *wind tunnel nozzle* must be designed so that it produces a parallel uniform flow at the entrance to the *test section* of the wind tunnel; that is, at the *nozzle exit section*. Moreover, the Mach number of the uniform flow discharged from the nozzle should be equal to the design Mach number M_D. Figure 16.26 illustrates schematically those requirements. The turning contour must be designed to yield the required exit flow conditions.

The analytical procedure for designing a wind tunnel nozzle is based on the techniques presented in Section 16–3. The subsonic and transonic contours of the wall of the wind tunnel must first be specified. Of course, the thermodynamic properties of the fluid must also be known. A transonic initial-value line is then established by employing one of the techniques discussed in Section 15–5. The

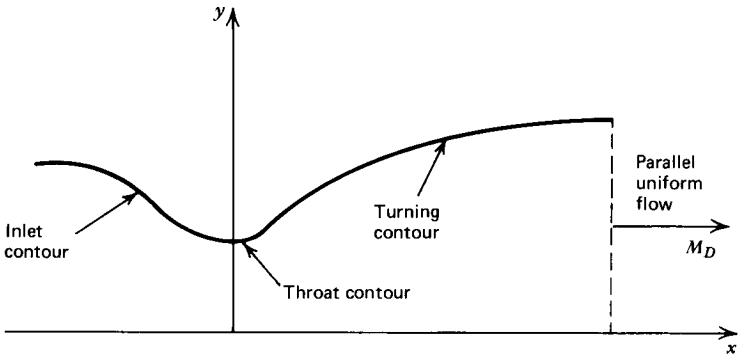

Figure 16.26 Supersonic wind tunnel nozzle design requirements.

contour of the wall immediately downstream from the throat is then specified; for example, a circular arc. Figure 16.27 illustrates the nature of the resulting initial-value and boundary-value problem. Curve AB is the inlet contour, curve BC is the initial expansion contour, and curve BD is the supersonic initial-value line.

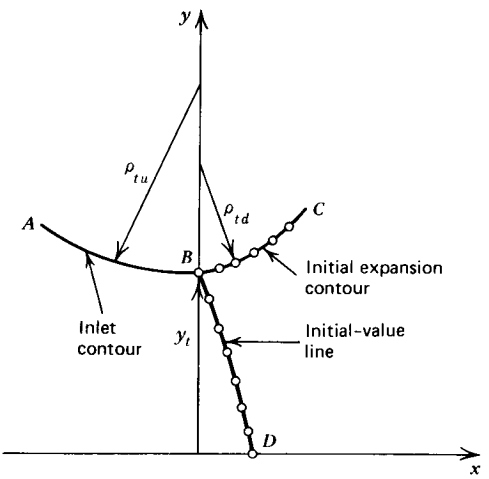

Figure 16.27 Initial-value line and initial expansion contour for supersonic nozzle design.

The initial-value and boundary-value problem is then analyzed by the method presented in Section 16–4(a) to determine the initial expansion flow field, which is illustrated schematically in Fig. 16.28. The flow field for the initial expansion is completely determined by the inlet and initial expansion contours, and is termed the *kernel*. The Mach number distribution along the axis, $M_{CL} = M(x)$, is determined from that flow field. As indicated in Fig. 16.28, the design Mach number M_D is then located on the x axis. The right-running characteristic which results in M_D, denoted by IK in Fig. 16.28, and the flow properties along line IK, may be determined by interpolation of the flow property values between the two right-running characteristics that intersect the x axis upstream and downstream from point K.

It is required that the *exit flow field* from the nozzle be a parallel uniform flow with $M = M_D$ and $\theta = 0$. In that region, all of the characteristics must, therefore, be straight lines at the angle $\alpha_D = \sin^{-1}(1/M_D)$, as illustrated in Fig. 16.29. Thus, a

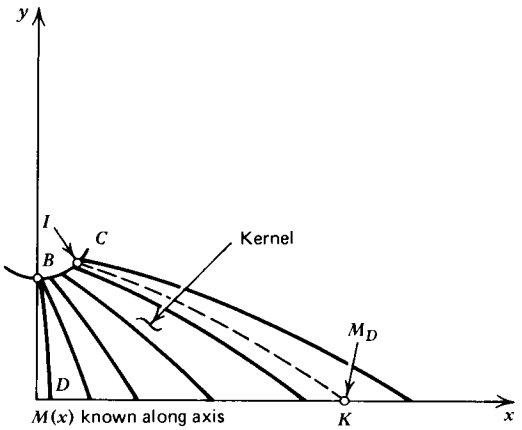

Figure 16.28 Location of the design Mach number on the centerline of a wind tunnel nozzle.

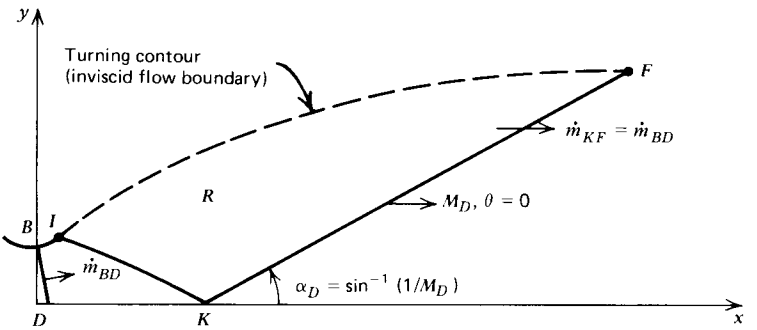

Figure 16.29 Determination of the exit flow conditions for a wind tunnel nozzle.

straight characteristic making the angle α_D with the x axis is extended from point K into the downstream flow field to the point F; the mass flow rate crossing line KF must equal the known mass flow rate crossing the initial-value line BD. Figure 16.29 illustrates schematically the resulting conditions.

The remaining problem is that of determining the flow field inside of the turning region R (Fig. 16.29), and the required shape for the *turning contour* of the wall, denoted by IF. Again, the problem is an initial-value problem, with data specified on two characteristics of opposite families (i.e., a *Goursat problem*). Figure 16.30 illustrates schematically how the unit process for an interior point [see Section 12–5(c)] is applied in region R, starting along line KF, to determine the supersonic flow field inside of the turning region R. Each new wall point is located by performing a mass balance along the corresponding characteristic from the initial point on line KF; the procedure is repeated at successive points along line KF until the entire turning contour IF has been determined.

In general, the nozzles required for producing parallel uniform exit flows are extremely long, with a nearly cylindrical cross section for a large portion of the downstream contour. In such long nozzles, the boundary layer growth cannot be neglected. The boundary layer displacement thickness must, therefore, be determined (see Section 5–10). The actual nozzle wall is obtained by displacing the turning contour IF by an amount equal to the boundary layer thickness. By applying that boundary layer thickness correction, the requirement that the contour

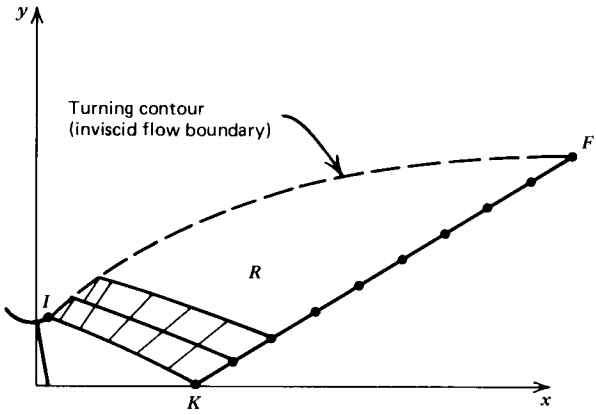

Figure 16.30 Determination of the turning contour.

IF is an inviscid streamline is thus preserved. An example of a technique for determining the boundary layer thickness is presented in Reference 5.

In the design of a two-dimensional planar wind tunnel, and many wind tunnels are planar, the turning region R may be determined by applying the simple wave concepts discussed in Section 12–6. A *simple wave region* is one where the characteristics of one family are straight lines having constant properties. It is shown in Section 12–6 that, in the case of a two-dimensional planar flow, the region adjoining a uniform flow region is always a simple wave region. Consequently, the turning region for a two-dimensional planar wind tunnel is a simple wave region. Figure 16.31 illustrates straight characteristics from selected points on line *IK*; the termination of each straight characteristic is determined by applying the mass balance requirement. The exact turning contour *IF* may, therefore, be determined without resorting to numerical integration.

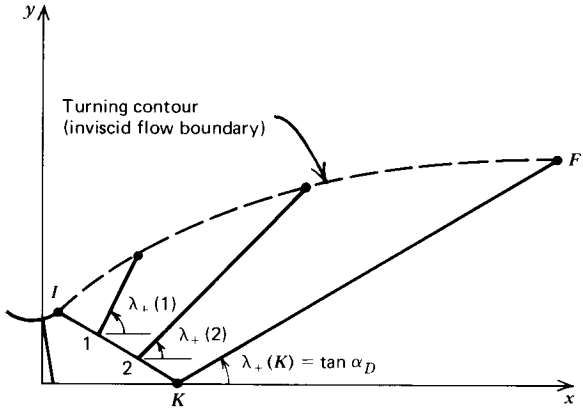

Figure 16.31 Determination of the turning contour for a simple wave region.

Example 16.7 A family of axisymmetric wind tunnel nozzles is to be designed for a blow-down air system. The thermodynamic properties of the air are $\gamma = 1.4$, $R = 287.04$ J/kg-K, $T = 300$ K, and $P = 30 \cdot 10^5$ N/m^2. It is desired that the nozzles produce parallel uniform flows having exit Mach numbers ranging from 1.5 to 4.0

in increments of 0.5. Determine the required inviscid flow boundary IF, for a throat radius $y_t = 1.0$ m, an upstream throat radius of curvature $\rho_{tu} = 2.0$ m, and a downstream throat radius of curvature $\rho_{td} = 0.5$ m (see Fig. 16.27).

Solution

For the given fixed inlet conditions and throat contour, the initial-value line BD of Fig. 16.27 is identical for all six nozzles. Employing Sauer's method (see Section 15–5) with 11 equally spaced points, a satisfactory initial-value line is obtained. The remainder of the calculation procedure is based on applying the appropriate irrotational flow unit processes as discussed in Section 16–4(b). Figure 16.32 presents the results for the required contours, as plots of y/y_t as a function of x/y_t, with M_D as a parameter.

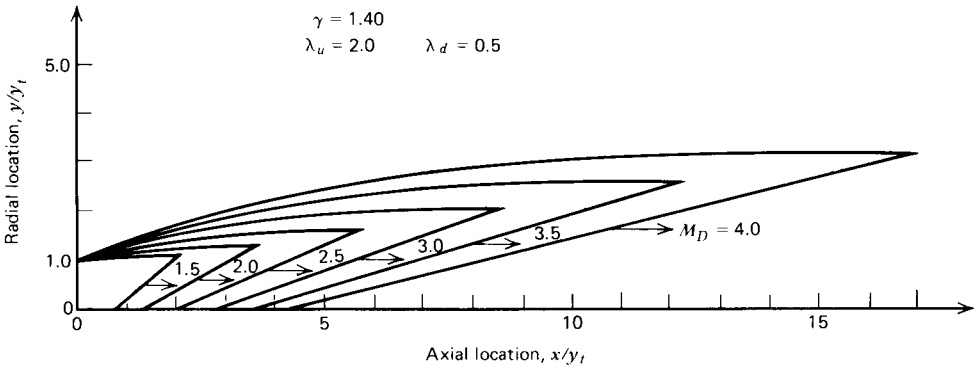

Figure 16.32 Nozzle designs having parallel uniform exit flow.

It is evident from Fig. 16.32 that the nozzles are quite long. By applying the scaling laws presented in Section 16–3(g), the contours presented in Fig. 16.32 may be scaled geometrically to any desired size. The nozzle contours are independent of the stagnation pressure. The velocity and the speed of sound, however, scale with $T^{-1/2}$. Hence, the velocity and the speed of sound change, but M remains the same when the stagnation temperature T changes. Consequently, the contours of the nozzles are independent of the stagnation temperature. Because, as stated earlier, flow fields do not scale with changes in γ, all of the calculations must be repeated if contours for different values of γ are needed.

16–4(c) Nozzle Design for Maximum Thrust

In Example 16.6, the propulsive performance of a 15-deg conical converging-diverging nozzle is discussed. It is shown that, compared to a nozzle that produces a parallel gas flow at its exit cross-section, the conical nozzle produces 1.72 percent less specific impulse, which is a significant reduction for a large rocket motor nozzle. Propulsive nozzles that produce an exit jet having a parallel uniform flow may be designed by the procedure presented in Section 16–4(b) for wind tunnel nozzles. Such nozzles, however, are excessively long and are consequently unacceptably heavy for propulsive nozzles for large chemical rocket motors. The same objections apply to their use as the propulsion nozzles for air-breathing jet engines. Truncated parallel flow nozzles[6] have been employed as propulsive nozzles.

A worthwhile improvement over the performance of the conical nozzle may be effected by designing the propulsive nozzle in accordance with the method described by Rao.[7] Nozzles designed by the latter method are known as *Rao nozzles.*

Rao[7] investigated the problem of determining the contour of the divergence for a propulsive nozzle that would maximize the thrust under the following two constraints: (1) a specified nozzle length L, and (2) a constant mass flow rate through the nozzle. Mathematically speaking, the above problem is one in *constrained,* rather than *free, maxima.* Its solution may be obtained by applying the method of *Lagrange multipliers* (see References 8 and 9). Rao applied the latter method of analysis to the isentropic frictionless (irrotational) flow of a gas through an axisymmetric converging-diverging nozzle subject to the two constraints presented above. It is assumed that the conditions at the inlet to the nozzle are known.

Figure 16.33*a* illustrates schematically the upper half of the longitudinal cross section of the nozzle contour; since the nozzle is axisymmetric only the upper half of the contour need be shown. The nozzle contour is denoted by $ATBE$, and the axis of the nozzle coincides with the x axis. The throat section is denoted by T, and the origin of the coordinate system 0 is at the intersection of the x axis and the throat section. The radial distance from the nozzle axis is denoted by y.

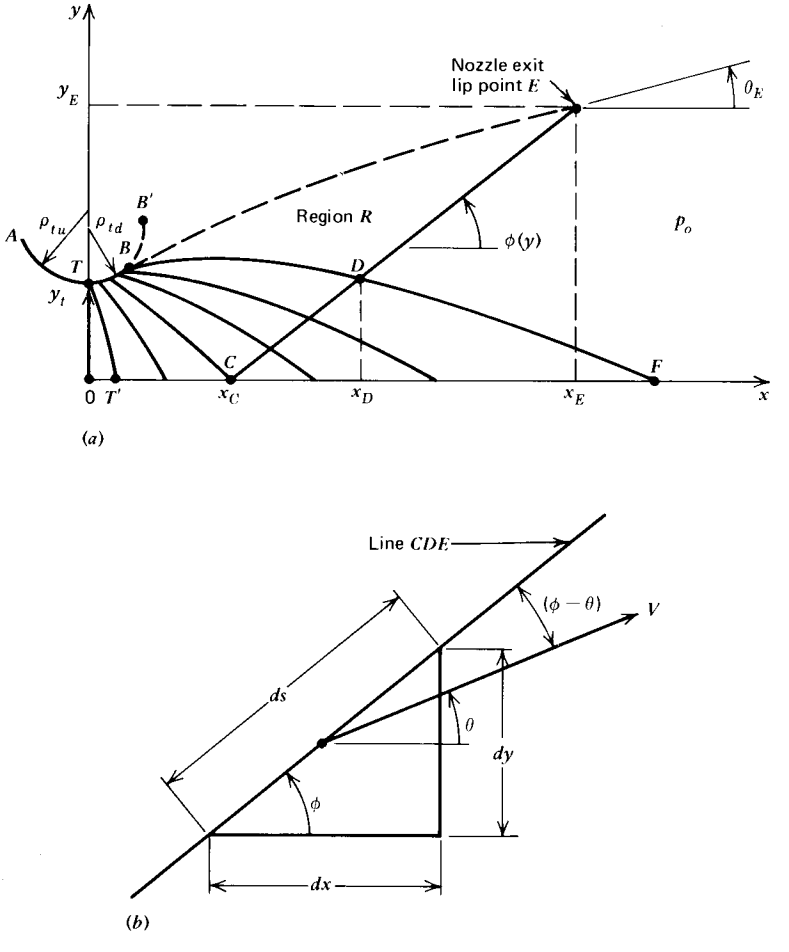

Figure 16.33 General features of the Rao nozzle for maximum thrust (taken from Reference 7). (*a*) Nozzle geometry and flow field model. (*b*) Flow across an element of the control surface.

The initial-value line TT'' in Fig. 16.33*a* is established by applying any of the transonic flow analysis methods discussed in Section 15–5. As in the case of designing a wind tunnel nozzle, the throat T and the initial expansion contour TB' are specified, and the *kernel* region for the flow field is determined by the method discussed in Section 16–4(a). The line CDE in Fig. 16.33*a* represents the intersection of a control surface with the meridional plane passing through the arbitrary point D in the *kernel*; the points C and E denote the intersections of that control surface with the *axis* and *exit lip* of the nozzle, respectively. The inclination of the line CDE at any point with respect to the nozzle axis is denoted by the angle ϕ, which is a function of y. The axial distance x_C and the angle $\phi(y)$ define the shape of the control surface.

Figure 16.33*b* illustrates an elementary arc ds of the control surface CDE at an arbitrary radius y. The elementary area dA corresponding to ds is given by

$$dA = 2\pi y\, ds = \frac{2\pi y\, dy}{\sin\phi} \tag{16.35}$$

From the geometry in Fig. 16.33*b*, we obtain

$$ds = \frac{dy}{\sin\phi} \tag{16.36}$$

Let V, ρ, and θ denote, respectively, the fluid velocity, density, and the flow (streamline) angle; they are assumed to be uniform over dA. Accordingly, the mass rate of flow of gas crossing the control surface, denoted by $\dot{m}_{CE}$, is given by

$$\dot{m}_{CE} = \int_C^E \rho V \frac{\sin(\phi - \theta)}{\sin\phi} 2\pi y\, dy = \text{constant} \tag{16.37}$$

Equation 16.37 specifies mathematically one of the constraints imposed on the analysis for maximizing the thrust.

The length of the control surface in the axial direction, denoted by L, is given by

$$L = x_C + \int_C^E \cot\phi\, dy \tag{16.38}$$

The length L selected for the nozzle determines the distance x_C. For the case at hand it may be assumed to be fixed. Since L is the second constraint imposed upon the analysis and x_C is assumed fixed, that constraint is specified by the equation

$$\int_C^E \cot\phi\, dy = \text{constant} \tag{16.39}$$

Let p_o and p denote the static pressures of the ambient atmosphere and that over ds, respectively. Hence, the thrust acting on the nozzle, denoted by F_{CE}, is given by

$$F_{CE} = \int_C^E \left[(p - p_o) + \rho V^2 \frac{\sin(\phi - \theta)\cos\theta}{\sin\phi} \right] 2\pi y\, dy \tag{16.40}$$

In Fig. 16.33*a* it is assumed that the point D on the control surface CDE lies at the intersection of the control surface and the right-running characteristic emanating from point B, on the prescribed initial expansion contour TBB'. Consequently, any changes in the nozzle contour downstream from point B have no influence on

the flow between points C and D. The portion of the control surface between points C and D is assumed, for convenience, to coincide with a left-running characteristic in the *kernel*. The location of point D is, however, not known because the extent of the initial expansion is unknown.

The problem is to maximize equation 16.40 in the presence of the constraints specified by equations 16.37 and 16.39, by applying the method of *Lagrange multipliers*. The details of the maximizing procedure are presented in Reference 7. Only the results are presented here.

It is found that along control surface DE, the angle ϕ is related to the flow (streamline) angle θ and the Mach angle α by the relation

$$\phi = \theta + \alpha \qquad (along\ DE) \tag{16.41}$$

Equation 16.41 shows that line DE of the control surface coincides with the last left-running characteristic of the flow field. At the point E

$$\sin 2\theta_E = \frac{(p_E - p_o)\cot \alpha_E}{\frac{1}{2}\rho_E V_E^2} \tag{16.42}$$

Equation 16.42 relates θ_E, $M_E = V_E/a_E$, and p_o. It is known as a *corner condition*. Two additional conditions are derived along the control surface DE, that is,

$$\frac{V\cos(\theta - \alpha)}{\cos \alpha} = C_1 \tag{16.43}$$

and

$$y\rho V^2 \sin^2 \theta \tan \alpha = C_2 \tag{16.44}$$

where C_1 and C_2 are constants.

The numerical procedure for designing a Rao nozzle is as follows (see Fig. 16.33*a*). At any arbitrary point D in the kernel, all of the flow properties are fixed by the throat and initial expansion contours. Thus, the constants C_1 and C_2 may be determined at point D, and equations 16.43 and 16.44 may be solved for M and θ as functions of y along the control surface DE. Consequently, the function $\phi(y)$ along line DE may be determined from equation 16.41, and equation 16.37 may be integrated to determine the location of point E. Integrating equations 16.39 and 16.40 between the limits D and E determines the thrust F_{DE} and the length x_E. The total thrust on the nozzle is obtained by adding the thrust obtained across line CD, in the kernel, to the thrust F_{DE}. Thus, all of the flow properties at point E are known, and equation 16.42 may be solved for the ambient static pressure p_o for which the nozzle contour is a maximum thrust contour, for the particular value of x_E.

The nozzle length x_E and the ambient pressure p_o are not known until the entire design procedure is completed. Consequently, an iterative procedure is required in which the choice of point D is varied to obtain the specified values for x_E and p_o. Such an iterative method is readily implemented by choosing several different points in the kernel as point D, and obtaining a map of x_E and p_o as a function of the different choices for point D. A direct approach, where M_E and p_o are specified, is presented by Rao,[7] but it is considerably more complex than the iterative procedure presented here. Moreover, the method described in Reference 7 still requires an iteration for obtaining a specific value for the nozzle length x_E.

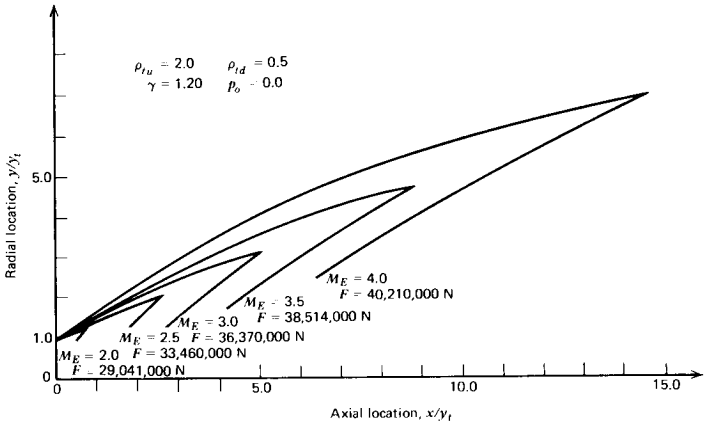

Figure 16.34 Rao nozzle designs.

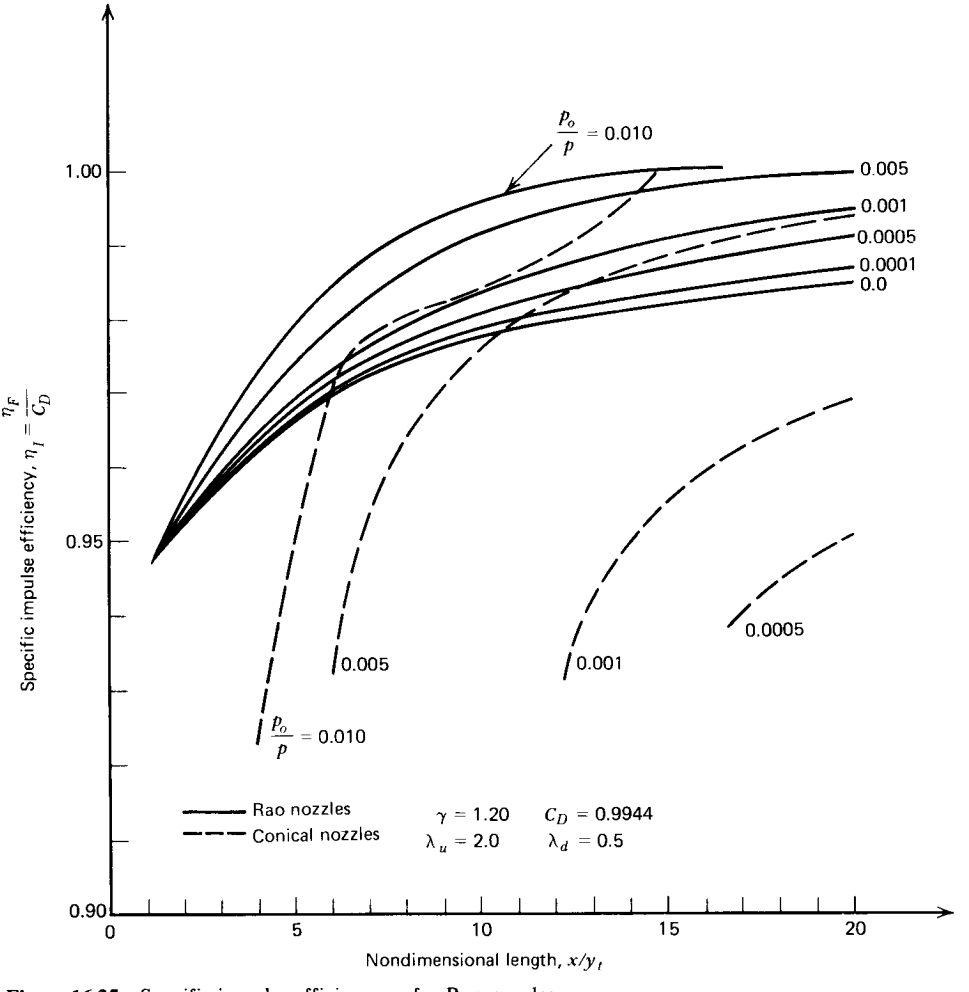

Figure 16.35 Specific impulse efficiency η_I for Rao nozzles.

The task still remains of determining the flow field in the turning region R, and the turning contour BE. The problem is an initial-value problem and by applying the method of characteristics in the manner illustrated schematically in Fig. 16.30, the turning contour BE may be determined [see Section 16–4(b)].

Rao nozzles are used extensively in the rocket engine industry. They develop the maximum thrust for a specified length. Also, they are much shorter, and hence lighter, than conventional conical nozzles producing the same thrust.

Example 16.8 A family of Rao nozzles is to be designed for $\gamma = 1.2$, $R = 320$ J/kg-K, $T = 3000$ K, and $P = 70 \cdot 10^5$ N/m^2. Those conditions are representative of the combustion gas flowing through a rocket motor. Refer to Fig. 16.33*a*; the throat radius $y_t = 1.0$ m, the upstream throat radius of curvature ρ_{tu} is 2.0 m, and the downstream throat radius of curvature ρ_{td} is 0.5 m. The ambient pressure $p_o = 0.0$. Determine the required inviscid flow boundary BE and the propulsive thrust for each of a series of Rao nozzles designed for exit Mach numbers M_E ranging from 2.0 to 4.0, in increments of 0.5.

Solution

The initial-value line that is common to all of the designs is determined by Sauer's technique with 11 equally spaced points. The remainder of the calculations are conducted in the manner described in Section 16–4(c). Figure 16.34 presents the resulting contours and thrusts. They may be scaled to any size, stagnation pressure, and stagnation temperature by applying the scaling rules presented in Section 16–3(g).

Figure 16.35 presents the specific impulse efficiency η_I (see Example 16.6) as a function of the nozzle length with the pressure ratio p_o/P as a parameter, for a family of Rao nozzles. The corresponding curves presented in Fig. 16.25 for a family of conical nozzles having the same throat geometry are illustrated by the dashed lines. By comparing the specific impulse efficiencies of the two families of nozzles for a given pressure ratio, it is apparent that Rao nozzles have a smaller divergence loss than do conical nozzles.

16–5 TAYLOR–MACCOLL FLOW AROUND A CONE

Supersonic flow around an infinite axisymmetric cone aligned with the free-stream flow direction occurs frequently in engineering applications. Since the upstream flow is supersonic, a shock wave is formed in the flow. When the cone angle δ_c and the free-stream Mach number M_1 fall within certain limits, the shock wave is attached to the vertex of the cone, as illustrated in Fig. 16.39. A flow satisfying the aforementioned conditions is called a Taylor–Maccoll flow.[10,11] The two most common examples of Taylor–Maccoll flow are the tips of projectiles and the central spike of supersonic diffusers [see Section 7–13(e)]. The general features of Taylor–Maccoll flow are described in Section 7–10(b).

In this section, the equations governing Taylor–Maccoll flow are derived, and a numerical procedure for solving those equations is discussed. A numerical example is presented to illustrate the application of the procedure, and a FORTRAN computer program for implementing the numerical computations is presented.

16–5(a) Governing Equations

The flow model for Taylor–Maccoll flow is illustrated in Fig. 16.36. For an infinite cone, no characteristic length appears in the flow field, and it is reasonable to

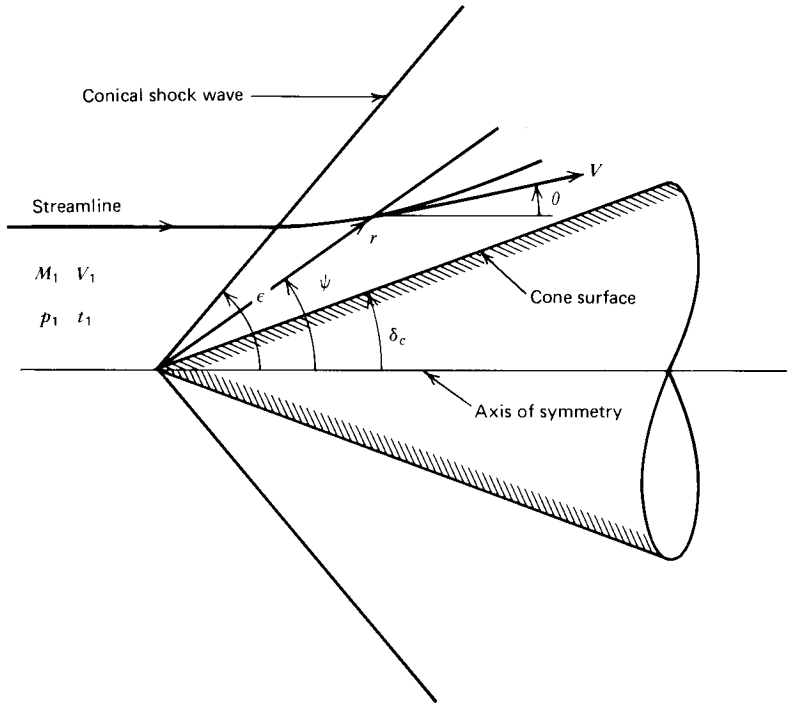

Figure 16.36 Flow model for Taylor-Maccoll flow over a cone.

assume that the flow properties depend only on the spherical angle ψ and not on the radius r. Consequently, we assume that flow properties are constant along any ray emanating from the vertex of the cone, and that the shock wave itself is conical. Such a flow is called a *conical flow*. The assumption that Taylor–Maccoll flow is a conical flow has been abundantly verified experimentally.

Since the oblique shock wave is conical, it has the same inclination to the free stream everywhere. Consequently, the strength of the shock wave is constant, and the flow properties immediately behind the shock wave are uniform. Thus, the flow behind the conical shock wave is irrotational, and the governing equations are the gas dynamic equation (equation 10.190) and the irrotationality condition. Those equations are given below. Thus,

$$(\mathbf{V}\cdot\nabla)\left(\frac{V^2}{2}\right)-a^2\nabla\cdot\mathbf{V}=0 \tag{16.45}$$

$$\boldsymbol{\omega}=\nabla\times\mathbf{V}=0 \tag{16.46}$$

where, for irrotational flow, equation 10.121 gives

$$a=a(V) \qquad (\textit{throughout the flow field}) \tag{16.47}$$

For a conical flow, it is convenient to express the governing equations in the spherical coordinate system illustrated in Fig. 16.37. The flow properties are independent of the angle ϕ due to the axial symmetry of the flow field, and the flow properties are independent of the radius r because of the conical nature of the flow field. Consequently, in spherical coordinates, the flow properties depend only on the spherical angle ψ, and the governing partial differential equations reduce to ordinary differential equations. The standard notation for the spherical angle is θ.

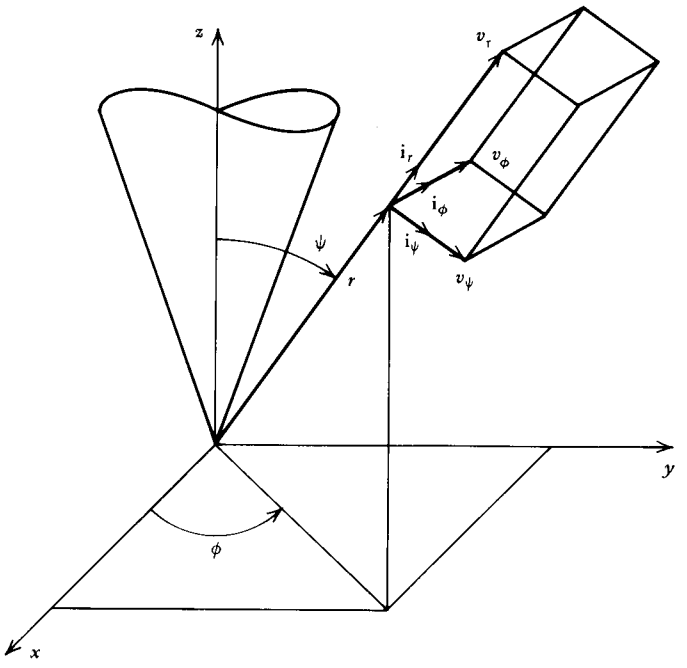

Figure 16.37 The spherical coordinate system.

However, to avoid confusion with the polar angle θ employed in cylindrical coordinates, the spherical angle is denoted by ψ in the present discussion.

In spherical coordinates, the velocity vector $\mathbf{V}$ and the vector operators $\nabla\cdot\mathbf{V}$, $(\mathbf{V}\cdot\nabla)$, and $\nabla\times\mathbf{V}$ take the following forms.[12]

$$\mathbf{V}=\mathbf{i}_r v_r+\mathbf{i}_\psi v_\psi+\mathbf{i}_\phi v_\phi \tag{16.48}$$

$$\nabla\cdot\mathbf{V}=\frac{1}{r^2}\frac{\partial}{\partial r}(r^2 v_r)+\frac{1}{r\sin\psi}\frac{\partial}{\partial\psi}(\sin\psi v_\psi)+\frac{1}{r\sin\psi}\frac{\partial v_\phi}{\partial\phi} \tag{16.49}$$

$$(\mathbf{V}\cdot\nabla)=v_r\frac{\partial}{\partial r}+\frac{v_\psi}{r}\frac{\partial}{\partial\psi}+\frac{v_\phi}{r\sin\psi}\frac{\partial}{\partial\phi} \tag{16.50}$$

$$\nabla\times\mathbf{V}=\mathbf{i}_r\left\{\frac{1}{r\sin\psi}\left[\frac{\partial}{\partial\psi}(\sin\psi v_\phi)-\frac{\partial v_\psi}{\partial\phi}\right]\right\}+\mathbf{i}_\psi\left[\frac{1}{r\sin\psi}\frac{\partial v_r}{\partial\phi}-\frac{1}{r}\frac{\partial}{\partial r}(rv_\phi)\right]$$

$$+\mathbf{i}_\phi\left\{\frac{1}{r}\left[\frac{\partial}{\partial r}(rv_\psi)-\frac{\partial v_r}{\partial\psi}\right]\right\} \tag{16.51}$$

Substituting equations 16.48 to 16.51 into equations 16.45 and 16.46, setting $v_\phi=0$, and disregarding derivatives with respect to r and ϕ, we obtain

$$v_\psi\left(v_r\frac{\partial v_r}{\partial\psi}+v_\psi\frac{\partial v_\psi}{\partial\psi}\right)-a^2\left(\frac{\partial v_\psi}{\partial\psi}+2v_r+v_\psi\cot\psi\right)=0 \tag{16.52}$$

$$v_\psi-\frac{\partial v_r}{\partial\psi}=0 \tag{16.53}$$

Since the flow properties depend only on the spherical angle ψ

$$\frac{\partial}{\partial \psi} = \frac{d}{d\psi} \tag{16.54}$$

In addition, the following change of notation is employed to simplify the appearance of equations 16.52 and 16.53. Thus,

$$\bar{u} \equiv v_r \qquad \text{and} \qquad \bar{v} \equiv v_\psi \tag{16.55}$$

where $\bar{u}$ and $\bar{v}$ are employed to avoid confusion with the velocity components u and v for a two-dimensional axisymmetric flow. Figure 16.38 illustrates the flow model in the $\bar{u}, \bar{v}$ notation, and the relationships between $\mathbf{V}$, $\bar{u}$, $\bar{v}$, ψ, u, v, and θ. Note that for Taylor–Maccoll flow, $\bar{v} = v_\psi$ is always a negative value since the positive direction for ψ is counterclockwise and v_ψ always points toward the cone, that is, in the negative ψ direction.

Substituting equations 16.54 and 16.55 into equations 16.52 and 16.53 yields

$$\bar{v}\left(\bar{u}\frac{d\bar{u}}{d\psi} + \bar{v}\frac{d\bar{v}}{d\psi}\right) - a^2\left(\frac{d\bar{v}}{d\psi} + 2\bar{u} + \bar{v}\cot\psi\right) = 0 \tag{16.56}$$

$$\frac{d\bar{u}}{d\psi} = \bar{v} \tag{16.57}$$

Substituting equation 16.57 into equation 16.56 and rearranging gives

$$\frac{d\bar{v}}{d\psi} = -\bar{u} + \frac{a^2(\bar{u} + \bar{v}\cot\psi)}{\bar{v}^2 - a^2} \tag{16.58}$$

Equations 16.57 and 16.58 may be written in dimensionless form by dividing by the critical speed of the free stream a^*. Thus,

$$\bar{u}^* \equiv \frac{\bar{u}}{a^*} \qquad \text{and} \qquad \bar{v}^* = \frac{\bar{v}}{a^*} \tag{16.59}$$

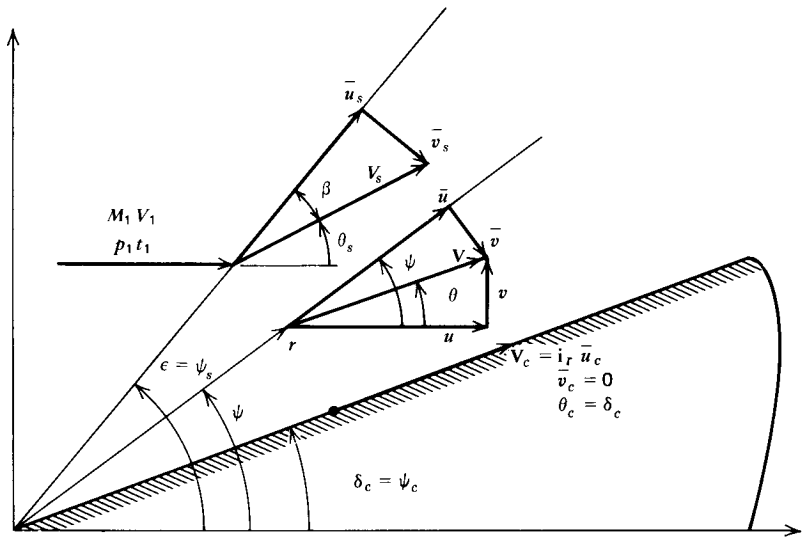

Figure 16.38 Relationships between V, $\bar{u}$, $\bar{v}$, ψ, u, v, and θ.

and equations 16.57 and 16.58 become

$$\frac{d\bar{u}^*}{d\psi} = \bar{v}^* \tag{16.60}$$

$$\frac{d\bar{v}^*}{d\psi} = -\bar{u}^* + \frac{(a/a^*)^2(\bar{u}^* + \bar{v}^* \cot\psi)}{(\bar{v}^*)^2 - (a/a^*)^2} = f(\psi, \bar{u}^*, \bar{v}^*) \tag{16.61}$$

Equations 16.60 and 16.61 comprise a set of two coupled ordinary differential equations for the determination of the nondimensional velocity components $\bar{u}^*$ and $\bar{v}^*$ in a steady conical irrotational flow. Those equations may be integrated by any standard integration method, for example, the fourth-order Runge–Kutta method presented in Appendix A–6(d). Before the integration can be performed, however, an equation of state relating a and a^* for the gas must be specified. In general, that relationship may take the form of an algebraic equation, a table, a graph, or a computer code. For a perfect gas, a particularly simple algebraic equation is obtained. From equation 3.94

$$\left(\frac{a}{a^*}\right)^2 = \frac{\gamma+1}{2} - \frac{\gamma-1}{2}\left(\frac{V}{a^*}\right)^2 = \frac{\gamma+1}{2} - \frac{\gamma-1}{2} M^{*2} \tag{16.62}$$

where

$$M^{*2} = \left(\frac{V}{a^*}\right)^2 = \bar{u}^{*2} + \bar{v}^{*2} \tag{16.63}$$

16–5(b) Numerical Integration of the Governing Equations for Taylor–Maccoll Flow

The direct problem of interest in a Taylor–Maccoll flow is the situation where the free-stream flow properties V_1, p_1, and t_1 and the cone semiangle δ_c are specified, and the shock wave angle ϵ and the velocity distributions $\bar{u}(\psi)$ and $\bar{v}(\psi)$ are to be determined. In that case, unfortunately, the initial conditions for $\bar{u}$ and $\bar{v}$ cannot be determined either behind the shock wave, since ϵ is unknown, or on the surface of the cone. Consequently, an iterative procedure is required to determine the solution.

Several iterative approaches are possible. The most straightforward is based on assuming a trial value for the shock wave angle $\epsilon^{(i)}$, where the superscript (i) denotes the trial number, and solving the governing equations to determine the corresponding value of the cone angle $\delta_c{}^{(i)}$. When the value of $\epsilon^{(i)}$ is determined that yields $\delta_c{}^{(i)} = \delta_c$, the solution is complete. The procedure is outlined below.

1. Assume a first trial value for the shock wave angle $\epsilon^{(1)}$. A reasonable estimate is given by

$$\epsilon^{(1)} = \delta_c + \frac{\alpha_1}{2} \tag{16.64}$$

where α_1 is the free-stream Mach angle $\alpha_1 = \sin^{-1}(1/M_1)$.

2. Determine the angular step size for the numerical integration algorithm. Thus,

$$\Delta\psi = -\frac{\epsilon^{(i)} - \delta_c}{N} \tag{16.65}$$

where N is the desired number of steps between the shock wave and the surface of the cone.

3. For the specified free-stream properties V_1, p_1, and t_1, and the assumed shock wave angle $\epsilon^{(i)}$, calculate the flow properties $\bar{u}_s^*$ and $\bar{v}_s^*$ immediately downstream of the oblique shock wave, as illustrated in Fig. 16.38. Those values of $\bar{u}_s^*$ and $\bar{v}_s^*$ serve as initial conditions for initiating the numerical integration of equations 16.60 and 16.61. For a perfect gas, the property ratios across an oblique shock wave are given by equations 7.90 to 7.92 in Section 7–7(b), which are repeated and renumbered below.

$$\frac{p_2}{p_1} = \frac{2\gamma}{\gamma+1}\left(M_1^2 \sin^2\epsilon - \frac{\gamma-1}{2\gamma}\right) \tag{16.66}$$

$$\frac{\rho_1}{\rho_2} = \frac{\tan\beta}{\tan\epsilon} = \frac{2}{\gamma+1}\left(\frac{1}{M_1^2 \sin^2\epsilon} + \frac{\gamma-1}{2}\right) \tag{16.67}$$

$$\frac{V_2}{V_1} = \frac{(V_2/a^*)}{(V_1/a^*)} = \frac{M_2^*}{M_1^*} = \frac{\sin\epsilon}{\sin\beta}\left[\frac{2}{(\gamma+1)M_1^2 \sin^2\epsilon} + \frac{\gamma-1}{\gamma+1}\right] \tag{16.68}$$

where point 2 denotes conditions immediately behind the shock wave, and

$$\beta = \epsilon - \theta_s \tag{16.69}$$

The values of $\bar{u}_s^*$ and $\bar{v}_s^*$ are determined as follows.

$$\bar{u}_s^* = M_2^* \cos\beta \tag{16.70}$$

$$\bar{v}_s^* = -M_2^* \sin\beta \tag{16.71}$$

where, from equations 3.189

$$M_1^* = \left[\frac{(\gamma+1)M_1^2}{2+(\gamma-1)M_1^2}\right]^{1/2} \tag{3.189}$$

Section 7–8 presents a numerical procedure for determing the properties behind an oblique shock wave for an imperfect gas.

4. Starting with the initial conditions determined in step 3, integrate equations 16.60 and 16.61 from the shock wave toward the surface of the cone. At the surface of the cone, which is a ray in the conical flow, the velocity must be parallel to the surface. Hence, $\bar{v}^* = 0$ at the surface of the cone. The initial value of $\bar{v}_s^*$ behind the shock wave is negative, and $\bar{v}^*$ increases toward zero as the spherical angle ψ decreases. The exact value of ψ_c where $\bar{v}_c^* = 0$ for an assumed value of the shock wave angle $\epsilon^{(i)}$ must be determined iteratively. When found, that value of ψ_c is equal to the cone semiangle $\delta_c^{(i)}$ corresponding to the shock wave angle $\epsilon^{(i)}$.

5. The procedure described in step 4 determines the flow field for a given combination of $\epsilon^{(i)}$ and $\delta_c^{(i)}$. However, the value of $\delta_c^{(i)}$ obtained is not, in general, the desired value of δ_c, so the assumed value for the shock wave angle $\epsilon^{(i)}$ must be revised and steps 2 to 4 above repeated. The first correction to the assumed value for $\epsilon^{(i)}$ may be determined by simply adjusting $\epsilon^{(1)}$ by the amount by which $\delta_c^{(1)}$ deviates from δ_c. Thus,

$$\epsilon^{(2)} = \epsilon^{(1)} + (\delta_c - \delta_c^{(1)}) \tag{16.72}$$

Subsequent trial values for $\epsilon^{(i)}$ may be determined by applying the secant method

[see Appendix A–4(b)] to the two most recent sets of values for $\epsilon^{(i)}$ and $(\delta_c - \delta_c^{(i)})$. Steps 2 to 4 are repeated until $(\delta_c - \delta_c^{(i)})$ falls within an acceptable convergence tolerance.

6. When the solution has converged, the velocity components $\bar{u}^*(\psi)$ and $\bar{v}^*(\psi)$ may be transformed into the two-dimensional velocity components $u^*(\psi)$ and $v^*(\psi)$, and the flow properties $V(\psi)$, $\theta(\psi)$, $p(\psi)$, and $\rho(\psi)$ may be calculated. From Fig. 16.38

$$M^* = \sqrt{u^{*2} + v^{*2}} \tag{16.73}$$

$$u^* = \bar{u}^* \cos\psi - \bar{v}^* \sin\psi \tag{16.74}$$

$$v^* = \bar{u}^* \sin\psi + \bar{v}^* \cos\psi \tag{16.75}$$

$$\theta = \tan^{-1}\left(\frac{v^*}{u^*}\right) \tag{16.76}$$

At any point in the conical flow field where the pressure is denoted by p and the density is denoted by ρ, we have

$$\frac{p}{p_1} = \left(\frac{p}{P}\right)\left(\frac{P_2}{p_2}\right)\left(\frac{p_2}{p_1}\right) \tag{16.77}$$

$$\frac{\rho}{\rho_1} = \left(\frac{\rho}{\rho_0}\right)\left(\frac{\rho_{02}}{\rho_2}\right)\left(\frac{\rho_2}{\rho_1}\right) \tag{16.78}$$

where P_2 and ρ_{02} are the stagnation values of the pressure and the density, respectively, behind the shock wave, p_2 and ρ_2 are the corresponding static values behind the shock wave, and P and ρ_0 are the stagnation properties corresponding to p and ρ, respectively. Since the conical flow is irrotational, $P_2 = P$ and $\rho_{02} = \rho_0$. For a perfect gas, the static values of pressure and density are related to the corresponding stagnation values and the dimensionless velocity M^* by equations 3.112 and 3.113, respectively, which are repeated and renumbered below.

$$\frac{p}{P} = \left(1 - \frac{\gamma - 1}{\gamma + 1} M^{*2}\right)^{\gamma/(\gamma-1)} \tag{16.79}$$

$$\frac{\rho}{\rho_0} = \left(1 - \frac{\gamma - 1}{\gamma + 1} M^{*2}\right)^{1/(\gamma-1)} \tag{16.80}$$

For an imperfect gas, the ratios p/P and ρ/ρ_0 may be determined by the procedures discussed in Section 4–5.

The numerical procedure described above is straightforward to implement, and convergence to a fractional tolerance of 10^{-6} is generally achieved with three or four trial values for ϵ. A computer program, subroutine TM, for implementing the above procedure, is presented below. In that program, the function statements AA(X, Y), PRR(X, Y), and RRR(X, Y) are based on equations 16.62, 16.79 and 16.80, respectively, which are applicable for a perfect gas. Subroutine SHCK, which calculates the properties behind an oblique shock wave, is based on equations 16.66 to 16.68, which are applicable for a perfect gas. The remainder of the program is valid for any equation of state. Consequently, if gases other than the perfect gas are to be considered, those three function statements and subroutine SHCK must be modified accordingly.

The program input consists of the specific heat ratio γ (denoted by G), the free-stream Mach number M_1 (denoted by M1), the cone angle δ_c (denoted by AC), and the number of angular increments NI between the shock wave and the surface of the cone. The output consists of the values of ψ, V/V_1, θ, p/p_1, and ρ/ρ_1, stored in order from the shock wave to the surface of the cone, in the arrays T(I), Q(I), A(I), P(I), and R(I). Any other properties of interest may be calculated from the above results.

```
      SUBROUTINE TM (EPS)

C     SUBROUTINE TM CALCULATES TAYLOR-MACCOLL FLOW OVER A CONE

      REAL M1,M1S,K1,K2,K3,K4,L1,L2,L3,L4
      COMMON /TAYMAC/ T(99),U(99),V(99)
      COMMON /ARRAYS/ X(99),Y(99),P(99),R(99),Q(99),A(99)

      AA(X,Y)=((G+1.0)-(G-1.0)*(X*X+Y*Y))/2.0
      PRR(X)=(1.0-(G-1.0)/(G+1.0)*X*X)**(G/(G-1.0))
      RRR(X)=(1.0-(G-1.0)/(G+1.0)*X*X)**(1.0/(G-1.0))
      F(X,Y,Z)=-X+AA(X,Y)*(X+Y/TAN(Z))/(Y*Y-AA(X,Y))
      NAMELIST /INTM/ G,M1,AC,NI $ RAD=57.2957795

   10 G=1.4 $ M1=3.0 $ AC=30.0 $ NI=11 $ READ (5,INTM) $ IF(EOF,5) 20,30
   20 RETURN
   30 WRITE(6,INTM) $ AC=AC/RAD $ EPS=AC+0.5*ASIN(1.0/M1) $ L=0

C     SOLVE FOR THE FLOW PROPERTIES BEHIND THE SHOCK WAVE

   40 CALL SHK (EPS,M1,M1S,G,QS,AS,PR,RR) $PR=PR/PRR(QS) $RR=RR/RRR(QS)
      U(1)=QS*COS(EPS-AS) $ V(1)=-QS*SIN(EPS-AS) $ T(1)=EPS
      K=0 $ I=1 $ DT=-(EPS-AC)/FLOAT(NI-1)

C     INTEGRATE FROM THE SHOCK WAVE TO THE CONE

   50 K1=V(I)*DT $ L1=F(U(I),V(I),T(I))*DT
      K2=(V(I)+0.5*L1)*DT $ L2=F(U(I)+0.5*K1,V(I)+0.5*L1,T(I)+0.5*DT)*DT
      K3=(V(I)+0.5*L2)*DT $ L3=F(U(I)+0.5*K2,V(I)+0.5*L2,T(I)+0.5*DT)*DT
      K4=(V(I)+L3)*DT $ L4=F(U(I)+K3,V(I)+L3,T(I)+DT)*DT
      U(I+1)=U(I)+(K1+2.0*K2+2.0*K3+K4)/6.0
      V(I+1)=V(I)+(L1+2.0*L2+2.0*L3+L4)/6.0 $ T(I+1)=T(I)+DT
      IF(K.GT.0)GO TO 70 $IF (V(I+1).GT.0.0) GO TO 60 $ I=I+1 $ GO TO 50
   60 VS=V(I+1) $ DTS=DT $ DT=DT*V(I)/(V(I)-V(I+1)) $ K=1 $ GO TO 50
   70 IF (ABS(V(I+1)).LT.1.0E-8) GO TO 80 $ SLOPE=(V(I+1)-VS)/(DT-DTS)
      DDT=-V(I+1)/SLOPE $ DTS=DT $ VS=V(I+1) $ DT=DT+DDT $ GO TO 50

C     ITERATE ON THE SHOCK WAVE ANGLE

   80 IF (ABS(T(I+1)-AC).LT.1.0E-6) GO TO 100 $ IF (L.GT.0) GO TO 90
      TS=T(I+1) $ ES=EPS $ EPS=EPS+(AC-TS) $ L=1 $ GO TO 40
   90 SLOPE=(T(I+1)-TS)/(EPS-ES) $ DE=(AC-T(I+1))/SLOPE $ ES=EPS
      TS=T(I+1) $ EPS=EPS+DE $ GO TO 40

C     SOLUTION HAS CONVERGED

  100 EP=EPS*RAD $ WRITE (6,1000) EP
      DO 110 I=1,NI $ Q(I)=SQRT(U(I)**2+V(I)**2) $ B=T(I)
      A(I)=ATAN((U(I)*SIN(B)+V(I)*COS(B))/(U(I)*COS(B)-V(I)*SIN(B)))
      P(I)=PR*PRR(Q(I)) $ R(I)=RR*RRR(Q(I)) $ TP=T(I)*RAD
      Q(I)=Q(I)/M1S $ AP=A(I)*RAD
  110 WRITE (6,1010) I,TP,Q(I),AP,P(I),R(I) $ RETURN

 1000 FORMAT (1H0,THE SHOCK WAVE ANGLE EPS = ,F7.4, DEGREES,/1H0,4X,
     1,I,8X,PSI,5X,V/V1,7X,THETA,6X,P/P1,7X,R/R1,,/1H )
 1010 FORMAT (I6,F12.3,F10.5,F11.3,2F11.4)
      END
```

```
      SUBROUTINE SHK (EPS,M1,M1S,G,Q,A,P,R)
C     SUBROUTINE SHK CALCULATES PROPERTY RATIOS FOR OBLIQUE SHOCK WAVE
      REAL MN,M1,M1S
      M1S=M1*SQRT((G+1.0)/(2.0+(G-1.0)*M1*M1))
      SINE=SIN(EPS) $ TANE=TAN(EPS) $ MN=(M1*SINE)**2
      TANB=TANE*2.0/(G+1.0)*(1.0/MN+(G-1.0)/2.0) $ BETA=ATAN(TANB)
      SINB=SIN(BETA) $ A=EPS-BETA
      Q=SINE/SINB*(2.0/(G+1.0)/MN+(G-1.0)/(G+1.0))*M1S
      P=2.0*G/(G+1.0)*(MN-(G-1.0)/2.0/G) $ R=TANE/TANB $ RETURN
      END
```

Figures 7.31, 7.33, and 7.34 present some results obtained with subroutine TM for $\gamma = 1.40$. In each of those figures, the abscissa is the free-stream Mach number M_1. Results for several values of the cone angle δ_c are presented in each figure. Figure 7.31 presents the conical shock wave angle ϵ, Fig. 7.33 presents the Mach number M_c on the surface of the cone, and Fig. 7.34 presents the cone surface to free-stream static pressure ratio p_c/p_1. Kopal[13] and Sims[14] present extensive tables for supersonic flow around cones.

Example 16.9. Calculate the flow properties of a Taylor–Maccoll flow of air at a Mach number $M_1 = 3.0$ over a cone having a semiangle $\delta_c = 30.0$ deg. Assume $\gamma = 1.40$, and employ 10 equal angular increments between the shock wave and the surface of the cone.

Solution

The solution procedure presented in Section 16–5(b) is employed. The numerical integration of equations 16.60 and 16.61 is performed by the fourth-order Runge–Kutta method discussed in Appendix A–6(d). For the present case, equations A.33 and A.34 may be written as

$$\bar{u}^*_{n+1} = \bar{u}^*_n + \frac{1}{6}(k_1 + 2k_2 + 2k_3 + k_4) \tag{a}$$

$$\bar{v}^*_{n+1} = \bar{v}^*_n + \frac{1}{6}(\ell_1 + 2\ell_2 + 2\ell_3 + \ell_4) \tag{b}$$

$$k_1 = \bar{v}^*_n \Delta\psi \tag{c}$$

$$k_2 = (\bar{v}^*_n + 0.5\ell_1)\Delta\psi \tag{d}$$

$$k_3 = (\bar{v}^*_n + 0.5\ell_2)\Delta\psi \tag{e}$$

$$k_4 = (\bar{v}^*_n + \ell_3)\Delta\psi \tag{f}$$

$$\ell_1 = f(\psi_n, \bar{u}^*_n, \bar{v}^*_n)\Delta\psi \tag{g}$$

$$\ell_2 = f(\psi_n + 0.5\Delta\psi, \bar{u}^*_n + 0.5k_1, \bar{v}^*_n + 0.5\ell_1)\Delta\psi \tag{h}$$

$$\ell_3 = f(\psi_n + 0.5\Delta\psi, \bar{u}^*_n + 0.5k_2, \bar{v}^*_n + 0.5\ell_2)\Delta\psi \tag{i}$$

$$\ell_4 = f(\psi_n + \Delta\psi, \bar{u}^*_n + k_3, \bar{v}^*_n + \ell_3)\Delta\psi \tag{j}$$

where the function $f(\psi, \bar{u}^*, \bar{v}^*)$ is defined by equation 16.61. The numerical solution follows the itemized procedure presented in Section 16–5(b).

1. *Determination of* $\epsilon^{(1)}$. For $M_1 = 3.0$

$$\alpha_1 = \sin^{-1}\left(\frac{1}{M_1}\right) = \sin^{-1}\left(\frac{1}{3.0}\right) = 19.4712 \text{ deg}$$

From equation 16.64, we obtain

$$\epsilon^{(1)} = 30.0 + 0.5(19.4712) = 39.7356 \text{ deg}$$

2. *Calculate the step size* $\Delta\psi$. From equation 16.65

$$\Delta\psi = -\frac{39.7356 - 30.000}{10} = -0.97360 \text{ deg} = -0.016993 \text{ rad}$$

3. *Determine the flow properties behind the shock wave.* From equation 3.189, we obtain

$$M_1^* = \left[\frac{2.4(3.0)^2}{2 + (0.4)(3.0)^2}\right]^{1/2} = 1.96396$$

For $\epsilon^{(1)} = 39.7356$ deg,

$$\sin\epsilon^{(1)} = \sin(39.7356) = 0.63925$$

$$\tan\epsilon^{(1)} = \tan(39.7356) = 0.83127$$

$$M_1^2 \sin^2\epsilon^{(1)} = (3.0)^2(0.63925)^2 = 3.67777$$

Solving equation 16.67 for β yields

$$\tan\beta = \frac{2(0.83127)}{2.4}\left(\frac{1}{3.67777} + \frac{0.4}{2}\right) = 0.32690$$

$$\beta = \tan^{-1}(0.32690) = 18.1026 \text{ deg}$$

$$\sin\beta = \sin(18.1026) = 0.31072$$

$$\cos\beta = \cos(18.1026) = 0.95050$$

From equation 16.69

$$\theta_s = \epsilon - \beta = 39.7356 - 18.1026 = 21.6330 \text{ deg}$$

Solving equation 16.68 for M_2^*, we obtain

$$M_2^* = \frac{(0.63925)(1.96396)}{(0.31072)}\left[\frac{2}{2.4(3.67777)} + \frac{0.4}{2.4}\right] = 1.58889$$

From equations 16.70 and 16.71

$$\bar{u}_s^* = (1.58889)(0.95050) = 1.51024$$

$$\bar{v}_s^* = -(1.58889)(0.31072) = -0.49371$$

4. *Integrate to the surface of the cone.* The application of equations (a) to (j) for the

first step is presented below. The complete results are tabulated in Table 16.17. For $\gamma = 1.40$, equation 16.62 becomes

$$\left(\frac{a}{a^*}\right)^2 = 1.2 - (0.2)(\bar{u}^{*2} + \bar{v}^{*2})$$

$$\left(\frac{a}{a^*}\right)_1^2 = 1.2 - (0.2)\left[(1.51024)^2 + (-0.49371)^2\right] = 0.69509$$

$$k_1 = (-0.49371)(-0.016993) = 0.008390$$

$$\ell_1 = \left\{-1.51024 + \frac{(0.69509)\left[1.51024 - 0.49371\cot(39.7356)\right]}{(-0.49371)^2 - (0.69509)}\right\}(-0.016993)$$

$$= 0.049644$$

$$\bar{u}_1^* + 0.5k_1 = 1.51024 + (0.5)(0.008390) = 1.51444$$

$$\bar{v}_1^* + 0.5\ell_1 = -0.49371 + (0.5)(0.049644) = -0.46889$$

$$\psi_1 + 0.5\Delta\psi = 39.7356 + (0.5)(-0.9736) = 39.2488 \text{ deg}$$

$$\left(\frac{a}{a^*}\right)_2^2 = 1.2 - (0.2)\left[(1.51444)^2 + (-0.46889)^2\right] = 0.69732$$

$$k_2 = (-0.46889)(-0.016993) = 0.007968$$

$$\ell_2 = \left\{-1.51444 + \frac{(0.69732)\left[1.51444 - 0.46889\cot(39.2488)\right]}{(-0.46889)^2 - (0.69732)}\right\}(-0.016993)$$

$$= 0.049077$$

$$\bar{u}_1^* + 0.5k_2 = 1.51024 + (0.5)(0.007968) = 1.51422$$

$$\bar{v}_1^* + 0.5\ell_2 = -0.49371 + (0.5)(0.049077) = -0.46917$$

$$\left(\frac{a}{a^*}\right)_3^2 = 1.2 - (0.2)\left[(1.51422)^2 + (-0.46917)^2\right] = 0.69740$$

$$k_3 = (-0.46917)(-0.016993) = 0.007973$$

$$\ell_3 = \left\{-1.51422 + \frac{(0.69740)\left[1.51422 - 0.46917\cot(39.2488)\right]}{(-0.46917)^2 - (0.69740)}\right\}(-0.016993)$$

$$= 0.049071$$

$$\bar{u}_1^* + k_3 = 1.51024 + 0.007973 = 1.51821$$

$$\bar{v}_1^* + \ell_3 = -0.49371 + 0.049071 = -0.44464$$

$$\psi + \Delta\psi = 39.7356 - 0.9736 = 38.7620$$

$$\left(\frac{a}{a^*}\right)_4^2 = 1.2 - (0.2)\left[(1.51821)^2 + (-0.44464)^2\right] = 0.69947$$

$$k_4 = (-0.44464)(-0.016993) = 0.007556$$

$$\ell_4 = \left\{-1.51821 + \frac{(0.69947)\left[1.51821 - 0.44464\cot(38.7620)\right]}{(-0.44464)^2 - (0.69947)}\right\}(-0.016993)$$

$$= 0.048645$$

$$\bar{u}_2^* = 1.51024 + \frac{1}{6}\left[0.008390 + 2(0.007968) + 2(0.007973) + 0.007556\right]$$

$$= 1.51821$$

$$\bar{v}_2^* = -0.49371 + \frac{1}{6}\left[0.049644 + 2(0.049077) + 2(0.049071) + 0.048645\right]$$

$$= -0.44461 \qquad \text{(k)}$$

Table 16.17 Results of the Numerical Integration for the First Trial Value of $\epsilon^{(1)} = 39.7356$ deg

Point	ψ, deg	$\bar{u}^*$	$\bar{v}^*$
1	39.7356	1.51024	−0.49371
2	38.7620	1.51821	−0.44461
3	37.7885	1.52540	−0.39627
4	36.8149	1.53173	−0.34829
5	35.8414	1.53724	−0.30038
6	34.8678	1.54194	−0.25232
7	33.8942	1.54581	−0.20388
8	32.9207	1.54886	−0.15489
9	31.9471	1.55107	−0.10513
10	30.9736	1.55243	−0.05438
11	30.0000	1.55291	−0.00239
12	29.0264	1.55250	0.05114
13	29.9565	1.55292	−0.0000356
14	29.9558	1.55292	−0.00000053

This completes the integration for the first step. The process is repeated successively until the value of $\bar{v}^*$ changes from negative to positive. When that occurs, an iterative procedure is employed to repeat the last step for different values of $\Delta\psi$ until the value of ψ for which $\bar{v}^* = 0$ is determined. Points 1 to 12 in Table 16.17 present the results obtained by the above procedure.

At point 11, $\psi = \psi_c = 30.000$ deg. However, at that point, $\bar{v}^* = -0.00239$, which indicates that the assumed value of $\epsilon^{(1)} = 39.7356$ deg is too small. At point 12, $\psi = 29.0264 < \psi_c$ and $\bar{v}^* = 0.05114$. Consequently, the value of ψ for which $\bar{v}^* = 0.0$ is less than 30.0 deg, and an iteration is required to determine the value of $\Delta\psi$ for the final step that yields $\bar{v}^* = 0$. During this iteration, let $\Delta\psi^{(1)} = -0.9736$ and $\bar{v}^{*(1)} = 0.05114$ denote the initial results of the iteration for the final value of $\Delta\psi$. For the second trial, linear interpolation between points 11 and 12 yields $\Delta\psi^{(2)} = -0.0435$ deg. Point 12 is now discarded, and a step is taken from point 11 with $\Delta\psi^{(2)} = -0.0435$. The results at point 13 are obtained, where $\psi^{(2)} = 29.9565$ deg and $\bar{v}^{*(2)} = -0.0000356$. One more iteration for the final value of $\Delta\psi$ is made by applying the secant method [see Appendix A–4(b)] to the two sets of $\Delta\psi, \bar{v}^*$ values. Thus,

$$\frac{\bar{v}^{*(3)} - \bar{v}^{*(2)}}{\Delta\psi^{(3)} - \Delta\psi^{(2)}} = \frac{\bar{v}^{*(2)} - \bar{v}^{*(1)}}{\Delta\psi^{(2)} - \Delta\psi^{(1)}}$$

$$\frac{\bar{v}^{*(3)} - (-0.0000356)}{\Delta\psi^{(3)} - (-0.0435)} = \frac{(-0.0000356) - (0.05114)}{(-0.0435) - (-0.9736)} = -0.05502$$

$$\Delta\psi^{(3)} = -0.0435 + \frac{\bar{v}^{*(3)} + 0.0000356}{-0.05502} \tag{l}$$

Solving equation (l) for $\bar{v}^{*(3)} = 0.0$, we obtain $\Delta\psi^{(3)} = -0.04415$ deg. Repeating the last step with $\Delta\psi^{(3)} = -0.04415$ yields $\psi^{(3)} = 29.9558$ deg and $\bar{v}^{*(3)} = -0.00000053$, which is close enough to zero. Those results are presented as point 14 in Table 16.17.

The cone angle $\delta_c^{(1)}$ corresponding to the assumed value of $\epsilon^{(1)} = 39.7356$ deg is thus $\delta_c^{(1)} = 29.9558$ deg.

5. *Determine subsequent trial values for* $\epsilon^{(i)}$. The value of $\delta_c^{(1)} = 29.9558$ deg determined in step 4 is not close enough to $\delta_c = 30.0$ deg, so a second trial value for $\epsilon^{(2)}$ is determined. From equation 16.72

$$\epsilon^{(2)} = 39.7356 + (30.0 - 29.9558) = 39.7798 \text{ deg}$$

Repeating steps 2 to 4 for $\epsilon^{(2)} = 39.7798$ deg, we obtain $\delta_c^{(2)} = 29.9960$ deg.

A third trial value for $\epsilon^{(3)}$ is obtained by applying the secant method [see Appendix A–4(b)] to the two sets of ϵ, δ_c values. Thus,

$$\frac{\delta_c^{(3)} - \delta_c^{(2)}}{\epsilon^{(3)} - \epsilon^{(2)}} = \frac{\delta_c^{(2)} - \delta_c^{(1)}}{\epsilon^{(2)} - \epsilon^{(1)}}$$

$$\frac{\delta_c^{(3)} - 29.9960}{\epsilon^{(3)} - 39.7798} = \frac{29.9960 - 29.9558}{39.7798 - 39.7356} = 0.90950$$

$$\epsilon^{(3)} = 39.7798 + \frac{\delta_c^{(3)} - 29.9960}{0.90950} \tag{m}$$

Solving equation (m) for $\delta_c^{(3)} = 30.0$ deg, we obtain $\epsilon^{(3)} = 39.7841$ deg. Repeating steps 2 to 4 for $\epsilon^{(3)} = 39.7841$ deg, we obtain $\delta_c^{(3)} = 30.0000$ deg, which is the desired value of δ_c. The results of the numerical integration for $\epsilon^{(3)}$ are presented in Table 16.18.

Table 16.18 Results of the Numerical Integration for the Final Value of $\epsilon^{(3)} = 39.7841$ deg

Point	ψ, deg	$\bar{u}^*$	$\bar{v}^*$
1	39.7841	1.50923	−0.49364
2	38.8057	1.51723	−0.44433
3	37.8273	1.52441	−0.39578
4	36.8489	1.53075	−0.34759
5	35.8705	1.53628	−0.29947
6	34.8921	1.54098	−0.25118
7	33.9137	1.54485	−0.20252
8	32.9352	1.54789	−0.15329
9	31.9568	1.55009	−0.10328
10	30.9784	1.55141	−0.05227
11	30.0000	1.55186	−0.000000072

6. *Determine the flow properties.* When the iteration for δ_c has converged, the values of $\bar{u}^*(\psi)$ and $\bar{v}^*(\psi)$ may be transformed into the two-dimensional velocity components $u^*(\psi)$ and $v^*(\psi)$, and the flow properties $V(\psi)$, $\theta(\psi)$, $p(\psi)$, and $\rho(\psi)$ may be determined. For example, the final values for ψ, $\bar{u}^*$, and $\bar{v}^*$ on the surface of the cone for the third trial value of $\psi^{(3)}$ are

$$\psi_c = 30.0000 \text{ deg} \qquad \bar{u}_c^* = 1.55186 \qquad \bar{v}_c^* = 0.00000$$

From equations 16.73 to 16.76, we obtain

$$M_c^* = \left[(1.55186)^2 + (0.00000)^2\right]^{1/2} = 1.55186$$

$$u_c^* = 1.55186\cos(30.0) - (0)\sin(30.0) = 1.34395$$

$$v_c^* = 1.55186\sin(30.0) + (0)\cos(30.0) = 0.77593$$

$$\theta_c = \tan^{-1}\left(\frac{0.77593}{1.34395}\right) = 30.0000 \text{ deg}$$

The value of M_2^* immediately behind the shock wave is found in the same manner to be $M_2^* = 1.58791$. Substituting the value $\epsilon^{(3)} = 39.7841$ deg into equations 16.66 and 16.67, we obtain

$$M_1^2 \sin^2\epsilon^{(3)} = (3.0)^2 \sin^2(39.7841) = 3.68521$$

$$\frac{p_2}{p_1} = \frac{2.8}{2.4}\left(3.68521 - \frac{0.4}{2.8}\right) = 4.13274$$

$$\frac{\rho_1}{\rho_2} = \frac{2}{2.4}\left(\frac{1}{3.68521} + \frac{0.4}{2}\right) = 0.39280$$

From equations 16.76 and 16.77, for $M_2^* = 1.58791$

$$\frac{p_2}{P_2} = \left[1 - \frac{0.4}{2.4}(1.58791)^2\right]^{1.4/0.4} = 0.14838$$

$$\frac{\rho_2}{\rho_{02}} = \left[1 - \frac{0.4}{2.4}(1.58791)^2\right]^{1/0.4} = 0.25593$$

From equations 16.76 and 16.77, for $M_c^* = 1.55186$

$$\frac{p_c}{P_c} = \left[1 - \frac{0.4}{2.4}(1.55186)^2\right]^{1.4/0.4} = 0.16597$$

$$\frac{\rho_c}{\rho_{oc}} = \left[1 - \frac{0.4}{2.4}(1.55186)^2\right]^{1/0.4} = 0.27726$$

Substituting the above results into equations 16.78 and 16.79, we obtain

$$\frac{p_c}{p_1} = \frac{(0.16597)(4.13274)}{(0.14839)} = 4.6228$$

$$\frac{\rho_c}{\rho_1} = \frac{(0.27726)}{(0.25593)(0.39280)} = 2.7580$$

Table 16.19 presents the flow properties for the Taylor–Maccoll flow of a gas with $\gamma = 1.40$ flowing at a Mach number $M_1 = 3.0$ over a cone having a semiangle $\delta_c = 30.0$ deg.

Table 16.19 Flow Properties for Taylor–Maccoll Flow for $\gamma = 1.40$, $M_1 = 3.0$, and $\delta_c = 30.0$ deg

Point	ψ, deg	$\frac{V_2}{V_1}$	θ, deg	$\frac{p}{p_1}$	$\frac{\rho}{\rho_1}$
1	39.784	0.80852	21.672	4.1327	2.5459
2	38.806	0.80498	22.483	4.2250	2.5863
3	37.827	0.80192	23.273	4.3057	2.6215
4	36.849	0.79926	24.056	4.3765	2.6522
5	35.870	0.79696	24.840	4.4383	2.6789
6	34.892	0.79498	25.634	4.4915	2.7018
7	33.914	0.79333	26.445	4.5364	2.7211
8	32.935	0.79200	27.280	4.5725	2.7366
9	31.957	0.79101	28.145	4.5996	2.7481
10	30.978	0.79039	29.049	4.6167	2.7554
11	30.000	0.79017	30.000	4.6228	2.7580

REFERENCES

1. R. Sauer, "General Characteristics of the Flow through Nozzles at Near Critical Speeds," NACA TM No. 1147, 1947.
2. D. Migdal and F. Landis, "Characteristics of Conical Supersonic Nozzles," *Journal of the American Rocket Society*, Vol. 32, No. 12, December 1962, pp. 1898–1901.
3. H. M. Darwell and H. Badham, "Shock Formation in Conical Nozzles," *Journal of the American Institute of Aeronautics and Astronautics*, Vol. 1, No. 8, August 1963, pp. 1932–1934.
4. D. Migdal and R. Kosson, "Shock Predictions in Conical Nozzles," *Journal of the American Institute of Aeronautics and Astronautics*, Vol. 3, No. 8, August 1965, pp. 1554–1555.
5. P. K. Sasman and R. J. Cresci, "Compressible Turbulent Boundary Layer with Pressure Gradient and Heat Transfer," *Journal of the American Institute of Aeronautics and Astronautics*, Vol. 4, No. 1, January 1966, pp. 19–25.

6. J. H. Ahlberg, S. Hamilton, D. Migdal, and E. N. Nilson, "Truncated Perfect Nozzles in Optimum Nozzle Design," *Journal of the American Rocket Society*, Vol. 31, No. 5, May 1961, pp. 614–620.
7. G. V. R. Rao, "Exhaust Nozzle Contour for Optimum Thrust," *Jet Propulsion*, Vol. 28, No. 6, June 1958, pp. 377–382.
8. A. Miele, *Theory of Optimum Aerodynamic Shapes*, Edited by A. Miele, Academic Press, New York, 1958, Chaps. 1–4.
9. L. E. Elsgolc, *Calculus of Variations*, Pergamon Press, London, 1962.
10. G. I. Taylor and J. W. Maccoll, "The Air Pressure on a Cone Moving at High Speeds," Proceedings of the Royal Society of London, Series A, Vol. 139, pp. 279–311, 1933.
11. J. W. Maccoll, "The Conical Shock Wave Formed by a Cone Moving at High Speed," Proceedings of the Royal Society of London, Series A, Vol. 159, pp. 459–472, 1937.
12. *Standard Mathematical Tables*, Twenty-Third Edition, Edited by S. M. Selby, CRC Press, Cleveland, Ohio, p. 567, 1975.
13. Z. Kopal, "Tables of Supersonic Flow around Cones," Report No. 1, Massachusetts Institute of Technology, Department of Electrical Engineering, Center of Analysis, 1947.
14. J. Sims, "Tables for Supersonic Flow around Right Circular Cones at Zero Angle of Attack," NASA SP-3004, 1964.

17
the method of characteristics applied to steady two-dimensional isentropic supersonic flow

17–1 PRINCIPAL NOTATION FOR CHAPTER 17

The notation presented in Section 16–1 and the additional notation listed below are employed in this chapter.

A,Q,R	coefficients in the finite difference equations.
S,T	
C_o	denotes characteristic curve C_o (i. e., the streamline).
ε	oblique shock wave angle.
λ_o	$=\tan(v/u)$, slope of C_o characteristics (i. e., the streamline).

17–2 INTRODUCTION

It is shown in Sections 10–7(a) and 10–7(b) that rotation (or vorticity) in the steady adiabatic inviscid flow of a compressible fluid is caused by the presence of gradients in the entropy and the stagnation enthalpy of the fluid *normal* to the streamlines. Entropy gradients *normal* to the streamlines are produced in supersonic external flows by shock waves. Stagnation enthalpy gradients and entropy gradients *normal* to the streamlines exist in the supersonic flow in a propulsive nozzle because of nonuniform combustion in the gas generator supplying hot gas to the nozzle. Dissipative flows such as nonequilibrium chemically reacting flow and gas flow with suspended condensed particles generate an increase in entropy *along* the streamlines.

In this chapter, the method of characteristics, which is applied to steady two-dimensional irrotational flow (i. e., entropy and stagnation enthalpy constant throughout the entire flow field) in Chapters 12 and 16, is applied to steady two-dimensional isentropic flow (i. e., entropy and stagnation enthalpy constant only along streamlines). Complete numerical algorithms are developed for the unit processes for the following types of points.

1. An interior point.
2. A direct wall point.
3. An indirect wall point.
4. An axis of symmetry point.
5. A free pressure boundary point.
6. An external shock wave point.

Numerical examples illustrating the above unit processes are presented, and FORTRAN computer programs for implementing the unit processes are given.

The following applications of steady two-dimensional isentropic supersonic flow are presented.

1. Analysis of the flow field in a nozzle of known shape.
2. Design of nozzles for parallel exit flow.

3. Design of propulsive nozzles for maximum thrust.
4. Analysis of the external flow field over a pointed body of known shape.

The absolute accuracy and the order of accuracy are of great concern in the numerical integration of differential equations. A brief discussion of accuracy criteria and the results of some accuracy studies for the numerical method of characteristics are presented in Section 17–6.

17–3 MATHEMATICAL ANALYSIS OF STEADY TWO-DIMENSIONAL ISENTROPIC FLOW

The method of characteristics is developed in this section for the steady two-dimensional supersonic flow of an inviscid compressible fluid in the absence of heat transfer, work, and body forces. Such flows are isentropic (i. e., the entropy is constant along streamlines), although there may be gradients in the entropy and stagnation properties normal to the streamlines, so that the flow is not *irrotational* but *rotational*. Rotational isentropic flow occurs, for example, in the supersonic flow downstream from a curved shock wave such as that formed in the front of a body moving at supersonic speed.

17–3(a) Governing Equations

Table 10.1 presents the governing equations for the steady adiabatic flow of an inviscid compressible fluid. They are the continuity equation, the Euler momentum equation, and the energy equation. As discussed in Section 10–9(b), for an *isentropic flow* the speed of sound equation may be employed in place of the energy equation. Hence, the following set of governing equations is obtained.

1. *Continuity equation*

$$\nabla \cdot (\rho \mathbf{V}) = 0 \tag{17.1}$$

2. *Momentum equation*

$$\rho \frac{D\mathbf{V}}{Dt} + \nabla p = 0 \tag{17.2}$$

3. *Speed of sound equation*

$$\frac{Dp}{Dt} - a^2 \frac{D\rho}{Dt} = 0 \tag{17.3}$$

For a two-dimensional flow, equations 17.1 to 17.3, when expressed in Cartesian coordinates, transform into the following set of equations [see Section 10–3(c)].

$$\rho u_x + \rho v_y + u\rho_x + v\rho_y + \delta \rho v / y = 0 \tag{17.4}$$

$$\rho u u_x + \rho v u_y + p_x = 0 \tag{17.5}$$

$$\rho u v_x + \rho v v_y + p_y = 0 \tag{17.6}$$

$$u p_x + v p_y - a^2 u \rho_x - a^2 v \rho_y = 0 \tag{17.7}$$

where $\delta = 0$ for planar flow, and $\delta = 1$ for axisymmetric flow. For a simple

thermodynamic system, the speed of sound a is a function of the pressure p and the density ρ. Thus,

$$a = a(p, \rho) \tag{17.8}$$

Equations 17.4 to 17.7 comprise a set of four equations involving the four variables u, v, p, and ρ. The above set of four equations may be reduced to three equations if the density derivatives $(u\rho_x + v\rho_y)$ are eliminated by substituting equation 17.7 into equation 17.4. The remaining three equations involving u, v, and p may then be solved in conjunction with equation 10.111, which is valid for an *isentropic flow*, and is repeated and renumbered here for convenience.

$$\rho = \rho(p) \quad (\textit{along a streamline}) \tag{17.9}$$

The foregoing simplification is not utilized here because it does not reduce appreciably the required computational effort for solving the equations. What is more important, however, is the fact that the aforementioned system of equations is quite similar to the set of equations governing nonequilibrium chemically reacting flows and gas-particle flows; those flows are considered in Chapter 18. Consequently, solving the aforementioned system of equations yields considerable insight into the numerical methods required for solving dissipative (i. e., nonisentropic) rotational flows.

17–3(b) Characteristic Equations

The characteristic and compatibility equations are derived by multiplying equations 17.4 to 17.7 by the unknown parameters σ_1 to σ_4 and summing (see Appendix B, Vol. 1). The procedure is indicated by the following equation.

$$\sigma_1(17.4) + \sigma_2(17.5) + \sigma_3(17.6) + \sigma_4(17.7) = 0 \tag{17.10}$$

From the summation indicated in equation 17.10, the coefficients of the x derivatives of u, v, p, and ρ are factored out. The result is

$$(\rho\sigma_1 + \rho u\sigma_2)\left[u_x + \frac{\rho v\sigma_2}{\rho\sigma_1 + \rho u\sigma_2}u_y\right] + (\rho u\sigma_3)\left[v_x + \frac{\rho\sigma_1 + \rho v\sigma_3}{\rho u\sigma_3}v_y\right]$$

$$+ (\sigma_2 + u\sigma_4)\left[p_x + \frac{\sigma_3 + v\sigma_4}{\sigma_2 + u\sigma_4}p_y\right]$$

$$+ (u\sigma_1 - a^2 u\sigma_4)\left[\rho_x + \frac{v\sigma_1 - a^2 v\sigma_4}{u\sigma_1 - a^2 u\sigma_4}\rho_y\right] + \sigma_1 \delta\rho v/y = 0 \tag{17.11}$$

The slopes of the characteristic curves, $dy/dx = \lambda$, are the coefficients of the y derivatives of u, v, p, and ρ. Thus,

$$\lambda = \frac{v\sigma_2}{\sigma_1 + u\sigma_2} = \frac{\sigma_1 + v\sigma_3}{u\sigma_3} = \frac{\sigma_3 + v\sigma_4}{\sigma_2 + u\sigma_4} = \frac{v\sigma_1 - a^2 v\sigma_4}{u\sigma_1 - a^2 u\sigma_4} \tag{17.12}$$

If u, v, p, and ρ are assumed to be continuous [see Section 12–3(b)], then $du/dx = u_x + \lambda u_y$, and so on, and equation 17.11 transforms to

$$\rho(\sigma_1 + u\sigma_2)\,du + \rho u\sigma_3\,dv + (\sigma_2 + u\sigma_4)\,dp + u(\sigma_1 - a^2\sigma_4)\,d\rho + \sigma_1(\delta\rho v/y)\,dx = 0 \tag{17.13}$$

Equation 17.13 is the *compatibility equation*, which is valid along the characteristic curves specified by equations 17.12. It remains to determine λ, and to eliminate σ_1 through σ_4 from equation 17.13.

Equations 17.12, when solved for σ_1 to σ_4, yield

$$\sigma_1(\lambda)+\sigma_2(u\lambda-v)+\sigma_3(0)+\sigma_4(0)=0 \tag{17.14}$$

$$\sigma_1(-1)+\sigma_2(0)+\sigma_3(u\lambda-v)+\sigma_4(0)=0 \tag{17.15}$$

$$\sigma_1(0)+\sigma_2(\lambda)+\sigma_3(-1)+\sigma_4(u\lambda-v)=0 \tag{17.16}$$

$$\sigma_1(u\lambda-v)+\sigma_2(0)+\sigma_3(0)+\sigma_4\left[-a^2(u\lambda-v)\right]=0 \tag{17.17}$$

For equations 17.14 to 17.17 to have a solution for the σ's other than zero, the determinant of the coefficient matrix for those four equations must vanish. By definition, let $S=(u\lambda-v)$. Then the following determinant must be zero.

$$\begin{vmatrix} \lambda & S & 0 & 0 \\ -1 & 0 & S & 0 \\ 0 & \lambda & -1 & S \\ S & 0 & 0 & -a^2S \end{vmatrix}=0 \tag{17.18}$$

Expanding the determinant yields

$$S^2\left[S^2-a^2(1+\lambda^2)\right]=0 \tag{17.19}$$

Equation 17.19 is a fourth-order algebraic equation in terms of λ; hence four roots and four characteristic curves should be found. The fourth-order equation is expressed as the product of two second-order factors. Setting either of those two factors equal to zero will yield two of the four roots; the other two roots are then found by setting the remaining factor equal to zero.

Setting the first quadratic factor, S^2, from equation 17.19 equal to zero, we obtain

$$\left(\frac{dy}{dx}\right)_o=\lambda_o=\frac{v}{u} \quad (\textit{appearing two times}) \tag{17.20}$$

Equation 17.20 is a repeated root, and is the differential equation for the streamline; the subscript o denotes the streamline. Hence, *in rotational flow, the streamline is a repeated characteristic.*

The remaining two roots are obtained from the second quadratic factor in equation 17.19. Substituting for $S=(u\lambda-v)$ into equation 17.19, we obtain

$$(u^2-a^2)\lambda^2-2uv\lambda+(v^2-a^2)=0 \tag{17.21}$$

Equation 17.21 is identical to equation 12.39 derived in Section 12–4(b) for a steady two-dimensional irrotational flow. It is the equation for the Mach lines and, of course, applies only to a supersonic flow. It follows, therefore, from Section 12–4(b), that the remaining two characteristics for a rotational flow are the Mach lines defined by equation 12.45, which is repeated and renumbered below.

$$\left(\frac{dy}{dx}\right)_{\pm}=\lambda_{\pm}=\tan(\theta\pm\alpha) \tag{17.22}$$

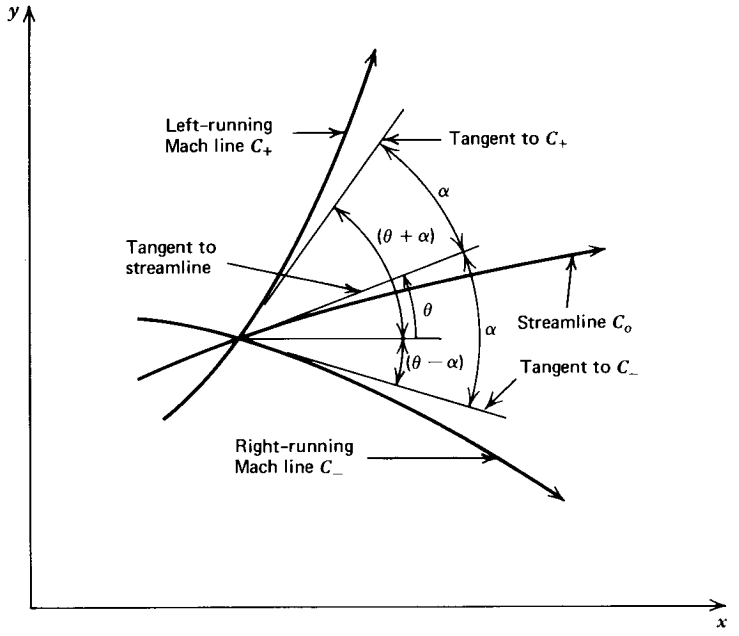

Figure 17.1 Characteristics for steady two-dimensional supersonic rotational flow.

Accordingly, in a rotational flow three distinct characteristics pass through each point of the flow field; the *streamline* and the two *Mach lines*. They are illustrated in Fig. 17.1.

17-3(c) Compatibility Equations

To eliminate the σ's from the compatibility equation (equation 17.13), equations 17.14 to 17.17 are solved for σ_1 to σ_4 in terms of λ. Along the streamlines, $\lambda = v/u$, and $S = (u\lambda - v) = 0$. Consequently, along the streamlines, equations 17.14 to 17.17 reduce to

$$\sigma_1\lambda = 0 \qquad \sigma_1 = 0 \qquad \sigma_2\lambda - \sigma_3 = 0 \qquad 0 = 0 \tag{17.23}$$

From equation 17.23, $\sigma_1 = 0$, $\sigma_3 = \lambda\sigma_2$, but σ_2 and σ_4 are completely unspecified; that is, they are arbitrary. Substituting those values for the σ's into equation 17.13, we obtain

$$\sigma_2[\rho u\,du + \rho v\,dv + dp] + \sigma_4[u\,dp - a^2 u\,d\rho] = 0 \tag{17.24}$$

Since σ_2 and σ_4 are both arbitrary, their coefficients must be identically zero. Thus, along streamlines

$$\rho u\,du + \rho v\,dv + dp = 0 \tag{17.25}$$

and

$$dp - a^2 d\rho = 0 \tag{17.26}$$

On the Mach lines, the quadratic factor in equation 17.19 is zero. Thus,

$$S^2 - a^2(1 + \lambda^2) = 0 \tag{17.27}$$

Along the Mach lines, therefore, equations 17.14 to 17.17 become

$$\sigma_2 = -\lambda\sigma_3$$

$$\sigma_1 = S\sigma_3$$

$$\sigma_4 = \sigma_3\left[(1+\lambda^2)/S\right] \tag{17.28}$$

$$\sigma_4 = \sigma_3(S/a^2) \tag{17.29}$$

Solving for S/a^2 from equation 17.27 and substituting the result into equation 17.29 yields equation 17.28, which shows that only one or the other of equations 17.28 and 17.29 is independent along the Mach lines. Hence, along the Mach lines

$$\sigma_2 = -\lambda\sigma_3 \qquad \sigma_1 = S\sigma_3 \qquad \sigma_4 = (S/a^2)\sigma_3 \tag{17.30}$$

where σ_3 is arbitrary. Substituting equation 17.30 into equation 17.13 and dividing by σ_3 yields the compatibility equation valid along the Mach lines. Thus,

$$(\rho v)\,du_{\pm} - (\rho u)\,dv_{\pm} + \left[\lambda_{\pm} - u(u\lambda_{\pm} - v)/a^2\right]dp_{\pm} - \delta\left[\rho v(u\lambda_{\pm} - v)/y\right]dx_{\pm} = 0 \tag{17.31}$$

where the subscript $\pm$ indicates the C_+ and C_-, or left- and right-running Mach lines, respectively.

An alternate form of equation 17.31 may be obtained in terms of V, θ, and M, by substituting equations 12.41 and 12.42 into equation 17.31. The result is

$$\frac{\sqrt{M^2-1}}{\rho V^2}\,dp_{\pm} \pm d\theta_{\pm} + \delta\left[\frac{\sin\theta\,dx_{\pm}}{yM\cos(\theta \pm \alpha)}\right] = 0 \tag{17.32}$$

where the upper subscripts on dp, $d\theta$, and dx correspond to the upper signs in $\pm\,d\theta$ and $\cos(\theta \pm \alpha)$, and vice versa. In terms of the velocity V, equation 17.25 becomes

$$\rho V\,dV + dp = 0 \tag{17.33}$$

which is *Bernoulli's equation*.

Table 17.1 Characteristic and Compatibility Equations for Steady Two-Dimensional Isentropic Rotational Supersonic Flow

Characteristic equations		
$\left(\frac{dy}{dx}\right)_o = \lambda_o = \frac{v}{u}$	(*streamline*)	(17.20)
$\left(\frac{dy}{dx}\right)_{\pm} = \lambda_{\pm} = \tan(\theta \pm \alpha)$	(*Mach lines*)	(17.22)
Compatibility equations		
$\rho V\,dV + dp = 0$	(*along streamlines*)	(17.33)
$dp - a^2\,d\rho = 0$	(*along streamlines*)	(17.26)
$\frac{\sqrt{M^2-1}}{\rho V^2}\,dp_{\pm} \pm d\theta_{\pm} + \delta\left[\frac{\sin\theta\,dx_{\pm}}{yM\cos(\theta \pm \alpha)}\right] = 0$	(*along Mach lines*)	(17.32)

From the foregoing it is seen that three distinct characteristics are obtained; the streamline and the two Mach lines. There are two compatibility equations valid on the streamline, and one compatibility equation valid on each Mach line. Consequently, there is a total of four compatibility equations. The derived system of characteristic and compatibility equations is sufficient for replacing the original system of four partial differential equations (equations 17.4 to 17.7). For convenience of reference, Table 17.1, on the preceding page, presents the characteristic and compatibility equations for steady two-dimensional isentropic rotational supersonic flow.

17–4 UNIT PROCESSES

The mathematical results obtained in Section 17–3 are employed in this section to develop numerical algorithms for the unit processes for steady two-dimensional isentropic rotational flow.

17–4(a) Finite Difference Equations

The numerical algorithm for solving a rotational flow problem is similar to that for solving an irrotational flow problem. Because there are three distinct characteristics instead of two, however, there is an extra degree of freedom in constructing the characteristic network for a rotational flow. A point must, therefore, be chosen where all three characteristics coincide, so that all four compatibility equations may be solved simultaneously for V, θ, p, and ρ. Because the intersection of any two of the three characteristics defines a unique point, the third characteristic must be passed through that point and extended backward to intersect the initial-value line. Since there are three characteristics, there are three choices for locating the solution point if the direct marching method, discussed in Section 12–5(b), is employed. In that method, a new point is determined by extending the characteristics from previous solution points in the flow direction, as shown in Fig. 12.10.

Figure 17.2 illustrates schematically the three available choices for determining the location of a solution point. Figure 17.2*a* illustrates the case where the solution point is at the intersection of the two Mach lines C_+ and C_-. Figure 17.2*b* applies when the solution point is at the intersection of the right-running Mach line C_- and the streamline C_o, and in Fig. 17.2*c* the solution point is at the intersection of the left-running Mach line C_+ and the streamline C_o. In each of the three cases illustrated, the third characteristic is extended backward from the solution point to intersect one of the previous characteristics, and the flow properties at the point of intersection are determined by interpolation.

Figure 17.3 illustrates diagrammatically the application of the inverse marching method. A solution point is chosen on a predetermined solution line, and all three characteristics are then extended backward to intersect the previous solution line. The flow properties at the points of intersection are determined by interpolation. The comments concerning the stability of the inverse method presented in Section 12–5(b) are also applicable here.

In the present analysis, the finite difference network is constructed for the direct marching method based on the Mach lines, illustrated schematically in Fig. 17.2*a*, and it is analogous to the finite difference network developed in Section 12–5 for irrotational flow (see Fig. 12.9). Consequently, the overall solution logic is similar to that developed in Section 16–4 for application to different flow fields.

Table 17.2 presents the finite difference equations corresponding to the characteristic and compatibility equations presented in Table 17.1, where the subscript

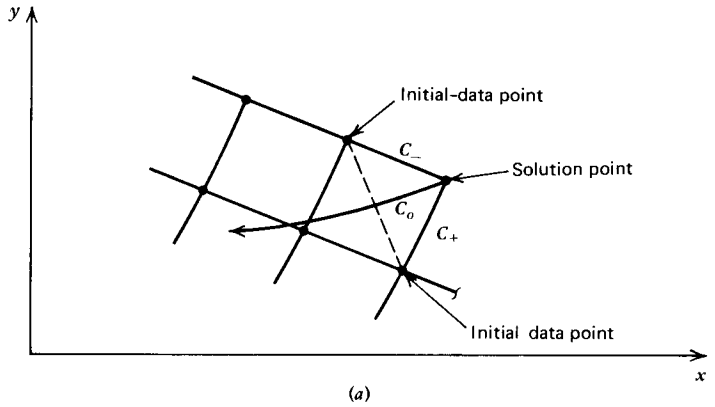

(*a*)

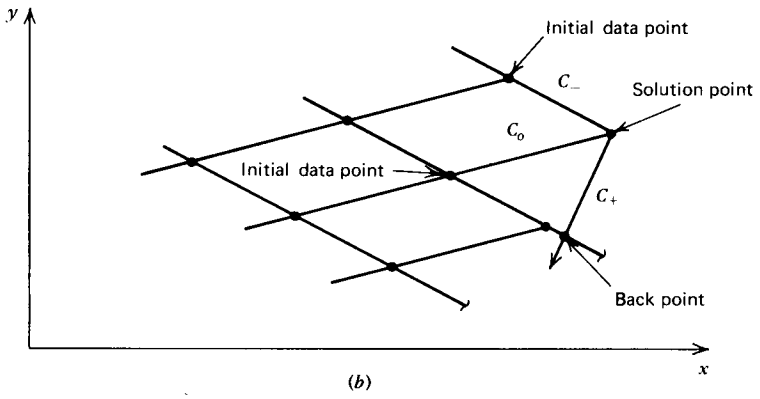

(*b*)

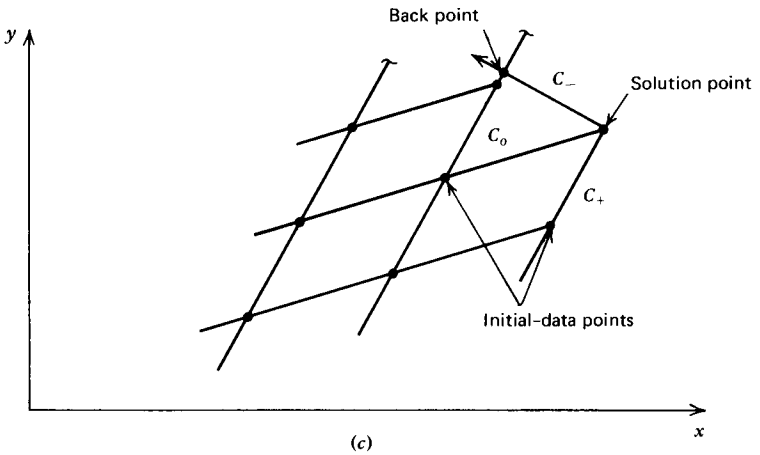

(*c*)

Figure 17.2 Direct marching methods for rotational flow. (*a*) Based on Mach lines. (*b*) Based on right-running Mach lines and streamline. (*c*) Based on left-running Mach lines and streamline.

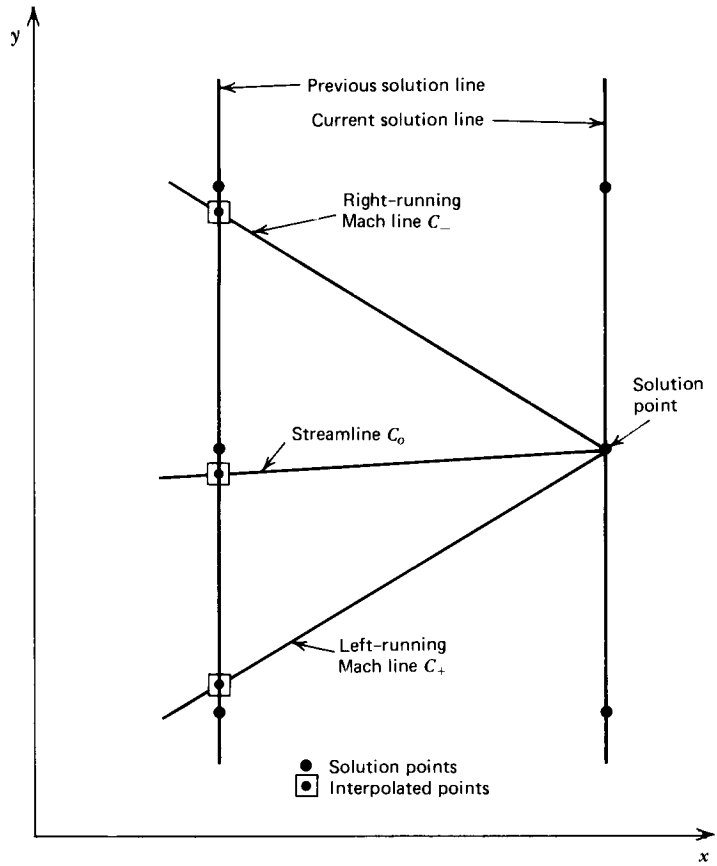

Figure 17.3 Inverse marching method for rotational flow.

Table 17.2 Finite Difference Equations for Steady Two-Dimensional Isentropic Rotational Supersonic Flow

$\Delta y_o = \lambda_o \Delta x_o$	(17.34)
$R_o \Delta V_o + \Delta p_o = 0$	(17.35)
$\Delta p_o - A_o \Delta \rho_o = 0$	(17.36)
$\Delta y_\pm = \lambda_\pm \Delta x_\pm$	(17.37)
$Q_\pm \Delta p_\pm \pm \Delta \theta_\pm + S_\pm \Delta x_\pm = 0$	(17.38)
$A = a^2$, N-m/kg (ft-lbf/lbm)	(17.39)
$Q = \dfrac{\sqrt{M^2-1}}{\rho V^2}$, m^2/N (ft^2/lbf)	(17.40)
$R = \rho V$, N-s/m^3 (lbf-sec/ft^3)	(17.41)
$S = \dfrac{\delta \sin\theta}{yM\cos(\theta \pm \alpha)}$, m^{-1} ($in.^{-1}$)	(17.42)
+, −, o denotes C_+, C_-, or C_o characteristic curve	

o denotes a streamline and the subscripts $\pm$ denote left- and right-running Mach lines, respectively.

The numerical algorithms for applying equations 17.34 to 17.38 are based on the modified Euler predictor-corrector method, discussed in Section 12–5(a). For the predictor step, all of the coefficients in the finite difference equations are calculated at the known initial points. For the corrector step, average values of the four primary dependent variables V, θ, p, and ρ are calculated along each of the three characteristics, and the coefficients of the finite difference equations are calculated by employing those average properties. The numerical integration algorithm is, therefore, termed an *average property method.*

Numerical algorithms, or unit processes, are developed in the following sections for determining the six types of points listed in Section 17–2.

17–4(b) Interior Point

Figure 17.4 illustrates two possible difference networks for determining an interior point. They depend on how the rearward running streamline is treated. The numerical method developed here is based on the network illustrated in Fig. 17.4*a*. Points 1 and 2 are initial-data points on the C_- and C_+ Mach lines and line 12 connects those points. The rearward running streamline C_o intersects line 12 at point 3. The properties at point 3 are determined by linear interpolation. The following four equations are obtained by writing equations 17.34 and 17.37 in finite difference form in terms of points 1, 2, 3, and 4, and from the equation of the diagonal line 12.

$$y_3 - \lambda_o x_3 = y_4 - \lambda_o x_4 \tag{17.43}$$

$$y_4 - \lambda_+ x_4 = y_2 - \lambda_+ x_2 \tag{17.44}$$

$$y_4 - \lambda_- x_4 = y_1 - \lambda_- x_1 \tag{17.45}$$

$$y_3 - \lambda_{12} x_3 = y_2 - \lambda_{12} x_2 \tag{17.46}$$

where λ_{12} is the slope of line 12. Equations 17.43 to 17.46 may be solved simultaneously for x_3, y_3, x_4, and y_4. As pointed out above, the properties V, θ, p, and ρ at point 3 are then obtained by linear interpolation.

For the *Euler predictor*, for brevity termed the *predictor*,

$$\lambda_+ = \tan(\theta_2 + \alpha_2) \tag{17.47}$$

$$\lambda_- = \tan(\theta_1 - \alpha_1) \tag{17.48}$$

The value of λ_o depends on the flow angle at point 3, which is not known until point 3 is located and the corresponding flow properties have been determined by linear interpolation. An iterative procedure must be employed for determining the location of point 3 during each pass through the modified Euler predictor-corrector algorithm. For the Euler *predictor*, the initial estimate for θ_3 is obtained as follows.

$$\theta_3 = \frac{\theta_1 + \theta_2}{2} \tag{17.49}$$

Equations 17.43 and 17.46 may then be solved simultaneously for x_3 and y_3, and the corresponding value of θ_3 may be determined by linear interpolation. The procedure may be repeated with the new value of θ_3 to obtain improved values of

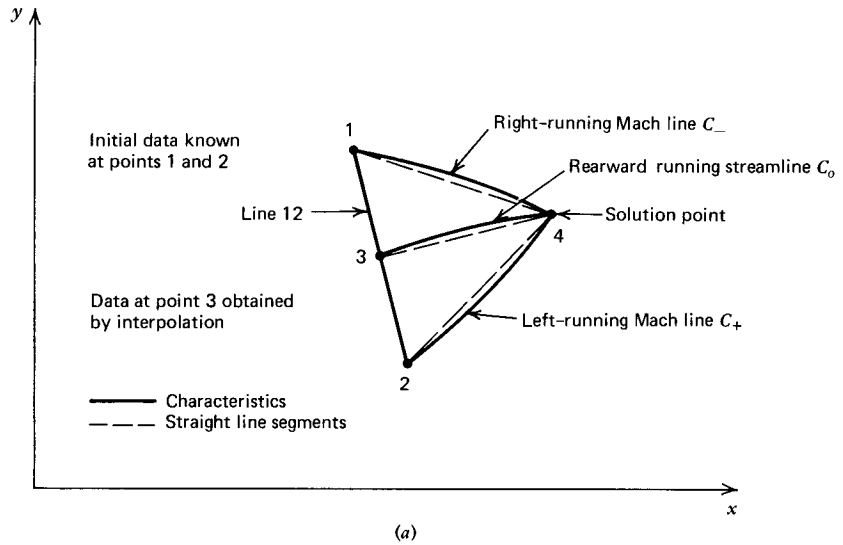

(*a*)

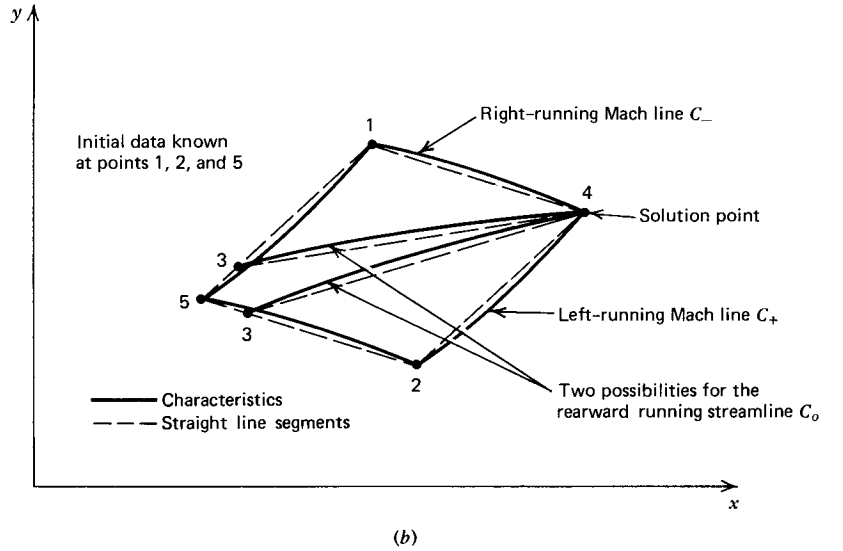

(*b*)

Figure 17.4 Unit process for an interior point. (*a*) Streamline intersection with the diagonal. (*b*) Streamline intersection with previous Mach lines.

x_3 and y_3, and correspondingly an improved value for θ_3. The procedure may be repeated a specified number of times, or until the values of x_3 and y_3 change from trial to trial by less than a specified tolerance.

The compatibility equation valid along the Mach lines, equation 17.38, may be written in finite difference form as follows.

$$Q_+ p_4 + \theta_4 = T_+ \tag{17.50}$$

$$Q_- p_4 - \theta_4 = T_- \tag{17.51}$$

where

$$T_+ = -S_+(x_4 - x_2) + Q_+ p_2 + \theta_2 \tag{17.52}$$

$$T_- = -S_-(x_4 - x_1) + Q_- p_1 - \theta_1 \tag{17.53}$$

For the Euler predictor

$$Q_+ = \frac{\sqrt{M_2^2 - 1}}{\rho_2 V_2^2} \qquad S_+ = \frac{\delta \sin\theta_2}{y_2 M_2 \cos(\theta_2 + \alpha_2)} \tag{17.54}$$

$$Q_- = \frac{\sqrt{M_1^2 - 1}}{\rho_1 V_1^2} \qquad S_- = \frac{\delta \sin\theta_1}{y_1 M_1 \cos(\theta_1 - \alpha_1)} \tag{17.55}$$

Equations 17.50 and 17.51 may be solved simultaneously for p_4 and θ_4.

Writing equations 17.35 and 17.36, the compatibility equations valid along streamlines, in finite difference form gives

$$R_o V_4 + p_4 = R_o V_3 + p_3 = T_{o1} \tag{17.56}$$

$$p_4 - A_o \rho_4 = p_3 - A_o \rho_3 = T_{o2} \tag{17.57}$$

For the Euler predictor

$$R_o = \rho_3 V_3 \quad A_o = a_3^2 \tag{17.58}$$

where $a_3 = a(p_3, \rho_3)$. Equations 17.56 and 17.57 may be solved for V_4 and ρ_4, thus completing the application of the Euler predictor algorithm.

Table 17.3 presents the computational equations for steady two-dimensional isentropic supersonic flow.

Improved values for the location of and the corresponding flow properties at point 4 may be obtained by repeating the steps discussed above for the Euler predictor algorithm, but employing average values of V, θ, p, and ρ along each

Table 17.3 Computational Equations for Steady Two-Dimensional Isentropic Rotational Supersonic Flow

$y_3 - \lambda_o x_3 = y_4 - \lambda_o x_4$	(17.43)
$y_4 - \lambda_+ x_4 = y_2 - \lambda_+ x_2$	(17.44)
$y_4 - \lambda_- x_4 = y_1 - \lambda_- x_1$	(17.45)
$y_3 - \lambda_{12} x_3 = y_2 - \lambda_{12} x_2$	(17.46)
$Q_+ p_4 + \theta_4 = T_+$	(17.50)
$Q_- p_4 - \theta_4 = T_-$	(17.51)
$R_o V_4 + p_4 = T_{o1}$	(17.56)
$p_4 - A_o \rho_4 = T_{o2}$	(17.57)

characteristic. Hence,

$$\lambda_+ = \tan(\theta_+ + \alpha_+) \tag{17.59}$$

where

$$p_+ = \frac{p_2 + p_4}{2} \qquad \theta_+ = \frac{\theta_2 + \theta_4}{2} \qquad V_+ = \frac{V_2 + V_4}{2} \qquad \rho_+ = \frac{\rho_2 + \rho_4}{2} \tag{17.60}$$

From equation 17.8,

$$a_+ = a(p_+, \rho_+) \tag{17.61}$$

Then,

$$M_+ = \frac{V_+}{a_+} \qquad \alpha_+ = \sin^{-1}\left(\frac{1}{M_+}\right) \tag{17.62}$$

The coefficients λ_-, λ_o, Q_+, Q_-, S_+, S_-, R_o, and A_o are determined in a similar manner. For example,

$$Q_+ = \frac{(M_+^2 - 1)^{1/2}}{\rho_+ V_+ V_+^2} \tag{17.63}$$

The corrector may be applied only once, or iterated to achieve a convergence tolerance.

The only problem remaining is the determination of the speed of sound a from equation 17.8. For a perfect gas, equation 17.8 takes the simple form

$$a^2 = \frac{\gamma p}{\rho} \tag{17.64}$$

Correspondingly, the temperature t is given by

$$t = t(p, \rho) \tag{17.65}$$

For a perfect gas

$$t = \frac{p}{\rho R} \tag{17.66}$$

For a real gas, equations 17.8 and 17.65 may be expressed in the form of two-dimensional tables, and the speed of sound a and temperature t may be determined by double interpolation in those tables. For mixtures of perfect gases having either equilibrium or frozen composition, the methods presented in Section 14–5 may be applied for compiling the aforementioned tables.

An irrotational flow is basically a special case of rotational flow. Consequently, irrotational flow problems may be solved by the numerical methods for solving rotational flows problems. Hence, the unit processes developed in the present chapter for rotational flows are applicable to irrotational flows. Whether an isentropic flow is irrotational or rotational depends only on the initial conditions, since by Kelvin's theorem, isentropic flows are rotation preserving (see Section 10–6).

A FORTRAN computer program, subroutine INTER, for implementing the unit process for an interior point is presented below. The terminology is the same as that presented in Tables 16.5 and 16.6.

The temperature t, Mach number M, and the speed of sound a are determined from the pressure p and the density ρ by calling subroutine **THERMO**. In this manner, the different unit processes to be determined by the method of characteristics are independent of the equations of state for the fluid. For illustrative purposes, a subroutine **THERMO** is presented below for a perfect gas. Other equations of state may be considered by developing an appropriate subroutine **THERMO**.

The iteration and convergence controls discussed in Sections 12–5(d) and 16–3(b) are applicable here. On the axis of symmetry, the ratio $\sin\theta_2/y_2$ in the coefficient S is approximated by the ratio $\sin\theta_1/y_1$ for the predictor. For the corrector, that ratio is based on the average values of θ and y, which are nonzero.

The data required by subroutine **INTER** are the values of x_1, y_1, p_1, ρ_1, V_1, θ_1, x_2, y_2, p_2, ρ_2, V_2, and θ_2. The data may be in either SI units or EE units. The results are the values of x_4, y_4, p_4, ρ_4, V_4, and θ_4.

The unit processes for an interior point, a direct wall point, an inverse wall point, an axis of symmetry point, and a free pressure boundary point, are presented in Sections 17–4(b), to 17–4(f), respectively. Those unit processes may be employed in conjunction with a master logic program for solving a variety of problems involving steady two-dimensional isentropic rotational supersonic flow fields.

```
      SUBROUTINE INTER

C     SUBROUTINE INTER CALCULATES THE SOLUTION AT AN INTERIOR POINT

      COMMON /CONTRL/ DELTA,NI,NT,ICOR,E1,E2,E3,E4,E5,IUNITS,PI,RAD
      COMMON /PROPTY/ G,RG,CP,TS,PS,PA,GC,GL $ REAL M
      COMMON /DATA/ X1,Y1,U1,V1,Q1,A1,P1,R1,T1,M1,X2,Y2,U2,V2,Q2,A2,P2,
     1R2,T2,M2,X3,Y3,U3,V3,Q3,A3,P3,R3,T3,M3,X4,Y4,U4,V4,Q4,A4,P4,R4,T4,
     2M4,LP,LM,LE,L12,L0 $ REAL M1,M2,M3,M4,LP,LM,LE,L12,L0

C     CALCULATE THE COEFFICIENTS FOR THE PREDICTOR

      ITER=0 $ L12=(Y1-Y2)/(X1-X2) $ CALL THERMO (Q2,P2,R2,T,C,M)
      LP=TAN(A2+ASIN(1.0/M)) $ QP=GC*SQRT(M**2-1.0)/(R2*Q2**2)
      SP=DELTA/(M*COS(A2+ASIN(1.0/M))) $ IF (Y2.EQ.0.0) SP=SP*SIN(A1)/Y1
      IF (Y2.GT.0.0) SP=SP*SIN(A2)/Y2 $ CALL THERMO (Q1,P1,R1,T,C,M)
      LM=TAN(A1-ASIN(1.0/M)) $ QM=GC*SQRT(M**2-1.0)/(R1*Q1**2)
      SM=DELTA*SIN(A1)/(Y1*M*COS(A1-ASIN(1.0/M))) $A3=0.5*(A1+A2) $A4=A3

C     SOLUTION OF THE FINITE DIFFERENCE EQUATIONS, LOCATE POINT 4

   10 X4=(Y1-Y2-LM*X1+LP*X2)/(LP-LM) $ Y4=Y1+LM*(X4-X1)
      IF (Y4.LT.0.0) RETURN
      TP=-SP*(X4-X2)+QP*P2+A2 $ TM=-SM*(X4-X1)+QM*P1-A1 $ K=1

C     LOCATE POINT 3 AND INTERPOLATE FOR THE PROPERTIES THERE

   20 L0=TAN(0.5*(A3+A4)) $ X3=(Y4-Y2-L0*X4+L12*X2)/(L12-L0)
      Y3=Y4+L0*(X3-X4) $ D=(Y3-Y2)/(Y1-Y2) $ A3=A2+D*(A1-A2)
      IF(ITER.EQ.0)A4=A3 $IF(K.GT.1.AND.ABS(Y3-YC).LT.0.000001) GO TO 30
      XC=X3 $ YC=Y3 $ K=K+1 $ GO TO 20
   30 Q3=Q2+D*(Q1-Q2) $ P3=P2+D*(P1-P2) $ R3=R2+D*(R1-R2)
      IF (ITER.GT.0) GO TO 40 $ Q4=Q3 $ P4=P3 $ R4=R3
   40 P=0.5*(P3+P4) $ R=0.5*(R3+R4) $ Q=0.5*(Q3+Q4) $ R0=R*Q/GC
      CALL THERMO (Q,P,R,T,C,M) $ A0=C**2/GC $T01=R0*G3+P3 $T02=P3-A0*R3

C     CALCULATE THE PROPERTIES AT POINT 4, AND TEST FOR CONVERGENCE

      P4=(TP+TM)/(QP+QM) $ A4=TP-QP*P4 $ Q4=(T01-P4)/R0 $ R4=(P4-T02)/A0
      IF (ITER.EQ.ICOR) RETURN $ IF (ITER.EQ.0) GO TO 50
      IF ((ABS(X4-XD).GT.E1).OR.(ABS(Y4-YD).GT.E1)) GO TO 50
      IF ((ABS(P4-PD).GT.E2*PD).OR.(ABS(R4-RD).GT.E3*RD)) GO TO 50
      IF ((ABS(Q4-QD).LT.E4*QD).AND.(ABS(A4-AD).LT.E5*AD)) RETURN
```

```
C     CALCULATE THE COEFFICIENTS FOR THE CORRECTOR

   50 ITER=ITER+1 $ XD=X4 $ YD=Y4 $ PD=P4 $ RD=R4 $ QC=Q4 $ AD=A4
      P=0.5*(P2+P4) $ R=0.5*(R2+R4) $ Q=0.5*(Q2+Q4) $ A=0.5*(A2+A4)
      Y=0.5*(Y2+Y4) $ CALL THERMO (Q,P,R,T,C,M) $ LP=TAN(A+ASIN(1.0/M))
      QP=GC*SQRT(M**2-1.0)/(R*Q**2) $ P=0.5*(P1+P4) $ R=0.5*(R1+R4)
      SP=DELTA*SIN(A)/(Y*M*COS(A+ASIN(1.0/M))) $ Q=0.5*(Q1+Q4)
      A=0.5*(A1+A4) $ Y=0.5*(Y1+Y4) $ CALL THERMO (Q,P,R,T,C,M)
      LM=TAN(A-ASIN(1.0/M)) $ QM=GC*SQRT(M**2-1.0)/(R*Q**2)
      SM=DELTA*SIN(A)/(Y*M*COS(A-ASIN(1.0/M))) $ GO TO 10
      END


      SUBROUTINE THERMO (Q,P,R,T,C,M)

C     SUBROUTINE THERMO CALCULATES T, C, AND M FOR GIVEN Q, P, AND R

      COMMON /PROPTY/ G,RG,CP,TS,PS,PA,GC,GL $ REAL M

      T=P/(RG*R) $ C=SQRT(G*GC*RG*T) $ M=Q/C $ RETURN
      END
```

Example 17.1. Solve Example 16.1 employing the unit process for an interior point in a steady two-dimensional isentropic rotational flow field. Assume that γ, R, P, and T are constant throughout the flow field. Consequently, the flow is actually irrotational. The basic features of the numerical analysis of rotational flow may be demonstrated, however, because irrotational flow, as pointed out in Section 17–4(b), is a special case of rotational flow. The unit process is illustrated schematically in Fig. 17.4*a*. From Example 16.1, $\gamma = 1.20$, $R = 320.0$ J/kg-K, $P = 70.0 \cdot 10^5$ N/m^2, and $T = 3000$ K. The initial data are presented in Table 17.4.

Table 17.4 Initial-Value Data (Example 17.1)

	Point 1	Point 2
x, m	0.131460	0.135683
y, m	0.040118	0.037123
V, m/s	2603.5	2609.2
θ, deg	18.191	16.422
p, N/m^2	34,042	32,781
ρ, kg/m^3	0.086151	0.083482

Solution

The initial data may be determined from the values of u and v given in Example 16.1 by employing the following equations.

$$V = (u^2 + v^2)^{1/2} \tag{a}$$

$$\theta = \tan^{-1}\left(\frac{v}{u}\right) \tag{b}$$

$$t = T - \frac{V^2}{2c_p} \tag{c}$$

$$p = P\left(\frac{t}{T}\right)^{\gamma/(\gamma-1)} \tag{d}$$

$$\rho = \frac{p}{Rt} \tag{e}$$

The results for the initial-value data are presented in Table 17.4. The numerical calculations are presented below for the predictor and one application of the corrector. Those results and the results of two additional applications of the corrector are summarized in Table 17.5.

(a) *The speed of sound equation.* From equation 17.64

$$a=\left(\frac{\gamma p}{\rho}\right)^{1/2}=\left(\frac{1.2p}{\rho}\right)^{1/2} \qquad (f)$$

(b) *Flow properties at the initial-value points (see Table 17.4).*

$$a_1=\left[\frac{1.2(34{,}042)}{(0.08615)}\right]^{1/2}=688.60 \text{ m/s}$$

$$M_1=\frac{2603.5}{688.60}=3.7809$$

$$\alpha_1=\sin^{-1}\left(\frac{1}{3.7809}\right)=15.337 \text{ deg}$$

$$a_2=\left[\frac{1.2(32{,}781)}{(0.083482)}\right]^{1/2}=686.44 \text{ m/s}$$

$$M_2=\frac{2609.2}{686.44}=3.8010$$

$$\alpha_2=\sin^{-1}\left(\frac{1}{3.8010}\right)=15.253 \text{ deg}$$

(c) *Calculation of the coefficients for the predictor.* From equations 17.47, 17.54, 17.48, and 17.55, respectively,

$$\lambda_+=\tan(\theta_2+\alpha_2)=\tan(16.422+15.253)=0.61702$$

$$Q_+=\frac{\left[(3.8010)^2-1\right]^{1/2}}{(0.083482)(2609.2)^2}=6.4523\cdot 10^{-6} \text{ m}^2/\text{N}$$

$$S_+=\frac{\sin(16.422)}{(0.037123)(3.8010)\cos(16.422+15.253)}=2.3542 \text{ m}^{-1}$$

$$\lambda_-=\tan(\theta_1-\alpha_1)=\tan(18.191-15.337)=0.04986$$

$$Q_-=\frac{\left[(3.7809)^2-1\right]^{1/2}}{(0.086151)(2603.5)^2}=6.2441\cdot 10^{-6} \text{ m}^2/\text{N}$$

$$S_-=\frac{\sin(18.191)}{(0.040118)(3.7809)\cos(18.191-15.337)}=2.0607 \text{ m}^{-1}$$

(d) *Determination of x_4 and y_4 for the predictor.* From equations 17.44 and 17.45,

$$y_4-0.61702x_4=0.037123-(0.61702)(0.135683)$$

$$y_4-0.04986x_4=0.040118-(0.04986)(0.131460)$$

Table 17.5 Values of the Solution, for Successive Trials, for the Interior Point Unit Process (Example 17.1)

	(0)	(1)	(2)	(3)
λ_+	0.61702	0.62398	0.62393	0.62391
λ_-	0.04986	0.04554	0.04482	0.04487
λ_o	0.30842	0.30996	0.30954	0.30955
x_4, m	0.14133	0.14119	0.14118	0.14118
y_4, m	0.040610	0.040561	0.040554	0.040554
x_3, m	0.13397	0.13399	0.13399	0.13399
y_3, m	0.038339	0.038327	0.038326	0.038327
R_o, N-S/m^3	220.45	207.61	208.72	208.67
$A_o \cdot 10^{-6}$, N-m/kg	0.47243	0.46615	0.46716	0.46707
$T_{o1} \cdot 10^{-6}$, N/m^2	0.60799	0.57451	0.57741	0.57728
$T_{o2} \cdot 10^{-3}$, N/m^2	−6.6586	−6.1276	−6.2130	−6.2048
$Q_+ \cdot 10^6$, m^2/N	6.4523	6.8598	6.8149	6.8173
S_+, m^{-1}	2.3542	2.2918	2.2932	2.2933
T_+, unitless	0.48483	0.49886	0.49741	0.49748
$Q_- \cdot 10^6$, m^2/N	6.2441	6.7392	6.6959	6.6982
S_-, m^{-1}	2.0607	1.9751	1.9763	1.9764
T_-, unitless	−0.12528	−0.10730	−0.10876	−0.10869
p_4, N/m^2	28,319	28,793	28,765	28,767
θ_4, deg	17.309	17.266	17.267	17.267
V_4, m/s	2629.5	2628.6	2628.6	2628.6
ρ_4, kg/m^3	0.074036	0.074913	0.074874	0.074875

Column (0)—predictor values. Column (2)—first iteration of the corrector.
Column (1)—corrector values. Column (3)—second iteration of the corrector.

from which we obtain

$$x_4 = 0.141335 \text{ m} \qquad \text{and} \qquad y_4 = 0.040610 \text{ m}$$

From equations 17.52 and 17.53,

$$T_+ = -(2.3542)(0.141335 - 0.135683) + (6.4523 \cdot 10^{-6})(32{,}781) + (16.422/57.2958)$$

$$T_+ = 0.48483$$

$$T_- = -(2.0607)(0.141335 - 0.131460) + (6.2441 \cdot 10^{-6})(34{,}042) - (18.191/57.2958)$$

$$T_- = -0.12528$$

(e) *Location of point 3 for the predictor.* The location of point 3 is determined iteratively employing the average property method. For the first pass, assume $\theta_3 = (\theta_1 + \theta_2)/2$. Thus,

$$\lambda_o = \tan\left(\frac{\theta_1 + \theta_2}{2}\right) = \tan\left(\frac{18.191 + 16.422}{2}\right) = 0.31159$$

The slope of line 12 is

$$\lambda_{12} = \frac{y_1 - y_2}{x_1 - x_2} = \frac{0.040118 - 0.037123}{0.131460 - 0.135683} = -0.70921$$

From equations 17.43 and 17.46,

$$y_3-(0.31159)x_3=0.040610-(0.31159)(0.141335)$$

$$y_3-(-0.70921)x_3=0.037123-(-0.70921)(0.135683)$$

which yield

$$x_3=0.133992 \text{ m} \qquad \text{and} \qquad y_3=0.038322 \text{ m}$$

Interpolating for θ_3 yields

$$\theta_3=\theta_2+\left(\frac{y_3-y_2}{y_1-y_2}\right)(\theta_1-\theta_2)=16.422+\frac{(0.038322-0.037123)}{(0.040118-0.037123)}(18.191-16.422)$$

$$\theta_3=17.130 \text{ deg}$$

Repeating the procedure iteratively employing the latest values of θ_3, we obtain

$$x_3=0.13397 \text{ m} \qquad y_3=0.038340 \text{ m} \qquad \theta_3=17.141 \text{ deg}$$

$$x_3=0.13397 \text{ m} \qquad y_3=0.038339 \text{ m} \qquad \theta_3=17.140 \text{ deg}$$

Interpolating for the remaining flow properties gives

$$p_3=33{,}293 \text{ N/m}^2 \qquad \rho_3=0.084565 \text{ kg/m}^3 \qquad V_3=2606.9 \text{ m/s}$$

(f) *Determination of* p_4, θ_4, V_4, *and* ρ_4 *for the predictor.* From equations (f), 17.58, 17.56, and 17.57, respectively,

$$a_3=\left[\frac{1.2(33{,}293)}{(0.084565)}\right]^{1/2}=687.34 \text{ m/s}$$

$$R_o=(0.084565)(2606.9)=220.45 \text{ N-s/m}^3$$

$$A_o=(687.34)^2=0.47243\cdot 10^6 \text{ N-m/kg}$$

$$T_{o1}=(220.45)(2606.9)+33{,}293=0.60799\cdot 10^6 \text{ N/m}^2$$

$$T_{o2}=33{,}293-(0.47243\cdot 10^6)(0.084565)=-6.6586\cdot 10^3 \text{ N/m}^2$$

Substituting the values of the coefficients into equations 17.50, 17.51, 17.56, and 17.57, respectively, we obtain

$$(6.4523\cdot 10^{-6})p_4+\theta_4=0.48483 \qquad \text{(g)}$$

$$(6.2441\cdot 10^{-6})p_4-\theta_4=-0.12528 \qquad \text{(h)}$$

$$220.45V_4+p_4=0.60799\cdot 10^6 \qquad \text{(i)}$$

$$p_4-(0.47243\cdot 10^6)\rho_4=-6.6586\cdot 10^3 \qquad \text{(j)}$$

Solving equations (g) and (h) simultaneously gives

$$p_4=28{,}319 \text{ N/m}^2 \qquad \theta_4=17.309 \text{ deg}$$

Solving equations (i) and (j) yields

$$V_4 = 2629.5 \text{ m/s} \qquad \rho_4 = 0.074036 \text{ kg/m}^3$$

The application of the predictor is complete. Column (0) in Table 17.5 presents the above results.

(g) *Calculation of the coefficients for the corrector.* Along Mach line 24,

$$p_+ = \frac{p_2 + p_4}{2} = \frac{32{,}781 + 28{,}319}{2} = 30{,}550 \text{ N/m}^2$$

$$\theta_+ = \frac{16.422 + 17.309}{2} = 16.866 \text{ deg}$$

$$V_+ = \frac{2609.2 + 2629.5}{2} = 2619.4 \text{ m/s}$$

$$\rho_+ = \frac{0.083482 + 0.074036}{2} = 0.078759 \text{ kg/m}^3$$

$$y_+ = \frac{0.037123 + 0.040610}{2} = 0.038867 \text{ m}$$

$$a_+ = \left[\frac{1.2(30{,}550)}{(0.078759)} \right]^{1/2} = 682.25 \text{ m/s}$$

$$M_+ = \frac{2619.4}{682.25} = 3.8392$$

$$\alpha_+ = \sin^{-1}\left(\frac{1}{3.8392} \right) = 15.098 \text{ deg}$$

$$\lambda_+ = \tan(16.866 + 15.098) = 0.62398$$

$$Q_+ = \frac{\left[(3.8392)^2 - 1 \right]^{1/2}}{(0.078759)(2619.4)^2} = 6.8598 \cdot 10^{-6} \text{ m}^2/\text{N}$$

$$S_+ = \frac{\sin(16.866)}{(0.038867)(3.8392)\cos(16.866 + 15.098)} = 2.2918 \text{ m}^{-1}$$

Along Mach line 14

$$p_- = \frac{p_1 + p_4}{2} = \frac{34{,}042 + 28{,}319}{2} = 31{,}181 \text{ N/m}^2$$

$$\theta_- = \frac{18.191 + 17.309}{2} = 17.750 \text{ deg}$$

$$V_- = \frac{2603.5 + 2629.5}{2} = 2616.5 \text{ m/s}$$

$$\rho_- = \frac{0.086151 + 0.074036}{2} = 0.080094 \text{ kg/m}^3$$

$$y_- = \frac{0.040118 + 0.040610}{2} = 0.040364 \text{ m}$$

$$a_- = \left[\frac{1.2(31{,}181)}{(0.080094)} \right]^{1/2} = 683.49 \text{ m/s}$$

$$M_- = \frac{2616.5}{683.49} = 3.8281$$

$$\alpha_- = \sin^{-1}\left(\frac{1}{3.8281} \right) = 15.143 \text{ deg}$$

$$\lambda_- = \tan(17.750 - 15.143) = 0.04554$$

$$Q_- = \frac{\left[(3.8281)^2 - 1 \right]^{1/2}}{(0.080094)(2616.5)^2} = 6.7392 \cdot 10^{-6} \text{ m}^2/\text{N}$$

$$S_- = \frac{\sin(17.750)}{(0.040364)(3.8281)\cos(17.750 - 15.143)} = 1.9751 \text{ m}^{-1}$$

(h) *Determination of x_4 and y_4 for the corrector.* From equations 17.44 and 17.45,

$$y_4 - (0.62398)x_4 = 0.037123 - (0.62398)(0.135683)$$

$$y_4 - (0.04554)x_4 = 0.040118 - (0.04554)(0.131460)$$

which yield

$$x_4 = 0.141193 \text{ m} \qquad \text{and} \qquad y_4 = 0.040561 \text{ m}$$

From equations 17.52 and 17.53,

$$T_+ = -(2.2918)(0.141193 - 0.135683) + (6.8598 \cdot 10^{-6})(32{,}781) + (16.422/57.2958)$$

$$T_+ = 0.49886$$

$$T_- = -(1.9751)(0.141193 - 0.131460) + (6.7392 \cdot 10^{-6})(34{,}042) - (18.191/57.29578)$$

$$T_- = -0.10730$$

(i) *Location of point 3 for the corrector.* The location of point 3 is determined iteratively. For the first pass, assume θ_3 retains its value from the predictor pass. Thus

$$\lambda_o = \tan\left(\frac{\theta_3 + \theta_4}{2} \right) = \tan\left(\frac{17.140 + 17.309}{2} \right) = 0.31002$$

From equations 17.43 and 17.46,

$$y_3 - (0.31002)x_3 = 0.040561 - (0.31002)(0.141193)$$

$$y_3 - (-0.70921)x_3 = 0.037123 - (-0.70921)(0.135683)$$

which yield

$$x_3 = 0.133986 \text{ m} \qquad y_3 = 0.038327 \text{ m}$$

Interpolating for θ_3 gives

$$\theta_3 = 16.422 + \frac{(0.038327 - 0.037123)}{(0.040118 - 0.037123)}(18.191 - 16.422) = 17.133 \text{ deg}$$

Repeating the above procedure iteratively gives

$$x_3 = 0.13399 \text{ m} \qquad y_3 = 0.038327 \text{ m} \qquad \theta_3 = 17.133 \text{ deg}$$

Interpolating for the remaining flow properties, we obtain

$$p_3 = 33{,}288 \text{ N/m}^2 \qquad \rho_3 = 0.084555 \text{ kg/m}^3 \qquad V_3 = 2606.9 \text{ m/s}$$

(j) *Determination of* p_4, θ_4, V_4, *and* ρ_4 *for the corrector*. The average properties along the streamline C_0 are

$$p_o = \frac{p_3 + p_4}{2} = \frac{33{,}288 + 28{,}319}{2} = 30{,}804 \text{ N/m}^2$$

$$\rho_o = \frac{(0.084555 + 0.074036)}{2} = 0.079296 \text{ kg/m}^3$$

$$V_o = \frac{2606.9 + 2629.5}{2} = 2618.2 \text{ m/s}$$

Substituting into equations (f), 17.58, 17.56, and 17.57, respectively, we obtain

$$a_o = \left[\frac{1.2(30{,}804)}{(0.079296)}\right]^{1/2} = 682.75 \text{ m/s}$$

$$R_o = (0.079296)(2618.2) = 207.61 \text{ N-s/m}^3$$

$$A_o = (682.75)^2 = 0.46615 \cdot 10^6 \text{ N-m/kg}$$

$$T_{o1} = (207.61)(2606.9) + 33{,}288 = 0.57451 \cdot 10^6 \text{ N/m}^2$$

$$T_{o2} = 33{,}288 - (0.46615 \cdot 10^6)(0.084555) = -6.1276 \cdot 10^3 \text{ N/m}^2$$

Substituting into the compatibility equations (equations 17.50, 17.51, 17.56, and 17.57), we obtain

$$(6.8598 \cdot 10^{-6})p_4 + \theta_4 = 0.49886 \tag{k}$$

$$(6.7392 \cdot 10^{-6})p_4 - \theta_4 = -0.10730 \tag{l}$$

$$207.61 V_4 + p_4 = 0.57451 \cdot 10^6 \tag{m}$$

$$p_4 - (0.46615 \cdot 10^6)\rho_4 = -6.1276 \cdot 10^3 \tag{n}$$

Solving equations (k) to (n) yields

$$p_4 = 28{,}793 \text{ N/m}^2, \qquad \theta_4 = 17.266 \text{ deg}$$

$$V_4 = 2628.6 \text{ m/s}, \qquad \rho_4 = 0.074913 \text{ kg/m}^3$$

Column (1) in Table 17.5 lists the above results.

(k) *Iteration of the corrector.* Columns (2) and (3) in Table 17.5 present the results of two iterations of the corrector. Iteration of the corrector is seen to have only a small effect on the final results.

17–4(c) Direct Wall Point

The unit processes for determining a direct wall point, an inverse wall point, an axis of symmetry point, and a free pressure boundary point may be developed by procedures analogous to those employed for irrotational flow presented in Sections 16–3(c) to 16–3(f), respectively. In all of those four cases, one of the Mach lines and its associated compatibility equation are replaced by the appropriate conditions.

Figure 17.5 illustrates the unit process for determining the location and the flow properties for a direct wall point (point 4) from the initial data points (points 2 and 3). Along the wall, the following boundary conditions are given.

$$y = y(x) \qquad (\textit{specified}) \tag{17.67}$$

$$\frac{dy}{dx} = \tan\theta = \frac{v}{u} \qquad (\textit{specified}) \tag{17.68}$$

Equations 17.67 and 17.68 comprise the aforementioned two conditions for replacing one characteristic equation and one compatibility equation for determining the location and the flow properties at a direct wall point.

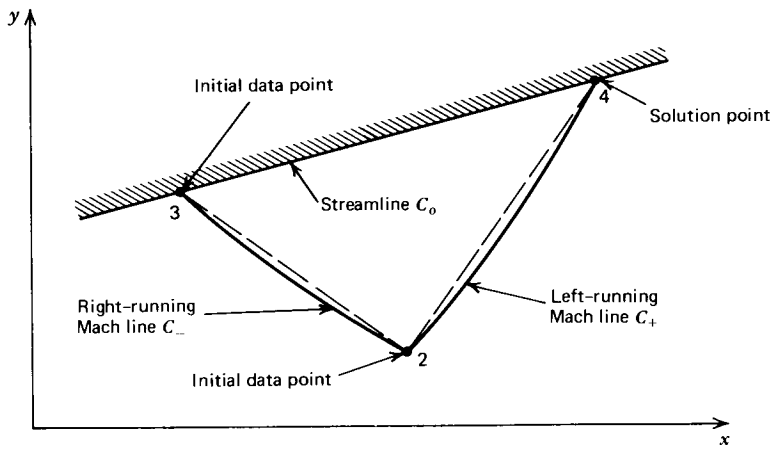

Figure 17.5 Unit process for a direct wall point.

A FORTRAN computer program, subroutine DRWALL, for implementing the unit process for a direct wall point is presented below. Subroutine DRWALL must be employed in conjunction with subroutine BOUNDY described in Section 16–3(c), which specifies the wall contour.

```
      SUBROUTINE DRWALL

C     SUBROUTINE DRWALL CALCULATES THE SOLUTION AT A DIRECT WALL POINT

      COMMON /CONTRL/ DELTA,NI,NT,ICOR,E1,E2,E3,E4,E5,IUNITS,PI,RAD
      COMMON /PROPTY/ G,RG,CP,TS,PS,PA,GC,GL $ REAL M
      COMMON /DATA/ X1,Y1,U1,V1,Q1,A1,P1,R1,T1,M1,X2,Y2,U2,V2,Q2,A2,P2,
     1R2,T2,M2,X3,Y3,U3,V3,Q3,A3,P3,R3,T3,M3,X4,Y4,U4,V4,Q4,A4,P4,R4,T4,
     2M4,LP,LM,LE,L12,LO $ REAL M1,M2,M3,M4,LP,LM,LE,L12,LO

C     CALCULATE THE COEFFICIENTS FOR THE PREDICTOR

      ITER=0 $ Q4=Q3 $ P4=P3 $ R4=R3 $ CALL THERMO(Q2,P2,R2,T,C,M)
      LP=TAN(A2+ASIN(1.0/M)) $ QP=GC*SQRT(M**2-1.0)/(R2*Q2**2)
      SP=DELTA*SIN(A2)/(Y2*M*COS(A2+ASIN(1.0/M)))

C     SOLUTION OF THE FINITE DIFFERENCE EQUATIONS

   10 CALL BOUNDY (2) $ TP=-SP*(X4-X2)+QP*P2+A2 $ P=0.5*(P3+P4)
      R=0.5*(R3+R4) $Q=0.5*(Q3+Q4) $RO=R*Q/GC $ CALL THERMO(Q,P,R,T,C,M)
      AO=C**2/GC $ TO1=RO*Q3+P3 $ TO2=P3-AO*R3
      P4=(TP-A4)/QP $ Q4=(TO1-P4)/RO $ R4=(P4-TO2)/AO

C     CHECK FOR CONVERGENCE OR COMPLETION OF SPECIFIED ITERATIONS

      IF (ITER.EQ.ICOR) RETURN $ IF (ITER.EQ.0) GO TO 20
      IF ((ABS(X4-XO).GT.E1).OR.(ABS(Y4-YO).GT.E1)) GO TO 20
      IF ((ABS(P4-PO).GT.E2*PO).OR.(ABS(R4-RO).GT.E3*RO)) GO TO 20
      IF ((ABS(Q4-QO).LT.E4*QO).AND.(ABS(A4-AO).LT.E5*AO)) RETURN

C     CALCULATE THE COEFFICIENTS FOR THE CORRECTOR

   20 ITER=ITER+1 $ PO=P4 $ RO=R4 $ QO=Q4 $ AO=A4 $ XO=X4 $ YO=Y4
      P=0.5*(P2+P4) $ R=0.5*(R2+R4) $ Q=0.5*(Q2+Q4) $ A=0.5*(A2+A4)
      Y=0.5*(Y2+Y4) $ CALL THERMO (Q,P,R,T,C,M) $ LP=TAN(A+ASIN(1.0/M))
      SP=DELTA*SIN(A)/(Y*M*COS(A+ASIN(1.0/M)))
      QP=GC*SQRT(M**2-1.0)/(R*Q**2) $ GO TO 10
      END
```

Example 17.2. Solve Example 16.2 employing the unit process for determining a direct wall point for a steady two-dimensional rotational supersonic flow. The unit process is illustrated in Fig. 17.5.

Solution

The initial data at point 2 may be determined by the process employed in Example 17.1. In addition, the properties at a prior wall point, point 3 in Fig. 17.5, are required. Those initial data are presented in Table 17.6. The computational procedure is illustrated below. The results of the calculations are summarized in Table 17.7.

Table 17.6 Initial-Value Data (Example 17.2)

	Point 2	Point 3
x, mm	60.480	55.943
y, mm	59.625	58.845
V, m/s	2274.2	2252.9
θ, deg	30.122	30.752
p, N/m$^2 \cdot 10^5$	1.9597	2.1453
ρ, kg/m^3	0.37046	0.39947

Table 17.7 Values of the Solution, for Successive Trials, for the Direct Wall Point Unit Process (Example 17.2)

	(0)	(1)	(2)	(3)
λ_+	1.2187	1.2133	1.2135	1.2135
x_4, mm	63.461	63.486	63.486	63.486
y_4, mm	63.258	63.273	63.272	63.272
R_o, N-s/m^3	899.97	857.33	857.82	857.84
$A_o \cdot 10^{-6}$, N-m/kg	0.64444	0.63711	0.63766	0.63762
$T_{o1} \cdot 10^{-6}$, N/m^2	2.2421	2.1460	2.1471	2.1472
$T_{o2} \cdot 10^{-3}$, N/m^2	−42.906	−39.976	−40.194	−40.181
$Q_+ \cdot 10^6$, m^2/N	1.3953	1.4234	1.4219	1.4219
S_+, m^{-1}	4.6485	4.4754	4.4762	4.4761
T_+, unitless	0.78532	0.79121	0.79091	0.79092
$p_4 \cdot 10^5$, N/m^2	1.8680	1.8730	1.8729	1.8729
θ_4, deg	30.061	30.058	30.058	30.058
V_4, m/s	2283.7	2284.7	2284.7	2284.7
ρ_4, kg/m^3	0.35645	0.35673	0.35675	0.35675

Column (0)—predictor values. Column (2)—first iteration of the corrector.
Column (1)—corrector values. Column (3)—second iteration of the corrector.

(a) *Specification of the nozzle contour.* The wall specifications are the same as in Example 16.2. From equation (h) in Example 16.2, we obtain

$$y = 22.1852 + 0.71568x - 0.0010787x^2 \tag{a}$$

$$\tan\theta = 0.71568 - 0.0021574x \tag{b}$$

where x and y are specified in mm.

(b) *The speed of sound equation.* From equation (f) in Example 17.1,

$$a = \left(\frac{1.2p}{\rho}\right)^{1/2} \tag{c}$$

(c) *Flow properties at point 2.*

$$a_2 = \left[\frac{1.2(1.9597 \cdot 10^5)}{(0.37046)}\right]^{1/2} = 796.74 \text{ m/s}$$

$$M_2 = \frac{2274.2}{796.74} = 2.8544$$

$$\alpha_2 = \sin^{-1}\left(\frac{1}{2.8544}\right) = 20.508 \text{ deg}$$

(d) *Calculation of the coefficients along left-running Mach line 24 for the predictor.* From equations 17.47 and 17.54,

$$\lambda_+ = \tan(\theta_2 + \alpha_2) = \tan(30.122 + 20.508) = 1.2187$$

$$Q_+ = \frac{\left[(2.8544)^2 - 1\right]^{1/2}}{(0.37046)(2274.2)^2} = 1.3953 \cdot 10^{-6} \text{m}^2/\text{N}$$

$$S_+ = \frac{\sin(30.122)}{(0.059625)(2.8544)\cos(30.122 + 20.508)} = 4.6485 \text{ m}^{-1}$$

(e) *Determination of x_4, y_4, and θ_4 for the predictor.* From equation 17.44,

$$y_4-(1.2187)x_4=59.625-(1.2187)(60.480) \tag{d}$$

Solving equations (a) and (d) simultaneously, we obtain

$$x_4=63.461\,\text{mm} \qquad y_4=63.258\,\text{mm}$$

From equation 17.52,

$$T_+=-(4.6485)(0.063461-0.060480)+(1.3953\cdot10^{-6})(1.9597\cdot10^5)+(30.122/57.2958)$$

$$T_+=0.78532$$

Substituting $x_4=63.461$ into equation (b) gives

$$\theta_4=\tan^{-1}\left[0.71568-(0.0021574)(63.461)\right]=30.061\,\text{deg}$$

(f) *Calculation of the coefficients along streamline 34 for the predictor.* From equations (c), 17.58, 17.56, and 17.57,

$$a_3=\left[\frac{1.2(2.1453\cdot10^5)}{(0.39947)}\right]^{1/2}=802.77\,\text{m/s}$$

$$R_o=(0.39947)(2252.9)=899.97\,\text{N-s/m}^3$$

$$A_o=(802.77)^2=0.64444\cdot10^6\,\text{N-m/kg}$$

$$T_{o1}=(899.97)(2252.9)+2.1453\cdot10^5=2.2421\cdot10^6\,\text{N/m}^2$$

$$T_{o2}=2.1453\cdot10^5-(0.64444\cdot10^6)(0.39947)=-42.906\cdot10^3\,\text{N/m}^2$$

(g) *Determination of p_4, V_4, and ρ_4 for the predictor.* Substituting the values of the coefficients and θ_4 into equations 17.50, 17.56, and 17.57, yields

$$(1.3953\cdot10^{-6})p_4+(30.061/57.2958)=0.78532 \tag{e}$$

$$899.97V_4+p_4=2.2421\cdot10^6 \tag{f}$$

$$p_4-(0.64444\cdot10^6)\rho_4=-42.906\cdot10^3 \tag{g}$$

Solving equations (e), (f), and (g), we obtain

$$p_4=1.8680\cdot10^5\,\text{N/m}^2 \qquad V_4=2283.7\,\text{m/s} \qquad \rho_4=0.35645\,\text{kg/m}^3$$

The predictor calculations are complete. The results are summarized in column (0) in Table 17.7.

(h) *Application of the corrector.* The modified Euler corrector is applied by repeating steps (c) to (g) employing the average values of the flow properties, as illustrated in Example 17.1. Column (1) in Table 17.7 presents the results for the corrector. Two iterations of the corrector are applied, and the results are summarized in columns (2) and (3) of Table 17.7. Thus, we see that iteration of the corrector has very little effect on the results.

17–4(d) Inverse Wall Point

In regions of the wall along which there are large gradients in the flow properties, it is advantageous to employ the unit process for an inverse wall point described in

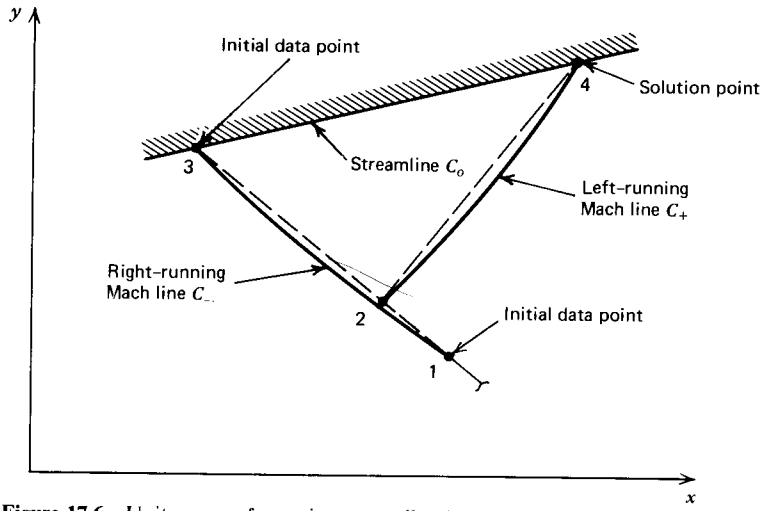

Figure 17.6 Unit process for an inverse wall point.

Section 16–3(d). Figure 17.6 illustrates the inverse unit process for determining a wall point in a rotational flow; a wall point determined by that procedure is termed an *inverse wall point*. The interior point, point 2, is located at the intersection of the rearward projected left-running Mach line emanating from the inverse wall point (point 4) and the right-running Mach line through the previously determined wall point, point 3, as discussed in Section 16–3(d). The application of the numerical method is identical to that discussed in Section 16–3(d), with the additional condition that the streamline adjacent to the wall is a characteristic, denoted by C_o, along which two compatibility equations are valid between the points 3 and 4. In all other respects, the application of the unit process for an inverse wall point for a rotational flow is the same as that discussed in Section 16–3(d) for an irrotational flow.

A FORTRAN computer program, subroutine INWALL, for the unit process for an inverse wall point is presented below.

```
      SUBROUTINE INWALL
C     SUBROUTINE INWALL CALCULATES THE SOLUTION AT AN INVERSE WALL POINT
      COMMON /CONTRL/ DELTA,NI,NT,ICOR,E1,E2,E3,E4,E5,IUNITS,PI,RAD
      COMMON /PROPTY/ G,RG,CP,TS,PS,PA,GC,GL $ REAL M
      COMMON /DATA/ X1,Y1,U1,V1,Q1,A1,P1,R1,T1,M1,X2,Y2,U2,V2,Q2,A2,P2,
     1R2,T2,M2,X3,Y3,U3,V3,Q3,A3,P3,R3,T3,M3,X4,Y4,U4,V4,Q4,A4,P4,R4,T4,
     2M4,LP,LM,LE,L12,L0 $ REAL M1,M2,M3,M4,LP,LM,LE,L12,L0
C     CALCULATE PROPERTIES FOR THE PREDICTOR
      ITER=0 $ LM=(Y3-Y1)/(X3-X1) $ P4=0.5*(P1+P3) $ R4=0.5*(R1+R3)
      Q4=0.5*(Q1+Q3) $ XA=X3 $ P2=P4 $ R2=R4 $ Q2=Q4 $ A2=0.5*(A1+A3)
C     DETERMINE THE LOCATION AND PROPERTIES AT POINT 2
   10 Q=0.5*(Q2+Q4) $ A=0.5*(A2+A4) $ P=0.5*(P2+P4) $ R=0.5*(R2+R4)
      CALL THERMO (Q,P,R,T,C,M) $ LP=TAN(A+ASIN(1.0/M))
      X2=(Y4-Y1+LM*X1-LP*X4)/(LM-LP) $ Y2=Y4+LP*(X2-X4)
      D=(X2-X1)/(X3-X1) $ Q2=Q1+D*(Q3-Q1) $ A2=A1+D*(A3-A1)
      P2=P1+D*(P3-P1) $ R2=R1+D*(R3-R1)
      IF (ITER.GT.0) GO TO 15 $ P4=P2 $ R4=R2 $ Q4=Q2
   15 IF (ABS(X2-XA).LT.0.000001) GO TO 20 $ XA=X2 $ GO TO 10
```

```
C     CALCULATE COEFFICIENTS AND SOLVE THE FINITE DIFFERENCE EQUATIONS

   20 P=0.5*(P2+P4) $ R=0.5*(R2+R4) $ Q=0.5*(Q2+Q4) $ A=0.5*(A2+A4)
      Y=0.5*(Y2+Y4) $ CALL THERMO (Q,P,R,T,C,M) $ LP=TAN(A+ASIN(1.0/M))
      QP=GC*SQRT(M**2-1.0)/(R*Q**2) $ SP=DELTA*SIN(A)/(Y*M*COS(A+
     1ASIN(1.0/M))) $ TP=-SP*(X4-X2)+QP*P2+A2 $ IF (ITER.GT.0) GO TO 25
      P4=P3 $ R4=R3 $ Q4=Q3
   25 P=0.5*(P3+P4) $ R=0.5*(R3+R4) $ Q=0.5*(Q3+Q4) $ RO=R*Q/GC
      CALL THERMO (Q,P,R,T,C,M) $ AO=C**2/GC $TO1=RO*Q3+P3 $TO2=P3-AO*R3
      P4=(TP-A4)/QP $ Q4=(TO1-P4)/RO $ R4=(P4-TO2)/AO

C     CHECK FOR CONVERGENCE OR COMPLETION OF SPECIFIED ITERATIONS

      IF (ITER.EQ.ICOR) RETURN $ IF (ITER.EQ.0) GO TO 40
      IF ((ABS(P4-PO).GT.E2*PO).OR.(ABS(R4-RO).GT.E3*RO)) GO TO 40
      IF (ABS(Q4-QO).LT.E4*QO) RETURN
   40 ITER=ITER+1 $ PO=P4 $ RO=R4 $ QO=Q4 $ GO TO 10
      END
```

Example 17.3. Solve Example 16.3 employing the unit process for an inverse wall point for rotational flow. The unit process is illustrated diagrammatically in Fig. 17.6.

Solution

The initial data at points 1 and 3, as well as the location and the wall slope at point 4, are obtainable from the data presented in Example 16.3 by employing equations (a) to (e) of Example 17.1. Those data are presented in Table 17.8. The numerical calculations are presented below for the predictor. The results are summarized in Table 17.9.

Table 17.8 Initial-Value Data (Example 17.3)

	Point 1	Point 3	Point 4
x, mm	5.495	5.085	5.283
y, mm	26.020	26.080	26.170
V, m/s	1728.9	1726.8	—
θ, deg	24.090	24.000	25.000
p, N/m$^2 \cdot 10^5$	11.545	11.604	—
ρ, kg/m^3	1.6240	1.6309	—

(a) *The speed of sound equation.* From equation (f) of Example 17.1,

$$a = \left(\frac{1.2p}{\rho}\right)^{1/2} \tag{a}$$

(b) *Equation of Mach line* 13. Along Mach line 13,

$$\lambda_- = \frac{y_3 - y_1}{x_3 - x_1} = \frac{26.080 - 26.020}{5.085 - 5.495} = -0.14634$$

From equation 17.37,

$$y_2 = y_1 + \lambda_-(x_2 - x_1) = 26.020 - 0.14634(x_2 - 5.495)$$

$$y_2 = 26.824 - 0.14634x_2 \tag{b}$$

where x and y are specified in mm.

Table 17.9 Solution Values, for Successive Trials, for the Inverse Wall Point Unit Process (Example 17.3)

	(0)	(1)	(2)	(3)
λ_+	1.5309	1.5147	1.5149	1.5149
x_2, mm	5.212	5.211	5.211	5.211
y_2, mm	26.061	26.062	26.062	26.062
R_o, N-s/m^3	2816.2	2774.5	2775.3	2775.3
$A_o \cdot 10^{-6}$, N-m/kg	0.85381	0.85022	0.85036	0.85036
$T_{o1} \cdot 10^{-6}$, N/m^2	6.0235	5.9513	5.9527	5.9527
$T_{o2} \cdot 10^{-3}$, N/m^2	−232.08	−226.22	−226.45	−226.45
$Q_+ \cdot 10^6$, m^2/N	0.32505	0.33148	0.33135	0.33135
S_+, m^{-1}	15.537	15.304	15.307	15.307
T_+, unitless	0.79486	0.80232	0.80216	0.80216
p_4, N/m$^2 \cdot 10^5$	11.030	11.041	11.041	11.041
V_4, m/s	1747.2	1747.1	1747.1	1747.1
ρ_4, kg/m^3	1.5637	1.5647	1.5646	1.5646

Column (0)—predictor values. Column (2)—first iteration of the corrector.
Column (1)—corrector values. Column (3)—second iteration of the corrector.

(c) *Location of point 2 for the predictor.* The location of point 2 is determined iteratively, employing the average property method. For the first pass, assume that the properties at point 2 are equal to the average of the values of the properties at points 1 and 3. Thus,

$$p_2 = \frac{p_1 + p_3}{2} = \frac{(11.545 + 11.604) \cdot 10^5}{2} = 11.575 \cdot 10^5 \text{ N/m}^2$$

$$\theta_2 = \frac{24.090 + 24.000}{2} = 24.045$$

$$V_2 = \frac{1728.9 + 1726.8}{2} = 1727.9 \text{ m/s}$$

$$\rho_2 = \frac{1.6240 + 1.6309}{2} = 1.6275 \text{ kg/m}^3$$

$$a_2 = \left[\frac{1.2(11.575 \cdot 10^5)}{(1.6275)} \right]^{1/2} = 923.82 \text{ m/s}$$

$$M_2 = \frac{1727.9}{923.81} = 1.8703$$

$$\alpha_2 = \sin^{-1}\left(\frac{1}{1.8703} \right) = 32.322 \text{ deg}$$

$$\theta_+ = \frac{\theta_2 + \theta_4}{2} = \frac{24.045 + 25.000}{2} = 24.523 \text{ deg}$$

$$\lambda_+ = \tan(24.523 + 32.320) = 1.5307$$

The Mach line 24 is specified by equation 17.44. Thus

$$26.170 - (1.5307)(5.283) = y_2 - (1.5307)x_2 \qquad \text{(c)}$$

Solving equations (b) and (c) simultaneously, we obtain

$$x_2 = 5.212 \text{ mm} \qquad y_2 = 26.061 \text{ mm}$$

Interpolating for the flow properties at point 2 yields

$$p_2 = p_1 + \left(\frac{x_2 - x_1}{x_3 - x_1}\right)(p_3 - p_1)$$

$$p_2 = 11.545 \cdot 10^5 + \left(\frac{5.212 - 5.495}{5.085 - 5.495}\right)(11.604 - 11.545)10^5$$

$$p_2 = 11.586 \cdot 10^5 \text{ N/m}^2$$

$$\theta_2 = 24.090 + (0.69024)(24.000 - 24.090) = 24.028 \text{ deg}$$

$$V_2 = 1728.9 + (0.69024)(1726.8 - 1728.9) = 1727.5 \text{ m/s}$$

$$\rho_2 = 1.6240 + (0.69024)(1.6309 - 1.6240) = 1.6288 \text{ kg/m}^3$$

Repeating the entire procedure iteratively, we obtain

$$x_2 = 5.212 \text{ mm} \qquad y_2 = 26.061 \text{ mm} \qquad p_2 = 11.586 \cdot 10^5 \text{ N/m}^2$$

$$\theta_2 = 24.028 \text{ deg} \qquad V_2 = 1727.5 \text{ m/s} \qquad \rho_2 = 1.6288 \text{ kg/m}^3$$

No further iterations are required.

(c) *Calculation of the coefficients along Mach line* 24 *for the predictor.* From equations 17.47, 17.54, and 17.52, employing the average property method, we obtain

$$\theta_+ = \frac{\theta_2 + \theta_4}{2} = \frac{24.028 + 25.000}{2} = 24.514 \text{ deg}$$

$$y_+ = \frac{26.061 + 26.170}{2} = 26.116 \text{ mm}$$

$$a_2 = \left[\frac{1.2(11.586 \cdot 10^5)}{(1.6288)}\right]^{1/2} = 923.90 \text{ m/s}$$

$$M_2 = \frac{1727.5}{923.90} = 1.8697$$

$$\alpha_2 = \sin^{-1}\left(\frac{1}{1.8697}\right) = 32.333 \text{ deg}$$

$$\lambda_+ = \tan(24.514 + 32.333) = 1.5309$$

$$Q_+ = \frac{\left[(1.8697)^2 - 1\right]^{1/2}}{(1.6288)(1727.5)^2} = 0.32505 \cdot 10^{-6} \text{ m}^2/\text{N}$$

$$S_+ = \frac{\sin(24.514)}{(0.026116)(1.8697)\cos(24.514 + 32.333)} = 15.537 \text{ m}^{-1}$$

$$T_+ = -(15.537)(0.005283 - 0.005212) + (0.32505 \cdot 10^{-6})(11.586 \cdot 10^5) + (24.028/57.2958) = 0.79486$$

(d) *Calculation of the coefficients along streamline* 34 *for the predictor.* From equations (a), 17.58, 17.56, and 17.57,

$$a_3 = \left[\frac{1.2(11.604 \cdot 10^5)}{(1.6309)} \right]^{1/2} = 924.02 \text{ m/s}$$

$$R_o = (1.6309)(1726.8) = 2816.2 \text{ N-s/m}^3$$

$$A_o = (924.02)^2 = 0.85381 \cdot 10^6 \text{ N-m/kg}$$

$$T_{o1} = (2816.2)(1726.8) + 11.604 \cdot 10^5 = 6.0235 \cdot 10^6 \text{ N/m}^2$$

$$T_{o2} = 11.604 \cdot 10^5 - (0.85381 \cdot 10^6)(1.6309) = -232.08 \cdot 10^3 \text{ N/m}^2$$

(e) *Determination of* p_4, V_4, *and* ρ_4 *for the predictor.* Substituting the values of the coefficients into equations 17.50, 17.56, and 17.57, we obtain

$$(0.32505 \cdot 10^{-6}) p_4 + (25.000/57.2958) = 0.79486 \tag{d}$$

$$2816.2 V_4 + p_4 = 6.0235 \cdot 10^6 \tag{e}$$

$$p_4 - (0.85381 \cdot 10^6)\rho_4 = -232.08 \cdot 10^3 \tag{f}$$

Solving equations (d), (e), and (f) yields

$$p_4 = 11.030 \cdot 10^5 \text{ N/m}^2 \qquad V_4 = 1747.2 \text{ m/s} \qquad \rho_4 = 1.5637 \text{ kg/m}^3$$

Column (0) in Table 17.9 summarizes the results of the predictor calculations.
(f) *Application of the corrector.* The modified Euler corrector is applied by repeating steps (c) to (e) employing the average values of the flow properties, as illustrated in Example 17.1. Column (1) in Table 17.9 presents the results obtained for the corrector. The results of two iterations of the corrector are presented in columns (2) and (3) of Table 17.9. Iteration of the corrector has only a very minor effect on the final solution.

17–4(e) Axis of Symmetry Point

The unit process for determining an axis of symmetry point in a steady two-dimensional rotational supersonic flow is analogous to that employed for determining a direct wall point described in Section 17–4(c). For an axis of symmetry point, however, there are the additional conditions that $y_4 = \theta_4 = 0$. Figure 17.7 illustrates schematically the unit process for an axis of symmetry point (point 4). For an axis of symmetry point, the coefficient S (see equation 17.42) is indeterminant on the axis itself. During the predictor pass, S is calculated at point 1 where it is nonzero, and during the corrector passes, S is based on the average values of sin θ and y, each of which is nonzero.

Subroutine AXIS presented below determines an axis of symmetry point in a steady two-dimensional isentropic rotational supersonic flow field.

```
      SUBROUTINE AXIS
C     SUBROUTINE AXIS CALCULATES THE SOLUTION AT AN AXIS POINT
      COMMON /CONTRL/ DELTA,NI,NT,ICOR,E1,E2,E3,E4,E5,IUNITS,PI,RAD
      COMMON /PROPTY/ G,RG,CP,TS,PS,PA,GC,GL $ REAL M
      COMMON /DATA/ X1,Y1,U1,V1,Q1,A1,P1,R1,T1,M1,X2,Y2,U2,V2,Q2,A2,P2,
     1R2,T2,M2,X3,Y3,U3,V3,Q3,A3,P3,R3,T3,M3,X4,Y4,U4,V4,Q4,A4,P4,R4,T4,
     2M4,LP,LM,LE,L12,L0 $ REAL M1,M2,M3,M4,LP,LM,LE,L12,L0
```

```
C     CALCULATE THE COEFFICIENTS FOR THE PREDICTOR

      ITER=0 $ Q4=Q3 $ P4=P3 $ R4=R3 $ CALL THERMC (Q1,P1,R1,T,C,M)
      LM=TAN(A1-ASIN(1.0/M)) $ QM=GC*SQRT(M**2-1.0) /(R1*Q1**2)
      SM=DELTA*SIN(A1)/(Y1*M*COS(A1-ASIN(1.0/M))) $ A4=0.0 $ Y4=0.0

C     SOLUTION OF THE FINITE DIFFERENCE EQUATIONS

   10 X4=X1-Y1/LM $ TM=-SM*(X4-X1)+QM*P1-A1 $ P=0.5*(F3+P4)
      R=0.5*(R3+R4) $Q=0.5*(Q3+Q4) $RO=R*Q/GC $ CALL THERMO(Q,P,R,T,C,M)
      A0=C**2/GC $ T01=R0*Q3+P3 $ T02=P3-A0*R3
      P4=(TM-A4)/QM $ Q4=(T01-P4)/R0 $ R4=(P4-T02)/A0

C     CHECK FOR CONVERGENCE OR COMPLETION OF SPECIFIED ITERATIONS

      IF (ITER.EQ.ICOR) RETURN $ IF (ITER.EQ.0) GO TO 20
      IF ((ABS(X4-XD).GT.E1).OR.(ABS(Q4-QD).GT.E4*QD)) GO TO 20
      IF ((ABS(P4-PD).LT.E2*PD).AND.(ABS(R4-RD).LT.E3*RD)) RETURN

C     CALCULATE THE COEFFICIENTS FOR THE CORRECTOR

   20 ITER=ITER+1 $ PD=P4 $ RD=R4 $ QD=Q4 $ XD=X4
      P=0.5*(P1+P4) $ R=0.5*(R1+R4) $ Q=0.5*(Q1+Q4) $ A=0.5*(A1+A4)
      Y=0.5*(Y1+Y4) $ CALL THERMO (Q,P,R,T,C,M) $ LM=TAN(A-ASIN(1.0/M))
      SM=DELTA*SIN(A)/(Y*M*COS(A-ASIN(1.0/M)))
      QM=GC*SQRT(M**2-1.0)/(R*Q**2) $ GO TO 10
      END
```

Example 17.4. Solve Example 16.4 by applying the unit process for an axis point for rotational flow. The unit process is illustrated schematically in Fig. 17.7.

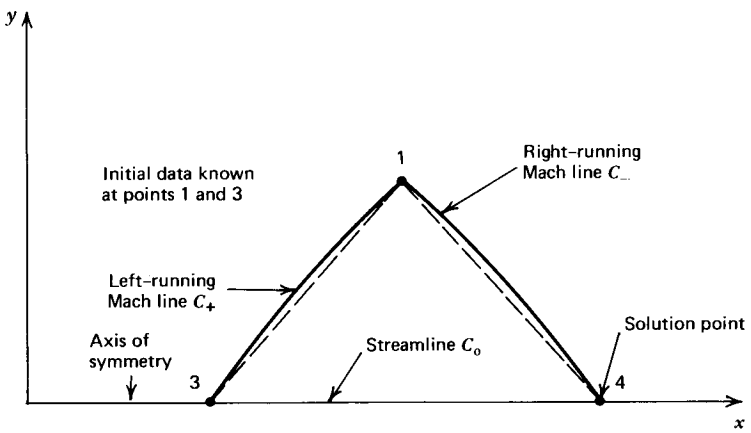

Figure 17.7 Unit process for an axis of symmetry point.

Solution

The initial data at point 1 are calculable from those given in Example 16.4 by applying equations (a) to (e) of Example 17.1. The flow properties must also be known at a previously determined point along the axis of symmetry, point 3 in Fig. 17.7. The initial data at points 1 and 3 are presented in Table 17.10. The numerical calculations are presented below for the predictor. The results are summarized in Table 17.11.

Table 17.10 Initial-Value Data (Example 17.4)

	Point 1	Point 3
x, mm	79.625	76.195
y, mm	1.290	0.000
V, m/s	2306.3	2280.4
θ, deg	0.8866	0.0000
p, N/m$^2\cdot 10^5$	1.7025	1.9077
ρ, kg/m^3	0.32947	0.36225

Table 17.11 Values of the Solution, for Successive Trials, for the Axis of Symmetry Unit Process (Example 17.4)

	(0)	(1)	(2)	(3)
λ_-	−0.34585	−0.35007	−0.35039	−0.35033
x_4, mm	83.355	83.310	83.307	83.307
R_o, N-s/m^3	826.07	760.84	762.06	762.14
$A_o\cdot 10^{-6}$, N-m/kg	0.63195	0.61963	0.62120	0.62103
$T_{o1}\cdot 10^{-6}$, N/m^2	2.0746	1.9258	1.9286	1.9287
$T_{o2}\cdot 10^{-3}$, N/m^2	−38.154	−33.692	−34.260	−34.199
$Q_-\cdot 10^6$, m^2/N	1.5708	1.6537	1.6486	1.6486
S_-, m^{-1}	4.3335	4.2919	4.2957	4.2950
T_-, unitless	0.23579	0.25025	0.24938	0.24939
p_4, N/m$^2\cdot 10^5$	1.5011	1.5133	1.5127	1.5127
V_4, m/s	2329.6	2332.2	2332.2	2332.2
$\rho_4\cdot 10^3$, kg/m^3	0.29791	0.29860	0.29866	0.29865

Column (0)—predictor values. Column (2)—first iteration of the corrector.
Column (1)—corrector values. Column (3)—second iteration of the corrector.

(a) *The speed of sound equation.* From equation (f) of Example 17.1,

$$a=\left(\frac{1.2p}{\rho}\right)^{1/2} \tag{a}$$

(b) *Flow properties at point 1.*

$$a_1=\left[\frac{1.2(1.7025\cdot 10^5)}{(0.32947)}\right]^{1/2}=787.46 \text{ m/s}$$

$$M_1=\frac{2306.3}{787.46}=2.9288$$

$$\alpha_1=\sin^{-1}\left(\frac{1}{2.9288}\right)=19.964 \text{ deg}$$

(c) *Calculation of the coefficients along right-running Mach line 14 for the predictor.*

From equations 17.48 and 17.55

$$\lambda_- = \tan(0.887 - 19.964) = -0.34585$$

$$Q_- = \frac{\left[(2.9288)^2 - 1\right]^{1/2}}{(0.32947)(2306.3)^2} = 1.5708 \cdot 10^{-6} \text{ m}^2/\text{N}$$

$$S_- = \frac{\sin(0.8866)}{(0.001290)(2.9288)\cos(0.887 - 19.964)} = 4.3335 \text{ m}^{-1}$$

(d) *Determination of x_4 for the predictor.* From equation 17.45,

$$0.0 - (-0.34585)x_4 = 1.290 - (-0.34585)(79.625) \tag{b}$$

Solving equation (b), we obtain $x_4 = 83.355$ mm. From equation 17.53,

$$T_- = -(4.3335)(0.083355 - 0.079625) + (1.5708 \cdot 10^{-6})(1.7025 \cdot 10^5) - (0.8866/57.2958) = 0.23579$$

(e) *Calculation of the coefficients along the streamline 34 for the predictor.* From equations (a), 17.58, 17.56, and 17.57,

$$a_3 = \left[\frac{1.2(1.9077 \cdot 10^5)}{(0.36225)}\right]^{1/2} = 794.95 \text{ m/s}$$

$$R_o = (0.36225)(2280.4) = 826.07 \text{ N-s/m}^3$$

$$A_o = (794.95)^2 = 0.63195 \cdot 10^6 \text{ N-m/kg}$$

$$T_{o1} = (826.07)(2280.4) + 1.9077 \cdot 10^5 = 2.0746 \cdot 10^6 \text{ N/m}^2$$

$$T_{o2} = 1.9077 \cdot 10^5 - (0.63195 \cdot 10^6)(0.36225) = -38.145 \cdot 10^3 \text{ N/m}^2$$

(f) *Determination of p_4, V_4, and ρ_4 for the predictor.* Substituting the above values of the coefficients into equations 17.51, 17.56, and 17.57, we obtain

$$(1.5708 \cdot 10^{-6})p_4 + 0.0 = 0.23579 \tag{c}$$

$$826.07 V_4 + p_4 = 2.0746 \cdot 10^6 \tag{d}$$

$$p_4 - (0.63195 \cdot 10^6)\rho_4 = -38.145 \cdot 10^3 \tag{e}$$

Solving equations (c), (d), and (e) gives

$$p_4 = 1.5011 \cdot 10^5 \text{ N/m}^2 \qquad V_4 = 2329.6 \text{ m/s} \qquad \rho_4 = 0.29791 \text{ kg/m}^3$$

The predictor calculations are summarized in column (0) of Table 17.11.

(g) *Application of the corrector.* For the application of the modified Euler corrector, average values of the flow properties are employed and steps (b) to (f) are repeated, as illustrated in Example 17.1. Column (1) in Table 17.11 summarizes the corrector calculations. Columns (2) and (3) in Table 17.11 present the results of two iterations of the corrector. It is evident that repetitive application of the corrector has little influence on the final results.

17-4(f) Free Pressure Boundary Point

Figure 17.8 illustrates the procedure for determining a point on the boundary of a supersonic two-dimensional free jet, where the static pressure is equal to the ambient pressure [see Section 16–3(f)]. It is assumed that there is no diffusion of gas from the surroundings into the gaseous jet, and vice versa. For an isentropic flow, the velocity and density along each streamline are unique functions of the pressure. Consequently, on the boundary of a free jet, the magnitudes of the pressure, density, and velocity remain constant; that is, the flow properties at any point on the boundary are the same as those at point 3. Accordingly, the problem reduces to that for determining the location of point 4 and the value of θ_4.

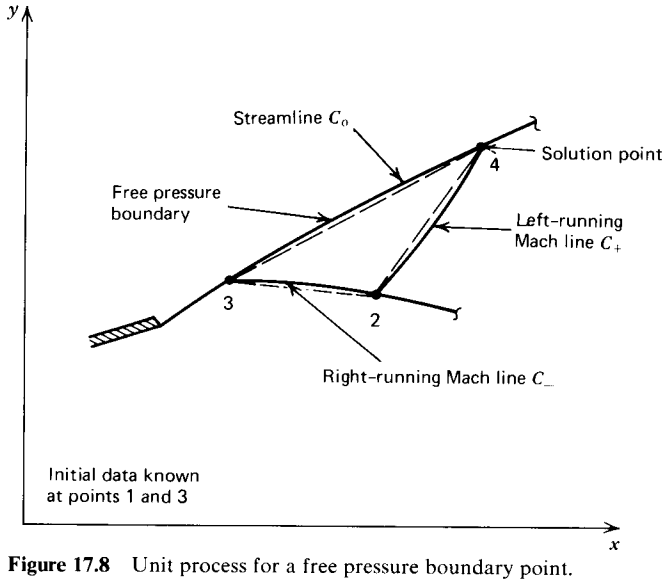

Figure 17.8 Unit process for a free pressure boundary point.

The boundary of a free jet is a streamline, specified by equation 17.43, which is repeated below for convenience.

$$y_3 - \lambda_o x_3 = y_4 - \lambda_o x_4 \tag{17.43}$$

In Fig. 17.8, left-running Mach line 24 is specified by equation 17.44. Thus,

$$y_4 - \lambda_+ x_4 = y_2 - \lambda_+ x_2 \tag{17.44}$$

Equations 17.43 and 17.44 may be solved simultaneously to obtain x_4 and y_4. The value of θ_4 is determined by means of equation 17.50, which is repeated below. Thus,

$$\theta_4 = T_+ - Q_+ p_4 \tag{17.50}$$

A FORTRAN computer program, subroutine JET, for implementing the unit process for a free pressure boundary point is presented below.

Example 17.5. Solve Example 16.5 employing the unit process for a free pressure boundary point for rotational flow. Figure 17.8 is a schematic illustration of the unit process, and Table 17.12 presents the initial-value data.

```
      SUBROUTINE JET

C     SUBROUTINE JET CALCULATES THE SOLUTION AT A JET BOUNDARY POINT

      COMMON /CONTRL/ DELTA,NI,NT,ICOR,E1,E2,E3,E4,E5,IUNITS,PI,RAD
      COMMON /PROPTY/ G,RG,CP,TS,PS,PA,GC,GL $ REAL M
      COMMON /DATA/ X1,Y1,U1,V1,Q1,A1,P1,R1,T1,M1,X2,Y2,U2,V2,Q2,A2,P2,
     1R2,T2,M2,X3,Y3,U3,V3,Q3,A3,P3,R3,T3,M3,X4,Y4,U4,V4,Q4,A4,P4,R4,T4,
     2M4,LP,LM,LE,L12,L0 $ REAL M1,M2,M3,M4,LP,LM,LE,L12,L0

C     CALCULATE THE COEFFICIENTS FOR THE PREDICTOR

      ITER=0 $ Q4=Q3 $ P4=P3 $ R4=R3 $ CALL THERMC (Q2,P2,R2,T,C,M)
      LP=TAN(A2+ASIN(1.0/M)) $ QP=GC*SQRT(M**2-1.0)/(R2*Q2**2)
      SP=DELTA*SIN(A2)/(Y2*M*COS(A2+ASIN(1.0/M))) $ L0=TAN(A3)

C     SOLUTION OF THE FINITE DIFFERENCE EQUATIONS

   10 X4=(Y3-Y2-L0*X3+LP*X2)/(LP-L0) $ Y4=Y3+L0*(X4-X3)
      TP=-SP*(X4-X2)+QP*P2+A2 $ A4=TP-QP*P4

C     CHECK FOR CONVERGENCE OR COMPLETION OF SPECIFIED ITERATIONS

      IF (ITER.EQ.ICOR) RETURN $ IF (ITER.EQ.0) GO TO 20
      IF ((ABS(X4-XD).GT.E1).OR.(ABS(Y4-YD).GT.E1)) GO TO 20
      IF (ABS(A4-AD).LT.E5*AD) RETURN

C     CALCULATE THE COEFFICIENTS FOR THE CORRECTOR

   20 ITER=ITER+1 $ AD=A4 $ XD=X4 $ YD=Y4 $ P=0.5*(P2+P4)
      R=0.5*(R2+R4) $ Q=0.5*(Q2+Q4) $ A=0.5*(A2+A4) $ Y=0.5*(Y2+Y4)
      CALL THERMO (Q,P,R,T,C,M) $ LP=TAN(A+ASIN(1.0/M))
      SP=DELTA*SIN(A)/(Y*M*COS(A+ASIN(1.0/M))) $ A=0.5*(A3+A4)
      QP=GC*SQRT(M**2-1.0)/(R*Q**2) $ L0=TAN(A) $ GO TO 10
      END
```

Table 17.12 Initial-Value Data (Example 17.5)

	Point 2	Point 3
x, m	0.34225	0.32979
y, m	0.12312	0.12351
V, m/s	2532.3	2511.7
θ, deg	14.165	15.317
p, N/m^2	53,164	60,000
ρ, kg/m^3	0.12491	0.13813

Solution

The initial data presented in Table 17.12 are calculated from the data in Example 16.5 by applying equations (a) to (e) of Example 17.1. The calculations for the predictor are presented below. The results of those calculations and those for three applications of the corrector are presented in Table 17.13.

On the boundary of a free jet, the pressure, density, and velocity of the fluid are constant and equal to their respective values at point 3. Thus,

$$p_4 = 60{,}000 \text{ N/m}^2 \qquad V_4 = 2511.7 \text{ m/s} \qquad \rho_4 = 0.13813 \text{ kg/m}^3$$

All that remains is to determine the location of point 4 and the value of θ_4.

Table 17.13 Values of the Solution, for Successive Trials, for a Free Pressure Boundary Point (Example 17.5)

	(0)	(1)	(2)	(3)
λ_+	0.59040	0.56952	0.57162	0.57155
λ_o	0.27389	0.24351	0.24519	0.24513
x_4, m	0.35428	0.35277	0.35282	0.35282
y_4, m	0.13022	0.12911	0.12916	0.12916
$Q_+ \cdot 10^6$, m^2/N	4.2439	4.0221	4.0221	4.0221
S_+, m^{-1}	0.65141	0.58707	0.59422	0.59395
T_+, unitless	0.46502	0.45488	0.45478	0.45478
θ_4, deg	12.054	12.236	12.230	12.230

Column (0)—predictor values. Column (2)—first iteration of the corrector.
Column (1)—corrector values. Column (3)—second iteration of the corrector.

(a) *The speed of sound equation.* From equation (f) of Example 17.1,

$$a = \left(\frac{1.2p}{\rho} \right)^{1/2} \tag{a}$$

(b) *Flow properties at point 2.*

$$a_2 = \left[\frac{1.2(53{,}164)}{(0.12491)} \right]^{1/2} = 714.66 \text{ m/s}$$

$$M_2 = \frac{2532.3}{714.66} = 3.5434$$

$$\alpha_2 = \sin^{-1}\left(\frac{1}{3.5434} \right) = 16.393 \text{ deg}$$

(c) *Calculation of the coefficients along Mach line 24 for the predictor.* From equations 17.47 and 17.54,

$$\lambda_+ = \tan(14.165 + 16.393) = 0.59040$$

$$Q_+ = \frac{\left[(3.5434)^2 - 1 \right]^{1/2}}{(0.12491)(2532.3)^2} = 4.2439 \cdot 10^{-6} \text{ m}^2/\text{N}$$

$$S_+ = \frac{\sin(14.165)}{(0.012312)(3.5434)\cos(14.165 + 16.393)} = 0.65141 \text{ m}^{-1}$$

Along the jet boundary 34,

$$\lambda_o = \tan(\theta_3) = \tan(15.317) = 0.27389$$

(d) *Determination of x_4, y_4, and θ_4 for the predictor.* From equations 17.43 and 17.44,

$$y_4 - (0.27389)x_4 = 0.12351 - (0.27389)(0.32979) \tag{b}$$

$$y_4 - (0.59040)x_4 = 0.12312 - (0.59040)(0.34226) \tag{c}$$

Solving for x_4 and y_4, we obtain

$$x_4 = 0.35428 \text{ m} \qquad y_4 = 0.13022 \text{ m}$$

From equation 17.52,

$$T_+ = -(0.65141)(0.35428 - 0.34226) + (4.2439 \cdot 10^{-6})(53{,}164) + (14.165/57.2958)$$

$$T_+ = 0.46502$$

Substituting the values of Q_+ and T_+ into equation 17.50 yields

$$(4.2439 \cdot 10^{-6})(60{,}000) + \theta_4 = 0.46502 \qquad \text{(d)}$$

from which $\theta_4 = 12.054$ deg. Column (0) in Table 17.13 presents the results obtained by applying the predictor.

(e) *Application of the corrector.* The modified Euler corrector is applied by repeating steps (b) to (d) employing the average values of the flow properties, as illustrated in Example 17.1. Column (1) in Table 17.13 presents the results obtained by applying the corrector. Columns (2) and (3) in Table 17.13 present the results of two iterations of the corrector. Iteration of the corrector has only a very minor effect on the flow properties at point 4.

17–4(g) External Shock Wave Point

A practical example of a steady two-dimensional rotational supersonic flow field is the flow field downstream from the curved shock wave formed in front of a two-dimensional body moving with supersonic speed in atmospheric air. Figure 17.9 illustrates schematically two models for the aforementioned flow situation.

If the nose of the moving body is sharp, as illustrated schematically in Fig. 17.9*a*, the shock wave may be attached to the tip of the nose. In the supersonic flow field behind the attached shock wave, a right-running Mach line is shown emanating

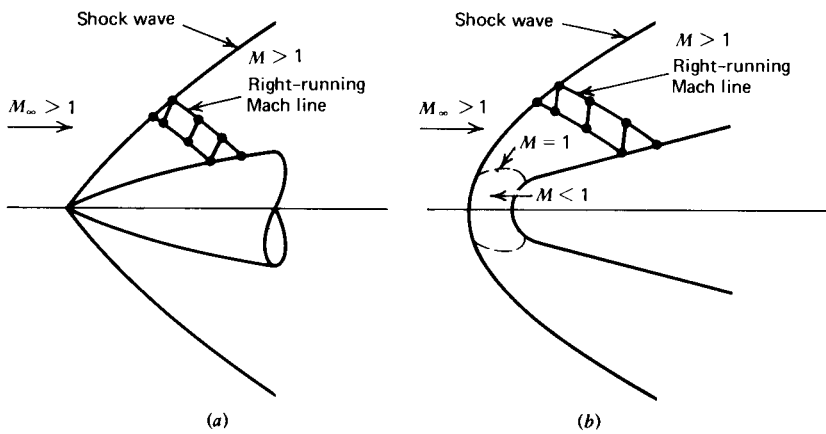

Figure 17.9 Shock wave formed by a body moving at supersonic speeds. (*a*) Attached shock wave. (*b*) Detached shock wave.

from the shock wave and extending to the body. If the nose of the body is blunt, as illustrated schematically in Fig. 17.9*b*, the shock wave is detached from the moving body, and a subsonic flow field is formed in the region immediately upstream from the blunt nose of the body. The flow field downstream from the subsonic flow region is supersonic, and a right-running Mach line is shown in that supersonic flow field. Because of their curvatures, the strengths of the shock waves illustrated in Figs. 17.9*a* and 17.9*b* decrease in the direction away from the surface of the moving body. Consequently, each streamline passing through the shock wave has its entropy increased by a different amount causing an entropy gradient. Thus, the supersonic flow that is irrotational upstream from the shock wave becomes rotational downstream from the shock wave. The stagnation enthalpy on each streamline, however, remains constant.

Figure 17.10 illustrates schematically the unit process for determining an *external shock wave point*. Point 1 is a known point on the downstream side of the shock wave, and point 2 is a known point on the previous right-running Mach line 12. The flow properties M_∞, V_∞, p_∞, ρ_∞, and θ_∞ of the free stream are known. Point 4, on the downstream side of the shock wave, is the external shock wave point. It is located at the intersection of the shock wave from point 1 and the left-running Mach line 24. The slope of the shock wave 14 is based on the average value of the two wave angles ε_1 and ε_4 at the points 1 and 4, respectively. The latter wave angles are functions of the free-stream Mach number M_∞ and the flow turning angles θ_1 and θ_4. M_∞, θ, and ε may be related by the procedures presented in Sections 7–7 and 7–8.

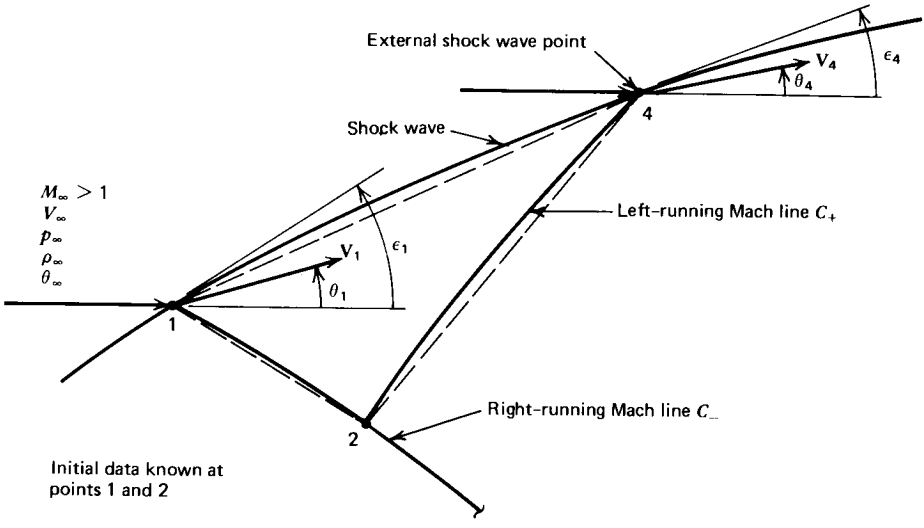

Figure 17.10 Unit process for an external shock wave point.

An iterative procedure is required for determining the location of point 4 and the flow properties at that point. A value is assumed for the wave angle ε_4 at point 4. The equation for the shock wave 14 is

$$y_4 - y_1 = \lambda_S (x_4 - x_1) = \tan\left(\frac{\varepsilon_1 + \varepsilon_4}{2}\right)(x_4 - x_1) \tag{17.69}$$

The equation of the left-running Mach line 24 is

$$y_4 - y_2 = \lambda_+ (x_4 - x_2) \tag{17.70}$$

The location of point 4 is obtained by solving equations 17.69 and 17.70 simultaneously for x_4 and y_4.

From the given values of the free-stream properties (i.e., M_∞, p_∞, ρ_∞, etc.) and the assumed value of the wave angle ε_4, the flow properties at point 4 on the downstream side of the shock wave may be calculated by the methods presented in Sections 7–7 and 7–8. The single compatibility equation valid along the left-running Mach line 24 (i.e., equation 17.50) must also be satisfied. Since all of the flow properties at point 4 are determinable from the solution for the oblique shock wave and all of the flow properties at point 2 are known, the application of the compatibility equation along Mach line 24 determines the correctness of the assumed value for ε_4.

One approach for checking the correctness of ε_4 is to substitute the value of θ_4 obtained from the solution for the oblique shock wave for the assumed value of ε_4 into equation 17.50, and then to solve the latter equation for the corresponding value of $p_{4,\mathrm{LRC}}$; the subscript LRC denotes that the value of p_4 is determined along the left-running characteristic 24. The latter value for p_4 may then be compared with the value of $p_{4,S}$ determined from the analysis of the oblique shock wave. If $p_{4,\mathrm{LRC}}$ differs from $p_{4,S}$ by less than some prescribed tolerance, the assumed value of ε_4 is acceptable. If not, a new value for ε_4 is selected, and the entire procedure is repeated until convergence of the two values for p_4 occurs.

It is convenient to choose $\varepsilon_4 = \varepsilon_1$ as the *first* trial value for ε_4. The *second* trial value for ε_4 may be either some arbitrary perturbation about ε_1, for example, $0.99\varepsilon_1$, or it may be determined by solving the oblique shock wave relationships for the shock angle required for obtaining a pressure ratio across the shock wave equal to $p_{4,\mathrm{LRC}}/p_\infty$, assuming that the other flow properties remain constant. In either case, the entire procedure is repeated with the second trial value for ε_4, and the corresponding values of $p_{4,\mathrm{LRC}}$ and $p_{4,S}$ are calculated. In this manner, two sets of values for ε_4 and $\Delta p_4 = p_{4,\mathrm{LRC}} - p_{4,S}$ are calculated. The secant method discussed in Appendix A–4(b) may be employed for predicting the value of ε_4 that corresponds to $\Delta p_4 = 0$. Due to the nonlinear nature of the governing equations, that value of ε_4 will not be exact, so that it may be necessary to repeat the application of the secant method until the value of Δp_4 is within an acceptable tolerance.

The procedure described above for determining the location and the flow properties at an external shock wave point is relatively straightforward. For nonuniform free-stream conditions, the procedure is similar, except that the values of the free-stream properties at point 4 vary with the location of that point.

A FORTRAN computer program, subroutine SHOCK, for implementing the external shock wave point is presented below. The terminology is consistent with the terminology employed in the other programs presented in this section. The shock wave angle ε is denoted by EPS. The thermodynamic properties of the fluid are specified by subroutine THERMO presented in Section 17–4(b). The properties behind the shock wave (i.e., V_4, θ_4, p_4, and ρ_4) are determined by subroutine SHCK from the known upstream properties (i.e., M_∞, V_∞, θ_∞, p_∞, and ρ_∞) and the local shock wave angle ε_4. Subroutine THERMO presented in Section 17–4(b) and subroutine SHCK presented below are applicable to a perfect gas. Subroutine SHCK is based on the analysis presented in Section 7–7. Other equations of state may be considered by replacing subroutines THERMO and SHCK with appropriate programs.

```
      SUBROUTINE SHOCK (EPS1,EPS4)

C     SUBROUTINE SHOCK CALCULATES THE SOLUTION AT AN EXTERNAL SHOCK WAVE

      COMMON /CONTRL/ DELTA,NI,ICOR,E1,E2,E3,E4,E5,IUNITS,PI,RAD
      COMMON /PROPTY/ G,RG,CP,TS,PS,PA,GC,GL $ REAL M,MU,LS
      COMMON /SHK/ MU,PU,TU,RU,QU,EPS
      COMMON /DATA/ X1,Y1,U1,V1,Q1,A1,P1,R1,T1,M1,X2,Y2,U2,V2,Q2,A2,P2,
     1R2,T2,M2,X3,Y3,U3,V3,Q3,A3,P3,R3,T3,M3,X4,Y4,U4,V4,Q4,A4,P4,R4,T4,
     2M4,LP,LM,LE,L12,L0 $ REAL M1,M2,M3,M4,LP,LM,LE,L12,L0

      ITER=0 $ EPS4=EPS1 $ G1=(G+1.0)/2.0/G $ G2=(G-1.0)/2.0/G
   10 CALL SHOCK (EPS4) $ P4S=P4 $ LS=TAN(0.5*(EPS1+EPS4))
      Q=0.5*(Q2+Q4) $ P=0.5*(P2+P4) $ R=0.5*(R2+R4) $ A=0.5*(A2+A4)
      CALL THERMO (Q,P,R,T,C,M) $ LP=TAN(A+ASIN(1.0/M))
      X4=(Y1-Y2-LS*X1+LP*X2)/(LP-LS) $ Y4=Y1+LS*(X4-X1) $ Y=0.5*(Y2+Y4)
      QP=GC*SQRT(M**2-1.0)/(R*Q**2)
      SP=DELTA*SIN(A)/(Y*M*COS(A+ASIN(1.0/M))) $ TP=-SP*(X4-X2)+QP*P2+A2
      P4LRC=(TP-A4)/QP $ DP=P4LRC-P4S

C     CHECK FOR CONVERGENCE

      IF (ABS(DP).LT.E2) GO TO 30 $ IF (ITER.EQ.ICOR) GO TO 30
      IF (ITER.GT.0) GO TO 20 $ ES=EPS4 $ DPS=DP
      EPS4=ASIN(SQRT(G1*P4LRC/PU+G2)/MU) $ ITER=ITER+1 $ GO TO 10
   20 SLOPE=(DP-DPS)/(EPS4-ES) $ DE=-DP/SLOPE $ ES=EPS4 $ DPS=DP
      EPS4=EPS4+DE $ ITER=ITER+1 $ GO TO 10

C     LOCATE POINT 3 MIDWAY BETWEEN POINTS 2 AND 4

   30 DEL=0.5 $ X3=X2+DEL*(X4-X2) $ Y3=Y2+DEL*(Y4-Y2) $Q3=Q2+DEL*(Q4-Q2)
      A3=A2+DEL*(A4-A2) $ P3=P2+DEL*(P4-P2) $ R3=R2+DEL*(R4-R2) $ RETURN
      END


      SUBROUTINE SHOCK (E)

C     SUBROUTINE SHOCK CALCULATES PROPERTY RATIOS FOR OBLIQUE SHOCK WAVE

      COMMON /CONTRL/ DELTA,NI,ICOR,E1,E2,E3,E4,E5,IUNITS,PI,RAD
      COMMON /PROPTY/ G,RG,CP,TS,PS,PA,GC,GL $ REAL M,MN,MU
      COMMON /SHK/ MU,PU,TU,RU,QU,EPS
      COMMON /DATA/ X1,Y1,U1,V1,Q1,A1,P1,R1,T1,M1,X2,Y2,U2,V2,Q2,A2,P2,
     1R2,T2,M2,X3,Y3,U3,V3,Q3,A3,P3,R3,T3,M3,X4,Y4,U4,V4,Q4,A4,P4,R4,T4,
     2M4,LP,LM,LE,L12,L0 $ REAL M1,M2,M3,M4,LP,LM,LE,L12,L0

      SINE=SIN(E) $ TANE=TAN(E) $ MN=(MU*SINE)**2
      TANB=TANE*2.0/(G+1.0)*(1.0/MN+(G-1.0)/2.0) $ BETA=ATAN(TANB)
      SINB=SIN(BETA) $ A4=E-BETA
      Q4=QU*SINE/SINB*(2.0/(G+1.0)/MN+(G-1.0)/(G+1.0))
      P4=PU*2.0*G/(G+1.0)*(MN-(G-1.0)/2.0/G) $ R4=RU*TANE/TANB $ RETURN
      END
```

Example 17.6. A supersonic air stream is flowing over a symmetrical two-dimensional, planar, pointed body similar to the one illustrated schematically in Fig. 17.9*a*. The free-stream flow properties and the flow properties at points 1 and 2 illustrated in Fig. 17.10 are given in Table 17.14. Assume that the air behaves as a perfect gas with $\gamma = 1.40$ and $R = 287.04$ J/kg-K. Apply the unit process for an external shock wave point to determine the location and flow properties at point 4.

Solution

The calculations are presented below for the first and second trial values for ε_4. Those results and the results for two additional values of ε_4 are summarized in Table 17.15.

Table 17.14 Initial-Value Data (Example 17.6)

	Free-stream	Point 1	Point 2
x, m	—	0.22113	0.26991
y, m	—	0.28317	0.26988
V, m/s	1041.6	691.51	697.16
θ, deg	0.000	30.000	29.536
p, $N/m^2 \cdot 10^5$	1.0	6.3559	6.2132
ρ, kg/m^3	1.1613	3.6782	3.6189
t, K	300.0	—	—
M	3.0	—	—
ε, deg	—	52.014	—

Table 17.15 Values of the Solution, for Successive Trials, for the External Shock Wave Point Unit Process (Example 17.6)

	(1)	(2)	(3)	(4)
ε_4, deg	52.014	50.420	51.197	51.193
V_4, m/s	691.51	712.41	702.26	702.31
θ_4, deg	30.000	29.106	29.550	29.548
p_4, $N/m^2 \cdot 10^5$	6.3559	6.0707	6.2102	6.2095
ρ_4, kg/m^3	3.6782	3.6004	3.6389	3.6387
λ_S	1.2806	1.2445	1.2619	1.2619
λ_+	3.6754	3.3018	3.4737	3.4727
x_4, m	0.30154	0.30588	0.30375	0.30376
y_4, m	0.38615	0.38862	0.38743	0.38744
$Q_+ \cdot 10^6$, m^2/N	0.56829	0.58100	0.57482	0.57485
T_+, unitless	0.86859	0.87649	0.87265	0.87267
$p_{4,\mathrm{LRC}}$, $N/m^2 \cdot 10^5$	6.0707	6.3423	6.2088	6.2095
Δp, N/m^2	−28,524	27,162	−142	−0.68

(a) *The speed of sound equation.* From equation (f) of Example 17.1,

$$a = \left(\frac{1.4p}{\rho} \right)^{1/2} \tag{a}$$

(b) *Flow properties at point 4.* The flow properties at point 4, immediately after the shock wave, depend only on the upstream flow properties and the shock wave angle ε_4. The flow property ratios across an oblique shock wave for a perfect gas are given by equations 7.90 to 7.92 in Section 7–7(b). Those equations are repeated below for convenience.

$$\frac{p_{4,S}}{p_\infty} = \frac{2\gamma}{\gamma+1}\left(M_\infty^2 \sin^2\varepsilon - \frac{\gamma-1}{2\gamma} \right) \tag{7.90}$$

$$\frac{\rho_\infty}{\rho_4} = \frac{\tan\beta}{\tan\varepsilon} = \frac{2}{\gamma+1}\left(\frac{1}{M_\infty^2 \sin^2\varepsilon} + \frac{\gamma-1}{2} \right) \tag{7.91}$$

$$\frac{V_4}{V_\infty} = \frac{\sin\varepsilon}{\sin\beta}\left[\frac{2}{(\gamma+1)M_\infty^2 \sin^2\varepsilon} + \frac{\gamma-1}{\gamma+1} \right] \tag{7.92}$$

where ε is the shock wave angle, δ is the flow deflection angle, and $\beta = \varepsilon - \delta$ (see Fig. 7.16). For the special case considered here where $\theta_\infty = 0.0$, $\theta_4 = \delta_4$. For the first trial assume that $\varepsilon_4 = \varepsilon_1$, so that the flow properties at point 4 are the same as those at point 1.

(c) *Determination of x_4 and y_4 for the first trial.* For the first trial, the slope of the oblique shock wave 14 is based on the properties at point 1. Thus,

$$\lambda_S = \tan(\varepsilon_1) = \tan(52.014) = 1.2806$$

The slope of Mach line 24 is based on the average values of the flow properties at points 2 and 4, and the flow properties at point 4 are the same as those at point 1. Thus,

$$V_+ = \frac{V_2 + V_4}{2} = \frac{697.16 + 691.51}{2} = 694.34 \text{ m/s}$$

$$\theta_+ = \frac{29.536 + 30.000}{2} = 29.768 \text{ deg}$$

$$p_+ = \frac{(6.2132 + 6.3559)10^5}{2} = 6.2846 \cdot 10^5 \text{ N/m}^2$$

$$\rho_+ = \frac{3.6189 + 3.6782}{2} = 3.6486 \text{ kg/m}^3$$

$$a_+ = \left[\frac{1.4(6.2846)10^5}{3.6486} \right]^{1/2} = 491.07 \text{ m/s}$$

$$M_+ = \frac{V_+}{a_+} = \frac{694.34}{491.07} = 1.4139$$

$$\alpha_+ = \sin^{-1}\left(\frac{1}{M_+}\right) = \sin^{-1}\left(\frac{1}{1.4139}\right) = 45.011 \text{ deg}$$

$$\lambda_+ = \tan(\theta_+ + \alpha_+) = \tan(29.768 + 45.011) = 3.6754$$

From equations 17.69 and 17.70, we obtain

$$y_4 - 0.28317 = 1.2806(x_4 - 0.22113) \qquad \text{(b)}$$

$$y_4 - 0.26988 = 3.6754(x_4 - 0.26991) \qquad \text{(c)}$$

Solving equations (b) and (c) simultaneously yields

$$x_4 = 0.30154 \text{ m} \qquad y_4 = 0.38615 \text{ m}$$

(d) *Calculation of the coefficients along Mach line 24 for the first trial.* From equations 17.54 and 17.52, we obtain

$$Q_+ = \frac{\left[(1.4139)^2 - 1\right]^{1/2}}{(3.6486)(694.34)^2} = 0.56829 \cdot 10^{-6} \text{ m}^2/\text{N}$$

$S_+ = 0.0$ for two-dimensional, planar flow (i.e., $\delta = 0$)

$$T_+ = (0.56799 \cdot 10^{-6})(6.2132 \cdot 10^5) + (29.536/57.2958) = 0.86859$$

(e) *Determination of* $\Delta p = p_{4,\mathrm{LRC}} - p_{4,S}$ *for the first trial.* Substituting the values of the coefficients into equation 17.50 yields,

$$(0.56829 \cdot 10^{-6}) p_{4,\mathrm{LRC}} + (30.000/57.2958) = 0.86859 \tag{d}$$

Solving equation (d), we obtain $p_{4,\mathrm{LRC}} = 6.0707 \cdot 10^5$ N/m^2. Then,

$$\Delta p = p_{4,\mathrm{LRC}} - p_{4,S} = (6.0707 - 6.3559)10^5 = -28{,}524 \text{ N/m}^2$$

The first trial is complete. The results are summarized in column (1) of Table 17.15.

(f) *Determination of* ε_4 *for the second trial.* For the second trial, equation 7.90 is solved for the value of ε_4 corresponding to $p_4 = p_{4,\mathrm{LRC}}$ determined by the first trial. Thus,

$$\sin\varepsilon_4 = \left[\frac{\gamma+1}{2\gamma}\left(\frac{p_{4,\mathrm{LRC}}}{p_\infty}\right) + \frac{\gamma-1}{2\gamma}\right]^{1/2} \frac{1}{M_\infty}$$

$$\sin\varepsilon_4 = \left[\frac{2.4}{2.8}\left(\frac{6.0707}{1.0000}\right) + \frac{0.4}{2.8}\right]^{1/2}\left(\frac{1}{3.0}\right) = 0.77074$$

$$\varepsilon_4 = \sin^{-1}(0.77074) = 50.420 \text{ deg}$$

(g) *Flow properties at point 4.* For $\varepsilon_4 = 50.420$ deg,

$$\sin\varepsilon_4 = \sin(50.420) = 0.77074$$

$$\tan\varepsilon_4 = \tan(50.420) = 1.2097$$

From equation 7.91, we obtain

$$M_\infty^2 \sin^2\varepsilon_4 = (3.0)^2(0.77074)^2 = 5.3464$$

$$\tan\beta_4 = \frac{2\tan\varepsilon_4}{\gamma+1}\left(\frac{1}{M_\infty^2\sin^2\varepsilon_4} + \frac{\gamma-1}{2}\right)$$

$$\tan\beta_4 = \frac{2(1.2097)}{2.4}\left[\frac{1}{(3.0)^2(0.77074)^2} + \frac{0.4}{2}\right] = 0.39017$$

$$\beta_4 = \tan^{-1}(0.39017) = 21.314 \text{ deg}$$

$$\theta_4 = \delta_4 = \varepsilon_4 - \beta_4 = 50.420 - 21.314 = 29.106 \text{ deg}$$

From equations 7.90 to 7.92, we obtain

$$p_{4,S} = 1.0 \cdot 10^5\left(\frac{2.8}{2.4}\right)\left(5.3464 - \frac{0.4}{2.8}\right) = 6.0707 \cdot 10^5 \text{ N/m}^2$$

$$\rho_4 = 1.1613\left(\frac{2.4}{2}\right)\left(\frac{1}{5.3464} + \frac{0.4}{2}\right)^{-1} = 3.6004 \text{ kg/m}^3$$

$$V_4 = \frac{1041.6(0.77074)}{\sin(21.314)}\left[\frac{2}{2.4(5.3464)} + \frac{0.4}{2.4}\right] = 712.41 \text{ m/s}$$

(h) *Determination of x_4 and y_4 for the second trial.* Along shock wave 14,

$$\lambda_S = \tan\left(\frac{\varepsilon_1 + \varepsilon_4}{2}\right) = \tan\left(\frac{52.014 + 50.420}{2}\right) = 1.2445$$

Along Mach line 24,

$$V_+ = \frac{V_2 + V_4}{2} = \frac{697.16 + 712.41}{2} = 704.79 \text{ m/s}$$

$$\theta_+ = \frac{29.536 + 29.106}{2} = 29.321 \text{ deg}$$

$$p_+ = \frac{(6.2132 + 6.0707)10^5}{2} = 6.1420 \cdot 10^5 \text{ N/m}^2$$

$$\rho_+ = \frac{3.6189 + 3.6004}{2} = 3.6097 \text{ kg/m}^3$$

$$a_+ = \left[\frac{1.4(6.1420 \cdot 10^5)}{3.6097}\right]^{1/2} = 488.07 \text{ m/s}$$

$$M_+ = \frac{704.79}{488.07} = 1.4440$$

$$\alpha_+ = \sin^{-1}\left(\frac{1}{1.4440}\right) = 43.829 \text{ deg}$$

$$\lambda_+ = \tan(29.321 + 43.829) = 3.3018$$

From equations 17.69 and 17.70, we obtain

$$y_4 - 0.28317 = 1.2445(x_4 - 0.22113) \tag{e}$$

$$y_4 - 0.26988 = 3.3018(x_4 - 0.26991) \tag{f}$$

Solving equations (e) and (f) simultaneously gives

$$x_4 = 0.30588 \text{ m} \qquad y_4 = 0.38864 \text{ m}$$

(i) *Calculation of the coefficients along Mach line 24 for the second trial.* From equations 17.54 and 17.52, we obtain

$$Q_+ = \frac{\left[(1.4440)^2 - 1\right]^{1/2}}{(3.6097)(704.79)^2} = 0.58100 \cdot 10^{-6} \text{ m}^2/\text{N}$$

$$T_+ = (0.58100 \cdot 10^{-6})(6.2132 \cdot 10^5) + (29.536/57.2958) = 0.87649$$

(j) *Determination of Δp for the second trial.* From equation 17.50,

$$(0.58100 \cdot 10^{-6})p_{4,\text{LRC}} + (29.106/57.2958) = 0.87649$$

$$p_{4,\text{LRC}} = 6.3423 \cdot 10^5 \text{ N/m}^2$$

$$\Delta p = p_{4,\text{LRC}} - p_{4,S} = (6.3423 - 6.0707)10^5 = 27{,}160 \text{ N/m}^2$$

The second trial is complete. The results are summarized in column (2) of Table 17.15.

(k) *Determination of* ε_4 *for the third trial.* The third trial value of ε_4 is determined by applying the secant method [see Appendix A–4(b)] to the two pairs of $\varepsilon, \Delta p$ values. Thus,

$$\frac{\Delta p_3 - \Delta p_2}{\varepsilon_3 - \varepsilon_2} = \frac{\Delta p_2 - \Delta p_1}{\varepsilon_2 - \varepsilon_1} = \frac{27{,}160 - (-28{,}524)}{50.420 - 52.014} = -34{,}934 \frac{\text{N/m}^2}{\text{deg}} \qquad \text{(g)}$$

where the subscripts 1, 2, and 3 denote the first, second, and third trials, respectively. Solving equation (g) to determine the value of ε_3 that drives Δp_3 to zero, we obtain the third trial value for ε_4. Thus,

$$\varepsilon_4 = 50.420 - \frac{27{,}160}{-34{,}934} = 51.197 \text{ deg}$$

(l) *Subsequent trials for* ε_4. Columns (3) and (4) in Table 17.15 present the results of trials 3 and 4. The procedure presented above is truly a relaxation process to determine the value of ε_4. Consequently, three or four trials are always necessary to achieve a desired convergence tolerance.

17–5 APPLICATIONS OF STEADY TWO-DIMENSIONAL ISENTROPIC SUPERSONIC FLOW

There are many flows of engineering interest that are rotational, yet isentropic along the streamlines. Examples of isentropic rotational flows are nozzle flow where each streamline has a different stagnation enthalpy and pressure due to nonhomogeneous combustion, and the flow field behind a curved shock wave where, as pointed out in Section 17–4(g), the entropy along each streamline is different because of the variable strength of the curved oblique shock wave. Examples of such flows are discussed here.

17–5(a) Analysis of the Flow Field for a Nozzle of Known Shape

Consider a nozzle of known shape where the fluid has different values of the stagnation enthalpy and the stagnation pressure on each streamline. Such a flow field may be analyzed by employing the same overall procedure that is described in Section 16–4(a). The latter analysis is applicable to the steady two-dimensional irrotational supersonic flow in a nozzle of known shape. To apply the procedure of Section 16–4(a) to the rotational flow in a nozzle, the initial-value line must take into account the variable stagnation properties of the rotational flow. The unit processes for rotational flow, developed in Section 17–4, are then applicable. The direct marching method, following right- and left-running Mach lines, may be applied in the manner discussed in Section 16–4(a).

In the case of a rotational flow, the determination of the initial-value line is a more difficult problem than it is for an irrotational flow. Taulbee and Boraas[1] developed a linearized transonic solution in closed form for flows having a stagnation enthalpy gradient normal to the streamlines, but having a constant stagnation pressure. All other closed form solutions for the initial-value line for a rotational flow are based on some artificial modification of the initial-value line for an irrotational flow. An example of the latter artificial technique is employed in the

accuracy studies presented in Section 17–6. Methods that solve the full nonlinear governing equations in the subsonic and transonic regions of the flow field can take into account variations in the stagnation conditions between streamlines. Several such methods are discussed in Section 15–5(e).

A master logic program, program NOZZLE, for implementing the flow field analysis for a nozzle of known shape is presented in Section 16–4(a) for irrotational flow. That program is also directly applicable to rotational flow. The subroutine THERMO presented in Section 16–3(b) for irrotational flow (i.e., entropy uniform over the entire flow field) must be replaced by the subroutine THERMO presented in Section 17–4(b) for rotational flow (i.e., entropy constant only along streamlines). In addition, the subroutine MOVE presented in Section 16–4(a) must be replaced by the subroutine MOVE presented below. Subroutine IVLINE must, of course, determine the rotational flow initial-value line. The two programs are compatible in all other respects. In fact, the subroutine IVLINE presented in Section 15–5(c) for irrotational flow may be employed with the rotational flow unit process subroutines when the initial-value line is irrotational. In that case, the entire flow field remains irrotational, since for isentropic flow the rotation of the flow field remains constant (see Kelvin's theorem, Section 10–6).

The input parameters presented in Table 16.15 are applicable in the present case with the following modifications. E1 is the length convergence tolerance in absolute length units as before (e.g., meters), but E2 to E5 are fractional convergence tolerances for pressure, density, velocity magnitude, and flow angle, respectively. TS and PS apply only to the irrotational flow initial-value line program presented in Section 15–5(c), subroutine IVLINE.

The procedure presented here may be applied to a nozzle of any contour where there is a steady two-dimensional rotational flow for which there is a known (or determinable) initial-value line.

```
      SUBROUTINE MOVE (I,J)
C     SUBROUTINE MOVE TRANSFERS DATA TO AND FROM GRID POINTS AND ARRAYS
      COMMON /ARRAYS/ X(99),Y(99),U(99),V(99),Q(99),A(99),P(99),R(99)
      COMMON /DATA/ X1,Y1,U1,V1,Q1,A1,P1,R1,T1,M1,X2,Y2,U2,V2,Q2,A2,P2,
     1R2,T2,M2,X3,Y3,U3,V3,Q3,A3,P3,R3,T3,M3,X4,Y4,U4,V4,Q4,A4,P4,R4,T4,
     2M4,LP,LM,LE,L12,L0 $ REAL M1,M2,M3,M4,LP,LM,LE,L12,L0
      GO TO (10,20,30,40,50,60), I
   10 X1=X(J) $ Y1=Y(J) $ P1=P(J) $ R1=R(J) $ Q1=Q(J) $ A1=A(J) $ RETURN
   20 X2=X(J) $ Y2=Y(J) $ P2=P(J) $ R2=R(J) $ Q2=Q(J) $ A2=A(J) $ RETURN
   30 X3=X(J) $ Y3=Y(J) $ P3=P(J) $ R3=R(J) $ Q3=Q(J) $ A3=A(J) $ RETURN
   40 X4=X(J) $ Y4=Y(J) $ P4=P(J) $ R4=R(J) $ Q4=Q(J) $ A4=A(J) $ RETURN
   50 X(J)=X4 $ Y(J)=Y4 $ P(J)=P4 $ R(J)=R4 $ Q(J)=Q4 $ A(J)=A4
      U4=Q4*COS(A4) $ V4=Q4*SIN(A4) $ U(J)=U4 $ V(J)=V4
      CALL THERMO (Q4,P4,R4,T4,C,M4) $ RETURN
   60 X3=X2 $ Y3=Y2 $ P3=P2 $ R3=R2 $ Q3=Q2 $ A3=A2 $ RETURN
      END
```

17–5(b) Nozzle Design for Parallel Flow

For a rotational flow, a nozzle may be designed to furnish a parallel flow at the nozzle exit by the procedures discussed in Section 16–4(b) for wind tunnel design. However, since the stagnation properties may vary from streamline to streamline in a rotational flow, the exit flow will not be uniform. One property may be specified

on each streamline at the exit, for example, the Mach number or the static pressure, and the remaining flow properties are determined on each streamline from the equation of state for that streamline. Consequently, the exit flow field is neither unique nor uniform.

In general, the flow in a wind tunnel is irrotational, so there is little, if any, need to consider rotational flow in designing a uniform flow nozzle for a wind tunnel. In Section 16–4(c), a method is discussed for designing truncated parallel flow nozzles for propulsive applications. The same concept may be employed for designing truncated parallel flow nozzles for rotational flow fields by combining the numerical techniques for rotational flow, presented in Section 17–4, with the design methodology for uniform flow truncated nozzles presented in Section 16–4(b).

17–5(c) Nozzle Design for Maximum Thrust.

It is pointed out in Section 16–4(c) that a truncated parallel flow nozzle does not yield the maximum thrust attainable from a given nozzle length. The design method due to Rao,[2] presented in Section 16–4(c), determines the contour for a maximum thrust nozzle for a two-dimensional irrotational supersonic flow. Rao's method has been extended by Guderley[3] to the design of maximum thrust nozzles having two-dimensional supersonic flows with an entropy gradient normal to the streamlines.

A further extension by Guderley and Armitage[4] is based on the optimization of the entire flow region influenced by the nozzle wall. The domain of dependence of the nozzle wall is denoted as region R in Fig. 17.11. The analysis, however, is based on irrotational flow. Scofield and Hoffman[5] extended the analysis of Reference (4) to include rotational flow; consequently, a method is available for designing maximum thrust nozzles for rotational flow. The details of the method, due to space limitations, are not included in this book. Briefly, it involves applying the calculus of variations to a functional comprising all of the governing equations for region R (see Fig. 17.11), the thrust integral expressed along the nozzle wall IF, the equation of a streamline applied along IF, and a general design condition such as a constant nozzle surface area specified along IF. The application of the design equations requires that the two-dimensional rotational supersonic flow field be calculable for an assumed contour, which is then relaxed to obtain the *maximum thrust contour*. The method of analysis developed here for rotational flow is essential to the application of the design technique.

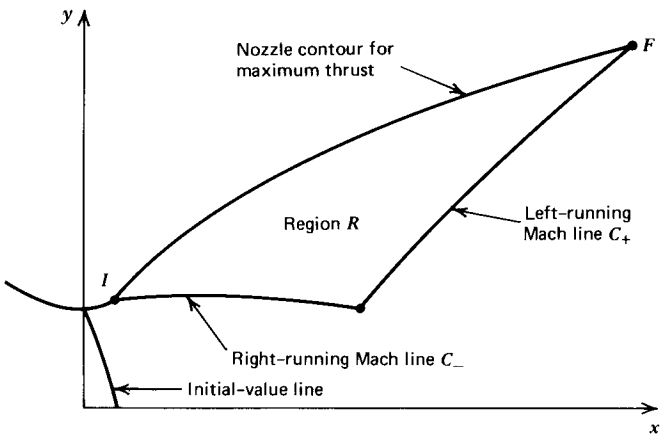

Figure 17.11 Model for maximum thrust nozzle design for rotational flow.

17–5(d) External Flow Fields

An important example of a rotational flow field is the flow field behind a curved shock wave; as pointed out in Section 17–4(g), such flow fields are present when a body travels at a supersonic speed. Figure 17.12 illustrates several possibilities. Figure 17.12*a* illustrates a pointed body with an attached shock wave and a completely supersonic flow behind the shock wave. On the other hand, Fig. 17.12*b* illustrates the case where the shock wave is detached, and a subsonic flow field is formed in the region surrounding the tip of the body. Figures 17.12*c* and 17.12*d* illustrate blunt bodies; such bodies always create a detached shock wave with a subsonic region behind the shock wave. The techniques developed in Section 17–4 may be applied to the rotational flow in the supersonic region behind the shock wave.

The determination of a supersonic initial-value line when a subsonic region is present is a formidable problem. Some success has been achieved with the *method of integral relations*.[6] The technique of obtaining the subsonic solution as the limiting value of a *time-dependent solution* with the same boundary conditions shows promise as a numerical method for dealing with such problems.[7,8] A technique based on assuming the shock position and then marching inward to the body has been developed by Lomax and Inouye.[9] It is an inverse (marching) method that is mathematically improperly posed because the governing equations

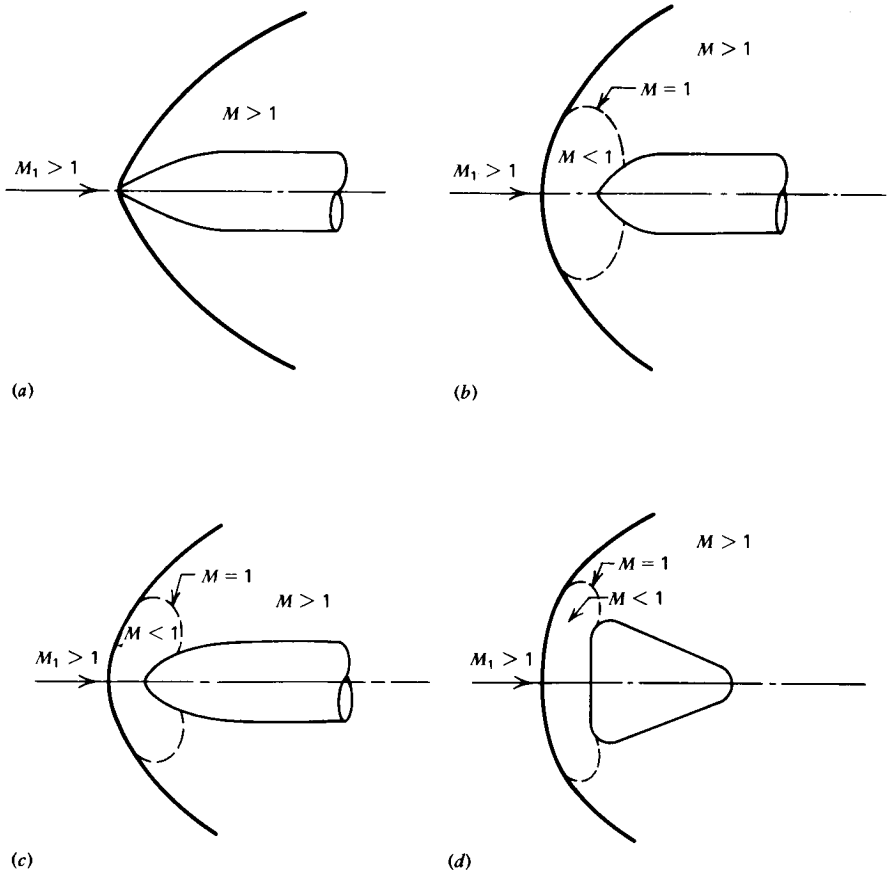

Figure 17.12 Supersonic external flows with several types of shock waves. (*a*) Attached shock wave. (*b*) Detached shock wave. (*c*) Detached shock wave. (*d*) Detached shock wave.

in the subsonic region are elliptic. Consequently, a simultaneous solution is required for all of the boundary conditions and all of the properties for the internal flow. Furthermore, the method involves a trial-and-error procedure, because the assumed shape of the shock wave may not yield a flow field that is compatible with the geometry of the moving body. It does, however, appear to be a promising method, and it yields useful results for free-stream Mach numbers larger than approximately 2.0.

Assuming that the initial-value line for the supersonic flow can be determined, the unit processes for steady two-dimensional rotational supersonic flow may be applied for determining the supersonic portion of the flow field behind the shock wave. It should be noted that the body must be at zero angle of attack with respect to the incident flow, or the resulting flow field will be three dimensional.

For the case illustrated in Fig. 17.12*a*, no subsonic region is present, and the unit processes presented in Section 17.4 may be applied to determine the supersonic flow field behind the attached shock wave. The tip of the body is a singular point in the flow field, and a starting technique is required to initiate the solution from that point.

If the body contour is a straight line at the tip, then the flow field in that region is either a wedge flow [see Sections 7–10(a)] or a conical flow [see Sections 7–10(b) and 16–5], and the flow properties may be determined by the procedures presented in those sections. In that case, an initial-value line such as that illustrated schematically in Fig. 17.13 may be determined. Point *I* lies on the body at the location where the straight body contour *OI* joins the curved body contour *IC*. Line *IJ* is a left-running Mach line along which the flow properties may be determined from the wedge flow or the conical flow in region *R*. In that region, the shock wave *OJ* is straight. If the flow is a two-dimensional planar flow, region *R* is a uniform flow region [see Section 7–10(a)], and the streamlines are straight lines as illustrated in Fig. 7.30*b*. If the flow is a two-dimensional axisymmetric flow, region *R* is a

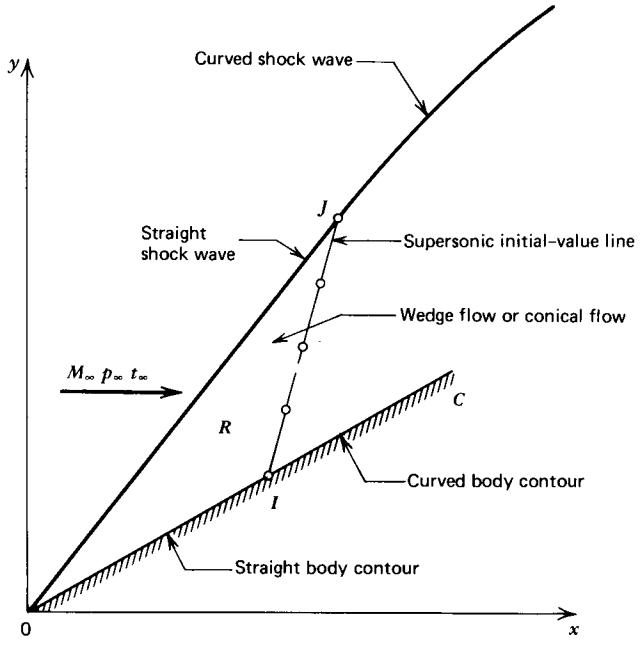

Figure 17.13 Supersonic initial-value line for a body having a wedge or a cone at the tip.

conical flow region and the flow properties are constant along rays from point O [see Sections 7–10(b) and 16–5]. In a conical flow, the streamlines converge toward the body surface as illustrated in Fig. 7.30*a*.

If the body contour is curved at the tip, then the flow field must be determined right from the tip by employing the methods presented in Section 17–4. In that case, an iterative predictor-corrector procedure is employed. The flow model is illustrated in Fig. 17.14. Point 3 is located at the tip of the body. The flow properties at that point are those for a wedge having a semiangle of $\delta_w = \theta_3$ if the flow is planar [see Section 7–10(a)], or those for a cone having a semiangle $\delta_c = \theta_3$ if the flow is axisymmetric [see Sections 7–10(b) and 16–5]. Points 1 and 4 are located by an iterative procedure where the shock wave angle ϵ_1 at point 1 is the iteration parameter.

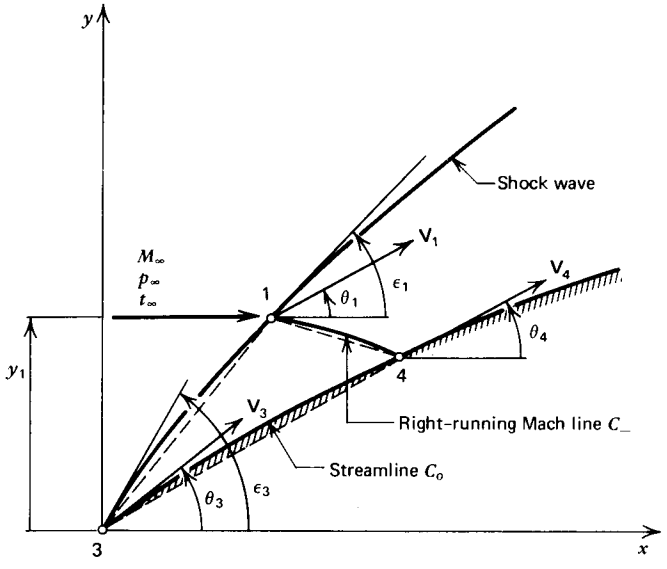

Figure 17.14 Application of the external shock wave point unit process from the tip of a curved body.

First, the free-stream streamline passing through point 1 is chosen by specifying the value of y_1. Typically, y_1 might be set equal to 10 percent of the maximum radius of the body. For the predictor, the shock wave angle ϵ_1 is set equal to the known shock wave angle ϵ_3 at point 3, and the flow angle θ_4 at point 4 is set equal to the flow angle θ_3 at point 3. The flow properties at point 1 are determined from the property ratios across an oblique shock wave, which are calculated by the procedures described in Section 7–7 or 7–8. Point 4 is located at the intersection of the right-running Mach line 14 (see equation 17.45) with the streamline 34 (see equation 17.43). The compatibility equation along right-running Mach line 14 (equation 17.51) and the compatibility equations along streamline 34 (equations 17.56 and 17.57) are solved simultaneously for the flow properties V_4, p_4, and ρ_4, to complete the application of the predictor.

At this stage in the calculations, a corrector could be applied to point 4, holding the value of ϵ_1 fixed at the predictor value. It is more efficient, however, to correct the value of ϵ_1 and the solution for point 4 simultaneously.

Point 4 must lie on the body contour. If the assumed value for ϵ_1 is correct, then point 4 will lie on the body. If the assumed value for ϵ_1 is not correct, then point 4

will not lie on the body, and the value for ϵ_1 must be varied iteratively until point 4 falls within an acceptable distance from the body.

The second trial value for ϵ_1 may be specified arbitrarily as some multiple of the first value, for example, 99 percent of the first value. The entire procedure is repeated for the second trial value for ϵ_1, and a new location for point 4 is determined. During the corrector pass, average values of the flow properties are employed along lines 13, 14 and 34. Once again, the distance between point 4 and the body is checked for convergence. If that distance falls within an acceptable tolerance, the solution is complete. If not, the secant method [see Appendix A–4(b)] is employed to determine the next trial value for ϵ_1. The entire procedure is repeated until convergence is obtained.

When the first shock wave point and the first body point are determined, the external shock wave unit process [see Section 17–4(g)] is employed to determine the next shock wave point, as illustrated schematically in Fig. 17.15. After the solution at point 4 is determined, a point (point 3 in Fig. 17.15) is inserted somewhere along line 24 to maintain a reasonable grid spacing. In subroutine SHOCK presented in Section 17–4(g), point 3 is located midway between points 2 and 4. Line 234 in Fig. 17.15 is analogous to line *IJ* in Fig. 17.13. Consequently, the solution now proceeds in the same manner from both types of initial-value lines.

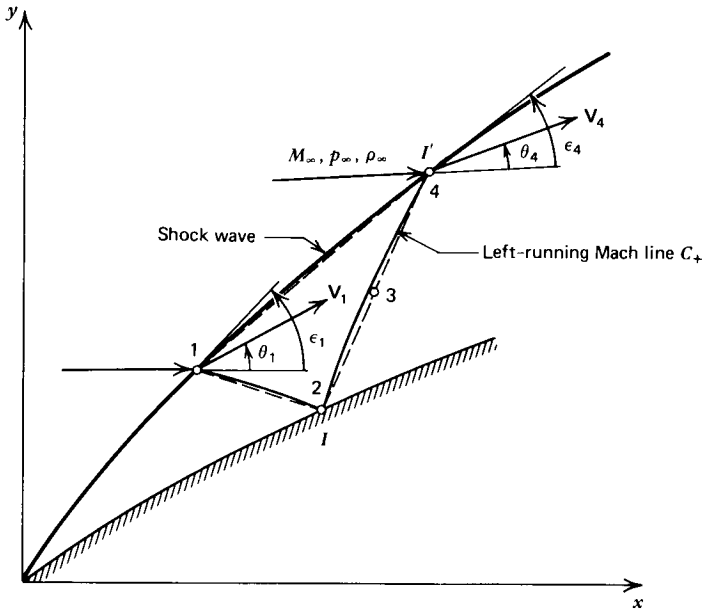

Figure 17.15 Application of the external shock wave point unit process from the first body point.

The next step in the solution is the determination of the point on the body where the right-running Mach line from the second point on the initial-value line intersects the body. Figure 17.16 illustrates the unit process for a body point. This unit process is analogous to the unit process for a direct wall point presented in Section 17–4(c), where the solid boundary is above the flowing gas. Subroutine BODY, presented at the end of this section, is a straightforward modification of subroutine DRWALL presented in Section 17–4(c). The characteristic and compatibility equations employed in subroutine DRWALL for the left-running Mach line 24

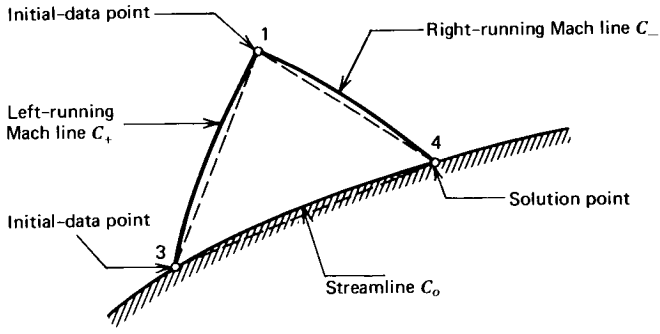

Figure 17.16 Unit process for a body point.

(see Fig. 17.5) are replaced with the characteristic and compatibility equations for the right-running Mach line 14 (see Fig. 17.16). In all other respects, subroutine BODY is identical to subroutine DRWALL. Of course, the subroutine BOUNDY employed by subroutine BODY must specify the shape of the body under consideration.

The body point unit process is applied from points 1 and 3 along the initial-value line as illustrated in Fig. 17.17. Then, as illustrated in Fig. 17.18, the interior point unit process is applied from the next point on the initial-value line, and the right-running Mach line is continued until it intersects the body. For the initial-value line illustrated in Fig. 17.13, that procedure is repeated from successive points along the initial-value line until the shock wave point is reached. The extent of the corresponding flow field is illustrated in Fig. 17.18.

The external shock wave unit process is then applied as illustrated in Fig. 17.19 to determine the next shock wave point and the inserted point from the previous shock wave point. Line 234 in Fig. 17.19 is analogous to line 234 in Fig. 17.15. The sequence of steps illustrated in Fig. 17.18 is then repeated from the two new points, thus extending two more right-running Mach lines from the shock wave to the body, as illustrated in Fig. 17.19.

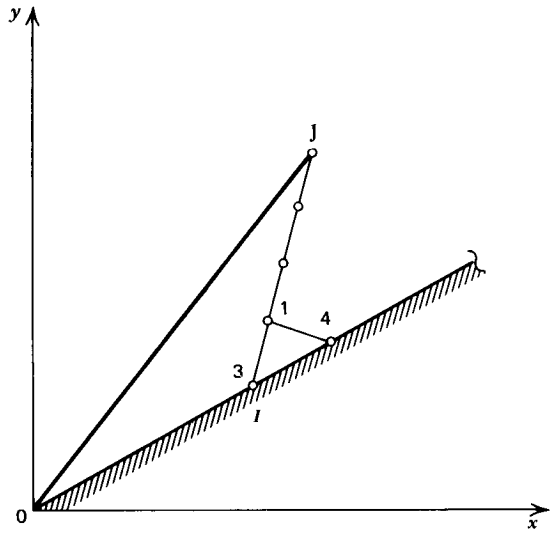

Figure 17.17 Application of the body point unit process.

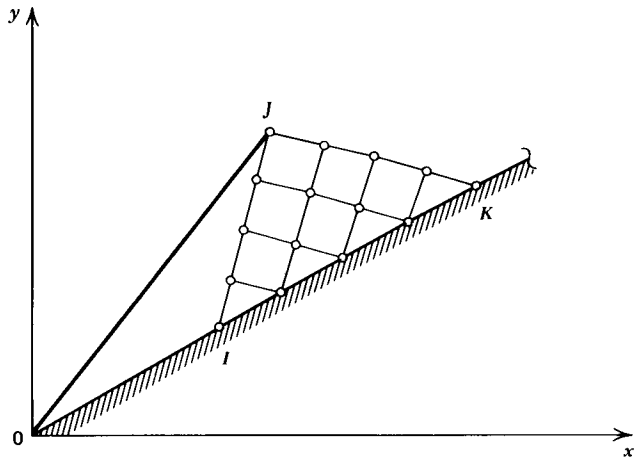

Figure 17.18 Extent of the flow field from the initial-value line.

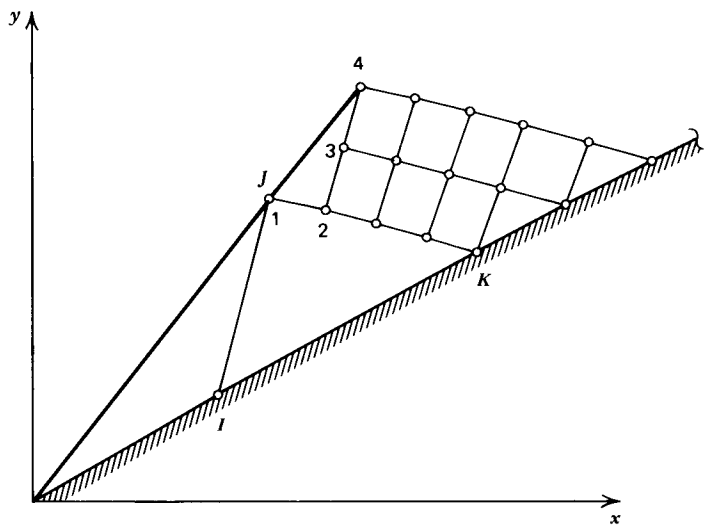

Figure 17.19 Application of the external shock wave point unit process from the previous right-running Mach line.

The process of determining a shock wave point and extending two right-running Mach lines to the body continues until the last right-running Mach line DE that intersects the body is determined. The complete flow field over the body is then known, as illustrated in Fig. 17.20.

The flow field in the region R illustrated in Fig. 17.20 may be determined in the manner described above, where the right-running Mach lines emanating from the shock wave are terminated when they intersect the left-running Mach line EF emanating from the last body point.

The flow field downstream from left-running Mach line EF in Fig. 17.20 may be determined from the flow field in the base region of the body. The base region is dominated by viscous flow effects that cause separation, recirculation, and recompression shock waves.[10,11] Figure 17.21 illustrates the general features of the base flow region. It is apparent that the base flow region is extremely complex. The calculation of the external flow region downstream from the base flow region

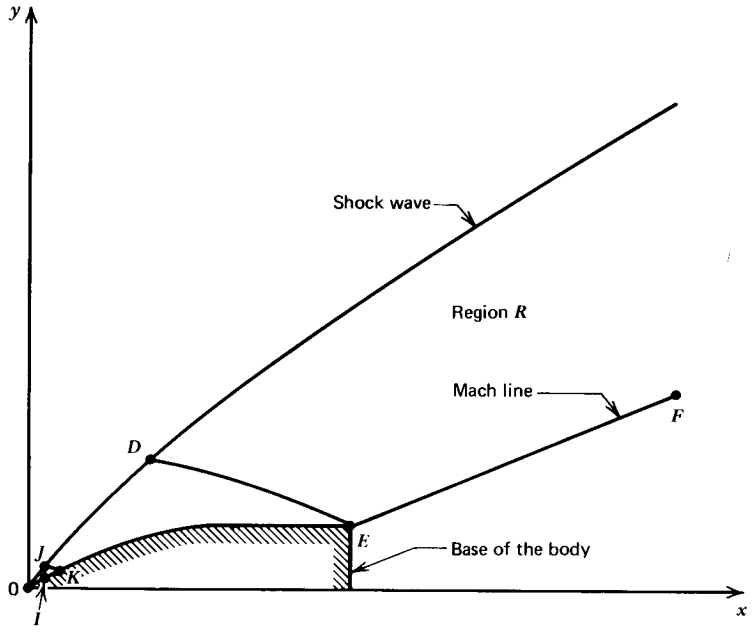

Figure 17.20 Complete external flow field over a pointed body.

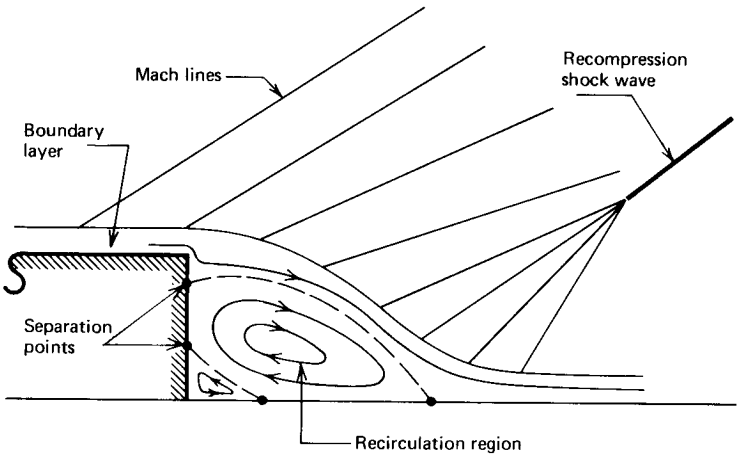

Figure 17.21 General features of the flow in the base region.

requires the determination of the base flow region itself, an analysis that is not well developed and beyond the scope of this book.

A master logic program, program EXTRNL, for implementing the solution procedure developed in the preceding discussion for the supersonic flow over a pointed body is presented below. The free-stream flow properties M_∞, p_∞, and t_∞ are denoted by MU, PU, and TU, respectively. The thermodynamic properties of the gas are specified by subroutine THERMO. When the gas is a perfect gas, the subroutine THERMO presented in Section 17–4(b) is applicable. When the gas is an imperfect gas, subroutine THERMO must account for the imperfect gas effects. The subroutine MOVE presented on page 240 transfers data between the storage arrays and the computational subroutines.

```
      PROGRAM EXTRNL (INPUT,OUTPUT,TAPE5=INPUT,TAPE6=OUTPUT)

C     MAIN PROGRAM FOR EXTERNAL FLOW FIELD ANALYSIS

      COMMON /CONTRL/ DELTA,NI,ICOR,E1,E2,E3,E4,E5,IUNITS,PI,RAD
      COMMON /PROPTY/ G,RG,CP,TS,PS,PA,GC,GL $ REAL M,MU
      COMMON /BODY/ TA,ZETA,XE,YE $ COMMON /SHK/ MU,PU,TU,RU,QU,EPS
      COMMON /ARRAYS/ X(99),Y(99),P(99),R(99),Q(99),A(99)
      COMMON /DATA/ X1,Y1,U1,V1,Q1,A1,P1,R1,T1,M1,X2,Y2,U2,V2,Q2,A2,P2,
     1R2,T2,M2,X3,Y3,U3,V3,Q3,A3,P3,R3,T3,M3,X4,Y4,U4,V4,Q4,A4,P4,R4,T4,
     2M4,LP,LM,LE,L12,L0 $ REAL M1,M2,M3,M4,LP,LM,LE,L12,L0
      NAMELIST /INFO/ IUNITS,DELTA,NI,ICOR,E1,E2,E3,E4,E5,G,RG,MU,PU,
     1TU,TA,ZETA,XE,YE,KWRITE

C     DEFINE DEFAULT VALUES, READ INPUT DATA, AND INITIALIZE PARAMETERS

   10 DELTA=0.0 $ NI=5 $ ICOR=3 $ E1=0.0 $ E2=0.0 $ E3=0.0 $ E4=0.0
      E5=0.0 $ IUNITS=2 $ G=1.4 $ RG=287.04 $ TU=300.0 $ PU=1.0E5
      MU=3.0 $ TA=30.0 $ ZETA=0.1 $ XE=10.0 $ YE=1.0 $ IEND=0 $ KWRITE=1
      READ (5,INFO) $ IF (EOF,5) 20,30
   20 CALL EXIT
   30 GC=32.174 $ GL=144.0 $ IF (IUNITS.EQ.1) GO TO 35 $ GC=1.0 $ GL=1.0
   35 PI=3.1415926 $RAD=57.2957795 $TA=TA/RAD $ CALL EOUNDY(1) $PU=PU*GL
      RU=PU/RG/TU $CU=SQRT(G*GC*RG*TU) $QU=MU*CU $WRITE(6,INFO)

C     CALCULATE THE FLOW FIELD FROM THE INITIAL-VALUE LINE

   40 CALL IVLINE $ DO 80 I=1,NI $ J2=I $ WRITE (6,1010)
      DO 80 J=1,J2 $ IF(J.GT.1) GO TO 50 $ CALL MOVE (4,I)
      IF (I.EQ.1) CALL MOVE (7,0) $ KW=1 $ GO TO 70
   50 CALL MOVE (1,J-1) $ IF (J.EQ.J2) GO TO 60 $ CALL MOVE (2,J)
      CALL INTER $ KW=KWRITE $ GO TO 70
   60 CALL MOVE (6,0) $ CALL BODY $ KW=1
   70 CALL MOVE (5,J) $ PP=P4/GL $ AP=A4*RAD
      IF (KW.EQ.1) WRITE (6,1020) I,J,X4,Y4,U4,V4,M4,Q4,AP,PP,R4,T4
   80 CONTINUE $ I1=NI+1 $ J1=1

C     CALCULATE THE FLOW FIELD FROM A SHOCK WAVE POINT

      DO 120 I=I1,1000 $ CALL MOVE (1,1) $ CALL MOVE (2,2)
      CALL SHOCK (EPS,EPS4) $ EPS=EPS4 $ J1=J1+1
      IF (X4.LT.XE) GO TO 85 $ IF (IEND.EQ.1) GO TO 10 $ IEND=1
   85 IR=NI+2*(I-NI-1) $ CALL MOVE (5,1) $ CALL MOVE (3,2)
      DO 120 K=1,2 $ J2=J2+1 $ WRITE (6,1010)
      DO 120 J=J1,J2 $ L=J+3-J1-K $ N=L+K-1 $ IF (J.GT.J1) GO TO 90
      CALL MOVE (4,L) $ KW=1 $ GO TO 110
   90 CALL MOVE(1,L-1) $ IF (J.EQ.J2) GO TO 100 $ CALL MOVE (2,N)
      CALL INTER $ KW=KWRITE $ GO TO 110
  100 CALL MOVE (6,0) $ CALL BODY $ KW=1
  110 CALL MOVE (5,L) $ PP=P4/GL $ AP=A4*RAD $ IO=IR+K
      IF (KW.EQ.1) WRITE (6,1020) IO,J,X4,Y4,U4,V4,M4,Q4,AP,PP,R4,T4
  120 CONTINUE $ GO TO 10

 1010 FORMAT (1H0,4X,1HI,4X,1HJ,6X,1HX,9X,1HY,9X,1HU,9X,1HV,9X,1HM,9X,
     11HQ,9X,1HA,9X,1HP,12X,1HR,12X,1HT/1H )
 1020 FORMAT (1H ,2I5,2F10.4,2F10.1,F10.4,F10.1,F10.4,2E13.4,F10.1)
      END


      SUBROUTINE MOVE (I,J)

C     SUBROUTINE MOVE TRANSFERS DATA TO AND FROM GRID POINTS AND ARRAYS

      COMMON /ARRAYS/ X(99),Y(99),P(99),R(99),Q(99),A(99)
      COMMON /DATA/ X1,Y1,U1,V1,Q1,A1,P1,R1,T1,M1,X2,Y2,U2,V2,Q2,A2,P2,
     1R2,T2,M2,X3,Y3,U3,V3,Q3,A3,P3,R3,T3,M3,X4,Y4,U4,V4,Q4,A4,P4,R4,T4,
     2M4,LP,LM,LE,L12,L0 $ REAL M1,M2,M3,M4,LP,LM,LE,L12,L0
```

```
      GO TO (10,20,30,40,50,60,70), I

10    X1=X(J) $ Y1=Y(J) $ Q1=Q(J) $ A1=A(J) $ P1=P(J) $ R1=R(J) $ RETURN
20    X2=X(J) $ Y2=Y(J) $ Q2=Q(J) $ A2=A(J) $ P2=P(J) $ R2=R(J) $ RETURN
30    X(J)=X3 $ Y(J)=Y3 $ Q(J)=Q3 $ A(J)=A3 $ P(J)=P3 $ R(J)=R3 $ RETURN
40    X4=X(J) $ Y4=Y(J) $ Q4=Q(J) $ A4=A(J) $ P4=P(J) $ R4=R(J) $ RETURN
50    U4=Q4*COS(A4) $ V4=Q4*SIN(A4) $ CALL THERMO (Q4,P4,R4,T4,C,M4)
      X(J)=X4 $ Y(J)=Y4 $ Q(J)=Q4 $ A(J)=A4 $ P(J)=P4 $ R(J)=R4 $ RETURN
60    X3=X2 $ Y3=Y2 $ Q3=Q2 $ A3=A2 $ P3=P2 $ R3=R2 $ RETURN
70    X2=X4 $ Y2=Y4 $ Q2=Q4 $ A2=A4 $ P2=P4 $ R2=R4 $ RETURN
      END
```

The body geometry considered by the program is illustrated in Fig. 17.22. The tip of the body is pointed (i.e., it is either a wedge or a cone), and the semiangle is denoted by δ_a. The radius of the main portion of the body is denoted by y_e. Point a is located by specifying y_a as some fraction of y_e, for example, $y_a = \zeta y_e$. The transition section ab between the tip and the main portion of the body is specified by the following second-order equation.

$$y = a + bx + cx^2 \tag{17.71}$$

The coefficients a, b, and c are chosen so that the transition section joins smoothly with the tip and the main body. Consequently, the body geometry is completely specified by the parameters δ_a, ζ, x_e, and y_e. Subroutine **BOUNDY** presented below specifies the body geometry discussed above. The locations of points a and b and the values of the coefficients a, b, and c are calculated by an initial call of subroutine **BOUNDY** from program **EXTRNL** with the variable **INITAL** equal to 1. Subsequent calls from subroutine **BODY** with **INITAL** equal to 2 determine the

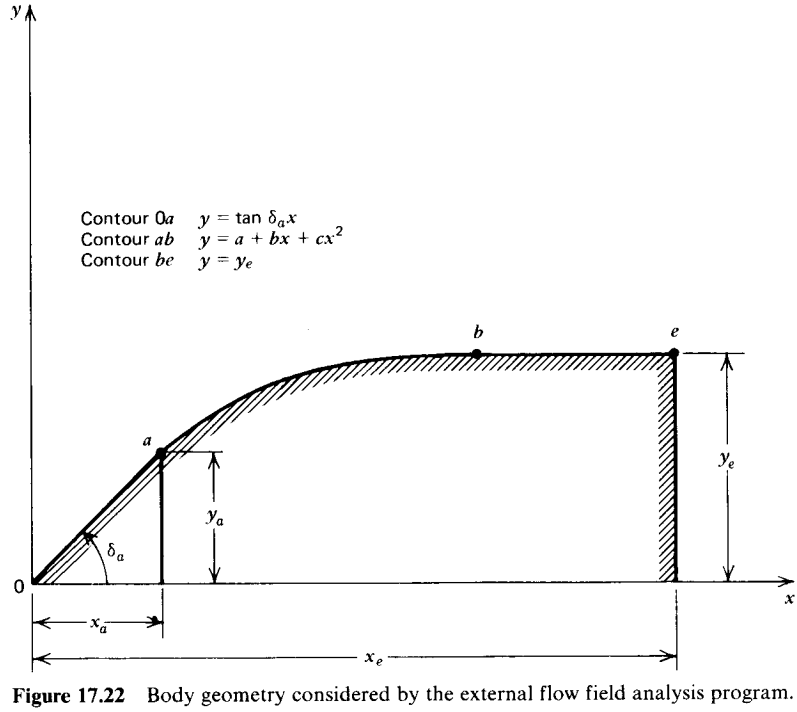

Figure 17.22 Body geometry considered by the external flow field analysis program.

point of intersection of the right-running Mach line 14 with the body (x_4 and y_4) and the value of the body angle θ_4 at the point of intersection (see Fig. 17.16). Other body shapes, including tabular specifications, may be studied by replacing the subroutine BOUNDY presented below with one that describes the body shape of interest.

```
      SUBROUTINE BODY

C     SUBROUTINE BODY CALCULATES THE SOLUTION AT A DIRECT WALL POINT

      COMMON /CONTRL/ DELTA,NI,ICOR,E1,E2,E3,E4,E5,IUNITS,PI,RAD
      COMMON /PROPTY/ G,RG,CP,TS,PS,PA,GC,GL $ REAL M
      COMMON /DATA/ X1,Y1,U1,V1,Q1,A1,P1,R1,T1,M1,X2,Y2,U2,V2,Q2,A2,P2,
     1R2,T2,M2,X3,Y3,U3,V3,Q3,A3,P3,R3,T3,M3,X4,Y4,U4,V4,Q4,A4,P4,R4,T4,
     2M4,LP,LM,LE,L12,L0 $ REAL M1,M2,M3,M4,LP,LM,LE,L12,L0

C     CALCULATE THE COEFFICIENTS FOR THE PREDICTOR

      ITER=0 $ Q4=Q3 $ P4=P3 $ R4=R3 $ CALL THERMO (Q1,P1,R1,T,C,M)
      LM=TAN(A1-ASIN(1.0/M)) $ QM=GC*SQRT(M**2-1.0)/(R1*Q1**2)
      SM=DELTA*SIN(A1)/(Y1*M*COS(A1-ASIN(1.0/M)))

C     SOLUTION OF THE FINITE DIFFERENCE EQUATIONS

   10 CALL BOUNDY (2) $ TM=-SM*(X4-X1)+QM*P1-A1 $ P=0.5*(P3+P4)
      R=0.5*(R3+R4) $Q=0.5*(Q3+Q4) $R0=R*Q/GC $ CALL THERMO(Q,P,R,T,C,M)
      A0=C**2/GC $ T01=R0*Q3+P3 $ T02=P3-A0*R3
      P4=(TM+A4)/QM $ Q4=(T01-P4)/R0 $ R4=(P4-T02)/A0

C     CHECK FOR CONVERGENCE OR COMPLETION OF SPECIFIED ITERATIONS

      IF (ITER.EQ.ICOR) RETURN $ IF (ITER.EQ.0) GO TO 20
      IF ((ABS(X4-XD).GT.E1).OR.(ABS(Y4-YD).GT.E1)) GO TO 20
      IF ((ABS(P4-PD).GT.E2*PD).OR.(ABS(R4-RD).GT.E3*RD)) GO TO 20
      IF ((ABS(Q4-QD).LT.E4*QD).AND.(ABS(A4-AD).LT.E5*AD)) RETURN

C     CALCULATE THE COEFFICIENTS FOR THE CORRECTOR

   20 ITER=ITER+1 $ PD=P4 $ RD=R4 $ QD=Q4 $ AD=A4 $ XD=X4 $ YD=Y4
      P=0.5*(P1+P4) $ R=0.5*(R1+R4) $ Q=0.5*(Q1+Q4) $ A=0.5*(A1+A4)
      Y=0.5*(Y1+Y4) $ CALL THERMO (Q,P,R,T,C,M) $ LM=TAN(A-ASIN(1.0/M))
      SM=DELTA*SIN(A)/(Y*M*COS(A-ASIN(1.0/M)))
      QM=GC*SQRT(M**2-1.0)/(R*Q**2) $ GO TO 10
      END


      SUBROUTINE BOUNDY (INITAL)

C     SUBROUTINE BOUNDY LOCATES THE INTERSECTION OF A RIGHT-RUNNING
C     CHARACTERISTIC WITH A SECOND-ORDER QUADRATIC WALL CONTOUR

      COMMON /CONTRL/ DELTA,NI,ICOR,E1,E2,E3,E4,E5,IUNITS,PI,RAD
      COMMON /BODY/ TA,ZETA,XE,YE
      COMMON /DATA/ X1,Y1,U1,V1,Q1,A1,P1,R1,T1,M1,X2,Y2,U2,V2,Q2,A2,P2,
     1R2,T2,M2,X3,Y3,U3,V3,Q3,A3,P3,R3,T3,M3,X4,Y4,U4,V4,Q4,A4,P4,R4,T4,
     2M4,LP,LM,LE,L12,L0 $ REAL M1,M2,M3,M4,LP,LM,LE,L12,L0

      GO TO (10,20), INITAL

C     CALCULATE THE COEFFICIENTS A, B, AND C

   10 TT=TAN(TA) $ YA=ZETA*YE $ XA=YA/TT $ IBODY=1
      C=-TT**2/4.0/YE/(1.0-ZETA) $ B=TT-2.0*C*XA $ A=YA-B*XA-C*XA*XA
      XB=-B/2.0/C $ RETURN
```

```
C     LOCATE THE INTERSECTION OF A CHARACTERISTIC AND THE NOSE

   20 GO TO (30,50), IBODY
   30 X4=((LM-B)+SQRT((LM-B)**2-4.0*C*(A-Y1+LM*X1)))/(2.0*C)
      IF (X4.LT.XB) GO TO 40 $ IBODY=2 $ GO TO 50
   40 Y4=A+B*X4+C*X4**2 $ A4=ATAN(B+2.0*C*X4) $ RETURN

C     LOCATE THE INTERSECTION OF A CHARACTERISTIC AND THE CYLINDER

   50 Y4=YE $ X4=X1+(Y4-Y1)/LM $ A4=0.0 $ RETURN
      END
```

The supersonic initial-value line illustrated in Fig. 17.13 is determined by subroutine IVLINE. If the body is planar, for example, a wedge faired into a plate, then the flow properties along the initial-value line may be determined from the wedge flow properties [see Section 7–10(a)]. If the body is axisymmetric, for example, a cone faired into a cylinder, then the flow properties along the initial-value line may be determined from the properties of the conical flow [see Sections 7–10(b) and 16–5]. Subroutine IVLINE employs subroutines TM and SHK described in Section 16–5 to obtain the solution for the Taylor-Maccoll flow over a cone.

```
      SUBROUTINE IVLINE

C     SUBROUTINE IVLINE DETERMINES AN EXTERNAL FLOW INITIAL-VALUE LINE

      COMMON /CONTRL/ DELTA,NI,ICCR,E1,E2,E3,E4,EE,IUNITS,PI,RAD
      COMMON /PROPTY/ G,RG,CP,TS,PS,PA,GC,GL $ REAL M,MU,MU2,LS,LI
      COMMON /BODY/ TA,ZETA,XE,YE $ COMMON /SHK/ MU,PL,TU,RU,QU,EPS
      COMMON /TAYMAC/ T(99),U(99),V(99)
      COMMON /ARRAYS/ X(99),Y(99),P(99),R(99),Q(99),A(99)
      COMMON /DATA/ X1,Y1,U1,V1,Q1,A1,P1,R1,T1,M1,X2,Y2,U2,V2,Q2,A2,P2,
     1R2,T2,M2,X3,Y3,U3,V3,Q3,A3,P3,R3,T3,M3,X4,Y4,U4,V4,Q4,A4,P4,R4,T4,
     2M4,LP,LM,LE,L12,L0 $ REAL M1,M2,M3,M4,LP,LM,LE,L12,L0

      IF (DELTA.EQ.1.0) GO TO 60

C     CALCULATE THE INITIAL-VALUE LINE PROPERTIES FOR A WEDGE FLOW

      X1=0.0 $ Y1=0.0 $ TANA=TAN(TA) $ YA=ZETA*YE $ XA=YA/TANA $ ITER=0
      J=1 $G1=2.0/(G+1.0) $G2=(G-1.0)/2.0 $MU2=MU*MU $ E=ASIN(1.0/MU)+TA
   10 B=E-TA $ TANB=TAN(B) $ TANE=TAN(E) $ SINE2=SIN(E)**2
      FE=TANB/TANE-G1*(1.0/MU2/SINE2+G2)
      IF (ABS(FE).LT.1.0E-8) GO TO 30 $ IF (ITER.GT.0) GO TO 20
      FES=FE $ ES=E $ E=0.99*E $ ITER=ITER+1 $ GO TO 10
   20 SLOPE=(FE-FES)/(E-ES) $ DE=-FE/SLOPE $ ES=E $ FES=FE
      E=E+DE $ ITER=ITER+1 $ GO TO 10
   30 CALL SHOCK (E) $ CALL THERMO (Q4,P4,R4,T,C,M) $EPS=E $WRITE(6,1030)
      LI=TAN(A4+ASIN(1.0/M)) $EP=E*RAD $WRITE (6,1010) EP $WRITE(6,1000)
      LS=TAN(E) $ X4=(Y1-YA-LS*X1+LI*XA)/(LI-LS) $ Y4=Y1+LS*(X4-X1)
      DY=(Y4-YA)/FLOAT(NI-1) $ DX=DY/LI $ X4=XA-DX $ Y4=YA-DY
      AP=A4*RAD $ PP=P4/GL $ DO 50 I=1,NI $ X4=X4+DX $ Y4=Y4+DY
      CALL MOVE (5,I) $ WRITE (6,1020) I,J,X4,Y4,U4,V4,M4,Q4,AP,PP,R4,T4
   50 CONTINUE $ WRITE (6,1030) $ RETURN

C     CALCULATE THE INITIAL-VALUE LINE PROPERTIES FOR A CONICAL FLOW

   60 CALL TM (EPS) $ DO 70 I=1,NI
      K=I+NI $ Q(K)=Q(I)*QU $ A(K)=A(I) $ P(K)=P(I)*PU $ T(K)=T(I)
   70 R(K)=R(I)*RU $ DO 80 I=1,NI $ K=2*NI+1-I $ Q(I)=Q(K) $ A(I)=A(K)
      P(I)=P(K) $ R(I)=R(K)
   80 T(I)=T(K) $ Y(1)=ZETA*YE $ X(1)=Y(1)/TAN(TA) $ J=1 $ WRITE(6,1000)
      DO 100 I=1,NI $ IF (I.EQ.1) GO TO 90 $ TT=TAN(T(I))
```

```
      QP=0.5*(Q(I-1)+Q(I)) $ AP=0.5*(A(I-1)+A(I)) $ PP=0.5*(P(I-1)+P(I))
      RP=0.5*(R(I-1)+R(I)) $ AA=SQRT(G*GC*PP/RP)
      LI=TAN(AP+ASIN(AA/QP)) $ X(I)=(LI*X(1)-Y(1))/(LI-TT) $Y(I)=TT*X(I)
   90 CALL THERMO (Q(I),P(I),R(I),TT,C,M) $ AP=A(I)*RAD $ PP=P(I)/GL
      U4=Q(I)*COS(A(I)) $ V4=Q(I)*SIN(A(I))
  100 WRITE (6,1020) I,J,X(I),Y(I),U4,V4,M,Q(I),AP,PP,R(I),TT
      WRITE (6,1030) $ RETURN

 1000 FORMAT (1H0,4X,1HI,4X,1HJ,6X,1HX,9X,1HY,9X,1HU,9X,1HV,9X,1HM,9X,
     11HQ,9X,1HA,9X,1HP,12X,1HR,12X,1HT/1H )
 1010 FORMAT (1H0≠THE SHOCK WAVE ANGLE EPS = ≠F7.4≠ DEGREES≠/1H0)
 1020 FORMAT (1H ,2I5,2F10.4,2F10.1,F10.4,F10.1,F10.4,2E13.4,F10.1)
 1030 FORMAT (1H1)
      END
```

Input to the program is accomplished through the NAMELIST INFO. Table 17.16 presents the input data required by the program, along with the default values defined within the program for each parameter. The input data may be specified in either SI units or EE units, and the results are presented in the same units.

The method presented here may be applied to a pointed body of any shape over which there is a steady two-dimensional isentropic supersonic flow for which there is a known or calculable initial-value line. An example illustrating the application of the program is presented in Example 17.7.

Table 17.16 Input Parameters for the External Flow Field Analysis Program

Parameter Symbol		Description and Units	Default Value
DELTA	δ	0 denotes planar flow, 1 denotes axisymmetric flow	0.0
NI		number of points on the initial-value line	5
ICOR		number of applications of the corrector	3
EI		length convergence tolerance, m (in.)	0.0
E2–E5		fractional convergence tolerances for p, ρ, V, and θ, respectively	0.0
IUNITS		2 denotes SI units, 1 denotes EE units	2
G	γ	specific heat ratio	1.40
RG	R	gas constant J/kg-K (ft-1 bf/1bm-	287.04
MU	M_∞	free-stream Mach number	3.0
PU	p_∞	free-stream static pressure, N/m^2 (1bf/in.^{2})	$1.0 \cdot 10^5$
TU	t_∞	free-stream static temperature, K (R)	300.0
TA	θ_a	tip attachment angle, deg	30.0
ZETA	ζ	y_a/y_e	0.1
YE	y_e	radius of main body, m (in.)	1.0
XE	x_e	length of body, m (in.)	10.0
KWRITE		0 write out solution at shock wave and body points only, 1 write out solution at all of the points	1

Example 17.7. Air is flowing at the Mach number $M_\infty = 3.0$ over a two-dimensional planar body having a pointed tip. The body geometry is of the type illustrated in Fig. 17.22, where $\theta_a = 30$ deg, $y_a = 0.1 y_e$, $y_e = 0.1$ m, and $x_e = 1.0$ m. Calculate the external flow field over the body and the pressure distributions behind the shock wave and on the surface of the body, employing the procedure presented in Section 17–5(d). Assume that $\gamma = 1.40$ and $R = 287.04$ J/kg-K for air.

Solution

The flow field over the body is obtained by employing the computer programs described in this chapter. From Fig. 17.22,

$$y_a = \zeta y_e \tag{a}$$

$$x_a = \frac{y_a}{\tan\theta_a} \tag{b}$$

Substituting the given geometrical specifications into equations 17.71, we obtain

$$y_a = a + bx_a + cx_a^2 \tag{c}$$

$$\left(\frac{dy}{dx}\right)_a = \tan\theta_a = b + 2cx_a \tag{d}$$

$$y_b = a + bx_b + cx_b^2 = y_e \tag{e}$$

$$\left(\frac{dy}{dx}\right)_b = \tan\theta_b = b + 2cx_b = 0 \tag{f}$$

Equations (c) to (f) may be solved simultaneously for x_b, a, b, and c. After considerable manipulation, the following results are obtained.

$$c = \frac{\tan^2\theta_a}{4y_e(1-\zeta)} \tag{g}$$

$$b = \tan\theta_a - 2cx_a \tag{h}$$

$$a = y_a - bx_a - cx_a^2 \tag{i}$$

$$x_b = -\frac{b}{2c} \tag{j}$$

Figure 17.23 presents the body geometry and the shock wave and Mach line pattern over the body. The results are presented in nondimensional form by dividing all x and y values by the body height y_e. The pressure ratio distributions p/p_∞ behind the shock wave and on the surface of the body are presented in Fig. 17.24. Both pressure ratios decrease toward unity in the downstream direction, with the pressure ratio on the body decreasing much more rapidly and becoming nearly unity as soon as the constant body height region is reached.

17–6 ACCURACY STUDIES FOR STEADY TWO-DIMENSIONAL ISENTROPIC FLOW[12]

In Sections 16–3 and 17–5 the method of characteristics is applied to irrotational and rotational flows, respectively, and unit processes are developed for the flow field calculations. In this section, the results of some accuracy studies are presented for ten different numerical algorithms based on the equations developed in the aforementioned sections.

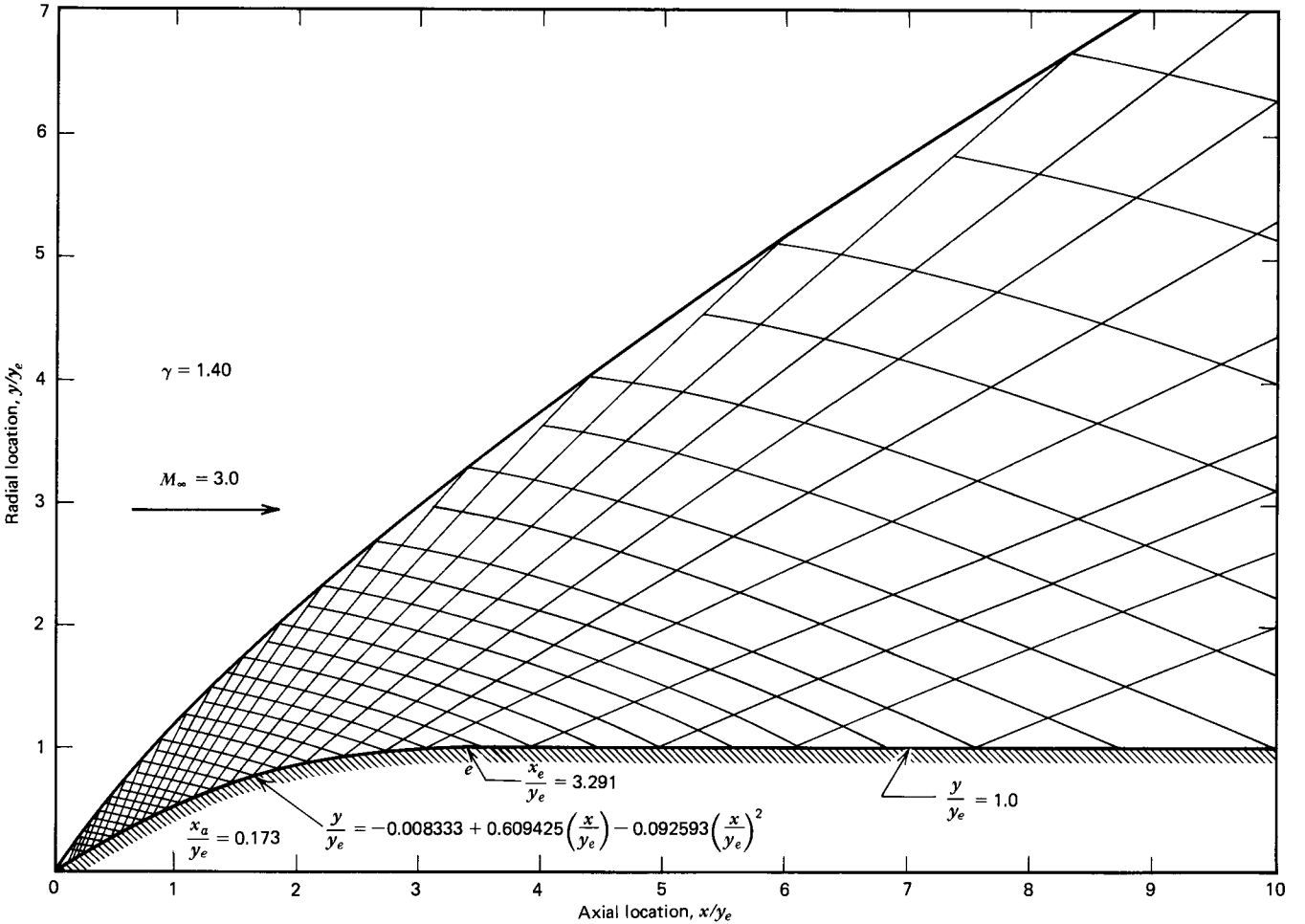

Figure 17.23 External flow field over the pointed body considered in Example 17.7.

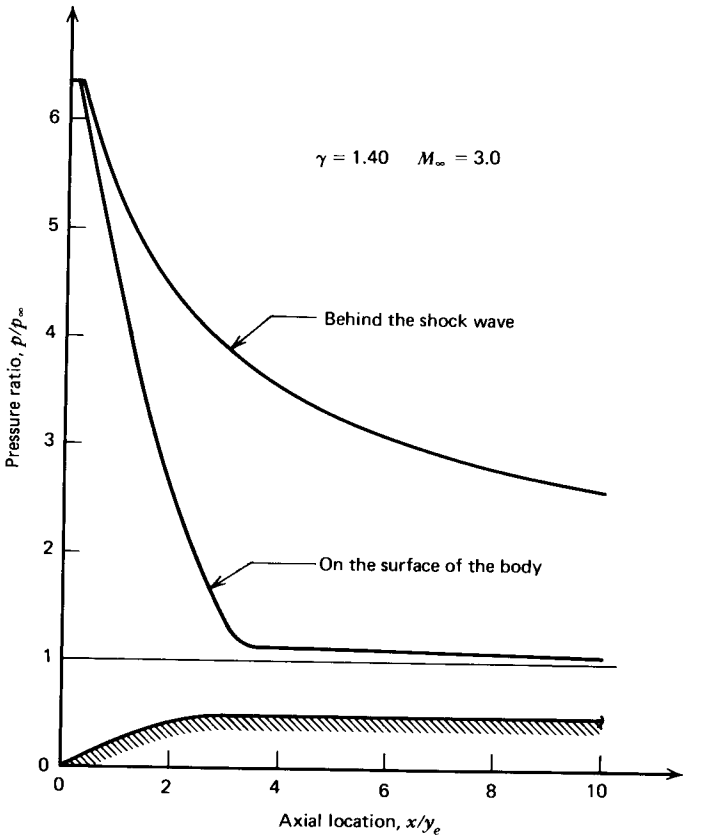

Figure 17.24 Pressure ratio p/p_∞, behind the shock wave and on the surface of the body for supersonic flow over the pointed body considered in Example 17.7.

The numerical algorithms developed in Sections 16–3 and 17–5 achieve second-order accuracy by determining the coefficients of the differentials during the corrector step based on the average values of the flow properties, a procedure that is known as an *average property method.* An alternate procedure for achieving second-order accuracy is that based on determining the coefficients of the differentials at each point in the characteristic network, and then calculating the average values of the coefficients along each characteristic. The latter procedure is called an *average coefficient method.* Comparisons of those two methods are presented in the present section, for both irrotational and rotational flows.

17–6(a) Accuracy Criteria for Numerical Methods of Integration

Two different, but related, criteria are frequently employed for judging the accuracy of a numerical method of integration. They are (1) the *absolute error*, and (2) the *order of the error.* Two procedures are customarily employed for determining those criteria. The first procedure involves calculating the flow properties for a flow which has an exact solution, and then computing the *absolute error*, denoted by *Error*. Thus,

$$Error = C - E \tag{17.72}$$

where C is the value of the *computed solution* based on a numerical method, and E is the *exact solution.*

It may be assumed that the *Error* depends on the step size h employed in the numerical integration in the following manner:

$$Error = C - E = A_1 h + A_2 h^2 + \cdots + A_n h^n + \cdots \tag{17.73}$$

where the coefficients A_n must be determined numerically. For a numerical method having nth-order accuracy, the coefficients A_1 through A_{n-1} are not present. If the step size h is sufficiently small, the coefficients A_{n+1}, A_{n+2}, and the like, become insignificant compared to A_n. Consequently, the error is proportional to h^n.

The *order* of a numerical method may be determined by calculating the *Error* for two different step sizes, one of which is half of the other, and then determining the ratio of the corresponding values of the *Error*; the latter is equal to $h^n/(h/2)^n$, or 2^n. For a second-order method (i.e., $n=2$), that ratio is 4. Hence, the order of a numerical method may be determined, when an exact solution is available, by calculating the values of the solution for two different step sizes, one of which is half the size of the other.

The procedure outlined above is the best way for determining the order of a numerical method. Unfortunately, in the case of multidimensional flows, very few exact solutions are known. One exact solution is for either an expanding source flow or a diffusing sink flow in a conical passage (see Section 4–9). Some accuracy studies pertinent to source and sink flows are presented in the present section. Source flow is, however, a well-behaved flow with straight streamlines. To study flows having curved streamlines, flow passages having a parabolic wall shape are considered. However, no exact solutions for such flows are available.

The *second* procedure for determining the *Error* and its order for a numerical integration method is based on making a numerical approximation to the exact solution. The numerical approximation involves applying equation 17.73 for a given step size h, and then successively halving the step size and recomputing the flow properties of the flow field until sufficient numerical results are available for determining all of the coefficients A_n in equation 17.73 that are significant, and the exact solution E. From those results the order of the numerical method of integration may be determined by the procedure discussed above. It is that type of procedure that is employed here for analyzing the flow in passages having parabolic walls.

For example, if three integration step sizes are employed, the following results are obtained:

$$C_1 = E + A_1 h + A_2 h^2 + \cdots \tag{17.74a}$$

$$C_2 = E + A_1\left(\frac{h}{2}\right) + A_2\left(\frac{h}{2}\right)^2 + \cdots \tag{17.74b}$$

$$C_3 = E + A_1\left(\frac{h}{4}\right) + A_2\left(\frac{h}{4}\right)^2 \cdots \tag{17.74c}$$

where C_1, C_2, and C_3 are the computed values of the solution for the step sizes h, $h/2$, and $h/4$, respectively. Equations 17.74 may be solved simultaneously for E, the exact solution, and the coefficients A_1 and A_2. If A_3 has a significant magnitude, a fourth step size must be employed so that a fourth equation will be obtained, thus making the determination of A_3 possible. For a second-order method, A_1 should be zero, and equation 17.73 becomes

$$C = E + A_2 h^2 + \cdots + A_n h^n + \cdots \tag{17.75}$$

In general, for an nth-order method, all of the coefficients preceding A_n should be zero, and equation 17.73 must be modified accordingly. Subtracting equations 17.74 successively, we obtain

$$C_1 - C_2 = A_1 \frac{h}{2} + A_2\left(\frac{3h^2}{4}\right) + \cdots \tag{17.76a}$$

$$C_2 - C_3 = A_1 \frac{h}{4} + A_2\left(\frac{3h^2}{16}\right) + \cdots \tag{17.76b}$$

For a *first-order* method, A_1 should be much larger than A_2, so that

$$\frac{C_1 - C_2}{C_2 - C_3} \approx \frac{A_1\left(\frac{h}{2}\right)}{A_1\left(\frac{h}{4}\right)} = 2 = 2^1 \tag{17.77}$$

For a *second-order* method, A_1 is zero and A_2 should be much larger than A_3, so that

$$\frac{C_1 - C_2}{C_2 - C_3} \approx \frac{A_2\left(\frac{3h^2}{4}\right)}{A_2\left(\frac{3h^2}{16}\right)} = 4 = 2^2 \tag{17.78}$$

In general,

$$\frac{C_1 - C_2}{C_2 - C_3} \approx 2^n \tag{17.79}$$

From the foregoing it follows that the *order n* of a numerical integration method applied to a flow that has no exact solution may be determined by calculating the numerical solution at three step sizes, each one-half the preceding, and determining the ratio of the successive differences in the computed solution (see equation 17.79). The aforementioned procedure is applicable only when the step size h is small enough so that the coefficients A_{n+1}, and the like, are insignificant when compared with A_n.

Hence, it is seen that the ratio of the *Errors* for successively halved step sizes can always be determined, and it should be approximately 4 for a *second-order method.* The exact step size for which the ratio of the *Errors* becomes equal to 4 depends on many factors, the main one being the gradients in the flow properties. For a well-behaved flow, such as a source flow, the numerical integration method may approach second order at a relatively large step size. On the other hand, for a highly distorted flow, such as occurs near a Prandtl-Meyer corner [see Section 8–4(a)], the numerical integration method may approach second order only for very small step sizes. If the order of a numerical integration method is determined for a smooth flow, it would be expected that the same order would be realized even for a distorted flow if the step size is sufficiently small. For that reason the study of source flow is a useful adjunct for determining the order of a numerical algorithm.

The studies of the accuracy of numerical integration methods presented in the sequel comprise comparisons with both known exact solutions and numerically approximated exact solutions. The results are presented in two forms. The *first form*

presents the solution (both location and flow properties) at a given point in the characteristic network as a function of step size. The *second form* presents the solution for a particular flow property (primarily the velocity magnitude V) along either the wall or the centerline of a flow passage for several different step sizes. The step size utilized for correlating the results is the uniform angular step size $h=(\Delta\theta/\alpha)$ on the initial-value line, illustrated schematically in Fig. 17.25. Because the characteristic network follows Mach lines and their reflections from the wall and centerline, the overall network is self-regulating, and halving the step size on the initial-value line effectively halves the step size throughout the entire flow field. The self-regulation is illustrated schematically in Fig. 17.25, where the solid lines correspond to $h=(\Delta\theta/\alpha)=1.0$ and the solid and dashed lines together correspond to $h=(\Delta\theta/\alpha)=0.5$.

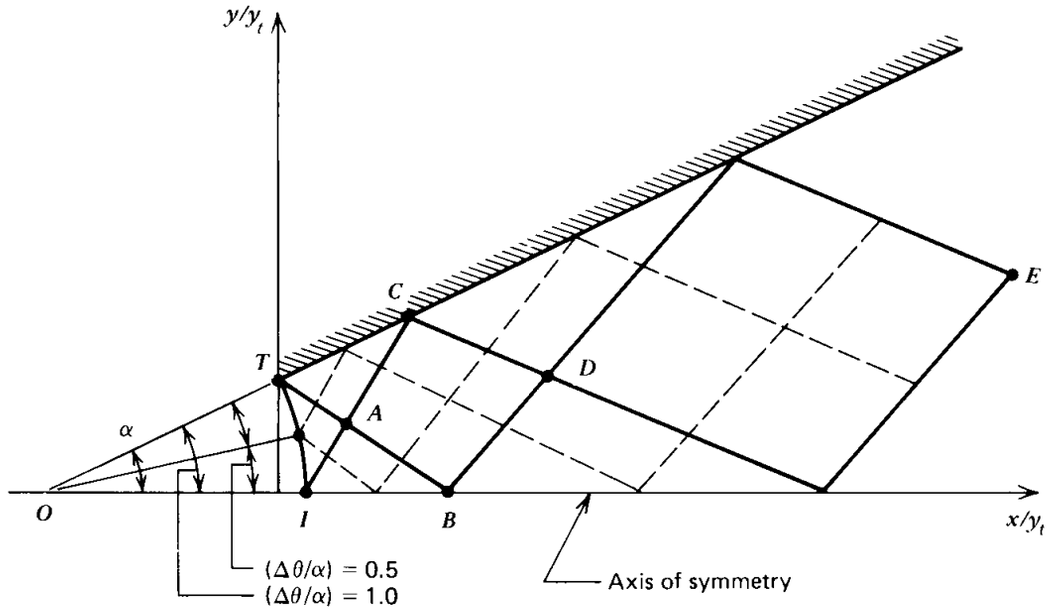

Figure 17.25 Initial-value line spacing and the corresponding characteristic network for an expanding flow.

It should be noted, however, that the concepts of accuracy and the order of accuracy presented here, as well as that of the Euler predictor-corrector integration method, are applicable to total differential equations. The characteristic and compatibility equations are strictly speaking, however, not total differential equations because the independent direction of differentiation is not the same in all of the simultaneous equations. A better description of those equations would be *total differential relationships* that may be solved by numerical techniques that are applicable to solving total differential equations. Consequently, it is not obvious that all of the concepts discussed above should be applicable to the numerical method of characteristics. Nevertheless, the results presented in the present section verify that those concepts do indeed apply to the numerical method of characteristics.

17–6(b) Summary of the Numerical Algorithms Investigated

Five numerical integration methods are investigated to determine their accuracies. The methods studied are described below. Methods 1, 2, and 3 are applicable to irrotational flows, and methods 4 and 5 to rotational flows.

(1) *Method 1* is based on equation 12.47.

$$(u^2-a^2)\,du_{\pm}+\left[2uv-(u^2-a^2)\lambda_{\pm}\right]dv_{\pm}-\delta\,(a^2v/y)\,dx_{\pm}=0 \qquad (12.47)$$

(2) *Method 2* is based on equation 12.49.

$$du_{\pm}+\lambda_{\mp}\,dv_{\pm}-\delta\,(a^2v/y)\,dx_{\pm}=0 \qquad (12.49)$$

(3) *Method 3* is based on equation 12.51, which is rearranged to read as follows.

$$\frac{\sqrt{M^2-1}}{V}\,dV_{\pm}\mp d\theta_{\pm}-\delta\left[\frac{\sin\theta}{yM\cos(\theta\pm\alpha)}\right]dx_{\pm}=0 \qquad (12.51)$$

(4) *Method 4* is based on equations 17.31, 17.25, and 17.26 for rotational flow.

$$(\rho v)\,du_{\pm}-(\rho u)\,dv_{\pm}+\left[\lambda_{\pm}-u(u\lambda_{\pm}-v)/a^2\right]dp_{\pm}$$
$$-\delta\left[\rho v(u\lambda_{\pm}-v)/y\right]dx_{\pm}=0 \qquad (17.31)$$

$$\rho u\,du+\rho v\,dv+dp=0 \qquad (17.25)$$

$$dp-a^2\,d\rho=0 \qquad (17.26)$$

(5) *Method 5* is based on equations 17.32, 17.33, and 17.26 for rotational flow.

$$\frac{\sqrt{M^2-1}}{\rho V^2}\,dp_{\pm}\pm d\theta_{\pm}+\delta\left[\frac{v}{yMV\cos(\theta\pm\alpha)}\right]dx_{\pm}=0 \qquad (17.32)$$

$$\rho V\,dV+dp=0 \qquad (17.33)$$

$$dp-a^2\,d\rho=0 \qquad (17.26)$$

Consequently, five sets of compatibility equations are considered. The numerical integration methods applicable to rotational flow are also applicable to irrotational flow. Hence, all five sets of compatibility equations are valid for analyzing irrotational flows. Two sets of compatibility equations are available for computing rotational flows.

For each of the five sets of compatibility equations, numerical algorithms based on both the *average coefficient method* and the *average property method* are considered. The methods presented in Sections 16–3 and 17–5 are average property methods. As an example of an average coefficient method, consider the average value for the first coefficient in equation 12.47. It is calculated as follows.

$$Q_{+}=\frac{Q_2+Q_4}{2}=\frac{(u_2^2-a_2^2)+(u_4^2-a_4^2)}{2} \qquad (17.80)$$

Investigating both the average coefficient method and the average property method requires applying 10 different numerical algorithms to irrotational flows and 4 to rotational flows. In the following sections, the aforementioned methods are compared for the same initial flow conditions. To simplify the presentation of the results, the legend presented in Table 17.17 is employed for identifying the 10 numerical algorithms; the *open symbols* denote the *average coefficient methods*, and the *closed symbols* denote the *average property methods*.

Table 17.17 Legend for the Numerical Algorithms

□	Method 1	Irrotational flow, average coefficient method
■	Method 1	Irrotational flow, average property method
⋈	Method 2	Irrotational flow, average coefficient method
⧓	Method 2	Irrotational flow, average property method
○	Method 3	Irrotational flow, average coefficient method
●	Method 3	Irrotational flow, average property method
◇	Method 4	Rotational flow, average coefficient method
◆	Method 4	Rotational flow, average property method
△	Method 5	Rotational flow, average coefficient method
▲	Method 5	Rotational flow, average property method

17–6(c) General Features of the Numerical Studies

Reference 12 presents accuracy studies for both irrotational and rotational flows, different source angles, various specific heat ratios, a range of initial Mach numbers M_i, both source flows and sink flows in conical and parabolic passages, and a large range of values for the step size h, for the 10 numerical algorithms presented in Table 17.17. The effect of predicting, correcting, and iterating to a specified tolerance is illustrated. Representative samples of those results are presented here.

For the subject studies, the initial-value line is a circular arc segment of a source flow that is tangent to the solid wall of the flow passage at its point of intersection with the wall, point T in Fig. 17.25. The initial-value line TI is divided into a number of equally spaced angular increments. The figure illustrates diagrammatically a few selected characteristics: those originating on the initial-value line at both the wall TAB and at the centerline IAC, and also their reflections throughout the flow field. The locations of the characteristics are determined by integrating numerically the pertinent characteristic equations. Similarly, the flow properties along a characteristic are determined by integrating numerically the appropriate compatibility equations along it. The accuracy studies should consider not only the accuracy achieved in locating the characteristics, but also the accuracy of the values of the flow properties computed along each characteristic. Numerical results are presented for the location of points A, B, C, and D (see Fig. 17.25), and for the flow properties at those points.

For the studies, it is assumed that the flowing fluid has the following thermodynamic properties: $\gamma = 1.20$, $R = 60$ ft-lbf/lbm-R (322.82 J/kg-K), $T = 6000$ R (3333.3 K), and $P = 1000$ lbf/in.^{2} ($6895 \cdot 10^5$ N/m^2). The number of points on the initial-value line is varied from 3 to 161. The configuration of the wall boundary is specified as being either conical or parabolic.

For a source flow, the error in the computed value of every flow property at each point may be determined by comparing the values obtained from the numerical solution with those obtained from the exact solution for the source flow. Figure 17.26 presents the exact solution for a 15-deg source flow, where the velocity V_{source} is plotted as a function of x/y_i, with M_i, the initial flow Mach number, as a parameter. The exact solution is the one-dimensional isentropic flow solution (see Section 4–9). For values of M_i close to unity, the initial expansion is highly nonlinear, and a second-order method may not demonstrate its second-order accuracy unless the step size is very small. In general, when the exact solution behaves approximately as a second-order polynomial, the second-order numerical

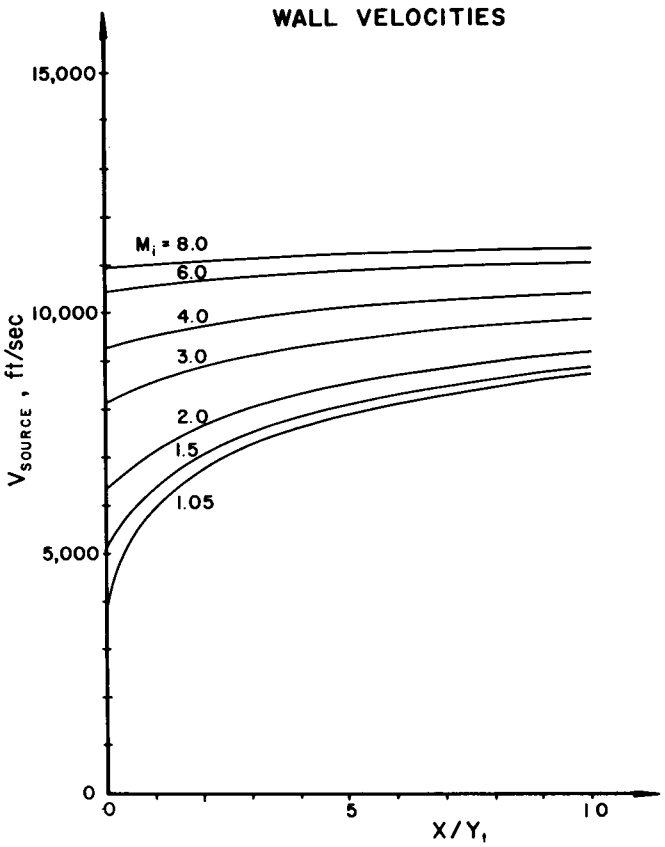

Figure 17.26 Exact wall velocities for a 15-deg source flow, $\gamma = 1.2$, with M_i as a parameter.

methods yield high accuracy. At the larger values for the initial Mach number M_i, the solution becomes almost linear, and a second-order numerical method should exhibit its second-order behavior even with a relatively large step size. Consequently, the solutions for the larger values of M_i should be more accurate than those for the smaller value of M_i. All of these essential qualities are verified by the results of the numerical studies presented here.

Once some error has accumulated, the solution is then effectively following a different member of the family of solutions to the differential equations. Hence, when a large error is produced for a flow near the sonic condition, the numerical solution then tends to follow a different solution curve. For expanding flows, however, all of the solution curves are converging. Consequently, large initial errors tend to decrease as the numerical solution approaches the higher flow velocities. For diffusing flows, however, the opposite effect occurs; that is, the family of solution curves diverges, so that even for small initial errors, the final error may be large.

The effects of gradients in the stagnation pressure and the stagnation temperature are similar to the effects of gradients in the other flow properties. The numerical integration of the differential equations pertinent to a flow having large stagnation property gradients requires smaller step sizes if an accuracy comparable to that for a flow with no stagnation property gradients is to be determined. The

combination of large stagnation property gradients and small values of the initial Mach number results in the most severe limitations on the accuracy obtainable by integrating the differential equations numerically.

17–6(d) Accuracy of the Numerical Methods for Analyzing Expanding Flows

The nominal case discussed in Section 17–6(c) is analyzed by employing the 10 numerical algorithms discussed in Section 17–6(b). The initial Mach number is $M_i = 1.05$, and it is assumed that there are no stagnation property gradients. The corrector is applied repeatedly until the values of the properties converge to a fractional tolerance of 0.00001. Results are presented for x, y, V, and θ at the points A, B, C, and D (see Fig. 17.25) as a function of the step size $h = (\Delta\theta/\alpha)$ on the initial-value line. The exact values at $h = (\Delta\theta/\alpha) = 0$ are obtained by the numerical approximation of the exact solution as discussed in Section 17–6(a).

Figure 17.27 presents the results obtained at point A. It is evident from the figure that each of the 10 numerical integration methods considered (see Table 17.17) is

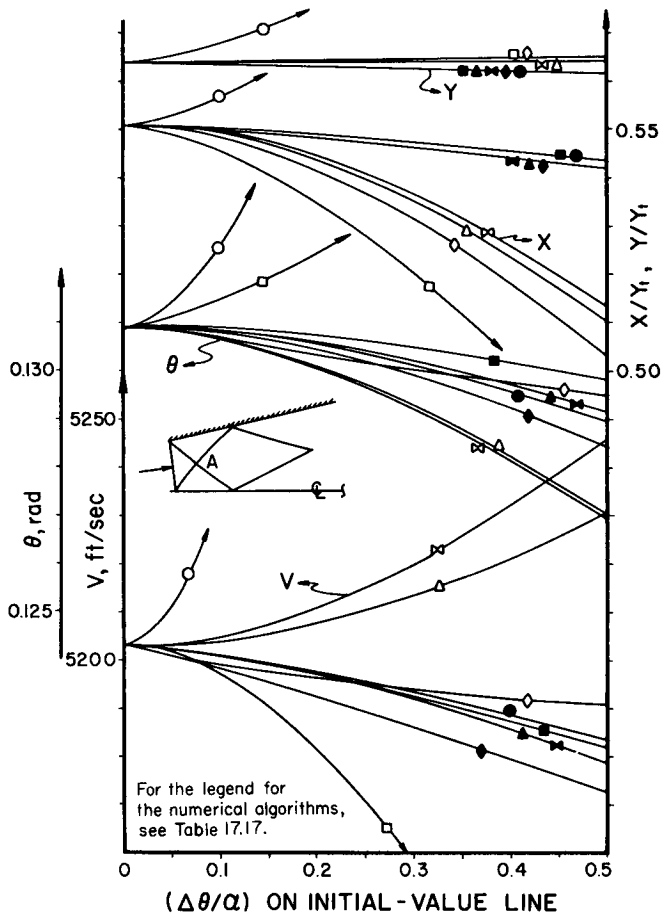

Figure 17.27 Solution at point A for a 15-deg source flow initial-value line with $M_i = 1.05$, 15 deg half-angle diverging contour, $\gamma = 1.2$.

inherently of second order, but some of them yield better absolute accuracy than others. For example, methods 1 and 3, which are average coefficient methods (i.e., □ and ○), both exhibit poor absolute accuracy. In general, more accurate results are obtained with the average property methods rather than with the average coefficient methods. The results presented in Fig. 17.27 are based exclusively on the calculation of interior points in the flow field; no effects because of either boundary (wall or axis of symmetry) are experienced at point A. A surprising result is the change in the absolute accuracy of method 3 from very poor for the average coefficient method to very good for the average property method.

Figure 17.28 presents similar results at point B. The solution at point B is influenced by both the unit processes for an interior point and for an axis of symmetry point. Because θ and y are zero at point B, only the values of V and x are presented in the figure. Each of the 10 methods exhibits second-order accuracy. The prediction of the x locations is more accurate for the average property methods.

Figure 17.29 presents the numerical solutions obtained for the properties at point C. The results for point C are influenced by the unit processes for a wall point and

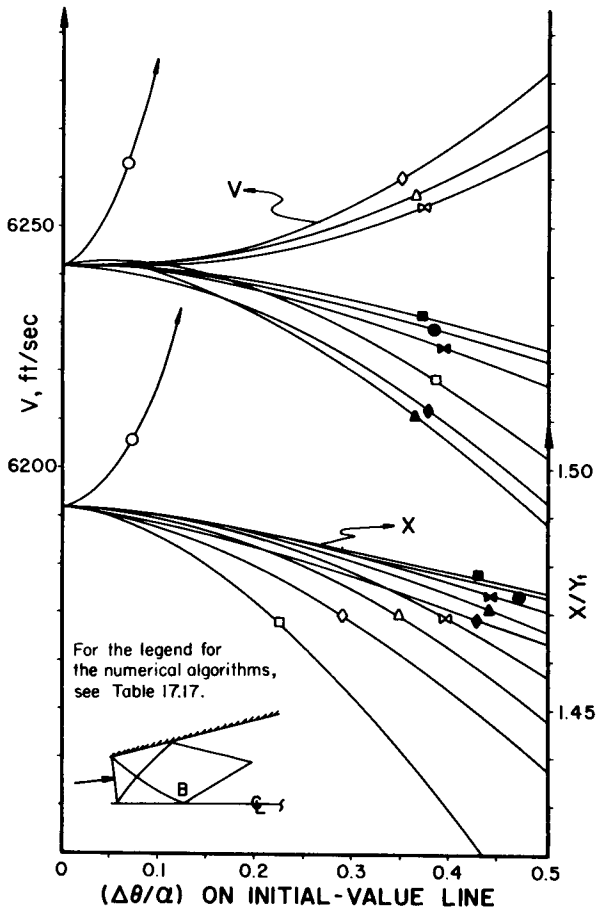

Figure 17.28 Solution at point B for a 15-deg source flow initial-value line with $M_i = 1.05$, 15 deg half-angle diverging contour, $\gamma = 1.2$.

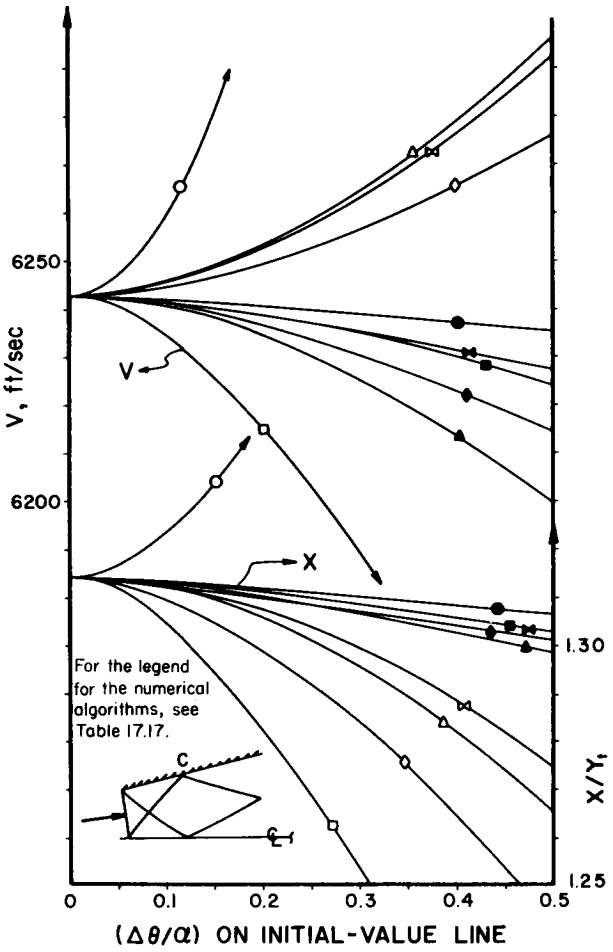

Figure 17.29 Solution at point C for a 15-deg source flow initial-value line with $M_i = 1.05$, 15 deg half-angle diverging contour, $\gamma = 1.2$.

an interior point. Since $y = x \tan\theta$ and $\theta = 15$ deg, Fig. 17.29 presents only the values of V and x. It is seen that all of the average property methods yield more accurate results than the average coefficient methods.

Figure 17.30 presents the numerical results for the solutions at point D, for the case of a parabolic wall contour. The solution at point D is influenced by the unit processes for the interior point, the wall point, and the axis of symmetry point. Several of the average coefficient methods overshoot the solution and do not exhibit their second-order character until the step size is relatively small. All of the average property methods, however, are clearly second order, and they are more accurate than the average coefficient methods.

Based on the results presented in Figs. 17.27 through 17.30, the average property methods appear to be more accurate than the average coefficient methods. Most of the methods do exhibit, however, a reasonable absolute accuracy even for a step size of $h = (\Delta\theta/\alpha) = 0.5$, which specifies only three points on the initial-value line. All of the methods exhibit second-order behavior, although the scatter increases as the solution progresses down the flow passage. Because the flow is irrotational, the methods for both irrotational flow and for rotational flow are considered in the

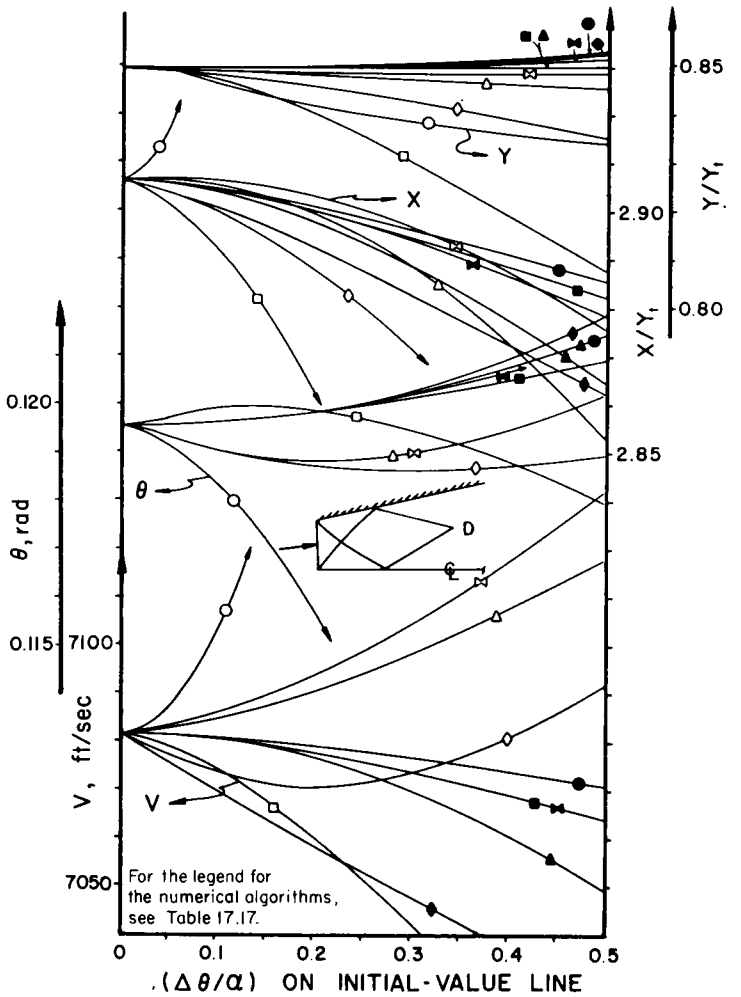

Figure 17.30 Solution at point D for a 15-deg source flow initial-value line with $M_i = 1.05$, parabolic contour from 15 deg entrance to 10 deg exit, $\gamma = 1.2$.

comparison. The accuracies of the methods for rotational flow are comparable to those obtainable with the methods applicable to irrotational flow.

Rotational flow fields result when the flow across the initial-value line is rotational. Initial-value lines for rotational flow are obtained by specifying a uniform static pressure and Mach number across the source flow line, a stagnation pressure increase of 100 lbf/in.^{2}, and a stagnation temperature increase of 1000 R from the wall to the axis of symmetry. Figure 17.31 presents the results for the solutions at point A, assuming an initial Mach number of 1.05. Since the flow is rotational, the results are presented only for Methods 4 and 5. The latter methods are second order when the step size is sufficiently small. It is seen that the average property methods are more accurate than the average coefficient methods. The results indicate that the gradients in the stagnation properties must be given serious consideration when selecting the step size, especially in the case of flows near the sonic condition. The combination of high velocity gradients near the sonic condition combined with large stagnation property gradients has an adverse effect on the absolute accuracy of the numerical integration methods.

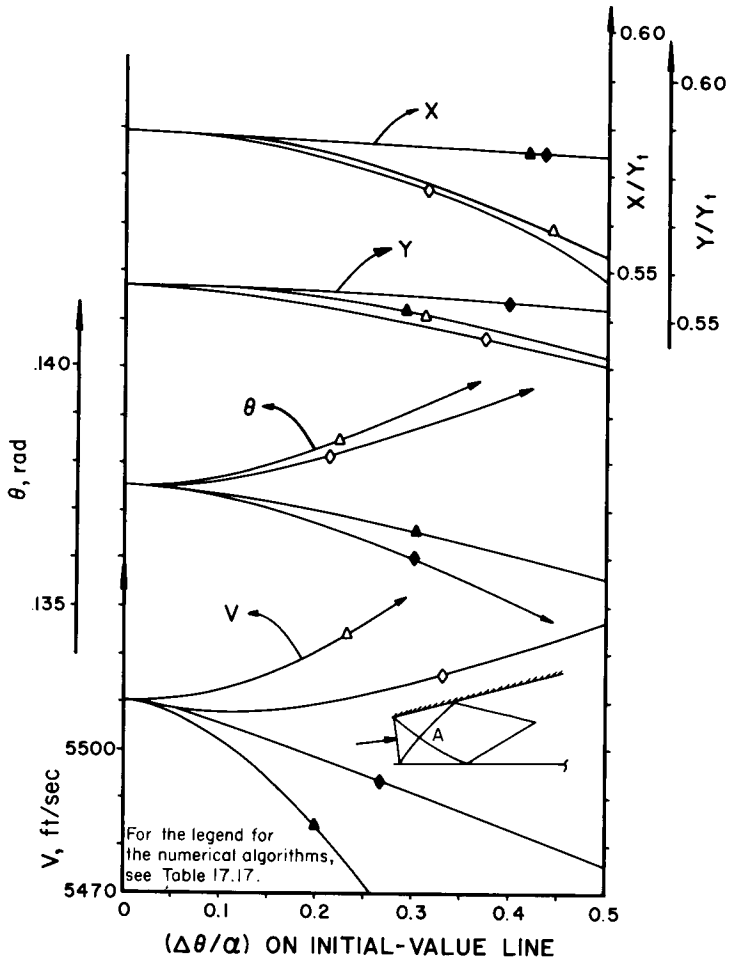

Figure 17.31 Solution at point A for a rotational initial-value line with $\Delta P = 100$ lbf/in.^{2} and $\Delta T = 1000$ R, $M_i = 1.05$, 15 deg half-angle diverging contour, $\gamma = 1.2$.

Method 5 is representative of the accuracy that may be obtained by the method of characteristics. The results obtained for the wall velocities are presented for method 5 to illustrate further the properties of that algorithm. Figure 17.32 presents the error in the velocity $\Delta V = V - V_{\text{source}}$ along the wall as a function of x/y_t, with the step size $h = (\Delta\theta/\alpha)$ as a parameter, for an initial Mach number $M_i = 1.05$. The full line curves apply to the calculations based on the average property method, and the broken line curves to the average coefficient method. The second-order behavior of those numerical integration methods is clearly evident.

The large initial errors obtained with the average coefficient method are disconcerting. Those errors are due to the large velocity gradient at the initial-value line, where $M_i = 1.05$. When the Mach number is close to unity, as in the cases studied, the magnitudes of the coefficients in the differential equations may change by a factor as large as two at a point in a characteristic net. For example, the coefficient $(u^2 - a^2)$ of du in method 1 (see equation 17.80) approximately doubles in value for a flow Mach number change from $M = 1.05$ to $M = 1.10$. The fact that the error in

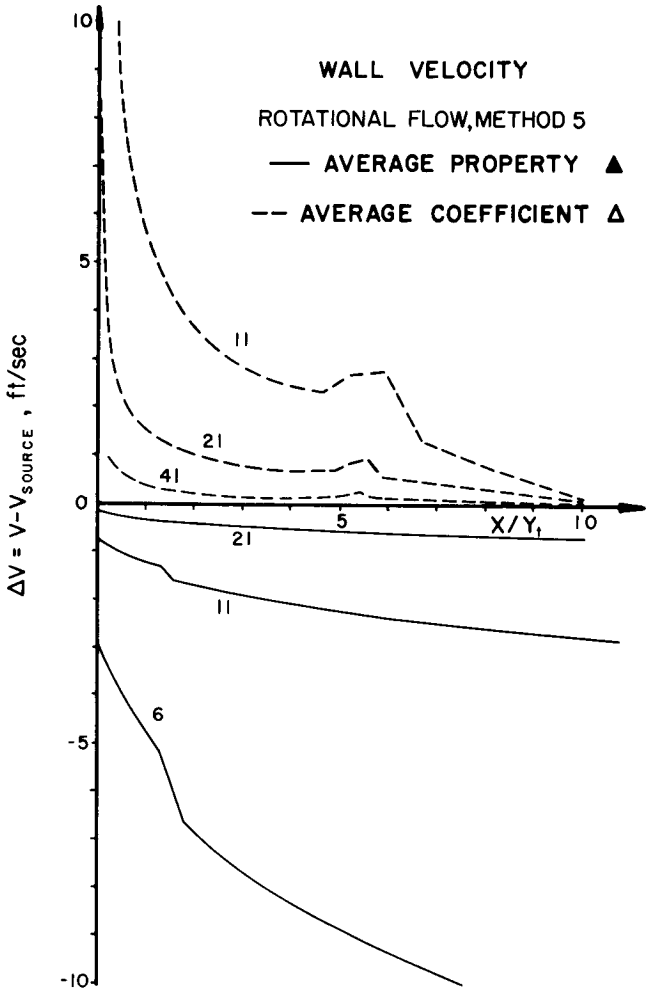

Figure 17.32 Wall velocity for a 15-deg source flow initial-value line with $M_i = 1.05$, 15 deg half-angle diverging contour, $\gamma = 1.2$, Method 5, with 6, 11, 21 and 41 points on the initial-value line.

the velocity ΔV decreases with increasing x/y_t and approaches zero is due to a fortuitous combination of the inherent characteristics of the numerical algorithm and the converging nature of the family of solution curves. The results presented in Fig. 17.32 suggest that in the vicinity of the sonic condition the step size for the numerical integration should be very small.

Figure 17.33 presents the error in the velocity ΔV along the wall as a function of x/y_t, with the initial Mach number M_i as a parameter. As in Fig. 17.32, the solid line curves apply to the average property method and the broken line curves apply to the average coefficient method. For the average coefficient method, it is seen that as M_i is increased, the initial error decreases and approaches zero. The error then increases monotonically with increasing values of x/y_t. It is evident, from Figs. 17.32 and 17.33 that, for flows near the sonic condition, the average property method gives the best accuracy, especially when the step size on the initial-value line is small.

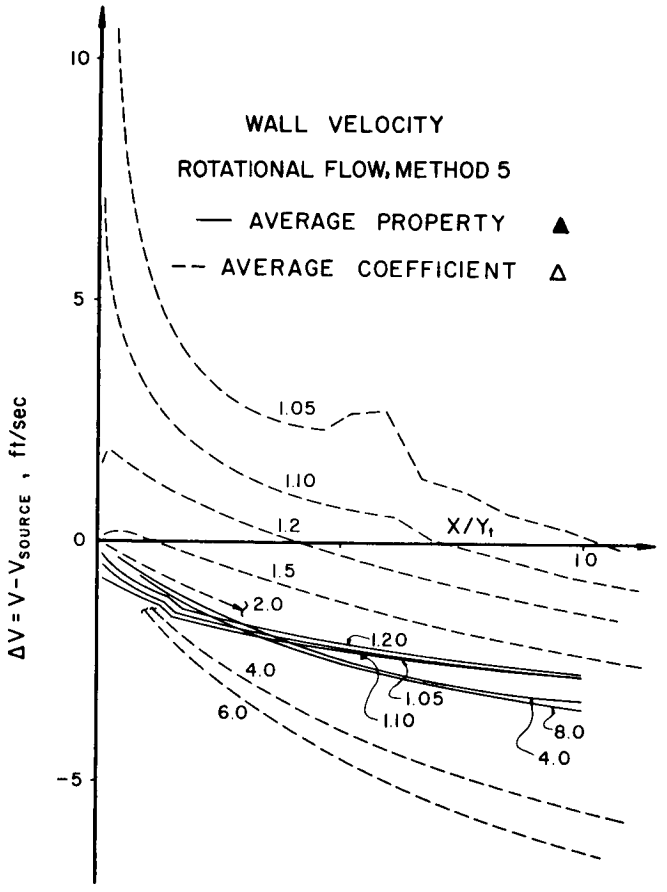

Figure 17.33 Wall velocity for a 15-deg source flow initial-value line with 11 points, 15 deg half-angle diverging contour, $\gamma = 1.2$, with $M_i = 1.05$, 1.1, 1.2, 1.5, 2, 4, 6 and 8. Method 5.

17–6(e) Comparison of the Accuracies of the Algorithms for Predicting, Correcting, and Iterating

Figure 17.34 presents the error in the velocity ΔV along the wall for method 5 employing the average property method. The dashed curves are for the Euler predictor, which theoretically should be first order, as it clearly is. The solid curves are for one application of the modified Euler corrector, which theoretically should be, and is, second order. It is apparent that by applying the corrector a significant improvement in the absolute accuracy is obtained. The results presented in Fig. 17.34 demonstrate clearly the desirability of the higher-order method.

It is not clear, however, whether or not the repeated application of the corrector is worthwhile. Figure 17.35 presents the results obtained with one, two, and three applications of the modified Euler corrector, for method 5. The basic character of the average coefficient method is unchanged by the repeated applications of the corrector. The basic character of the average property method, however, appears to change from an *overpredicting* to an *underpredicting* method. In both cases, how-

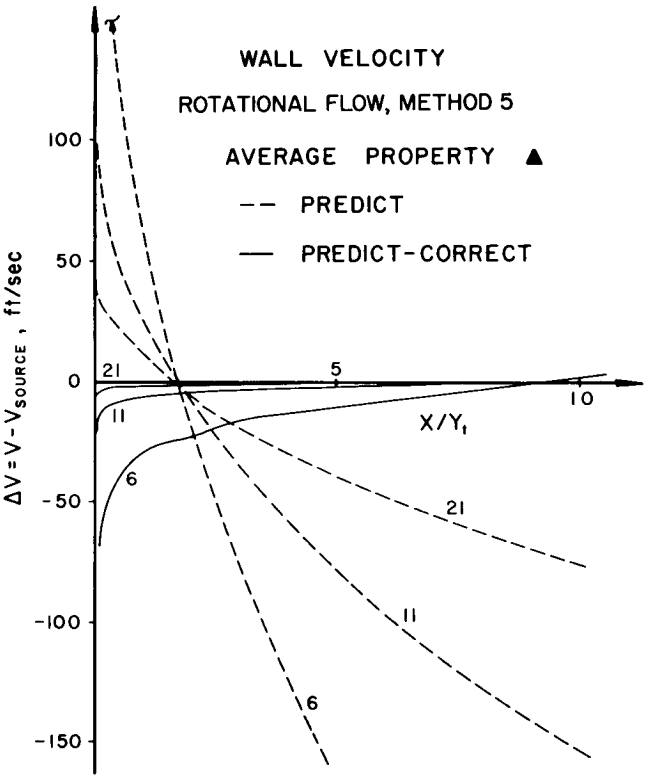

Figure 17.34 Wall velocity for a 15-deg source flow initial-value line with $M_i = 1.05$, 15 deg half-angle diverging contour, $\gamma = 1.2$, Method 5, with 6, 11, and 21 points on the initial-value line, illustrating predict only and predict-correct once results.

ever, there appears to be little gain in the accuracy obtainable by repeated application of the corrector, other than the reduction in the initial error in the case of the average property method. Certainly no more than two applications of the corrector are warranted.

Figure 17.36 presents the error in the velocity ΔV along the wall as a function of x/y_t for the case where the corrector is applied repetitively until the solution converges to a specified fractional tolerance. The results demonstrate clearly that no benefit is gained by converging the calculated result to a fractional tolerance smaller than 0.001. The results for a tolerance of 10^{-8} in some cases require twice as much computer time as those for a tolerance of 10^{-3}, with no significant change in the numerical solution. To obtain a fractional tolerance of 0.01 generally requires a single predict-correct solution, particularly for the average coefficient method. In the case of the average property method, however, the relatively large initial error (see Fig. 17.35) obtained with a single application of the corrector is practically eliminated. The results presented in Figs. 17.35 and 17.36 suggest that a predict and correct-once method should be employed in conjunction with a coarse convergence tolerance, which allows more applications of the corrector in regions where the property changes are large.

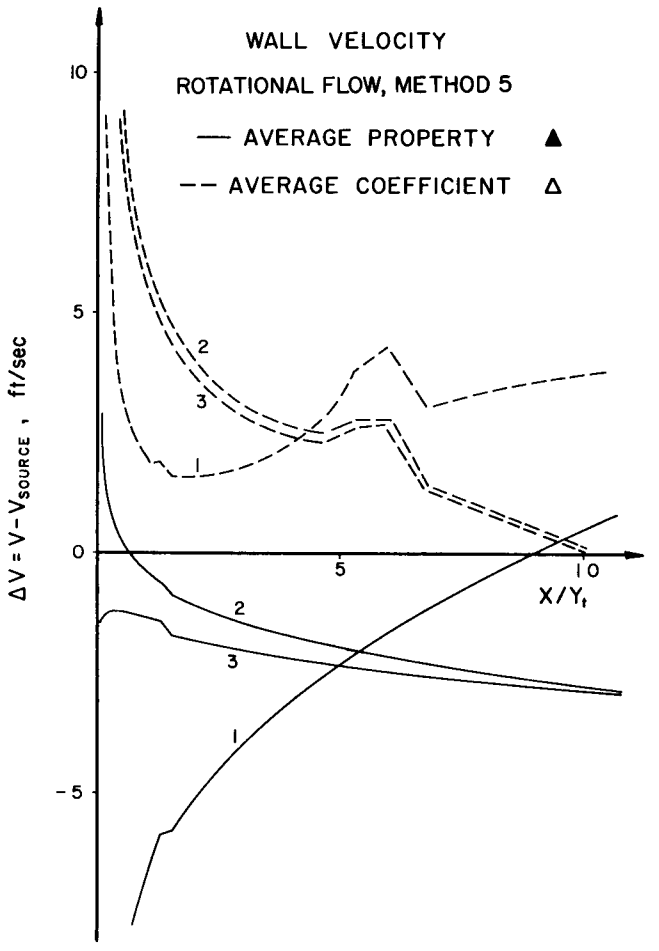

Figure 17.35 Wall velocity for a 15-deg source flow initial-value line with $M_i = 1.05$, 15 deg half-angle diverging contour, $\gamma = 1.2$, Method 5, with 11 points on the initial-value line, illustrating the effect of the number of applications of the corrector.

17–6(f) Accuracy of the Numerical Methods for Analyzing Diffusing Flows

It is pointed out in Section 17–6(c) that, for expanding flows, the family of solution curves is converging, while for diffusing flows they are diverging. Consequently, the solutions curves are more closely spaced at the high supersonic flow Mach numbers, but they diverge as the Mach number decreases, as may be inferred from Fig. 17.26 by recalling that in a diffusing supersonic flow the flow Mach number decreases in the flow direction. Figure 17.33 shows that the initial error is small for a flow having a large initial Mach number, and that the error grows in a bounded manner. Accordingly, for a diffusing flow the initial error inherent to a numerical method for calculating the solution is small because the initial Mach number is large. The error grows rapidly, however, as the flow Mach number approaches small values. Near the sonic condition, the error may grow without bound.

Figure 17.37 presents the error in the pressure Δp along the wall as a function of x/y_t, for a 15-deg sink flow with an initial Mach number $M_i = 3.0$, with the number

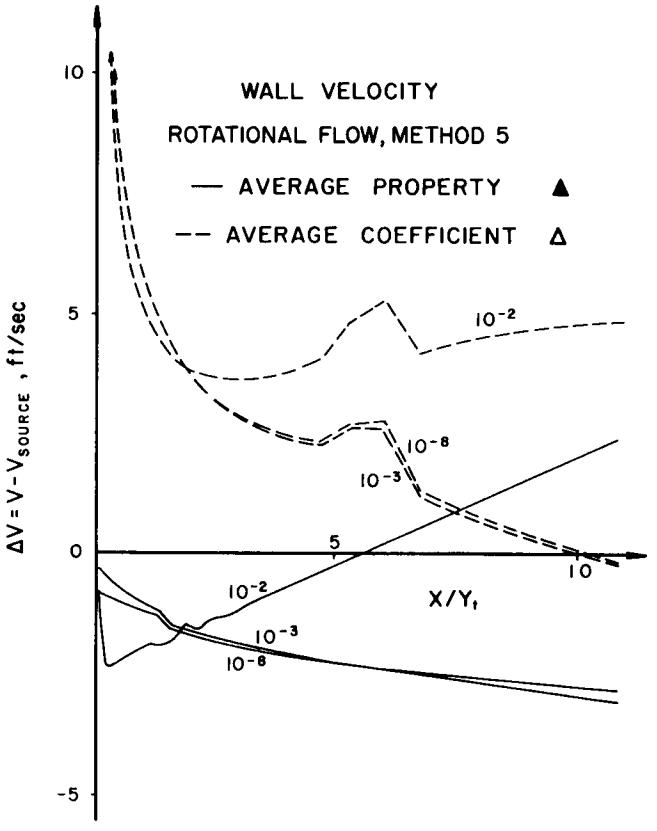

Figure 17.36 Wall velocity for a 15-deg source flow initial-value line with $M_i = 1.05$, 15 deg half-angle diverging contour, $\gamma = 1.2$, Method 5, with 11 points on the initial-value line, illustrating the effect of a fractional convergence tolerance.

of points on the initial-value line as a parameter. The numerical method is clearly second order, and the initial errors are extremely small. As to be expected, the absolute error Δp grows rapidly as the flow decelerates, and it appears that the growth rate for Δp is unbounded. For a diffusing flow, the application of iteration appears to be advantageous. The above results suggest that a method employing a coarse grid may be employed in the high Mach number region of a diffusing flow, and that the grid spacing should be decreased as the Mach number decreases, approaching 21 to 41 points across the flow field when the sonic condition is approached.

17–6(g) Some Results for Planar Flow

In general, the conclusions presented for an axisymmetric flow are also valid for a planar flow. The major difference is in the magnitude of the absolute error, which is much smaller for a planar flow, because for the latter flow the property gradients are much smaller. Figure 17.38 presents the error in velocity ΔV along the wall and the centerline as functions of x/y_t based on method 5 employing the average property method. It is seen that the initial error ΔV is small and that it grows in a bounded manner. The centerline and wall solutions have comparable accuracies, principally because there is no nonhomogeneous term in the governing differential

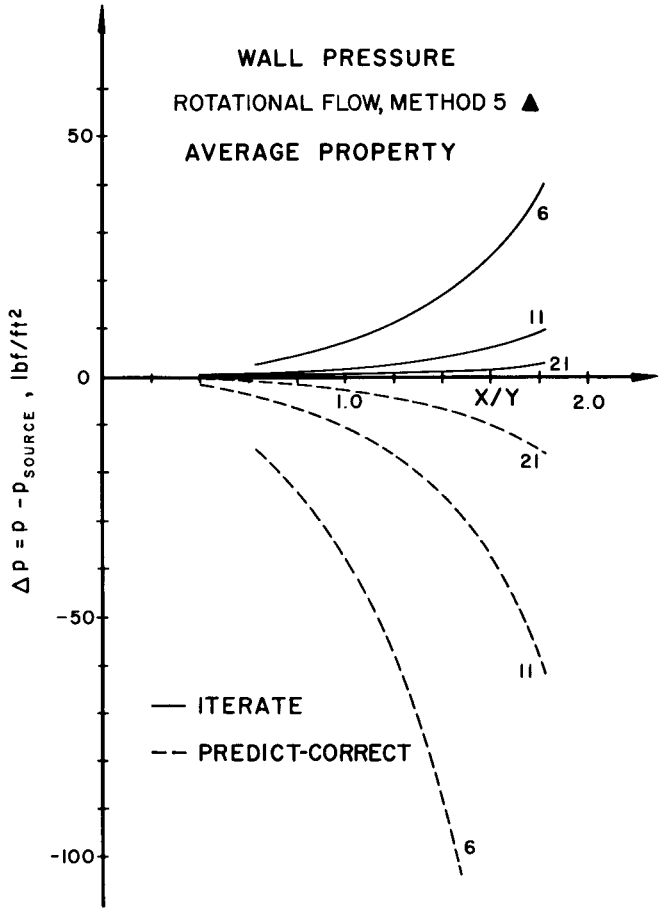

Figure 17.37 Wall pressure for a 15-deg sink flow initial-value line with $M_i = 3.0$, 15 deg half-angle converging contour, $\gamma = 1.2$, Method 5, with 6, 11, and 21 points on the initial-value line.

equation as there is in axisymmetric flow. The solution is clearly second order.

Comparison of the results presented in Fig. 17.38 with those presented in Fig. 17.32 indicates that the error ΔV for planar flow is one-tenth of that for axisymmetric flow. Hence, to obtain an accuracy comparable to that for the equivalent axisymmetric flow, the step size for the numerical integration of a two-dimensional planar flow may be larger than that employed for analyzing a comparable axisymmetric two-dimensional flow.

17-6(h) Conclusions from the Accuracy Studies

The results of the accuracy studies, although strictly speaking valid only for the specific flows investigated, do suggest some general guidelines for the application of the numerical method of characteristics to two-dimensional supersonic flows.

For rotational flows, a characteristic network based on following the Mach lines and extending the streamline back to intersect the line between the two initial points is satisfactory. For irrotational flows, the results obtained with the methods applicable to a rotational flow are of comparable accuracy to the results obtained with the irrotational flow methods.

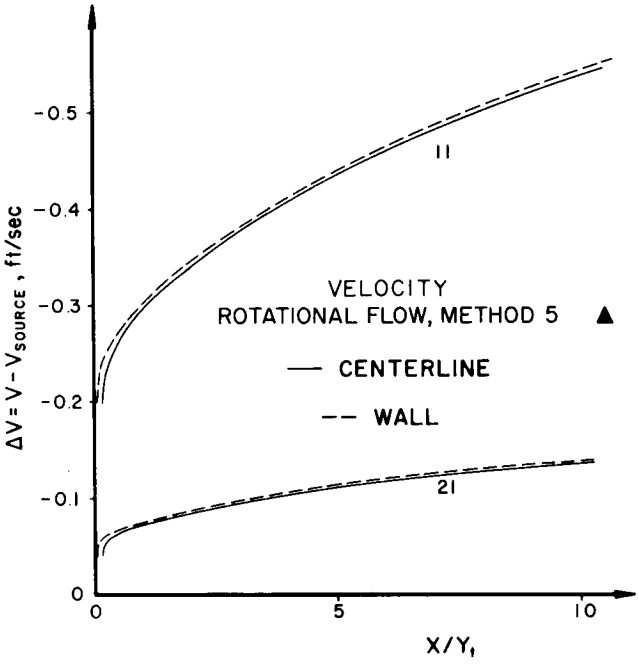

Figure 17.38 Wall and centerline velocities for a 15-deg source flow initial-value line with $M_i = 1.05$, 15 deg half-angle diverging contour, $\gamma = 1.2$, Method 5, with 11 and 21 points on the initial-value line, for a planar two-dimensional flow field.

In most cases, the results obtained employing the average property method are more accurate than those obtained by the average coefficient method. Consequently, the average property method is recommended.

The results of the studies concerned with *predict*, *predict-correct*, and *iterate*, suggest that a method employing a single predict-correct with an overriding coarse convergence tolerance in the regions of high gradients is advantageous. In regions of either large velocity or stagnation property gradients, satisfactory accuracy is obtainable if a large number of grid points is utilized.

For an expanding flow, the number of points may be decreased as the solution progresses, but for a diffusing flow, the number of points should be increased.

In summary, the results of the accuracy studies presented herein indicate that high accuracy is attainable in the analysis of steady two-dimensional supersonic flow by the numerical method of characteristics.

REFERENCES

1. D. B. Taulbee and S. Boraas, "Transonic Nozzle Flow with Nonuniform Total Energy," *Journal of the American Institute of Aeronautics and Astronautics*, Vol. 9, No. 10, pp. 2102–2104, October 1971.
2. G. V. R. Rao, "Exhaust Nozzle Contour for Optimum Thrust," *Jet Propulsion*, Vol. 28, pp. 377–382, 1958.
3. G. Guderley, "On Rao's Method for Computation of Exhaust Nozzles," *Zeitschrift für Flugwissenschaften*, Vol. 7, pp. 345–350, 1959.
4. K. G. Guderley and J. V. Armitage, "General Approach to Optimum Rocket Nozzles," Chap. 11, *Theory of Optimum Aerodynamic Shapes*, Edited by A. Miele, Academic Press, New York, 1965.

5. M. Peter Scofield and Joe D. Hoffman, "Maximum Thrust Nozzles for Nonequilibrium Simple Dissociating Gas Flows," *Journal of the American Institute of Aeronautics and Astronautics*, Vol. 9, No. 9, pp. 1824–1832, September 1971.
6. O. M. Belotserkovskii, "Flow with a Detached Shock Wave about a Symmetric Profile," *Journal of Applied Mathematics and Mechanics*, Vol. 22, pp. 279–296, 1958.
7. G. Moretti and M. Abbett, "A Time-Dependent Computational Method for Blunt Body Flows," *Journal of the American Institute of Aeronautics and Astronautics*, Vol. 4, No. 12, pp. 2136–2141, December 1966.
8. C. P. Li, "Time Dependent Solutions of Nonequilibrium Airflow past a Blunt Body," *Journal of Spacecraft and Rockets*, Vol. 9, No. 8, pp. 571–572, August 1972.
9. H. Lomax and M. Inouye, "Numerical Analysis of Flow Properties about Blunt Bodies Moving at Supersonic Speeds in an Equilibrium Gas," NASA TR-R-204, 1964.
10. L. D. Kayser and J. E. Danberg, "Experimental Study of Separation from the Base of a Cone at Supersonic Speeds," *Journal of the American Institute of Aeronautics and Astronautics*, Vol. 12, No. 11, pp. 1607–1609, November 1974.
11. I. S. Donaldson, "On the Separation of a Supersonic Flow at a Sharp Corner," *Journal of the American Institute of Aeronautics and Astronautics*, Vol. 5, No. 6, pp. 1086–1088, June 1967.
12. J. D. Hoffman, "Accuracy Studies of the Numerical Method of Characteristics for Axisymmetric, Steady Supersonic Flows," *Journal of Computational Physics*, Vol. 11, No. 2, pp. 210–239, February 1973.

18
the method of characteristics applied to the steady two-dimensional flow of nonequilibrium chemically reacting gas mixtures and gas-particle mixtures

18–1 PRINCIPAL NOTATION FOR CHAPTER 18

The notation presented in Sections 14–1 and 16–1 and the additional notation presented below are employed in this chapter.

a_f $= \sqrt{\gamma_f RT}$, frozen speed of sound.
c_{pf} frozen specific heat at constant pressure.
C_o denotes characteristic curve C_o (i. e., the streamline).
h absolute enthalpy of the gas mixture.
h_i sensible enthalpy of species i.
h_i° energy of formation of species i.
R gas constant of the gas mixture.
R_i gas constant of species i.
t time.
T static temperature of the gas.
T_p static temperature of condensed particles.
u_p, v_p velocity components in the x,y direction of condensed particles.
V_p $= \sqrt{u_p{}^2 + v_p{}^2}$, magnitude of particle velocity.
$\boldsymbol{V}_p$ velocity of condensed particle.

Greek Letters

γ_f frozen specific heat ratio.
λ_o $= \tan(v/u)$, slope of C_o characteristic (i.e., the streamline).
ψ term in energy equation defined by equation 18.15 for nonequilibrium chemically reacting flow.
ψ term in energy equation defined by equation 18.53 for gas-particle flow.
ψ_p particle stream function.

Subscripts

j denotes particle j ($j = 1, \ldots, n$) in a gas-particle flow.

18–2 INTRODUCTION

The method of characteristics is applied to steady two-dimensional irrotational (i. e., entropy and stagnation enthalpy constant throughout the flow field) supersonic flow in Chapters 12 and 16. In Chapter 17, the method of charcteristics is applied to steady two-dimensional rotational isentropic (i. e., entropy and stagnation enthalpy constant only along streamlines) supersonic flow in the absence of dissipative effects such as friction, heat transfer, finite rate chemical reactions, drag of condensed phases, and so on. Two important types of flow in which dissipative effects occur are the flow of nonequilibrium chemically reacting gas mixtures and the flow of gas-particle mixtures. Steady one-dimensional flow of nonequilibrium chemically reacting gas mixtures is considered in Section 14–6, and steady one-dimensional flow of gas-particle mixtures is considered in Section 14–7. In this chapter, the method of characteristics is applied to the steady two-dimensional supersonic flow of nonequilibrium chemically reacting gas mixtures and the flow of gas-particle mixtures.

18–3 STEADY TWO-DIMENSIONAL FLOW OF NONEQUILIBRIUM CHEMICALLY REACTING GAS MIXTURES

The steady one-dimensional flow of nonequilibrium chemically reacting gas mixtures is analyzed in Section 14–6. In this section, that analysis is extended to steady two-dimensional supersonic flow. The governing equations are presented, and the characteristic and compatibility equations are derived. The numerical implementation of those equations is discussed briefly.

18–3(a) Governing Equations

Table 10.1 presents the governing equations for a steady multidimensional adiabatic flow that performs no work, is inviscid, and has negligible body forces. Those equations are valid for a nonequilibrium chemically reacting flow when combined with the following two considerations.

1. The enthalpy h in equation 10.168a is the absolute enthalpy, which comprises the sensible enthalpy and the energy of formation [see Section 14–3(a)].
2. The law of the conservation of mass must be applied to each chemical species involved in the nonequilibrium reactions.

Accordingly, from Table 10.1 and Section 14–3(a), it follows that the governing equations for the steady multidimensional flow of a nonequilibrium chemically reacting gas mixture are the following.

$$\nabla \cdot (\rho \mathbf{V}) = 0 \tag{18.1}$$

$$\rho \frac{D\mathbf{V}}{Dt} + \nabla p = 0 \tag{18.2}$$

$$\frac{D}{Dt}\left(h + \frac{V^2}{2}\right) = 0 \tag{18.3}$$

$$\nabla \cdot (\rho_i \mathbf{V}) = \sigma_i \quad (i = 1, \ldots, n) \tag{18.4}$$

$$h = \sum_{i=1}^{n} C_i (h_i + h_i^\circ) \tag{18.5}$$

where σ_i is the species source function derived in Section 14–3(e), h_i is the sensible enthalpy, and h_i° is the energy of formation of species i. Section 14–6 discusses the application of the above equations to steady one-dimensional flow.

The above set of equations may be rearranged to yield a set of equations that is more amenable to numerical computations. Substituting $C_i = \rho_i / \rho$ into equation 18.4 and expanding yields

$$\nabla \cdot (C_i \rho \mathbf{V}) = C_i \nabla \cdot (\rho \mathbf{V}) + \rho \mathbf{V} \cdot \nabla C_i = \sigma_i \qquad (i = 1, \ldots, n) \tag{18.6}$$

Substituting equation 18.1 into equation 18.6, we obtain

$$\rho \frac{DC_i}{Dt} = \sigma_i \quad (i = 1, \ldots, n) \tag{18.7}$$

where $\mathbf{V} \cdot \nabla C_i = DC_i / D_t$ for steady flow.

Forming the scalar product of the velocity vector $\mathbf{V}$ with equation 18.2, we obtain

$$\rho \mathbf{V} \cdot \frac{D\mathbf{V}}{Dt} + \mathbf{V} \cdot \nabla p = \rho \frac{D}{Dt}\left(\frac{V^2}{2}\right) + \frac{Dp}{Dt} = 0 \tag{18.8}$$

Substituting for $D(V^2/2)/Dt$ from equation 18.8 into equation 18.3 gives

$$\rho \frac{Dh}{Dt} - \frac{Dp}{Dt} = 0 \tag{18.9}$$

Substituting for h from equation 18.5 into equation 18.9 yields

$$\frac{Dp}{Dt} = \rho \sum_{i=1}^{n} (h_i + h_i^\circ) \frac{DC_i}{Dt} + \rho \sum_{i=1}^{n} C_i \frac{Dh_i}{Dt} \tag{18.10}$$

where $Dh_i^\circ / Dt = 0$. For a thermally perfect gas,

$$h_i = \int_{T_o}^{T} c_{pi}\, dT \tag{18.11}$$

and

$$p = \rho T \sum_{i=1}^{n} C_i R_i \tag{18.12}$$

where T denotes the *static temperature*.* Substituting equations 18.7 and 18.11 into equation 18.10 yields

$$\frac{Dp}{Dt} = \sum_{i=1}^{n} (h_i + h_i^\circ)\sigma_i + \rho c_{pf} \frac{DT}{Dt} \tag{18.13}$$

where $c_{pf} = \sum_{i=1}^{n} C_i c_{pi}$ is termed the *frozen specific heat* at constant pressure. The substantial derivative DT/Dt may be determined from equation 18.12, where DC_i/Dt is obtained from equation 18.7. Substituting that result into equation 18.13 and rearranging, we obtain

$$\frac{Dp}{Dt} - a_f^2 \frac{D\rho}{Dt} = \psi \tag{18.14}$$

where $c_{pf} = \gamma_f R/(\gamma_f - 1)$, $a_f^2 = \gamma_f RT$, and

$$\psi \equiv \sum_{i=1}^{n} \psi_i \equiv \sum_{i=1}^{n} \left[\gamma_f R_i T - (\gamma_f - 1)(h_i + h_i^\circ) \right] \sigma_i \tag{18.15}$$

Hence, the steady multidimensional flow of a nonequilibrium chemically reacting mixture of thermally perfect gases is governed by equations 18.1, 18.2, 18.7, and 18.14.

For a steady two-dimensional flow, the above set of equations takes the form shown in Table 18.1, where $\delta = 0$ for planar flow and $\delta = 1$ for axisymmetric flow.

Comparing the above equations to the corresponding governing equations for isentropic flow presented in Section 17–3(a), it is seen that the only differences are the nonhomogeneous term ψ in the energy equation, equation 18.19, and the addition of the species *continuity equations*, equation 18.20, to the set of equations. Consequently, the development of a numerical algorithm based on the method of characteristics for solving the governing equations for nonequilibrium chemically reacting flow is quite similar to that presented in Sections 17–3 and 17–4 for isentropic flow.

*In this chapter, t denotes the time, and T denotes the static temperature, not the stagnation temperature.

Table 18.1 Governing Equations for Steady Two-Dimensional Flow of a Mixture of Nonequilibrium Chemically Reacting Perfect Gases

$$\rho u_x + \rho v_y + u\rho_x + v\rho_y + \delta\rho v/y = 0 \tag{18.16}$$

$$\rho u u_x + \rho v u_y + p_x = 0 \tag{18.17}$$

$$\rho u v_x + \rho v v_y + p_y = 0 \tag{18.18}$$

$$up_x + vp_y - a_f^2 u\rho_x - a_f^2 v\rho_y = \psi \tag{18.19}$$

$$\rho u C_{ix} + \rho v C_{iy} = \sigma_i \qquad (i = 1, \ldots, n) \tag{18.20}$$

18–3(b) Characteristic and Compatibility Equations

The characteristic and compatibility equations are derived by the method employed in Section 17–3 for isentropic flow. The procedure is simplified by noting that equation 18.20 may be put directly into characteristic form. Rearranging equation 18.20, we obtain

$$\rho u\left(C_{ix} + \frac{v}{u} C_{iy}\right) = \sigma_i \qquad (i = 1, \ldots, n) \tag{18.21}$$

From Table 10.2, equation 10.184, along a streamline,

$$\lambda = \frac{dy}{dx} = \frac{v}{u} \tag{18.22}$$

Consequently, along a streamline, equation 18.21 may be written in the form

$$\rho u\, dC_i = \sigma_i dx \qquad (i = 1, \ldots, n) \tag{18.23}$$

since $(C_{ix} + \lambda C_{iy}) = dC_i/dx$ when $\lambda = v/u$.

Following the procedure employed in section 17–3(b), the remaining four equations are multiplied by the unknown parameters σ_1 through σ_4 and summed, as indicated below.

$$\sigma_1(18.16) + \sigma_2(18.17) + \sigma_3(18.18) + \sigma_4(18.19) = 0 \tag{18.24}$$

After performing the summation, the coefficients of the x derivatives of u, v, p, and ρ are factored out. The result is exactly the same as equation 17.11 with the addition of the nonhomogeneous term $\sigma_4\psi$. The latter term may be combined with the term $\sigma_1\delta\rho v/y$ in equation 17.11 to yield the new nonhomogeneous term

$$\sigma_1\delta\rho v/y - \sigma_4\psi \tag{18.25}$$

Since the terms containing derivatives are unchanged, the same characteristics that are obtained for an isentropic flow are obtained for a nonequilibrium chemically reacting flow; that is, the streamline and the Mach lines [see equations 17.20 and 17.22, Section 17–3(b)]. The characteristics are illustrated in Fig. 18.1. Note that the speed of sound appearing in equation 18.19 is the *frozen speed of sound* a_f. Consequently, the Mach lines for a nonequilibrium chemically reacting flow are termed the *frozen Mach lines*. Equations 17.20 and 17.22 are repeated and renumbered below.

$$\left(\frac{dy}{dx}\right)_o = \lambda_o = \frac{v}{u} \qquad (\textit{streamline}) \tag{18.26}$$

$$\left(\frac{dy}{dx}\right)_{\pm} = \lambda_{\pm} = \tan(\theta \pm \alpha) \qquad (\textit{Mach lines}) \tag{18.27}$$

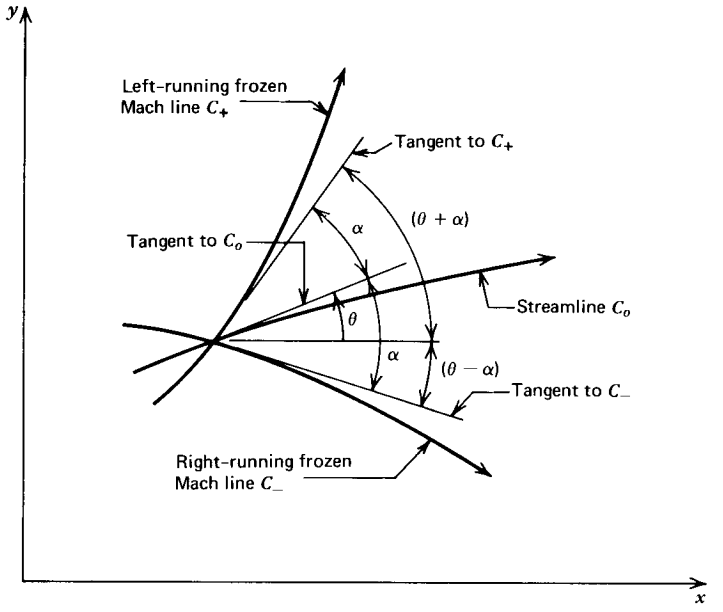

Figure 18.1 Characteristics for steady two-dimensional supersonic flow of a nonequilibrium chemically reacting gas mixture.

The compatibility equations may be obtained by adding the term $-\sigma_4\psi$ to equation 17.13. Thus,

$$\rho(\sigma_1 + u\sigma_2)\,du + \rho u\sigma_3\,dv + (\sigma_2 + u\sigma_4)\,dp + u\left(\sigma_1 - a_f^2\sigma_4\right)d\rho + (\sigma_1\delta\rho v/y - \sigma_4\psi)\,dx = 0 \tag{18.28}$$

Following the procedure presented in Section 17–3(c), along the streamlines equation 18.28 becomes

$$\sigma_2(\rho u\,du + \rho v\,dv + dp) + \sigma_4\left(u\,dp - a_f^2 u\,d\rho - \psi\,dx\right) = 0 \tag{18.29}$$

Since σ_2 and σ_4 each may be arbitrary, we obtain

$$\rho u\,du + \rho v\,dv + dp = 0 \tag{18.30}$$

$$u\,dp - a_f^2 u\,d\rho = \psi\,dx \tag{18.31}$$

Equations 18.30 and 18.31 are the compatibility equations that are valid along the streamlines.

Following the steps presented in Section 17–3(c), along the Mach lines equation 18.28 becomes

$$(\rho v)\,du_\pm - (\rho u)\,dv_\pm + \left[\lambda_\pm - u(u\lambda_\pm - v)/a_f^2\right]dp_\pm - (u\lambda_\pm - v)\left[\delta\rho v/y - \psi/a_f^2\right]dx_\pm = 0 \tag{18.32}$$

where the subscript $\pm$ indicates the C_+ and C_-, or left- and right-running Mach lines, respectively.

Alternate forms of equations 18.30 and 18.32 may be obtained in terms of V, θ, and M by introducing equations 12.41 and 12.42. Thus,

$$dp + \rho V\, dV = 0 \tag{18.33}$$

$$\frac{\sqrt{M^2-1}}{\rho V^2}\, dp_{\pm} \pm d\theta_{\pm} + \left(\frac{\delta \sin\theta}{yM} - \frac{\psi}{\rho V^2 a_f} \right) \frac{dx_{\pm}}{\cos(\theta \pm \alpha)} = 0 \tag{18.34}$$

Summarizing, along the streamlines, equations 18.23 (repeated n times because there are n chemical species), 18.31, and 18.33 are applicable, and equation 18.34 is applicable along both of the Mach lines. Hence, $4+n$ equations are available for determining the $4+n$ properties p, θ, B, ρ, and C_i $(i=1,\ldots,n)$. Table 18.2 presents the characteristic and compatibility equations for the steady two-dimensional flow of nonequilibrium chemically reacting gas mixture.

Table 18.2 Characteristic and Compatibility Equations for Steady Two-Dimensional Flow of a Nonequilibrium Chemically Reacting Gas Mixture

Characteristic equations		
$\left(\frac{dy}{dx}\right)_o = \lambda_o = \frac{v}{u}$	*(streamline)*	(18.26)
$\left(\frac{dy}{dx}\right)_{\pm} = \lambda_{\pm} = \tan(\theta \pm \alpha)$	*(Mach lines)*	(18.27)
Compatibility equations		
$dp + \rho V\, dV = 0$	*(along streamlines)*	(18.33)
$dp - a_f^2\, d\rho = \frac{\psi}{u}\, dx$	*(along streamlines)*	(18.31)
$\rho u\, dC_i = \sigma_i\, dx \ (i=1,\ldots,n)$	*(along streamlines)*	(18.23)
$\frac{\sqrt{M^2-1}}{\rho V^2}\, dp_{\pm} \pm d\theta_{\pm} + \left[\frac{\delta \sin\theta}{yM} - \frac{\psi}{\rho V^2 a_f} \right] \frac{dx_{\pm}}{\cos(\theta \pm \alpha)} = 0$	*(along Mach lines)*	(18.34)

18–3(c) Implementation of the Numerical Analysis

The unit processes for a nonequilibrium chemically reacting flow are quite similar to those for an isentropic flow discussed in Section 17–4. The computational effort required is increased considerably by the presence of the finite rate chemical reactions.

Section 14–6 describes the numerical procedure for analyzing a steady one-dimensional nonequilibrium chemically reacting flow, and Section 17–4 describes the numerical procedure for analyzing a steady two-dimensional isentropic flow. The analysis of a steady two-dimensional nonequilibrium chemically reacting flow is essentially a combination of the procedures described in the aforementioned two sections. The unit processes are modifications of the unit processes for isentropic flow by the addition of the species continuity equations; the latter are integrated numerically along the streamlines of the flow by employing the numerical methods applied in analyzing the steady one-dimensional flow.

Section 17–4(a) discusses the three possible characteristic networks which may be constructed from the streamline and the Mach lines. They are illustrated diagrammatically in Fig. 17.2. The network based on the Mach lines, Fig. 17.2*a*, is employed in the unit process for an interior point in isentropic flow. The flow properties at the intersection of the rearward running streamline C_o and the line between points 1 and 2 are determined by interpolation. In a nonequilibrium chemically reacting flow, even small errors in the interpolation of species concentrations may cause serious accuracy problems in the numerical integration of the species continuity equations along a streamline. A more suitable choice for the characteristic network is one based on following the streamline and either of the two Mach lines, as illustrated in Figs. 17.2*b* and 17.2*c*. In either case, the interpolation for the species concentrations along the streamline is eliminated. At the *back point* on a characteristic, the flow properties p, ρ, V, and θ are determined by interpolation. Those properties vary slowly through the characteristic grid, however, so that their values may be interpolated quite accurately.

Reference 1 presents a computer program for calculating nonequilibrium chemically reacting flows in nozzles. The computer program considers the six elements C, H, O, N, F, and Cl, 19 gaseous species containing those elements, and 48 chemical reactions that may occur between those species. The unit processes are based on extending the streamline and the left-running Mach line from two known points, and projecting a right-running Mach line rearward so that it intersects the previous left-running Mach line, as illustrated in Fig. 18.2.

The major difficulty in analyzing a steady two-dimensional nonequilibrium chemically reacting flow is, therefore, the complexity of the numerical algorithm due to the large number of individual chemical species and their associated chemical reactions that must be considered. The difficulty is not due to a lack of understanding of the basic flow processes. Space limitations preclude including the

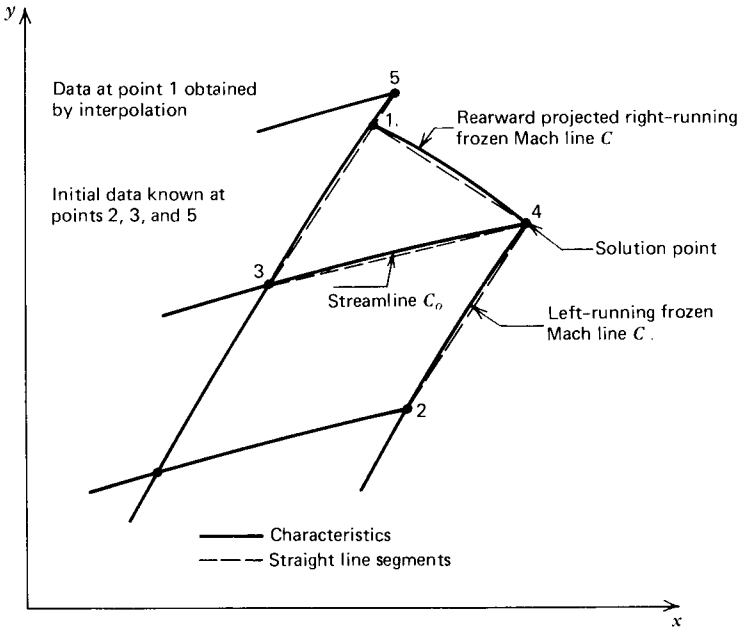

Figure 18.2 Finite difference network for an interior point for steady two-dimensional nonequilibrium chemically reacting flow.

development here of the unit processes for nonequilibrium chemically reacting flow. Those unit processes are discussed in Reference 1.

18–3(d) Example of Steady Two-Dimensional Nonequilibrium Chemically Reacting Flow

Example 14.7 presents the results of a steady one-dimensional analysis of the nonequilibrium chemically reacting flow of the products of combustion of the H_2–F_2 system described in Example 14.3. That same chemical system is analyzed in the present section by the method of characteristics program presented in Reference 1 to illustrate the two-dimensional flow effects.

The physical apparatus is a gas-fueled rocket motor burning hydrogen and fluorine as the propellants at a combustion pressure of $6.895 \cdot 10^5$ N/m^2. The oxidizer to fuel ratio by mass is 12.0, and the temperature of the reactants is 298.15 K. The combustion temperature, composition, and entropy are determined in Example 14.3.

The properties of both a frozen expansion and an equilibrium expansion from the combustor through an adiabatic frictionless nozzle having an area ratio of 50 in the divergence are determined in Example 14.6. Figure 14.9 presents the composition as a function of nozzle area ratio, and Fig. 14.10 presents the temperature, velocity, and Mach number as a function of nozzle area ratio.

The flow properties for a steady one-dimensional expansion from the combustor through the nozzle taking into account the finite reaction rates of the gases are determined in Example 14.7. The reaction mechanism is specified by equation 14.82, the backward reaction rates are presented in Table 14.3, and the equilibrium constants are presented in Table D.1. The nozzle is a De Laval nozzle having a conical converging section with a semiangle of 45 deg and a conical diverging section with a semiangle of 15 deg. The throat diameter is 0.0254 m and the radius of curvature of the circular arc throat is 0.0508 m. The results of the analysis are presented in Figs. 14.9 and 14.10.

The chemical system and nozzle geometry considered in the above discussion may be analyzed by the computer program presented in Reference 1 to determine the two-dimensional flow effects. The only additional piece of data required is the number of points desired on the initial-value line. The results that follow are obtained with 11 points on the initial-value line.

Figure 18.3 presents the mole fractions of H and H_2 as functions of the nondimensional length x/y_t for three cases: one-dimensional flow, flow along the wall for the two-dimensional analysis, and flow along the axis for the two-dimensional analysis. The three curves for each species are quite similar, indicating that two-dimensional flow effects are not strong in this nozzle. That should be expected since the radius of curvature of the nozzle circular arc throat is large compared to the throat radius ($\lambda = \rho_t/y_t = 2.0$) and the nozzle wall is straight (a conical wall with $\alpha = 15$ deg).

The temperature T, velocity V, and the Mach number M are presented in Fig. 18.4 as functions of the nozzle area ratio ε for the same three cases described above. Again, the two-dimensional flow effects are not great, but a significant effect is present.

By comparing the results presented in Figs. 18.3 and 18.4 with the one-dimensional equilibrium flow and frozen flow results presented in Figs. 14.9 and 14.10, it is apparent that the differences in the chemical model (i.e., equilibrium, frozen, or nonequilibrium chemistry) has a much greater influence on the composition and

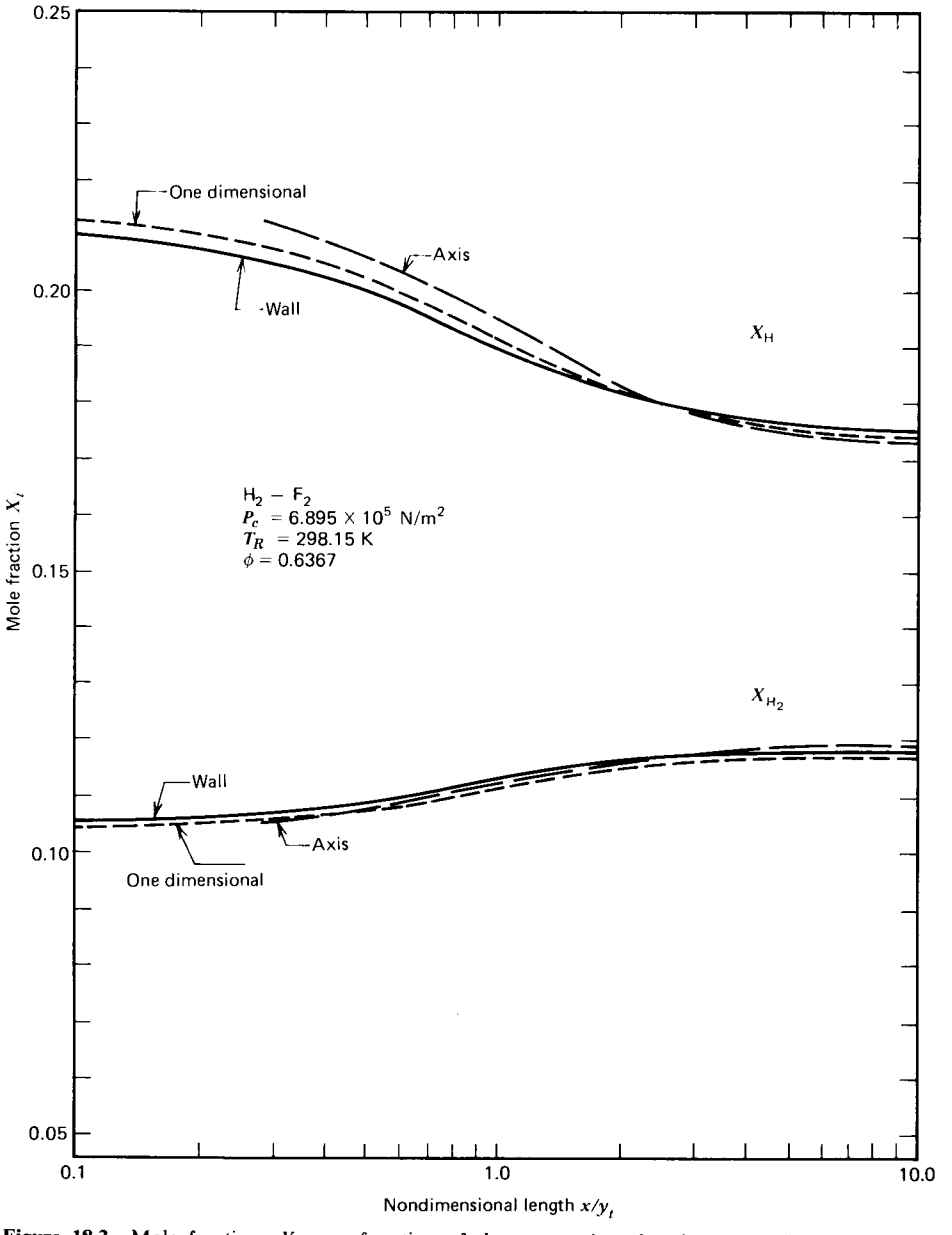

Figure 18.3 Mole fractions X_i as a function of the area ratio ϵ for the nonequilibrium chemically reacting flow of the products of combustion of the H_2–F_2 reaction through a nozzle.

flow properties than the two-dimensional flow effects. For less reactive chemical systems and for more radical nozzle geometries, the relative influence of chemistry and nozzle geometry may be reversed. No general conclusions may be made, and each combination of a specific chemical system and a specific nozzle geometry must be analyzed to determine the relative influence of chemistry and geometry.

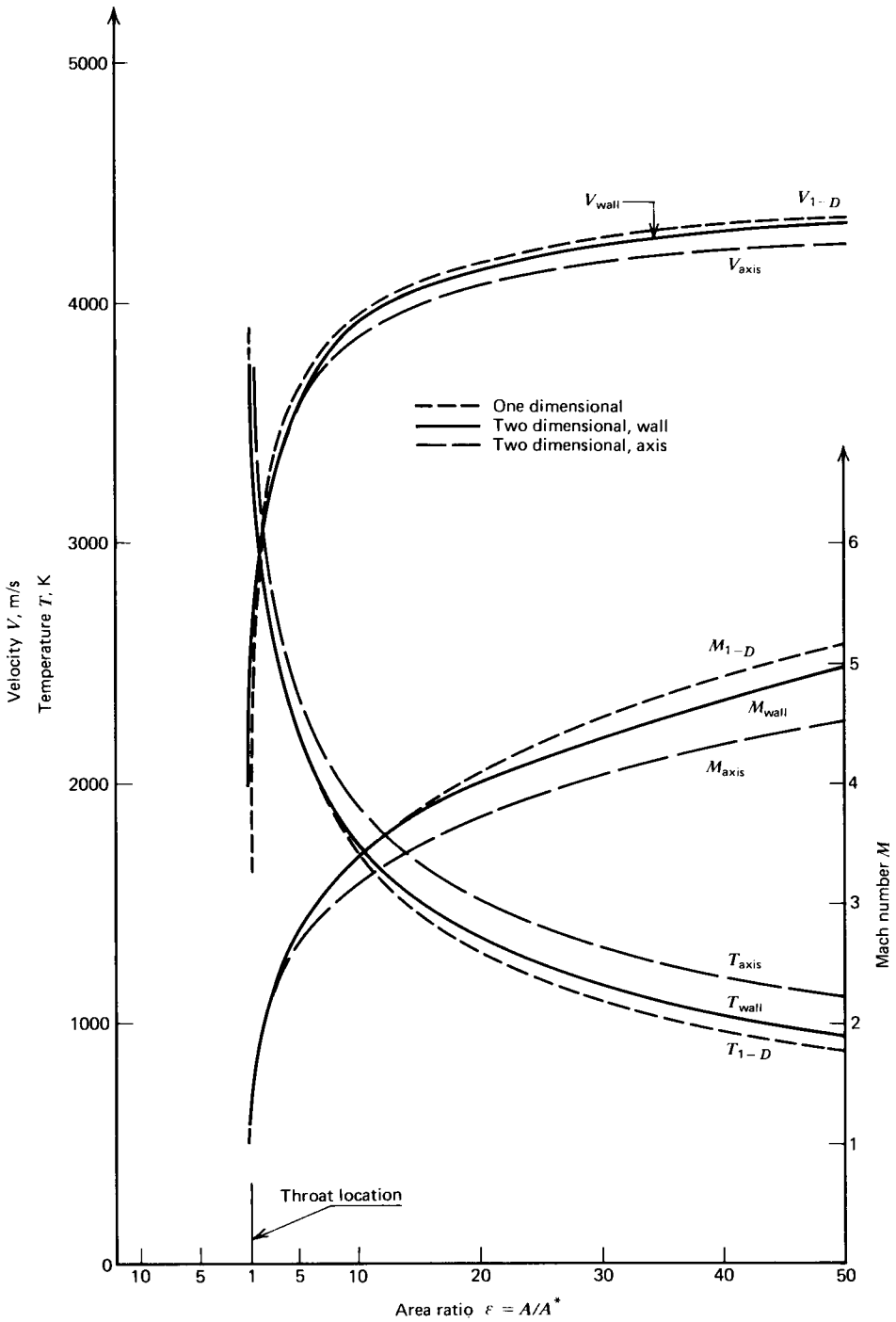

Figure 18.4 Temperature T, velocity V, and Mach number M for the nonequilibrium chemically reacting flow of the products of combustion of the H_2–F_2 reaction through a nozzle.

18–4 STEADY TWO-DIMENSIONAL FLOW OF GAS-PARTICLE MIXTURES

In Section 14–7, the steady one-dimensional flow of a gas-particle mixture is considered. That analysis is extended here to the case of steady two-dimensional supersonic flow. The governing equations are presented, and the characteristic and compatibility equations are derived. The implementation of a numerical method for solving those equations is discussed briefly.

18–4(a) Governing Equations

The model for the steady multidimensional flow of a gas-particle mixture is illustrated schematically in Fig. 18.5. The assumptions presented in Section 14–7 are applicable. They are restated here for convenience.

1. The flow is steady.
2. There is no work, external heat transfer, or wall friction, and the effect of gravity is negligible.
3. The particles exert a body force $\delta \mathbf{D}$ on the gas and transfer the heat δQ to the gas.
4. The particles occupy negligible volume, do not interact with each other, have a uniform internal temperature, are incompressible, and are spherical in shape.

As pointed out in Section 14–7, the *particle flow properties* may be determined by analyzing the behavior of an individual particle as it passes through the control volume. The body force $\delta \mathbf{D}$ and the heat transfer δQ denote the total drag and heat transfer, respectively, due to all of the particles in the control volume. As in Section 14–7(a), the symbols for the flow properties without a subscript denote *gas properties*, and those with the subscript p denote *particle properties*

The governing equations for the steady one-dimensional flow of a gas-particle mixture, derived in Section 14–7(a), can be generalized so that they apply to a steady multidimensional flow.

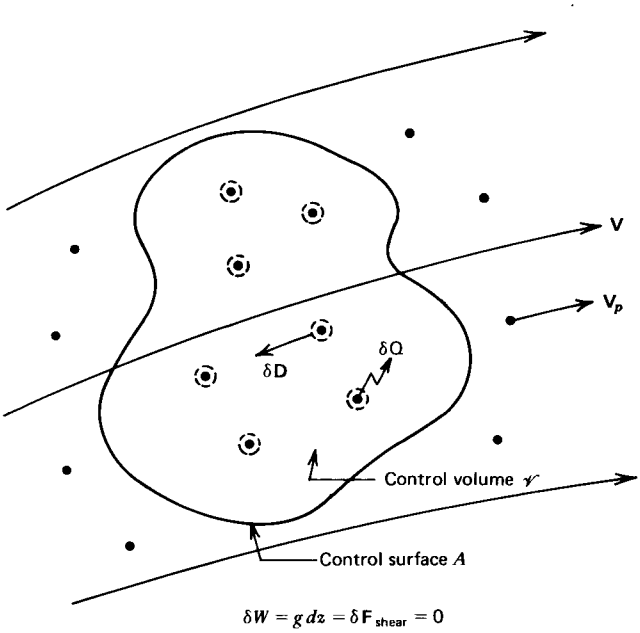

Figure 18.5 Flow model for gas-particle flow.

1. *Particle continuity equation.* In terms of the particle density ρ_p, the law of the conservation of mass for the particles is given by

$$\nabla \cdot (\rho_p \mathbf{V}_p) = 0 \tag{18.35}$$

where ρ_p is the total mass of particles per unit volume of the flowing medium, and $\mathbf{V}_p$ is the particle velocity.

2. *Particle momentum equation.* Because momentum is a vector quantity, the particle momentum equation for steady one-dimensional flow, equation 14.181, applies to each direction of a multidimensional flow. Consequently, equation 14.181 applies in each of the three coordinate directions for a Cartesian coordinate system. In vector form, the *particle momentum equation* is

$$\frac{D\mathbf{V}_p}{Dt} = A_p(\mathbf{V} - \mathbf{V}_p) \tag{18.36}$$

where A_p is defined by equation 14.182.

3. *Particle energy equation.* The particle energy equation for one-dimensional flow, equation 14.191, may be extended to multidimensional flow by noting that the left-hand side of that equation is analogous to the substantial derivative in a multidimensional flow. Thus*,

$$\frac{Dh_p}{Dt} = B_p(T - T_p) \tag{18.37}$$

where B_p is defined by equation 14.192.

4. *Particle equation of state.* The particle equation of state is given by

$$T_p = f(h_p) \tag{18.38}$$

Equation 14.199 is an explicit relationship for the particle equation of state when the particle specific heat is constant.

5. *Gas continuity equation.* From Table 10.1, we obtain

$$\nabla \cdot (\rho \mathbf{V}) = 0 \tag{18.39}$$

6. *Gas momentum equation.* Equation 14.202 may be extended to multidimensional flow by noting that, for multidimensional flow,

$$V\frac{dV}{dx} \Rightarrow \frac{D\mathbf{V}}{Dt} \qquad \text{and} \qquad \frac{dp}{dx} \Rightarrow \nabla p \tag{18.40}$$

Thus, equation 14.202 becomes

$$\rho \frac{D\mathbf{V}}{Dt} + \rho_p \frac{D\mathbf{V}_p}{Dt} + \nabla p = 0 \tag{18.41}$$

Substituting equation 18.36 into equation 18.41, we obtain

$$\rho \frac{D\mathbf{V}}{Dt} + \nabla p = -\rho_p A_p(\mathbf{V} - \mathbf{V}_p) \tag{18.42}$$

Equation 18.42 is analogous to Euler's momentum equation for inviscid flow, equation 17.2, but with a nonhomogeneous term which accounts for the effects of the particle drag.

* In this section T denotes the static temperature and not the stagnation temperature.

7. *Gas energy equation.* Equation 14.205 for one-dimensional flow may be extended to multidimensional flow by changing all of the derivatives to substantial derivatives. Thus,

$$\rho \frac{Dh}{Dt} + \rho \frac{D}{Dt}\left(\frac{V^2}{2}\right) + \rho_p \frac{Dh_p}{Dt} + \rho_p \frac{D}{Dt}\left(\frac{V_p^2}{2}\right) = 0 \tag{18.43}$$

Forming the scalar product of $\mathbf{V}_p$ with equation 18.36 gives

$$\mathbf{V}_p \cdot \frac{D\mathbf{V}_p}{Dt} = \frac{D}{Dt}\left(\frac{V_p^2}{2}\right) = A_p(\mathbf{V}_p \cdot \mathbf{V} - \mathbf{V}_p \cdot \mathbf{V}_p) \tag{18.44}$$

Forming the scalar product of $\mathbf{V}$ with equation 18.42 yields

$$\rho \frac{D}{Dt}\left(\frac{V^2}{2}\right) + \frac{Dp}{Dt} = -\rho_p A_p(\mathbf{V} \cdot \mathbf{V} - \mathbf{V} \cdot \mathbf{V}_p) \tag{18.45}$$

Substituting equations 18.37, 18.44, and 18.45 into equation 18.43, we obtain

$$\rho \frac{Dh}{Dt} - \frac{Dp}{Dt} = \rho_p A_p(\mathbf{V} \cdot \mathbf{V} - 2\mathbf{V} \cdot \mathbf{V}_p + \mathbf{V}_p \cdot \mathbf{V}_p) + \rho_p B_p(T_p - T) \tag{18.46}$$

8. *Gas equation of state (see equations 14.207 to 14.210).*

$$h = h(p, \rho) \tag{18.47}$$

$$T = T(p, \rho) \tag{18.48}$$

For a perfect gas, equations 18.47 and 18.48 take the forms

$$h = \int_{T_o}^{T} c_p \, dT + h_o \tag{18.49}$$

$$p = \rho RT \tag{18.50}$$

For a perfect gas, equation 18.46 may be simplified by employing equations 18.49 and 18.50 to express Dh/Dt in terms of the derivatives of the pressure and the density. Thus,

$$\rho \frac{Dh}{Dt} = \rho c_p \frac{DT}{Dt} = \frac{\rho c_p}{R} \frac{D}{Dt}\left(\frac{p}{\rho}\right) = \frac{1}{\gamma - 1}\left(\gamma \frac{Dp}{Dt} - a^2 \frac{D\rho}{Dt}\right) \tag{18.51}$$

Substituting equation 18.51 into equation 18.46 yields

$$\frac{Dp}{Dt} - a^2 \frac{D\rho}{Dt} = \psi \tag{18.52}$$

where

$$\psi = (\gamma - 1)\rho_p\left[A_p(\mathbf{V} \cdot \mathbf{V} - 2\mathbf{V} \cdot \mathbf{V}_p + \mathbf{V}_p \cdot \mathbf{V}_p) + B_p(T_p - T)\right] \tag{18.53}$$

Equation 18.52 is identical in form to the energy equation for a nonequilibrium chemically reacting flow, equation 18.14. Of course, the parameter ψ is different for each of those flows.

The flow of a gas-particle mixture is governed by the six differential equations 18.39, 18.42, 18.52, 18.35, 18.36, and 18.37, and the three equations of state 18.49,

18.50, and 18.38. Those equations comprise a system of nine equations for determining the nine flow properties ρ, $\mathbf{V}$, h, p, T, ρ_p, $\mathbf{V}_p$, h_p, and T_p.

For a steady two-dimensional flow, the above differential equations, in Cartesian coordinates, take the forms shown in Table 18.3, where $\delta = 0$ for planar flow and $\delta = 1$ for axisymmetric flow.

Table 18.3 Governing Equations for Steady Two-Dimensional Flow of Gas-Particle Mixtures

$$\rho u_x + \rho v_y + u\rho_x + v\rho_y + \delta\rho v/y = 0 \tag{18.54}$$

$$\rho u u_x + \rho v u_y + p_x = -\rho_p A_p (u - u_p) \tag{18.55}$$

$$\rho u v_x + \rho v v_y + p_y = -\rho_p A_p (v - v_p) \tag{18.56}$$

$$up_x + vp_y - a^2 u\rho_x - a^2 v\rho_y = \psi \tag{18.57}$$

$$\rho_p u_{px} + \rho_p v_{py} + u_p \rho_{px} + v_p \rho_{py} + \delta\rho_p v_p/y = 0 \tag{18.58}$$

$$u_p u_{px} + v_p u_{py} = A_p (u - u_p) \tag{18.59}$$

$$u_p v_{px} + v_p v_{py} = A_p (v - v_p) \tag{18.60}$$

$$u_p h_{px} + v_p h_{py} = B_p (T - T_p) \tag{18.61}$$

Comparing equations 18.54 to 18.57 to the corresponding equations governing isentropic flow presented in Section 17–3(a), it is seen that the left-hand sides of the two sets of equations are identical. The right-hand sides of the gas-particle flow equations contain, however, nonhomogeneous terms that take into account the effects of the particle drag and heat transfer. Consequently, the procedures for deriving the characteristic and compatibility equations for gas-particle flow, and the implementation of their numerical solution, is similar to the procedures discussed in Section 17–3 for isentropic flow and in Section 18–3 for nonequilibrium chemically reacting flow.

18–4(b) Characteristic and Compatibility Equations

The characteristic and compatibility equations for gas-particle flow may be determined by the procedure employed in Section 17–3 for isentropic flow. The procedure is simplified, however, by putting the momentum and energy equations for the particles directly into characteristic form by rewriting equations 18.59 to 18.61 in the following forms.

$$u_p \left(u_{px} + \frac{v_p}{u_p} u_{py} \right) = A_p (u - u_p) \tag{18.62}$$

$$u_p \left(v_{px} + \frac{v_p}{u_p} v_{py} \right) = A_p (v - v_p) \tag{18.63}$$

$$u_p \left(h_{px} + \frac{v_p}{u_p} h_{py} \right) = B_p (T - T_p) \tag{18.64}$$

Along a particle streamline,

$$\lambda_p = \left(\frac{dy}{dx} \right)_p = \frac{v_p}{u_p} \tag{18.65}$$

Hence, along *particle streamlines*, $(u_{px}+\lambda_p u_{py})=du_p/dx$, and so on, so that equations 18.62 to 18.64 become

$$u_p\,du_p = A_p(u-u_p)\,dx \tag{18.66}$$

$$u_p\,dv_p = A_p(v-v_p)\,dx \tag{18.67}$$

$$u_p\,dh_p = B_p(T-T_p)\,dx \tag{18.68}$$

The last three equations are the *particle compatibility equations*.

When the procedure employed in Section 17–3 is applied to the remaining five equations (i.e., the gas continuity, momentum, and energy equations and the particle continuity equation), only four compatibility equations are obtained. No compatibility equation is found that involves the particle density ρ_p; a deficiency that arises because the particles do not interact with each other. Consequently, the particle properties u_p, v_p, and h_p do not depend on the particle density ρ_p, and the particle density ρ_p depends only on the spacing of the particle streamlines and the particle velocity. Since the latter are determined solely by the particle momentum equations, equations 18.66 and 18.67 in characteristic form, the particle density is also determined by those equations. There is no other effect, analogous to the gas pressure, that influences the particle density.

Accordingly, the particle density is determined simply by taking into account the mass of particles flowing between the individual particle streamlines; the latter are determined by following the particle trajectories through the gas flow field. The accounting for the particles is accomplished by means of the *particle stream function* ψ_p, which is defined by

$$\psi_{px} \equiv -y^{\delta}\rho_p v_p \qquad \text{and} \qquad \psi_{py} \equiv y^{\delta}\rho_p u_p \tag{18.69}$$

Substituting equation 18.69 into the particle continuity equation, equation 18.35, yields

$$-\frac{\partial^2\psi_p}{\partial x\partial y}+\frac{\partial^2\psi_p}{\partial y\partial x}=0 \tag{18.70}$$

which is satisified identically. For a two-dimensional flow, $\psi_p=\psi_p(x,y)$. Thus,

$$d\psi_p = \psi_{px}\,dx+\psi_{py}\,dy \tag{18.71}$$

Substituting equation 18.69 into equation 18.71 gives

$$d\psi_p = -y^{\delta}\rho_p v_p\,dx+y^{\delta}\rho_p u_p\,dy \tag{18.72}$$

Rearranging equation 18.72, we obtain

$$d\psi_p = y^{\delta}\rho_p(u_p\,dy-v_p\,dx) \tag{18.73}$$

Along the particle streamlines, $(u_p\,dy-v_p\,dx)=0$. Thus,

$$d\psi_p = 0 \qquad (\textit{along a particle streamline}) \tag{18.74}$$

Hence, the particle density may be obtained by applying equation 18.73 between points in the flow field where the particle *stream function* ψ is known.

The characteristic and compatibility equations corresponding to equations 18.54 to 18.57 are found by multiplying those four equations by the unknown parameters

σ_1 to σ_4 and summing the products, as indicated by the following equation.

$$\sigma_1(18.54)+\sigma_2(18.55)+\sigma_3(18.56)+\sigma_4(18.57)=0 \tag{18.75}$$

Performing the summation indicated by equation 18.75 and factoring out the coefficients of the x derivatives of u, v, p, and ρ, we obtain equation 17.11, but with the following nonhomogeneous term.

$$\sigma_1\delta\rho v/y+\sigma_2\rho_p A_p(u-u_p)+\sigma_3\rho_p A_p(v-v_p)-\sigma_4\psi=0 \tag{18.76}$$

Since the terms containing derivatives in equation 18.75 are identical to the corresponding terms in equation 17.11, the characteristics that are determined by means of equation 17.11 for an isentropic flow are the same ones that are obtained for a gas-particle flow; that is, the gas streamline and the Mach lines [see Section 17–3(b), equations 17.20 and 17.22]. Those equations are repeated and renumbered below.

$$\left(\frac{dy}{dx}\right)_o=\lambda_o=\frac{v}{u} \qquad (\textit{gas streamline}) \tag{18.77}$$

$$\left(\frac{dy}{dx}\right)_{\pm}=\lambda_{\pm}=\tan(\theta\pm\alpha) \qquad (\textit{Mach lines}) \tag{18.78}$$

The compatibility equation for a gas-particle flow is obtained by replacing the nonhomogeneous term in equation 17.13 with the nonhomogeneous term defined by equation 18.76. Thus,

$$\begin{aligned}&\rho(\sigma_1+u\sigma_2)\,du+\rho u\sigma_3\,dv+(\sigma_2+u\sigma_4)\,dp+u(\sigma_1-a^2\sigma_4)\,dp\\&+\left[\sigma_1\delta\rho v/y+\sigma_2\rho_p A_p(u-u_p)+\sigma_3\rho_p A_p(v-v_p)-\sigma_4\psi\right]dx=0\end{aligned} \tag{18.79}$$

Following the steps outlined in Section 17–3(c), it follows that, along the gas streamlines, equation 18.79 becomes

$$\begin{aligned}&\sigma_2\left\{\rho u\,du+\rho v\,dv+dp+\rho_p A_p\left[(u-u_p)\,dx+(v-v_p)\,dy\right]\right\}\\&\qquad+\sigma_4\left\{u\,dp-a^2u\,d\rho-\psi\,dx\right\}=0\end{aligned} \tag{18.80}$$

For arbitrary values for σ_2 and σ_4, we obtain

$$\rho u\,du+\rho v\,dv+dp=-\rho_p A_p\left[(u-u_p)\,dx+(v-v_p)\,dy\right]=\beta \tag{18.81}$$

$$u\,dp-a^2u\,d\rho=\psi\,dx \tag{18.82}$$

Employing the procedure outlined in Section 17–3(c), it follows that, along the Mach lines, equation 18.79 becomes

$$\begin{aligned}&(\rho v)\,du_{\pm}-(\rho u)\,dv_{\pm}+\left[\lambda_{\pm}-u(u\lambda_{\pm}-v)/a^2\right]dp_{\pm}\\&-(u\lambda_{\pm}-v)\left[\delta(\rho v/y)-\psi/a^2\right]dx_{\pm}\\&+\rho_p A_p\left[(u-u_p)\,dy_{\pm}-(v-v_p)\,dx_{\pm}\right]=0\end{aligned} \tag{18.83}$$

where the subscript $\pm$ denotes the C_+ and C_-, or left- and right-running Mach lines, respectively.

Summarizing, equations 18.81 and 18.82 are applicable along the gas streamlines, and equation 18.83 is applicable along each of the two Mach lines. Along the particle streamlines, equations 18.66 to 18.68 are valid, and equation 18.73 may be employed for determining the particle density. Consequently, eight equations are available for determining the eight flow properties u, v, p, ρ, u_p, v_p, h_p, and ρ_p. Table 18.5 summarizes the characteristic and compatibility equations for steady two-dimensional gas-particle flow.

Table 18.5 Characteristic and Compatibility Equations for Steady Two-Dimensional Gas-Particle Flow

Characteristic equations		
$\left(\frac{dy}{dx}\right)_o = \lambda_o = \frac{v}{u}$	(*gas streamline*)	(18.77)
$\left(\frac{dy}{dx}\right)_p = \lambda_p = \frac{v_p}{u_p}$	(*particle streamline*)	(18.65)
$\left(\frac{dy}{dx}\right)_{\pm} = \lambda_{\pm} = \tan(\theta \pm \alpha)$	(*Mach lines*)	(18.78)
Compatibility equations		
$\rho u\, du + \rho v\, dv + dp = \beta$	(*along gas streamlines*)	(18.81)
$dp - a^2 d\rho = \frac{\psi}{u} dx$	(*along gas streamlines*)	(18.82)
$\rho v\, du_{\pm} - \rho u\, dv_{\pm} + \left[\lambda_{\pm} - \frac{u(u\lambda_{\pm} - v)}{a^2}\right] dp_{\pm}$ $-(u\lambda_{\pm} - v)\left(\frac{\delta \rho v}{y} - \frac{\psi}{a^2}\right) dx_{\pm}$ $+ \rho_p A_p[(u - u_p)\, dy_{\pm} - (v - v_p)\, dx_{\pm}] = 0$	(*along Mach lines*)	(18.83)
$u_p\, du_p = A_p(u - u_p)\, dx$	(*along particle streamlines*)	(18.66)
$u_p\, dv_p = A_p(v - v_p)\, dx$	(*along particle streamlines*)	(18.67)
$u_p\, dh_p = B_p(T - T_p)\, dx$	(*along particle streamlines*)	(18.68)
$d\psi_p = y^{\delta} \rho_p (u_p\, dy - v_p\, dx)$	(*everywhere*)	(18.73)

The analysis presented above is applicable when all of the particles have the same size and chemical composition. The analysis may be extended to take into account a discrete number of particle sizes and different chemical compositions. That is accomplished by including the continuity, momentum, and energy equations for each individual particle size and each different chemical composition in the system of governing equations. The effect of the drag and heat transfer of all of the particles on the gas is determined by summing those effects for all of the individual particles. Thus, equations 18.54 to 18.61 take the forms shown in Table 18.4, where j denotes either a particular size or chemical composition for a particle, and n denotes the number of such particle groups in the gas-particle mixture.

Table 18.4 Governing Equations for Steady Two-Dimensional Flow of a Gas-Particle Mixture Having a Discrete Number of Individual Particles

$$\rho u_x + \rho v_y + u\rho_x + v\rho_y + \delta\rho v/y = 0 \tag{18.84}$$

$$\rho u u_x + \rho v u_y + p_x = -\sum_{j=1}^{n} \rho_{pj} A_{pj}(u - u_{pj}) \tag{18.85}$$

$$\rho u v_x + \rho v v_y + p_y = -\sum_{j=1}^{n} \rho_{pj} A_{pj}(v - v_{pj}) \tag{18.86}$$

$$up_x + vp_y - a^2 u\rho_x - a^2 v\rho_y = \psi \tag{18.87}$$

$$\rho_{pj} u_{pjx} + \rho_{pj} v_{pjy} + u_{pj}\rho_{pjx} + v_{pj}\rho_{pjy} + \delta\rho_{pj} v_{pj}/y = 0 \quad (j = 1, \ldots, n) \tag{18.88}$$

$$u_{pj} u_{pjx} + v_{pj} u_{pjy} = A_{pj}(u - u_{pj}) \quad (j = 1, \ldots, n) \tag{18.89}$$

$$u_{pj} v_{pjx} + v_{pj} v_{pjy} = A_{pj}(v - v_{pj}) \quad (j = 1, \ldots, n) \tag{18.90}$$

$$u_{pj} h_{pjx} + v_{pj} h_{pjy} = B_{pj}(T - T_{pj}) \quad (j = 1, \ldots, n) \tag{18.91}$$

$$\psi = (\lambda - 1) \sum_{j=1}^{n} \rho_{pj} \{ A_{pj}(\mathbf{V}\cdot\mathbf{V} - 2\mathbf{V}\cdot\mathbf{V}_{pj} + \mathbf{V}_{pj}\cdot\mathbf{V}_{pj}) + B_{pj}(T_{pj} - T) \} \tag{18.92}$$

Following the procedure described above for a single particle, we obtain equations 18.66 to 18.68 and 18.73, each repeated n times. Accordingly, equation 18.81 becomes

$$\rho u\, du + \rho v\, dv + dp = -\sum_{j=1}^{n} \rho_{pj} A_{pj} [(u - u_{pj})\, dx + (v - v_{pj})\, dy] \tag{18.93}$$

Equation 18.82 is unchanged, except that ψ is now defined by equation 18.92. Equation 18.83 becomes

$$\begin{aligned} &(\rho v)\, du_{\pm} - (\rho u)\, dv_{\pm} + [\lambda_{\pm} - u(u\lambda_{\pm} - v)/a^2]\, dp_{\pm} \\ &- (u\lambda_{\pm} - v)[\delta(\rho v/y) - \psi/a^2]\, dx_{\pm} \\ &+ \sum_{j=1}^{n} \rho_{pj} A_{pj} [(u - u_{pj})\, dy_{\pm} - (v - v_{pj})\, dx_{\pm}] = 0 \end{aligned} \tag{18.94}$$

18–4(c) Implementation of the Numerical Analysis

The unit processes for gas-particle flow are similar to those discussed in Section 17–4 for steady two-dimensional isentropic flow, and those discussed in Section 18–3 for steady two-dimensional nonequilibrium chemically reacting flow. The presence of the condensed particles, however, adds an extra characteristic (the *particle streamline*) to the characteristic network. Figure 18.6 illustrates schematically the characteristic network for an interior point. The Mach lines from the known points 1 and 2 determine the location of the solution point, point 4. Points 3 and 5 are determined by extending the gas and particle streamlines, respectively, rearward from point 4 to intersect line 12. When more than one particle size or chemical composition is present, the streamline for each discrete particle must be added to the characteristic network, as indicated schematically in Fig. 18.7.

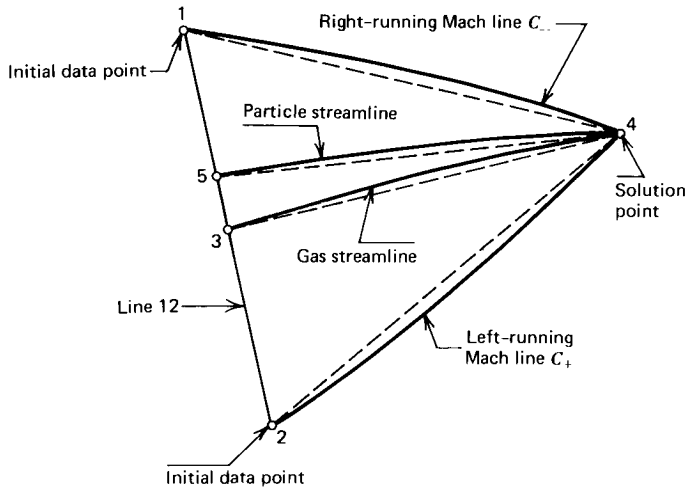

Figure 18.6 Unit process for an interior point for a single discrete particle.

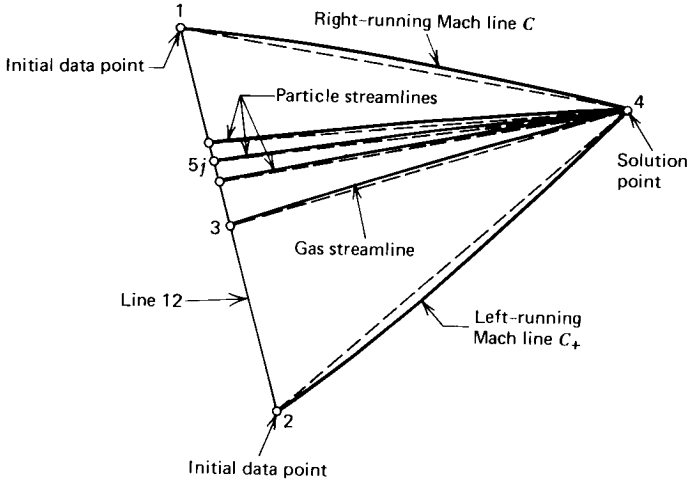

Figure 18.7 Unit process for an interior point for multiple discrete particles.

The characteristic and compatibility equations derived in Section 18-4(b) may be written in finite difference form for the characteristic network illustrated in Fig. 18.6, as is done in Section 17-4(b) for isentropic flow. Those equations may be solved simultaneously for the location of point 4 and the values of the flow properties at that point.

In gas-particle flow, an additional complication arises because of the inertia of the condensed particles. The particle streamlines (or trajectories) are determined by following the individual particles through the flow field for the gas. Since the particles exert no pressure, particle streamlines near a solid boundary (wall) are unaware of and uninfluenced by the presence of the wall. Consequently, the particle streamlines are not required to be parallel to the wall. The particles may, therefore, impinge on the wall. They may also detach from the wall thereby forming a *particle free region* between the so-called *limiting particle streamline* and the wall. Figure 18.8 illustrates diagrammatically the phenomenology associated with

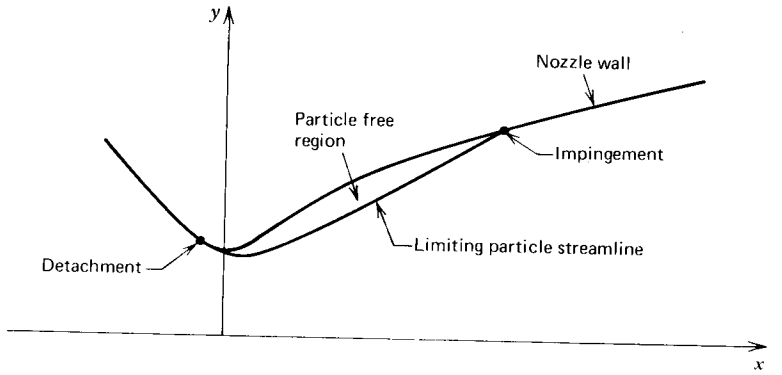

Figure 18.8 Gas-particle flow in a De Laval nozzle illustrating detachment, impingement, and the limiting particle streamline.

the gas-particle flow in a De Laval nozzle; it illustrates both the particle free region caused by the particle detachment, and particle impingement.

Because of the possibility of forming a particle free region and a limiting particle streamline, the unit processes in the vicinity of the limiting particle streamline must be modified. The unit processes developed in Section 17–4 for isentropic flow are applicable to the gas flowing in the particle free region. In the region below the limiting particle streamline in Fig. 18.8, the unit processes based on the characteristic and compatibility equations derived in Section 18–4(b) are applicable. At the limiting particle streamline itself, a combination of both of the aforementioned two types of unit processes is required.

Figure 18.9 illustrates one method for constructing the unit process at the limiting particle streamline. Figure 18.9*a* illustrates the locating of point 4 at the intersection of the right- and left-running Mach lines through points 1 and 2, respectively. Figure 18.9*b* illustrates the first step of the unit process for locating point 9, which is the intersection of the C_- Mach line 19 and the limiting particle streamline 79. The locations of points 6 and 8 on line 12 are determined by the rearward projections of the C_+ Mach line 69 and the gas streamline 89. The compatibility equation 18.83 applies along the C_- Mach line 19, and the compatibility equations 18.81 and 18.82 apply along the gas streamline 89. Equations 18.66 to 18.68 apply along the particle streamline 79, equation 18.83 applies along left-running Mach line 69, and equation 18.73 applies in region 6796. If the slope of the gas streamline 89 is smaller than that of the particle streamline 79, then the terms β and ψ in equations 18.81 and 18.82, respectively, which include the effect of the particle drag and heat transfer, are zero. By employing the aforementioned equations, the flow properties at point 9 may be determined. With point 9 a known point, the network illustrated in Fig. 18.9*c* in which there is a continuous flow of particles may be employed for determining the flow properties at point 4. A similar method may be developed for the case where the limiting particle streamline is located below point 4, which is illustrated diagrammatically in Fig. 18.10.

When more than a single discrete particle is to be taken into account, the method illustrated schematically in Fig. 18.9 becomes quite complicated. In that case, an approximation may be employed wherein the complete unit process for gas-particle flow, illustrated in Fig. 18.7, is employed, but the effects of particle drag and heat transfer along right-running Mach line 14 (or left-running Mach line 24) are weighted in proportion to the portion of the Mach line 14 (or 24) that contains

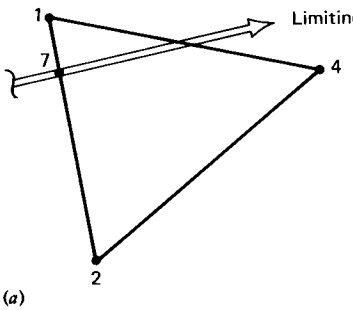

(*a*)

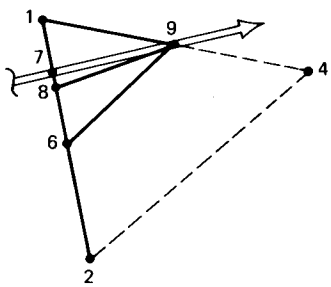

(*b*)

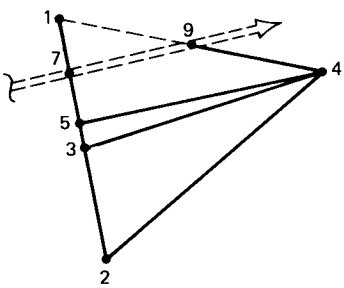

(*c*)

Figure 18.9 Unit process at the limiting particle streamline. (*a*) Overall unit process. (*b*) Determination of the limiting particle streamline properties. (*c*) Determination of the flow properties at point 4.

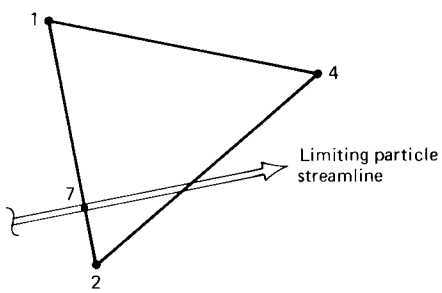

Figure 18.10 Unit process when the limiting particle streamline falls below point 4.

particles. The latter approach was employed by Hoffman[2], and proved to be an acceptable approximation.

The analysis of steady two-dimensional gas-particle flow by the method of characteristics, although relatively straightforward, requires unit processes that become complicated, especially when more than a single particle size must be considered. The same remark is applicable to the modifications to the unit processes in the vicinity of the limiting particle streamline. Space limitations preclude including the details for developing the unit processes for gas-particle flow in this book. References 2 and 3 develop those unit processes in some detail.

18–4(d) Examples of Steady Two-Dimensional Gas-Particle Flow

Some results for steady one-dimensional gas-particle flow obtained by Kliegel[4] are presented in Section 14–7(a) for the flow of the combustion products of a typical

metalized solid propellant in a rocket motor propulsive nozzle. The nozzle geometry is illustrated in Fig. 14.16*a*. The flow properties in the nozzle are presented in Figs. 14.16*b* to 14.16*f*. The particle size distribution comprises five discrete particle sizes having the mass ratios presented in Table 14.5. Results obtained by Kliegel[4] for the corresponding steady two-dimensional gas-particle flow are presented in this section.

Figures 18.11 to 18.14, taken from Reference 4, present calculated results for five discrete particle sizes for the gas-particle flow in the nozzle configuration illustrated in Fig. 14.16*a*. Figure 18.11 presents the limiting particle streamlines for each of the five discrete particle sizes. A particle free region exists between the wall and the limiting particle streamline for the 1.58μm particle. The limiting particle streamlines for the larger (and correspondingly heavier) particles fall closer and closer to the nozzle axis as the particle diameter increases. For the conical wall considered in

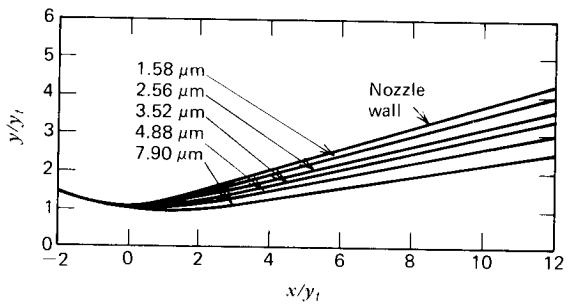

Figure 18.11 Limiting particle streamlines in the nozzle shown in Fig. 14.16*a* (taken from Reference 4).

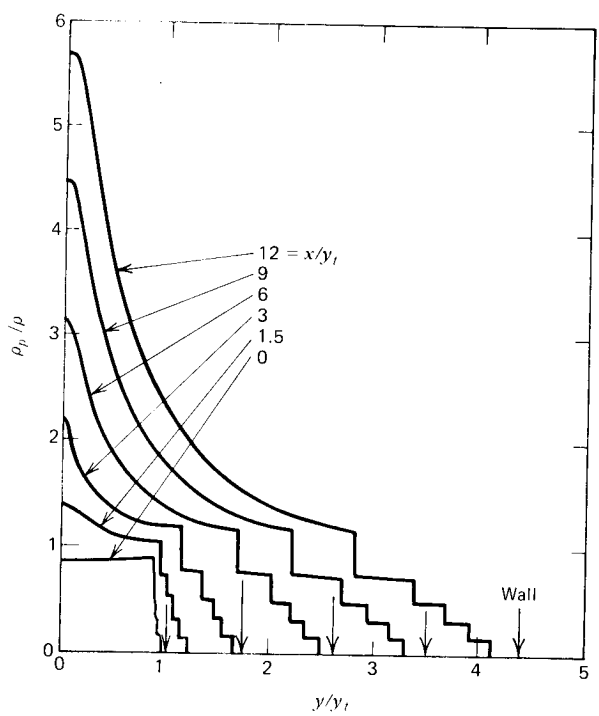

Figure 18.12 Particle-gas density ratio at various stations in the nozzle shown in Fig. 14.16*a* (taken from Reference 4).

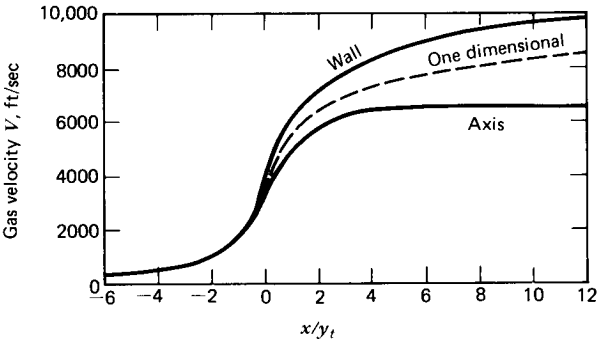

Figure 18.13 Axis and wall gas velocity profiles in the nozzle shown in Fig. 14.16*a* (taken from Reference 4).

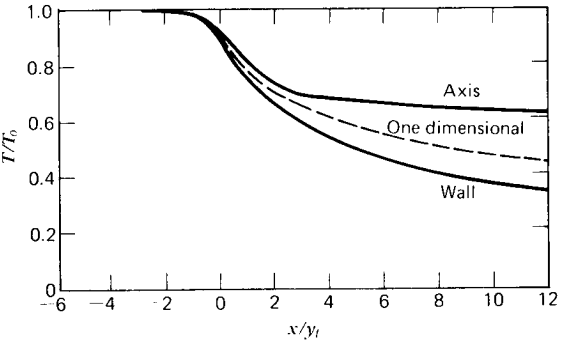

Figure 18.14 Axis and wall gas temperature profiles in the nozzle shown in Fig. 14.16*a* (taken from Reference 4).

the analysis, none of the particles impinge on the downstream portion of the nozzle.

Figure 18.12 is a plot of the particle-to-gas density ratio ρ_p/ρ as a function of the nondimensional distance y/y_t normal to the nozzle axis, for different stations in the nozzle denoted by the nondimensional distance x/y_t. The discontinuities in the curves occur at the limiting particle streamlines. It is seen that the particles tend to concentrate near the nozzle axis.

Figure 18.13 presents the gas velocity profiles along the nozzle wall and along the nozzle axis. The one-dimensional velocity profile presented in Fig. 14.16*b* is presented in Fig. 18.13 for comparison. The velocity of the gas at the wall is larger than the one-dimensional value, and the velocity of the gas at the centerline is smaller than the one-dimensional value. Because of the high concentration of the particles on the nozzle axis (with the accompanying large drag force on the gas), the gas flowing along the nozzle axis attains a maximum velocity and then decreases slightly in the vicinity of the nozzle exit.

Figure 18.14 presents the gas temperature profiles along the nozzle wall and along the nozzle axis. The gas temperature is lower along the wall and higher along the axis than the corresponding one-dimensional values. The gas temperature on the nozzle axis decreases very slowly because of the large concentration of particles along the nozzle axis and the accompanying large particle-to-gas heat transfer rate.

Figures 18.15 to 18.18, taken from Reference 5, present the results of a paramet-

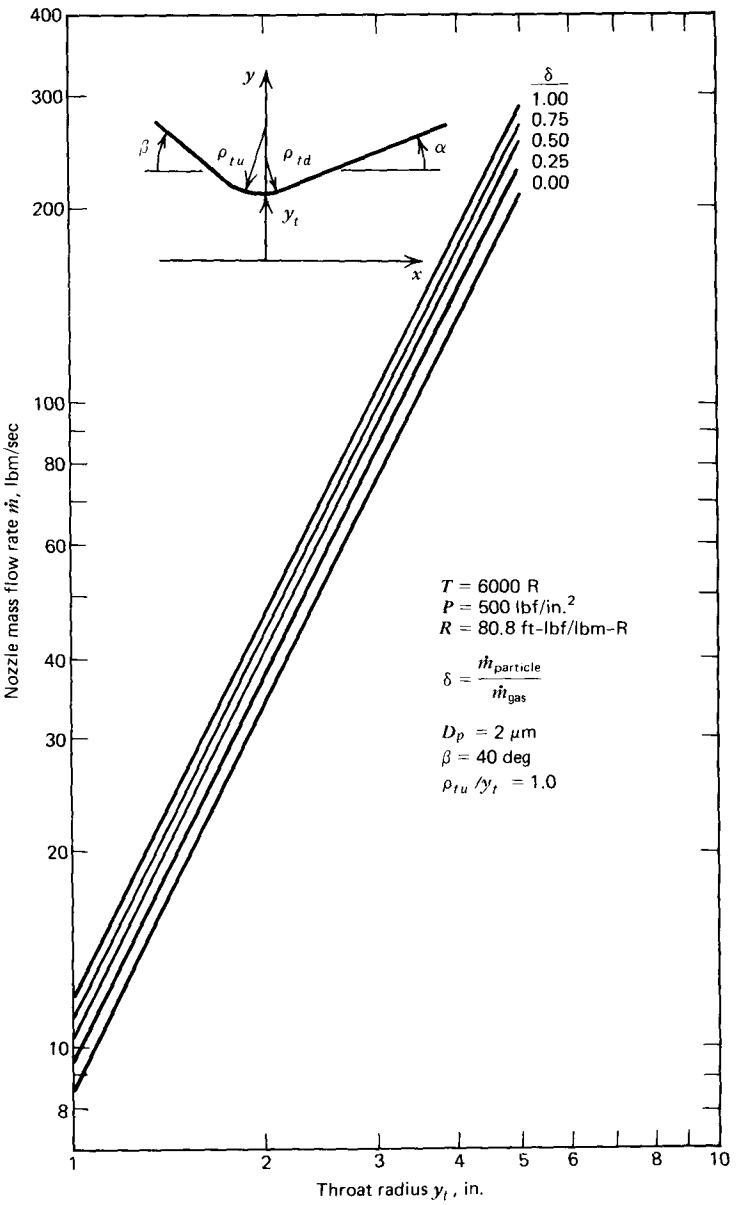

Figure 18.15 Mass flow rate $\dot{m}$ versus throat radius y_t for gas-particle flow in a converging-diverging nozzle (taken from Reference 5).

ric study of gas-particle flow in conical propulsive nozzles for a typical metalized solid propellant. The nozzle geometry is illustrated in Fig. 18.15, which also presents the mass flow rate $\dot{m}$ as a function of the throat radius y_t with the particle-to-gas *mass flow rate ratio* δ as a parameter. Those results were obtained by solving the one-dimensional gas-particle flow equations presented in Section 14–7(a) in the converging portion of the nozzle to obtain the particle lags K and L (see equations 14.228 and 14.229) at the nozzle throat. The constant lag analysis described in Section 14–7(b) was employed for defining an *effective specific heat ratio* $\bar{\gamma}$ in the throat region of the nozzle, and Sauer's analysis (see Section 15–5)

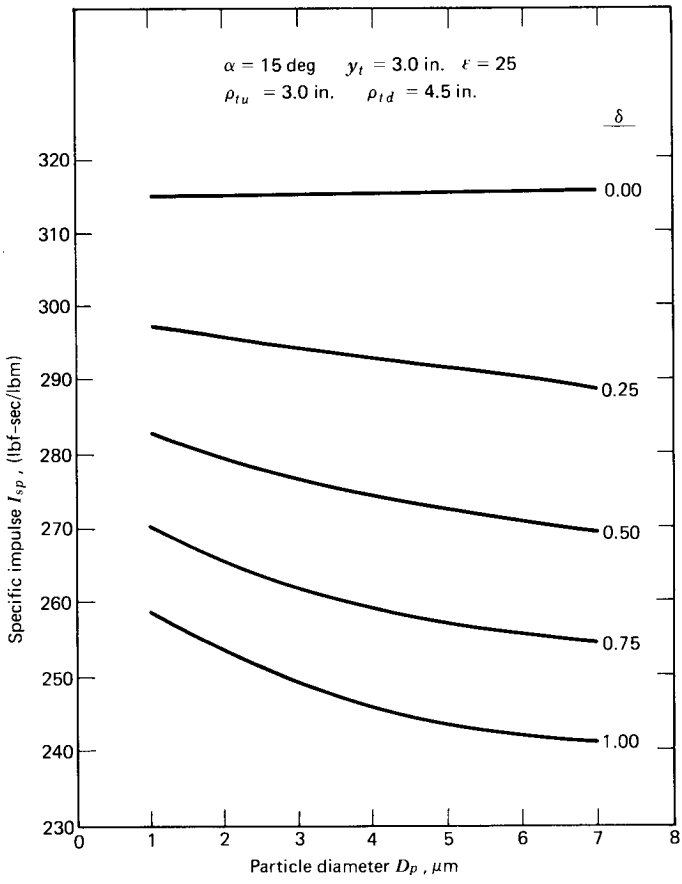

Figure 18.16 Specific impulse I_{sp} versus particle diameter D_p for a converging-diverging nozzle with a 15-deg semiangle conical divergence (taken from Reference 5).

was employed for determining the initial-value line corresponding to $\bar{\gamma}$, from which the method of characteristics was initiated. *Particle trajectories* were traced through the transonic gas flow field to determine the properties of the particles on the supersonic initial-value line. The mass flow rates presented in Fig. 18.15 were obtained by integrating across the aforementioned initial-value line. Although the latter procedure involves several approximations, the results obtained have proved to be reasonable[2]. From Fig. 18.15, it is apparent that the mass flow rate increases linearly with the square of the throat radius y_t, and depends slightly on the mass flow rate ratio δ.

Figure 18.16 presents the specific impulse $I_{sp} = F/\dot{m}$ [see Section 4–10(b)] as a function of the particle diameter D_p with the mass flow rate ratio δ as a parameter. For a fixed value of δ, the specific impulse decreases as the particle size increases because of the larger drag and smaller heat transfer associated with the larger particles. For a given particle size, increasing δ increases the losses due to the drag associated with the increased particle mass flow rate, so that the specific impulse I_{sp} decreases.

Figure 18.17 presents the specific impulse I_{sp} as a function of the nozzle

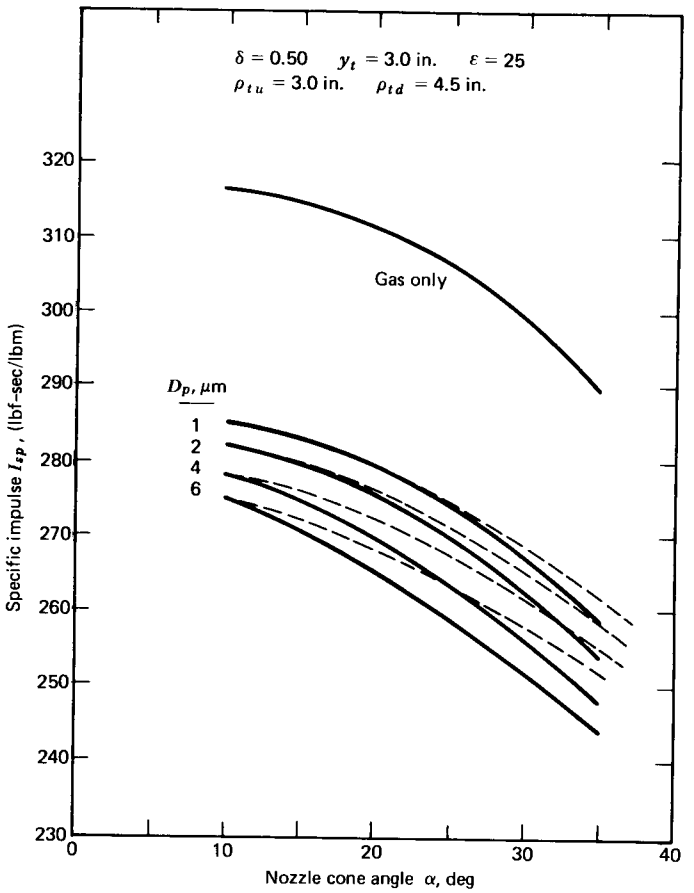

Figure 18.17 Specific impulse I_{sp} versus cone angle α for a nozzle having a conical divergence (taken from Reference 5).

semiangle α with the particle diameter D_p as a parameter, for a mass flow rate ratio $\delta = 0.5$. The decrease in the specific impulse I_{sp} with increasing values of the semiangle α is attributable to the increased divergence loss discussed in Section 4–10(d). The divergence factor $\lambda = (1 + \cos\alpha)/2$ derived in Section 4–10(d) is applicable for a pure gas flow. The dashed curves in Fig. 18.17 illustrate the application of that divergence factor using the I_{sp} values for $\alpha = 10$ deg as a base. It is seen that the specific impulse I_{sp} decreases more rapidly than that predicted by the value of λ, indicating that the two-dimensional flow effects in gas-particle flow are larger than in a pure gas flow, especially for the larger particles.

Figure 18.18 presents the specific impulse I_{sp} for a conical nozzle with a semiangle $\alpha = 15$ deg as a function of the throat radius y_t, with the mass flow rate ratio δ as a parameter, for a 2 μm particle. For small values of the throat radius y_t, the gradients in the flow properties are large, and the velocity and temperature of the particles lag the velocity and temperature of the gas, thereby causing a reduction in the thrust, and hence the specific impulse I_{sp}, obtainable from the nozzle. For large values of the throat radius y_t, the aforementioned particle lags are small, so that the thrust, and hence the specific impulse I_{sp}, approaches the equilibrium value associated with no particle lag.

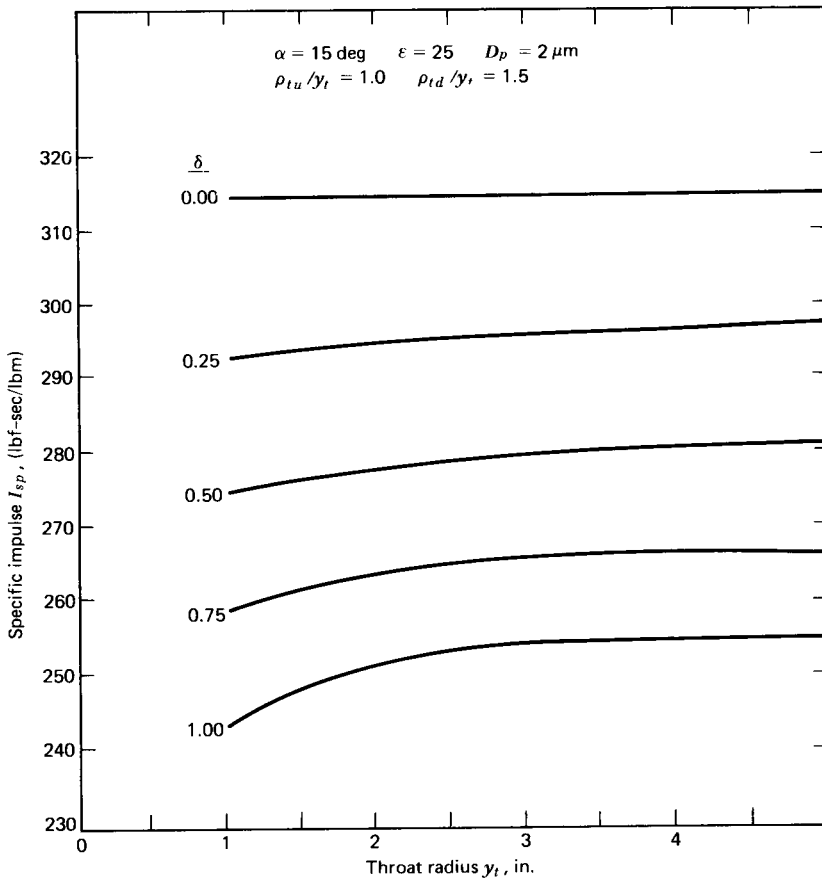

Figure 18.18 Specific impulse I_{sp} versus throat radius y_t for a converging-diverging nozzle with a 15-deg semiangle conical divergence (taken from Reference 5).

REFERENCES

1. J. R. Kliegel, G. R. Nickerson, H. M. Frey, V. Quan, and J. E. Melde, "ICRPG Two-Dimensional Kinetic Reference Program," Dynamic Science, Monrovia, California, July 1968.
2. J. D. Hoffman, "An Analysis of the Effects of Gas-Particle Mixtures on the Performance of Rocket Nozzles," Ph. D. Thesis, Purdue University, West Lafayette, Indiana, January 1963.
3. J. R. Kliegel and G. R. Nickerson, "Axisymmetric Two-Phase Perfect Gas Performance Program," Report No. 02874-6006-R000, TRW Systems, Redondo Beach, California, April 1967.
4. J. R. Kliegel, "Gas Particle Nozzle Flows," *Ninth International Symposium on Combustion*, Academic Press, New York, pp. 811–826, 1963.
5. J. D. Hoffman and S. A. Lorenc, "A Parametric Study of Gas-Particle Flows in Conical Nozzles," *Journal of the American Institute of Aeronautics and Astronautics*, Vol. 3, No. 1, pp. 103–106, January 1965.

19
the method of characteristics applied to unsteady one-dimensional flow

19–1 PRINCIPAL NOTATION FOR CHAPTER 19

The notation presented in Section 16–1 and the notation presented in this section are applicable to the present chapter.

A flow cross-sectional area.
$C_{\pm}$ denotes the unsteady flow Mach lines.
C_o denotes the pathline.
$\mathfrak{f}$ Fanning friction coefficient.
$\delta F_{\mathfrak{f}}$ frictional force.
h static specific enthalpy.
H stagnation specific enthalpy.
L length of flow passage.
$\dot{m}_i$ mass addition.
δQ heat transfer.
t time.
T absolute static temperature.
u one-dimensional velocity of the gas.
U one-dimensional velocity of a shock wave relative to the gas.

Greek Letters

β combined friction and mass addition term in the momentum equation.
δ denotes planar, cylindrical, spherical, or quasi-one-dimensional flow (see Table 19.1).
ε mass addition term in the continuity equation.
$\lambda_{\pm}$ $= 1/(u \pm a)$, slope of the Mach lines.
λ_o $= 1/u$, slope of the pathline.
ψ combined friction, heat transfer, and mass addition term in the energy equation.

Subscripts

i denotes mass addition.
L denotes the left-hand side of a discontinuity surface.
o denotes the pathline, or a reference property.
R denotes the right-hand side of a discontinuity surface.
$\pm$ denotes the $C_{\pm}$ Mach lines.

Superscripts

$*$ denotes nondimensional property.

19–2 INTRODUCTION

Unsteady flow phenomena occur in all types of engineering applications.[1-5] The present chapter is concerned with *unsteady one-dimensional flows* in which *large amplitude changes* in the properties of the flowing gas occur. Several applications in which unsteady flows are important are mentioned in Section 13–2.

The governing equations for unsteady one-dimensional *homentropic* flow are derived in Chapter 13, and the corresponding characteristic and compatibility

equations are determined. The general features of unsteady one-dimensional *continuous* flow are discussed there, and a numerical algorithm is presented for the determination of an interior point in such a flow field.

In this chapter the governing equations are derived for the unsteady one-dimensional and quasi-one-dimensional flow of a compressible fluid including the effects of area change, friction, heat transfer, and mass addition, but neglecting work and body forces. The corresponding characteristic and compatibility equations are determined. Numerical algorithms are developed for applying the latter equations to several unit processes that occur commonly in unsteady flows. Examples are presented for illustrating the application of those unit processes to several unsteady one-dimensional flow problems.

19–3 MATHEMATICAL ANALYSIS OF UNSTEADY ONE-DIMENSIONAL FLOW

The governing equations for unsteady one-dimensional and quasi-one-dimensional flow are derived in this section. The equations include the effects of friction, heat transfer, and mass addition, but neglect the effects of work and body forces. The corresponding characteristic and compatibility equations are determined.

19–3(a) Governing Equations for Unsteady One-Dimensional Isentropic Flow

A truly *one-dimensional flow* is one where the flow properties depend only on one space coordinate x and the time t.* Consequently, the pathlines of the fluid particles are straight lines. Thus, planar flow in a constant-area duct, flow having cylindrical symmetry, and flow with spherical symmetry are *one-dimensional flows*. Flow in a duct having a slowly varying cross-section where the duct height is small compared to the radius of curvature of the axis of the duct is termed a *quasi-one-dimensional flow*. Hence, in the above terminology, the isentropic flow considered in Chapter 4 is a quasi-one-dimensional flow. The governing equations for unsteady one-dimensional isentropic flow are derived in the present section, and those for unsteady quasi-one-dimensional isentropic flow are derived in Section 19–3(b).

The governing equations for unsteady one-dimensional isentropic flow are obtained from Table 2.2 by assuming that $\mathbf{B} = d\mathbf{F}_{\text{shear}} = \delta\dot{W} = \delta\dot{Q} = g\,dz = 0$. Thus,

Continuity equation

$$\rho_t + \nabla \cdot (\rho \mathbf{V}) = 0 \tag{19.1}$$

Momentum equation

$$\rho \frac{D\mathbf{V}}{Dt} + \nabla p = 0 \tag{19.2}$$

Energy equation

$$\rho \frac{D}{Dt}\left(h + \frac{V^2}{2}\right) - p_t = 0 \tag{19.3}$$

Entropy equation

$$\frac{Ds}{Dt} = 0 \tag{19.4}$$

*In Chapter 19 the time is denoted by t and the static temperature is denoted by T.

Figure 19.1 illustrates the Cartesian, cylindrical, and spherical coordinate systems for a one-dimensional flow. In all three cases, x denotes the spatial coordinate and u the flow velocity. Expressing equation 19.1 in the aforementioned three coordinate systems, we obtain the following three forms for the continuity equation.

$$\rho_t + u\rho_x + \rho u_x = 0 \qquad (Cartesian) \tag{19.5a}$$

$$\rho_t + u\rho_x + \rho u_x + \frac{\rho u}{x} = 0 \qquad (cylindrical) \tag{19.5b}$$

$$\rho_t + u\rho_x + \rho u_x + \frac{2\rho u}{x} = 0 \qquad (spherical) \tag{19.5c}$$

The last three equations may be reduced to the following single continuity equation by introducing the parameter δ. Thus,

$$\rho_t + u\rho_x + \rho u_x + \frac{\delta \rho u}{x} = 0 \tag{19.6}$$

where $\delta = 0$ for a planar flow, $\delta = 1$ for a cylindrical flow, and $\delta = 2$ for a spherical flow.

Equation 19.2, the momentum vector equation, when expressed in any of the aforementioned three coordinate systems, yields the following momentum equation.

$$\rho u_t + \rho u u_x + p_x = 0 \tag{19.7}$$

Since the flow is assumed to be isentropic (i.e., the entropy of each particle remains constant), the speed of sound equation (see equation 1.180) may be employed in place of the energy equation as a governing equation. Hence,

$$a^2 = \left(\frac{\partial p}{\partial \rho}\right)_s = \frac{dp}{d\rho} \qquad (for\ isentropic\ flow) \tag{19.8a}$$

where

$$a = a(p, \rho) \tag{19.8b}$$

Since equation 19.8a is a *particle* or *material* derivative [see Section 2–3(f)], it may be written as the following *substantial derivative*.

$$\frac{Dp}{Dt} - a^2 \frac{D\rho}{Dt} = 0 \tag{19.9}$$

Equation 19.9 yields the following equation for all three coordinate systems.

$$p_t + up_x - a^2(\rho_t + u\rho_x) = 0 \tag{19.10}$$

The entropy equation, equation 19.4, transforms to the following equation in all three coordinate systems.

$$s_t + us_x = 0 \tag{19.11}$$

Equations 19.6, 19.7, 19.10, and 19.11 comprise a set of four equations for determining the four flow properties u, p, ρ, and s. Equations 19.6, 19.7, and 19.10

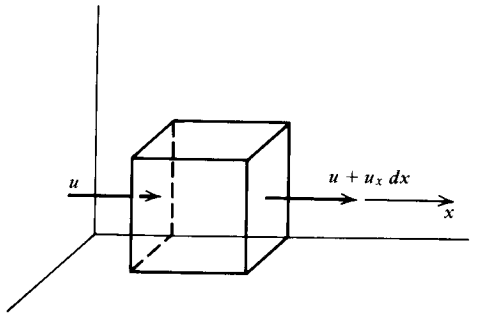

(a)

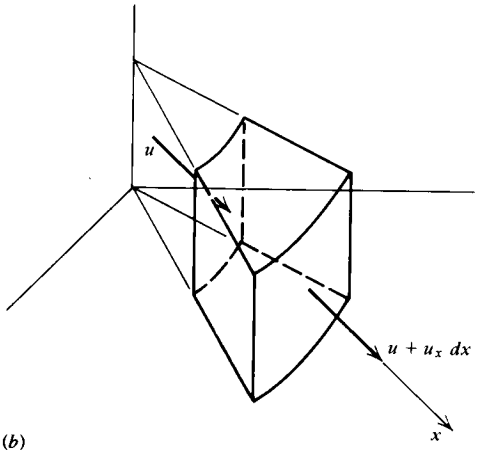

(b)

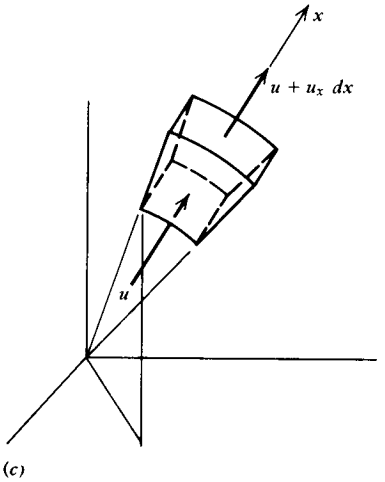

(c)

Figure 19.1 Coordinate systems for unsteady one-dimensional flow. (*a*) Cartesian coordinates. (*b*) Cylindrical coordinates. (*c*) Spherical coordinates.

comprise a set of three equations for determining the three flow properties u, p, and ρ, since the entropy s appears only in equation 19.11. In most practical flow problems, the value of the entropy s per se is not of direct interest. Consequently, in the discussions in the remainder of the present chapter, the set of governing equations is restricted to equations 19.6, 19.7, and 19.10.

19–3(b) Governing Equations for Unsteady Quasi-One-Dimensional Isentropic Flow

If the cross-sectional area of a flow passage varies very slowly and the radius of curvature of the central axis of the passage is large compared to the passage height, the flow inside of the passage is said to be a *quasi-one-dimensional flow*. In that case, the flow area is a function of x and t. The flow properties are assumed to be uniform across all surfaces perpendicular to the mean flow direction (see Section 3–3). Figure 19.2 illustrates schematically the quasi-one-dimensional flow model for an inviscid adiabatic flow in the absence of work and body forces. The continuity and momentum equations for the quasi-one-dimensional flow model illustrated in Fig. 19.2 are obtained by applying the *integral form* of the governing equations presented in Table 2.1.

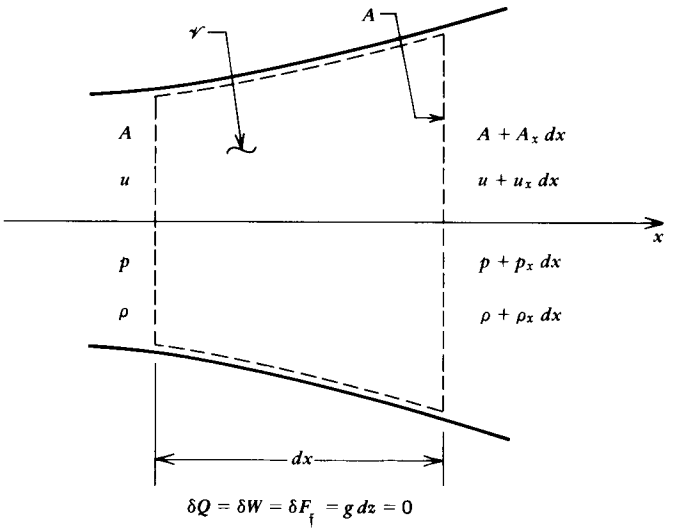

Figure 19.2 Flow model for unsteady quasi-one-dimensional flow.

1. *Continuity equation.* From equation 2.86, Table 2.1,

$$\int_{\forall} \rho_t \, d\forall + \int_A \rho \mathbf{V} \cdot d\mathbf{A} = 0 \tag{19.12}$$

If the flow area A varies with time, the first term in equation 19.12 must be written as $\partial [\int_{\forall} \rho \, d\forall]/\partial t$. In the present chapter, however, it is assumed that the flow area A is only a function of x. Figure 19.3 illustrates schematically the flow model for obtaining the continuity equation. Applying equation 19.12 to that flow model, we obtain

$$\rho_t A \, dx + [\rho A u + (\rho A u)_x \, dx] - \rho A u = 0 \tag{19.13}$$

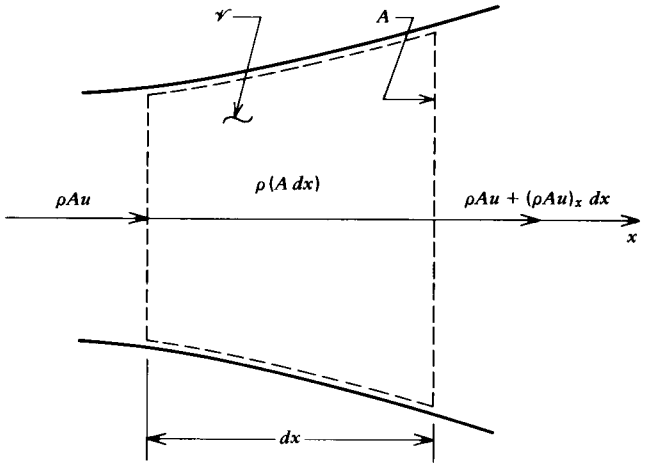

Figure 19.3 Flow model for the continuity equation.

Simplifying equation 19.13 yields

$$\rho_t A\,dx + (\rho u)_x A\,dx + \rho u A_x\,dx = 0 \tag{19.14}$$

Equation 19.14 may be rewritten as

$$\rho_t + u\rho_x + \rho u_x + \frac{\delta \rho u}{x} = 0 \tag{19.15}$$

where

$$\delta = \frac{x}{A} A_x = \frac{x}{A}\frac{dA}{dx} = x\frac{d(\ln A)}{dx} \tag{19.16}$$

Equation 19.15 is identical to equation 19.6, which is applicable to one-dimensional flow, but for a quasi-one-dimensional flow δ is defined by equation 19.16.

2. *Momentum equation.* From equation 2.87, Table 2.1, with the restrictions $\mathbf{B} = \mathbf{F}_{\text{shear}} = 0$, we obtain

$$-\int_A p\,d\mathbf{A} = \int_{\mathcal{V}} (\rho \mathbf{V})_t\,d\mathcal{V} + \int_A \mathbf{V}(\rho \mathbf{V}\cdot d\mathbf{A}) \tag{19.17}$$

Figure 19.4 illustrates schematically the flow model for deriving the momentum equation. Applying equation 19.17 to the flow model illustrated in Fig. 19.4, we obtain

$$pA + p\,dA - \left[pA + (pA)_x\,dx\right] = (\rho u)_t A\,dx + \left[\rho A u^2 + (\rho A u^2)_x\,dx\right] - \rho A u^2 \tag{19.18}$$

Noting that $(pA)_x\,dx = p\,dA + p_x A\,dx$, and canceling terms in equation 19.18, we obtain

$$-p_x A\,dx = (\rho u)_t A\,dx + (\rho A u^2)_x\,dx \tag{19.19}$$

Equation 19.19 may be rearranged to yield

$$u\left[\rho_t A\,dx + (\rho A u)_x\,dx\right] + \rho u_t A\,dx + \rho u u_x A\,dx + p_x A\,dx = 0 \tag{19.20}$$

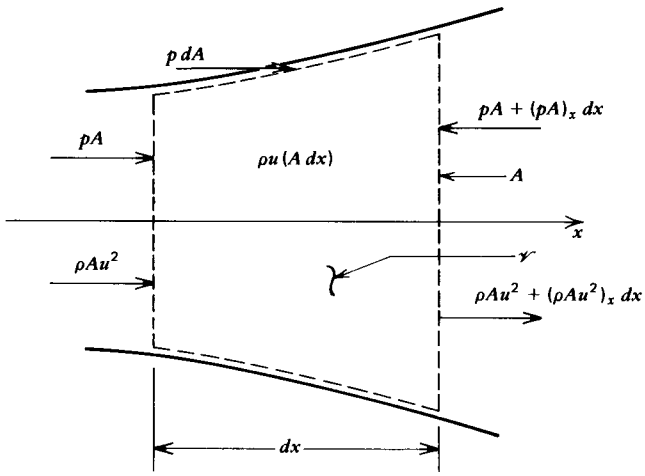

Figure 19.4 Flow model for the momentum equation.

The expression enclosed by the square brackets is identical to the continuity equation, equation 19.14, and is, therefore, equal to zero. Consequently, the momentum equation for unsteady *quasi-one-dimensional* isentropic flow becomes

$$\rho u_t + \rho u u_x + p_x = 0 \tag{19.21}$$

Equation 19.21 is identical to equation 19.7, which is the momentum equation for unsteady *one-dimensional* isentropic flow.

The energy equation for an isentropic flow may be replaced by the speed of sound equation, equation 19.10, as demonstrated in Section 19–3(a). Equation 19.10 is a substantial derivative and is, therefore, directly applicable to unsteady *quasi-one-dimensional* flow.

Equation 19.11, the entropy equation for unsteady *one-dimensional* flow, is also a substantial derivative and is, therefore, directly applicable to unsteady *quasi-one-dimensional* flow.

Hence, the governing equations for unsteady *quasi-one-dimensional* isentropic flow are equations 19.15, 19.21, 19.10, and 19.11. Reference to Section 19–3(a) shows that the latter equations are identical to the governing equations for unsteady *one-dimensional* isentropic flow. The parameter δ in the continuity equation has the values $\delta = 0$, 1, or 2 for *one-dimensional* planar, cylindrical, or spherical flow, respectively, and the value $\delta = xd(\ln A)/dx$ for *quasi-one-dimensional* flow.

19–3(c) Governing Equations for Unsteady One-Dimensional Generalized Flow

The analysis of unsteady quasi-one-dimensional flow presented in Section 19–3(b) may be extended to take into account the effects of friction, heat transfer, and mass addition. Figure 19.5 illustrates schematically the corresponding flow model. The continuity and momentum equations derived in Section 19–3(b) may be extended directly to take into account the effects of friction, heat transfer, and mass addition on the flow by including those effects in equations 19.15 and 19.21, respectively. The appropriate form of the energy equation is obtained by applying the integral form of the energy equation (equation 2.88, Table 2.1,) to the flow model illustrated in Fig. 19.5.

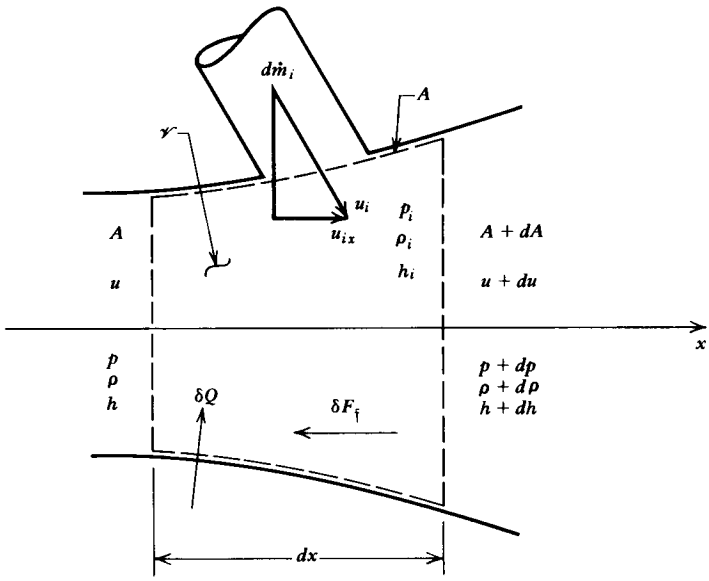

Figure 19.5 Flow model for unsteady quasi-one-dimensional flow with friction, heat transfer, and mass addition.

1. *Continuity equation.* The presence of friction and heat transfer in the flow do not enter the continuity equation directly. The effect of mass addition $d\dot{m}_i$ may be taken into account by adding the term $\varepsilon \equiv (d\dot{m}_i/dx)/A$ to equation 19.15. Hence, the continuity equation including the effect of mass addition is

$$\rho_t + u\rho_x + \rho u_x + \frac{\delta \rho u}{x} = \frac{1}{A}\frac{d\dot{m}_i}{dx} = \varepsilon \tag{19.22}$$

2. *Momentum equation.* The effect of heat transfer does not enter explicitly into the momentum equation. The effect of friction, however, manifests itself as a friction force δF_f acting in a direction opposite to that of the flow (see Fig. 19.5). The relationship between δF_f and the flow properties ρ and u is derived in Section 3–5(d), equation 3.17, which is repeated and renumbered below for convenience. Thus,

$$\delta F_f = \frac{\rho u^2}{2}\frac{4f\,dx}{\mathfrak{D}}A \tag{19.23}$$

where f is the Fanning friction coefficient discussed in Section 5–4(b). Consequently, the effect of friction may be taken into account by adding the term $\delta F_f/(A\,dx) = (\rho u^2/2)(4f/\mathfrak{D})$ to the momentum equation, equation 19.21. From equation 9.8, the effect of mass addition on the momentum equation may be obtained by adding the term $\rho u^2(1-y)(d\dot{m}_i/dx)/\dot{m}$ to equation 19.21, where $y \equiv u_{ix}/u_i$. Adding the aforementioned two terms to equation 19.21, we obtain

$$\rho u_t + \rho u u_x + p_x = \beta \tag{19.24}$$

where

$$\beta \equiv -\left[\frac{\rho u^2}{2}\frac{4f}{\mathfrak{D}} + \rho u^2(1-y)\frac{d(\ln \dot{m}_i)}{dx}\right] \tag{19.25}$$

and $d(\ln \dot{m}_i) = d\dot{m}_i/\dot{m}$.

3. *Energy equation.* A flow involving either friction, heat transfer, or mass addition is not isentropic. Consequently, equation 19.10 is not applicable to the flow model illustrated in Fig. 19.5. To derive the appropriate form of the energy equation, equation 2.88, Table 2.1, is applied to the differential control volume illustrated in Fig. 19.6; it should be noted that $\delta \dot{W}_{\text{shear}} = \delta \dot{W}_{\text{shaft}} = 0$, and that the internal energy u in equation 2.88 is replaced by $u = h - pv$ (see equation 1.53).* We obtain

$$-\delta\dot{Q} + \frac{\partial}{\partial t}\left[(\rho A\,dx)\left(h - pv + \frac{u^2}{2}\right)\right] + \left\{(\rho uA)\left(h + \frac{u^2}{2}\right)\right.$$

$$\left. + \frac{\partial}{\partial x}\left[(\rho uA)\left(h + \frac{u^2}{2}\right)\right]dx\right\} - \left\{(\rho uA)\left(h + \frac{u^2}{2}\right) + d\dot{m}_i\left(h_i + \frac{u_i^2}{2}\right)\right\} = 0 \quad (19.26)$$

In equation 19.26, it is assumed that the mass $d\dot{m}_i$ added to the main stream flow mixes completely with the main stream and leaves the control volume with the same energy per unit mass as that of the main stream. Expanding equation 19.26 and rearranging terms, we obtain

$$-\delta\dot{Q} + H\left[\frac{\partial}{\partial t}(\rho A\,dx) + \frac{\partial}{\partial x}(\rho uA)\,dx\right] + (\rho A\,dx)\frac{\partial H}{\partial t}$$

$$+ (\rho uA)\frac{\partial H}{\partial x}\,dx - \frac{\partial}{\partial t}\left[(\rho A\,dx)\,pv\right] - H_i\,d\dot{m}_i = 0 \quad (19.27)$$

where $H = h + u^2/2$ and $H_i = h_i + u_i^2/2$ are the stagnation enthalpies of the main stream and the mass addition stream, respectively. Substituting from equation 19.22 into the first term enclosed by the square brackets in equation 19.27, we obtain

$$-\delta\dot{Q} + H\,d\dot{m}_i + (\rho A\,dx)(H_t + uH_x) - p_t A\,dx - H_i\,d\dot{m}_i = 0 \quad (19.28)$$

Dividing equation 19.28 by $A\,dx$ yields

$$\rho(H_t + uH_x) - p_t = \rho u\,\delta Q_x - dH_i \quad (19.29)$$

where

$$dH_i = \frac{(H - H_i)\,d\dot{m}_i}{A\,dx} = \frac{\rho u(H - H_i)\,d\dot{m}_i}{\dot{m}\,dx} = \rho u(H - H_i)\frac{d(\ln \dot{m}_i)}{dx} \quad (19.30)$$

and $\delta Q_x = \delta Q/dx$. The term dH_i arises because of the difference between the stagnation enthalpy of the main stream H and that of the mass addition stream H_i.

An alternate form of the energy equation may be obtained by rewriting the first two terms in the momentum equation, equation 19.24, as follows:

$$u_t + uu_x = \frac{1}{u}\left[\left(\frac{u^2}{2}\right)_t + u\left(\frac{u^2}{2}\right)_x\right] = \frac{1}{u}\frac{D}{Dt}\left(\frac{u^2}{2}\right) \quad (19.31)$$

Substituting equation 19.31 into equation 19.24, we obtain

$$\rho\frac{D}{Dt}\left(\frac{u^2}{2}\right) = -up_x + u\beta \quad (19.32)$$

*In all of the equations of this chapter u denotes the velocity of the fluid in the x direction, except in the expressions for h and h_i where u denotes the specific internal energy of the fluid.

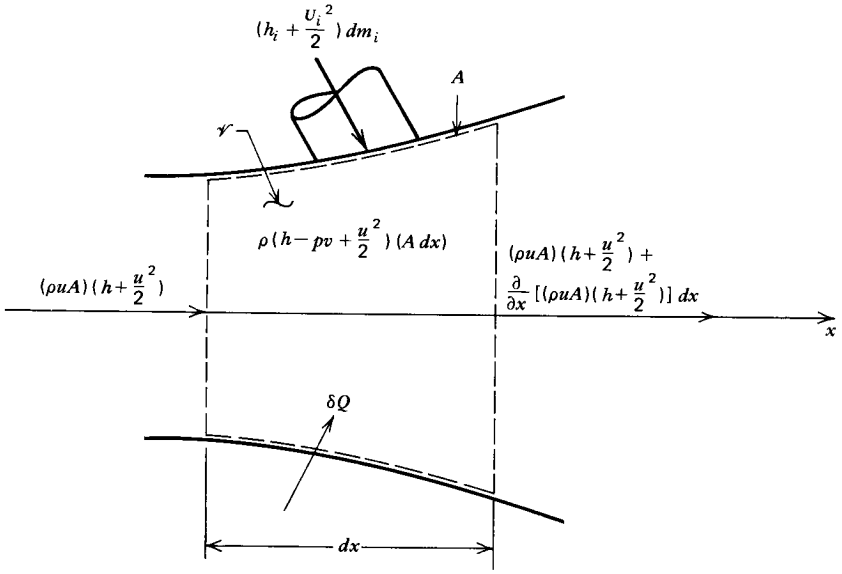

Figure 19.6 Flow model for the energy equation for unsteady quasi-one-dimensional flow with friction, heat transfer, and mass addition.

Substituting equation 19.32 into equation 19.29 gives

$$\rho \frac{Dh}{Dt} - \frac{Dp}{Dt} = \rho u\,\delta Q_x - dH_i - u\beta \tag{19.33}$$

Equations 19.22, 19.24, and 19.29 or 19.33 comprise a system of three equations for determining the four flow properties u, p, ρ, and h. An additional relationship is provided by the equation of state. Thus,

$$h = h(p, \rho) \tag{19.34}$$

Consequently, there is a sufficient number of relationships for determining the flow properties u, p, ρ, and h when the independent driving potentials dA, $d\dot{m}_i$, $4\mathfrak{f}/\mathfrak{D}$, and δQ are either specified or calculable in terms of u, p, ρ, and h.

The aforementioned system of equations is applicable to any fluid. To apply the method of characteristics, however, the static specific enthalpy h must be eliminated from equation 19.33. If the flowing fluid is a perfect gas, $dh = c_p\,dt$ and $p = \rho RT$. Hence,

$$dh = c_p\,dT = \frac{c_p}{R} d\left(\frac{p}{\rho}\right) = \frac{c_p}{\rho R}\,dp - \frac{pc_p}{\rho^2 R}\,d\rho \tag{19.35}$$

For a perfect gas, $p = \rho RT$, $c_p = \gamma R/(\gamma - 1)$, and $a^2 = \gamma RT$, so that equation 19.35 becomes

$$dh = c_p T\left(\frac{dp}{p} - \frac{d\rho}{\rho}\right) = \frac{a^2}{\gamma - 1}\left(\frac{dp}{p} - \frac{d\rho}{\rho}\right) \tag{19.36}$$

Expressing equation 19.36 as a *substantial derivative*, we obtain

$$\frac{Dh}{Dt} = \frac{a^2}{\gamma - 1}\left(\frac{1}{p}\frac{Dp}{Dt} - \frac{1}{\rho}\frac{D\rho}{Dt}\right) \tag{19.37}$$

Substituting for Dh/Dt from equation 19.37 into equation 19.33 and simplifying yields

$$\frac{Dp}{Dt} - a^2 \frac{D\rho}{Dt} = \psi \tag{19.38}$$

where

$$\psi = (\gamma - 1)(\rho u \, \delta Q_x - dH_i - u\beta) \tag{19.39}$$

Accordingly, the expanded form of equation 19.38 is

$$p_t + up_x - a^2(\rho_t + u\rho_x) = \psi \tag{19.40}$$

Equation 19.40 differs from the speed of sound equation for isentropic flow, equation 19.10, by the additional term ψ, where ψ is defined by equation 19.39.

Equations 19.22, 19.24, and 19.40 comprise a set of three equations for determining the three flow properties u, p, and ρ, for the unsteady quasi-one-dimensional flow of a perfect gas in the presence of friction, heat transfer, and mass addition. Those equations are applicable to both one-dimensional and quasi-one-dimensional flows, the flow geometry being specified by the value of δ in the term $\delta\rho u/x$ in equation 19.22.

For convenience of reference, the governing equations for unsteady one-dimensional and quasi-one-dimensional flow are renumbered and assembled in Table 19.1. For an isentropic flow, $\varepsilon = \beta = \psi = 0$.

Table 19.1 Governing Equations for Unsteady One-Dimensional and Quasi-One-Dimensional Flow

Continuity equation

$$\rho_t + u\rho_x + \rho u_x + \frac{\delta \rho u}{x} = \varepsilon \tag{19.41}$$

Momentum equation

$$\rho u_t + \rho u u_x + p_x = \beta \tag{19.42}$$

Energy equation

$$p_t + up_x - a^2(\rho_t + u\rho_x) = \psi \tag{19.43}$$

Nonhomogeneous terms

$\delta = 0$ for Cartesian coordinates

$\delta = 1$ for cylindrical coordinates

$\delta = 2$ for spherical coordinates

$\delta = x \dfrac{d(\ln A)}{dx}$ for quasi-one-dimensional flow

$$\varepsilon = \frac{1}{A}\frac{d\dot{m}_i}{dx} \tag{19.44}$$

$$\beta = -\left[\frac{\rho u^2}{2}\frac{4\mathfrak{f}}{\mathfrak{D}} + \rho u^2(1-y)\frac{d(\ln \dot{m}_i)}{dx}\right] \tag{19.45}$$

$$\psi = (\gamma - 1)(\rho u \, \delta Q_x - dH_i - u\beta) \tag{19.46}$$

19–3(d) Characteristic and Compatibility Equations

Table 19.1 presents the governing equations for unsteady one-dimensional and quasi-one-dimensional flow. They include the effects of friction, heat transfer, and mass addition. The geometry of the flow passage is specified by the parameter δ. The parameters ε, β, and ψ account for the combined effects of friction, heat transfer, and mass addition. For an isentropic flow, ε, β, and ψ are all zero.

The characteristic and compatibility equations corresponding to the equations presented in Table 19.1 are derived by multiplying equations 19.41, 19.42, and 19.43 by the unknown parameters σ_1, σ_2, and σ_3, respectively, and summing (see Appendix B in Volume I.). The following equation indicates the procedure.

$$\sigma_1(19.41)+\sigma_2(19.42)+\sigma_3(19.43)=0 \tag{19.47}$$

Performing the summation indicated in equation 19.47 and factoring out the coefficients of the x derivatives, we obtain

$$(\rho\sigma_1+\rho u\sigma_2)\left[u_x+\frac{\rho\sigma_2}{\rho\sigma_1+\rho u\sigma_2}u_t\right]+(\sigma_2+u\sigma_3)\left[p_x+\frac{\sigma_3}{\sigma_2+u\sigma_3}p_t\right]$$

$$+\left(u\sigma_1-a^2u\sigma_3\right)\left[\rho_x+\frac{\sigma_1-a^2\sigma_3}{u\sigma_1-a^2u\sigma_3}\rho_t\right]+\left(\sigma_1\frac{\delta\rho u}{x}-\sigma_1\varepsilon-\sigma_2\beta-\sigma_3\psi\right)=0 \tag{19.48}$$

The slopes of the characteristic curves, $dt/dx=\lambda$, are the coefficients of the derivatives u_t, p_t, and ρ_t. Thus,

$$\lambda=\frac{\sigma_2}{\sigma_1+u\sigma_2}=\frac{\sigma_3}{\sigma_2+u\sigma_3}=\frac{\sigma_1-a^2\sigma_3}{u\sigma_1-a^2u\sigma_3} \tag{19.49}$$

Assuming that u, p, and ρ are continuous, then $du/dx=u_x+\lambda u_t$, and so on, and equation 19.48 transforms to

$$\rho(\sigma_1+u\sigma_2)\,du+(\sigma_2+u\sigma_3)\,dp+\left(u\sigma_1-a^2u\sigma_3\right)d\rho$$

$$+\left(\sigma_1\frac{\delta\rho u}{x}-\sigma_1\varepsilon-\sigma_2\beta-\sigma_3\psi\right)dx=0 \tag{19.50}$$

Equation 19.50 is the *compatibility equation*, which is valid along the characteristic curves determined by equation 19.49. All that remains is to eliminate the unknown parameters σ_1, σ_2, and σ_3 from equations 19.49 and 19.50.

Solving equations 19.49 for σ_1, σ_2, and σ_3, we obtain

$$\sigma_1(\lambda)+\sigma_2(u\lambda-1)+\sigma_3(0)=0 \tag{19.51}$$

$$\sigma_1(0)+\sigma_2(\lambda)+\sigma_3(u\lambda-1)=0 \tag{19.52}$$

$$\sigma_1(u\lambda-1)+\sigma_2(0)+\sigma_3a^2(1-u\lambda)=0 \tag{19.53}$$

For equations 19.51 to 19.53 to have a solution other than $\sigma_1=\sigma_2=\sigma_3=0$, the determinant of the coefficient matrix for those equations must vanish. Thus,

$$\begin{vmatrix} \lambda & (u\lambda-1) & 0 \\ 0 & \lambda & (u\lambda-1) \\ (u\lambda-1) & 0 & -a^2(u\lambda-1) \end{vmatrix}=0 \tag{19.54}$$

Expanding the above determinant, we obtain

$$(u\lambda - 1)\left[(u\lambda - 1)^2 - a^2\lambda^2\right] = 0 \tag{19.55}$$

Equation 19.55 is a cubic equation in λ, and consequently, has three roots. If the roots are all real, there are three real characteristic curves.

Setting the linear factor $(u\lambda - 1)$ in equation 19.55 equal to zero yields the following characteristic curve.

$$\left(\frac{dt}{dx}\right)_o = \lambda_o = \frac{1}{u} \tag{19.56}$$

Equation 19.56, written in the more conventional form $dx/dt = u$, is seen to be the equation of the pathline of the fluid particles; the subscript o is employed for denoting the pathline. Accordingly, in unsteady one-dimensional flow, the *pathlines are characteristics*.

From the quadratic term in equation 19.55, the following two additional roots and the corresponding characteristic curves are obtained. Thus,

$$\begin{aligned} (u\lambda - 1)^2 &= a^2\lambda^2 \\ u\lambda - 1 &= \pm a\lambda \\ \left(\frac{dt}{dx}\right)_{\pm} &= \lambda_{\pm} = \frac{1}{u \pm a} \end{aligned} \tag{19.57}$$

Figure 19.7 illustrates schematically the characteristics in the xt plane; that is, the *physical plane*. The C_+ and C_- characteristics, corresponding to the + and − signs, respectively, in equation 19.57, lie on either side of the pathline C_o, but are not symmetrical with respect to C_o. Four possible cases are illustrated in Fig. 19.7, depending on whether u is positive or negative, and whether u is less than or greater than the local speed of sound a; that is, whether the flow is subsonic or supersonic. In each of the four cases, λ is real and the characteristics exist. Hence, the equations governing the unsteady one-dimensional flow of a compressible fluid are hyperbolic for both subsonic flow and supersonic flow.

One of the properties of a characteristic curve is that it is the path along which information is propagated through a flow field (see Section 12–3). Along the C_+ and C_- characteristics, the speed of propagation is

$$\left(\frac{dx}{dt}\right)_{\pm} = \frac{1}{\lambda_{\pm}} = u \pm a \tag{19.58}$$

Hence, the propagation speed along the $C_{\pm}$ characteristics is equal to the speed of sound relative to the moving fluid. In that regard, the $C_{\pm}$ characteristics in unsteady flow are analogous to the Mach lines in a steady flow, and are called the *Mach lines of the unsteady flow*. Consequently, in an unsteady one-dimensional or quasi-one-dimensional flow three characteristic curves pass through each point of the flow field; the pathline C_o and the right- and left-running Mach lines $C_{\pm}$, illustrated in Fig. 19.7.

The compatibility equations that are valid along the characteristic curves are obtained from equation 19.50 by solving equations 19.51 to 19.53 for the σ's and substituting the results into equation 19.50. Along pathlines, therefore, $(u\lambda - 1) = 0$, and equations 19.51 to 19.53 become

$$\sigma_1 = 0 \qquad \sigma_2 = 0 \qquad \sigma_3 \text{ is arbitrary} \tag{19.59}$$

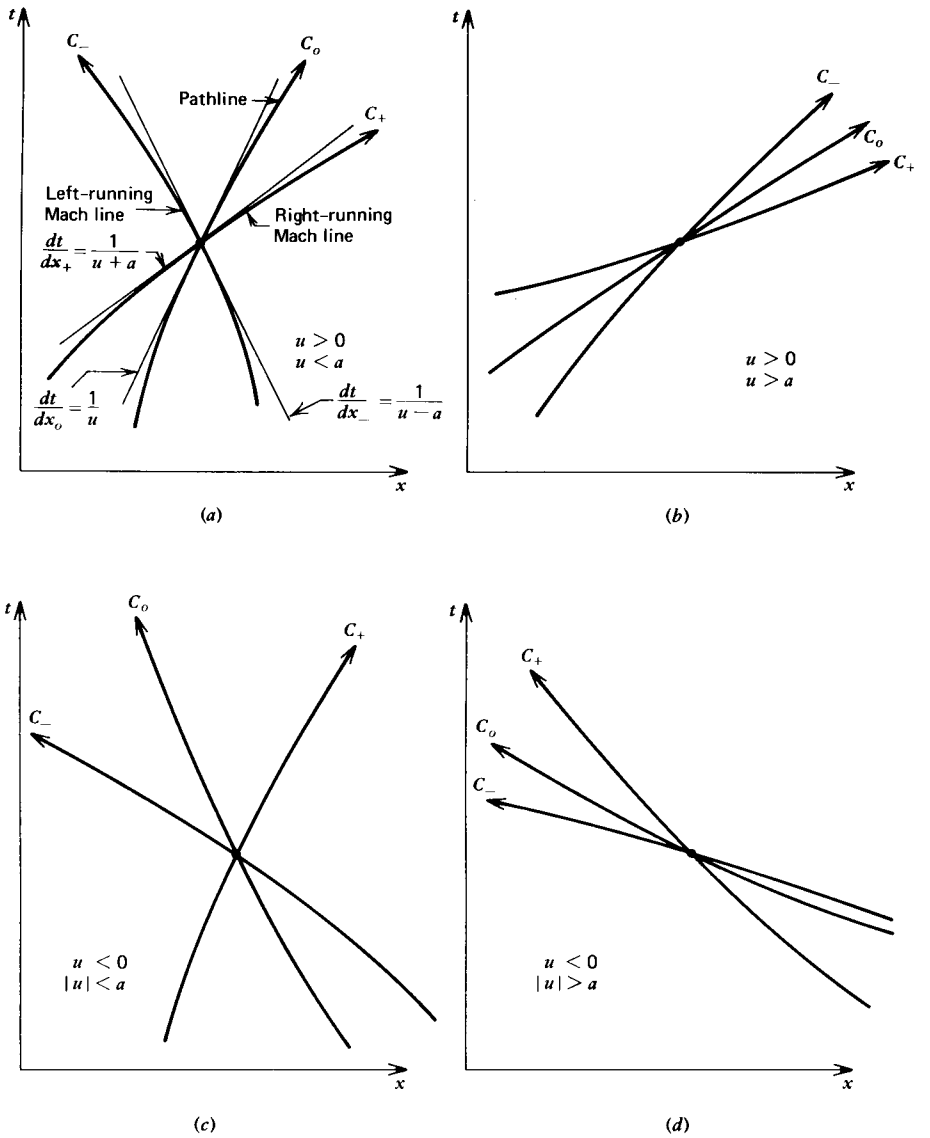

Figure 19.7 Characteristics for unsteady one-dimensional flow. (*a*) Subsonic flow from left to right. (*b*) Supersonic flow from left to right. (*c*) Subsonic flow from right to left. (*d*) Supersonic flow from right to left.

Substituting equation 19.59 into equation 19.50, we obtain

$$dp - a^2 d\rho = \frac{\psi}{u} dx \tag{19.60}$$

Along the Mach lines, $(u\lambda - 1)^2 = a^2\lambda^2$, and equations 19.51 to 19.53 become

$$\sigma_1 = -\sigma_2 \frac{(u\lambda - 1)}{\lambda} = \sigma_3 \frac{(u\lambda - 1)^2}{\lambda^2} = a^2\sigma_3 \tag{19.61}$$

$$\sigma_2 = -\sigma_3 \frac{(u\lambda - 1)}{\lambda} \tag{19.62}$$

$$\sigma_1 = a^2\sigma_3 \tag{19.63}$$

Equations 19.61 and 19.63 are not independent. Consequently, there are only two independent relationships between σ_1, σ_2, and σ_3, so that one of the σ's is arbitrary. Choosing σ_3 to be arbitrary, equations 19.62 and 19.63 may be substituted into equation 19.50 to express σ_1 and σ_2 in terms of σ_3. Since σ_3 is nonzero, it may be divided out of the result, yielding the following compatibility equation that is valid along the Mach lines.

$$\rho\left[a^2-\frac{u(u\lambda-1)}{\lambda}\right]du+\left[-\frac{(u\lambda-1)}{\lambda}+u\right]dp$$

$$+(a^2u-a^2u)\,d\rho+\left[\frac{\delta\rho ua^2}{x}-a^2\varepsilon+\frac{(u\lambda-1)}{\lambda}\beta-\psi\right]dx=0 \quad (19.64)$$

Recalling that $(u\lambda-1)^2=a^2\lambda^2$ and $\lambda_\pm=1/(u\pm a)$ along the Mach lines, equation 19.64 may be simplified to yield

$$dp_\pm \pm \rho a\,du_\pm=\left(-\frac{\delta\rho ua^2}{x}+a^2\varepsilon\pm a\beta+\psi\right)dt_\pm \quad (19.65)$$

where the upper subscript + attached to the differentials and the upper sign + in the coefficients $\pm\rho a$ and $\pm a\beta$ correspond to the C_+ characteristic, and the lower subscript − and the lower sign − correspond to the C_- characteristic. For the special case of isentropic flow in a constant-area duct (i.e., $\delta=\varepsilon=\beta=\psi=0$), equation 19.65 reduces to the well-known classical result[1–5] (see equation 13.28)

$$dp_\pm \pm \rho a\,du_\pm=0 \quad (19.66)$$

Summarizing, for unsteady one-dimensional and quasi-one-dimensional flow, there are three distinct characteristic curves: the pathline C_o and the two Mach lines $C_\pm$. There is one compatibility equation valid on each of those three characteristic curves. The derived system of characteristic and compatibility equations may replace the original system of partial differential equations (equations 19.41 to 19.43). Table 19.2 presents the aforementioned characteristic and compatibility equations.

To apply the characteristic and compatibility equations presented in Table 19.2, a characteristic grid or network must be devised where the three characteristic

Table 19.2 Characteristic and Compatibility Equations for Unsteady One-Dimensional and Quasi-One-Dimensional Flow

Characteristic equations		
$\left(\frac{dt}{dx}\right)_o=\lambda_o=\frac{1}{u}$	(*pathline*)	(19.56)
$\left(\frac{dt}{dx}\right)_\pm=\lambda_\pm=\frac{1}{u\pm a}$	(*Mach lines*)	(19.57)
Compatibility equations		
$dp_o-a^2d\rho_o=\frac{\psi}{u}dx_o$	(*along pathlines*)	(19.60)
$dp_\pm \pm \rho a\,du_\pm=\left(-\frac{\delta\rho ua^2}{x}+a^2\varepsilon\pm a\beta+\psi\right)dt_\pm$	(*along Mach lines*)	(19.65)

curves intersect at a common point, so that the three compatibility equations may be solved simultaneously at the point of intersection for the flow properties u, p, and ρ at that point. Figure 19.8 illustrates schematically the intersection of the three characteristic curves at a common point. Several finite difference grids and overall marching algorithms for obtaining the appropriate characteristic network are discussed in Section 19–6(a).

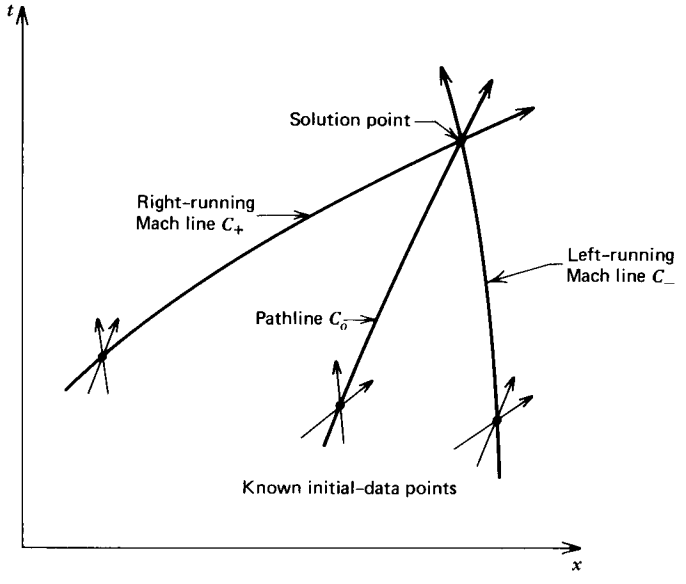

Figure 19.8 Intersection of all three characteristics at a common solution point.

19–4 UNSTEADY ONE-DIMENSIONAL PLANAR CONTINUOUS FLOW

The equations governing unsteady one-dimensional and quasi-one-dimensional continuous flow are derived in Section 19–3. Those equations include the effects of area change, friction, heat transfer, and mass addition. Two types of discontinuities may occur in unsteady flows: shock waves and contact surfaces. Shock waves and contact surfaces are generally treated as mathematical discontinuities that separate regions of continuous flow. The general features of unsteady one-dimensional continuous flow are discussed in Section 13–4 and reviewed briefly in the present section. The general features of unsteady one-dimensional flow with discontinuities are discussed in Section 19–5.

In Section 13–4, the general features of unsteady one-dimensional flow are discussed for the special case of planar homentropic flow. The general features of planar homentropic flow are qualitatively applicable to unsteady one-dimensional and quasi-one dimensional flow with area change, friction, heat transfer, and mass addition. A brief summary of the major points developed in Section 13–4 is presented below.

For the case of unsteady one-dimensional homentropic flow considered in Chapter 13, two families of characteristics exist: the left-running and right-running Mach lines. For the case of unsteady one-dimensional flow with area change, friction, heat transfer, mass addition, and entropy gradients, three families of characteristics exist: the pathline and the left-running and right-running Mach lines. In both cases, the Mach lines of the flow determine the general features of the flow process.

As illustrated in Fig. 19.7, two families of Mach lines exist: left-running Mach lines and right-running Mach lines. The orientation of the Mach lines depends on whether the flow is from left-to-right or from right-to-left, and on whether the flow is subsonic or supersonic. Each family of Mach lines may represent either a compression wave or an expansion wave.

In unsteady one-dimensional flow, *uniform flow regions*, *simple wave regions*, and *nonsimple wave regions* occur. A uniform flow region is one in which all of the thermodynamic properties of the fluid are uniform and its velocity is constant. A simple wave region is one where the changes in the flow properties are caused by waves of only one family. The propagation of a pressure disturbance into a uniform region results in the formation of a simple wave region. The reflection of waves at the boundaries of simple wave regions results in waves of both families that interact and create nonsimple wave regions.

Simple compression and expansion waves occur when a disturbance moves into an undisturbed fluid. Simple compression waves accelerate the fluid in the direction of the propagation of the wave, and increase the pressure, velocity, and speed of sound of the fluid, thus increasing the wave propagation speed. Compression waves converge, and the pathlines bend toward the waves. Figure 19.9 illustrates the wave pattern for a simple compression wave.

Simple expansion waves accelerate the fluid in the direction opposite to the propagation of the wave, and decrease the pressure and speed of sound of the fluid. Consequently, the wave propagation speed decreases, the waves diverge, and the pathlines bend away from the waves. The wave pattern for a simple expansion wave is illustrated in Fig. 19.10.

Centered compression and expansion waves occur when there are discontinuous changes in the fluid properties at a point. For example, centered waves are created in a shock tube by the instantaneous rupture of a diaphragm separating a region of high pressure from a region of low pressure. A centered compression wave (i.e., a shock wave) propagates into the low pressure region, and a centered expansion wave propagates into the high pressure region. Figure 19.11 illustrates the initial wave pattern in a shock tube.

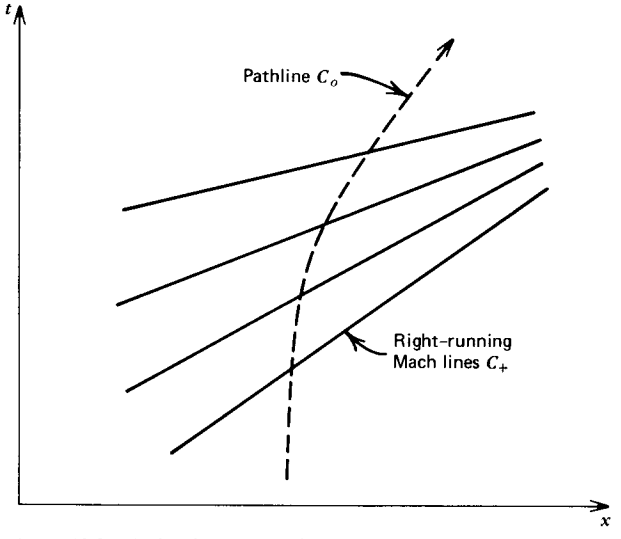

Figure 19.9 A simple compression wave.

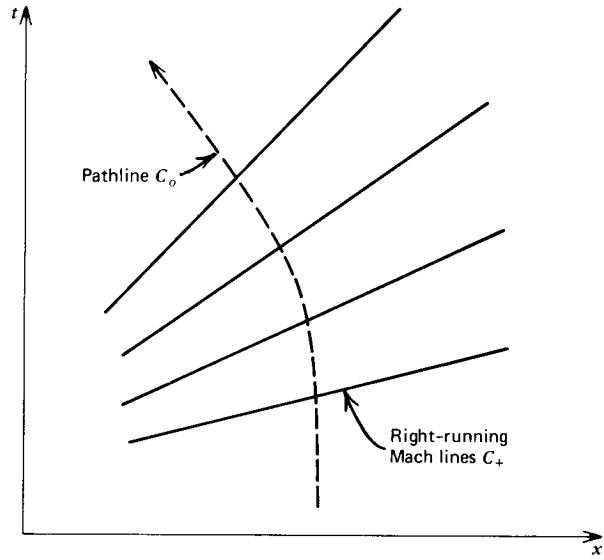

Figure 19.10 A simple expansion wave.

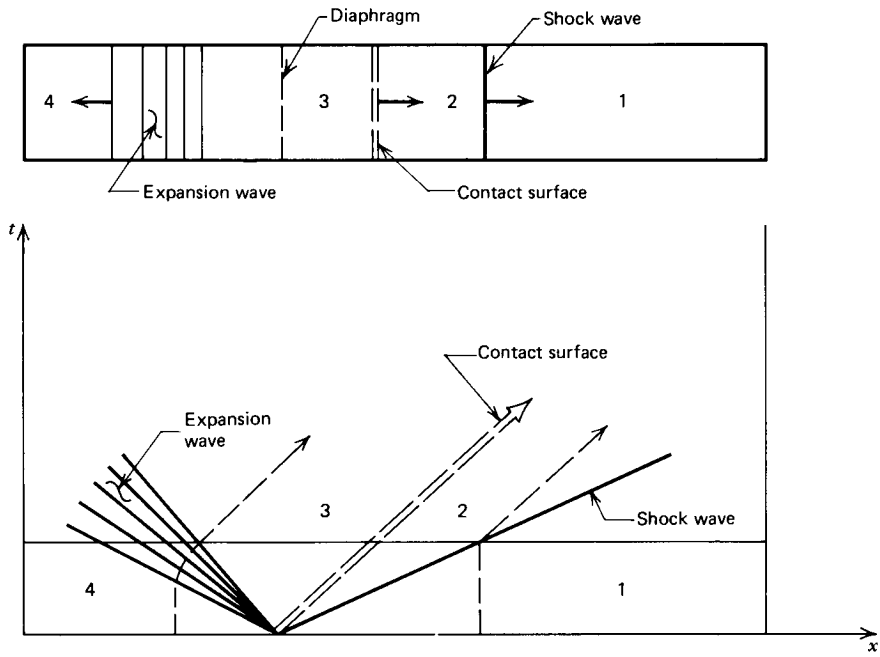

Figure 19.11 The initial wave pattern in a shock tube.

When either a continuous compression wave or expansion wave impinges on a boundary of the flow region, a reflected wave is generated. Waves are reflected from closed ends and open ends of a duct, from shock waves, and from contact surfaces. Reflections from the closed and open ends of a duct are discussed below, and interactions of continuous waves with shock waves and contact surfaces are discussed in Section 19–5.

When a continuous wave is incident on a closed end, a wave of the same type is reflected. Thus, incident compression waves reflect as compression waves and incident expansion waves reflect as expansion waves. When a continuous wave is incident on an open end where the pressure in the exit plane is constant and the flow is subsonic, a wave of the opposite type is reflected. Thus, incident compression waves reflect as expansion waves and incident expansion waves reflect as compression waves. If the flow is supersonic, no waves are reflected. The wave reflection rules for an open end hold for both outflow and inflow. Figures 19.12 and 19.13 illustrate the reflection of compression waves and expansion waves, respectively, from the ends of a flow passage.

When continuous waves intersect, the resultant wave pattern depends on the type of waves involved (i.e., compression or expansion) and the direction of propagation of the incident waves (i.e., whether both waves travel in the same direction or the waves travel in the opposite directions). Compression waves of the same family converge as illustrated in Fig. 19.14, and may ultimately coalesce to

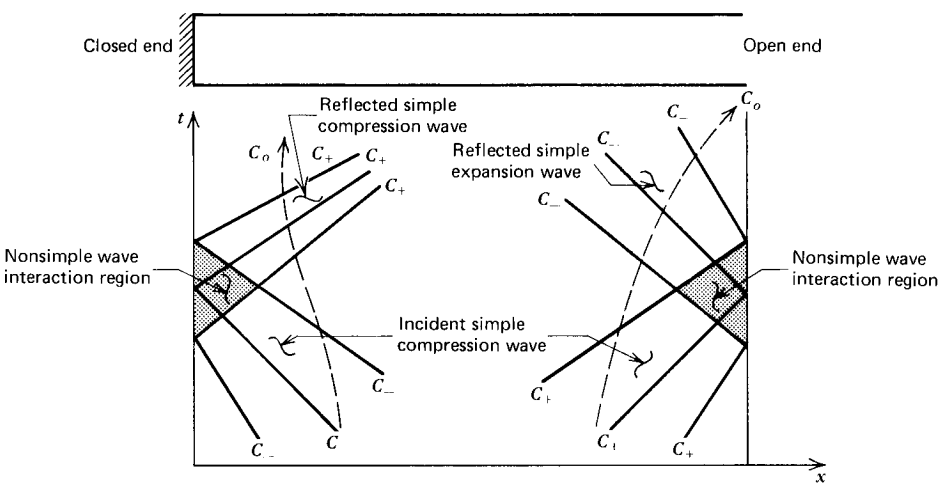

Figure 19.12 Reflection of compression waves from the end of a tube.

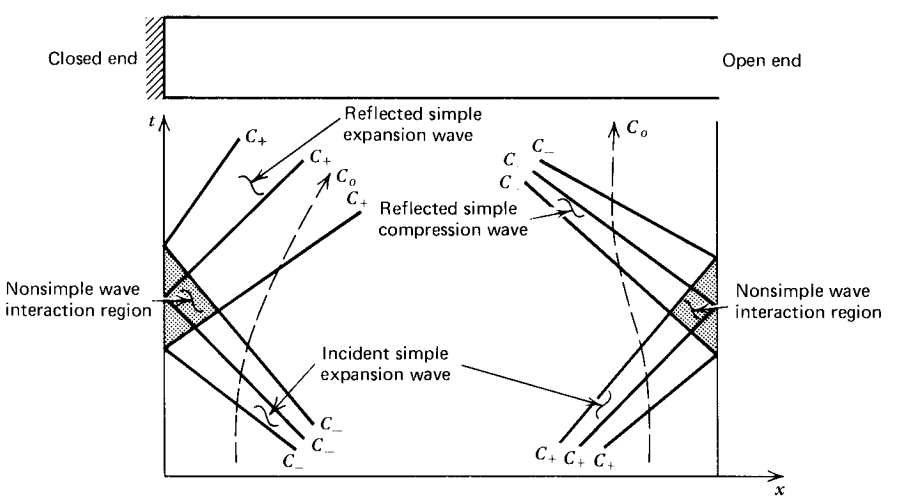

Figure 19.13 Reflection of expansion waves from the end of a tube.

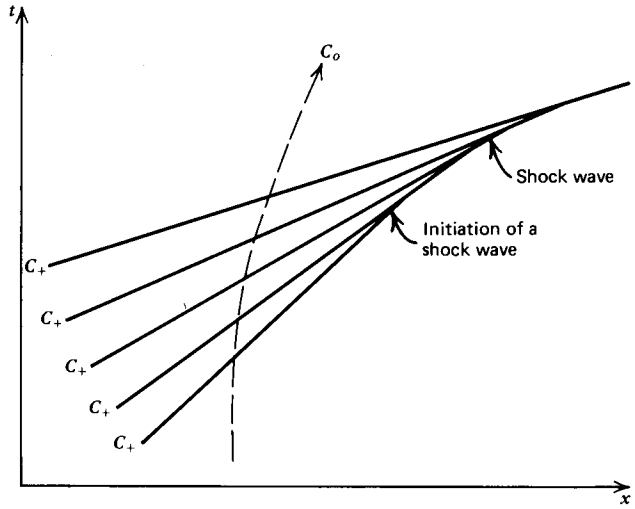

Figure 19.14 Coalescence of compression waves to form a shock wave.

form a shock wave (see Section 19–5). Expansion waves traveling in the same direction diverge as illustrated in Fig. 19.10, and no interaction can occur.

When two compression waves traveling in opposite directions interact, two compression waves are transmitted through the interaction region as illustrated in Fig. 19.15. Similarly, when two expansion waves traveling in opposite directions interact, two expansion waves are transmitted through the interaction region as illustrated in Fig. 19.16. When a wave of one type (i.e., compression or expansion) traveling in a given direction (i.e., right or left) interacts with a wave of the other type traveling in the opposite direction, waves of the same type are transmitted through the interaction region as illustrated in Fig. 19.17.

The general features of unsteady one-dimensional continuous flow described in this section apply strictly speaking to planar homentropic flow. Those features are, however, qualitatively applicable to continuous flow with area change, friction,

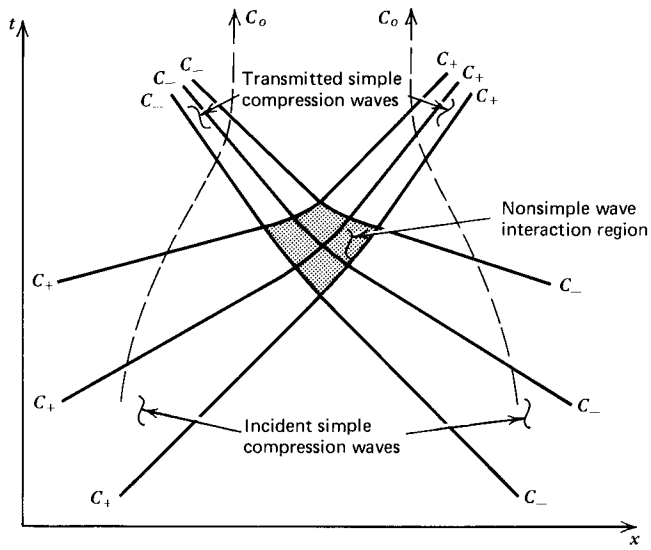

Figure 19.15 Intersection of two simple compression waves.

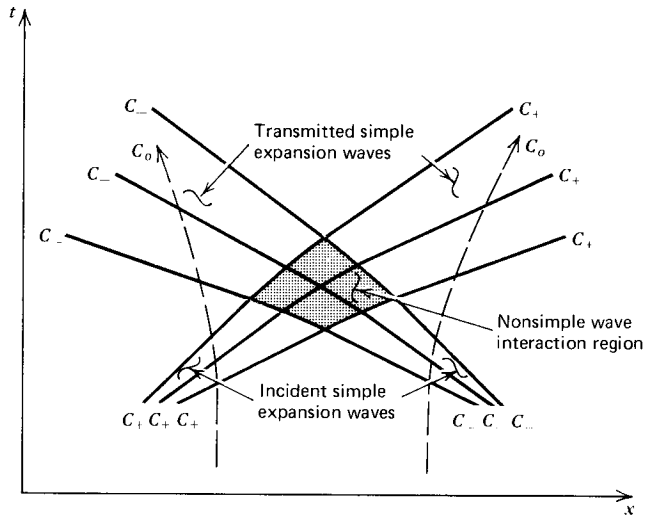

Figure 19.16 Intersection of two simple expansion waves.

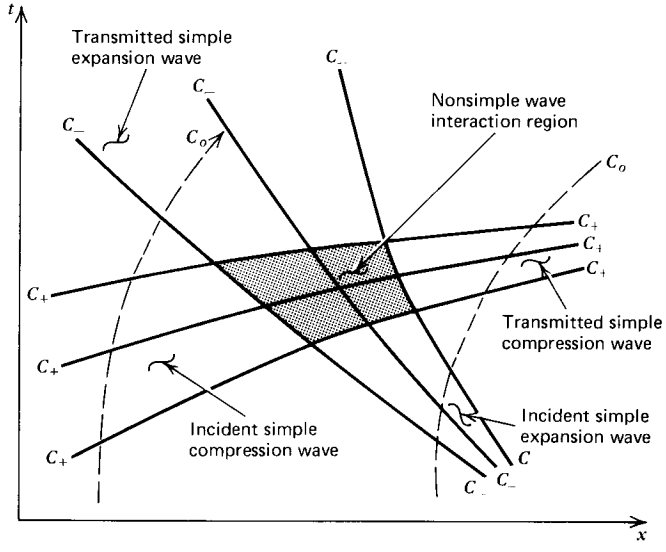

Figure 19.17 Intersection of a simple compression wave and a simple expansion wave.

heat transfer, and mass addition, and to the continuous flow regions between shock waves and contact surfaces. The boundaries of a flow field, such as an open end or a closed end, are points, and the effects of area change, friction, heat transfer, and mass addition are negligible. Consequently, the rules of wave interaction at boundaries presented in this section are directly applicable to the unsteady quasi-one-dimensional generalized flow case.

19–5 UNSTEADY ONE-DIMENSIONAL PLANAR FLOW WITH DISCONTINUITIES

In Section 19–4, the properties of continuous waves are discussed. It is shown there that continuous compression waves always converge, as illustrated in Fig. 19.14, and that the waves may coalesce and form a *shock wave* or *shock front*. As more

and more of the compression waves coalesce, the wave steepens and becomes more shock fronted, as illustrated in Fig. 19.18. There are discontinuities in the properties of the fluid as it flows through the shock wave, which may be treated as a boundary of the continuous flow regions located on each side of it. Shock waves are also formed when the velocity of the fluid at a solid boundary of the flow field is discontinuous, as in the instantaneous acceleration of a piston illustrated in Fig. 13.8*a*.

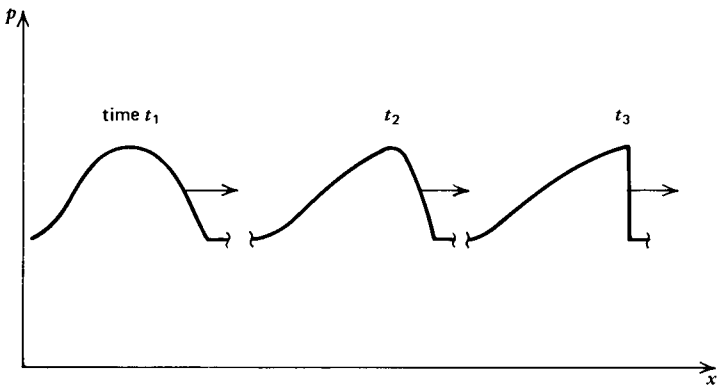

Figure 19.18 Strengthening of a finite amplitude compression wave.

In addition to the shock wave, there is another type of discontinuity termed a *contact surface*. The latter is an interface that separates two flow regions, but it moves with those regions. The velocity and pressure of the gas on each side of the contact surface are the same, but the other thermodynamic properties may be different. Unlike the shock wave, there is no flow of gas across a contact surface. Figure 19.19 illustrates diagrammatically a contact surface.

A contact surface arises on the rupture of a diaphragm separating two regions containing different gases, or two regions containing the same gas but at different thermodynamic states. Such a contact surface is generated in a shock tube, which is discussed in Section 19–5(c). Contact surfaces also arise at the interface between the regions containing gaseous reactants and products in a combustion chamber, and at the point of intersection of two shock waves. The properties of contact surfaces are discussed in Section 19–5(b).

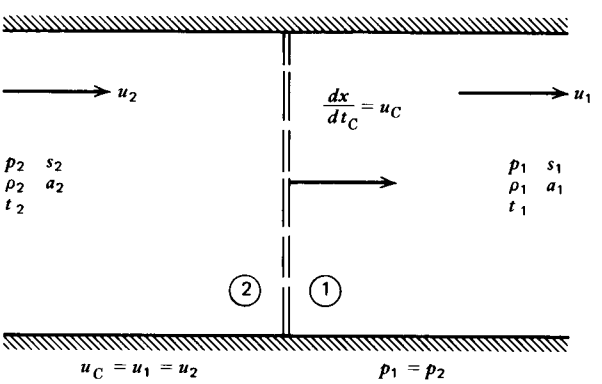

Figure 19.19 Illustration of a contact surface.

19–5(a) Shock Waves

Figure 19.20*a* illustrates schematically a normal shock wave being propagated to the right with the velocity U relative to the gas into which it moves. The gas moves with the velocity u_1. The absolute velocity of propagation of the shock wave is, therefore, $(dx/dt)_S = u_1 + U$. Figure 19.20*b* illustrates how the moving shock wave may be transformed into a stationary shock wave by a relative coordinate transformation wherein the observer moves at the same velocity, $u_1 + U$, as the shock wave (see Section 7–3). The resulting stationary shock wave may, therefore, be analyzed

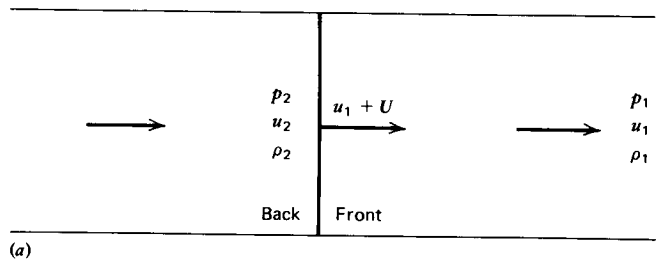

(*a*)

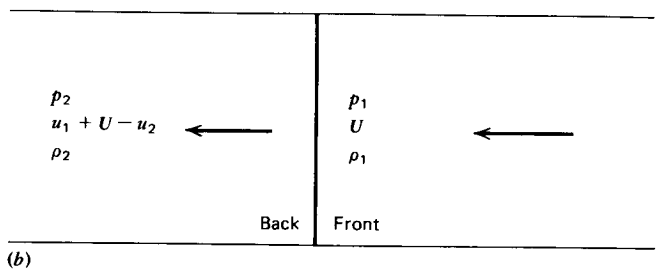

(*b*)

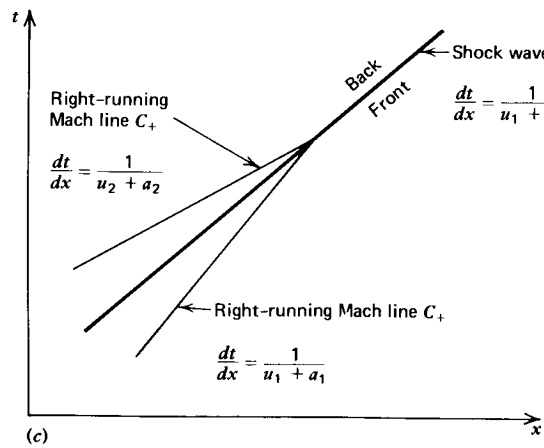

(*c*)

Figure 19.20 Relationship between the slope of a shock wave and the slopes of the upstream and downstream Mach lines. (*a*) Moving shock wave. (*b*) Stationary shock wave. (*c*) Slopes in the xt plane.

by the methods presented in Chapter 7. Even when the moving shock wave has a nonuniform propagation velocity the above transformation is permissible, because the shock wave is so thin that the unsteady flow effects within it are negligible.

It is shown in Chapter 7 that the Mach number M_1 ahead of a normal shock wave relative to an observer moving with the shock wave is always supersonic. Hence, in Fig. 19.20*b*, the velocity $U > a_1$. Consequently,

$$u_1 + U > u_1 + a_1 \tag{19.67}$$

The C_+ Mach lines in front of the shock wave travel at the velocity $dx/dt_+ = u_1 + a_1$. Consequently, they will always be overtaken by the shock wave. It is also shown in Chapter 7 that the Mach number M_2 behind a normal shock wave relative to an observer moving with the shock wave is subsonic. Referring to Fig. 19.20*b*, $U + u_1 - u_2 < a_2$. Consequently,

$$u_1 + U < u_2 + a_2 \tag{19.68}$$

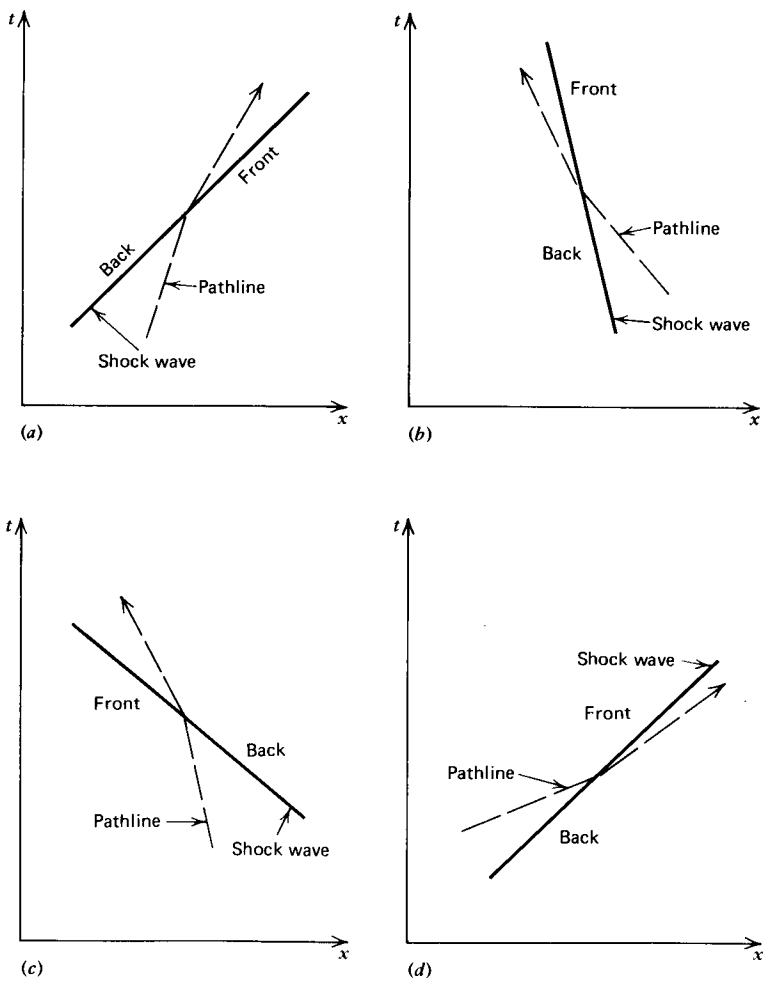

Figure 19.21 Illustration of right- and left-facing, right- and left-traveling shock waves. (*a*) Right-facing right-traveling shock wave. (*b*) Right-facing left-traveling shock wave. (*c*) Left-facing left-traveling shock wave. (*d*) Left-facing right-traveling shock wave.

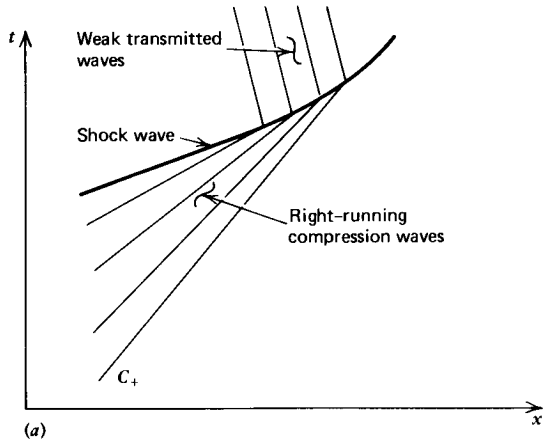

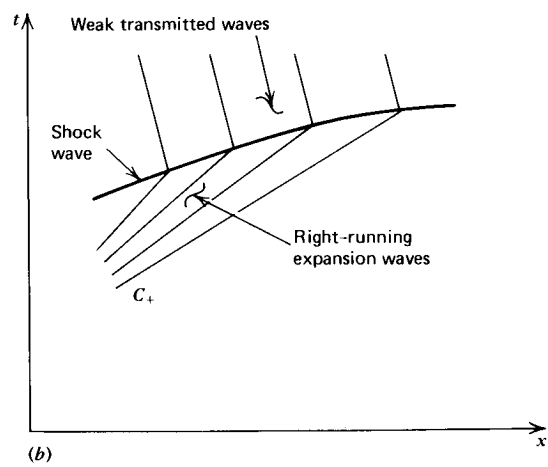

Figure 19.22 Interaction of a right-facing right-traveling shock wave with right-running continuous waves. (*a*) Overtaking compression waves. (*b*) Overtaking expansion waves.

Since the C_+ Mach lines behind the shock wave travel at the velocity $dx/dt_+ = u_2 + a_2$, they will always overtake the shock wave. Figure 19.20*c* illustrates the aforementioned relationships. Consequently, the following general rules relate the speeds of propagation of shock waves and continuous waves.

Rule 1. Shock waves are always overtaken by continuous waves of the same family in the region behind the shock wave.

Rule 2. Shock waves always overtake continuous waves of the same family in the region ahead of the shock wave.

Shock waves may be classified as *right-facing* or *left-facing* depending on whether the fluid particles enter the shock wave from the *right* or the *left*, respectively. Relative to a stationary observer, shock waves may also be classified as *right-traveling* or *left-traveling* depending on whether they propagate to the *right* or to the *left*, respectively, as time increases. Figure 19.21 illustrates the four possible combinations of right- and left-facing and right- and left-traveling shock waves. Of course,

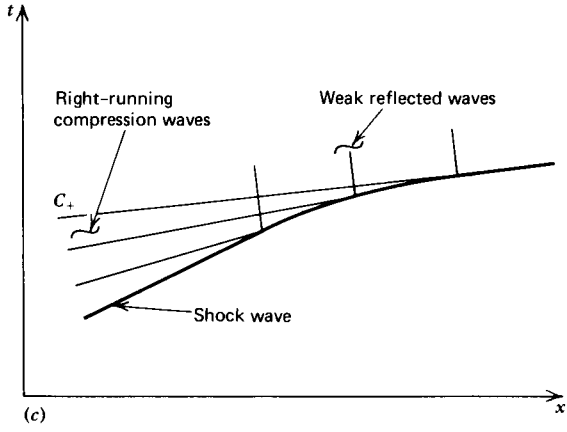

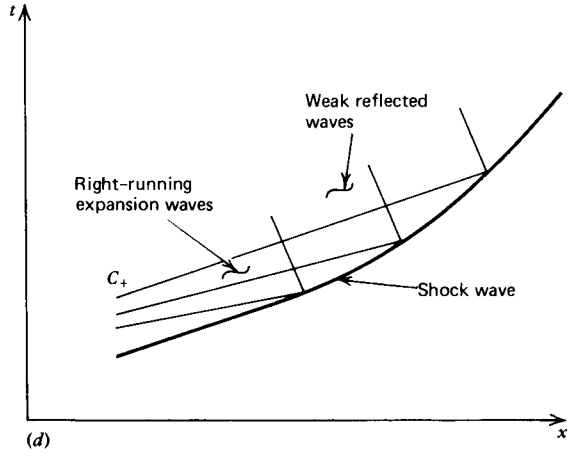

Figure 19.22 (*Continued*) (*c*) Overtaken by compression waves. (*d*) Overtaken by expansion waves.

stationary shock waves may also occur for certain periods, even in an unsteady flow.

Figure 19.22 illustrates the interaction of a shock wave with continuous waves. When a shock wave overtakes a family of compression waves, the shock wave is weakened and its speed decreases, as illustrated in Fig. 19.22*a*. On the other hand, when a shock wave overtakes a family of expansion waves, the shock wave is strengthened and its speed increases, as illustrated in Fig. 19.22*b*. When a shock wave is overtaken by a family of compression waves, illustrated in Fig. 19.22*c*, the continuous compression waves coalesce into the shock wave thereby strengthening it and increasing its velocity. When a family of expansion waves overtakes a shock wave, they coalesce into the shock wave and weaken it and decrease its speed, as illustrated in Fig. 19.22*d*. In all of the four cases illustrated in Fig. 19.22, left-running waves are propagated from the back side of the shock wave.

When a fluid particle passes through a shock wave, its entropy increases. Accordingly, the flow across a shock wave is nonisentropic. When the shock wave

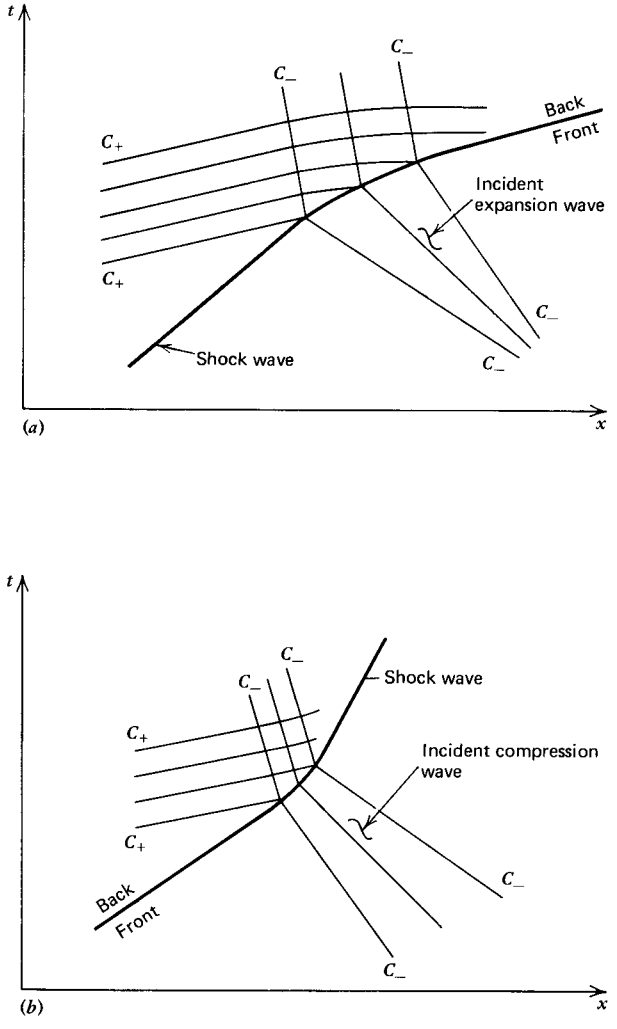

Figure 19.23 Interaction of a right-facing right-traveling shock wave with left-running continuous waves. (*a*) Interaction with an expansion wave. (*b*) Interaction with a compression wave.

strength is changing, as is usually the case, each fluid particle passing through the shock wave experiences a different increase in entropy. As a result, the flow field behind a shock wave is not *homentropic*, and the state plane, described in Section 13–4(a), cannot be constructed for that region of the flow. In the special case where the shock strength is constant, the entropy change across the shock wave is uniform, and the flow behind the shock wave is homentropic. In that case, the state plane has physical significance, although a different state plane must be constructed for the regions in front of and behind the shock wave.

It is possible for shock waves of one family (right- or left-facing) to interact with continuous waves traveling in the opposite direction. Figure 19.23*a* illustrates the interaction of a right-facing shock wave with a left-running expansion wave. As the shock wave penetrates the expansion wave, both the strength and the speed of the shock wave increase, while simultaneously the strength and the speed of the expansion wave decrease. There are no reflected right-running waves in front of the shock wave, because a shock wave *always overtakes waves traveling in the same*

direction. Similarly, there are no right-running waves generated on the back side of the shock wave, since those waves travel faster than the shock wave and, therefore, would be absorbed immediately into the shock wave. Right-running waves traveling in back of the shock wave will penetrate the transmitted expansion wave and coalesce with the shock wave.

Figure 19.23*b* illustrates the interaction of a right-facing shock wave with a left-running compression wave. As the shock wave interacts with the compression wave, its strength and speed decrease, as do the strength and speed of the compression wave. There are no right-running waves reflected in front of the shock wave nor any right-running waves generated from the back side of the shock wave. Right-running waves traveling behind the shock wave will penetrate the transmittted compression wave and eventually coalesce with the shock wave.

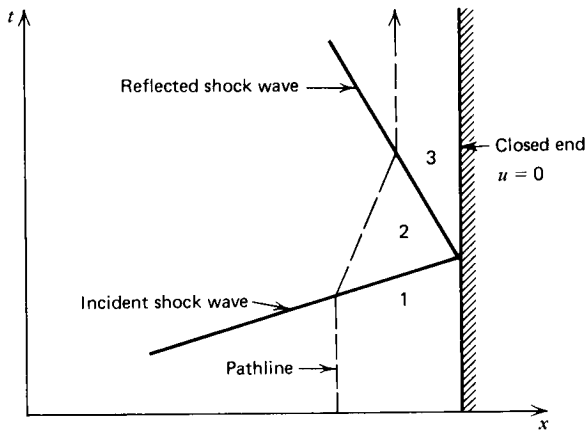

Figure 19.24 Reflection of a right-facing right-traveling shock wave from a solid boundary.

Figure 19.24 illustrates the reflection of a shock wave from the closed end of a duct. The incident shock wave imparts a finite pressure change Δp and a finite velocity change Δu to the fluid. At the solid boundary, the fluid velocity must remain equal to zero. Consequently, a reflected wave is generated which imparts the finite velocity change $-\Delta u$ to the fluid. Since the velocity change acts in the same direction as the reflected wave is propagated, the reflected wave must be a compression wave. Because a finite velocity change is required, a finite pressure change is similarly required, and the reflected compression wave is a shock wave. It may be shown that, for a perfect gas,[2,4,5]

$$\frac{p_3 - p_1}{p_2 - p_1} = 1 + \frac{\left(1 + \dfrac{\gamma - 1}{\gamma + 1}\right)}{\left(\dfrac{p_1}{p_2} + \dfrac{\gamma - 1}{\gamma + 1}\right)} \tag{19.69}$$

$$\frac{p_3}{p_2} = \frac{\left(\dfrac{3\gamma - 1}{\gamma + 1}\right)\dfrac{p_2}{p_1} - \dfrac{\gamma - 1}{\gamma + 1}}{\left(\dfrac{\gamma - 1}{\gamma + 1}\right)\dfrac{p_2}{p_1} + 1} \tag{19.70}$$

It is shown in Section 7–4 that the pressure ratio p_2/p_1 across the incident shock wave depends on the Mach number $M_1=(u_1+U)/a_1$, and the specific heat ratio γ. As M_1 approaches infinity, the pressure ratio p_2/p_1 similarly approaches infinity (see Table 7.2). From equations 19.69 and 19.70,

$$\lim_{\frac{p_2}{p_1}\to\infty}\left(\frac{p_3}{p_2}\right)=\frac{3\gamma-1}{\gamma-1} \qquad (=8 \text{ for } \gamma=1.4) \tag{19.71}$$

$$\lim_{\frac{p_2}{p_1}\to\infty}\left(\frac{p_3-p_1}{p_2-p_1}\right)=\frac{3\gamma-1}{\gamma-1} \qquad (=8 \text{ for } \gamma=1.4) \tag{19.72}$$

For weak shock waves, M_1 approaches unity, p_2/p_1 approaches unity (see Table 7.2), and equations 19.69 and 19.70 yield

$$\lim_{\frac{p_2}{p_1}\to 1}\left(\frac{p_3}{p_2}\right)=1 \tag{19.73}$$

$$\lim_{\frac{p_2}{p_1}\to 1}\left(\frac{p_3-p_1}{p_2-p_1}\right)=2 \tag{19.74}$$

Equation 19.74 shows that for weak pressure distrubances (i.e., acoustic waves), the pressure changes of the incident and reflected waves are equal; that is, $(p_3-p_2)=(p_2-p_1)$. For a shock wave, however, equation 19.69 shows that the pressure change for the reflected shock wave (p_3-p_2) is larger than the pressure change of the incident shock wave (p_2-p_1). That fact is employed in a shock tube to obtain extremely high pressures in the region behind the reflected shock wave.

The interaction of a shock wave with the open end of a duct can yield several different results. The interaction should account for the unsteady flow effects in the exhaust region. If the initial flow behind the shock wave is subsonic, a reasonable approximation for the pressure in the exhaust region is obtained by assuming that the pressure at the duct exit plane is equal to the constant ambient pressure. In that case, the incident shock wave imparts a finite velocity increment Δu and pressure increment Δp to the fluid. At the duct exit plane, since the pressure remains constant by assumption, a reflected wave having a pressure increment $-\Delta p$ is generated; that is, the wave is an expansion wave. Because Δp is a finite pressure change, the reflected expansion wave must be a centered expansion wave, as illustrated in Fig. 19.25. If the subsonic Mach number behind the incident shock wave is large, the assumption that the pressure in the exit plane is constant may be in serious error. If the pressure in back of the incident shock wave is considerably larger than the ambient pressure, then the assumption requires the pressure at the end of the duct to drop instantaneously to the ambient pressure, which may result in a flow having a supersonic Mach number at the duct exit. In that case no waves are reflected because the speed of the reflected waves is smaller than the flow speed. In such a case, the assumption that the duct exit pressure equals the ambient pressure is questionable, and the unsteady external flow field should be calculated. When the Mach number behind the incident shock wave is supersonic, no waves are reflected from an open end, because in that case the entire interaction is swept out of the duct.

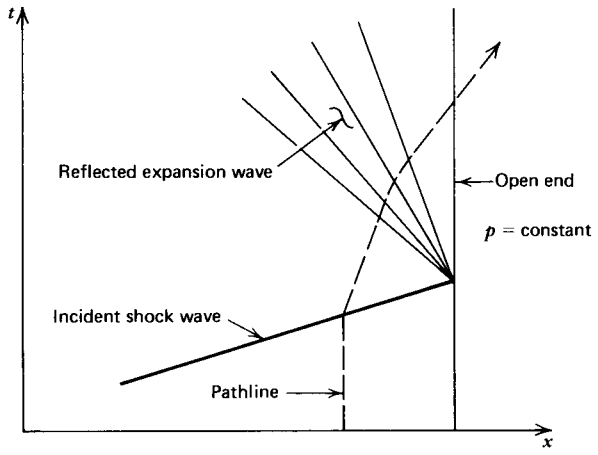

Figure 19.25 Reflection of a right-facing right-traveling shock wave from an open end.

When a shock wave impinges on the open end of a duct with inflow, the situation may become quite complex. The interaction depends on the source of the inflowing gas. Typical sources of the inflowing gas are the discharge from the exhaust manifold of an internal combustion engine, the flow into an intake pipe, and various types of combustion gas generators. In each case, a specific model which takes into account the external flow effects must be devised.

19–5(b) Contact Surfaces

In the following discussion, it is assumed that a contact surface, once formed, retains its identity throughout the flow process. It is, therefore, assumed that such transport processes as viscous mixing, diffusion, and heat conduction are negligible.

Figure 19.26 illustrates the formation of a contact surface at the point of intersection of two shock waves. The intersection of two right-facing shock waves is illustrated in Fig. 19.26*a*. At the point of intersection, the incident shock waves coalesce into a single shock wave, termed the *transmitted* shock wave, and an expansion wave is reflected back from the point of intersection into the oncoming flow. A pathline to the left of the point of intersection passes through both of the incident shock waves, while a pathline to the right of the point of intersection passes through the transmitted shock wave. The transmitted shock wave is stronger than the combined strengths of the incident shock waves. Consequently, there is a larger entropy change across the transmitted shock wave, and the pathline passing through the point of intersection becomes an interface between two regions of different entropy; that is, it becomes a *contact surface*.

Figure 19.26*b* illustrates the intersection of two shock waves facing in opposite directions. Both transmitted shock waves are weaker than the incident shock waves, and a contact surface originates at the point of intersection.

Figure 19.27*a* illustrates the interaction of a continuous expansion wave with a contact surface. The expansion wave is transmitted through the contact surface, and a reflected wave is generated. Similarly, when a compression wave intersects a contact surface, see Fig. 19.27*b*, the compression wave is transmitted through the

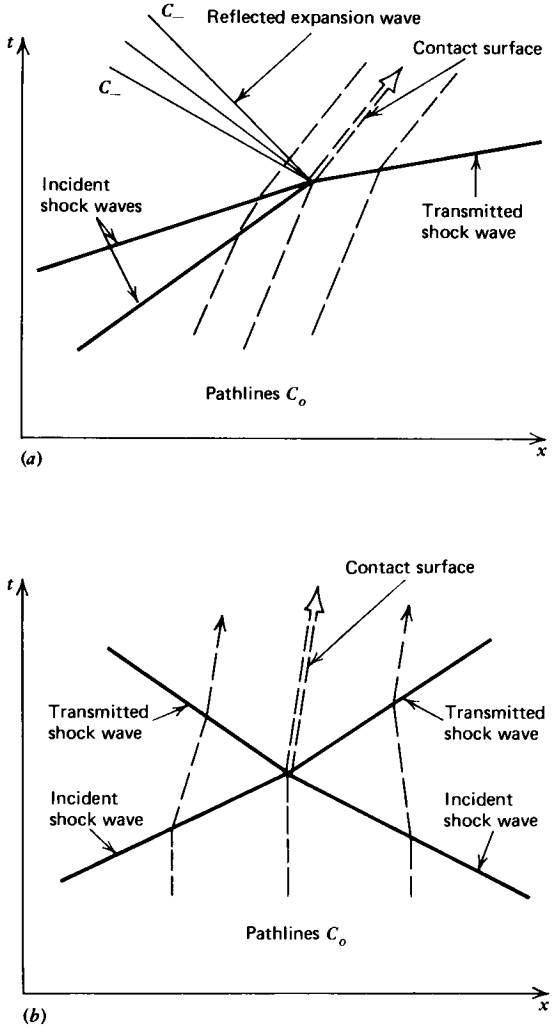

Figure 19.26 Intersection of shock waves. (*a*) Intersection of shock waves of the same family. (*b*) Intersection of shock waves of opposite families.

contact surface and a reflected wave is generated. In both of the cases illustrated in Fig. 19.27, the reflected waves are usually much weaker than the transmitted waves.

Figure 19.28 illustrates the interaction of a shock wave with a contact surface. A transmitted shock wave penetrates the contact surface, and a reflected wave is generated at the point of intersection. The reflected wave may be either a shock wave as illustrated in Fig. 19.28*a*, or an expansion wave as illustrated in Fig. 19.28*b*. The type of wave that is reflected depends on the thermodynamic and flow properties of the gas on the two sides of the contact surface ahead of the point of intersection.

19–5(c) The Shock Tube[6]

An important practical application of unsteady one-dimensional flow is the *shock tube*. Figure 19.29*a* illustrates the essential features of a shock tube, which is

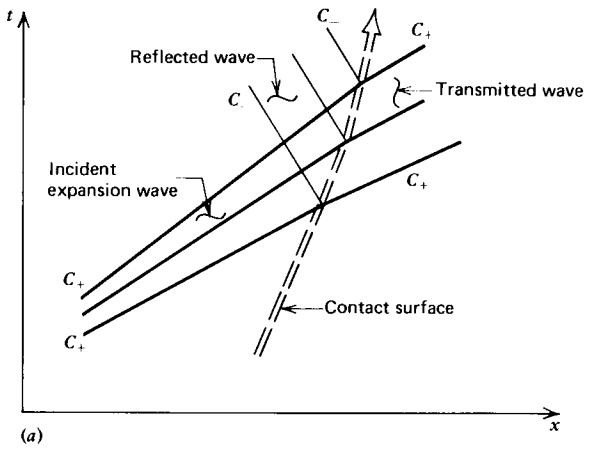

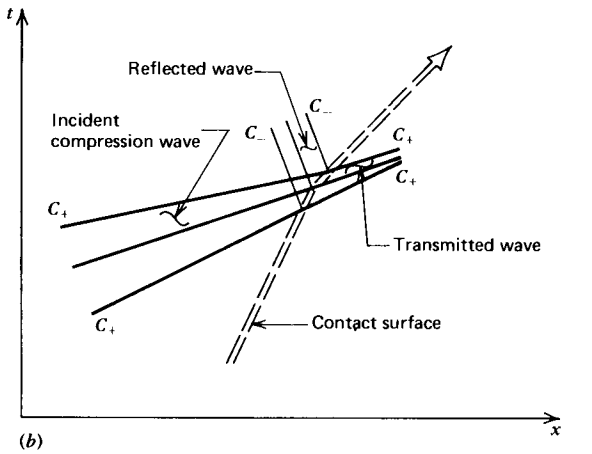

Figure 19.27 Interaction of continuous waves with a contact surface. (*a*) Expansion waves. (*b*) Compression waves.

ordinarily a long constant-area duct divided into two sections separated by a diaphragm. The section to the left of the diaphragm is filled with a high pressure gas, called the *driver gas*. The section to the right of the diaphragm is filled with a low pressure gas, called the *driven gas*. The driver gas and the driven gas may be the same gas or different gases. When the diaphragm is removed (by rupturing it), a right-facing shock wave travels into the low pressure gas and a left-facing expansion wave propagates into the high pressure gas. Figure 19.29*b* illustrates the main features of the flow inside of the shock tube at a later time t_1 after rupture of the diaphragm. Figure 19.29*c* illustrates diagrammatically the corresponding pressure distribution, and Fig. 19.29*d* illustrates the wave pattern in the *xt* plane. If both ends of the shock tube are closed, as is the case for the example presented in Fig. 19.29, reflected waves are generated at each end of the shock tube and propagate back into the tube. A *contact surface* is formed between the two gases originally separated into the high and low pressure regions by the diaphragm.

Regions 1 and 4 in the *xt* plane are stationary regions where $u=0$ and the thermodynamic properties of the fluid are constant. Region 2 behind the shock

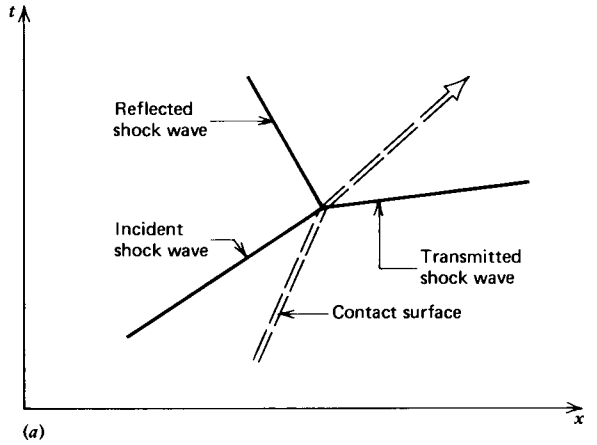

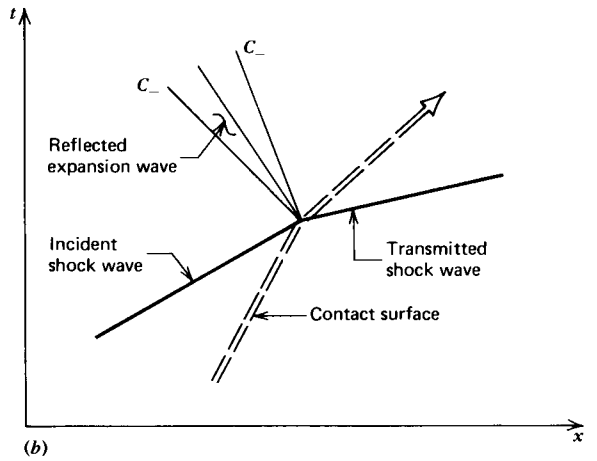

Figure 19.28 Intersection of a shock wave and a contact surface. (*a*) Reflected shock wave. (*b*) Reflected expansion wave.

wave is a uniform flow region, as is region 3 behind the contact surface. Region 5 behind the reflected shock wave is a stationary region. Point *a*, the location of the rupture of the diaphragm, is the origin of a centered expansion wave, and may be analyzed by the method presented in Section 13–4(c). Since region 4 is a uniform region, region 6 adjacent to it must be a simple wave region. Consequently, the Mach lines in the expansion fan are straight lines having constant flow properties along each Mach line. The direction and the flow properties of each Mach line are those determined at the origin of the centered expansion wave, point *a* [see Section 13–4(c)].

Where a Mach line of the expansion fan of region 6 intersects the wall as at point *b*, a reflected wave is generated, so that region 7 is a nonsimple wave region; that is, waves of both families are present in that region. Consequently, the flow field in region 7 must be determined by the general methods presented in Section 19–6. For a perfect gas, analytical expressions may be obtained[5] for the path of the first reflected expansion wave of a reflected centered expansion wave, such as line

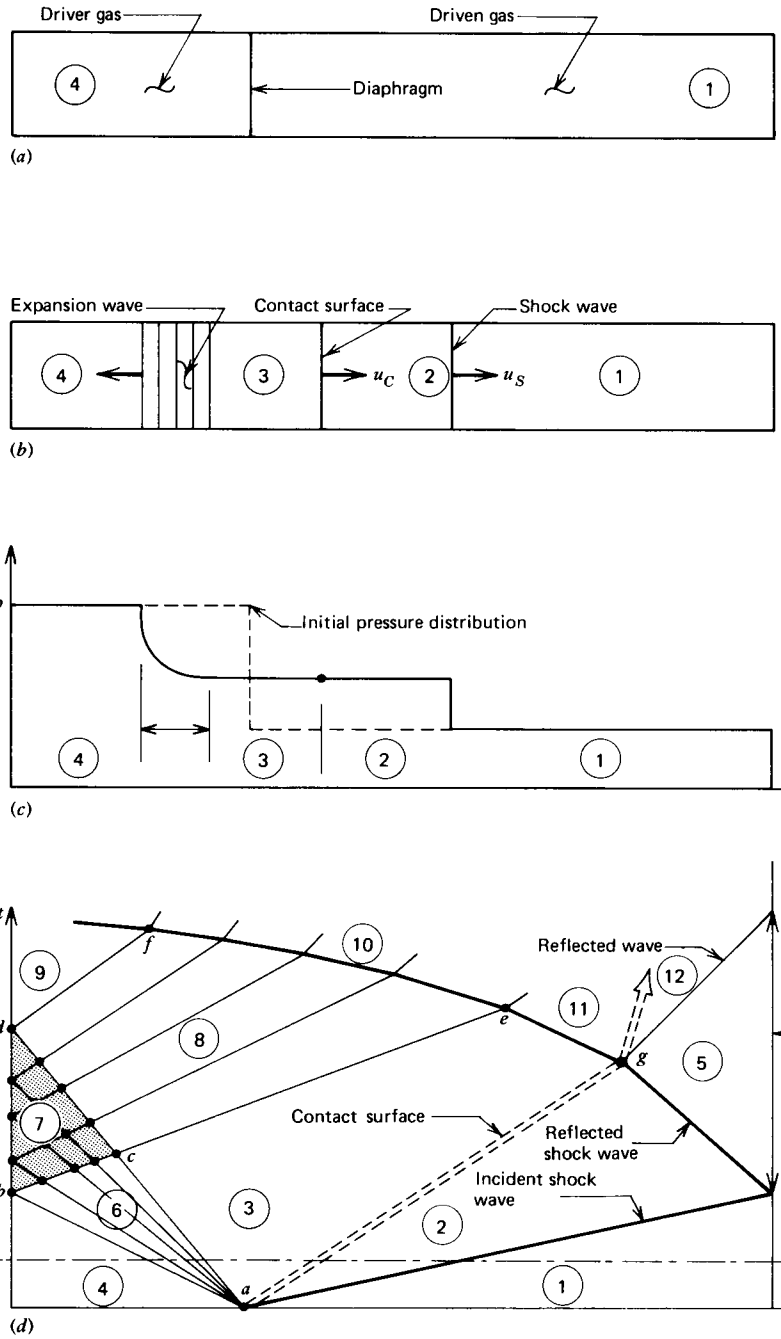

Figure 19.29 The shock tube. (*a*) Flow field before rupture of the diaphragm. (*b*) Flow field at time t_1 after rupture of the diaphragm. (*c*) Pressure distribution at time t_1. (*d*) Wave pattern in the physical plane.

bc in Fig. 19.29*d*. Region 7 is, however, an isentropic flow region, so that all of the reflected Mach lines which emerge from region 7 and cross Mach line *cd* have the same entropy. The reflected Mach line that emerges from the nonsimple wave region at point *c* is adjacent to region 3, which is a uniform flow region. Consequently, region 8 is a simple wave region. The Mach lines in region 8 are straight lines having the slope and the properties with which they emerge from region 7 along Mach line *cd*. Region 9 is accordingly, a stationary region.

When the expansion waves in region 8 interact with the shock wave *ef*, the shock wave becomes curved, and the entropy distribution in region 10 is nonuniform. Hence, the simple wave is destroyed. When the nonsimple expansion wave in region 10 interacts with the contact surface and the reflected waves at the right end of the shock tube, all remnants of simple wave flow are destroyed, and the general method of characteristics presented in this chapter must be employed for determining the resulting flow field.

Owczarek[5] presents an analysis of a simple shock tube, for a perfect gas, where it is shown that

$$\frac{p_2}{p_1} = 1 + \frac{1}{2}\left(\frac{a_4}{a_1}\right)^2\left(\frac{\gamma_1 M_3}{\psi}\right)^2\left\{\left(\frac{\gamma_1+1}{2\gamma_1}\right) + \left[\left(\frac{\gamma_1+1}{2\gamma_1}\right)^2 + 4\left(\frac{a_1}{a_4}\right)^2\left(\frac{\psi}{\gamma_1 M_3}\right)^2\right]^{1/2}\right\} \tag{19.75}$$

$$\frac{p_4}{p_1} = \left(\frac{p_2}{p_1}\right)\psi^{2\gamma_4/(\gamma_4-1)} \tag{19.76}$$

$$M_2^2 = \frac{2}{\gamma_1(\gamma_1-1)}\left(\frac{\dfrac{p_2}{p_1} + \dfrac{p_1}{p_2} - 2}{\dfrac{\gamma_1+1}{\gamma_1-1} + \dfrac{p_2}{p_1}}\right) \tag{19.77}$$

$$M_S^2 = 1 + \frac{\gamma_1+1}{2\gamma_1}\left(\frac{p_2}{p_1} - 1\right) \tag{19.78}$$

where $\psi = 1 + (\gamma_4 - 1)M_3/2$, $(a_4/a_1)^2 = (\gamma_4 R_4 t_4/\gamma_1 R_1 T_1)$, the subscripts denote the uniform flow regions identified in Fig. 19.29, and the Mach numbers are those relative to a stationary observer.

The shock tube is employed in many different types of experiments. For example, the high-pressure stationary region behind the reflected shock wave may serve as the gas source for a shock-tube-driven wind tunnel (see Fig. 7.40*d*). The available test times are quite small, usually of the order of a few milliseconds. For the shock-tube-driven wind tunnel, the maximum test time Δt is the time interval between the arrival of the initial shock wave and the arrival of the wave reflected from the intersection of the contact surface and the reflection of the incident shock wave.

The flow field in a shock tube illustrates the many complex interactions that may occur between uniform regions, simple wave regions, and nonsimple wave regions.

When uniform and simple wave regions are present in a flow field, considerable computational time and effort may be saved by identifying those regions and employing the properties of simple waves to determine the solution in those regions. The general method of characteristics, which requires considerably more computational time and effect, is then employed only in the analysis of the nonsimple wave regions. For example, in the flow field illustrated in Fig. 19.29, only region 7 and the regions above shock wave *ef* must be determined by the general method of characteristics. The interaction of the contact surface and the reflected shock wave at point *g* requires special care to ensure that the flow properties in regions 2, 3, 5, 11, and 12 are compatible.

Unsteady one-dimensional planar isentropic flow occurs frequently in engineering applications in conjunction with regions of uniform flow. Consequently, a knowledge of the special features of simple wave flow may be helpful in analyzing such situations. In the majority of engineering applications, however, the necessary requirements for producing simple wave flow are not met, and in those cases the general method of characteristics presented in this chapter must be employed.

Example 19.1. A shock tube employs air for both the driver and the driven gas. The pressure in the low-pressure side is 1 atm, that in the high pressure side is 100 atm, and the temperature in both sides is 300 K. The physical arrangement and region identification are illustrated in Fig. 19.29. Assume $\gamma = 1.40$. Calculate (a) the Mach number M_3 behind the contact surface, (b) the pressure $p_2 = p_3$ behind the shock wave, (c) the Mach number M_2 behind the shock wave, (d) the shock wave Mach number M_S, and (e) the pressure p_5 behind the reflected shock wave at the end of the tube.

Solution

The solutions for M_3 and p_2 are obtained by the simultaneous solution of equations 19.75 and 19.76. Due to the nonlinear nature of those equations, the solution must be accomplished by an iterative procedure where a value for M_3 is assumed, p_2/p_1 is determined from equation 19.75, and p_4/p_1 is calculated from equation 19.76. The procedure is repeated until the specified value of p_4/p_1 is obtained. Since the same gas is used on both sides of the diaphragm and the temperature is uniform, $a_1 = a_4$. For $\gamma = 1.40$, equations 19.75 and 19.76 become

$$\frac{p_2}{p_1} = 1 + 0.98(M_3/\psi)^2 \left\{ 0.85714 + \left[0.73469 + \frac{2.04082}{(M_3/\psi)^2} \right]^{1/2} \right\} \tag{a}$$

$$\frac{p_4}{p_1} = \frac{p_2}{p_1}\psi^7 \tag{b}$$

$$\psi = 1.0 + 0.2M_3 \tag{c}$$

Trial 1. Assume $M_3 = 2.50$. Then,

$$\psi = 1 + 0.2(2.5) = 1.50 \qquad (M_3/\psi)^2 = (2.5/1.5)^2 = 2.7778$$

$$\frac{p_2}{p_1} = 1 + 0.98(2.7778) \left\{ 0.85714 + \left[0.73469 + \frac{2.04082}{(2.7778)} \right]^{1/2} \right\} = 6.63315$$

$$\frac{p_4}{p_1} = (6.63315)(1.50)^7 = 113.33$$

Trial 2. Assume $M_3 = 2.40$.

$$\psi = 1.48 \qquad \left(\frac{M_3}{\psi}\right)^2 = 2.62966 \qquad \frac{p_2}{p_1} = 6.37646 \qquad \frac{p_4}{p_1} = 99.177$$

Trial 3. Employ the secant method to determine the next trial value of M_3 [see Appendix A–4(b)].

$$\frac{100 - 99.177}{M_3 - 2.40} = \frac{113.33 - 99.177}{2.5 - 2.4} = 141.53 \qquad M_3 = 2.4058$$

$$\psi = 1.48116 \qquad \left(\frac{M_3}{\psi}\right)^2 = 2.63824 \qquad \frac{p_2}{p_1} = 6.39134 \qquad \frac{p_4}{p_1} = 99.955$$

Trial 4.

$$\frac{100 - 99.955}{M_3 - 2.4058} = \frac{99.177 - 99.955}{2.4 - 2.4058} = 131.14 \qquad M_3 = 2.4061$$

$$\psi = 1.48123 \qquad \left(\frac{M_3}{\psi}\right)^2 = 2.63865 \qquad \frac{p_2}{p_1} = 6.39208 \qquad \frac{p_4}{p_1} = 100.000$$

(a) Thus, $M_3 = 2.4061$.

(b) $p_2 = p_1\left(\frac{p_2}{p_1}\right) = (1)(6.39208) = 6.39208$ atm

(c) From equation 19.77,

$$M_2^2 = \frac{2}{1.4(0.4)}\left[\frac{6.39208 + \dfrac{1}{6.39208} - 2}{6 + 6.39208}\right] = 1.31089 \qquad M_2 = 1.1449$$

(d) From equation 19.78,

$$M_S^2 = 1 + \frac{2.4}{2.8}(6.39208 - 1) = 5.62178 \qquad M_2 = 2.3710$$

(e) To obtain the pressure behind the reflected shock wave, refer to Fig. 19.24 and equation 19.70, where p_3 denotes the required pressure. Thus,

$$\frac{p_3}{p_2} = \frac{\left[\dfrac{3(1.4) - 1}{2.4}\right](6.39208) - \left(\dfrac{0.4}{2.4}\right)}{\left(\dfrac{0.4}{2.4}\right)(6.39208) + 1} = 4.0459$$

$$p_3 = (6.39208)(4.0459) = 25.862 \text{ atm}$$

19–6 UNIT PROCESSES

The characteristic and compatibility equations for unsteady one-dimensional and quasi-one-dimensional flow are derived in Section 19–3. The general features of unsteady continuous flow are discussed in Section 19–4, and the general features of unsteady flow with discontinuities are discussed in Section 19–5. In the present

section, numerical algorithms are developed for the general case where the unsteady flow includes area change, friction, heat transfer, and mass addition. Unit processes are developed for determining the flow properties for the following types of points.

1. A point interior to the flow field, termed an *interior point.*
2. A point on a solid boundary, termed a *solid boundary point.*
3. A point at an open end, called an *open end point.*
4. Subsonic outflow through a quasi-steady isentropic nozzle, termed a *nozzle point.*
5. A point on a shock wave, called a *shock wave point.*
6. A point on a contact surface, termed a *contact surface point.*
7. A moving projectile, termed a *projectile point.*
8. A centered expansion wave.

19–6(a) Finite Difference Grids and Overall Marching Algorithms

The governing partial differential equations for unsteady one-dimensional and quasi-one-dimensional flow are presented in Table 19.1. The corresponding characteristic and compatibility equations are presented in Table 19.2. Since the aforementioned governing equations are hyperbolic, they may be integrated by a marching type of numerical method, such as the method of characteristics discussed in Chapter 12. The application of the latter numerical method requires developing numerical algorithms that are appropriate to the problem under consideration.

It is shown in Section 19–3(d) that three characteristics pass through every point in the xt plane: the pathline C_0, and a right- and left-running Mach line, C_+ and C_-, respectively. It is useful in developing the numerical algorithms for applying the method of characteristics to employ finite difference grids constructed with the characteristic curves, substituting short lengths of straight lines to approximate the corresponding short sections of the characteristic curves. It is shown in Section 15–5 that there are two different methods for proceeding (marching) through a flow field with a numerical algorithm; the *direct marching method* and the *inverse marching method.*

The general procedure for constructing a finite difference grid employing the *direct marching method* is to locate the solution point by extending to intersection any two of the three C_o, C_+, and C_- characteristics from two known initial-data points; the latter two points having been determined by previous calculations. The third characteristic is then passed through the solution point and extended rearward to intersect some line along which the flow properties are known. Since there are three different characteristics C_o, C_+, and C_-, three different types of finite difference grids are possible, as illustrated in Fig. 19.30. In that figure, and in all such grids presented hereafter, short straight lines replace the short sections of the characteristics curves.

Figure 19.30*a* illustrates the grid based on the C_+ and C_- characteristics (Mach lines). Points 1 and 2 are initial-data points and point 4 is the solution point. The pathline C_o may be projected rearward from point 4 either to establish point 3 on the diagonal line 12, or to intersect the C_- Mach line through point 1 at point 3′.

Figures 19.30*b* and 19.30*c* illustrate the finite difference grids based on following the Mach lines of one family (called the *primary Mach lines*) and the pathlines. The solution point is point 4, and the initial-data points are points 1 and 3 in Fig.

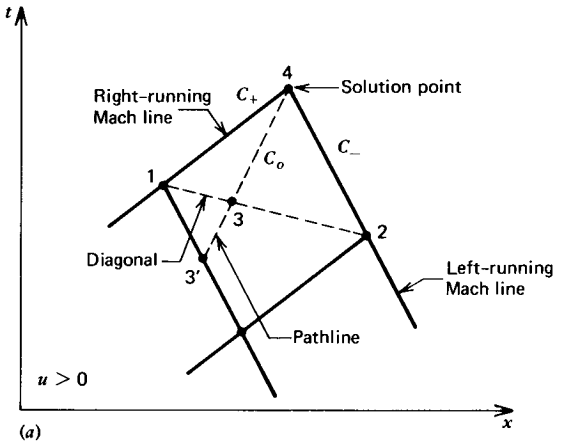

(a)

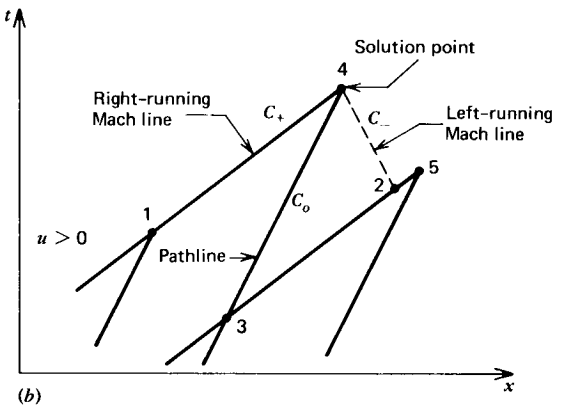

(b)

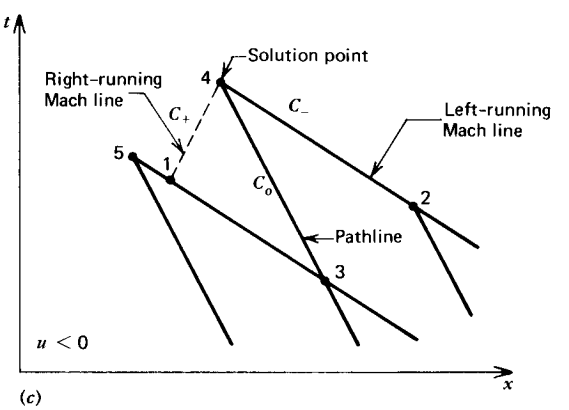

(c)

Figure 19.30 Finite difference grids for direct marching methods. (*a*) Grid based on both Mach lines. (*b*) Grid based on right-running Mach line and pathline. (*c*) Grid based on left-running Mach line and pathline.

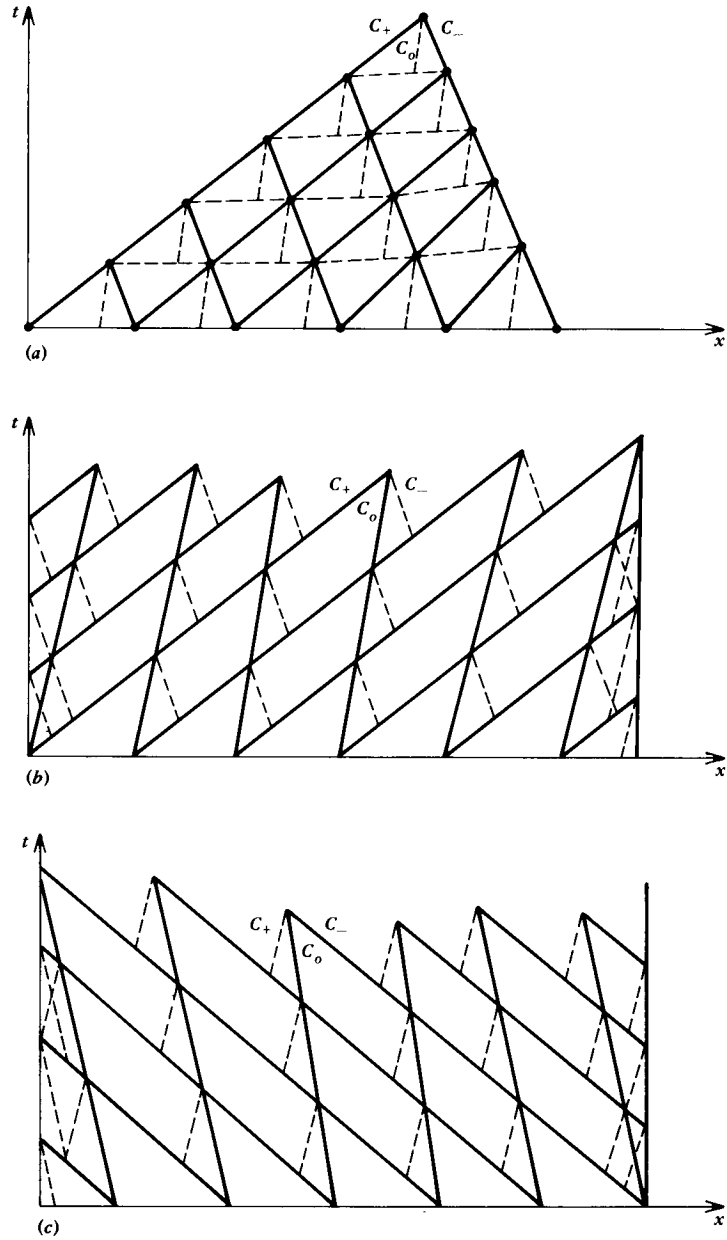

Figure 19.31 Overall marching algorithms for direct marching methods. (*a*) Based on Mach lines. (*b*) Based on right-running Mach lines and pathlines. (*c*) Based on left-running Mach lines and pathlines.

19.30*b* and points 2 and 3 in Fig. 19.30*c*. The third initial-data point (point 2 or point 1) is located by extending rearward the *secondary Mach line* from point 4 to intersect the previous primary *Mach line*.

The three grids illustrated in Fig. 19.30 require employing interpolation for determining the values of the flow properties at one of the initial-data points. The grid illustrated in Fig. 19.30*a* yields the most accurate results, because the interpolation does not involve data from points lying outside of the domain of dependence for point 4, the solution point. Figure 19.31*a* illustrates graphically an

over-all marching algorithm based on employing the grid of Fig. 19.30*a* with the direct marching method. Figures 19.31*b* and 19.31*c* are the corresponding algorithms based on the grids illustrated in Figs. 19.30*b* and 19.30*c*, respectively.

Figure 19.32 illustrates schematically the finite difference grid, in the *xt* plane, based on the *inverse marching method.*[7] In the latter method the locations of the solution points, such as point 4, are specified a priori. The three characteristics intersecting at point 4 are extended rearward to intersect a line on which are located initial-data points from previous calculations. In the study of unsteady flow, it is often advantageous to determine the flow properties at prespecified points located on lines of constant time, termed *t-lines*. In the case of an algorithm based on the finite difference grid illustrated in Fig. 19.32, the calculation of the flow properties at the initial-data points (such as points 1, 2, and 3) requires interpolation employing previous solution points (points 5, 7, and 6). The interpolation reduces the accuracy of the results obtainable by the numerical algorithm.

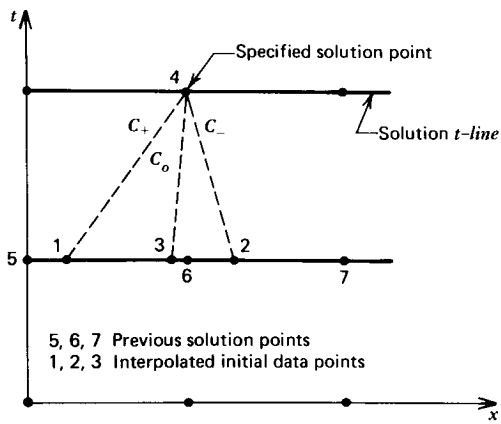

Figure 19.32 Finite difference grid for the inverse marching method.

Furthermore, to insure that the solution is stable, the Courant-Friedrichs-Lewy (CFL) stability criterion[8] must be satisfied. The criterion requires that the initial-data points (such as points 1, 2, and 3 in Fig. 19.32) fall between the previous solution points (such as points 5, 6, and 7) that are employed in the interpolation for determining the flow properties at points 1, 2, and 3. Consequently, the interpolation is based on properties outside of the domain of dependence of point 4, which further reduces the accuracy of the numerical integration. Interpolation based on the properties of points lying within or on the boundary of the domain of dependence of the solution point (see Fig. 19.30*a*) slightly decreases the accuracy of the results, but interpolation based on the properties of points lying outside of the domain of dependence of the solution point causes a smearing of the solution, which may be a more serious error. That is the price that must be paid, however, for employing the inverse marching method. Figure 19.33 illustrates the overall marching algorithm based on the grid for the inverse marching method shown in Fig. 19.32.

As discussed in Section 19–5 and illustrated in Fig. 19.14, continuous compression waves coalesce and form shock waves. The detection of the initiation of such *imbedded shock waves* is based on locating the point where characteristics of the same family intersect. It is easy to detect the point of initiation of the shock waves

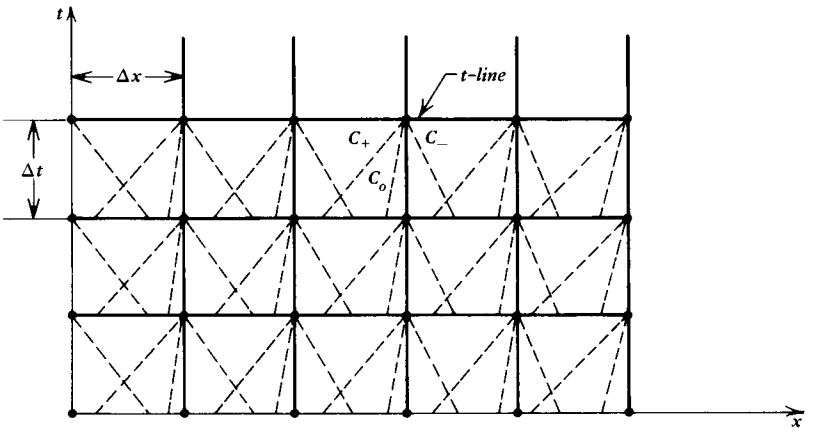

Figure 19.33 Overall marching algorithm for the inverse marching method.

of either family in the case of the overall marching algorithm illustrated in Fig. 19.31*a*. In the case of the overall marching algorithm illustrated in Fig. 19.31*b*, the initiation of a right-running shock wave may be detected easily because the solution grid is constructed with continuous right-running Mach lines. The detection of the initiation of a left-running shock wave, however, is more difficult and less accurate. That detection is based on the magnitude of the left-facing pressure gradient. Similar remarks apply to the detection of right-facing shock waves when the marching algorithm illustrated in Fig. 19.31*c* is employed. When the inverse marching method illustrated in Fig. 19.33 is employed, the detection of both right- and left-facing shock waves is difficult.

When the solution is desired on *t-lines* and it is known that shock waves of one family may appear, a *modified inverse marching method* may be employed where the solution point is located at the intersection of a *t-line* and the Mach line of the family that may coalesce into a shock wave, called the *primary Mach line*. Figures 19.34*a* and 19.34*b* illustrate schematically the corresponding grids and overall marching algorithms. In some applications it may be desirable to follow continuous pathlines as they cross *t-lines*, for example, in the case of nonequilibrium chemically reacting flows. The corresponding grid and overall marching algorithm are illustrated in Fig. 19.34*c*.

In each of the three grids illustrated in Fig. 19.34, interpolation is required at the intersection of the two rearward running characteristics with the previous *t-line*. Some smearing of the solution always results because the interpolation is based on the values of flow properties at a point outside of the domain of dependence of the solution point, as is required by the CFL stability criterion. In the case of the grids and algorithms illustrated in Figs. 19.34*a* and 19.34*b*, however, smearing is eliminated along the primary Mach line that locates the solution point. Nevertheless, smearing is introduced along the other Mach line so that the accuracy of the overall solution is degraded. Coalescence of the primary Mach lines to form a shock wave may be detected easily, but, as indicated earlier, the detection of the initiation of shock waves due to the coalescence of Mach lines of the other family is more difficult.

When the overall marching algorithm is based on following either one or both families of Mach lines, the coalescence of the Mach lines to form shock waves results in a reduction in the number of solution points. Correspondingly, there is an increase in the spacing between the solution points. If strong shock waves are

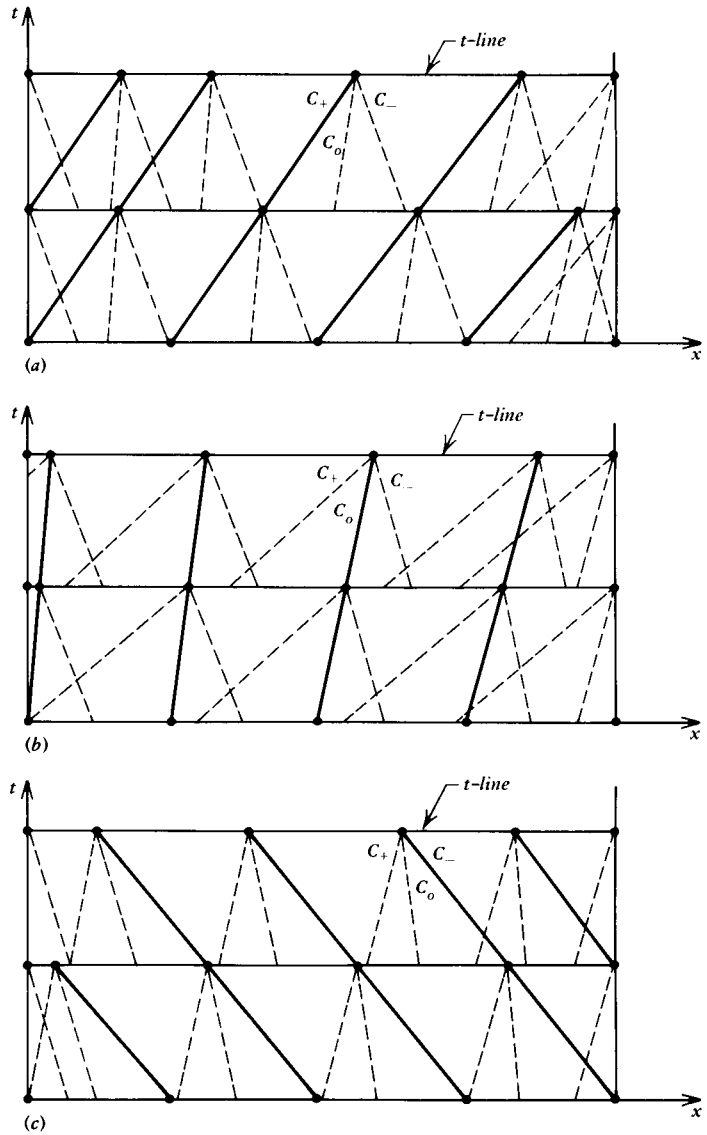

Figure 19.34 Finite difference grids and overall marching algorithms for the modified inverse marching methods. (*a*) Based on right-running Mach lines. (*b*) Based on left-running Mach lines. (*c*) Based on pathlines.

formed, the reduction in the number of solution points may be severe enough to negate the usefulness of the solution. In such a situation, new solution points must be added to the array of existing solution points by interpolation, as illustrated in Fig. 19.35. In those cases where the number of solution points exceeds what is needed so that they are more closely spaced than necessary, it is, of course, a simple matter to drop some of the points from the solution array.

The variety of finite difference grids and overall marching algorithms presented in the foregoing discussion illustrates the wide range of possibilities available for implementing a numerical integration of the partial differential equations governing unsteady one-dimensional flow. The choice of a particular finite difference grid and the corresponding overall marching algorithm depends strongly on the specific

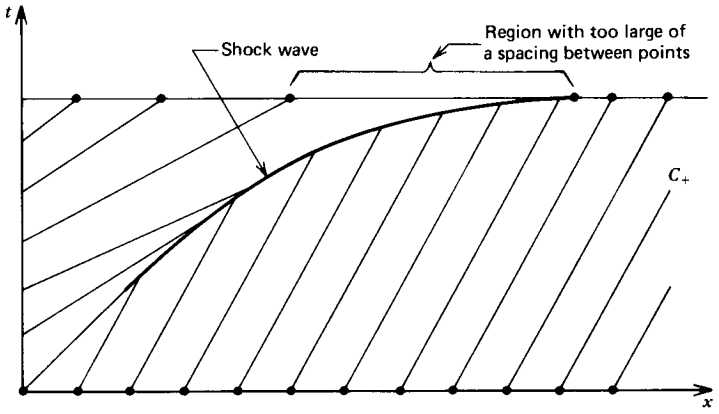

Figure 19.35 Decrease in the number of solution points due to overtaking of Mach lines by a shock wave.

flow problem being studied. Shock waves are an inherent feature of unsteady flows, and it is important that the solution method be capable of detecting them.

It should be noted that the general features of finite difference grids and overall marching algorithms discussed above also apply to the steady two-dimensional flows discussed in Chapters 12 and 16 to 18.

19–6(b) Finite Difference Equations

The numerical procedure for solving an unsteady one-dimensional flow problem is similar to that discussed in Section 17–4 for solving a steady two-dimensional supersonic rotational flow problem. As discussed in Section 19–6(a), a variety of finite difference grids and overall marching algorithms may be constructed, and the selection of a particular grid and its overall marching algorithm depends strongly on the wave pattern in the flow field under investigation. To illustrate the construction of the numerical algorithms for the unit processes listed in Section 19–6, the *inverse marching method* illustrated in Figs. 19.32 and 19.33 is employed. The latter method is the more straightforward of the two marching methods discussed, because the locations of the solution points are prespecified, usually as equally spaced points on a *t-line*. The disadvantages of the method are as follows: (1) the solution is smeared by the interpolation required for determining the flow properties at the initial-data points, and (2) the detection of the initiation of shock waves is difficult.

Figure 19.36 illustrates schematically the finite-difference grid for the unit process for determining the flow properties at an interior point. As mentioned earlier, the segments of the characteristic curves between the initial-data points and the solution point are approximated by the straight dashed lines connecting those points. Table 19.3 presents the finite difference equations corresponding to the characteristic and compatibility equations presented in Table 19.2, where the subscript o denotes the pathline and the subscripts + and − denote right- and left-running Mach lines, respectively.

The finite time step Δt is chosen so that the intersections of the rearward projected Mach lines 14 and 24 fall between the previous solution points (points 5 and 7) that are to be employed in interpolating for the values of the flow properties at the initial-data points, points 1, 2, and 3. The size of the time step Δt to the

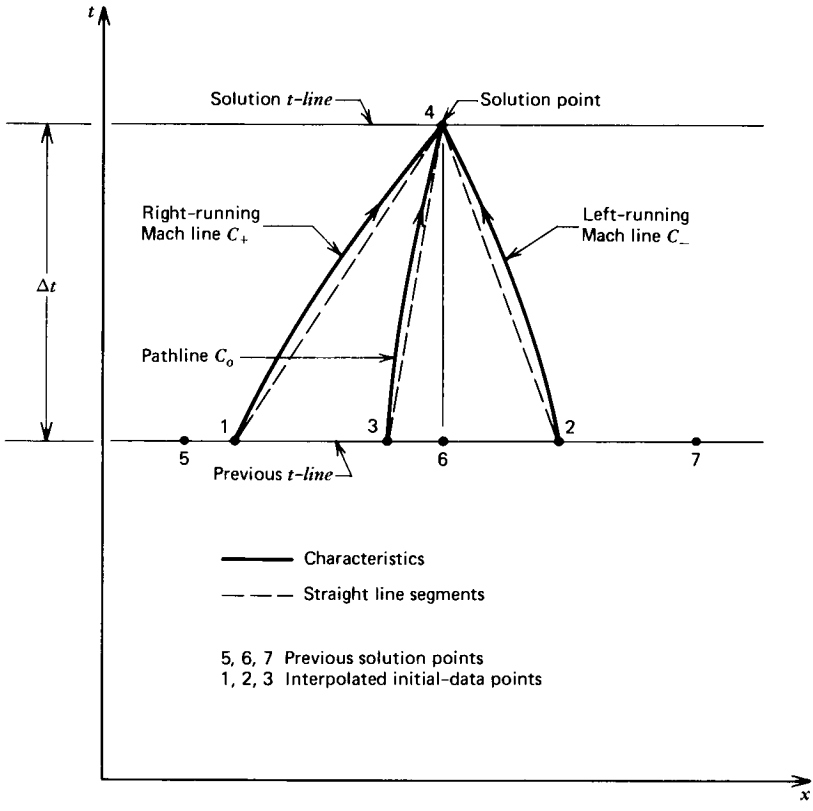

Figure 19.36 Finite difference grid for an interior point based on the inverse marching method.

Table 19.3 Finite Difference Equations for Unsteady One-Dimensional and Quasi-One-Dimensional Flow

$\Delta t_o = \lambda_o \Delta x_o$	(*pathline*)	(19.79)
$\Delta p_o - A_o \Delta \rho_o = B_o \Delta x_o$	(*along a pathline*)	(19.80)
$\Delta t_\pm = \lambda_\pm \Delta x_\pm$	(*Mach lines*)	(19.81)
$\Delta p_\pm \pm Q_\pm \Delta u_\pm = S_\pm \Delta t_\pm$	(*along Mach lines*)	(19.82)
$\lambda_o = \dfrac{1}{u_o}$, s/m (sec/ft)		(19.83)
$\lambda_\pm = \dfrac{1}{u_\pm \pm a_\pm}$, s/m (sec/ft)		(19.84)
$A = a^2$, N-m/kg (ft-lbf/lbm)		
$B = \dfrac{\psi}{u}$, N/m^3 (lbf/ft^3)		
$Q = \rho a$, N-s/m^3 (lbf-sec/ft^3)		
$S = -\dfrac{\delta \rho u a^2}{x} + a^2 \varepsilon \pm a\beta + \psi$, N/m^2-s (lbf/ft^2-sec)		
$+, -, o$ denotes C_+, C_-, or C_o characteristic curve		

solution *t-line* is chosen so that it corresponds to the smallest value of Δt for all of the solution points located on the *t-line*. From Table 19.3, equation 19.81, the time step Δt is given by

$$\Delta t_{\pm} = \lambda_{\pm} \Delta x = \frac{\Delta x}{u \pm a} \tag{19.85}$$

The $\Delta t_{\pm}$ has its minimum value when $u \pm a$ is a maximum. For an inverse marching method where Δx is constant, we obtain

$$\Delta t_{\min} = \frac{\Delta x}{(|u| + a)_{\max}} \tag{19.86}$$

The numerical algorithms for applying equations 19.79 to 19.84 of Table 19.3 are based on the *modified Euler predictor-corrector* method discussed in Section 12–5(a). In the predictor step, all of the coefficients in the finite difference equations are calculated at the known initial-data points. The corrector step employs the average values of the three primary dependent variables u, p, and ρ for each characteristic curve, and the coefficients of the finite difference equations are calculated for the aforementioned average values of the flow properties. Hence, the resulting numerical algorithms are *average property* algorithms.

19–6(c) Interior Point

Figure 19.36 illustrates schematically, in the xt plane, the finite difference grid for determining the location and properties of point 4, an interior point. The locations of the initial-data points 1, 2, and 3 are determined by writing equations 19.79 and 19.81 in finite difference form in terms of points 1, 2, 3, and 4. Thus,

$$\Delta t_o = \lambda_o (x_4 - x_3) \tag{19.87}$$

$$\Delta t_+ = \lambda_+ (x_4 - x_1) \tag{19.88}$$

$$\Delta t_- = \lambda_- (x_4 - x_2) \tag{19.89}$$

where $\Delta t = \Delta t_o = \Delta t_+ = \Delta t_-$ for the inverse marching finite difference grid. Since Δt and x_4 are known, equations 19.87 to 19.89 may be solved simultaneously for x_1, x_2, and x_3. The properties u, p, and ρ at points 1, 2, and 3 are then obtained by linear interpolation.

From Table 19.3, the slopes λ_o, λ_+, and λ_- are given by equations 19.83 and 19.84. Since they are not known, they must be determined iteratively. For the Euler *predictor*, the initial estimates for the slopes are calculated using the following approximation:

$$\lambda_o = \frac{1}{u_6} \qquad \lambda_+ = \frac{1}{u_5 + a_5} \qquad \lambda_- = \frac{1}{u_7 - a_7} \tag{19.90}$$

Equations 19.87 to 19.89 may then be solved for x_1, x_2, and x_3, and the corresponding values of u, p, and ρ at those points may be determined by linear interpolation. For example

$$u_1 = u_6 + \left(\frac{u_5 - u_6}{x_5 - x_6} \right)(x_1 - x_6) = m_u x_1 + b_u \tag{19.91}$$

where

$$m_u = \frac{u_5 - u_6}{x_5 - x_6} \tag{19.92}$$

$$b_u = u_6 - m_u x_6 \tag{19.93}$$

Similar linear interpolation formulas may be written for u_2 and u_3, and also for the corresponding values of p and ρ. Then,

$$\lambda_o = \frac{1}{u_3} \qquad \lambda_+ = \frac{1}{u_1 + a_1} \qquad \lambda_- = \frac{1}{u_2 - a_2} \tag{19.94}$$

The procedure may be repeated to obtain improved values of x_1, x_2, and x_3, and the corresponding values of u, p, and ρ. The procedure may be repeated a specified number of times, or until the values of x_1, x_2, and x_3 change by less than a specified tolerance from trial to trial.

The compatibility equation (equation 19.82, Table 19.3) which is valid along the Mach lines can be expressed in finite difference form in terms of points 1, 2, and 4. Thus,

$$p_4 + Q_+ u_4 = T_+ \tag{19.95}$$

$$p_4 - Q_- u_4 = T_- \tag{19.96}$$

where

$$T_+ = S_+ \Delta t + p_1 + Q_+ u_1 \tag{19.97}$$

$$T_- = S_- \Delta t + p_2 - Q_- u_2 \tag{19.98}$$

For the Euler *predictor*,

$$Q_+ = \rho_1 a_1 \qquad S_+ = -\frac{\delta \rho_1 u_1 a_1^2}{x_1} + a_1^2 \varepsilon_1 + a_1 \beta_1 + \psi_1 \tag{19.99}$$

$$Q_- = \rho_2 a_2 \qquad S_- = -\frac{\delta \rho_2 u_2 a_2^2}{x_2} + a_2^2 \varepsilon_2 - a_2 \beta_2 + \psi_2 \tag{19.100}$$

Equations 19.95 and 19.96 may be solved simultaneously for p_4 and u_4.

The compatibility equation (equation 19.80, Table 19.3) which is valid along pathlines, expressed in finite difference form in terms of points 3 and 4, yields

$$p_4 - A_o \rho_4 = T_o \tag{19.101}$$

where

$$T_o = B_o (x_4 - x_3) + p_3 - A_o \rho_3 \tag{19.102}$$

For the Euler *predictor*,

$$A_o = a_3^2 \qquad B_o = \frac{\psi_3}{u_3} \tag{19.103}$$

Equation 19.101 may be solved for ρ_4.

Table 19.4 Computational Equations for Unsteady One-Dimensional and Quasi-One-Dimensional Flow

$\Delta t = \lambda_o (x_4 - x_3)$	(19.104)
$\Delta t = \lambda_+ (x_4 - x_1)$	(19.105)
$\Delta t = \lambda_- (x_4 - x_2)$	(19.106)
$p_4 + Q_+ u_4 = T_+$	(19.107)
$p_4 - Q_- u_4 = T_-$	(19.108)
$p_4 - A_o \rho_4 = T_o$	(19.109)

Table 19.4 presents the computational equations for unsteady one-dimensional and quasi-one-dimensional flow.

The steps presented above may be repeated according to the Euler corrector algorithm, to furnish corrected values for the flow properties at point 4. The coefficients of the compatibility equations presented in Table 19.4 are determined by applying the Euler *corrector* algorithm employing average values of u, p, and ρ along each characteristic. Thus,

$$\lambda_o = \frac{1}{u_o} \qquad \lambda_+ = \frac{1}{u_+ + a_+} \qquad \lambda_- = \frac{1}{u_- - a_-} \tag{19.110}$$

where

$$u_o = \frac{u_3 + u_4}{2} \qquad u_+ = \frac{u_1 + u_4}{2} \qquad u_- = \frac{u_2 + u_4}{2} \tag{19.111}$$

From equation 19.8b,

$$a_+ = a(p_+, \rho_+) \qquad a_- = a(p_-, \rho_-) \tag{19.112}$$

where

$$p_+ = \frac{p_1 + p_4}{2} \qquad \rho_+ = \frac{\rho_1 + \rho_4}{2} \qquad p_- = \frac{p_2 + p_4}{2} \qquad \rho_- = \frac{\rho_2 + \rho_4}{2} \tag{19.113}$$

The coefficients Q_+, Q_-, S_+, S_-, T_+, T_-, A_o, and B_o are determined in a similar manner. The corrector may be applied only once, or iterated to achieve a specified convergence tolerance.

The only problem remaining is the determination of the speed of sound a from equation 19.8b. For a perfect gas, equation 19.8b takes the simple form

$$a^2 = \frac{\gamma p}{\rho} \tag{19.114}$$

For a real gas, the speed of sound a may be expressed as a two-dimensional tabular function of p and ρ. For equilibrium and frozen mixtures of perfect gases, the methods presented in Section 14–5 may be employed for compiling those tables.

A FORTRAN computer program, subroutine INTER, for implementing the unit process for an interior point is presented below. The terminology employed in the program is presented in Table 19.5. FORTRAN names for each variable are chosen to resemble the symbols employed in the finite difference algorithm presented in

this section. All of the control variables, the initial data, and the solution values are transmitted between the main program and the subroutine by COMMON statements.

The speed of sound a is determined from the pressure p and density ρ by calling subroutine THERMO. The specific subroutine THERMO presented below determines the speed of sound for a perfect gas.

The number of applications of the modified Euler corrector is governed by the control variables ICOR, E1, E2, E3, and E4, as discussed in Section 16–3(b) for steady two-dimensional irrotational flow.

The initial data required by subroutine INTER are the values of Δt, x_4, x_5, u_5, p_5, ρ_5, x_6, u_6, p_6, ρ_6, x_7, u_7, p_7, and ρ_7. The data may be specified in either SI or EE units. The results are the values of u_4, p_4, and ρ_4.

The interior point subroutine presented here may be combined with the subroutines presented in the following sections for other unit processes to obtain a versatile program capable of solving a variety of unsteady one-dimensional flow problems. All of the subroutines presented here are limited to planar isentropic flow (i.e., $\delta = \varepsilon = \beta = \psi = 0$). Any of the effects specified by the variables δ, ε, β, and ψ may be included in the subject subroutines by adding the appropriate quantities to the nonhomogeneous terms T_+, T_-, and T_o defined by equations 19.97, 19.98, and 19.102, respectively.

Table 19.5 Terminology for the Unsteady One-Dimensional Flow Unit Process Programs

	Control Variables
ICOR	Number of applications of the corrector desired
E1, E2, E3	Fractional convergence tolerance for u, p, and ρ, respectively
E4	Convergence tolerance for location, m (in.)
GC	g_c, 1.0 m-kg/N-s^2 in SI units, 32.174 ft-lbm/lbf-sec^2 in EE units
GL	1.0 in SI units, 144.0 in EE units
GN	1.0 in SI units, 12.0 in EE units
	Thermodynamic Properties
G	γ, specific heat ratio, dimensionless
RG	R, gas constant, J/kg-K (ft-lbf/lbm-R)
G1	γ_1, specific heat ratio on the left side of a contact surface or a projectile
G2	γ_2, specific heat ratio on the right side of a contact surface or a projectile
RG1	R_1, gas constant on the left side of a contact surface or a projectile
RG2	R_2, gas constant on the right side of a contact surface or a projectile
	Flow Field Variables
X	x, physical location, m (in.)
U	u, velocity, m/s (ft/sec)
P	p, pressure, N/m^2 (lbf/in.^{2})
R	ρ, density, kg/m^3 (lbm/-ft^3)
3, 4, 5, 6, 7, 8, 3L, 3R, 4L, and 4R	denote points in the finite difference grids for the unit processes

```
      SUBROUTINE INTER

C     SUBROUTINE INTER CALCULATES THE SOLUTION AT AN INTERIOR POINT

      REAL LP,LM,LO,MUL,MPL,MRL,MUR,MPR,MRR
      COMMON /CONTRL/ ICOR,IE,E1,E2,E3,E4,GC,GL,GN,DT,G,RG,G1,G2,RG1,RG2
      COMMON /D1/ X4,U4,P4,R4,X5,U5,P5,R5,X6,U6,P6,R6,X7,U7,P7,R7,PA,ME

C     DEFINE INITIAL PROPERTIES AND DETERMINE INTERPOLATING POLYNOMIALS

      ITER=0 $ X1S=X5 $ X2S=X7 $ X3S=X6
      U1=U5 $ P1=P5 $ R1=R5 $ U2=U7 $ P2=P7 $ R2=R7 $U3=U6 $P3=P6 $R3=R6
      DX=X5-X6 $ MUL=(U5-U6)/DX $ BUL=U6-MUL*X6 $ MPL=(P5-P6)/DX
      BPL=P6-MPL*X6 $ MRL=(R5-R6)/DX $ BRL=R6-MRL*X6
      DX=X6-X7 $ MUR=(U6-U7)/DX $ BUR=U7-MUR*X7 $ MPR=(P6-P7)/DX
      BPR=P7-MPR*X7 $ MRR=(R6-R7)/DX $ BRR=R7-MRR*X7

C     LOCATE POINT 1 AND DETERMINE COEFFICIENTS ALONG LINE 14

   10 IF (ITER.GT.0) GO TO 20 $ U4=U1 $ P4=P1 $ R4=R1
   20 U=0.5*(U1+U4) $ P=0.5*(P1+P4) $ R=0.5*(R1+R4) $CALL THERMO (P,R,A)
      LP=1.0/(U+A) $ X1=X4-DT*GN/LP $ IF(ABS(X1-X1S).LT.0.0001) GO TO 40
      X1S=X1 $ IF (X1.GT.X6) GO TO 30 $ U1=MUL*X1+BUL $ P1=MPL*X1+BPL
      R1=MRL*X1+BRL $ GO TO 10
   30 U1=MUR*X1+BUR $ P1=MPR*X1+BPR $ R1=MRR*X1+BRR $ GO TO 10
   40 QP=R*A/GC $ TP=GL*P1+QP*U1

C     LOCATE POINT 2 AND DETERMINE COEFFICIENTS ALONG LINE 24

   50 IF (ITER.GT.0) GO TO 60 $ U4=U2 $ P4=P2 $ R4=R2
   60 U=0.5*(U2+U4) $ P=0.5*(P2+P4) $ R=0.5*(R2+R4) $CALL THERMO (P,R,A)
      LM=1.0/(U-A) $ X2=X4-DT*GN/LM $ IF(ABS(X2-X2S).LT.0.0001) GO TO 80
      X2S=X2 $ IF (X2.GT.X6) GO TO 70 $ U2=MUL*X2+BUL $ P2=MPL*X2+BPL
      R2=MRL*X2+BRL $ GO TO 50
   70 U2=MUR*X2+BUR $ P2=MPR*X2+BPR $ R2=MRR*X2+BRR $ GO TO 50
   80 QM=R*A/GC $ TM=GL*P2-QM*U2

C     LOCATE POINT 3 AND DETERMINE COEFFICIENTS ALONG LINE 34

   90 IF (ITER.GT.0) GO TO 100 $ U4=U3 $ P4=P3 $ R4=R3
  100 U=0.5*(U3+U4) $ P=0.5*(P3+P4) $ R=0.5*(R3+R4) $CALL THERMO (P,R,A)
      IF (ABS(U).GT.1.0E-6) GO TO 110 $ LO=0.0 $ X3=X4 $ GO TO 120
  110 LO=1.0/U $ X3=X4-DT*GN/LO
  120 IF (ABS(X3-X3S).LT.0.0001) GO TO 140 $ X3S=X3
      IF (X3.GT.X6) GO TO 130 $ U3=MUL*X3+BUL $ P3=MPL*X3+BPL
      R3=MRL*X3+BRL $ GO TO 90
  130 U3=MUR*X3+BUR $ P3=MPR*X3+BPR $ R3=MRR*X3+BRR $ GO TO 90
  140 AO=A**2/GC $ TO=GL*P3-AO*R3

C     CALCULATE THE PROPERTIES AT POINT 4, AND TEST FOR CONVERGENCE

      U4=(TP-TM)/(QP+QM) $ P4=(TP-QP*U4)/GL $ R4=(GL*P4-TO)/AO
      IF (ITER.EQ.ICOR) RETURN $ IF (ITER.EQ.0) GO TO 150
      IF ((ABS(U4-UD).GT.E1*UD).OR.(ABS(P4-PD).GT.E2*PD)) GO TO 150
      IF (ABS(R4-RD).LT.E3*RD) RETURN
  150 ITER=ITER+1 $ UD=U4 $ PD=P4 $ RD=R4 $ GO TO 10
      END


      SUBROUTINE THERMO (P,R,A)

C     SUBROUTINE THERMO CALCULATES THE SPEED OF SOUND FOR A PERFECT GAS

      COMMON /CONTRL/ ICOR,IE,E1,E2,E3,E4,GC,GL,GN,DT,G,RG,G1,G2,RG1,RG2

      A=SQRT(GC*GL*G*P/R) $ RETURN
      END
```

Example 19.2. A small high-pressure solid propellant rocket motor experiences unsteady flow effects during the blowdown of the combustion chamber after propellant burnout. The diameter of the combustion chamber is $D = 0.0635$ m, its length is $L = 0.254$ m, and the diameter of the throat of the short converging nozzle at the end of the combustion chamber is 0.05453 m. The combustion gases may be treated as a perfect gas with $\gamma = 1.20$. At a given instant of time during the blowdown, the flow properties at three adjacent locations in the combustion chamber (points 5, 6, and 7 in Fig. 19.36) are those presented in Table 19.6. Calculate the flow properties at point 4 (see Fig. 19.36) at a time 0.016604 ms later, assuming that the flow is planar and isentropic, that is, $\delta = \varepsilon = \beta = \psi = 0$.

Table 19.6 Initial-Value Data (Example 19.2)

	Point 5	Point 6	Point 7
x, m	0.10160	0.12700	0.15240
u, m/s	188.28	235.30	282.53
$p \cdot 10^{-5}$, N/m^2	111.77	110.78	109.54
ρ, kg/m^3	14.064	13.959	13.827

Solution

(a) *Speed of sound equation.* For a perfect gas, the speed of sound is given by equation 19.114. Thus,

$$a = \left(\frac{\gamma p}{\rho}\right)^{1/2} = \left[\frac{1.20(p \text{ N/m}^2)}{(\rho \text{ kg/m}^3)}\left(\frac{\text{kg}-\text{m}}{\text{N}-\text{s}^2}\right)\right]^{1/2} = \left(\frac{1.2p}{\rho}\right)^{1/2} \text{m/s} \tag{a}$$

(b) *Interpolating polynomials.* Interpolating polynomials are required along lines 56 and 67. For u along line 56, we obtain from equations 19.91 to 19.93

$$u = m_u x + b_u = \left(\frac{u_5 - u_6}{x_5 - x_6}\right)x + (u_6 - m_u x_6)$$

$$u = \left(\frac{188.28 - 235.30}{0.10160 - 0.12700}\right)x + [235.30 - (1851.2)(0.12700)]$$

$$u = 1851.2x + 0.20 \text{ m/s} \tag{b}$$

where u is in m/s and x is in m. Similarly,

$$p = (-38.976x + 115.73)10^5 \text{ N/m}^2 \tag{c}$$

$$\rho = -4.1339x + 14.484 \text{ kg/m}^3 \tag{d}$$

Along line 67,

$$u = 1859.4x - 0.85 \text{ m/s} \tag{e}$$

$$p = (-48.819x + 116.98)10^5 \text{ N/m}^2 \tag{f}$$

$$\rho = -5.1969x + 14.619 \text{ kg/m}^3 \tag{g}$$

(c) *Locate point 1 and calculate the coefficients for the predictor.* For the first pass through the predictor, set the values of the average flow properties along the C_+ right-running Mach line 14 equal to those at point 5. Thus,

$$u_+ = 188.28 \text{ m/s} \qquad p_+ = 111.77 \cdot 10^5 \text{ N/m}^2 \qquad \rho_+ = 14.064 \text{ kg/m}^3$$

From equation (a), we obtain

$$a_+ = \left[\frac{1.2(111.77)10^5}{14.064} \right]^{1/2} = 976.56 \text{ m/s}$$

Substituting the values for u_+ and a_+ into equation 19.110, we obtain

$$\lambda_+ = \frac{1}{u_+ + a_+} = \frac{1}{188.28 + 976.56} = 0.85849 \text{ ms/m} \tag{h}$$

From equation 19.105,

$$x_1 = x_4 - \frac{\Delta t}{\lambda_+} = 0.12700 - \frac{0.016604}{0.85849} = 0.10766 \text{ m} \tag{i}$$

Since x_1 lies between x_5 and x_6, u_1, p_1, and ρ_1 may be determined from equations (b), (c), and (d), respectively. Thus,

$$u_1 = 199.50 \text{ m/s} \qquad p_1 = 111.53 \cdot 10^5 \text{ N/m}^2 \qquad \rho_1 = 14.039 \text{ kg/m}^3$$

The above procedure yields tentative values for the location and flow properties at point 1. Those values may be improved by repeating the above steps iteratively, each time employing the most recent values of u_1, p_1, and ρ_1. The results of three passes, including the first pass, are summarized in the following table.

Pass	x_1, m	u_1, m/s	p_1, N/m^2·10^5	ρ_1, kg/m^3	a_1, m/s
1	0.10766	199.50	111.53	14.039	976.40
2	0.10748	199.16	111.54	14.040	976.40
3	0.10748	199.16	111.54	14.040	976.40

Substituting the final values of u_1, p_1, and ρ_1 into equations 19.99 and 19.97 gives

$$Q_+ = \rho_+ a_+ = (14.040)(976.40) = 13{,}708 \text{ N-s/m}^3 \tag{j}$$

$$T_+ = p_1 + Q_+ u_1 = 111.54 \cdot 10^5 + (13{,}708)(199.16) = 13.885 \cdot 10^6 \text{ N/m}^2 \tag{k}$$

(d) *Locate point 2 and calculate the coefficients for the predictor.* For the first pass through the predictor, set the values of the average flow properties along line 24 equal to those at point 7. Then,

$$a_- = \left[\frac{1.2(109.54)10^5}{13.827} \right]^{1/2} = 975.02 \text{ m/s}$$

Substituting into equation 19.110 gives

$$\lambda_- = \frac{1}{u_- - a_-} = \frac{1}{282.53 - 975.02} = -1.4441 \text{ ms/m} \tag{l}$$

From equation 19.106,

$$x_2 = x_4 - \frac{\Delta t}{\lambda_-} = 0.12700 - \frac{0.016604}{-1.4441} = 0.13850 \text{ m} \tag{m}$$

Since x_2 lies between x_6 and x_7, x_2 may be substituted into equations (e), (f), and (g), to yield

$$u_2 = 256.68 \text{ m/s} \qquad p_2 = 110.22 \cdot 10^5 \text{ N/m}^2 \qquad \rho_2 = 13.899 \text{ kg/m}^3$$

Repeating the above procedure two more times, we obtain the following results.

Pass	x_2, m	u_2, m/s	p_2, N/m$^2 \cdot 10^5$	ρ_2, kg/m^3	a_2, m/s
1	0.13850	256.68	110.22	13.899	975.49
2	0.13894	257.49	110.20	13.897	975.47
3	0.13892	257.46	110.20	13.897	975.47

From equations 19.100 and 19.98, we obtain

$$Q_- = \rho_- a_- = (13.897)(975.47) = 13{,}556 \text{ N-s/m}^3$$

$$T_- = p_2 - Q_- u_2 = 110.20 \cdot 10^5 - (13{,}556)(257.46) = 7.5291 \cdot 10^6 \text{ N/m}^2$$

(e) *Locate point 3 and calculate the coefficients for the predictor.* For the first pass through the predictor, set $u_o = u_6$. Then,

$$\lambda_o = \frac{1}{u_o} = \frac{1}{235.30} = 4.2499 \text{ ms/m} \tag{n}$$

Substituting the value of λ_o into equation 19.104 gives

$$x_3 = x_4 - \frac{\Delta t}{\lambda_o} = 0.12700 - \frac{0.016604}{4.2499} = 0.12309 \text{ m} \tag{o}$$

Since x_3 lies between x_5 and x_6, u_3 may be determined from equation (b). Thus, $u_3 = 228.07$ m/s. Repeating the above procedure, we obtain

Pass	x_3, m	u_3, m/s
1	0.12309	228.07
2	0.12321	228.29
3	0.12321	228.29

Substituting the final value for x_3 into equations (c), (d), and (a), we obtain

$$p_3 = 110.93 \cdot 10^5 \text{ N/m}^2 \qquad \rho_3 = 13.975 \text{ kg/m}^3 \qquad a_3 = 975.98 \text{ m/s}$$

From equations 19.103 and 19.102,

$$A_o = a_o^2 = (975.98)^2 = 952{,}530 \text{ N-m/kg} \tag{p}$$

$$T_o = p_3 - A_o\rho_3 = 110.93 \cdot 10^5 - (0.95253 \cdot 10^6)(13.975)$$

$$= -2.2186 \cdot 10^6 \text{ N/m}^2 \tag{q}$$

f) *Determine u_4, p_4, and ρ_4 for the predictor.* The values of the coefficients determined in steps (c), (d), and (e) may be substituted into equations 19.107 to 19.109 to yield three equations for the determination of u_4, p_4, and ρ_4. Thus,

$$p_4 + 13{,}708u_4 = 13.884 \cdot 10^6 \tag{r}$$

$$p_4 - 13{,}556u_4 = 7.5291 \cdot 10^6 \tag{s}$$

$$p_4 - 952{,}530\rho_4 = -2.2186 \cdot 10^6 \tag{t}$$

Solving equations (r), (s), and (t), we obtain

$$u_4 = 233.09 \text{ m/s} \qquad p_4 = 106.89 \cdot 10^5 \text{ N/m}^2 \qquad \rho_4 = 13.551 \text{ kg/m}^3$$

The application of the Euler predictor algorithm is complete. The results obtained for the predictor are presented in column (0) in Table 19.7.

(g) *Locate point 1 and calculate the coefficients for the corrector.* For the application of the Euler corrector algorithm, average values of the flow properties along the C_+, C_-, and C_o characteristics are employed. Point 1 must be located iteratively.

Table 19.7 Values of the Solution, for Successive Trials, for the Interior Point Unit Process (Example 19.2)

	(0)	(1)	(2)	(3)
λ_+, ms/m	0.85066	0.83992	0.83984	0.83984
x_1, m	0.10748	0.10723	0.10723	0.10723
λ_-, ms/m	−1.3928	−1.3722	−1.3723	−1.3723
x_2, m	0.13892	0.13910	0.13910	0.13910
λ_o, ms/m	4.3804	4.3348	4.3334	4.3334
x_3, m	0.12321	0.12317	0.12317	0.12317
Q_+, N-s/m^3	13,708	13,447	13,447	13,447
$T_+ \cdot 10^{-6}$, N/m^2	13.884	13.827	13.827	13.827
Q_-, N-s/m^3	13,556	13,369	13,370	13,370
$T_- \cdot 10^{-6}$, N/m^2	7.5291	7.5722	7.5720	7.5720
A_o, N-m/kg	952,530	949,600	949,660	949,650
$T_o \cdot 10^{-6}$, N/m^2	−2.2186	−2.1775	−2.1783	−2.1783
u_4, m/s	233.09	233.24	233.24	233.24
$p_4 \cdot 10^{-5}$, N/m^2	106.89	106.91	106.91	106.91
ρ_4, kg/m^3	13.551	13.551	13.551	13.551

For the first iteration for the location of point 1,

$$u_+ = \frac{u_1 + u_4}{2} = \frac{199.16 + 233.09}{2} = 216.12 \text{ m/s} \tag{u}$$

$$p_+ = \frac{p_1 + p_4}{2} = \frac{(111.54 + 106.89)10^5}{2} = 109.22 \cdot 10^5 \text{ N/m}^2 \tag{v}$$

$$\rho_+ = \frac{\rho_1 + \rho_4}{2} = \frac{14.040 + 13.551}{2} = 13.795 \text{ kg/m}^3 \tag{w}$$

Substituting into equations (a), (h), and (i), we obtain values of a_+, λ_+, and x_1. Improved values for u_1, p_1, and ρ_1 may be determined from the interpolating polynomials, and the procedure may be repeated iteratively to obtain improved values for x_1. The following results are obtained.

Pass	x_1, m	u_1, m/s	p_1, N/m^2·10^5	ρ_1, kg/m^3
1	0.10723	198.70	111.55	14.041
2	0.10723	198.70	111.55	14.041

From equations (j) and (k), we obtain

$$Q_+ = 13{,}447 \text{ N-s/m}^3 \qquad T_+ = 13.827 \cdot 10^6 \text{ N/m}^2$$

(h) *Locate point 2 and calculate the coefficients for the corrector.* Employing average properties along line 24 in a manner analogous to that presented in part (g) for line 14, we obtain the following results.

Pass	x_2, m	u_2, m/s	p_2, N/m^2·10^5	ρ_2, kg/m^3
1	0.13190	257.80	110.19	13.896
2	0.13190	257.80	110.19	13.896

$$Q_- = 13{,}369 \text{ N-s/m}^3 \qquad T_- = 7.5722 \cdot 10^6 \text{ N/m}^2$$

(i) *Locate point 3 and calculate the coefficients for the corrector.* The following results are obtained along line 34.

Pass	x_3, m	u_3, m/s
1	0.12317	228.29
2	0.12317	228.29

$$A_o = 949{,}600 \text{ N-m/kg} \qquad T_o = -2.1775 \cdot 10^6 \text{ N/m}^2$$

(j) *Determine* u_4, p_4, *and* ρ_4 *for the corrector.* Substituting the values of the coefficients into equations 19.107 to 19.109, we obtain

$$p_4 + 13{,}447u_4 = 13.827 \cdot 10^6$$

$$p_4 - 13{,}369u_4 = 7.5722 \cdot 10^6$$

$$p_4 - 949{,}600\rho_4 = -2.1775 \cdot 10^6$$

Solving the above equations yields

$$u_4 = 233.24 \text{ m/s} \qquad p_4 = 106.91 \cdot 10^5 \text{ N/m}^2 \qquad \rho_4 = 13.551 \text{ kg/m}^3$$

The application of the modified Euler corrector algorithm is complete. The results are presented in column (1) of Table 19.7.

(k) *Iteration of the corrector.* The results obtained by two iterations of the corrector are presented in columns (2) and (3) of Table 19.7. From those results, it is clear that iteration of the corrector has only a very small effect on the final results.

19–6(d) Solid Boundary Point

The unit process for a solid boundary point is applicable at the closed end of a flow passage and at the surface of a moving solid object, such as either a piston or a projectile moving inside a tube. Figure 19.37*a* illustrates the case where the solid boundary is stationary and located at the left-hand side of the flow field, and Fig. 19.37*b* illustrates the case where the solid boundary is one that moves to the right.

For the stationary boundary illustrated in Fig. 19.37*a* the location x_4 of the solution point is known, and at x_4 the fluid velocity is $u_4 = 0$. For the moving boundary illustrated in Fig. 19.37*b*, x_4 and u_4 are determined by the motion of the boundary. The pathline 34 corresponds to the path of the boundary. If the motion of the boundary is prescribed, as for example a moving piston with a given velocity-time curve, then the values of x_4 and u_4 may be determined for given values of t_4. A stationary boundary is, therefore, a special case of a moving boundary for which x_4 is fixed and $u_4 = 0$. If the motion of the solid boundary depends on the properties of the flow field, as in the case of a moving projectile having an acceleration proportional to the pressure acting on its base, then the motion of the boundary and the properties of the flow field must be determined simultaneously. For either a stationary or a moving boundary the values of x_4 and u_4 are, therefore, determined by the motion of the boundary. The pressure p_4 and density ρ_4 are, however, determined from the compatibility equations (equations 19.108 and 19.109).

Points 2 and 4 are determined from the characteristic equations, equations 19.104 and 19.106, by applying the Euler predictor method as illustrated in Section 19–6(c) for an interior point. As stated earlier, u_4 is known from the prescribed motion of the boundary, and p_4 and ρ_4 are determined from the compatibility equations. The values of p_4 and ρ_4 obtained by applying the Euler predictor may be improved by applying the Euler corrector method.

A computer program, subroutine SOLID, for implementing the unit process for a solid boundary point is presented below. The terminology presented in Table 19.5 is also applicable to this subroutine. The initial data required by the program are

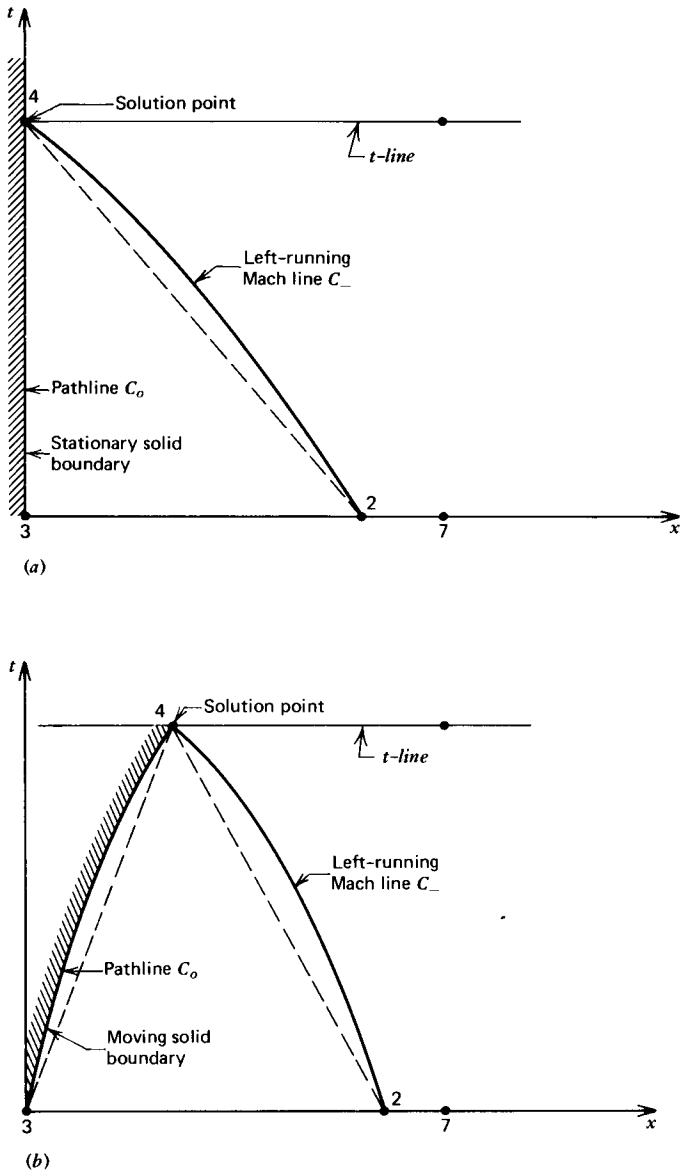

Figure 19.37 Unit process for a solid boundary point. (*a*) Stationary solid boundary. (*b*) Moving solid boundary.

Δt, x_3, u_3, p_3, ρ_3, u_4, x_7, u_7, p_7, and ρ_7. The data may be specified in either SI or EE units. The results are the values of x_4, p_4, and ρ_4. The particular form of the unit process programmed in subroutine SOLID assumes that the velocity u_4 at point 4 is specified. Thus, for a stationary boundary, $u_3 = u_4 = 0.0$. If the velocity of the solid boundary is to be determined by an interaction with the flow field, then the interaction model must be added to the initial steps in subroutine SOLID.

```
      SUBROUTINE SOLID (X3,U3,P3,R3)

C     SUBROUTINE SOLID CALCULATES THE SOLUTION AT A SOLID BOUNDARY POINT

      REAL LP,LM,LO,MUL,MPL,MRL,MUR,MPR,MRR
      COMMON /CONTRL/ ICOR,IE,E1,E2,E3,E4,GC,GL,GN,DT,G,RG,G1,G2,RG1,RG2
      COMMON /D1/ X4,U4,P4,R4,X5,U5,P5,R5,X6,U6,P6,R6,X7,U7,P7,R7,PA,ME

C     DEFINE INITIAL PROPERTIES AND DETERMINE INTERPOLATING POLYNOMIALS

      ITER=0 $ X2S=X7 $ U2=U7 $ P2=P7 $ R2=R7 $ USOLID=U4
      DX=X3-X7 $ MUR=(U3-U7)/DX $ BUR=U7-MUR*X7 $ MPR=(P3-P7)/DX
      BPR=P7-MPR*X7 $ MRR=(R3-R7)/DX $ BRR=R7-MRR*X7

C     LOCATE POINT 4

      U=0.5*(U3+U4) $ IF (ABS(U).GT.1.0E-6) GO TO 10 $ X4=X3 $ GO TO 20
   10 LO=1.0/U $ X4=X3+DT*GN/LO

C     LOCATE POINT 2 AND DETERMINE COEFFICIENTS ALONG LINE 24

   20 IF (ITER.GT.0) GO TO 30 $ U4=U2 $ P4=P2 $ R4=R2
   30 U=0.5*(U2+U4) $ P=0.5*(P2+P4) $ R=0.5*(R2+R4) $CALL THERMO (P,R,A)
      LM=1.0/(U-A) $ X2=X4-DT*GN/LM $ IF(ABS(X2-X2S).LT.0.0001) GO TO 40
      X2S=X2 $ U2=MUR*X2+BUR $ P2=MPR*X2+BPR $ R2=MRR*X2+BRR $ GO TO 20
   40 QM=R*A/GC $ TM=GL*P2-QM*U2

C     CALCULATE THE COEFFICIENTS ALONG LINE 34

      IF (ITER.GT.0) GO TO 50 $ P4=P3 $ U4=U3 $ R4=R3
   50 U=0.5*(U3+U4) $ P=0.5*(P3+P4) $ R=0.5*(R3+R4) $CALL THERMO (P,R,A)
      AO=A**2/GC $ TO=GL*P3-AO*R3

C     CALCULATE THE PROPERTIES AT POINT 4, AND TEST FOR CONVERGENCE

      U4=USOLID $ P4=(TM+QM*U4)/GL $ R4=(GL*P4-TO)/AO
      IF (ITER.EQ.ICOR) RETURN $ IF (ITER.EQ.0) GO TO 60
      IF ((ABS(P4-PD).LT.E2*PD).AND.(ABS(R4-RD).LT.E3*RD)) RETURN
   60 ITER=ITER+1 $ PD=P4 $ RD=R4 $ GO TO 20
      END
```

Example 19.3 Table 19.8 presents the flow properties at the head end and at the first point downstream from the head end at a given instant of time for the rocket motor described in Example 19.2. Employ the unit process for a solid boundary point, illustrated in Fig. 19.37*a*, and determine the flow properties at the head end at a time 0.016604 ms later.

Solution

(a) *Speed of sound equation.* From equation (a) of Example 19.2,

$$a = \left(\frac{1.20p}{\rho}\right)^{1/2} \tag{a}$$

(b) *Interpolating polynomials.* Along line 37, from equations 19.91 to 19.93,

$$m_u = \frac{u_3 - u_7}{x_3 - x_7} = \frac{0.00 - 47.16}{0.0 - 0.02540} = 1856.7$$

$$b_u = u_7 - m_u x_7 = 47.16 - (1856.7)(0.02540) = 0.00$$

Table 19.8 Initial-Value Data (Example 19.3)

	Point 3	Point 7
x, m	0.00000	0.02450
u, m/s	0.00	47.16
$p \cdot 10^{-5}$, N/m^2	113.49	113.42
ρ, kg/m^3	14.251	14.239

Hence,

$$u = m_u x + b_u = 1856.7x + 0.0 \text{ m/s} \tag{b}$$

By analogy to equation (b), we obtain

$$p = (-2.7559x + 113.49)10^5 \text{ N/m}^2 \tag{c}$$

$$\rho = -0.47244x + 14.251 \text{ kg/m}^3 \tag{d}$$

(c) *Locate point 2 and calculate the coefficients for the predictor.* For the first pass through the predictor, set the values of the average flow properties along line 24 equal to those at point 7. Then,

$$a_- = \left[\frac{1.20(113.42)10^5}{14.239} \right]^{1/2} = 977.68 \text{ m/s}$$

From Table 19.8, $u_- = u_7 = 47.16$ m/s. Substituting for u_- and a_- into equation 19.110 yields

$$\lambda_- = \frac{1}{47.16 - 977.68} = -1.0747 \text{ ms/m}$$

From equation 19.106, we obtain

$$x_2 = 0.0 - \frac{0.016604}{-1.0747} = 0.015450 \text{ m}$$

Substituting the value of x_2 into the interpolating polynomials gives

$$u_2 = 28.68 \text{ m/s} \qquad p_2 = 113.45 \cdot 10^5 \text{ N/m}^2 \qquad \rho_2 = 14.244 \text{ kg/m}^3$$

Repeating the above steps until the value of x_2 converges yields the following results.

Pass	x_2, m	u_2, m/s	$p_2 \cdot 10^{-5}$, N/m^2	ρ_2, kg/m^3	a_2, m/s
1	0.015450	28.68	113.45	14.244	977.63
2	0.015756	29.26	113.45	14.244	977.64
3	0.015747	29.26	113.45	14.244	977.64

Substituting the values from pass 3 into equations 19.100 and 19.98 gives

$$Q_- = (14.244)(977.64) = 13{,}925 \text{ N-s/m}^3$$

$$T_- = 113.45 \cdot 10^5 - (13{,}925)(29.26) = 10{,}937{,}000 \text{ N/m}^2$$

(d) *Calculate the coefficients along line 34.* For the predictor, set the average values of the flow properties along line 34 equal to those at point 3. Then,

$$a_o = a_3 = \left[\frac{1.20(113.49)10^5}{14.251} \right]^{1/2} = 977.57 \text{ m/s}$$

From equations 19.103 and 19.102,

$$A_o = (977.57)^2 = 955{,}640 \text{ J/kg}$$

$$T_o = 113.49 \cdot 10^5 - (955{,}640)(14.251) = -2{,}269{,}800 \text{ N/m}^2$$

(e) *Determine u_4, p_4, and ρ_4 for the predictor.* For a stationary wall, $u_4 = 0.0$. Substituting the values of the coefficients Q_- and T_- determined in step (c) and the values of A_o and T_o from step (d) into equations 19.108 and 19.109 (Table 19.4), we obtain

$$p_4 - 13{,}925(0.0) = 10{,}937{,}000 \tag{e}$$

$$p_4 - 955{,}640\rho_4 = -2{,}269{,}800 \tag{f}$$

Solving equations (e) and (f) gives $p_4 = 109.37 \cdot 10^5$ N/m^2 and $\rho_4 = 13.820$ kg/m^3, which completes the application of the Euler predictor algorithm. The results are presented in column (0) of Table 19.9.

(f) *Application of the corrector.* The modified Euler corrector algorithm is applied by employing average values of the flow properties along the characteristics, as illustrated in Example 19.2. The results are presented in column (1) of Table 19.9.

Table 19.9 Values of the Solution, for Successive Trials, for the Solid Boundary Unit Process (Example 19.3)

	(0)	(1)	(2)	(3)
λ_-, ms/m	−1.0544	−1.0401	−1.0402	−1.0402
x_2, m	0.015747	0.015964	0.015962	0.015962
Q_-, N-s/m^3	13,925	13,696	13,697	13,697
T_-, N/m^2	10,937,000	10,939,000	10,939,000	10,939,000
A_o, J/kg	955,640	952,700	952,760	952,760
T_o, N/m^2	−2,269,800	−2,228,000	−2,228,800	−2,228,800
u_4, m/s	0.0	0.0	0.0	0.0
$p_4 \cdot 10^{-5}$, N/m^2	109.37	109.39	109.39	109.39
ρ_4, kg/m^3	13.820	13.820	13.820	13.820

Two iterations of the corrector give the values presented in columns (2) and (3) of Table 19.9. It is apparent from Table 19.9 that iteration of the corrector has a minor effect on the final results.

19–6(e) Open End Point

The unit process for determining the flow properties at the open end of a duct is more complicated than that for the closed end. At an open end, the flow may be either an inflow or an outflow. Furthermore, the flow Mach number at the open end may be either subsonic or supersonic. The general features of wave interaction at the open end of a duct are discussed in Section 19–4. Figure 19.38 illustrates the

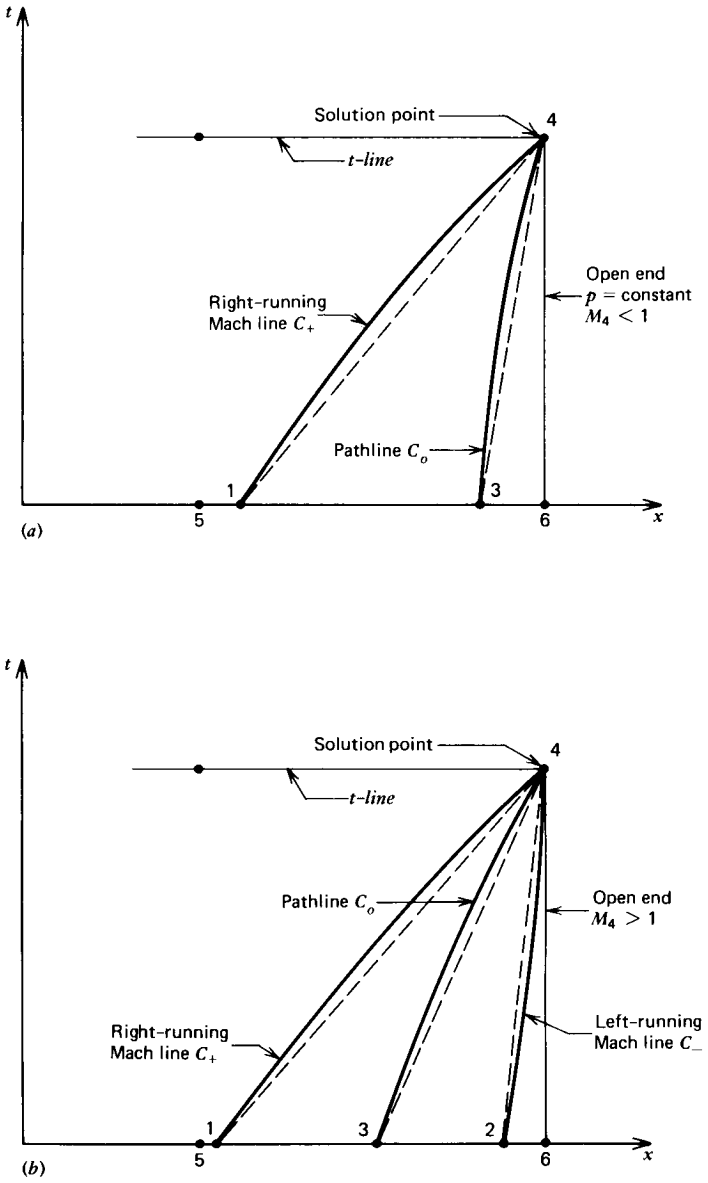

Figure 19.38 Unit process for outflow at an open end. (*a*) Subsonic outflow. (*b*) Supersonic outflow.

unit process for an open end point with outflow at the right-hand side of the internal flow field. An analogous unit process may be developed when the open end of the duct is on the left-hand side of the internal flow field.

The boundary condition at the open end is determined by the unsteady two- and three-dimensional external flow field surrounding the exit plane of the duct. As discussed in Section 13–4(d), for subsonic outflow, a reasonable approximation may be obtained by assuming that the pressure p_4 at the open end is equal to the ambient pressure. Figure 19.38*a* illustrates the unit process for an open end with subsonic outflow. The boundary condition imposed on the internal flow is that the pressure $p_4 = p_{\text{ambient}}$. When the details of the external flow field must be considered, their overall effect on the open-end boundary condition is still expressed by specifying the pressure p_4 that the *external* flow field presents to the internal flow. In that case, however, the determination of p_4 requires obtaining the solution of the unsteady two- or three-dimensional external flow field. Consequently, it may be

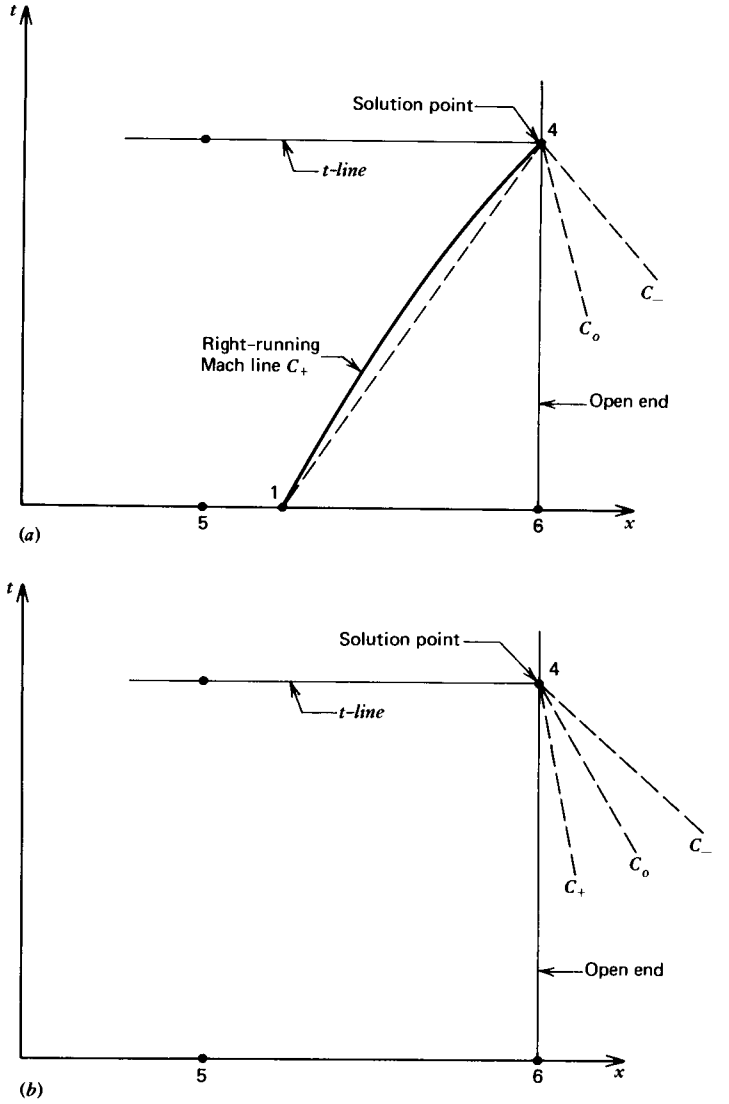

Figure 19.39 Unit process for inflow at an open end. (*a*) Subsonic inflow. (*b*) Supersonic inflow.

assumed that the boundary condition for an open end with subsonic outflow is that p_4 is known.

Figure 19.38*b* illustrates the unit process for an open end point when the outflow is supersonic. The three characteristic curves C_o, C_+, and C_- originate inside of the flow passage, so that no boundary condition is required.

For subsonic outflow (see Fig. 19.38*a*), x_4 and p_4 are specified. Points 1 and 3 are located by applying the characteristic equations (equations 19.104 and 19.105, Table 19.4), employing the Euler predictor method presented in Section 19–6(c). At point 4, u_4 and ρ_4 are determined from the corresponding compatibility equations, equations 19.107 and 19.109. Improved values for the properties at point 4 may be obtained by the repetitive application of the above procedure.

As stated earlier, for supersonic outflow at an open end, all three characteristics originate from within the internal flow field. Consequently, the flow properties at point 4 are independent of the external flow field, and the unit process for an interior point, presented in Section 19–6(c), may be employed for determining the flow properties at point 4.

Figure 19.39 illustrates the unit process for inflow at an open end point. In the case of subsonic inflow, illustrated in Fig. 19.39*a*, only a single characteristic, the right-running Mach line C_+, reaches point 4 from inside the flow passage. Consequently, two boundary conditions must be specified from the external flow field. But those boundary conditions depend on the particular type of external flow, so that no general conclusions are possible. In the case of supersonic inflow, illustrated in Fig. 19.39*b*, all three characteristics through point 4 originate in the external flow field. Consequently, the flow properties at point 4 are completely determined by the external flow field and are independent of the internal flow field.

Subroutine OPEN presented below implements the unit process for an open end with subsonic outflow where the approximation that the pressure in the exit plane is equal to the ambient pressure is employed. The terminology presented in Table 19.5 is applicable. The initial data required by the program are Δt, x_4, x_5, u_5, p_5, ρ_5, x_6, u_6, p_6, and ρ_6. The data may be specified in either SI or EE units. In addition, the control parameter IE must be set equal to zero to specify a constant-area open end. IE = 1 specifies that the open end is terminated by a quasi-steady isentropic choked nozzle having an inlet Mach number ME. The latter unit process is described in Section 19–6(f). The results are the values of u_4 and ρ_4.

```
      SUBROUTINE OPEN

C     SUBROUTINE OPEN CALCULATES THE SOLUTION AT AN OPEN END OR NOZZLE

      REAL LP,LM,LO,MUL,MPL,MRL,MUR,MPR,MRR,ME,M4,M4I
      COMMON /CONTRL/ ICOF,IE,E1,E2,E3,E4,GC,GL,GN,DT,G,RG,G1,G2,RG1,RG2
      COMMON /D1/ X4,U4,P4,R4,X5,U5,P5,R5,X6,U6,P6,R6,X7,U7,P7,R7,PA,ME

C     DEFINE INITIAL PROPERTIES AND DETERMINE INTERPOLATING POLYNOMIALS

      ITER=0 $ X1S=X5 $ X3S=X6
      U1=U5 $ P1=P5 $ R1=R5 $ U3=U6 $ P3=P6 $ R3=R6
      DX=X5-X6 $ MUL=(U5-U6)/DX $ BUL=U6-MUL*X6 $ MPL=(P5-P6)/DX
      BPL=P6-MPL*X6 $ MRL=(R5-R6)/DX $ BRL=R6-MRL*X6

C     LOCATE POINT 1 AND DETERMINE COEFFICIENTS ALONG LINE 14

   10 IF (ITER.GT.0) GO TO 20 $ U4=U1 $ P4=P1 $ R4=R1
   20 U=0.5*(U1+U4) $ P=0.5*(P1+P4) $ R=0.5*(R1+R4) $CALL THERMO (P,R,A)
```

```
      LP=1.0/(U+A) $ X1=X4-DT*GN/LP $ IF(ABS(X1-X1S).LT.0.0001) GO TO 30
      X1S=X1 $ U1=MUL*X1+BUL $ P1=MPL*X1+BPL $ R1=MRL*X1+BRL $ GO TO 10
   30 QP=R*A/GC $ TP=GL*P1+QP*U1

C     LOCATE POINT 3 AND DETERMINE COEFFICIENTS ALONG LINE 34

   40 IF (ITER.GT.0) GO TO 50 $ U4=U3 $ P4=P3 $ R4=R3
   50 U=0.5*(U3+U4) $ P=0.5*(P3+P4) $ R=0.5*(R3+R4) $CALL THERMO (P,R,A)
      LO=1.0/U $ X3=X4-DT*GN/LO $ IF (ABS(X3-X3S).LT.0.0001) GO TO 60
      X3S=X3 $ U3=MUL*X3+BUL $ P3=MPL*X3+BPL $ R3=MRL*X3+BRL $ GO TO 40
   60 AO=A**2/GC $ TO=GL*P3-AO*R3

C     CALCULATE THE PROPERTIES AT POINT 4, AND TEST FOR CONVERGENCE

      IF (IE.EQ.0) GO TO 90 $ I=1 $ IF (ITER.EQ.0) P4=P6
   70 U4=(TP-GL*P4)/QP $R4=(GL*P4-TO)/AO $CALL THERMO(P4,R4,A4)$M4=U4/A4
      IF (ABS(M4-ME).LT.0.00001) GO TO 100 $ IF (I.GT.1) GO TO 80
      I=I+1 $ P4I=P4 $ M4I=M4 $ P4=1.01*P4 $ GO TO 70
   80 SL=(M4-M4I)/(P4-P4I) $ P4I=P4 $M4I=M4 $P4=P4+(ME-M4)/SL $ GO TO 70
   90 P4=PA $ U4=(TP-GL*P4)/QP $ R4=(GL*P4-TO)/AO
  100 IF (ITER.EQ.ICOR) RETURN $ IF (ITER.EQ.0) GO TO 110
      IF ((ABS(U4-UD).LT.E1*UD).AND.(ABS(R4-RD).LT.E3*RD)) RETURN
  110 ITER=ITER+1 $ UD=U4 $ RD=R4 $ GO TO 10
      END
```

Example 19.4. Guns and rifles are devices that accelerate a projectile along a tube (having either smooth or rifled walls) by a column of high-pressure gas acting on the base of the projectile. As the projectile moves into the stagnant gas in the tube ahead of the projectile, compression waves emanating from the front of the projectile set that gas in motion toward the muzzle of the launch tube. Consider a device where the launch tube length is $L = 0.762$ m, the tube internal diameter is $D = 0.0635$ m, the projectile length is $L_P = 0.2032$ m, and the projectile mass is $m_P = 0.90718$ kg. At the muzzle exit plane, the flow leaving the tube is exposed to a pressure of 1 atm. The gas propelling the projectile may be treated as a perfect gas with $\gamma = 1.20$. Assume that the gas ahead of the projectile has the same properties as the propelling gas. At a given instant of time, the flow properties at the muzzle exit plane and the first point inside of the launch tube (see Fig. 19.38*a*) are those presented in Table 19.10. Calculate the flow properties at the muzzle exit plane at a time 0.033159 ms later, assuming that the pressure at the exit plane is equal to the ambient pressure.

Table 19.10 Initial-Value Data (Example 19.4)

	Point 5	Point 6
x, m	0.71120	0.76200
u, m/s	144.09	146.21
$p \cdot 10^{-5}$, N/m^2	1.3873	1.0135
ρ, kg/m^3	1.3835	1.0648

Solution

(a) *Speed of sound equation.* From equation (a) of Example 19.2,

$$a = \left(\frac{1.2p}{\rho}\right)^{1/2} \tag{a}$$

(b) *Interpolating polynomials.* Along line 56, employing equations 19.91 to 19.93,

$$m_u = \frac{u_5 - u_6}{x_5 - x_6} = \frac{144.09 - 146.21}{0.71120 - 0.76200} = 41.732$$

$$b_u = u_6 - m_u x_6 = 146.21 - (41.732)(0.76200) = 114.41$$

Hence,

$$u = m_u x + b_u = 41.732x + 114.41 \text{ m/s} \tag{b}$$

By analogy to equation (b) we obtain

$$p = (-7.3583x + 6.6205)10^5 \text{ N/m}^2 \tag{c}$$

$$\rho = -6.2736x + 5.8453 \text{ kg/m}^3 \tag{d}$$

(c) *Locate point 1 and calculate the coefficients for the predictor.* For the first pass through the predictor, set the values of the average flow properties along line 14 equal to those at point 5. From equation (a),

$$a_+ = \left[\frac{1.2(1.3873)10^5}{1.3835}\right]^{1/2} = 346.89 \text{ m/s}$$

Substituting into equation 19.110, we obtain

$$\lambda_+ = \frac{1}{144.09 + 346.89} = 2.0369 \text{ ms/m}$$

From equation 19.105,

$$x_1 = 0.76200 - \frac{0.033159}{2.0369} = 0.74572 \text{ m}$$

Substituting the value of x_1 into equations (b), (c), and (d), gives

$$u_1 = 145.53 \text{ m/s} \qquad p_1 = 1.1333 \cdot 10^5 \text{ N/m}^2 \qquad \rho_1 = 1.1669 \text{ kg/m}^3$$

Repeating the above procedure, we obtain the following results.

Pass	x_1, m	u_1, m/s	$p_1 \cdot 10^{-5}$, N/m^2	ρ_1, kg/m^3	a_1, m/s
1	0.74572	145.53	1.1333	1.1669	341.38
2	0.74585	145.54	1.1323	1.1661	341.35
3	0.74586	145.54	1.1323	1.1661	341.35

Substituting the final values into equations 19.99 and 19.97 yields

$$Q_+ = (1.1661)(341.35) = 398.05 \text{ N-s/m}^3$$

$$T_+ = 1.1323 \cdot 10^5 + (398.05)(145.54) = 171{,}600 \text{ N/m}^2$$

(d) *Locate point 3 and calculate the coefficients for the predictor.* For the first pass through the predictor, let $u_o = u_6$. Thus,

$$\lambda_o = \frac{1}{146.21} = 6.8395 \text{ ms/m}$$

Substituting the value of λ_o into equation 19.104 yields

$$x_3 = 0.76200 - \frac{0.033159}{6.8395} = 0.75715 \text{ m}$$

Substituting that value of x_3 into equation (b) gives $u_3 = 146.01$ m/s. Repeating the above procedure, we obtain

Pass	x_3, m	u_3, m/s
1	0.75715	146.01
2	0.75716	146.01

From equations (c), (d), and (a), we obtain

$$p_3 = 1.0492 \cdot 10^5 \text{ N/m}^2 \qquad \rho_3 = 1.0952 \text{ kg/m}^3 \qquad a_3 = 339.05 \text{ m/s}$$

From equations 19.103 and 19.102,

$$A_o = (339.05)^2 = 114{,}960 \text{ N-m/kg}$$

$$T_o = 1.0492 \cdot 10^5 - (114{,}960)(1.0952) = -20{,}983 \text{ N/m}^2$$

(e) *Determine u_4, p_4, and ρ_4 for the predictor.* At an open end with subsonic outflow, the exit plane pressure may be approximated by the ambient pressure. Thus, $p_4 = 1.0135 \cdot 10^5$ N/m^2. Substituting that value of p_4 and the values of the coefficients determined in steps (c) and (d) into equations 19.107 and 19.109, we obtain

$$1.0135 \cdot 10^5 + 398.05 u_4 = 171{,}600 \tag{e}$$

$$1.0135 \cdot 10^5 - 114{,}960 \rho_4 = -20{,}983 \tag{f}$$

Solving equations (e) and (f) gives $u_4 = 175.38$ m/s and $\rho_4 = 1.0642$ kg/m^3. This completes the application of the Euler predictor algorithm. The results are presented in column (0) of Table 19.11.

Table 19.11 Values of the Solution, for Successive Trials, for the Open End Point Unit Process (Example 19.4)

	(0)	(1)	(2)	(3)
λ_+, ms/m	2.0538	1.9989	1.9942	1.9942
x_1, m	0.74586	0.74541	0.74537	0.74537
λ_o, ms/m	6.8490	6.2234	6.1791	6.1790
x_3, m	0.75716	0.75667	0.75663	0.75663
Q_+, N-s/m^3	398.05	379.43	379.42	379.42
T_+, N/m^2	171,160	168,770	168,770	168,770
A_o, N-m/kg	114,960	114,660	114,670	114,670
T_o, N/m^2	−20,983	−20,654	−20,662	−20,662
u_4, m/s	175.38	177.69	177.69	177.69
$p_4 \cdot 10^{-5}$, N/m^2	1.0135	1.0135	1.0135	1.0135
ρ_4, kg/m^3	1.0642	1.0640	1.0640	1.0640

(f) *Application of the corrector.* For the application of the modified Euler corrector algorithm, average values of the flow properties along lines 14 and 34 are employed. The procedure is illustrated in detail in Example 19.2 for the unit process for an interior point. Column (1) in Table 19.11 presents the results for the first application of the corrector for the present problem. Columns (2) and (3) in Table 19.11 present the results obtained for two iterations of the corrector. Iteration of the corrector is seen to have an insignificant effect on the final results.

19–6(f) Subsonic Outflow Through an Isentropic Nozzle

Figure 19.40 illustrates diagrammatically the flow model for a duct having an outflow of gas through a short converging nozzle. The flow in the nozzle may be considered to be quasi-steady. If the flow is also inviscid and adiabatic, then it is isentropic. The assumption that the flow is quasi-steady, one-dimensional, and isentropic means that the instantaneous values of the stagnation properties of the gas flowing in the nozzle are equal to those at the nozzle entrance plane. Hence, the flow properties at the nozzle entrance plane e may be related to those at the nozzle throat plane t by the methods presented in Chapter 4, for both perfect and imperfect gases. The boundary conditions at the nozzle throat plane, denoted by the subscript t, are that $p_t \geqslant p_{\text{ambient}}$. If $M_t < 1.0$, then $p_t = p_{\text{ambient}}$. If $M_t = 1.0$, then $p_t = p^* \geqslant p_{\text{ambient}}$. These are the steady-state boundary conditions discussed in Section 4–3(e).

The unit process for subsonic outflow through an isentropic nozzle is, therefore, analogous to the unit process for subsonic outflow through the open end of a duct, discussed in Section 19–6(e). There is, however, the modification that p_e is determined by the quasi-steady properties of the nozzle.

There are two cases. First, if the nozzle is choked, that is, $M_t = 1.0$, then M_e and p_e may be determined from the nozzle area ratio A_e/A_t by the methods presented in Chapter 4. Second, if the nozzle is unchoked, then $p_t = p_{\text{ambient}}$, and M_t may be determined from the pressure ratio p_t/P_t, where $P_t = P_e$ for quasi-steady isentropic flow. Knowing M_t and the area ratio A_e/A_t, then M_e and p_e may be determined by the methods of Chapter 4. Hence, in either case p_e is determinable, and the unit process for an open end may be employed for determining u_e and ρ_e.

A word of caution is in order, however. The analysis discussed above neglects unsteady flow effects inside the nozzle. The latter assumption is justified if the nozzle length is extremely short when compared with the length of the duct wherein the unsteady flow effects may be important. In some application, however, unsteady flow effects within the nozzle itself may be important, and the nozzle must be analyzed by the unsteady flow methods presented in the present chapter.

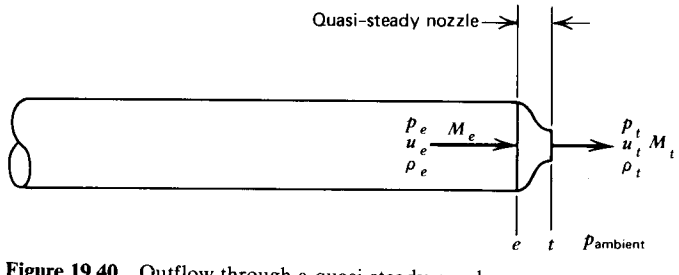

Figure 19.40 Outflow through a quasi-steady nozzle.

The numerical implementation of the unit process for a quasi-steady isentropic nozzle is accomplished in subroutine OPEN, presented in Section 19–6(e), by specifying the control parameter IE = 1. The initial data are the same as described in Section 19–6(e), with the addition of M_e, the Mach number at the nozzle entrance. The results are the values u_4, p_4, and ρ_4.

Example 19.5 The properties at the entrance to the nozzle of the rocket motor described in Example 19.2 at a given instant are presented in Table 19.12 (see Figs. 19.38*a* and 19.40). Calculate the properties of the flowing gas at the nozzle entrance at a time 0.016604 ms later. Assume that the flow through the nozzle is quasi-steady, one-dimensional, and isentropic.

Table 19.12 Initial-Value Data (Example 19.5)

	Point 5	Point 6
x, m	0.22860	0.25400
u, m/s	430.30	484.42
$p \cdot 10^{-5}$, N/m^2	103.91	101.10
ρ, kg/m^3	13.226	12.925

Solution

(a) *Nozzle entrance Mach number.* For a duct terminated by a quasi-steady isentropic nozzle, the nozzle throat pressure $p_t \geqslant p_{amb}$, and the Mach number $M_t \leqslant 1.0$. In the present problem, it is obvious that for the large value of static pressure at the entrance plane of the nozzle (i.e., $p_6 = 101.10 \cdot 10^5$ N/m^2) the nozzle is choked and $M_t = 1.0$. Consequently, the Mach number M_e at the nozzle entrance depends only on the nozzle area ratio ε. Thus,

$$\varepsilon = \frac{A_e}{A_t} = \left(\frac{D_e}{D_t}\right)^2 = \left(\frac{0.0635}{0.05453}\right)^2 = 1.3562$$

Solving equation 4.146 for $\varepsilon = 1.3562$ gives $M_e = 0.500$.

(b) *Speed of sound equation.* From equation (a) of Example 19.2,

$$a = \left(\frac{1.2p}{\rho}\right)^{1/2} \tag{a}$$

(c) *Interpolating polynomials.* Along line 56, employing equations 19.91 to 19.93,

$$m_u = \frac{u_5 - u_6}{x_5 - x_6} = \frac{430.30 - 484.42}{0.22860 - 0.25400} = 2130.7$$

$$b_u = u_6 - m_u x_6 = 484.42 - 2130.7(0.25400) = -56.780$$

Hence,

$$u = m_u x + b_u = 2130.7x - 56.780 \text{ m/s} \tag{b}$$

By analogy to equation (b), we obtain

$$p = (-110.63x + 129.20)10^5 \text{ N/m}^2 \tag{c}$$

$$\rho = -11.850x + 15.935 \text{ kg/m}^3$$

(d) *Locate point* 1 *and calculate the coefficients for the predictor.* Set the values of the average flow properties along line 14 equal to those at point 5 for the first pass through the predictor. From equation (a),

$$a_+ = \left[\frac{1.2(103.91)10^5}{13.226} \right]^{1/2} = 970.97 \text{ m/s}$$

Substituting $u_+ = u_5$ and a_+ into equation 19.110 gives

$$\lambda_+ = \frac{1}{430.30 + 970.97} = 0.71364 \text{ ms/m}$$

From equation 19.105, we obtain

$$x_1 = 0.25400 - \frac{0.016604}{0.71364} = 0.23073 \text{ m}$$

Substituting the above value of x_1 into equations (b), (c), and (d), we obtain

$$u_1 = 434.85 \text{ m/s} \qquad p_1 = 103.67 \cdot 10^5 \text{ N/m}^2 \qquad \rho_1 = 13.201 \text{ kg/m}^3$$

Repeating the above procedure, the following results are obtained.

Pass	x_1, m	u_1, m/s	$p_1 \cdot 10^{-5}$, N/m^2	ρ_1, kg/m^3	a_1, m/s
1	0.23073	434.85	103.67	13.201	970.79
2	0.23066	434.85	103.67	13.201	970.79

Substituting the final results into equations 19.99 and 19.97 gives

$$Q_+ = (13.201)(970.79) = 12{,}815 \text{ N-s/m}^3$$

$$T_+ = 103.67 \cdot 10^5 + (12{,}815)(434.85) = 15.940 \cdot 10^6 \text{ N/m}^2$$

(e) *Locate point* 3 *and calculate the coefficients for the predictor.* Let $u_o = u_6$ for the first pass through the predictor. Then,

$$\lambda_o = \frac{1}{484.42} = 2.0643 \text{ ms/m}$$

From equation 19.104, for $\lambda_o = 2.0643$ ms/m and $\Delta t = 0.016604$ ms, we obtain

$$x_3 = 0.25400 - \frac{0.016604}{2.0643} = 0.24596 \text{ m}$$

Substituting $x_3 = 0.24596$ m into equation (b) gives $u_3 = 467.28$ m/s. Repeating the above procedure iteratively, we obtain

Pass	x_3, m	u_3, m/s
1	0.24596	467.28
2	0.24624	467.89
3	0.24623	467.89

From equations (c), (d), and (a), we obtain

$$p_3 = 101.96 \cdot 10^5 \text{ N/m}^2 \quad \rho_3 = 13.017 \text{ kg/m}^3 \qquad a_3 = 969.50 \text{ m/s}$$

Substituting those values into equations 19.103 and 19.102 yields

$$A_o = (969.50)^2 = 939{,}930 \text{ N-m/kg}$$

$$T_o = 101.96 \cdot 10^5 - (939{,}930)(13.017) = -2.0392 \cdot 10^6 \text{ N/m}^2$$

(f) *Determine u_4, p_4, and ρ_4 for the predictor.* The procedure employed in the unit process for an open end, Section 19–6(e), where the value of p_4 is known, must be modified in the present case since M_4 is known instead of p_4. Due to the nonlinear nature of the relationship between M_4, u_4, p_4, and ρ_4, the solution for the flow properties at point 4 during each pass through the overall predictor-corrector algorithm must be obtained in an iterative manner.

Trial 1. Assume that $p_4 = p_6 = 101.10 \cdot 10^5$ N/m^2. Substituting the values of the coefficients into equations 19.107 and 19.109, we obtain

$$101.10 \cdot 10^5 + 12{,}815 u_4 = 15.940 \cdot 10^6 \tag{e}$$

$$101.10 \cdot 10^5 - 939{,}930 \rho_4 = -2.0392 \cdot 10^6 \tag{f}$$

Solving equations (e) and (f) yields $u_4 = 454.93$ m/s and $\rho_4 = 12.926$ kg/m^3. Substituting for p_4 and ρ_4 into equation (a) gives $a_4 = 968.80$ m/s, for which $M_4 = 0.46948$.

Trial 2. Assume that $p_4 = 1.01 p_6 = 102.11 \cdot 10^5$ N/m^2. Repeating the above procedure, we obtain $u_4 = 447.04$ m/s, $\rho_4 = 13.033$ kg/m^3, $a_4 = 969.62$ m/s, and $M_4 = 0.46105$.

Trial 3. The third trial value for p_4 is obtained by the secant method [see Appendix A–4(b)].

$$\frac{M_e^{(3)} - M_e^{(2)}}{p_4^{(3)} - p_4^{(2)}} = \frac{M_e^{(2)} - M_e^{(1)}}{p_4^{(2)} - p_4^{(1)}}$$

$$\frac{0.500 - 0.46105}{p_4 - 102.11 \cdot 10^5} = \frac{0.46105 - 0.46958}{(102.11 - 101.10)10^5} = -8.4455 \cdot 10^{-8} \tag{g}$$

Solving equation (g) gives $p_4 = 97.493 \cdot 10^5$ N/m^2. Repeating the steps presented in Trial 1 gives $u_4 = 483.08$ m/s, $\rho_4 = 12.542$ kg/m^3, $a_4 = 965.82$ m/s, and $M_4 = 0.50018$.

Trial 4. Applying the secant method again, we obtain

$$\frac{0.500 - 0.50018}{p_4 - 97.493 \cdot 10^5} = \frac{0.50018 - 0.46105}{(97.493 - 102.11)10^5} = -8.4752 \cdot 10^{-8} \tag{h}$$

Solving equation (h) yields $p_4 = 97.513 \cdot 10^5$ N/m^2. Repeating the above steps, we obtain $u_4 = 482.92$ m/s, $\rho_4 = 12.544$ kg/m^3, $a_4 = 965.84$ m/s, and $M_4 = 0.50000$, which is the desired result.

The application of the Euler predictor is complete. The results are presented in column (0) of Table 19.13.

(g) *Application of the corrector.* The modified Euler corrector algorithm is applied by employing average values of the flow properties along the characteristics, as illustrated in Example 19.2. The results are presented in column (1) of Table 19.13. Columns (2) and (3) of Table 19.13 presents the results obtained for two iterations of the corrector. The effect of iterating the corrector is quite small.

Table 19.13 Values of the Solution, for Successive Trials, for the Unit Process for a Quasi-Steady Nozzle (Example 19.5)

	(0)	(1)	(2)	(3)
λ_+, ms/m	0.71142	0.70086	0.70081	0.70081
x_1, m	0.23066	0.23031	0.23031	0.23031
λ_o, ms/m	2.1373	2.1041	2.1040	2.1040
x_3, m	0.24623	0.24611	0.24611	0.24611
Q_+, N-s/m^3	12,815	12,468	12,473	12,473
$T_+ \cdot 10^{-6}$, N/m^2	15.940	15.782	15.784	15.784
A_o, N-m/kg	939,930	936,460	936,600	936,590
$T_o \cdot 10^{-6}$, N/m^2	−2.0392	−1.9940	−1.9958	−1.9958
u_4, m/s	482.92	482.99	482.99	482.99
$p_4 \cdot 10^{-5}$, N/m^2	97.513	97.604	97.602	97.602
ρ_4, kg/m^3	12.544	12.552	12.552	12.552

19–6(g) Shock Wave Point

Figure 19.41 illustrates the unit process for determining a shock wave point on a right-facing right-traveling shock wave. A shock wave, like a contact surface, must be tracked through the flow field, and its location and properties must be determined at the points of intersection of the shock wave and the *t-lines*.

At any point on a shock wave, all of the flow properties are discontinuous, and it is advantageous to consider separately the two sides of the shock wave. In Fig. 19.41, points 3L and 4L denote the properties on the left-hand side of the shock

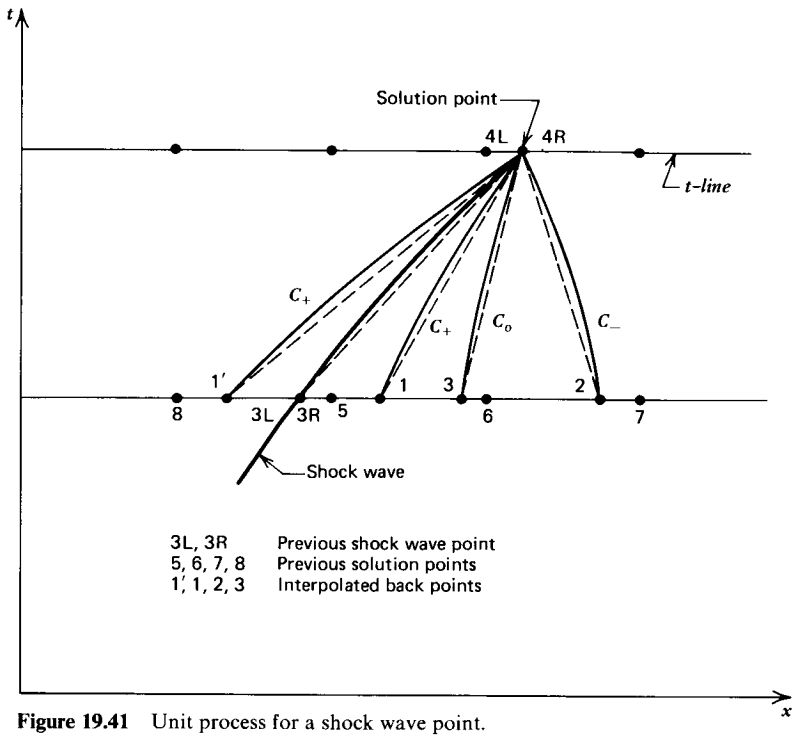

Figure 19.41 Unit process for a shock wave point.

wave, and points 3R and 4R those corresponding on the right-hand side. Accordingly, the unit process for a shock wave may be divided into two parts, as illustrated in Fig. 19.42. It is shown in Section 19–5(a) that a shock wave always overtakes continuous waves downstream from it and is always overtaken by continuous waves upstream to it (see Fig. 19.20c). Hence, the three characteristics C_o, C_+, and C_- pass through point 4R on the front side of the shock wave, but only the right-running Mach line 1′4L passes through point 4L on the back side of the shock wave. The location of point 4 is determined from the path of the shock

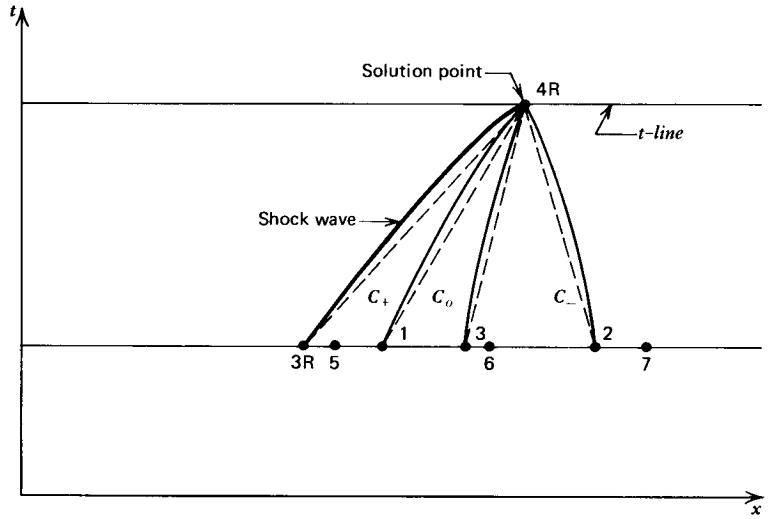

(*a*)

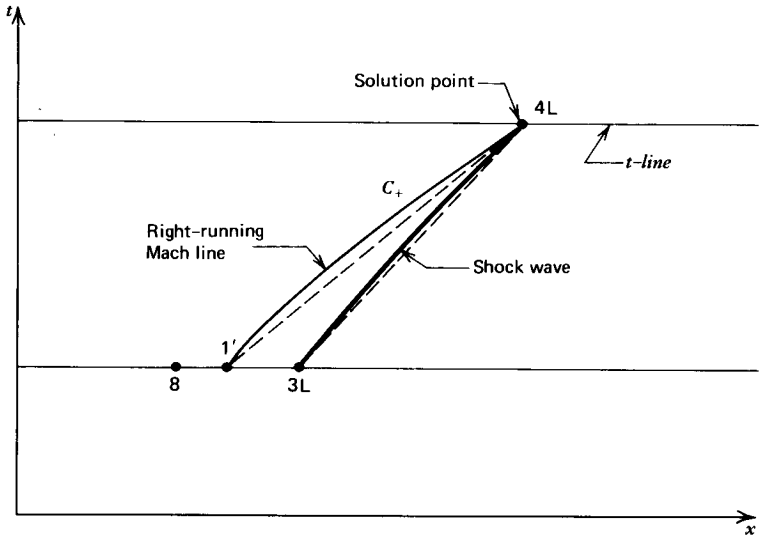

(*b*)

Figure 19.42 The shock wave unit process divided into two steps. (*a*) Right-hand side. (*b*) Left-hand side.

wave, given by

$$\left(\frac{dt}{dx}\right)_S = \lambda_S = \frac{1}{u_R + U} = \frac{1}{\left(\frac{u_{3R} + u_{4R}}{2}\right) + \left(\frac{U_3 + U_4}{2}\right)} \tag{19.115}$$

where u_R is the average velocity of the fluid on the right-hand side of the shock wave, and U is the average velocity of the shock wave relative to the fluid into which the shock wave is moving (see Fig. 19.43).

The finite change in the flow properties across a moving shock wave may be obtained by transforming the moving shock wave into a stationary frame of reference, as illustrated in Fig. 19.43, which is similar to Fig. 19.20. The resulting stationary shock wave may then be analyzed by the methods presented in Chapter 7. Alternately, a formal transformation of the governing equations for a stationary shock wave may be made to obtain a set of equations for a moving shock wave; because the latter transformation is easy to misapply, it is not employed in the present discussion.

The solution for a shock wave point requires the determination of the location of point 4 and the flow properties at points 4R and 4L. The following iterative procedure is applicable.

1. Assume the shock wave velocity U_4 and the flow velocity u_{4R} at point 4.
2. Solve equation 19.115 to locate point 4. Thus,

$$x_4 = x_3 + \frac{\Delta t}{\lambda_S} \tag{19.116}$$

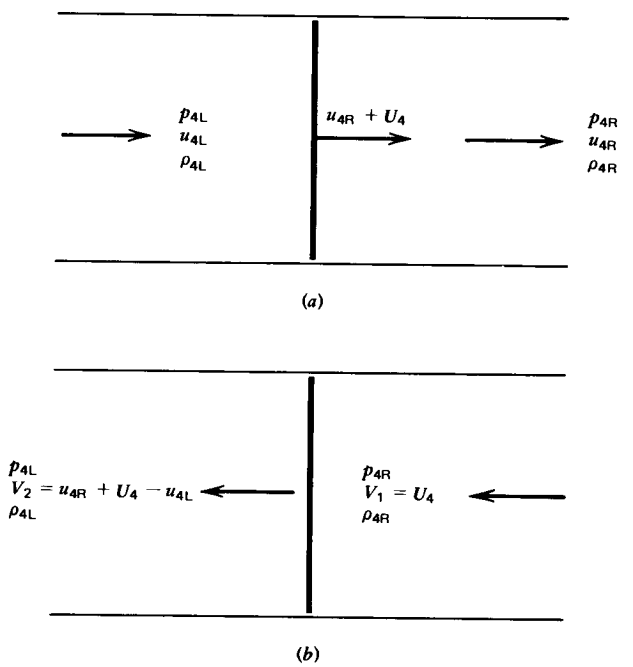

Figure 19.43 Transformation of a moving shock wave into a stationary shock wave. (*a*) Moving shock wave. (*b*) Stationary shock wave.

3. Employ the unit process for an interior point to determine the flow properties at point 4R [see Section 19–6(c)].
4. Determine the flow properties at point 4L behind the shock wave by the methods presented in Chapter 7. Identify the corresponding pressure by $p_{4L,S}$, where the subscript S denotes that p_{4L} is determined from the shock wave solution.
5. Locate point 1′ from equation 19.105, where λ_+ is based on average values of the flow properties along line 1′4L. Solve the corresponding compatibility equation (equation 19.107) for $p_{4L,RRC}$, where the subscript RRC denotes that p_{4L} is obtained along the right-running characteristic 1′4L.
6. Compare the value of $p_{4L,RRC}$ with $p_{4L,S}$. Iterate the value of the shock wave velocity U_4 until $\Delta p_{4L} = p_{4L,RRC} - p_{4L,S}$ falls within the desired convergence tolerance.

The application of the above procedure is straightforward, and the solution is generally obtained in three to five iterations. For the first iteration, U_4 may be set equal to U_3. For the second iteration, U_4 is increased slightly, say 1.0 percent, and a second value of Δp_{4L} is determined. The secant method presented in Appendix A–4(b) may then be employed to determine subsequent values of U_4.

The numerical implementation of the shock wave point unit process is accomplished in subroutine SHOCK. The initial data comprise Δt, x_3, w_3, u_{3R}, p_{3R}, ρ_{3R}, u_{3L}, p_{3L}, ρ_{3L}, x_5, u_5, p_5, ρ_5, x_6, u_6, p_6, ρ_6, x_7, u_7, p_7, ρ_7, x_8, u_8, p_8, and ρ_8, where w_3 denotes the shock wave speed U_3 at point 3. The results of the computations are x_4, w_4, u_{4R}, p_{4R}, ρ_{4R}, u_{4L}, p_{4L}, and ρ_{4L}. The determination of the property changes across the shock wave itself is performed in subroutine SHCK. The subroutine SHCK presented below is applicable to a perfect gas. The initial data, and the corresponding results, may be specified in either SI or EE units.

```
      SUBROUTINE SHOCK (X3)

C     SUBROUTINE SHOCK CALCULATES THE PROPERTIES AT A SHOCK WAVE

      REAL LP,LM,LO,MUL,MPL,MRL,MUR,MPR,MRR
      COMMON /CONTRL/ ICOR,IE,E1,E2,E3,E4,GC,GL,GN,DT,G,RG,G1,G2,RG1,RG2
      COMMON /D1/ X4,U4,P4,R4,X5,U5,P5,R5,X6,U6,P6,R6,X7,U7,P7,R7,PA,ME
      COMMON /D2/ W3,W4,X8,U8,P8,R8,X3L,U3L,P3L,R3L,X3R,U3R,P3R,R3R,X4L,
     1U4L,P4L,R4L,X4R,U4R,P4R,R4R,XP,AREA,MP

C     DEFINE INITIAL PROPERTIES AND DETERMINE INTERPOLATING POLYNOMIALS

      ITER=0 $ X1S=X8 $ U1=U8 $ P1=P8 $ R1=R8
      DX=X8-X3 $ MUL=(U8-U3L)/DX $ BUL=U3L-MUL*X3 $ MPL=(P8-P3L)/DX
      BPL=P3L-MPL*X3 $ MRL=(R8-R3L)/DX $ BRL=R3L-MRL*X3

C     LOCATE POINT 4

   10 IF (ITER.EQ.0) W4=W3 $ W=0.5*(W3+W4) $ LO=1.0/W $ X4=X3+DT*GN/LO

C     CALL INTER AND SHCK TO DETERMINE THE SOLUTION AT POINTS 4L AND 4R

      CALL INTER $ U4R=U4 $ P4R=P4 $ R4R=R4 $ CALL SHCK

C     LOCATE POINT 1 AND DETERMINE THE COEFFICIENTS ALONG LINE 14

   30 U=0.5*(U4L+U1) $P=0.5*(P4L+P1) $R=0.5*(R4L+R1) $CALL THERMO(P,R,A)
      LP=1.0/(U+A) $ X1=X4-DT*GN/LP $ IF(ABS(X1-X1S).LT.0.0001) GO TO 40
      X1S=X1 $ U1=MUL*X1+BUL $ P1=MPL*X1+BPL $ R1=MRL*X1+BRL $ GO TO 30
   40 QP=R*A/GC $ TP=GL*P1+QP*U1
```

```
C       CALCULATE P4RRC AND TEST FOR CONVERGENCE

        P4RRC=(TP-QP*U4L)/GL $ DP=P4L-P4RRC $ IF(ABS(DP).LT.E2*P4L) RETURN
        ITER=ITER+1 $ IF (ITER.GT.ICOR) RETURN $ IF (ITER.GT.1) GO TO 50
        W4I=W4 $ DPI=DP $ W4=1.01*W4 $ GO TO 10
     50 SL=(DP-DPI)/(W4-W4I) $ W4I=W4 $ DPI=DP $ W4=W4-DP/SL $ GO TO 10
        END


        SUBROUTINE SHCK

C       SUBROUTINE SHCK CALCULATES THE PROPERTIES ACROSS A SHOCK WAVE

        REAL LP,LM,LO,MUL,MPL,MRL,MUR,MPR,MRR,M1
        COMMON /CONTRL/ ICOR,IE,E1,E2,E3,E4,GC,GL,GN,DT,G,RG,G1,G2,RG1,RG2
        COMMON /D1/ X4,U4,P4,R4,X5,U5,P5,R5,X6,U6,P6,R6,X7,U7,P7,R7,PA,ME
        COMMON /D2/ W3,W4,X8,U8,P8,R8,X3L,U3L,P3L,R3L,X3R,U3R,P3R,R3R,X4L,
       1U4L,P4L,R4L,X4R,U4R,P4R,R4R,XP,AREA,MP

C       DEFINE QUASI-STEADY SHOCK WAVE PROPERTIES

        V1=W4 $ CALL THERMO (P4R,R4R,A1) $ M1=V1/A1

C       CALCULATE PROPERTY RATIOS ACROSS SHOCK WAVE FOR A PERFECT GAS

        V2V1=(2.0+(G-1.0)*M1**2)/((G+1.0)*M1**2) $ R2R1=1.0/V2V1
        P2P1=2.0*G*M1**2/(G+1.0)-(G-1.0)/(G+1.0)

C       CALCULATE PROPERTIES BEHIND QUASI-STEADY SHOCK WAVE

        V2=V2V1*V1 $ P4L=P2P1*P4R $ R4L=R2R1*R4R $ U4L=W4+U4R-V2 $ RETURN
        END
```

Example 19.6. A shock wave is propagating through a nonuniform region in a constant-area duct. The flow properties at a given instant corresponding to the points denoted in Fig. 19.41 are given in Table 19.14. Assume that the fluid is a perfect gas having $\gamma = 1.40$ and calculate the location and flow properties on both sides of the shock wave at a time 0.050 ms later. In the present example, point 5 is coincident with point 3R. The initial shock wave velocity is $U_3 = 815.61$ m/s.

Table 19.14 Initial-Value Data (Example 19.6)

	Point 8	Point 3L	Points 3R and 5	Point 6	Point 7
x, m	0.15240	0.20828	0.20828	0.25400	0.30480
u, m/s	592.44	559.00	0.00	25.67	53.91
$p \cdot 10^{-5}$, N/m^2	7.1402	6.4910	1.0135	0.91217	0.81082
ρ, kg/m^3	4.0874	3.8185	1.2014	1.1143	1.0244

Solution

(a) *Speed of sound equation.* From equation 19.114,

$$a = \left(\frac{1.4p}{\rho} \right)^{1/2} \tag{a}$$

(b) *Interpolating polynomials.* The flow properties at point 4R located on the right-hand side of the shock wave are obtained by the unit process for an interior point [see Section 19–6(c)]. Those calculations are not presented in this example, so

the corresponding interpolating polynomials are not presented. Along line 8–3L of Fig. 19.41, we obtain from equations 19.91 to 19.93,

$$m_u = \frac{u_8 - u_{3L}}{x_8 - x_{3L}} = \frac{592.44 - 559.00}{0.15240 - 0.20828} = -598.43$$

$$b_u = u_{3L} - m_u x_{3L} = 559.00 - (-598.43)(0.20828) = 683.64$$

Hence,

$$u = m_u x + b_u = -598.43x + 683.64 \text{ m/s} \tag{b}$$

In a similar manner, we obtain

$$p = (-11.618x + 8.9107)10^5 \text{ N/m}^2 \tag{c}$$

$$\rho = -4.8121x + 4.8208 \text{ kg/m}^3 \tag{d}$$

(c) *Determine the location of point* 4 *for the predictor.* For the predictor, assume that $u_{4R} = u_{3R} = u_R$ and $U_4 = U_3 = U$. Then, from equation 19.115, we obtain

$$\lambda_S = \frac{1}{u_R + U} = \frac{1}{0.0 + 815.61} = 1.2261 \text{ ms/m} \tag{e}$$

Substituting that value of λ_S into equation 19.116 gives

$$x_4 = x_3 + \frac{\Delta t}{\lambda_S} = 0.20828 + \frac{0.050}{1.2261} = 0.24906 \text{ m} \tag{f}$$

(d) *Determine the solution at point* 4R. As pointed out under (b), the solution at point 4R is determined by the unit process for an interior point [see Section 19–6(c)]. The location x_4 is known, and the location and flow properties at points 5, 6, and 7 are specified. The results are $u_{4R} = 31.48$ m/s, $p_{4R} = 0.89151 \cdot 10^5$ N/m^2, and $\rho_{4R} = 1.0961$ kg/m^3.

(e) *Determine the flow properties at point* 4L. The flow properties at point 4L behind the moving normal shock wave are determined by transforming the moving shock wave into a stationary shock wave, as illustrated in Fig. 19.43. For the stationary shock wave, V_1 and V_2 denote the velocities in front of and behind the shock wave, respectively, relative to the shock wave. From Fig. 19.43*b*,

$$V_1 = U_4 \tag{g}$$

$$u_{4L} = u_{4R} + U_4 - V_2 \tag{h}$$

where V_2 is found by the methods presented in Section 7–4 or 7–5. From equation (a),

$$a_1 = a_{4R} = \left(\frac{1.4p_{4R}}{\rho_{4R}}\right)^{1/2} = \left[\frac{1.4(0.89151)10^5}{1.0961}\right]^{1/2} = 337.45 \text{ m/s}$$

The Mach number M_1 ahead of the shock wave is

$$M_1 = \frac{V_1}{a_1} = \frac{U_4}{a_1} = \frac{815.61}{337.45} = 2.4170 \tag{i}$$

Substituting $M_1 = 2.4170$ into equations 7.49 and 7.50 (see Table 7.1), we obtain

$$\frac{p_{4L}}{p_{4R}} = \frac{2\gamma}{\gamma+1}M_1^2 - \frac{\gamma-1}{\gamma+1} = \frac{2(1.4)}{2.4}M_1^2 - \frac{0.4}{2.4} = 1.16667M_1^2 - 0.16667 \qquad \text{(j)}$$

$$\frac{p_{4L}}{p_{4R}} = 1.16667(2.4170)^2 - 0.16667 = 6.6488$$

$$p_{4L} = (6.6488)(0.89151)10^5 = 5.9275 \cdot 10^5 \text{ N/m}^2$$

$$\frac{\rho_{4L}}{\rho_{4R}} = \frac{V_1}{V_2} = \frac{(\gamma+1)M_1^2}{2+(\gamma-1)M_1^2} = \frac{2.4M_1^2}{2+0.4M_1^2} = \frac{2.4(2.4170)^2}{2+(0.4)(2.4170)^2} = 3.2329 \qquad \text{(k)}$$

$$\rho_{4L} = (3.2329)(1.0961) = 3.5435 \text{ kg/m}^3$$

$$V_2 = \frac{V_1}{3.2329} = \frac{815.61}{3.2329} = 252.28 \text{ m/s}$$

From equation (h),

$$u_{4L} = 31.48 + 815.61 - 252.28 = 594.81 \text{ m/s}$$

(f) *Locate point 1′ and calculate* $p_{4L,RRC}$*. Refer to Fig. 19.42b. Point 1′ is located at the intersection of the rearward running C_+ Mach line through point 4 and the previous *t-line*. The flow properties at point 4L are known. The flow properties at point 1′, however, must be determined by trial and error. For the first trial, set the values of the flow properties at point 1′ equal to those at point 8. Then,

$$u_+ = \frac{u_{1'} + u_{4L}}{2} = \frac{592.44 + 594.81}{2} = 593.63 \text{ m/s} \qquad \text{(l)}$$

$$p_+ = \frac{(7.1402 + 5.9275)10^5}{2} = 6.5338 \cdot 10^5 \text{ N/m}^2$$

$$\rho_+ = \frac{4.0874 + 3.5435}{2} = 3.8155 \text{ kg/m}^3$$

$$a_+ = \left[\frac{1.4(6.5338)10^5}{3.8155}\right]^{1/2} = 489.64 \text{ m/s}$$

$$\lambda_+ = \frac{1}{u_+ + a_+} = \frac{1}{593.63 + 489.64} = 0.92314 \text{ ms/m} \qquad \text{(m)}$$

$$x_{1'} = x_4 - \frac{\Delta t}{\lambda_+} = 0.24906 - \frac{0.050}{0.92314} = 0.19490 \text{ m} \qquad \text{(n)}$$

From equations (b), (c), and (d), we obtain

$$u_{1'} = 56.70 \text{ m/s} \qquad p_{1'} = 6.6465 \cdot 10^5 \text{ N/m}^2 \qquad \rho_{1'} = 3.8829 \text{ kg/m}^3$$

The following results are obtained by repeating the above procedure.

*$p_{4L,RRC}$ is the value of p_{4L} determined by the right-running Mach line C_+ through point 4L, and $p_{4L,S}$ is the value determined from the shock wave in part (e). When the solution converges, $p_{4L,S} = p_{4L,RRC}$.

Pass	$x_{1'}$, m	$u_{1'}$, m/s	$p_{1'} \cdot 10^{-5}$, N/m^2	$\rho_{1'}$, kg/m^3
1	0.19490	567.01	6.6465	3.8829
2	0.19567	566.55	6.6375	3.8792
3	0.19569	566.55	6.6375	3.8792

The average values of p, ρ, and a along line 1′–4L are

$$p_+ = 6.2825 \cdot 10^5 \text{ N/m}^2 \qquad \rho_+ = 3.7113 \text{ kg/m}^3 \qquad a_+ = 486.81 \text{ m/s}$$

From equations 19.99 and 19.97, we obtain

$$Q_+ = (3.7113)(486.81) = 1806.7 \text{ N-s/m}$$

$$T_+ = 6.6375 \cdot 10^5 + (1806.7)(566.55) = 1.6873 \cdot 10^6 \text{ N/m}^2$$

Substituting the value of $u_{4L} = 594.81$ m/s and the values of Q_+ and T_+ into equation 19.107, we obtain

$$p_{4L,RRC} + (1806.7)(594.81) = 1.6873 \cdot 10^6 \tag{o}$$

Solving equation (o) yields $p_{4L,RRC} = 6.1268 \cdot 10^5$ N/m^2. Then,

$$\Delta p_{4L} = p_{4L,RRC} - p_{4L,S} = (6.1268 - 5.9275)10^5 = 19{,}933 \text{ N/m}^2 \tag{p}$$

The foregoing procedure completes the first pass through the algorithm. The results are presented in column (1) of Table 19.15.

(g) *Relaxation of U_4 to drive Δp_{4L} toward zero.* Steps (c) through (f) must be repeated for different values of U_4 until Δp_{4L} falls within the desired closeness to zero. The second trial value for U_4 is arbitrarily specified as $U_4 = 1.01\ U_4$. Subsequent trial values for U_4 may be obtained by the secant method [see Appendix A–4(b)]. Thus, for the second trial,

$$U_4 = 1.01(815.61) = 823.77 \text{ m/s}$$

Repeating step (c), we obtain $x_4 = 0.24926$ m. From the unit process for an interior point, $u_{4R} = 31.59$ m/s, $p_{4R} = 0.89111 \cdot 10^5$ N/m^2, and $\rho_{4R} = 1.0957$ kg/m^3. Repeating step (e), we obtain $u_{4L} = 602.88$ m/s, $p_{4L} = 6.0477 \cdot 10^5$ N/m^2, and $\rho_{4L} = 3.5751$ kg/m^3. Performing the calculations presented in step (f), we obtain $p_{4L,RRC} = 5.9764 \cdot 10^5$ N/m^2 and $\Delta p_{4L} = -7128$ N/m^2. The results of the second trial are presented in column (2) of Table 19.15.

The third trial value of U_4 is obtained by the secant method based on the two previous trial values for U_4 and the corresponding values of Δp_{4L}. Thus,

$$\frac{\Delta p_{4L}^{(3)} - \Delta p_{4L}^{(2)}}{U_4^{(3)} - U_4^{(2)}} = \frac{\Delta p_{4L}^{(2)} - \Delta p_{4L}^{(1)}}{U_4^{(2)} - U_4^{(1)}}$$

$$\frac{0.0 - (-7128)}{U_4 - 823.77} = \frac{-7128 - 19{,}993}{823.77 - 815.61} = -3323.7 \tag{q}$$

Solving equation (q) yields the next trial value $U_4 = 821.62$ m/s. Repeating steps (c) through (f), we obtain $\Delta p_{4L} = 27$ N/m^2. The results obtained during the third trial are presented in column (3) of Table 19.15.

Table 19.15 Values of the Solution, for Successive Trials, for the Shock Wave Point Unit Process (Example 19.6)

	(1)	(2)	(3)	(4)
U_4, m/s	815.61	823.77	821.62	821.63
λ_S, ms/m	1.2261	1.2200	1.2216	1.2216
x_4, m	0.24906	0.24926	0.24921	0.24921
u_{4R}, m/s	31.48	31.59	31.56	31.56
$p_{4R} \cdot 10^{-5}$, N/m^2	0.89151	0.89111	0.89122	0.89122
ρ_{4R}, kg/m^3	1.0961	1.0957	1.0958	1.0958
V_1, m/s	815.61	823.77	821.62	821.63
V_2, m/s	252.28	252.47	252.42	252.42
u_{4L}, m/s	594.81	602.88	600.76	600.77
$p_{4L} \cdot 10^{-5}$, N/m^2	5.9275	6.0477	6.0159	6.0160
ρ_{4L}, kg/m^3	3.5435	3.5751	3.5668	3.5668
Q_+, N-s/m	1806.7	1819.2	1815.9	1815.9
$T_+ \cdot 10^{-6}$, N/m^2	1.6873	1.6944	1.6926	1.6926
$p_{4L,RRC} \cdot 10^{-5}$, N/m^2	6.1268	5.9764	6.0162	6.0160
Δp_{4L}, N/m^2	19,933	−7128	27	0

Applying the secant method again yields the fourth trial value $U_4 = 821.63$ m/s, for which $\Delta p_{4L} = 0.04$ N/m^2. The results of the fourth trial are presented in column (4) of Table 19.15.

From the results presented in Table 19.15, it is seen that the solution is satisfactory after three trials. Very little effect on the final results is observed for the fourth trial. However, in some cases, depending on the nonuniformity of the flow field, a fourth trial may be required.

19–6(h) Contact Surface Point

Figure 19.44 illustrates schematically the unit process for a *contact surface point*. Since a contact surface moves with the velocity of the fluid, it usually will not coincide with a grid point in the inverse marching method. Consequently, a contact surface, like a shock wave, must be tracked through the flow field, and the location and the flow properties at a point on that surface must be determined at the point where the contact surface intersects the *t-lines*.

Figure 19.44 illustrates the unit process for a contact surface point. At a point on a contact surface, the pressure and velocity are continuous, but the remaining flow properties may be discontinuous. As in the case of a shock wave, the contact surface may be conceived as being composed of two halves, as illustrated in Fig. 19.45. Points 3L and 4L in Fig. 19.44 denote two points on the left-hand side of the contact surface, and points 3R and 4R denote the corresponding points on its right-hand side. Accordingly, the solution point, point 4, becomes two halves of two interior points, points 4L and 4R. At each point the fluid has the same velocity and pressure; that is, $u_4 = u_{4L} = u_{4R}$ and $p_4 = p_{4L} = p_{4R}$. The remaining flow properties are determined by solving the appropriate compatibility equations along the right-running Mach line 1–4L and the pathline 3L–4L, and the left-running Mach line 2–4R and the pathline 3R–4R.

For the Euler predictor, the initial estimates for the slopes λ_0, λ_+ and λ_-, are obtained as follows.

$$\lambda_0 = \frac{1}{u_3} \qquad \lambda_+ = \frac{1}{u_{3L} + a_{3L}} \qquad \lambda_- = \frac{1}{u_{3R} - a_{3R}} \tag{19.117}$$

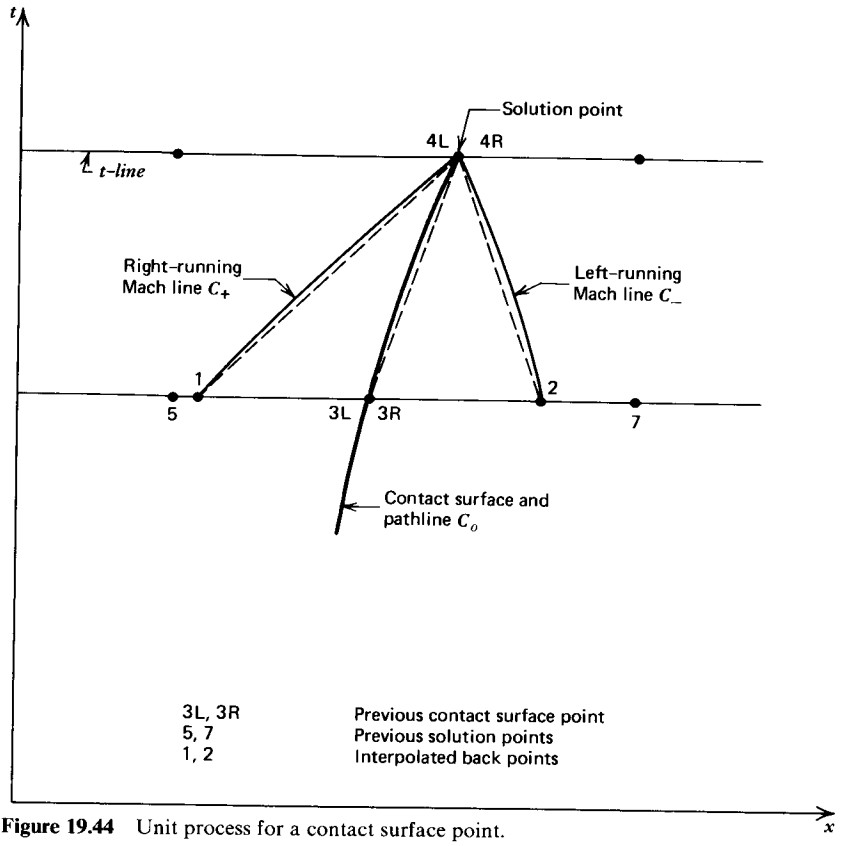

Figure 19.44 Unit process for a contact surface point.

Equation 19.104 is then solved to obtain x_4, and equations 19.105 and 19.106 are solved for x_1 and x_2. The values of the flow properties at points 1 and 2 are obtained by linear interpolation, and points 1 and 2 may be relocated by iteration.

Applying the finite difference forms of the compatibility equations (see Table 19.4) along lines 1–4L, 3L–4L, 3R–4R, and 2–4R, we obtain

$$p_4 + Q_+ u_4 = T_+ \tag{19.118}$$

$$p_4 - A_{oL}\rho_{4L} = T_{oL} \tag{19.119}$$

$$p_4 - Q_- u_4 = T_- \tag{19.120}$$

$$p_4 - A_{oR}\rho_{4R} = T_{oR} \tag{19.121}$$

Equations 19.118 and 19.120 may be solved simultaneously for p_4 and u_4, equation 19.119 may be solved for ρ_{4L}, and equation 19.121 may be solved for ρ_{4R}. The above procedure may be applied repetitively to determine improved values for the location and the flow properties at point 4.

A computer program for implementing the unit process for a contact surface, subroutine CONTACT, is presented below. The terminology is described in Table 19.5. The required initial data are Δt, x_3, u_3, p_3, ρ_{3L}, ρ_{3R}, x_5, u_5, p_5, ρ_5, x_7, u_7, p_7, and ρ_7. The data may be specified in either SI or EE units. The results are the values of x_4, u_4, p_4, ρ_{4L}, and ρ_{4R}.

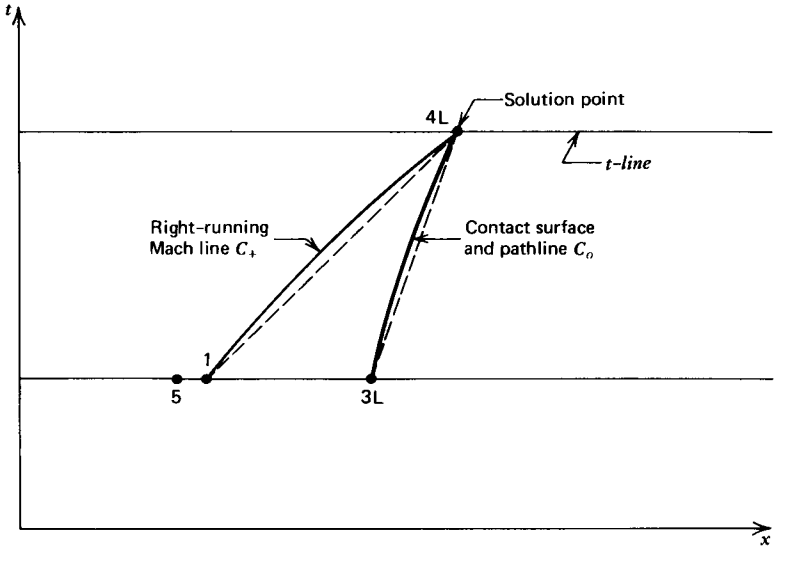

(*a*)

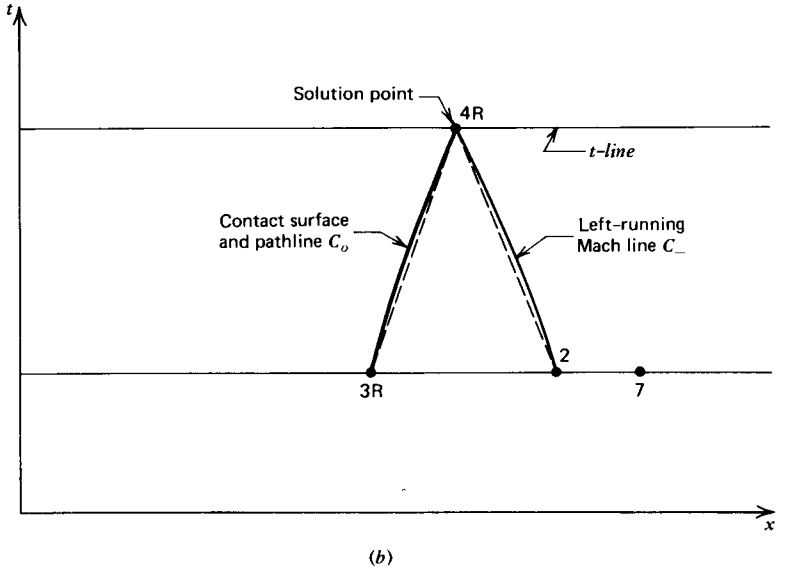

(*b*)

Figure 19.45 A contact surface point considered as two halves of two interior points. (*a*) Left-hand side. (*b*) Right-hand side.

```
      SUBROUTINE CONTACT (X3,U3,P3)
C     SUBROUTINE CONTACT CALCULATES THE SOLUTION AT A CONTACT SURFACE
      REAL LP,LM,LO,MUL,MPL,MRL,MUR,MPR,MRR,ME,M4
      COMMON /CONTRL/ ICOR,IE,E1,E2,E3,E4,GC,GL,GN,DT,G,RG,G1,G2,RG1,RG2
      COMMON /D1/ X4,U4,P4,R4,X5,U5,P5,R5,X6,U6,P6,R6,X7,U7,P7,R7,PA,ME
      COMMON /D2/ W3,W4,X8,U8,P8,R8,X3L,U3L,P3L,R3L,X3R,U3R,P3R,P3R,X4L,
     1U4L,P4L,R4L,X4R,U4R,P4R,R4R,XP,AREA,MP
```

```
C     DEFINE INITIAL PROPERTIES AND DETERMINE INTERPOLATING POLYNOMIALS

      ITER=0 $ X1S=X5 $ X2S=X7 $ U1=U5 $ P1=P5 $ R1=R5 $ U4=U3
      U2=U7 $ P2=P7 $ R2=R7 $ P4=P3 $ R4L=R3L $ R4R=R3R
      DX=X5-X3 $ MUL=(U5-U3)/DX $ BUL=U3-MUL*X3 $ MPL=(P5-P3)/DX
      BPL=P3-MPL*X3 $ MRL=(R5-R3L)/DX $ BRL=R3L-MRL*X3
      DX=X3-X7 $ MUR=(U3-U7)/DX $ BUR=U7-MUR*X7 $ MPR=(P3-P7)/DX
      BPR=P7-MPR*X7 $ MRR=(R3R-R7)/DX $ BRR=R7-MRR*X7

C     CALCULATE THE LOCATION OF THE CONTACT SURFACE

   10 U=0.5*(U3+U4) $ IF (ABS(U).GT.1.0E-6) GO TO 15 $ X4=X3 $ GO TO 20
   15 LO=1.0/U $ X4=X3+DT*GN/LO

C     LOCATE POINT 1 AND DETERMINE COEFFICIENTS ALONG LINE 14

   20 G=G1 $ IF (ITER.GT.0) GO TO 30 $ U4=U1 $ P4=P1 $ R4L=R1
   30 U=0.5*(U1+U4) $ P=0.5*(P1+P4) $ R=0.5*(R1+R4L) $CALL THERMO(P,R,A)
      LP=1.0/(U+A) $ X1=X4-DT*GN/LP $ IF(ABS(X1-X1S).LT.0.0001) GO TO 40
      X1S=X1 $ U1=MUL*X1+BUL $ P1=MPL*X1+BPL $ R1=MRL*X1+BRL $ GO TO 20
   40 QP=R*A/GC $ TP=GL*P1+QP*U1

C     LOCATE POINT 2 AND DETERMINE COEFFICIENTS ALONG LINE 24

   50 G=G2 $ IF (ITER.GT.0) GO TO 60 $ U4=U2 $ P4=P2 $ R4R=R2
   60 U=0.5*(U2+U4) $ P=0.5*(P2+P4) $ R=0.5*(R2+R4R) $CALL THERMO(P,R,A)
      LM=1.0/(U-A) $X2=X4-DT*GN/LM $ IF(ABS(X2-X2S).LT.0.0001) GO TO 70
      X2S=X2 $ U2=MUR*X2+BUR $ P2=MPR*X2+BPR $ R2=MRR*X2+BRR $ GO TO 50
   70 QM=R*A/GC $ TM=GL*P2-QM*U2

C     DETERMINE THE COEFFICIENTS ALONG LINE 34

      IF (ITER.GT.0) GO TO 80 $ P4=P3 $ R4L=R3L $ R4R=R3R
   80 P=0.5*(P3+P4) $ RL=0.5*(R3L+R4L) $ G=G1 $ CALL THERMO (P,RL,AL)
      RR=0.5*(R3R+R4R) $ G=G2 $ CALL THERMO (P,RR,AR) $ AOL=AL**2/GC
      TOL=GL*P3-AOL*R3L $ AOR=AR**2/GC $ TOR=GL*P3-AOR*R3R

C     CALCULATE THE PROPERTIES AT POINT 4, AND TEST FOR CONVERGENCE

      U4=(TP-TM)/(QP+QM) $ P4=(TP-QP*U4)/GL $ R4L=(GL*P4-TOL)/AOL
      R4R=(GL*P4-TOR)/AOR
      IF (ITER.EQ.ICOR) RETURN $ IF (ITER.EQ.0) GO TO 90
      IF ((ABS(U4-UD).GT.E1*UD).OR.(ABS(P4-PD).GT.E2*PD)) GO TO 90
      IF((ABS(R4L-RDL).GT.E3*RDL).OR.(ABS(R4R-RDR).GT.E3*RDR)) GO TO 90
      IF (ABS(X4-XD).LT.E4) RETURN
   90 ITER=ITER+1 $ XD=X4 $ UD=U4 $ PD=P4 $ RDL=R4L $ RDR=R4R $ GO TO 10
      END
```

Example 19.7. A contact surface is traveling along a constant-area flow passage. The flow properties at a given instant are given in Table 19.16 (see Figs. 19.44 and 19.45). Assume that the gases on both sides of the contact surface are perfect gases with $\gamma = 1.40$. The presence of the contact surface is due to the discontinuity in the gas density across the interface. Calculate the location and flow properties at the contact surface at a time 0.050 ms later.

Table 19.16 Initial-Value Data (Example 19.7)

	Point 5	Point 3L	Point 3R	Point 7
x, m	0.05080	0.11176	0.11176	0.15240
u, m/s	512.31	559.00	559.00	512.31
$p \cdot 10^{-5}$, N/m^2	5.8419	6.4911	6.4911	7.1402
ρ, kg/m^3	2.1575	2.3262	3.8185	4.0874

Solution

(a) *Speed of sound equation.* From equation 19.114,

$$a = \left(\frac{1.4p}{\rho} \right)^{1/2} \tag{a}$$

(b) *Interpolating polynomials.* Along line 5–3L, applying equations 19.91 to 19.93, we obtain

$$u = 765.91x + 473.40 \text{ m/s} \tag{b}$$

$$p = (10.650\,x + 5.3009)10^5 \text{ N/m}^2 \tag{c}$$

$$\rho = 2.7674x + 2.0169 \text{ kg/m}^3 \tag{d}$$

Along line 3R–7,

$$u = -1148.9x + 687.40 \text{ m/s} \tag{e}$$

$$p = (15.972x + 4.7061)10^5 \text{ N/m}^2 \tag{f}$$

$$\rho = 6.6166x + 3.0790 \text{ kg/m}^3 \tag{g}$$

(c) *Determine the location of point* 4 *for the predictor.* For the predictor, assume that $u_o = u_3$. Then,

$$\lambda_o = \frac{1}{u_o} = \frac{1}{559.00} = 1.7889 \text{ ms/m} \tag{h}$$

From equation 19.104, we obtain

$$x_4 = x_3 + \frac{\Delta t}{\lambda_o} = 0.11176 + \frac{0.050}{1.7889} = 0.13971 \text{ m} \tag{i}$$

(d) *Locate point* 1 *and calculate the coefficients for the predictor.* This step is similar to step (c) in Example 19.3, except that ρ_{3L} replaces ρ_3. The following results are obtained.

Pass	x_1, m	u_1, m/s	$p_1 \cdot 10^{-5}$, N/m^2	ρ_1, kg/m^3	a_1, m/s
1	0.08331	537.21	6.1881	2.2475	620.85
2	0.08181	536.06	6.1721	2.2433	620.64
3	0.08188	536.06	6.1721	2.2433	620.64

$$Q_+ = 1392.3 \text{ N-s/m}^3 \qquad T_+ = 1.3636 \cdot 10^6 \text{ N/m}^2$$

(e) *Locate point* 2 *and calculate the coefficients for the predictor.* This step is similar to step (d) in Example 19.3, with ρ_{3R} replacing ρ_3. The results are tabulated below.

Pass	x_2, m	u_2, m/s	$p_2 \cdot 10^{-5}$, N/m^2	ρ_2, kg/m^3	a_2, m/s
1	0.13882	527.91	6.9233	3.9976	492.41
2	0.13793	528.93	6.9092	3.9917	492.26
3	0.13788	528.93	6.9092	3.9917	492.26

$$Q_- = 1965.0 \text{ N-s/m}^3 \qquad T_- = -348{,}410 \text{ N/m}^2$$

(f) *Determine the coefficients along lines* 3L − 4L *and* 3R − 4R *for the predictor.* For the predictor, set the values of the average flow properties along lines 3L − 4L and 3R − 4R equal to those at point 3L and 3R, respectively. Then,

$$a_{oL} = 625.03 \text{ m/s} \qquad a_{oR} = 487.84 \text{ m/s}$$

$$A_{oL} = 390{,}660 \text{ N-m/kg} \qquad A_{oR} = 237{,}990 \text{ N-m/kg}$$

$$T_{oL} = -259{,}640 \text{ N/m}^2 \qquad T_{oR} = -259{,}640 \text{ N/m}^2$$

(g) *Determine* u_4, p_4, ρ_{4L}, *and* ρ_{4R} *for the predictor.* Substituting the values of the coefficients determined in steps (d), (e), and (f) into equations 19.118 to 19.121, we obtain

$$p_4 + 1392.3u_4 = 1.3636 \cdot 10^6 \tag{j}$$

$$p_4 - 390{,}660\rho_{4L} = -259{,}640 \tag{k}$$

$$p_4 - 1965.0u_4 = -348{,}410 \tag{l}$$

$$p_4 - 237{,}990\rho_{4R} = -259{,}640 \tag{m}$$

Solving the pairs of equations (j) and (l), and (k) and (m), simultaneously yields

$$u_4 = 509.93 \text{ m/s} \qquad p_4 = 6.5359 \cdot 10^5 \text{ N/m}^2$$

$$\rho_{4L} = 2.3377 \text{ kg/m}^3 \qquad \rho_{4R} = 3.8373 \text{ kg/m}^3$$

The application of the predictor is now completed. The results are presented in column (0) of Table 19.17.

(h) *Application of the corrector.* The modified Euler corrector algorithm is applied by repeating steps (c) through (g), employing average values of the properties

Table 19.17 Values of the Solution, for Successive Trials, for the Unit Process for a Contact Surface (Example 19.7)

	(0)	(1)	(2)	(3)
λ_o, ms/m	1.7899	1.8710	1.8699	1.8700
x_4, m	0.13971	0.13848	0.13850	0.13850
λ_+, ms/m	0.86453	0.87268	0.87251	0.87252
x_1, m	0.08188	0.08119	0.08119	0.08119
λ_-, ms/m	27.275	33.678	33.253	33.263
x_2, m	0.13788	0.13700	0.13700	0.13700
Q_+, N-s/m^3	1392.3	1426.8	1425.5	1425.5
$T_+ \cdot 10^{-6}$, N/m^2	1.3636	1.3807	1.3800	1.3800
Q_-, N-s/m^3	1965.0	1917.6	1916.0	1916.0
$T_- \cdot 10^{-6}$, N/m^2	−0.34841	−0.32682	−0.32594	−0.32594
A_{oL}, N-m/kg	390,660	391,040	390,930	390,930
T_{oL}, N/m^2	−259,640	−260,540	−260,270	−260,270
A_{oR}, N-m/kg	237,990	238,220	238,150	238,150
T_{oR}, N/m^2	−259,640	−260,540	−260,270	−260,270
u_4, m/s	509.93	510.55	510.53	510.53
$p_4 \cdot 10^{-5}$, N/m^2	6.5359	6.5223	6.5223	6.5223
ρ_{4L}, kg/m^3	2.3377	2.3342	2.3342	2.3342
ρ_{4R}, kg/m^3	3.8373	3.8316	3.8616	3.8316

as illustrated in Example 19.2. The results are presented in column (1) of Table 19.17. The results of two iterations of the corrector are presented in columns (2) and (3) of Table 19.17. Iteration of the corrector has only a minor effect on the final results.

19–6(i) Moving Projectile

The acceleration of a projectile through a tube by a column of high pressure gas expanding behind the projectile is the principle of operation of rifles, guns, and recoilless rifles. Figure 19.46 presents a schematic illustration of a recoilless rifle. The gas generator, usually a solid propellant, is the source of high pressure gas that flows into the launch tube and accelerates the projectile. Simultaneously, a portion of that gas is expanded through a propulsive nozzle thereby developing a jet thrust for counteracting the jet thrust developed by the gases flowing into the launch tube plus the drag between the projectile and the walls of the launch tube. The flows of gas discharged by the gas generator and the propulsive nozzle may be considered to be quasi-steady one-dimensional gas flows. The flows in the launch tube, however, both in front of and behind the projectile, are unsteady one-dimensional flows. The unit process for the projectile itself is discussed below.

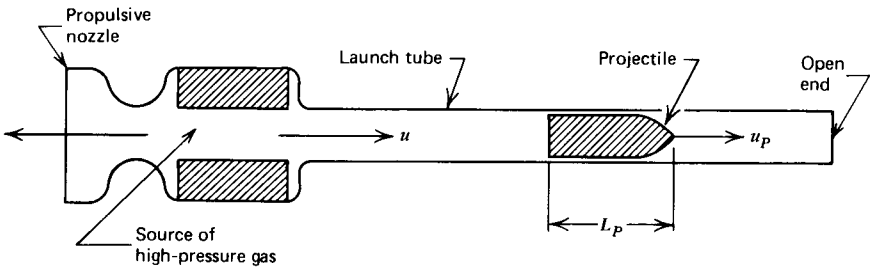

Figure 19.46 Schematic illustration of a recoilless rifle.

Figure 19.47 illustrates the unit process for the projectile, which is similar to that for a contact surface discussed in Section 19–6(h) and illustrated in Figs. 19.44 and 19.45. In Fig. 19.47, points 3L and 4L refer to the left-hand side of the projectile, and points 3R and 4R refer to the right-hand side. Both sides of the projectile have the same velocity, of course, but the pressures acting on them are different. Hence, the unit process for a projectile may be considered to consist of two halves of two interior points, each having the same velocity $u_4 = u_{4L} = u_{4R}$, but having different pressures p_{4L} and p_{4R}.

Point 4L may be determined from point 3L by solving equation 19.104, Table 19.4. Let u_P denote the projectile velocity. Then λ_o is given by

$$\lambda_o = \frac{1}{u_P} \tag{19.122}$$

From Fig. 19.46, if L_P denotes the length of the projectile, then the location of point 4R with reference to point 4L is given by

$$x_{4R} = x_{4L} + L_P \tag{19.123}$$

Equations 19.105 and 19.106, Table 19.4, may be solved for the location of points 1 and 2, respectively. For the Euler predictor, λ_+, λ_-, and λ_o are based on the flow

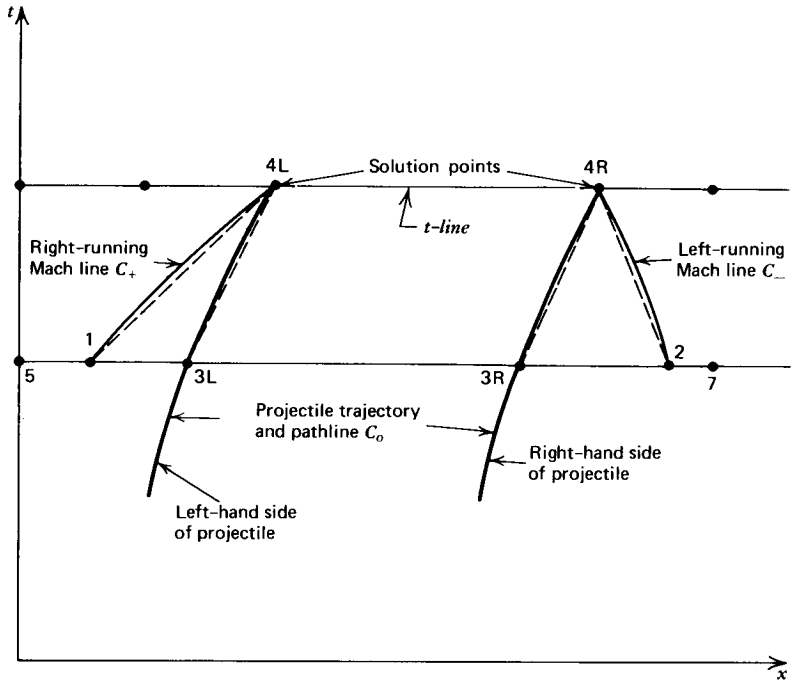

Figure 19.47 Unit process for a projectile.

properties at points 1, 2, and 3, respectively. For the corrector, the average values of the flow properties are employed for determining the slopes of the characteristics.

Applying the finite difference forms of the compatibility equations (see Table 19.4) along lines 1-4L, 3L-4L, 3R-4R, and 2-4R, we obtain

$$p_{4L} + Q_+ u_4 = T_+ \tag{19.124}$$

$$p_{4L} - A_{oL}\rho_{4L} = T_{oL} \tag{19.125}$$

$$p_{4R} - Q_- u_4 = T_- \tag{19.126}$$

$$p_{4R} - A_{oR}\rho_{4R} = T_{oR} \tag{19.127}$$

An additional relation between the flow properties is obtained by applying Newton's second law of motion to the projectile. Thus,

$$\sum F = m_P a_P = m_P \frac{du_P}{dt} \tag{19.128}$$

where m_P, a_P, and u_P denote the mass, acceleration, and velocity, respectively, of the projectile, and ΣF denotes the algebraic sum of all of the external forces acting on the projectile. A force diagram for the projectile is illustrated in Fig. 19.48. Applying equation 19.128, we obtain

$$p_L A - p_R A - D = m_P \frac{du_P}{dt} = m_P a_P \tag{19.129}$$

where p_L and p_R denote the pressure on the left-hand and right-hand sides,

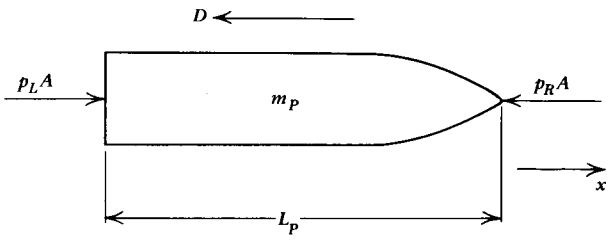

Figure 19.48 Force diagram for a moving projectile.

respectively, of the projectile, and D denotes the drag force exerted by the wall of the tube on the projectile. Writing equation 19.129 in finite difference form for the grid illustrated in Fig. 19.47, we obtain

$$u_4 = u_3 + \frac{1}{m_P}\left[A(p_L - p_R) - D\right](t_4 - t_3) \tag{19.130}$$

Equations 19.124 to 19.127 and 19.130 may be solved simultaneously for u_4, p_{4L}, p_{4R}, ρ_{4L}, and ρ_{4R}.

The above procedure may be applied iteratively to obtain improved values for the location of and the flow properties at point 4. A similar procedure may be developed for a left-traveling projectile.

A FORTRAN program, subroutine MISSILE, is presented below for the numerical implementation of the unit process for a moving projectile. The initial data comprise Δt, x_{3L}, u_{3L}, p_{3L}, ρ_{3L}, x_{3R}, u_{3R}, p_{3R}, ρ_{3R}, x_5, u_5, p_5, ρ_5, x_7, u_7, p_7, ρ_7, A, and m_P, where A is the area of the base of the projectile in m^2 (in.^{2}) and m_P is the mass of the projectile in kg (lbm). The initial data may be specified in either SI or EE units. The results of the calculations are x_{4L}, u_{4L}, p_{4L}, ρ_{4L}, x_{4R}, u_{4R}, p_{4R}, and ρ_{4R}.

```
      SUBROUTINE MISSILE
C     SUBROUTINE MISSILE CALCULATES PROPERTIES OF A MOVING PROJECTILE
      REAL LP,LM,LO,MUL,MPL,MRL,MUR,MPR,MRR,MP
      COMMON /CONTRL/ ICOR,IE,E1,E2,E3,E4,GC,GL,GN,DT,G,RG,G1,G2,RG1,RG2
      COMMON /D1/ X4,U4,P4,R4,X5,U5,P5,R5,X6,U6,P6,R6,X7,U7,P7,R7,PA,ME
      COMMON /D2/ W3,W4,X8,U8,P8,R8,X3L,U3L,P3L,R3L,X3R,U3R,P3R,R3R,X4L,
     1U4L,P4L,R4L,X4R,U4R,P4R,R4R,XP,AREA,MP
C     DEFINE INITIAL PROPERTIES AND DETERMINE INTERPOLATING POLYNOMIALS
      U1=U5 $ P1=P5 $ R1=R5 $ U2=U7 $ P2=P7 $ R2=R7 $ P4L=P3L $ P4R=P3R
      DX=X5-X3L $ MUL=(U5-U3L)/DX $ BUL=U3L-MUL*X3L $ MPL=(P5-P3L)/DX
      BPL=P3L-MPL*X3L $ MRL=(R5-R3L)/DX $ BRL=R3L-MRL*X3L
      DX=X3R-X7 $ MUR=(U3R-U7)/DX $ BUR=U7-MUR*X7 $ MPR=(P3R-P7)/DX
      BPR=P7-MPR*X7 $ MRR=(R3R-R7)/DX $ BRR=R7-MRR*X7 $ ITER=0
C     CALCULATE ACCELERATION, VELOCITY, AND LOCATION OF THE PROJECTILE
   10 AP=0.5*(P3L+P4L-P3R-P4R)*AREA*GC/MP $ UMISLE=U3L+AP*DT $U4L=UMISLE
      U=0.5*(U3L+U4L) $ LO=1.0/U $ DX=DT*GN/LO $ X4L=X3L+DX $ X4R=X3R+DX
C     LOCATE POINT 1 AND DETERMINE COEFFICIENTS ALONG LINE 14
   20 G=G1 $ IF (ITER.GT.0) GO TO 30 $ U4L=U1 $ P4L=P1 $ R4L=R1
   30 U=0.5*(U1+U4L) $P=0.5*(P1+P4L) $R=0.5*(R1+R4L) $CALL THERMO(P,R,A)
      LP=1.0/(U+A) $ X1=X4L-DT*GN/LP $IF(ABS(X1-X1S).LT.0.0001) GO TO 40
      X1S=X1 $ U1=MUL*X1+BUL $ P1=MPL*X1+BPL $ R1=MRL*X1+BRL $ GO TO 20
   40 QP=R*A/GC $ TP=GL*P1+QP*U1
```

```
C     LOCATE POINT 2 AND DETERMINE COEFFICIENTS ALONG LINE 24

   50 G=G2 $ IF (ITER.GT.0) GO TO 60 $ U4R=U2 $ P4R=P2 $ R4R=R2
   60 U=0.5*(U2+U4R) $P=0.5*(P2+P4R) $R=0.5*(R2+R4R) $CALL THERMO(P,R,A)
      LM=1.0/(U-A) $ X2=X4R-DT*GN/LM $IF(ABS(X2-X2S).LT.0.0001) GO TO 70
      X2S=X2 $ U2=MUR*X2+BUR $ P2=MPR*X2+BPR $ R2=MRR*X2+BRR $ GO TO 50
   70 QM=R*A/GC $ TM=GL*P2-QM*U2

C     DETERMINE THE COEFFICIENTS ALONG LINE 34

      IF (ITER.GT.0) GO TO 80 $ P4L=P3L $ R4L=R3L $ P4R=P3R $ R4R=R3R
   80 PL=0.5*(P3L+P4L) $ RL=0.5*(R3L+R4L) $ G=G1 $ CALL THERMO(PL,RL,AL)
      AOL=AL**2/GC $ TOL=GL*P3L-AOL*R3L $ PR=0.5*(P3R+P4R)
      RR=0.5*(R3R+R4R) $ G=G2 $ CALL THERMO (PR,RR,AR) $ AOR=AR**2/GC
      TOR=GL*P3R-AOR*R3R

C     CALCULATE THE PROPERTIES AT POINT 4, AND TEST FOR CONVERGENCE

      U4L=UMISLE $ P4L=(TP-QP*U4L)/GL $ R4L=(GL*P4L-TCL)/AOL
      U4R=UMISLE $ P4R=(TM+QM*U4R)/GL $ R4R=(GL*P4R-TOR)/AOR
      IF (ITER.EQ.ICOR) RETURN $ IF (ITER.EQ.0) GO TO 90
      IF ((ABS(X4L-XD).GT.E4).OR.(ABS(U4L-UD).GT.E1*UD)) GO TO 90
      IF ((ABS(P4L-PDL).GT.E2*PDL).OR.(ABS(R4L-RDL).GT.E3*RDL)) GO TO 90
      IF ((ABS(R4R-RDR).LT.E2*RDR).AND.(ABS(R4L-RDL).LT.E3*RDL)) RETURN
   90 ITER=ITER+1 $ XD=X4L $ UD=U4L $ PDL=P4L $ RDL=R4L $ PDR=P4R
      RDR=R4R $ GO TO 10
      END
```

Example 19.8. At a given instant, the properties on either side of the projectile described in Example 19.4 are those given in Table 19.18; the corresponding unit process is illustrated in Fig. 19.47. Determine the properties of the projectile at a time 0.03159 ms later. Neglect the drag force between the projectile and the wall of the tube.

Table 19.18 Initial-Value Data (Example 19.8)

	Point 5	Point 3L	Point 3R	Point 7
x, m	0.20320	0.25720	0.46040	0.50800
u, m/s	323.07	327.51	327.51	298.54
$p \cdot 10^{-5}$, N/m^2	599.62	593.41	3.1130	2.8303
ρ, kg/m^3	56.484	55.998	2.7163	2.5051

Solution

(a) *Speed of sound equation.* From equation (a) of Example 19.2,

$$a = \left(\frac{1.2p}{\rho} \right)^{1/2} \tag{a}$$

(b) *Interpolating polynomials.* Along line 5-3L, applying equations 19.91 to 19.93, we obtain

$$u = 82.22x + 306.36 \text{ m/s} \tag{b}$$

$$p = (-115.00x + 622.99)10^5 \text{ N/m}^2 \tag{c}$$

$$\rho = -9.0000x + 5.8313 \text{ kg/m}^3 \tag{d}$$

Along line 3R-7,

$$u = -608.61x + 607.72 \text{ m/s} \tag{e}$$

$$p = (-5.9391x + 5.8474)10^5 \text{ N/m}^2 \tag{f}$$

$$\rho = -4.4370x + 4.7591 \text{ kg/m}^3 \tag{g}$$

(c) *Determine the location and velocity at point 4 for the predictor.* The acceleration of the projectile is determined from equation 19.129 with $D = 0.0$. For the predictor, assume that $p_{4L} = p_{3L}$ and $p_{4R} = p_{3R}$. The base area A of the projectile is

$$A = \frac{\pi D_P^2}{4} = \frac{\pi(0.0635)^2}{4} = 0.0031669 \text{ m}^2$$

From equation 19.129,

$$a_P = \frac{(p_L - p_R)A}{m_P} = \frac{(593.41 - 3.1130)10^5(0.0031669)}{(0.90718)}$$

$$= 206{,}070 \text{ m/s}^2 \tag{h}$$

Substituting the value of a_P into equation 19.130, we obtain

$$u_4 = u_3 + a_P \Delta t = 327.51 + (206{,}070)(0.00003159) = 334.01 \text{ m/s} \tag{i}$$

Substituting the values of u_3 and u_4 into equation 19.122 yields

$$u_P = \frac{u_3 + u_4}{2} = \frac{327.51 + 334.01}{2} = 330.76 \text{ m/s} \tag{j}$$

$$\lambda_o = \frac{1}{u_P} = \frac{1}{330.76} = 3.0233 \text{ ms/m} \tag{k}$$

From equations 19.104 and 19.123, we obtain

$$x_{4L} = x_{3L} + \frac{\Delta t}{\lambda_o} = 0.25720 + \frac{0.03159}{3.0233} = 0.26765 \text{ m} \tag{l}$$

$$x_{4R} = x_{4L} + L_P = 0.26765 + 0.20320 = 0.47085 \text{ m} \tag{m}$$

(d) *Locate point 1 and calculate the coefficients for the predictor.* For the first pass through the predictor, set the values of the average flow properties along line 14 equal to those at point 5. From equation (a),

$$a_+ = \left[\frac{1.2(599.62)10^5}{56.484}\right]^{1/2} = 1128.7 \text{ m/s}$$

Substituting the above result into equation 19.110 yields

$$\lambda_+ = \frac{1}{323.07 + 1128.7} = 0.68883 \text{ ms/m}$$

From equation 19.105, we obtain

$$x_1 = x_{4L} - \frac{\Delta t}{\lambda_+} = 0.26765 - \frac{0.03159}{0.68883} = 0.22179 \text{ m} \tag{n}$$

Substituting $x_1 = 0.22179$ m into equations (b), (c), and (d), gives

$$u_1 = 324.60 \text{ m/s} \qquad p_1 = 597.48 \cdot 10^5 \text{ N/m}^2 \qquad \rho_1 = 56.317 \text{ kg/m}^3$$

The above procedure is repeated to obtain the following results.

Pass	x_1, m	u_1, m/s	$p_1 \cdot 10^{-5}$, N/m^2	ρ_1, kg/m^3	a_1, m/s
1	0.22179	324.60	597.48	56.317	1128.3
2	0.22175	324.60	597.48	56.317	1128.3

Substituting the results from Pass 2 into equations 19.99 and 19.97 gives

$$Q_+ = (56.317)(1128.3) = 63{,}544 \text{ N-s/m}^3$$

$$T_+ = 597.48 \cdot 10^5 + (63{,}544)(324.60) = 80.374 \cdot 10^6 \text{ N/m}^2$$

(e) *Locate point 2 and calculate the coefficients for the predictor.* Following a procedure analogous to that presented in part (d), the following results are obtained.

Pass	x_2, m	u_2, m/s	$p_2 \cdot 10^{-5}$, N/m^2	ρ_2, kg/m^3	a_2, m/s
1	0.47305	319.81	3.0379	2.6602	370.19
2	0.47244	320.18	3.0415	2.6629	370.22
3	0.47243	320.18	3.0415	2.6629	370.22

Substituting the values from Pass 3 into equations 19.100 and 19.98 yields

$$Q_- = (2.6629)(370.22) = 985.85 \text{ N-s/m}^3$$

$$T_- = 3.0415 \cdot 10^5 - (985.85)(320.18) = -11{,}501 \text{ N/m}^2$$

(f) *Determine the coefficients along lines 3L-4L and 3R-4R for the predictor.* For the predictor, set the average values of the flow properties along lines 3L-4L and 3R-4R equal to those at point 3L and 3R, respectively. Then,

$$a_{o\text{L}} = \left[\frac{1.2(593.41)10^5}{55.998} \right]^{1/2} = 1127.7 \text{ m/s}$$

$$a_{o\text{R}} = \left[\frac{1.2(3.1130)10^5}{2.7163} \right]^{1/2} = 370.84 \text{ m/s}$$

Substituting into equations 19.103 and 19.102, we obtain

$$A_{o\text{L}} = (1127.7)^2 = 1.2716 \cdot 10^6 \text{ N-m/kg}$$

$$A_{o\text{R}} = (370.84)^2 = 137{,}530 \text{ N-m/kg}$$

$$T_{o\text{L}} = 593.41 \cdot 10^5 - (1.2716 \cdot 10^6)(55.998) = -11.868 \cdot 10^6 \text{ N/m}^2$$

$$T_{o\text{R}} = 3.1130 \cdot 10^5 - (137{,}530)(2.7163) = -62{,}260 \text{ N/m}^2$$

(g) *Determine* u_4, p_{4L}, ρ_{4L}, p_{4R}, *and* ρ_{4R} *for the predictor.* For the predictor, $u_4 = 334.01$ m/s from part (c). Substituting that value for u_4 and the values of the coefficients determined in parts (d), (e), and (f), into equations 19.124 to 19.127, we obtain

$$p_{4L} + 63{,}544(334.01) = 80.374 \cdot 10^6 \tag{o}$$

$$p_{4L} - 1.2716 \cdot 10^6 \rho_{4L} = -11.868 \cdot 10^6 \tag{p}$$

$$p_{4R} - 985.85(334.01) = -11{,}501 \tag{q}$$

$$p_{4R} - 137{,}530\rho_{4R} = -62{,}260 \tag{r}$$

Solving equations (o) to (r), we obtain

$$p_{4L} = 591.50 \cdot 10^5 \text{ N/m}^2 \qquad \rho_{4L} = 55.847 \text{ kg/m}^3$$

$$p_{4R} = 3.1779 \cdot 10^5 \text{ N/m}^2 \qquad \rho_{4R} = 2.7635 \text{ kg/m}^3$$

The application of the Euler predictor algorithm is complete. The results are presented in column (0) of Table 19.19.

(h) *Application of the corrector.* The modified Euler corrector algorithm is applied by employing average values of the flow properties along the characteristics. The results are presented in column (1) of Table 19.19. Columns (2) and (3) of Table 19.19 present the results of two iterations of the corrector. Those results demonstrate that iteration of the corrector has a negligible effect on the final results.

Table 19.19 Values of the Solution, for Successive Trials, for the Unit Process for a Moving Projectile (Example 19.8)

	(0)	(1)	(2)	(3)
a_P, m/s^2	207,070	205,720	205,730	205,730
u_4, m/s	334.02	334.01	334.01	334.01
λ_o, ms/m	3.0233	3.0233	3.0233	3.0233
x_{4L}, m	0.26765	0.26765	0.26765	0.26765
x_{4R}, m	0.47085	0.47085	0.47085	0.47085
λ_+, ms/m	0.68827	0.68627	0.68627	0.68627
x_1, m	0.22175	0.22162	0.22162	0.22162
λ_-, ms/m	−19.985	−22.883	−22.872	−22.871
x_2, m	0.47243	0.47223	0.47223	0.47223
Q_+, N-s/m^3	63,544	63,253	63,255	63,255
$T_+ \cdot 10^{-6}$, N/m^2	80.374	80.281	80.282	80.282
Q_-, N-s/m^3	985.85	1006.4	1006.8	1006.8
T_-, N/m^2	−11,501	−18,086	−18,211	−18,214
$A_{oL} \cdot 10^{-6}$, N-m/kg	1.2716	1.2713	1.2713	1.2713
$T_{oL} \cdot 10^{-6}$, N/m^2	−11.868	−11.849	−11.850	−11.850
A_{oR}, N-m/kg	137,530	137,760	137,770	137,770
T_{oR}, N/m^2	−62,260	−62,904	−62,936	−62,937
$p_{4L} \cdot 10^{-5}$, N/m^2	591.50	591.54	591.54	591.54
ρ_{4L}, kg/m^3	55.847	55.851	55.851	55.851
$p_{4R} \cdot 10^{-5}$, N/m^2	3.1779	3.1806	3.1807	3.1807
ρ_{4R}, kg/m^3	2.7634	2.7654	2.7654	2.7654

19-6(j) Centered Expansion Wave

The formation of centered expansion waves in unsteady one-dimensional flow is discussed in earlier sections of this chapter. Examples are the expansion waves created by the instantaneous acceleration of a piston (see Fig. 13.8*b*), the rupture of a diaphragm (see Fig. 19.11), the expansion wave reflected from the open end of a duct when a shock wave interacts with the fixed pressure at that point (see Fig. 19.25), and the expansion wave that is reflected from the intersection of two shock waves of the same family (see Fig. 19.26*a*). The point in the xt plane from which the centered expansion wave is propagated, called the *origin* of the wave, is a singular point; at the origin the flow properties are multivalued. The solution at the origin of the centered expansion wave must be known in order to extend the solution beyond that point. The centered expansion wave is analogous to the Prandtl-Meyer centered expansion wave in steady two-dimensional planar flow discussed in Chapter 8.

The unit process for the origin of the centered expansion wave is illustrated schematically in Fig. 19.49*a*. Because the origin is a geometric point, area change, friction, heat transfer, and mass addition are not possible at that point. Consequently, the flow through the origin is isentropic, and the compatibility equations (see Table 19.2) become

$$dp_o - a^2 d\rho_o = 0 \tag{19.131}$$

$$dp_{\pm} \pm \rho a\, du_{\pm} = 0 \tag{19.132}$$

Equations 19.131 and 19.132 may be integrated in closed form for a perfect gas to yield relationships between u, p, and ρ at the origin of the centered expansion wave. Section 13-4(a) presents the results obtained for a perfect gas. For an imperfect gas, however, numerical integration is required.

When the flow properties u and a have been determined at the origin of the centered expansion wave, the direction of the Mach lines emanating from that point may be determined from the characteristic equation for the Mach lines. Thus,

$$\frac{dt}{dx_{\pm}} = \frac{1}{u_{\pm} \pm a_{\pm}} \tag{19.133}$$

Hence, the initial flow properties and the slopes of each Mach line emanating from the origin of the centered expansion wave are determinable.

The flow properties in the neighborhood of the origin of the centered expansion wave may be determined by applying an appropriate unit process for an interior point, such as that for the left-running centered expansion wave illustrated in Fig. 19.49*b*. The origin of the wave is point 2, and the initial-data points 1 and 2 are located along the previous left-running Mach line C_-. The solution point, point 4, is located at the intersection of the right-running Mach line C_+ through point 1 and the left-running Mach line C_- emanating from point 2, the origin of the centered expansion wave. Point 3 is a back point located at the intersection of the pathline C_o and the left-running Mach line 12. The number of Mach lines emanating from the origin of the centered expansion wave is chosen so that the property changes at the origin between Mach lines have approximately the same magnitudes as the property changes between other finite difference grid points in the neighborhood of the origin of the centered expansion wave.

The centered expansion wave illustrated in Fig. 19.49 is a left-running expansion wave. Analogous results pertain to right-running expansion waves.

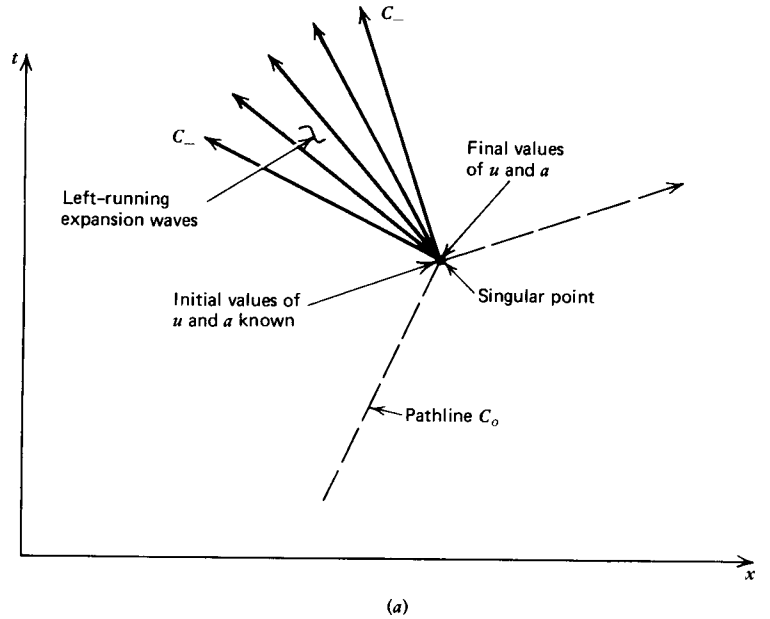

(a)

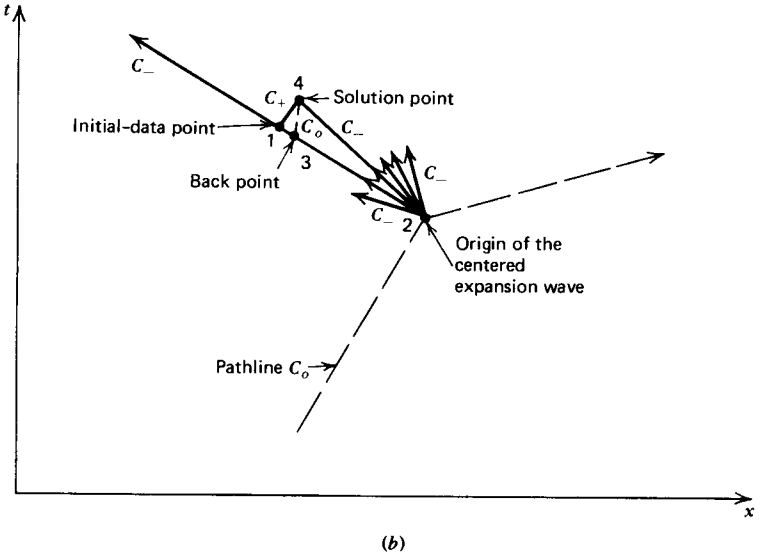

(b)

Figure 19.49 Unit process for a centered expansion wave. (*a*) Origin of a centered expansion wave. (*b*) Unit process for an interior point where point 2 is at the origin of a centered expansion wave.

19–7 APPLICATIONS

In this section, the methods of analysis described in the foregoing sections for unsteady one-dimensional flow are applied to determining the unsteady flow fields for the following engineering problems.

1. The blowdown of a solid propellant rocket motor combustion chamber.
2. The acceleration of a projectile in a recoilless rifle.

3. The starting process in a tube wind tunnel (Ludwieg tube).
4. Steady flow in a converging conical passage as the asymptotic limit at large time for the corresponding unsteady flow field.

19–7(a) Blowdown of a Solid Propellant Rocket Motor Combustion Chamber

An example of an unsteady one-dimensional flow is the *blowdown* of the combustion chamber of a solid propellant rocket motor after the propellant is consumed. Figure 19.50 illustrates schematically an internal burning solid propellant rocket motor just prior to propellant *burnout*. The rocket motor illustrated in Fig. 19.50 corresponds to that described in Examples 19.2, 19.3, and 19.5.

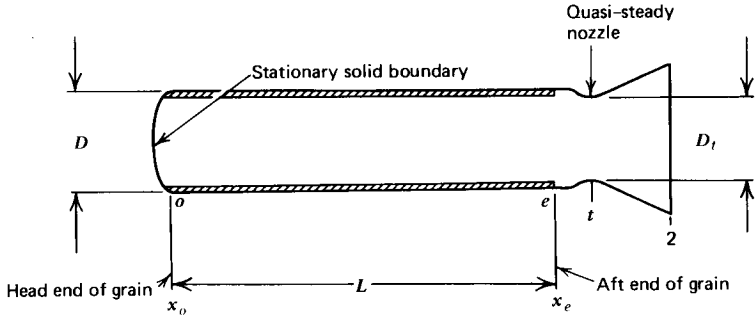

Figure 19.50 Schematic illustration of a typical small solid propellant rocket motor just prior to propellant burn-out.

A typical pressure-time history at the head end of the grain for such a rocket motor is illustrated schematically in Fig. 19.51. During the major portion of the total operating time of the rocket motor, the mass flow rate of combustion gas through the perforation in the solid propellant grain changes only slightly with time. The corresponding distribution of the flow properties for the gas along the

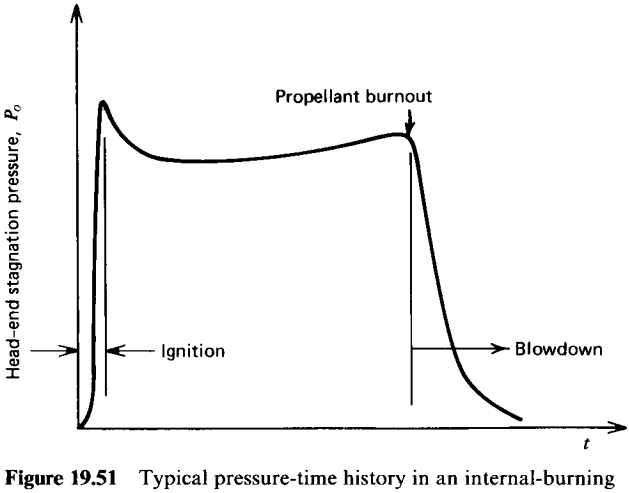

Figure 19.51 Typical pressure-time history in an internal-burning solid propellant rocket motor.

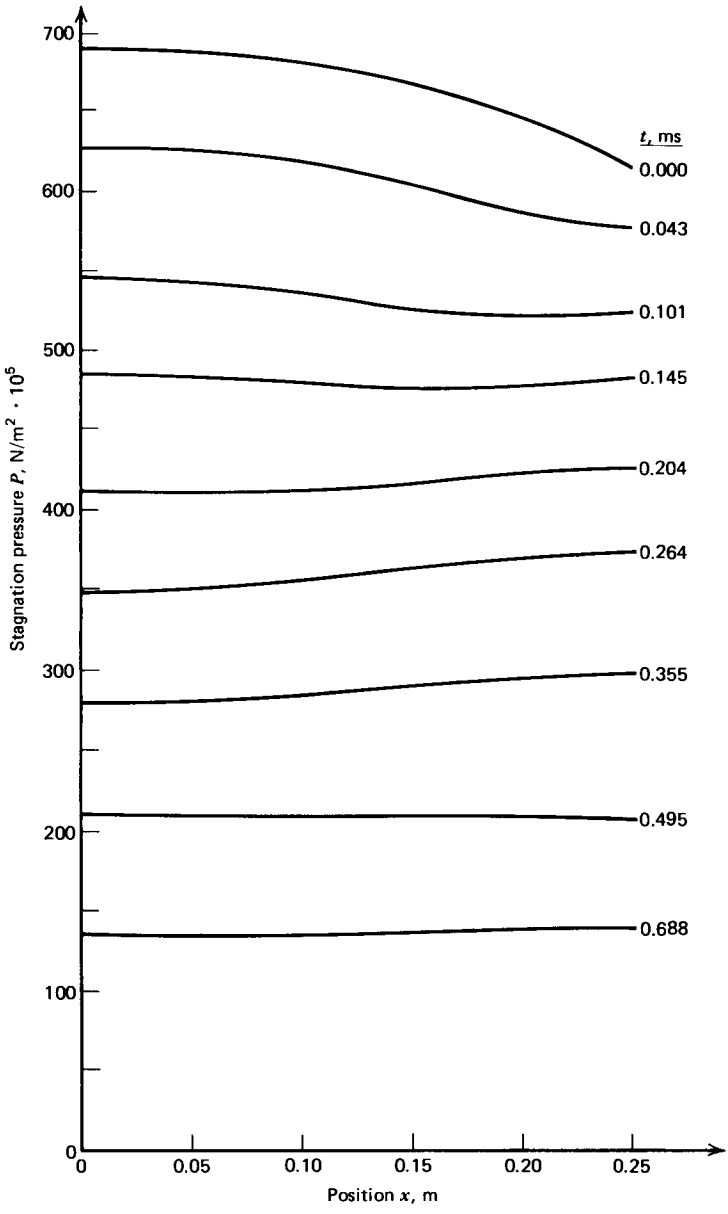

Figure 19.52 Stagnation pressure P at selected times t as a function of position x.

internal burning perforation may be determined by a quasi-steady flow analysis based on the flow model of Section 9–3 for a steady one-dimensional flow with mass addition. During the ignition and blowdown periods, however, the flow properties change so rapidly with time that the unsteady flow effects become significant.

The blowdown process illustrated in Fig. 19.51 may be described adequately by assuming that the rocket motor is a long constant-area tube having a stationary solid boundary at the left end, and quasi-steady isentropic flow through the nozzle

at the right end (see Fig. 19.50). The flow within the rocket motor after *burnout* is assumed to be isentropic. For illustrative purposes, consider the case where the head-end pressure $P_o = 689.5 \cdot 10^5$ N/m^2 at burnout and the linear burning rate for the propellant $\dot{r}$ is constant [see Section 9–3(c)]. In that case, the mass flux $G = \dot{m}/A$ is linearly proportional to x, the distance along the tube from the head end [see equation 9.42, Section 9–3(c)]. Accordingly, the distribution of flow properties of the gas along the perforation in the grain may be determined directly from Table C.14 in Volume I. The corresponding stagnation pressure distribution along the motor at burnout, denoted by $t = 0.000$ ms, is illustrated by the top curve in Fig. 19.52. The decrease in stagnation pressure along the motor is due to the effects of mass addition, which is a nonisentropic process.

After propellant burnout, the flow process within the rocket motor is isentropic, but not homentropic, because there is an initial variation in the entropy of the gas flowing along the flow passage due to the effects of mass addition prior to burnout. The flow properties at the different stations along the rocket motor during the blowdown period may be determined from the initial property distribution at burnout by employing the unsteady one-dimensional planar isentropic flow unit processes for an interior point [subroutine INTER, Section 19–6(c)], a stationary solid boundary point [subroutine SOLID, Section 19–6(e)], and a quasi-steady nozzle point [subroutine OPEN, Section 19–6(f)].

Figure 19.52 presents the stagnation pressure distribution along the motor at selected times during blowdown. A quasi-steady flow analysis would predict that throughout the blowdown process the stagnation pressure distribution would be similar to the initial stagnation pressure distribution; that is, P decreasing from the head end to the aft end. Because of the unsteady flow effects, however, initially the stagnation pressure at the head end decreases more rapidly than the stagnation pressure at the aft end, and the slope of the curve for the pressure distribution actually reverses itself. As time progresses, the stagnation pressure at the aft end decreases more rapidly than it does at the head end. Furthermore, the slope of the pressure distribution reverses a second time at $t = 0.495$ ms. At $t = 0.688$ ms, the slope of the pressure distribution reverses a third time.

The back and forth sloshing of the stagnation pressure distribution described above continues throughout the blowdown period, but the magnitude of the stagnation pressure change $(P_o - P_e)$ along the grain decreases during each oscillation. Figure 19.53 presents the ratio P_e/P_o as a function of time. The oscillatory nature of the unsteady flow is evident, as is the decreasing magnitude of the pressure ratio during each oscillation.

The net thrust developed by the rocket motor may be determined by applying the integral form of the momentum equation (equation 2.87, Table 2.1) to the control surface comprising the internal walls of the rocket motor and the exit plane of the nozzle divergence. Thus,

$$F = \int_{\forall} \frac{\partial}{\partial t}(\rho V)\, d\forall + \dot{m} V_2 + (p_2 - p_o) A_2 \tag{19.134}$$

where $\dot{m}$, V_2, and p_2 are time dependent, and the unsteady momentum change within the rocket motor may attain a value as large as 25 percent of the instantaneous jet thrust. The aforementioned unsteady flow effects may have a significant effect on the operation of the rocket motor during the blowdown period.

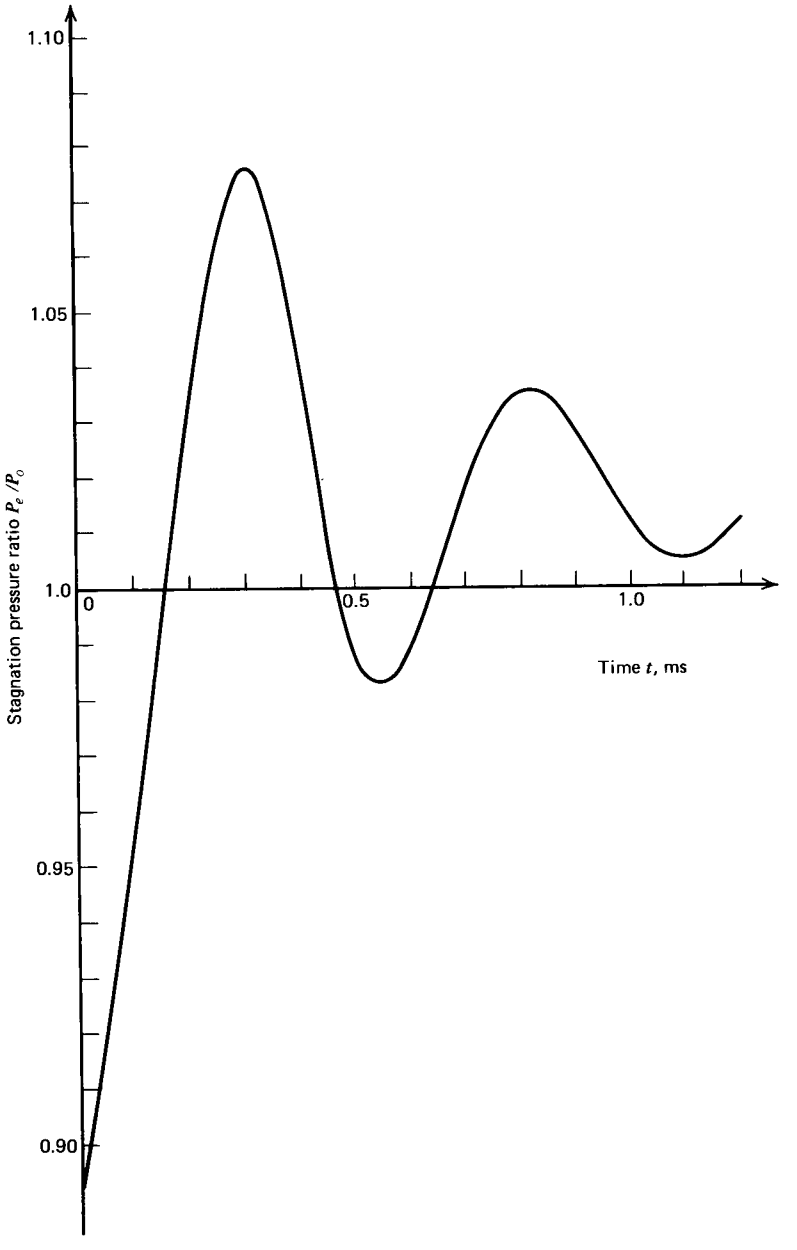

Figure 19.53 Values of the stagnation pressure ratio P_e/P_o as a function of time t during blow-down.

19–7(b) Acceleration of a Projectile

The principles of operation of the recoilless rifle are presented in Section 19–6(i). Figure 19.46 presents a schematic illustration of the general features of a recoilless rifle. The source of high-pressure gases is usually a solid propellant gas generator. The properties of the combustion gas produced by the gas generator may be determined with acceptable accuracy by an unsteady flow analysis where the flow properties, although changing with time, are assumed to be uniform throughout the

gas generator volume. An example of that type of analysis is presented in Example 4.2 for the depressurization of a spacecraft cabin after puncture of its wall. The flow through the propulsive nozzle of the recoilless rifle may be treated as a quasi-steady flow by the methods presented in Section 4–4 and 4–5. The flow in the launch tube, however, experiences large unsteady flow effects that must be taken into account if an accurate determination of the flow field in that tube is to be obtained.

The flow field properties at a general point in the launch tube may be determined by the unit process presented in Section 19–6(c) for an interior point [subroutine POINT]. The flow properties at the right-hand (open) end of the launch tube may be calculated by the unit process for an open end point [subroutine OPEN, Section 19–6(e)]. The acceleration, velocity, and location of the projectile are determined by the moving projectile unit process described in Section 19–6(i) (subroutine MISSILE).

The left-hand end of the launch tube is an open end with subsonic inflow. Figure 19.39 illustrates schematically the unit process for the case of inflow at the right-hand side of the flow passage. The unit process for an open end [subroutine OPEN, Section 19–6(e)], must, therefore, be modified so that two of the three flow properties u, p, and ρ are determined by the gas generator and the third flow property is determined by the compatibility equation that is valid along the single Mach line passing through the solution point from inside the launch tube. The most straightforward procedure for implementing the modified open end unit process is one where the Mach number M_4 at the solution point (point 4 in Fig. 19.39*a*) is assumed. From the calculable flow properties in the gas generator, u_4, p_4, and ρ_4 may be determined. The compatibility equation that is valid along the Mach line passing through point 4 is then employed for determining if the assumed value of M_4 is the correct value. An iterative procedure is implemented where M_4 is varied until the aforementioned compatibility equation is satisfied. The flow properties of the gas generator are affected by the unsteady mass flow rate out of the gas generator into the launch tube. Consequently, the aforementioned iteration procedure requires the simultaneous solution for the properties of the combustion gas produced by the gas generator and the flow properties at the inlet to the launch tube (point 4, Fig. 19.39*a*).

For illustrative purposes, consider the recoilless rifle described in Examples 19.4 and 19.8. To simplify the analysis of the gas generator, assume that it comprises a source of gases having a constant stagnation temperature $T=3330$ K and a stagnation pressure P that varies with time t, as illustrated in Fig. 19.54. The acceleration a_p, velocity u_p, and position x_p of the projectile as a function of time t, as determined by the unit processes described above, are also presented in Fig. 19.54.

The effects of the unsteady flow are illustrated more effectively in Figs. 19.55 and 19.56. Figure 19.55 presents curves of the gas velocity u as a function of the position in the launch tube x, for selected values of the time t. Figure 19.56 presents the gas velocity u at selected values of x as a function of the time t. In each of those figures, the heavy curve presents the projectile velocity u_p.

From Fig. 19.55, it is seen that during the early part of the motion of the projectile (up to $t=1.996$ ms), the gas velocity at the entrance to the launch tube increases with time, and increases slightly along the launch tube at each instant of time. As the projectile moves further down the tube, the velocity at the entrance to the launch tube decreases because of the decrease in the stagnation pressure in the

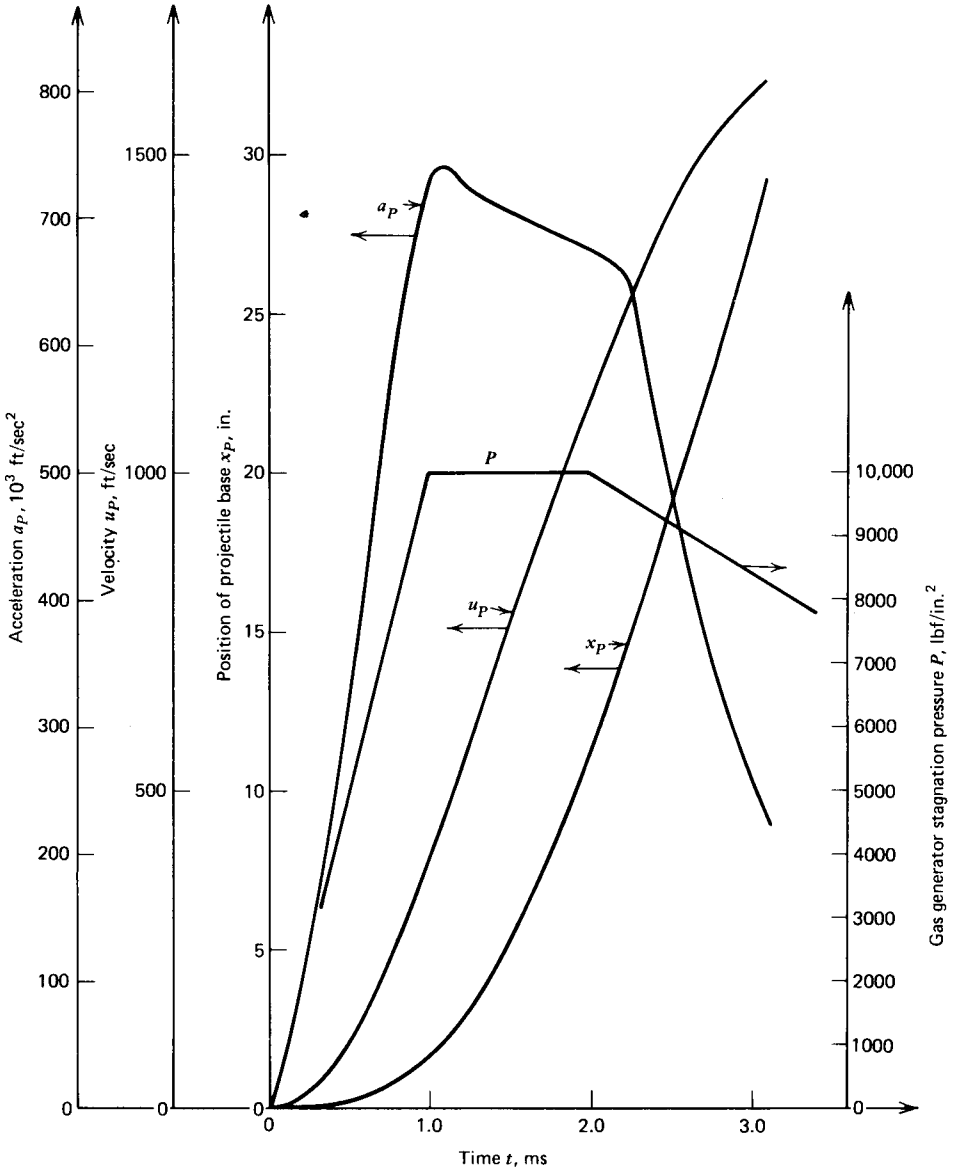

Figure 19.54 Stagnation pressure P in the gas generator, and accleration a_p, velocity u_p, and position x_p of a projectile as a function of time t.

gas generator. At $t=2.450$ ms, the gas velocity at the tube inlet is zero, and a reverse flow from the launch tube into the gas generator develops after that time. At $t=2.989$ ms, the velocity of the reversed gas flow exceeds 750 m/s at the entrance to the gas generator. Figure 19.56 presents the same results in a different format.

The results presented in Figs. 19.55 and 19.56 demonstrate clearly the complex nature of the flow field in a recoilless rifle launch tube. Quasi-steady flow analyses are totally inadequate for determining an accurate solution for such flow problems.

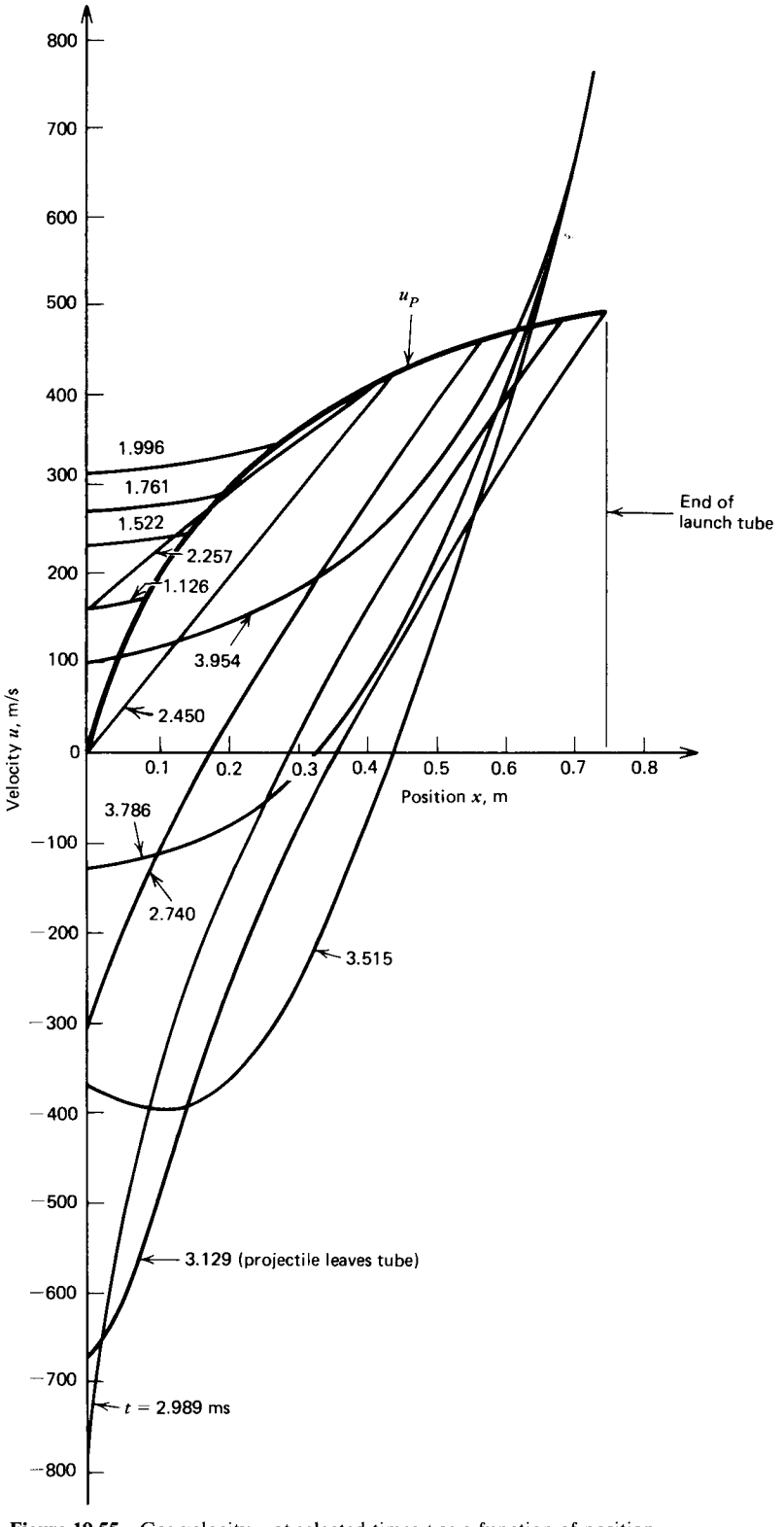

Figure 19.55 Gas velocity u at selected times t as a function of position x.

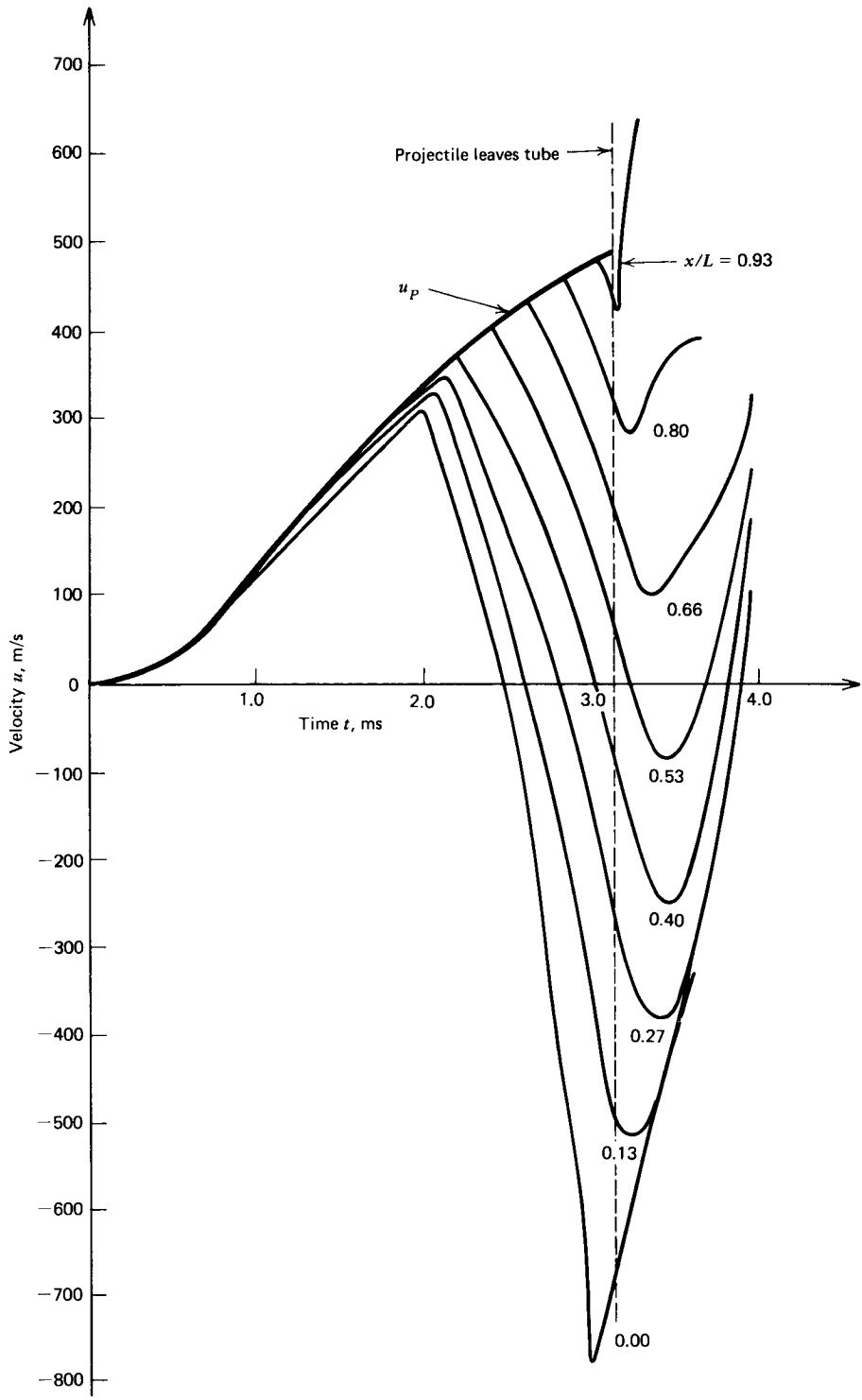

Figure 19.56 Gas velocity u at selected positions x as a function of time t.

19–7(c) Starting Process in a Tube Wind Tunnel (Ludwieg Tube)

The general features of supersonic wind tunnels are discussed in Section 7–12. Several physical arrangements for obtaining the gas for operating the wind tunnel, termed the *test gas*, are illustrated schematically in Fig. 7.40. The shock tube driven tunnel is discussed in detail in Section 19–5(c), and illustrated schematically in Fig. 19.29. The *tube wind tunnel* proposed by Ludwieg[9] is another device for obtaining the test gas. The physical arrangement of the tube wind tunnel is illustrated in Fig. 19.57*a*, and the *xt* wave diagram is illustrated in Fig. 19.57*b*.

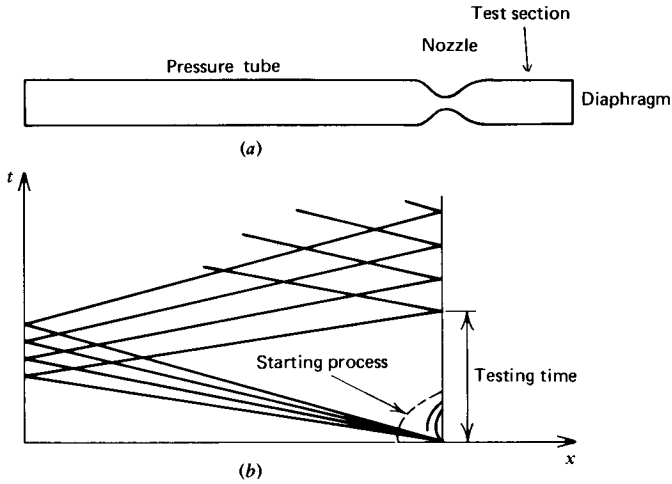

Figure 19.57 General characteristics of the tube wind tunnel (Ludwieg tube) (taken from Reference 11).

The tube wind tunnel comprises a long tube filled with high pressure gas which is closed at one end and has a wind tunnel nozzle, test section, and exhaust system at the other end. A diaphragm sealing the tube is placed somewhere in the nozzle or test section. When the diaphragm is removed (by rupturing it or by a quick opening valve), an expansion fan is propagated into the stagnant high pressure gas in the pressure tube, as illustrated schematically in the *xt* wave diagram presented in Fig. 19.57*b*. The expansion fan propagates through the tube, reflects from the closed end, and returns to the nozzle entrance plane. During the time between the removal of the diaphragm and the return of the expansion waves, a region of uniform flow exists at the nozzle entrance plane, and that region of uniform flow serves as a source of test gas for the supersonic wind tunnel. The duration of the testing time depends on the duration of the starting transient and the length of the pressure tube. Testing times of up to 500 ms have been obtained with a pressure tube length up to 80 m.[10]

The starting transient between the time of diaphragm removal and the establishment of steady flow in the test nozzle decreases the testing time. Warmbrod and Struck[11] determined the starting process in a tube wind tunnel having a test section Mach number $M_{test}=2.0$ by applying a numerical analysis employing the unsteady one-dimensional method of characteristics. The physical arrangement and wave diagram are presented in Fig. 19.58. When the diaphragm is ruptured, a shock wave and a contact surface propagate to the right and an expansion fan propagates

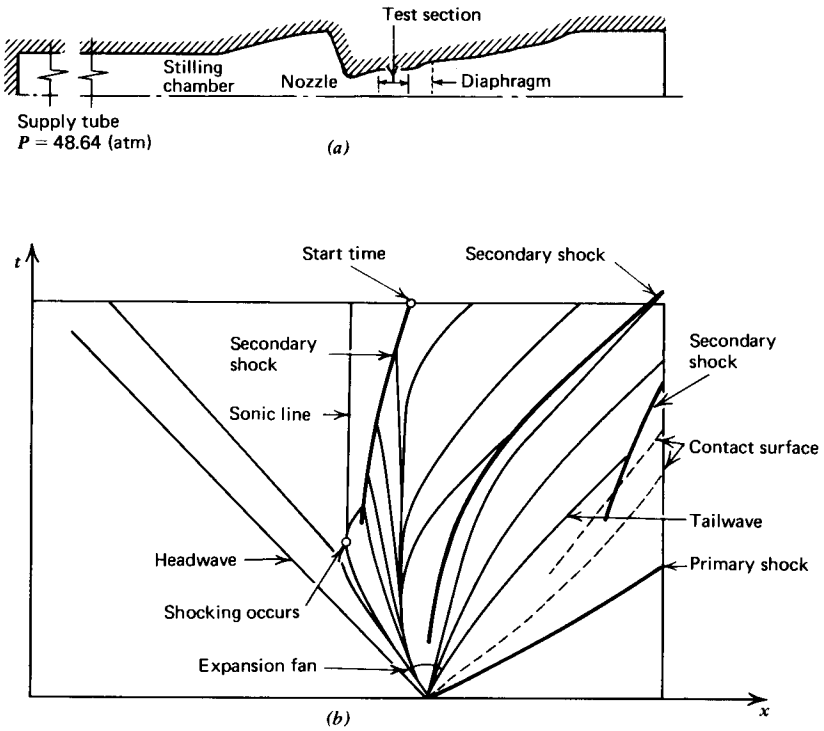

Figure 19.58 Starting process in a tube wind tunnel (Ludwieg tube) (taken from Reference 11).

to the left, as in a conventional shock tube. Because of the variable area of the test nozzle, a secondary shock wave is formed in the nozzle test section and slowly moves downstream through the test section. The starting process is completed when that secondary shock wave leaves the test section. The xt wave diagram presented in Fig. 19.58*b* illustrates the complexity of the starting process.

19–7(d) Steady Flow as the Asymptotic Limit of Unsteady Flow

An important application of unsteady flow analysis is to determine a steady flow field as the asymptotic limit at large time from an unsteady flow field having the same boundary conditions as the steady flow. The application of the aforementioned procedure to the solution of steady one-dimensional flow problems that have a singularity at the sonic point is discussed in Section 9–5(f). Anderson[12] successfully applied that procedure to obtain the solution to the steady one-dimensional flow in a nozzle in the presence of vibrational and chemical nonequilibrium. The aforementioned procedure is also useful for obtaining the solution to multidimensional flows for which the governing steady flow equations are elliptic, but the corresponding unsteady flow equations are hyperbolic. Cline[13] successfully applied the latter procedure to obtain the solutions to steady two-dimensional isentropic nozzle flows for converging, converging-diverging, and plug nozzles. Cline's results are presented in Section 15–5(e). Delaney[14] applied the same procedure to obtain the solutions to steady two-dimensional subsonic and transonic flows in turbine blade cascades. Delaney's results are presented in Section

20–9(b). Anderson and Cline employed fixed grid finite difference methods, whereas Delaney employed the method of characteristics.

Gale[15] employed the method of characteristics for determining the steady one-dimensional isentropic pressure distribution in a diverging conical nozzle having a semiangle of 15 degrees and an expansion ratio of 10. The boundary conditions are a constant stagnation pressure $P = 6.895 \cdot 10^5$ N/m^2 at the nozzle inlet, and an ambient pressure $p_o = 0.1\,P$. The initial conditions are a uniform stagnation pressure $P = 1.013 \cdot 10^5$ N/m^2 and a uniform Mach number $M = 1.22$ throughout the nozzle. Because of the assumed discontinuity in the stagnation pressure at the nozzle inlet, a shock wave is formed at that location. As illustrated in Fig. 19.59, the shock wave propagates through the nozzle quite rapidly, and the flow behind the shock wave approaches the steady flow pressure distribution.

The determination of the flow field for a steady flow as the asymptotic solution at large time for the corresponding unsteady flow is a computational method of

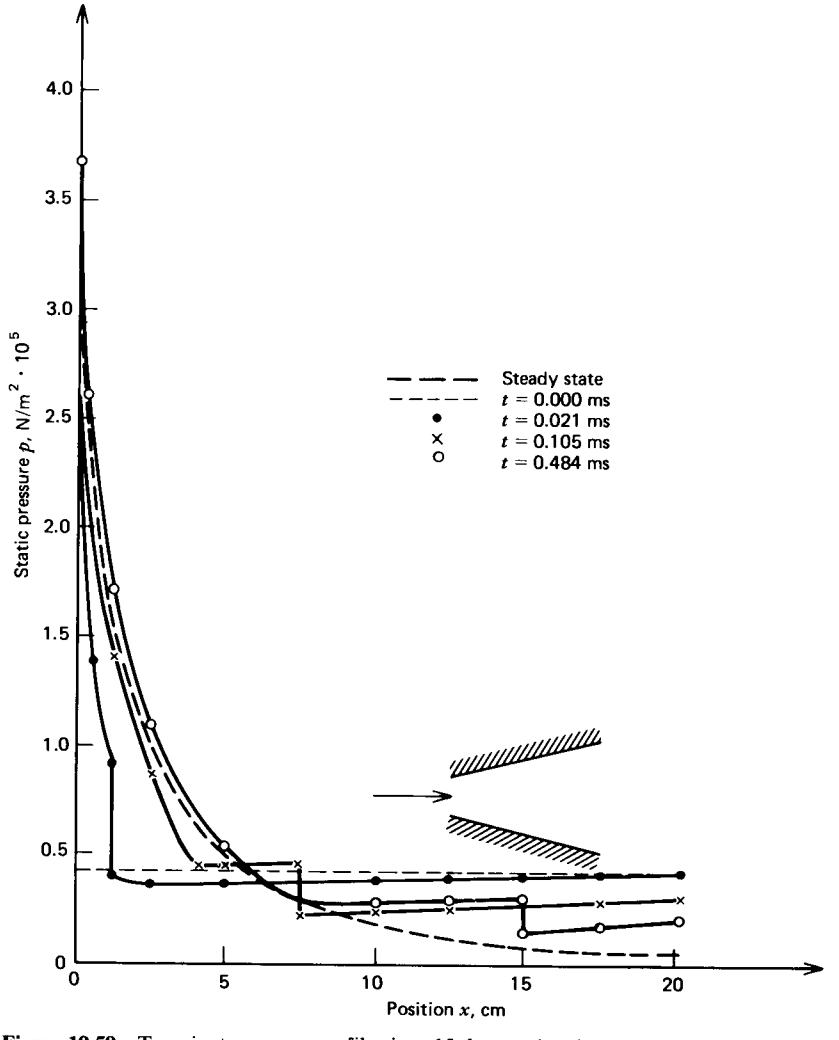

Figure 19.59 Transient pressure profiles in a 15-deg semiangle diverging conical nozzle having an area ratio of 10 (taken from Reference 15).

great value for solving steady one-dimensional flows having singularities, and also for multidimensional steady flows that are governed by elliptic equations but are governed by hyperbolic equations for the corresponding unsteady flows.

REFERENCES

1. R. Courant and K. O. Friedrichs, *Supersonic Flow and Shock Waves*, Chapter III, Interscience Publishers, New York, 1958.
2. G. Rudinger, *Wave Diagrams for Nonsteady Flow in Ducts*, Van Nostrand, Princeton, N. J., 1955.
3. K. P. Stanyukovich, *Unsteady Motion of Continuous Media*, Pergamon Press, New York, 1960.
4. A. H. Shapiro, *The Dynamics and Thermodynamics of Compressible Fluid Flow*, Vol. II, Chapters 23, 24, and 25, Ronald Press, New York, 1953.
5. J. A. Owczarek, *Fundamentals of Gas Dynamics*, Chapters 7 and 8, International Textbook Co., Scranton, Pa., 1964.
6. A. G. Gaydon and I. R. Hurle, *The Shock Tube in High-Temperature Chemical Physics*, Reinhold, New York, 1963.
7. D. R. Hartree, "Some Practical Methods of Using Characteristics in the Calculation of Nonsteady Compressible Flow," U. S. Atomic Energy Commission Report No. AECU-2713, 1953.
8. R. Courant, K. O. Friedrichs, and H. Lewy, " Uberdie Partiellen Differenzialgleichugen der Mathematisehen Physik," *Mathematische Annalen*, Vol. 100, pp. 32–74, 1928.
9. H. Ludwieg, "Der Rohrwindkanal," *Zeitschrift fur Flugwissenschaften*, Vol. 3, No. 7, pp. 206–216, 1955.
10. H. Ludwieg, T. Hottner, and H. Grauer-Cartensen, "Der Rohrwindkanal der Aerodynamischen Versuchsanstalt Göttingen," DFVLR-Aerodynamische Versuchsanstalt Göttingen, 70 A 31, 1970.
11. J. D. Warmbrod and H. Struck, "Application of the Characteristic Method in Calculating the Time Dependent, One-Dimensional, Compressible Flow in a Tube Wind Tunnel," NASA TM X-53769, 1968.
12. J. D. Anderson, Jr., "A Time-Dependent Analysis for Vibrational and Chemical Nonequilibrium Nozzle Flows," *Journal of the American Institute of Aeronautics and Astronautics*, Vol. 8, No. 3, pp. 545–550, March 1970.
13. M. C. Cline, "Computation of Steady Nozzle Flow by a Time Dependent Method," *Journal of the American Institute of Aeronautics and Astronautics*, Vol. 12, No. 4, pp. 419–420, April 1974.
14. R. A. Delaney, "A Second-Order Method of Characteristics for Two-Dimensional Unsteady Flow with Application to Turbomachinery Cascades," Ph. D. Thesis, Iowa State University, 1974.
15. H. W. Gale, "Numerical Analysis of Unsteady Compressible Gas Dynamics of Varied Area Channels: Applied to Gas Dynamic Laser Start," Ph.D. Thesis, Purdue University, May 1974.

20
the method of characteristics applied to steady three-dimensional and unsteady two-dimensional isentropic flow

20–1 PRINCIPAL NOTATION FOR CHAPTER 20

a	speed of sound.
$\mathbf{l}$	vector bicharacteristic ray.
$\mathbf{n}$	unit normal vector to a characteristic surface.
$\mathbf{N}$	normal vector to a characteristic surface.
p	absolute static pressure.
$\mathbf{s}$	distance along a particle path or bicharacteristic ray.
$\mathbf{S}$	vector direction in a stream surface independent of $\mathbf{V}$.
t	time.
u,v,w	velocity components in the Cartesian coordinate system.
U	$=\mathbf{V}\cdot\mathbf{N}$ or $\hat{\mathbf{V}}\cdot\mathbf{N}$.
V	velocity magnitude.
$\mathbf{V}$	velocity vector.
$\hat{\mathbf{V}}$	pseudo-velocity vector.
$\mathbf{W}_j$	vectors defined in Sections 15–4(b) and 15–5(b).
x,y,z	Cartesian coordinates.

Greek Letters

ρ	static density.
σ_i	arbitrary parameters employed in the method of characteristics.

Subscripts

i	$=1,\ldots,n$, denotes a particular σ_i.
j	$=1,\ldots,n$, denotes a particular $\mathbf{W}_j$.
t	denotes directional differentiation along a particle path or a bicharacteristic ray.
x,y,z,t	denotes partial differentiation with respect to that variable, except when x, y, or z are attached to either $\mathbf{N}$ or $\mathbf{n}$.

Operators

$d(\ )$	denotes the total differential of ( ).
$d_{\mathbf{W}_j}(\ )$	denotes the directional derivative of ( ) in the direction of $\mathbf{W}_j$.

20–2 INTRODUCTION

The method of characteristics is applied to flows having two independent variables in Chapters 12, 13, and 16 to 19. In Chapters 12 and 16 to 18, the two independent variables are the two space variables x and y, while in Chapters 13 and 19 the two independent variables are the one space variable x and the time t.

The method of characteristics is applied in this chapter to the following two types of flows having three independent variables.

1. Steady three-dimensional isentropic flow.
2. Unsteady two-dimensional isentropic flow.

For both types of flow, the governing equations are presented, and the characteristic and compatibility equations are determined.

A brief discussion is presented of several numerical algorithms that have been proposed for implementing the numerical solution of flows having three independent variables by the method of characteristics.

Two applications are considered; the steady three-dimensional isentropic flow in supersonic nozzles, and the unsteady two-dimensional isentropic flow in subsonic and transonic turbine cascades.

20–3 GENERAL FEATURES OF THE METHOD OF CHARACTERISTICS FOR THREE INDEPENDENT VARIABLES[1]

The general features of the method of characteristics for two-independent variables are discussed in Section 12 – 3. From the viewpoint of numerical computation, the advantage of the method of characteristics is that it permits reducing a system of partial differential equations in two independent variables to a system of ordinary differential equations that are valid along the characteristic curves. Moreover, the system of ordinary differential equations may then be integrated in a relatively straightforward manner by the numerical techniques that are applicable to ordinary differential equations.

When the flow involves three independent variables, such as either x, y, and z for a steady three-dimensional flow, or x, y, and t for an unsteady two-dimensional flow, it becomes necessary to deal with characteristic surfaces in space instead of characteristic curves in a plane. A surface is specified by its normal at the point being studied and its corresponding tangent plane. As a result, the analysis of a flow involving three independent variables becomes complicated by the geometry pertaining to surfaces, and the simplicity of the method of characteristics, when applied in two-dimensional flows, is significantly reduced.

Furthermore, the governing partial differential equations for a flow involving three independent variables cannot be reduced to a system of ordinary differential equations as can the corresponding equations for flows involving only two independent variables. Instead, the governing differential equations may be reduced to an *interior operator* [see Section 12–3(a)] in a surface of the three-dimensional space; that is, they are transformed into a system of partial differential equations valid in a two-dimensional surface termed a *characteristic surface*. Consequently, any applicable method of numerical integration must take into account the pertinent derivatives in two independent directions.

For flows with three independent variables (i.e., three space variables or two space variables and time), the characteristic surfaces comprise two families of surfaces. For steady three-dimensional flow, the characteristic surfaces in the xyz

space are the surfaces tangent to the local Mach conoid, called the *wave surfaces*, and the surfaces composed of the streamlines, called the *stream surfaces*. For unsteady two-dimensional flow, the characteristic surfaces in xyt space are the *wave surfaces* tangent to the local Mach conoid, and the *stream surfaces* composed of the pathlines. The lines of tangency between the wave surfaces and the Mach conoid are called *bicharacteristics*. Consequently, in both types of flow, there are two infinite families of characteristic surfaces. On those characteristic surfaces, the system of partial differential equations in three variables reduces to a system of partial differential equations in two variables. Numerical integration on such surfaces is less complex than integration on noncharacteristic surfaces where we must deal with the derivatives with respect to each of the three independent variables.

Any numerical algorithm based on the method of characteristics employs the fact that the original system of partial differential equations may be replaced by an equivalent system of independent compatibility equations that are applicable on the characteristic surfaces. The number of independent compatibility equations cannot exceed the number of partial differential equations comprising the original system of equations. For a complete system that number will equal the number of dependent variables. Rusanov[2] determined the number of independent compatibility equations that apply on both the stream surfaces and the wave surfaces for a steady three-dimensional flow, and also for an unsteady two-dimensional flow. Those results are discussed in Sections 20–4(d) and 20–5(d), respectively.

The procedure for determining the characteristic surfaces and the corresponding compatibility equations is discussed in Section 20–4 for steady three-dimensional isentropic flow,[3–6] and in Section 20–5 for unsteady two-dimensional isentropic flow.[7].

20–4 STEADY THREE-DIMENSIONAL ISENTROPIC FLOW[3–6]

In the present section, the governing equations for steady three-dimensional isentropic flow are presented, and the equations for the characteristic surfaces and the corresponding compatibility equations are determined.

20–4(a) Governing Equations

The governing equations in Cartesian coordinates for the steady three-dimensional isentropic flow of an inviscid compressible fluid are obtained from Table 10.2. Those equations are the momentum equations, equations 10.172, the continuity equation, equation 10.171, and the speed of sound equation, equation 10.173b. Thus,

$$\rho u u_x + \rho v u_y + \rho w u_z + p_x = 0 \tag{20.1}$$

$$\rho u v_x + \rho v v_y + \rho w v_z + p_y = 0 \tag{20.2}$$

$$\rho u w_x + \rho v w_y + \rho w w_z + p_z = 0 \tag{20.3}$$

$$\rho u_x + \rho v_y + \rho w_z + u\rho_x + v\rho_y + w\rho_z = 0 \tag{20.4}$$

$$u p_x + v p_y + w p_z - a^2(u\rho_x + v\rho_y + w\rho_z) = 0 \tag{20.5}$$

where $a = a(p, \rho)$. Equations 20.1 to 20.5 comprise a set of five first-order homogeneous partial differential equations for determining the five flow properties u, v, w, p, and ρ.

20–4(b) Characteristic and Compatibility Equations

The characteristic and compatibility equations corresponding to equations 20.1 to 20.5 are determined by multiplying those equations by the unknown parameters σ_1 to σ_5, respectively, and summing. The result is the following equation.

$$\sigma_1(20.1) + \sigma_2(20.2) + \sigma_3(20.3) + \sigma_4(20.4) + \sigma_5(20.5) = 0 \tag{20.6}$$

Performing the summation indicated in equation 20.6 and collecting the coefficients of like terms, we obtain

$$\begin{aligned}
&\rho(u\sigma_1 + \sigma_4)u_x + \rho v\sigma_1 u_y + \rho w\sigma_1 u_z \\
&\quad + \rho u\sigma_2 v_x + \rho(v\sigma_2 + \sigma_4)v_y + \rho w\sigma_2 v_z \\
&\quad + \rho u\sigma_3 w_x + \rho v\sigma_3 w_y + \rho(w\sigma_3 + \sigma_4)w_z \\
&\quad + (\sigma_1 + u\sigma_5)p_x + (\sigma_2 + v\sigma_5)p_y + (\sigma_3 + w\sigma_5)p_z \\
&\quad + u(\sigma_4 - a^2\sigma_5)\rho_x + v(\sigma_4 - a^2\sigma_5)\rho_y + w(\sigma_4 - a^2\sigma_5)\rho_z = 0
\end{aligned} \tag{20.7}$$

By *definition*, the following set of vectors $\mathbf{W}_j$ $(j = 1, \ldots, 5)$ have for their components in the Cartesian coordinate system the coefficients of the partial derivatives in equation 20.7. Thus,

$$\mathbf{W}_1 = \mathbf{i}\rho(u\sigma_1 + \sigma_4) + \mathbf{j}\rho v\sigma_1 + \mathbf{k}\rho w\sigma_1 \tag{20.8}$$

$$\mathbf{W}_2 = \mathbf{i}\rho u\sigma_2 + \mathbf{j}\rho(v\sigma_2 + \sigma_4) + \mathbf{k}\rho w\sigma_2 \tag{20.9}$$

$$\mathbf{W}_3 = \mathbf{i}\rho u\sigma_3 + \mathbf{j}\rho v\sigma_3 + \mathbf{k}\rho(w\sigma_3 + \sigma_4) \tag{20.10}$$

$$\mathbf{W}_4 = \mathbf{i}(\sigma_1 + u\sigma_5) + \mathbf{j}(\sigma_2 + v\sigma_5) + \mathbf{k}(\sigma_3 + w\sigma_5) \tag{20.11}$$

$$\mathbf{W}_5 = \mathbf{i}u(\sigma_4 - a^2\sigma_5) + \mathbf{j}v(\sigma_4 - a^2\sigma_5) + \mathbf{k}w(\sigma_4 - a^2\sigma_5) \tag{20.12}$$

Equation 20.7 may, therefore, be transformed to read

$$d_{\mathbf{W}_1}u + d_{\mathbf{W}_2}v + d_{\mathbf{W}_3}w + d_{\mathbf{W}_4}p + d_{\mathbf{W}_5}\rho = 0 \tag{20.13}$$

where $d_{\mathbf{W}_1}u$ is *defined* as the derivative of u in the direction of the vector $\mathbf{W}_1$, etc. Equation 20.13 is the compatibility equation for steady three-dimensional flow.

The following question is now posed. Can the σ_i $(i = 1, \ldots, 5)$ be chosen such that the vectors $\mathbf{W}_j$ $(j = 1, \ldots, 5)$ are linearly dependent, or, in other words, so that all of the vectors $\mathbf{W}_j$ lie in the same surface? If such σ_i do exist, then the surface that contains the vectors $\mathbf{W}_j$ is called the *characteristic surface*, its normal $\mathbf{N}$ (at each point on the surface) is called the *characteristic normal*, and equation 20.13 becomes an *interior operator* in the surface. Equation 20.13 is called the *compatibility condition* corresponding to a given characteristic surface.

The normal to a characteristic surface is defined as $\mathbf{N} = \mathbf{i}N_x + \mathbf{j}N_y + \mathbf{k}N_z$, where N_x, N_y, and N_z are the components of $\mathbf{N}$ parallel to the x, y, and z axes,

respectively. Since all of the vectors $\mathbf{W}_j$ lie in the characteristic surface, the vector $\mathbf{N}$ is perpendicular to the vectors $\mathbf{W}_j$. Consequently, their scalar product must equal zero. Hence,

$$\mathbf{N}\cdot\mathbf{W}_j=0 \qquad (j=1,\ldots,5) \tag{20.14}$$

Writing $\mathbf{N}$ and the vectors $\mathbf{W}_j$ (see equations 20.8 to 20.12) in their component forms, performing the corresponding scalar products indicated by equation 20.14, and letting

$$U\equiv uN_x+vN_y+wN_z=\mathbf{V}\cdot\mathbf{N} \tag{20.15}$$

five equations are obtained that may be written in matrix form as follows.

$$\begin{vmatrix} \rho U & 0 & 0 & \rho N_x & 0 \\ 0 & \rho U & 0 & \rho N_y & 0 \\ 0 & 0 & \rho U & \rho N_z & 0 \\ N_x & N_y & N_z & 0 & U \\ 0 & 0 & 0 & U & -a^2U \end{vmatrix} \begin{vmatrix} \sigma_1 \\ \sigma_2 \\ \sigma_3 \\ \sigma_4 \\ \sigma_5 \end{vmatrix} = 0 \tag{20.16}$$

Equation 20.16 represents a system of five linear homogeneous algebraic equations.

For equation 20.16 to have a nontrivial solution, the coefficient matrix must be singular, or in other words, its determinant must equal zero. Setting the determinant of the coefficient matrix of equation 20.16 equal to zero yields

$$(uN_x+vN_y+wN_z)^3\left[(uN_x+vN_y+wN_z)^2-a^2\left(N_x^2+N_y^2+N_z^2\right)\right]=0 \tag{20.17}$$

In equation 20.17 the velocity components u, v, and w are related to the fluid velocity $\mathbf{V}$ by $\mathbf{V}=\mathbf{i}u+\mathbf{j}v+\mathbf{k}w$, and the characteristic normal $\mathbf{N}$ may be expressed in terms of its components by $\mathbf{N}=\mathbf{i}N_x+\mathbf{j}N_y+\mathbf{k}N_z$.

For a steady three-dimensional isentropic flow, the characteristic surfaces are defined by equation 20.17, and the corresponding compatibility equation is equation 20.13.

20–4(c) Characteristic Surfaces

The characteristic surfaces are determined by solving equation 20.17 for the characteristic normal $\mathbf{N}$, and then determining the equation of the surface that is everywhere normal to $\mathbf{N}$. Equation 20.17 comprises a linear factor repeated three times multiplied by a quadratic factor. Setting either of those factors equal to zero satisfies equation 20.17, and yields an equation for determining $\mathbf{N}$.

Consider the first factor of equation 20.17. Setting that factor equal to zero, we obtain

$$uN_x+vN_y+wN_z=\mathbf{V}\cdot\mathbf{N}=0 \qquad (\textit{repeated three times}) \tag{20.18}$$

Because the actual magnitude of the characteristic normal $\mathbf{N}$ is immaterial, it may be replaced by its unit normal $\mathbf{n}=\mathbf{i}n_x+\mathbf{j}n_y+\mathbf{k}n_z$, where n_x, n_y, and n_z are the components of $\mathbf{n}$ in the x, y, and z directions, respectively. Hence,

$$\mathbf{n}\cdot\mathbf{n}=n_x^2+n_y^2+n_z^2=1 \tag{20.19}$$

Equation 20.18 may, therefore, be rewritten in the form

$$un_x + vn_y + wn_z = \mathbf{V} \cdot \mathbf{n} = 0 \tag{20.20}$$

Equations 20.19 and 20.20 are two equations relating the three components of the *characteristic unit normal* **n**. The remaining condition needed for determining **n** is arbitrary. Consequently, instead of a uniquely determined characteristic normal **n**, there is an infinite family of characteristic normals.

A physical interpretation of equations 20.19 and 20.20 may be obtained by assuming that the origin of the Cartesian coordinate system x,y,z is located at the point in space under consideration. The unit vector **n** thus originates at the origin, and the components of **n** (i.e., n_x, n_y, and n_z) correspond to the Cartesian coordinates x, y, and z. In that form, it is obvious that equation 20.19 is the equation of a unit sphere with its center at the origin, and equation 20.20 is the equation of a plane passing through the origin, where the orientation of the plane depends on the magnitude of the velocity components u, v, and w of the fluid. The locus of the end points of the characteristic unit normals is, therefore, the circle formed by the intersection of the plane and the unit sphere, as illustrated in Fig. 20.1. Since the unit normals **n** originate at the origin and the plane specified by equation 20.19 passes through the origin, all of the unit normals lie within that plane. That plane is called the *plane of normals*.

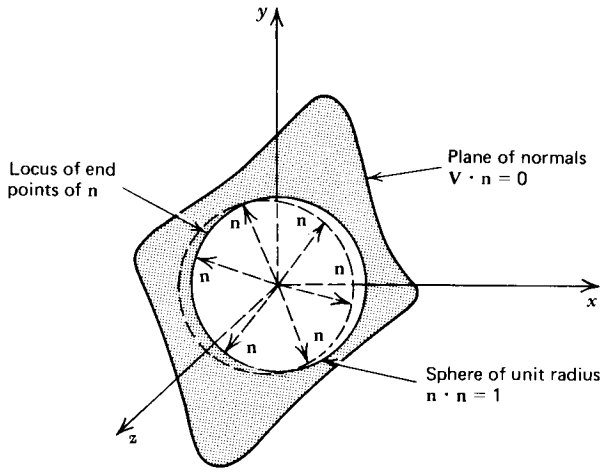

Figure 20.1 Plane of normals corresponding to stream surfaces in steady three-dimensional flow.

Equation 20.20 shows that the characteristic normal corresponding to the first factor in equation 20.17 is normal to a surface containing the streamline; the latter surface is called a *stream surface*. Figure 20.2 illustrates the stream surface corresponding to a particular characteristic normal **N**, or its unit normal **n**. At each point in space there is an infinite number of stream surfaces corresponding to the infinite number of characteristic normals.

The envelope formed by the infinite number of stream surfaces is the streamline. Let t denote the time of travel of a fluid particle along the streamline. Then the equations for the streamline in terms of the velocity components u, v, and w and

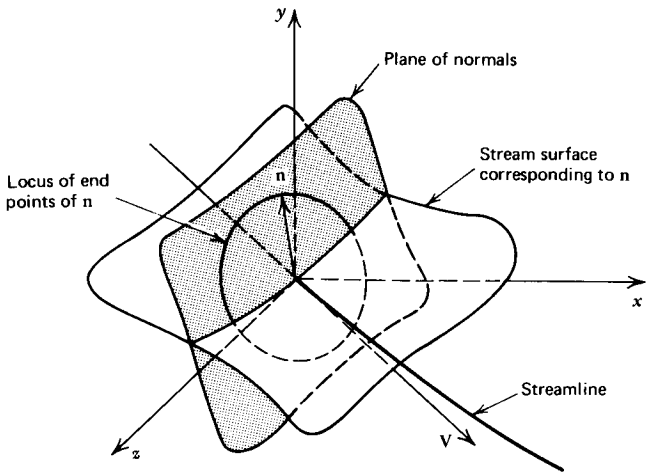

Figure 20.2 Stream surface corresponding to a particular characteristic normal.

the time t, are

$$\frac{dx}{dt} = u \qquad \frac{dy}{dt} = v \qquad \frac{dz}{dt} = w \tag{20.21}$$

The differential vector distance $d\mathbf{s}$ in any arbitrary direction is given by

$$d\mathbf{s} = \mathbf{i}\,dx + \mathbf{j}\,dy + \mathbf{k}\,dz \tag{20.22}$$

Along a streamline, dx, dy, and dz are given by equation 20.21. Consequently, $d\mathbf{s}$ along a streamline is given by

$$d\mathbf{s} = (\mathbf{i}u + \mathbf{j}v + \mathbf{k}w)\,dt = \mathbf{V}\,dt \tag{20.23}$$

where t denotes the time of travel of a fluid particle along the streamline.

Consider now the second factor in equation 20.17. Setting that factor equal to zero yields

$$(uN_x + vN_y + wN_z)^2 - a^2(N_x^2 + N_y^2 + N_z^2) = 0 \tag{20.24}$$

Rearranging equation 20.24 and taking the square root, we obtain

$$uN_x + vN_y + wN_z = \pm a(N_x^2 + N_y^2 + N_z^2)^{1/2} = \pm a|N| \tag{20.25}$$

where the choice of the positive or negative root is arbitrary. The sign merely determines the sense of $\mathbf{N}$ along the direction specified by the components of $\mathbf{N}$. Since the magnitude of $\mathbf{N}$ is immaterial, it may be replaced by the unit normal $\mathbf{n} = \mathbf{i}n_x + \mathbf{j}n_y + \mathbf{k}n_z$ to the characteristic surface. Hence,

$$\mathbf{n} \cdot \mathbf{n} = n_x^2 + n_y^2 + n_z^2 = 1 \tag{20.26}$$

Equation 20.25, with $\mathbf{N}$ replaced by $\mathbf{n}$, may, therefore, be written in the form

$$un_x + vn_y + wn_z = \mathbf{V} \cdot \mathbf{n} = \pm a \tag{20.27}$$

Equations 20.26 and 20.27 are two equations for determining the components of the characteristic unit normal **n**. Since the remaining condition needed for determining **n** is arbitrary, there is an infinite family of characteristic normals.

As discussed above for the stream surfaces, equation 20.26 is the equation for a unit sphere having the characteristic unit normal **n** emanating from its center, and equation 20.27 is the equation of a plane, where the orientation of the plane depends on the magnitudes of the velocity components u, v, and w and the speed of sound a of the fluid. The plane specified by equation 20.27 does not, however, pass through the center of the unit sphere in this case. The locus of the end points of the characteristic unit normals is, therefore, the circular curve formed by the intersection of the plane and the unit sphere, as illustrated in Fig. 20.3. The unit normals **n** originate at the center of the sphere, but the plane specified by equation 20.27 does not pass through the center of the sphere. Consequently, the infinite family of characteristic unit normals **n** forms a cone. That cone, illustrated in Fig. 20.4, is termed the *cone of normals*.

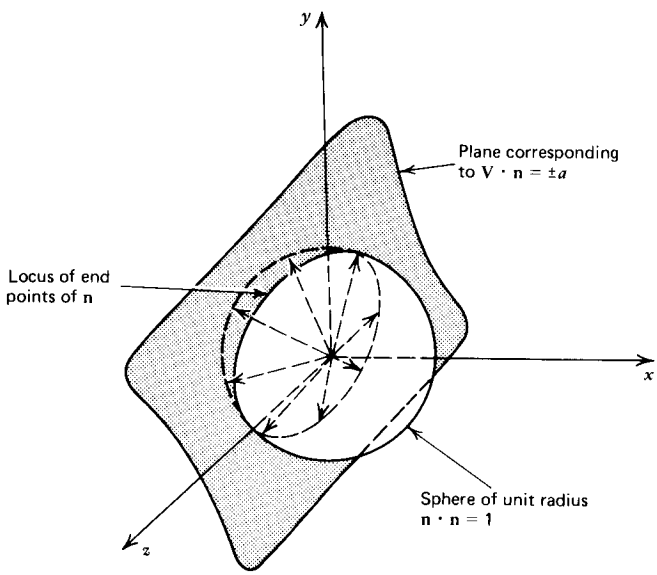

Figure 20.3 Locus of the end points of **n**.

Equation 20.27 shows that the magnitude of the component of the fluid velocity normal to a characteristic surface is equal to the local speed of sound a. Each such characteristic surface is called a *wave surface*. Figure 20.5 illustrates the wave surfaces corresponding to two particular characteristic normals. At each point in space there is an infinity of wave surfaces corresponding to the infinite number of characteristic normals.

The envelope formed by the infinity of wave surfaces is called the *characteristic manifold* or *Mach conoid*. At a point, the Mach conoid is tangent to the *Mach cone*, which is the *reciprocal cone* to the *cone of normals*. The determination of the equation of the Mach conoid is a straightforward, although lengthy, exercise in differential geometry that is not presented here.[33,34] For the present case, the

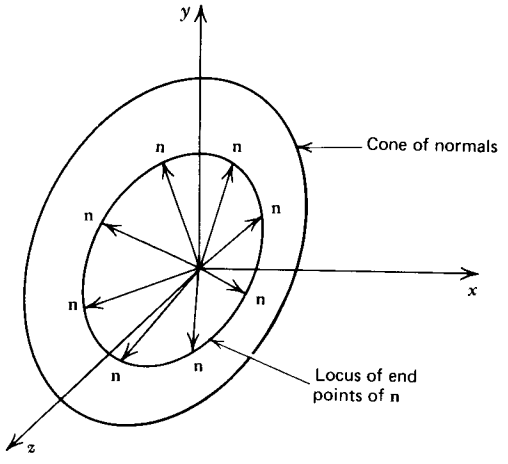

Figure 20.4 The cone of normals.

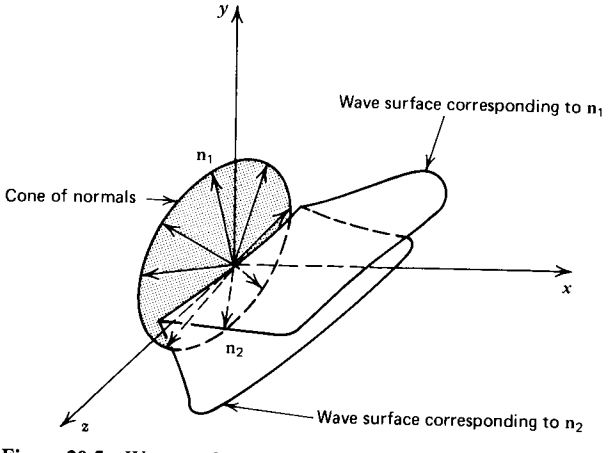

Figure 20.5 Wave surfaces corresponding to two particular characteristic normals.

equation of the Mach conoid is[3,5]

$$\begin{aligned}&\left[u^2-(V^2-a^2)\right](dx)^2+\left[v^2-(V^2-a^2)\right](dy)^2\\&\quad+\left[w^2-(V^2-a^2)\right](dz)^2+2uv(dx)(dy)\\&\quad+2uw(dx)(dz)+2vw(dy)(dz)=0\end{aligned}\tag{20.28}$$

where V is the *velocity magnitude*. Equation 20.28 determines the Mach conoid or characteristic manifold. The Mach conoid is real only if the quantity (V^2-a^2) is positive; that is, if the flow is supersonic. The curves of tangency between the wave surfaces and the Mach conoid are called the *bicharacteristics*.

The Mach cone corresponding to the Mach conoid specified by equation 20.28 is a right circular cone, whose axis is the tangent to the streamline at the vertex of the cone. The intersections of the Mach cone with surfaces perpendicular to its axis are circles. That the Mach cone is a right circular cone may be substantiated by the

physical interpretation of the Mach conoid as the envelope of all of the acoustic waves created by a small disturbance moving along a streamline at the velocity of the fluid particles. For example, in a uniform flow field parallel to the x axis, all of the streamlines are straight lines and all of the acoustic waves are spherical waves of constant speed emanating from successive points along the streamline and propagating outward into the xyz space, as illustrated in Fig. 20.6. The envelope of the acoustic waves is the Mach conoid, which is obviously a right circular cone in the uniform flow case. The Mach cone, which is the local tangent cone to the Mach conoid, is identical to the Mach conoid in this case, and is also a right circular cone. In a nonuniform flow field, the streamlines are not straight lines and the speed of the acoustic waves is not constant. The envelope of the acoustic waves, that is, the Mach conoid, is not a right circular cone in this case, illustrated in Fig. 20.7. The local tangent cone to the Mach conoid at each point in the flow field,

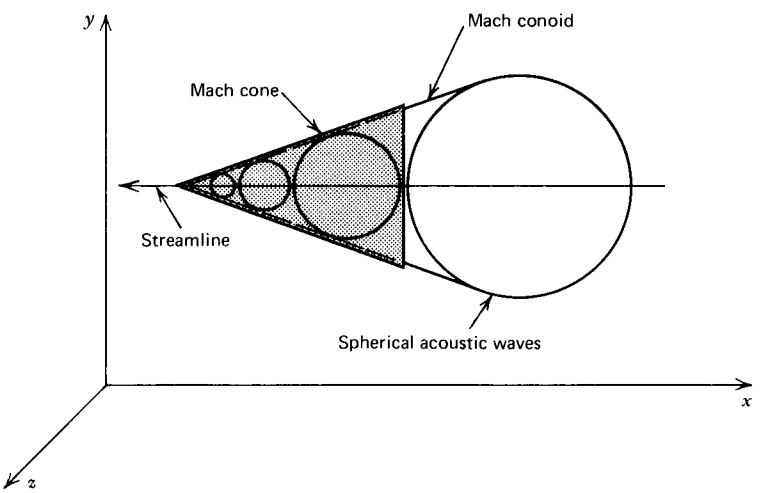

Figure 20.6 The Mach conoid and the Mach cone in a uniform steady three-dimensional flow field.

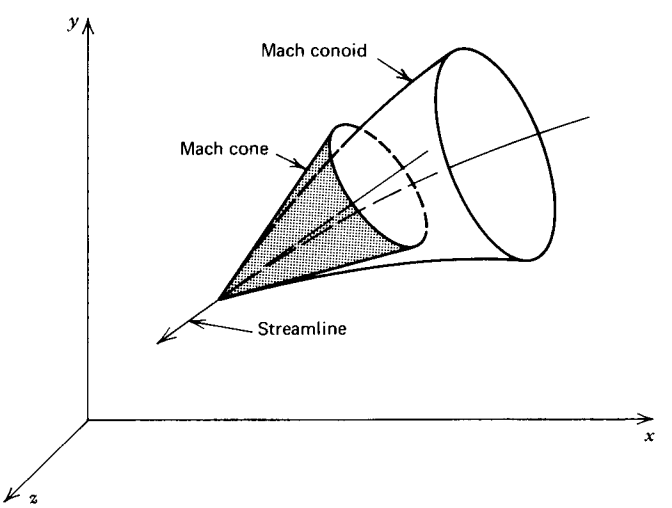

Figure 20.7 The Mach conoid and the Mach cone in a nonuniform steady three-dimensional flow field.

that is, the Mach cone, is, however, a right circular cone even in the nonuniform flow case. By contrast in unsteady two-dimensional flow [see Section 20–5(c)], the Mach cone is an oblique cone. The intersections of the Mach cone with the surfaces $t =$ constant are circles, while the intersections with the surfaces perpendicular to the axis of the cone are ellipses.

Figure 20.8 illustrates diagrammatically the relationship between the two families of wave surfaces, the stream surface, the Mach conoid, and two bicharacteristics, for an arbitrary point $P(x,y,z)$ on a *spacelike curve*; the latter is any curve located outside of the Mach conoid. It is seen that a single stream surface and two wave surfaces pass through the spacelike curve. If the spacelike curve is rotated through 360 degrees, the envelope of the infinity of stream surfaces defines the *streamline*, and the envelope of the infinity of wave surfaces defines the *Mach conoid*. The streamline and the bicharacteristics for a steady three-dimensional flow are analogous to the streamline and the Mach lines for a steady two-dimensional flow [see Section 17–3(b)].

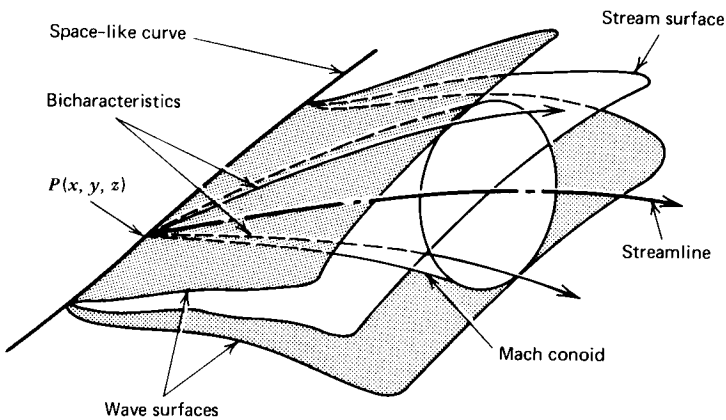

Figure 20.8 Stream surfaces, wave surfaces, streamline, Mach conoid, and bicharacteristics in steady three-dimensional supersonic flow.

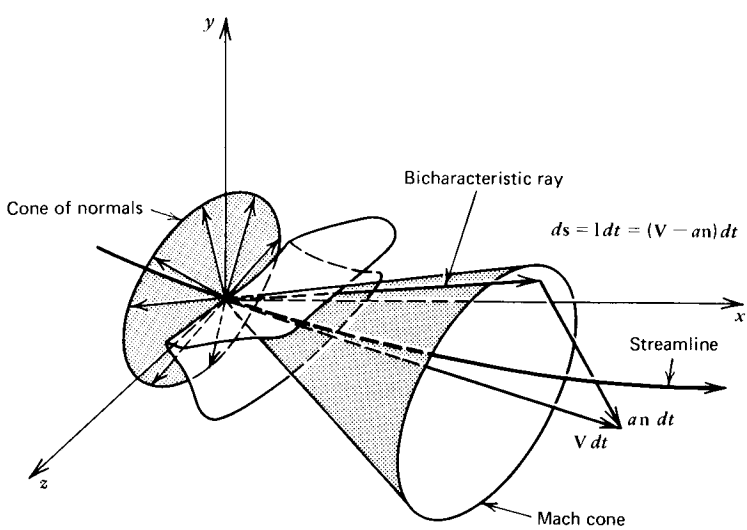

Figure 20.9 The Mach cone.

The geometry of the Mach cone is illustrated in Fig. 20.9, where $\mathbf{V}dt$, the distance traveled by a fluid particle during the time dt, is the axis of the Mach cone, $a\mathbf{n}\,dt$ is the distance traveled by an acoustic wave in the direction of the normal $\mathbf{n}$ during the time dt, and $d\mathbf{s}=\mathbf{l}\,dt$ is the corresponding ray along the bicharacteristic. The vector $\mathbf{l}$ is defined as

$$\mathbf{l}\equiv\mathbf{V}-a\mathbf{n}=\mathbf{i}(u-an_x)+\mathbf{j}(v-an_y)+\mathbf{k}(w-an_z) \tag{20.29}$$

Consequently, $d\mathbf{s}$ along a bicharacteristic ray is given by

$$d\mathbf{s}=\left[\mathbf{i}(u-an_x)+\mathbf{j}(v-an_y)+\mathbf{k}(w-an_z)\right]dt \tag{20.30}$$

where t denotes the time of travel of a fluid particle along the streamline that is the axis of the Mach cone.

20–4(d) Compatibility Equations

The method of characteristics determines the surfaces in the flow field along which the governing partial differential equations reduce to interior operators; that is, the direction of differentiation lies within the surface. For three-dimensional steady flow, those surfaces are the stream surfaces and the wave surfaces, illustrated in Fig. 20.8. The interior operator (i.e., the compatibility equation) valid on each of those surfaces is given by equation 20.13. To employ the compatibility equation, the unknown parameters σ_i must be determined.

Consider first the stream surface defined by equation 20.18. Substituting equation 20.18 into equation 20.16 yields

$$\begin{vmatrix} 0 & 0 & 0 & \rho N_x & 0 \\ 0 & 0 & 0 & \rho N_y & 0 \\ 0 & 0 & 0 & \rho N_z & 0 \\ N_x & N_y & N_z & 0 & 0 \\ 0 & 0 & 0 & 0 & 0 \end{vmatrix} \begin{vmatrix} \sigma_1 \\ \sigma_2 \\ \sigma_3 \\ \sigma_4 \\ \sigma_5 \end{vmatrix} = 0 \tag{20.31}$$

The rank of the coefficient matrix of equation 20.31 is two.* Consequently, there are three independent solutions for the σ_i on the stream surfaces. Expanding equation 20.31, it is seen that σ_4 equals zero, σ_5 is arbitrary, and σ_1, σ_2, and σ_3 must satisfy the relationship

$$\sigma_1 N_x+\sigma_2 N_y+\sigma_3 N_z=0 \tag{20.32}$$

Three possible solutions for the σ_i that satisfy equation 20.32 are

$$\sigma_1=u \qquad \sigma_2=v \qquad \sigma_3=w \qquad \sigma_4=\sigma_5=0 \tag{20.33}$$

$$\sigma_1=\sigma_2=\sigma_3=\sigma_4=0 \qquad \sigma_5 \text{ is arbitrary} \tag{20.34}$$

$$\sigma_1=S_x \qquad \sigma_2=S_y \qquad \sigma_3=S_z \qquad \sigma_4=\sigma_5=0 \tag{20.35}$$

where $\mathbf{S}=\mathbf{i}S_x+\mathbf{j}S_y+\mathbf{k}S_z$ is any vector in the stream surface that is not parallel to

*The largest matrix, in the main matrix, that has a determinant which does not equal zero, is a 2×2 matrix.

the velocity vector, and S_x, S_y, and S_z are the components of **S** in the x, y, and z directions, respectively. Equation 20.33 is obtained by comparing equation 20.18 and equation 20.32. Equation 20.33 applies on all of the stream surfaces (i.e., for all values of **N**), since the same values for the σ_i satisfy equation 20.32 for all values of **N** (see equation 20.18). The same conclusion is true for the set of σ_i defined by equation 20.34. Consequently, the two sets of solutions for the σ_i specified by equations 20.33 and 20.34 apply along the envelope of the stream surfaces, which is the streamline [see Section 20–4(c)], and the two compatibility equations corresponding to equations 20.33 and 20.34 apply along the streamline. The set of σ_i defined by equation 20.35, however, depends on the value of **N**, since for each value of **N** corresponding to a particular stream surface, a different value for **S** is obtained. Consequently, the corresponding compatibility equation is applicable only in that stream surface. Thus, an infinite number of compatibility equations are obtained for the set of σ_i defined by equation 20.35.

Substituting equations 20.33 to 20.35 into equation 20.7 yields the following three compatibility equations that are valid on the stream surfaces.

$$\rho u(uu_x + vu_y + wu_z) + \rho v(uv_x + vv_y + wv_z) + \rho w(uw_x + vw_y + ww_z) + (up_x + vp_y + wp_z) = 0 \tag{20.36}$$

$$up_x + vp_y + wp_z - a^2(u\rho_x + v\rho_y + w\rho_z) = 0 \tag{20.37}$$

$$\rho S_x(uu_x + vu_y + wu_z) + \rho S_y(uv_x + vv_y + wv_z) + \rho S_z(uw_x + vw_y + ww_z) + (S_x p_x + S_y p_y + S_z p_z) = 0 \tag{20.38}$$

Equations 20.36 to 20.38 are differential operators within the stream surface. Since there are only two independent directions of differentiation within a surface in three-dimensional space, equations 20.36 to 20.38, which are written in terms of partial derivatives with respect to the *three* Cartesian coordinate directions, may be written in terms of partial derivatives with respect to any *two* independent directions within the stream surface. In fact, equations 20.36 and 20.37 may be written in terms of *total* derivatives in the direction of the streamline.

Consider the general function $f(x,y,z)$. The total derivative of f is given by

$$df = f_x\,dx + f_y\,dy + f_z\,dz \tag{20.39}$$

Equation 20.39 may be written as

$$df = \nabla f \cdot d\mathbf{s} \tag{20.40}$$

where $d\mathbf{s}$ is the differential vector distance

$$d\mathbf{s} = \mathbf{i}\,dx + \mathbf{j}\,dy + \mathbf{k}\,dz \tag{20.41}$$

Along a streamline, $d\mathbf{s}$ is given by equation 20.23. Consequently, equation 20.40 becomes

$$df = \nabla f \cdot \mathbf{V}\,dt \tag{20.42}$$

which may be written as

$$f_t = \frac{df}{dt} = \nabla f \cdot \mathbf{V} = uf_x + vf_y + wf_z \tag{20.43}$$

where t denotes the time of travel of a fluid particle along a streamline, and f_t denotes the directional derivative of f along the streamline.

The terms inside of the parentheses in equations 20.36 and 20.37 are of the same form as equation 20.43. Consequently, those terms may be written as directional derivatives along the streamline. Thus, equations 20.36 and 20.37 may be written as

$$\rho u u_t + \rho v v_t + \rho w w_t + p_t = 0 \qquad (\textit{along the streamline}) \tag{20.44}$$

$$p_t - a^2 \rho_t = 0 \qquad (\textit{along the streamline}) \tag{20.45}$$

where $u_t = du/dt = (uu_x + vu_y + wu_z)$, etc., and t denotes the time of travel of a fluid particle along a streamline. Equation 20.38 cannot be written as a directional derivative along the streamline since, by definition, **S** is a vector in the stream surface that is *not* parallel to the velocity vector **V**.

Consider next the wave surfaces specified by equation 20.27. Again, the σ_i must be determined. Substituting equation 20.27 into equation 20.16, where the positive root is chosen arbitrarily and **N** has been replaced by **n**, we obtain

$$\begin{vmatrix} \rho a & 0 & 0 & \rho n_x & 0 \\ 0 & \rho a & 0 & \rho n_y & 0 \\ 0 & 0 & \rho a & \rho n_z & 0 \\ n_x & n_y & n_z & 0 & a \\ 0 & 0 & 0 & a & -a^3 \end{vmatrix} \begin{vmatrix} \sigma_1 \\ \sigma_2 \\ \sigma_3 \\ \sigma_4 \\ \sigma_5 \end{vmatrix} = 0 \tag{20.46}$$

The rank of the coefficient matrix of equation 20.46 is four.* Consequently, there is only one independent solution for the σ_i. Letting $\sigma_5 = -1$ yields the following solution for the σ_i.

$$\sigma_1 = an_x \qquad \sigma_2 = an_y \qquad \sigma_3 = an_z \qquad \sigma_4 = -a^2 \qquad \sigma_5 = -1 \tag{20.47}$$

The compatibility equation for the wave surface is obtained by substituting equation 20.47 into the general compatibility equation, equation 20.7. Thus,

$$\rho a n_x (uu_x + vu_y + wu_z) + \rho a n_y (uv_x + vv_y + wv_z) + \rho a n_z (uw_x + vw_y + ww_z)$$

$$+ (an_x - u) p_x + (an_y - v) p_y + (an_z - w) p_z - \rho a^2 (u_x + v_y + w_z) = 0 \tag{20.48}$$

Equation 20.48 represents a differential operator within the wave surface. There are only two independent directions of differentiation within a surface in three-dimensional space. Consequently, equation 20.48, which is written in terms of partial derivatives with respect to the *three* Cartesian coordinate directions, may be written in terms of partial derivatives with respect to any *two* independent directions within the wave surface. Those two independent directions may be chosen as the direction of the bicharacteristic (i.e., the tangent to a ray of the Mach conoid) and the normal to the bicharacteristic within the wave surface.

The total derivative of a general function $f(x,y,z)$ is given by equation 20.40, where $d\mathbf{s}$ is given by equation 20.41. Along a bicharacteristic ray, $d\mathbf{s}$ is given by

*The largest matrix, in the main matrix, that has a determinant which does not equal zero, is a 4×4 matrix.

equation 20.30. Consequently, equation 20.40 may be written as

$$f_t = \frac{df}{dt} = \nabla f \cdot \mathbf{l} = (u - an_x) f_x + (v - an_y) f_y + (w - an_z) f_z \tag{20.49}$$

where t denotes the time of travel of a fluid particle along the streamline that is the axis of the Mach cone, and f_t denotes the directional derivative of f along a bicharacteristic ray.

The following term may be added to and subtracted from equation 20.48.

$$\pm \left\{ \rho a^2 \left[n_x^2 u_x + n_y^2 v_y + n_z^2 w_z + (u_y + v_x) n_x n_y + (u_z + w_x) n_x n_z + (v_z + w_y) n_y n_z \right] \right\}$$

The result is

$$\begin{aligned}
&\rho a n_x \left[(u - an_x) u_x + (v - an_y) u_y + (w - an_z) u_z \right] \\
&\quad + \rho a n_y \left[(u - an_x) v_x + (v - an_y) v_y + (w - an_z) v_z \right] \\
&\quad + \rho a n_z \left[(u - an_x) w_x + (v - an_y) w_y + (w - an_z) w_z \right] \\
&\quad - \left[(u - an_x) p_x + (v - an_y) p_y + (w - an_z) p_z \right] \\
&\quad + \rho a^2 \left[(n_x^2 - 1) u_x + (n_y^2 - 1) v_y + (n_z^2 - 1) w_z \right. \\
&\quad \left. + (u_y + v_x) n_x n_y + (u_z + w_x) n_x n_z + (v_z + w_y) n_y n_z \right] = 0
\end{aligned} \tag{20.50}$$

By comparing the terms inside of the brackets of the first four terms of equation 20.50 with the directional derivative defined by equation 20.49, we may transform equation 20.50 to read as follows.

$$\begin{aligned}
&\rho a n_x u_t + \rho a n_y v_t + \rho a n_z w_t - p_t + \rho a^2 \left[(n_x^2 - 1) u_x + (n_y^2 - 1) v_y + (z_z^2 - 1) w_z \right. \\
&\qquad \left. + (u_y + v_x) n_x n_y + (u_z + w_x) n_x n_z + (v_z + w_y) n_y n_z \right] = 0
\end{aligned} \tag{20.51}$$

where $u_t = du/dt = \nabla u \cdot \mathbf{l}$, etc., and t denotes the time of travel of a fluid particle along the streamline that is the axis of the Mach cone. The terms inside of the brackets in equation 20.51 are the derivatives normal to the bicharacteristic direction written in terms of partial derivatives with respect to the *three* Cartesian coordinates x, y, and z. Those derivatives are termed the *cross-derivatives*.

Three independent compatibility equations are obtained on each stream surface (i.e., equations 20.38, 20.44, and 20.45), and one independent compatibility equation is obtained on each wave surface (i.e., equation 20.51). There are, however, an infinite number of characteristic surfaces at a point. Since the number of independent compatibility equations cannot exceed the number of independent equations of motion, it is necessary to determine which of the possible combinations of compatibility equations are independent. Rusanov[2] determined the possible combinations for steady three-dimensional isentropic supersonic flow. One of the several possible independent sets of compatibility equations comprises equations 20.44 and 20.45 along the flow streamlines, and equation 20.51 along any three wave surfaces. That set of compatibility equations is presented in Table 20.1. Those equations are employed in the numerical algorithms presented in Sections 20–7 and 20–8.

Table 20.1 Characteristic and Compatibility Equations for Steady Three-Dimensional Isentropic Supersonic Flow

Characteristic equations		
$\frac{dx}{dt}=u \quad \frac{dy}{dt}=v \quad \frac{dz}{dt}=w$	*(streamline)*	(20.21)
$[u^2-(V^2-a^2)](dx)^2+[v^2-(V^2-a^2)](dy)^2$ $+[w^2-(V^2-a^2)](dz)^2+2uv(dx)(dy)$ $+2uw(dx)(dz)+2vw(dy)(dz)=0$	*(Mach conoid)*	(20.28)
Compatibility equations		
$\rho u u_t+\rho v v_t+\rho w w_t+p_t=0$	*(along streamlines)*	(20.44)
$p_t-a^2\rho_t=0$	*(along streamlines)*	(20.45)
$\rho a n_x u_t+\rho a n_y v_t+\rho a n_z w_t-p_t$ $+\rho a^2[(n_x^2-1)u_x+(n_y^2-1)v_y+(n_z^2-1)w_z$ $+(u_y+v_x)n_x n_y+(u_z+w_x)n_x n_z+(v_z+w_y)n_y n_z]=0$	*(along bicharacteristics)*	(20.51)

Note: n_x, n_y, and n_z are the components of the unit normal $\mathbf{n}$ in the x, y, and z directions, respectively. The subscript t denotes directional derivatives in a characteristic direction.

20–5 UNSTEADY TWO-DIMENSIONAL ISENTROPIC FLOW

The governing equations for unsteady two-dimensional isentropic flow are presented in this section, and the equations for the characteristic surfaces and the corresponding compatibility equations are determined.

20–5(a) Governing Equations

The governing equations for unsteady two-dimensional isentropic flow are obtained from Table 2.2 by assuming that $\mathbf{B}=d\mathbf{F}_{\text{shear}}=\delta\dot{W}=\delta\dot{Q}=g\,dz=w=\partial(\ )/\partial z=0$. For isentropic flow, the energy equation (equation 2.92) may be replaced by the speed of sound equation written in the form of a substantial derivative (equation 19.9). Those equations written in Cartesian coordinates are as follows.

$$\rho u_t+\rho u u_x+\rho v u_y+p_x=0 \tag{20.52}$$

$$\rho v_t+\rho u v_x+\rho v v_y+p_y=0 \tag{20.53}$$

$$\rho u_x+\rho v_y+\rho_t+u\rho_x+v\rho_y=0 \tag{20.54}$$

$$p_t+up_x+vp_y-a^2(\rho_t+u\rho_x+v\rho_y)=0 \tag{20.55}$$

where $a=a(p,\rho)$. Equations 20.52 to 20.55 comprise a set of four first-order homogeneous partial differential equations for determining the four flow properties u, v, p, and ρ.

In the derivation of the characteristic and compatibility equations in this section, the time axis t is considered to be directed normal to the physical plane, so that the rules governing the vector scalar product are applicable in xyt space to equations 20.52 to 20.55. In addition, the *pseudo-velocity vector* $\hat{\mathbf{V}}$ is defined as

$$\hat{\mathbf{V}}=\mathbf{i}u+\mathbf{j}v+\mathbf{k}=\mathbf{V}+\mathbf{k} \tag{20.56}$$

where **k** is the unit vector in the direction of the *time* axis. The projection of $\hat{\mathbf{V}}$ on the physical plane (i.e., the *xy* plane) is the velocity vector $\mathbf{V}=\mathbf{i}u+\mathbf{j}v$. The path traced out by a fluid particle in *xyt* space is termed the *pseudo-pathline*. The projection of the pseudo-pathline on the physical plane is the particle *pathline*. By employing the concepts of the pseudo-velocity vector and the pseudo-pathline described above, the procedure for determining the characteristic and compatibility equations presented in this section for unsteady two-dimensional isentropic flow is analogous to the procedure employed in Section 20–4 for determining the characteristic and compatibility equations for steady three-dimensional isentropic supersonic flow.

20–5(b) Characteristic and Compatibility Equations

To determine the characteristic and compatibility equations for unsteady two-dimensional isentropic flow, equations 20.52 to 20.55 are multiplied by the unknown parameters σ_1 to σ_4, respectively, and summed. Thus,

$$\sigma_1(20.52)+\sigma_2(20.53)+\sigma_3(20.54)+\sigma_4(20.55)=0 \tag{20.57}$$

Performing the summation and collecting the coefficients of like terms, we obtain

$$\begin{aligned}&\rho(u\sigma_1+\sigma_3)u_x+\rho v\sigma_1 u_y+\rho\sigma_1 u_t\\&\quad+\rho u\sigma_2 v_x+\rho(v\sigma_2+\sigma_3)v_y+\rho\sigma_2 v_t\\&\quad+(\sigma_1+u\sigma_4)p_x+(\sigma_2+v\sigma_4)p_y+\sigma_4 p_t\\&\quad+u(\sigma_3-a^2\sigma_4)\rho_x+v(\sigma_3-a^2\sigma_4)\rho_y+(\sigma_3-a^2\sigma_4)\rho_t=0\end{aligned} \tag{20.58}$$

Define the following set of vectors $\mathbf{W}_j$ ($j=1,\ldots,4$), where the components of $\mathbf{W}_j$ in the *xyt* coordinate system are the coefficients of the partial derivatives in equation 20.58. Thus,

$$\mathbf{W}_1=\mathbf{i}\rho(u\sigma_1+\sigma_3)+\mathbf{j}\rho v\sigma_1+\mathbf{k}\rho\sigma_1 \tag{20.59}$$

$$\mathbf{W}_2=\mathbf{i}\rho u\sigma_2+\mathbf{j}\rho(v\sigma_2+\sigma_3)+\mathbf{k}\rho\sigma_2 \tag{20.60}$$

$$\mathbf{W}_3=\mathbf{i}(\sigma_1+u\sigma_4)+\mathbf{j}(\sigma_2+v\sigma_4)+\mathbf{k}\sigma_4 \tag{20.61}$$

$$\mathbf{W}_4=\mathbf{i}u(\sigma_3-a^2\sigma_4)+\mathbf{j}v(\sigma_3-a^2\sigma_4)+\mathbf{k}(\sigma_3-a^2\sigma_4) \tag{20.62}$$

Equation 20.58 may, therefore, be transformed to read

$$d_{\mathbf{W}_1}u+d_{\mathbf{W}_2}v+d_{\mathbf{W}_3}p+d_{\mathbf{W}_4}\rho=0 \tag{20.63}$$

where $d_{\mathbf{W}_1}u$ is defined as the derivative of u in the direction of the vector $\mathbf{W}_1$, etc. Equation 20.63 is, therefore, the *compatibility equation* for unsteady two-dimensional isentropic flow.

To determine the pertinent characteristic surfaces, the following question is posed. Can the arbitrary parameters σ_i ($i=1,\ldots,4$) be chosen so that the vectors $\mathbf{W}_j$ ($j=1,\ldots,4$) all lie in the same surface? If such a surface exists, it is the *characteristic surface*, and its normal **N** (at each point on the surface) is called the *characteristic normal*. Accordingly, equation 20.63 is then an *interior operator* on the aforementioned characteristic surface, and is the *compatibility equation* corresponding to the characteristic surface.

The characteristic normal **N** for unsteady two-dimensional flow is defined by

$$\mathbf{N}=\mathbf{i}N_x+\mathbf{j}N_y+\mathbf{k}N_t \tag{20.64}$$

Since **N** is perpendicular to the vectors $\mathbf{W}_j$ lying in the characteristic surface, it follows that their scalar products must vanish. Hence,

$$\mathbf{N}\cdot\mathbf{W}_j=0 \qquad (j=1,\ldots,4) \tag{20.65}$$

Futhermore, let

$$U=uN_x+vN_y+N_t=\hat{\mathbf{V}}\cdot\mathbf{N} \tag{20.66}$$

Performing the scalar product expressed by equation 20.65, we obtain the following system of equations expressed in matrix form.

$$\begin{vmatrix} \rho U & 0 & \rho N_x & 0 \\ 0 & \rho U & \rho N_y & 0 \\ N_x & N_y & 0 & U \\ 0 & 0 & U & -a^2U \end{vmatrix} \begin{vmatrix} \sigma_1 \\ \sigma_2 \\ \sigma_3 \\ \sigma_4 \end{vmatrix} = 0 \tag{20.67}$$

For equation 20.67 to have a solution other than the trivial solution $\sigma_1=\sigma_2=\sigma_3=\sigma_4=0$, the determinant of its coefficient matrix must vanish. Setting that determinant equal to zero yields

$$(uN_x+vN_y+N_t)^2\left[(uN_x+vN_y+N_t)^2-a^2\left(N_x^2+N_y^2\right)\right]=0 \tag{20.68}$$

In equation 20.68 the fluid velocity **V** is $\mathbf{V}=\mathbf{i}u+\mathbf{j}v$, and the characteristic normal **N** is expressed in terms of its components by $\mathbf{N}=\mathbf{i}N_x+\mathbf{j}N_y+\mathbf{k}N_t$.

For an unsteady two-dimensional isentropic flow, the characteristic surfaces are defined by equation 20.68, and the corresponding compatibility equation is equation 20.63.

20–5(c) Characteristic Surfaces

The characteristic surfaces are determined by solving equation 20.68 for the characteristic normal **N**, and then determining the surface that is everywhere normal to **N**. Equation 20.68 comprises a linear factor appearing twice multiplied by a quadratic factor. Setting either of those factors equal to zero satisfies equation 20.68, and yields an equation for determining **N**.

Setting the first factor of equation 20.68 equal to zero yields

$$uN_x+vN_y+N_t=\hat{\mathbf{V}}\cdot\mathbf{N}=0 \qquad (\textit{repeated two times}) \tag{20.69}$$

Because the magnitude of the characteristic normal **N** is arbitrary, it may be chosen so that its physical components N_x and N_y comprise the unit vector $\mathbf{n}=\mathbf{i}n_x+\mathbf{j}n_y$ in the physical plane (i.e., the xy plane). Hence,

$$\mathbf{n}\cdot\mathbf{n}=\left(n_x^2+n_y^2\right)=1 \tag{20.70}$$

Equation 20.69 may, therefore, be written as

$$un_x+vn_y+n_t=\hat{\mathbf{V}}\cdot\hat{\mathbf{n}}=\mathbf{V}\cdot\mathbf{n}+n_t=0 \tag{20.71}$$

where

$$\hat{\mathbf{n}} = \mathbf{i}n_x + \mathbf{j}n_y + \mathbf{k}n_t = \mathbf{n} + \mathbf{k}n_t \tag{20.72}$$

and

$$n_t = \frac{N_t}{\left(N_x^2 + N_y^2\right)^{1/2}} \tag{20.73}$$

Equations 20.70 and 20.71 are two equations relating the three components of the *characteristic normal* $\hat{\mathbf{n}}$. The remaining condition required for determining $\hat{\mathbf{n}}$ is arbitrary. Consequently, rather than a uniquely determined characteristic normal $\hat{\mathbf{n}}$, there is an infinite family of characteristic normals.

Equations 20.70 and 20.71 may be interpreted physically by assuming that the origin of the xyt coordinate system is located at the point in space under consideration. The unit vector $\mathbf{n}$ in the physical plane thus originates at the origin, and the components of $\mathbf{n}$ (i.e., n_x and n_y) correspond to the Cartesian coordinates x and y. In that form, it is obvious that equation 20.70 represents a unit circle with its center at the origin. The projection of the unit circle in the t direction yields the unit cylinder having the t axis for its axis, as illustrated in Fig. 20.10. Equation 20.71 represents a plane passing through the origin, where the orientation of the plane depends on the magnitudes of the velocity components u and v of the fluid. Therefore, the locus of the end points of the characteristic normal $\hat{\mathbf{n}}$ is the elliptical curve formed by the intersection of the plane and the unit cylinder, as illustrated in Fig. 20.10. Since the characteristic normals originate at the origin and the plane specified by equation 20.71 passes through the origin, all of the characteristic normals lie within that plane. That plane is termed the *plane of normals*.

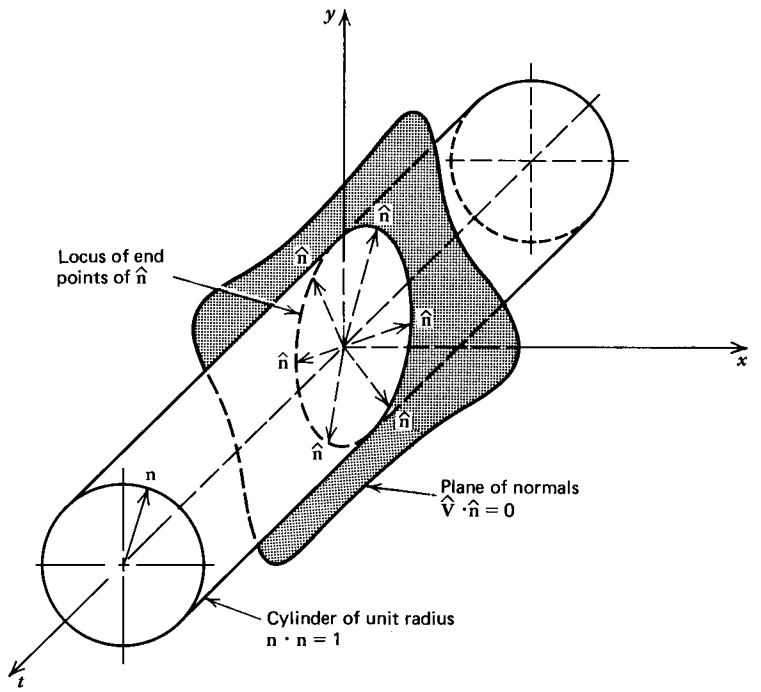

Figure 20.10 Plane of normals corresponding to stream surfaces in unsteady two-dimensional flow.

Equation 20.71 shows that the characteristic normal $\hat{\mathbf{n}}$ corresponding to the first factor in equation 20.68 is normal to a surface containing the pseudo-velocity vector $\hat{\mathbf{V}}$; the latter surface is called a stream surface. Figure 20.11 illustrates schematically the stream surface corresponding to a particular characteristic normal $\hat{\mathbf{n}}$. At each point in space there is an infinite number of stream surfaces corresponding to the infinite number of characteristic normals.

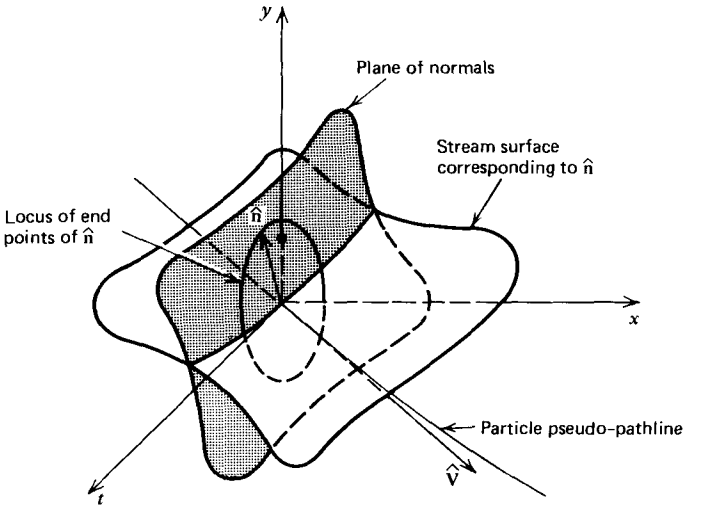

Figure 20.11 Stream surface corresponding to a particular characteristic normal.

The envelope formed by the infinite number of stream surfaces is the pseudo-pathline. Let t denote the time of travel of a fluid particle along the pseudo-pathline. Then the equations for the pseudo-pathline in terms of the velocity components u and v and the time t are

$$\frac{dx}{dt} = u \qquad \frac{dy}{dt} = v \qquad \frac{dt}{dt} = 1 \tag{20.74}$$

The differential vector $d\mathbf{s}$ in any arbitrary direction in xyt space is given by

$$d\mathbf{s} = \mathbf{i}\,dx + \mathbf{j}\,dy + \mathbf{k}\,dt \tag{20.75}$$

Along a pseudo-pathline, dx, dy, and dt are given by equation 20.74. Therefore, $d\mathbf{s}$ along a pseudo-pathline is given by

$$d\mathbf{s} = (\mathbf{i}u + \mathbf{j}v + \mathbf{k})\,dt = \hat{\mathbf{V}}\,dt \tag{20.76}$$

where t denotes the time of travel of a fluid particle along the pseudo-pathline.

Figure 20.12 illustrates the intersection of a stream surface in xyt space with the physical plane, that is, the xy plane. The curve of intersection is the particle pathline, which is the projection of the pseudo-pathline in the physical plane.

The procedure employed herein for determining the characteristic surfaces in xyt space is based on the concept of the pseudo-velocity vector $\hat{\mathbf{V}} = \mathbf{i}u + \mathbf{j}v + \mathbf{k} = \mathbf{V} + \mathbf{k}$. The physical significance of $\hat{\mathbf{V}}$ may be illustrated by comparing the present results with those obtained for unsteady one-dimensional flow in Chapter 19. In that case,

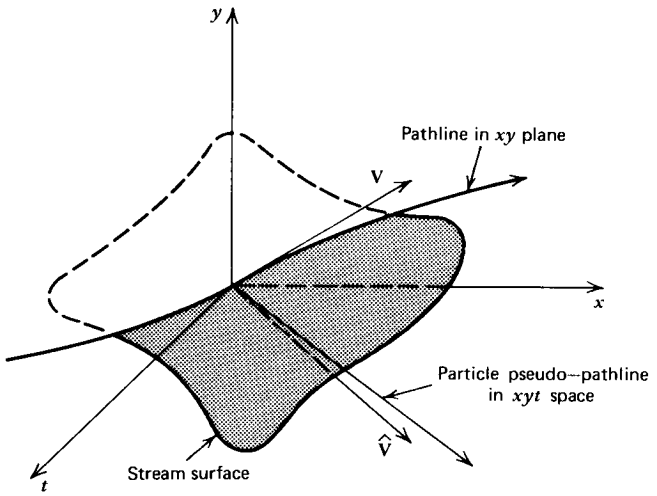

Figure 20.12 Intersection of a stream surface with the physical plane.

the pathline in xt space is a characteristic curve (see Table 19.2) specified by equation 19.56.

$$\left(\frac{dt}{dx}\right)_o = \lambda_o = \frac{1}{u} \tag{19.56}$$

For an unsteady one-dimensional flow we may define the pseudo-velocity vector $\hat{\mathbf{V}} = \mathbf{i}u + \mathbf{j}$, which is analogous to the pseudo-velocity vector $\hat{\mathbf{V}} = \mathbf{i}u + \mathbf{j}v + \mathbf{k}$ for unsteady two-dimensional flow. Figure 20.13 illustrates the pseudo-velocity vector $\hat{\mathbf{V}}$ in xt space. From the figure it is evident that for an unsteady one-dimensional flow, the pseudo-velocity vector $\hat{\mathbf{V}}$ defines the pseudo-pathline for the fluid particle in xt space. Accordingly, the pseudo-velocity vector $\hat{\mathbf{V}} = \mathbf{i}u + \mathbf{j}v + \mathbf{k}$ defines the pseudo-pathline for a fluid particle in xyt space. The projection of $\hat{\mathbf{V}} = \mathbf{i}u + \mathbf{j}v + \mathbf{k}$ on the xy plane defines the pseudo-pathline of a fluid particle in the physical plane.

Now consider the second factor in equation 20.68. Thus,

$$(uN_x + vN_y + N_t)^2 - a^2(N_x^2 + N_y^2) = 0 \tag{20.77}$$

where the subscripts x, y, and t denote the components of $\mathbf{N}$ in the x, y, and t

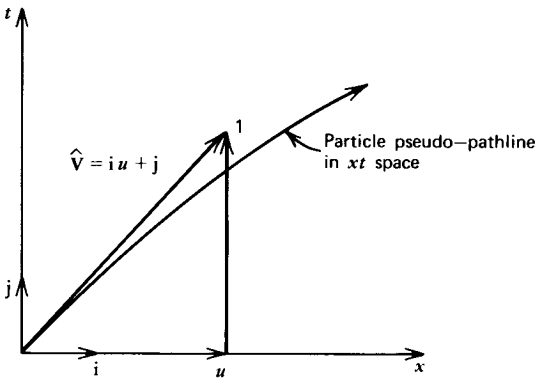

Figure 20.13 Pseudo-velocity vector in xt space.

directions, respectively. Rearranging equation 20.77 and taking the square root of each side yields

$$uN_x + vN_y + N_t = \pm a\left(N_x^2 + N_y^2\right)^{1/2} \tag{20.78}$$

In equation 20.78 the choice of the positive or negative root is arbitrary. The sign merely determines the sense of the characteristic normal $\mathbf{N}$ along the direction specified by its components. Because the length of $\mathbf{N}$ is immaterial, it may be chosen so that its physical components N_x and N_y comprise the unit normal $\mathbf{n} = \mathbf{i}n_x + \mathbf{j}n_y$ in the physical plane (i.e., the xy plane). Hence,

$$\mathbf{n} \cdot \mathbf{n} = n_x^2 + n_y^2 = 1 \tag{20.79}$$

Equation 20.79 is the equation of a cylinder of unit radius.

In equation 20.78 the left-hand side is the scalar product $\hat{\mathbf{V}} \cdot \mathbf{N}$, where $\hat{\mathbf{V}} = \mathbf{i}u + \mathbf{j}v + \mathbf{k}$. That equation may be transformed to read, in terms of the unit normal $\mathbf{n}$, as follows.

$$un_x + vn_y + n_t = \hat{\mathbf{V}} \cdot \hat{\mathbf{n}} = \mathbf{V} \cdot \mathbf{n} + n_t = \pm a \tag{20.80}$$

where

$$\hat{\mathbf{n}} = \mathbf{i}n_x + \mathbf{j}n_y + \mathbf{k}n_t = \mathbf{n} + \mathbf{k}n_t \tag{20.81}$$

and

$$n_t = \frac{N_t}{\left(N_x^2 + N_y^2\right)^{1/2}} \tag{20.82}$$

Equations 20.79 and 20.80 express two of the three needed equations for determining the characteristic normal $\hat{\mathbf{n}}$. The remaining condition required for determining $\hat{\mathbf{n}}$ is arbitrary. Consequently, there is an infinite family of characteristic normals; that is, there is no uniquely determined normal.

Equations 20.79 and 20.80 may be interpreted physically by the procedure employed for interpreting the stream surfaces. Equation 20.79 is the equation for a unit circle having the physical characteristic unit normal $\mathbf{n}$ emanating from its center. The projection of the unit circle in the t direction yields the unit cylinder, illustrated in Fig. 20.14, having the t axis for its axis. Equation 20.80 is the equation of a plane whose orientation depends on the velocity components u and v and the speed of sound a of the fluid. The plane specified by equation 20.80 does not, however, pass through the origin of the coordinate system. The locus of the end points of the characteristic normal $\hat{\mathbf{n}}$ is, therefore, the elliptical curve formed by the intersection of the plane and the unit cylinder, as illustrated in Fig. 20.14. The characteristic normals $\hat{\mathbf{n}}$ originate at the origin, but the plane specified by equation 20.80 does not pass through the origin. Consequently, the infinite family of characteristic normals $\hat{\mathbf{n}}$ forms a cone. That cone, which is termed the *cone of normals*, is illustrated in Fig. 20.15.

Equation 20.80 shows that the magnitude of the component of the pseudo-velocity $\hat{\mathbf{V}}$ normal to a characteristic surface is equal to the local speed of sound a. Each such characteristic surface is termed a *wave surface*. Figure 20.16 illustrates the wave surfaces corresponding to two particular characteristic normals. There is an infinity of wave surfaces at each point in space corresponding to the infinite number of characteristic normals.

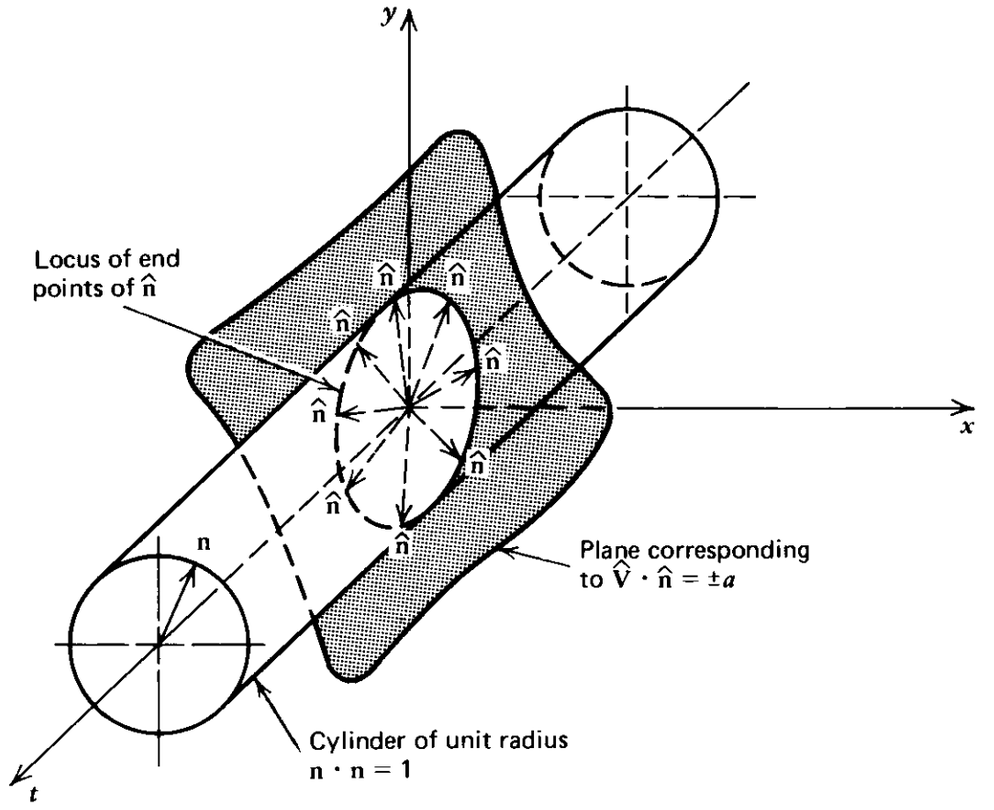

Figure 20.14 Locus of the end points of $\hat{\mathbf{n}}$.

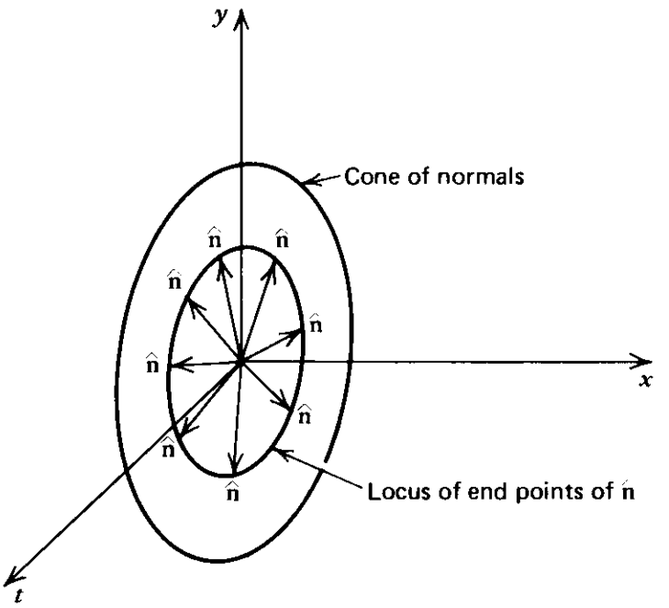

Figure 20.15 The cone of normals.

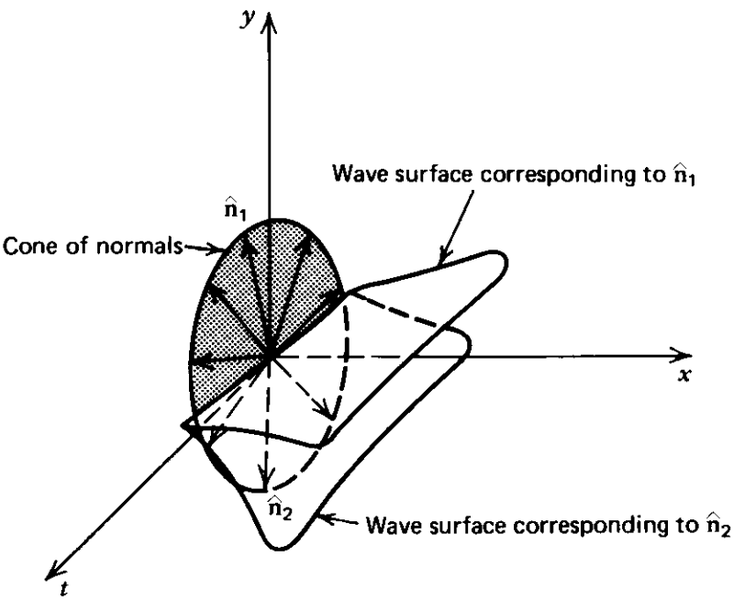

Figure 20.16 Wave surfaces corresponding to two particular characteristic normals.

The envelope formed by the infinity of wave surfaces is called the *characteristic manifold* or *Mach conoid*. At a point, the Mach conoid is tangent to the *Mach cone*, which is the *reciprocal cone* to the *cone of normals*. The determination of the equation of the Mach conoid is a straightforward, although lengthy, exercise in differential geometry that is not presented here.[33,34] For the present case, the equation of the Mach conoid is[7]

$$(dx - u\,dt)^2 + (dy - v\,dt)^2 = a^2\,dt^2 \tag{20.83}$$

Equation 20.83 determines the characteristic manifold or Mach conoid. The wave surfaces in unsteady two-dimensional flow are always real, in contrast to steady three-dimensional flow where the wave surfaces are real only if the flow is supersonic. The curves of tangency between the wave surfaces and the Mach conoid are called the *bicharacteristics*.

The Mach cone corresponding to the Mach conoid specified by equation 20.83 is an oblique cone, whose axis is tangent to the pseudo-pathline at the vertex of the cone. The intersections of the Mach cone with the surfaces t = constant are circles, while the intersections with the surfaces perpendicular to the axis of the cone are ellipses. That the Mach cone is an oblique cone may be substantiated by the physical interpretation of the Mach conoid as the envelope of all of the acoustic waves created by a small disturbance moving along a pseudo-pathline at the pseudo-velocity of the fluid particles. For example, in a uniform flow field parallel to the x axis, all of the pseudo-pathlines are straight lines and all of the acoustic waves are circular waves of constant speed emanating from successive points along the pseudo-pathline and propagating outward into the xy space, as illustrated in Fig. 20.17. The envelope of the acoustic waves is the Mach conoid, which is obviously an oblique cone in the uniform flow case since intersections of the Mach conoid with the surfaces t = constant are circles. The Mach cone, which is the local tangent cone to the Mach conoid, is identical to the Mach conoid in this case, and is also an oblique cone. In an unsteady nonuniform flow field, the pseudo-pathlines

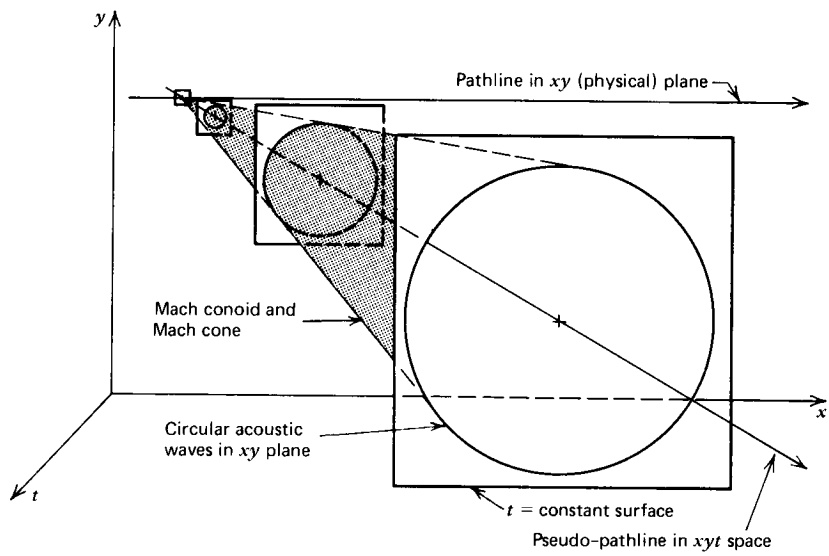

Figure 20.17 The Mach conoid and the Mach cone in a uniform unsteady two-dimensional flow field.

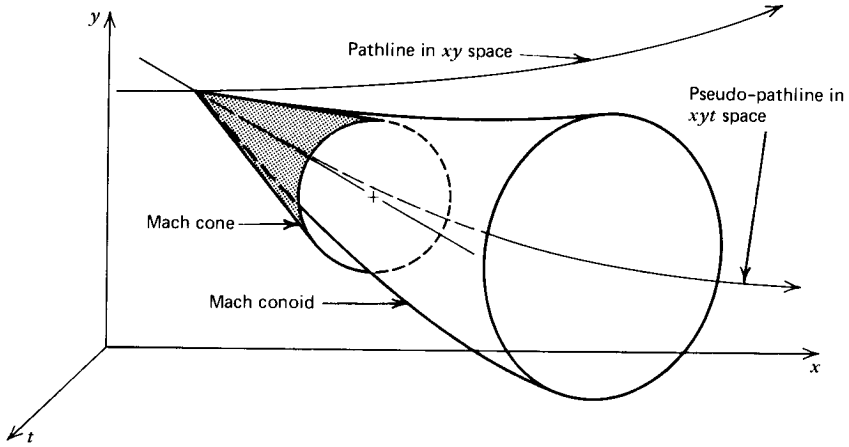

Figure 20.18 The Mach conoid and the Mach cone in a nonuniform unsteady two-dimensional flow field.

are not straight lines and the speed of the acoustic waves is not constant. The envelope of the acoustic waves, that is, the Mach conoid, is not an oblique cone in this case, as illustrated in Fig. 20.18. The local tangent cone to the Mach conoid at each point in xyt space, that is, the Mach cone, is, however, an oblique cone even in the nonuniform flow case. By contrast, in steady three-dimensional supersonic flow, the Mach cone is a right circular cone whose intersections with the surfaces perpendicular to the streamlines are circles.

Figure 20.19 illustrates schematically the relationship between the two families of wave surfaces, the stream surface, the Mach conoid, and two bicharacteristics, for an arbitrary point $P(x,y,t)$ lying on a *spacelike curve*; the latter is any curve located outside of the Mach conoid. A single stream surface and two wave surfaces pass through the spacelike curve. When the spacelike curve is rotated through 360 degrees, the envelope of the infinity of stream surfaces defines the *pseudo-pathline* in xyt space, and the envelope of the infinity of wave surfaces defines the *Mach conoid*. The pathline and the bicharacteristics for an unsteady two-dimensional flow are analogous to the pathline and the Mach lines for an unsteady one-dimensional flow [see Section 19–3(d)].

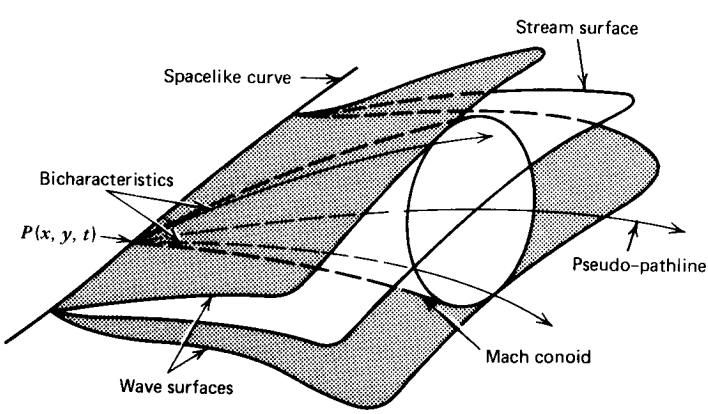

Figure 20.19 Stream surfaces, wave surfaces, pseudo-pathline, Mach conoid, and bicharacteristics in unsteady two-dimensional flow.

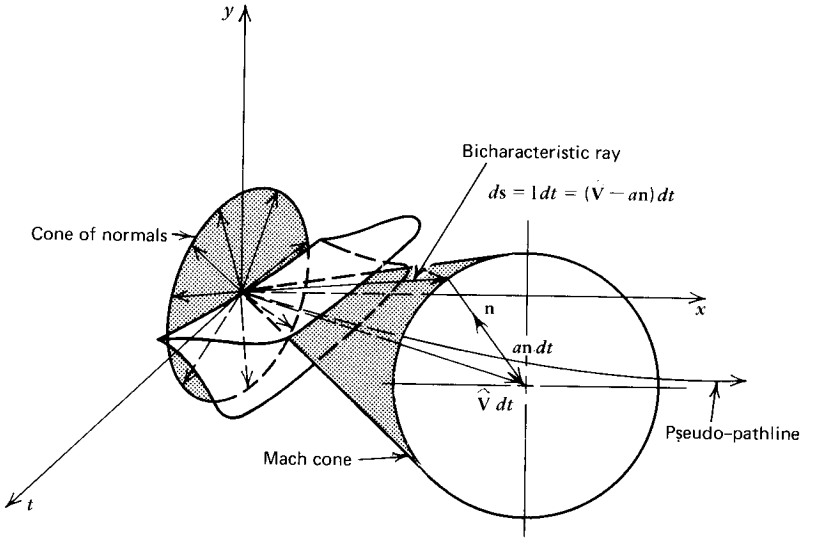

Figure 20.20 illustrates the geometry of the Mach cone, where $\hat{\mathbf{V}}\,dt$, the distance traveled along the pseudo-pathline by a fluid particle during the time dt, is the axis of the Mach cone, $a\mathbf{n}\,dt$ is the distance in xy space traveled by the acoustic wave in the direction of the physical unit normal $\mathbf{n}$ during the time dt, and $d\mathbf{s}=\mathbf{l}\,dt$ is the corresponding ray along the bicharacteristic. The vector $\mathbf{l}$ is defined as

$$\mathbf{l}\equiv\hat{\mathbf{V}}-a\hat{\mathbf{n}}=\mathbf{i}(u-an_x)+\mathbf{j}(v-an_y)+\mathbf{k} \tag{20.84}$$

Consequently, along a bicharacteristic ray, $d\mathbf{s}$ is given by

$$d\mathbf{s}=\left[\mathbf{i}(u-an_x)+\mathbf{j}(v-an_y)+\mathbf{k}\right]dt \tag{20.85}$$

where t denotes the time of travel of a fluid particle along the pseudo-pathline that is the axis of the Mach cone.

20–5(d) Compatibility Equations

The method of characteristics determines the surfaces in the flow field along which the governing partial differential equations combine to become interior operators; that is, the direction of differentiation lies within the surfaces. For an unsteady two-dimensional flow, the characteristic surfaces are the stream surfaces and the wave surfaces, illustrated in Fig. 20.19, and equation 20.63 is the corresponding interior operator; that is, the compatibility equation that is valid on the aforementioned characteristic surfaces. The unknown parameters σ_i must be determined before the compatibility equation can be applied.

First, consider the stream surface specified by equation 20.69. Substituting equation 20.69 into the system of equations represented by the matrix equation 20.67, we obtain

$$\begin{vmatrix} 0 & 0 & \rho N_x & 0 \\ 0 & 0 & \rho N_y & 0 \\ N_x & N_y & 0 & 0 \\ 0 & 0 & 0 & 0 \end{vmatrix} \begin{vmatrix} \sigma_1 \\ \sigma_2 \\ \sigma_3 \\ \sigma_4 \end{vmatrix} = 0 \tag{20.86}$$

The rank of the coefficient matrix of equation 20.86 is two.* Consequently, there are two independent solutions for the σ_i on the stream surfaces. Expanding equation 20.86, it is seen that σ_3 equals zero, σ_4 is arbitrary, and σ_1 and σ_2 satisfy the relationship

$$\sigma_1 N_x + \sigma_2 N_y = 0 \tag{20.87}$$

Two possible solutions for the σ_i which satisfy equation 20.87 are

$$\sigma_1 = \sigma_2 = \sigma_3 = 0 \qquad \sigma_4 \text{ is arbitrary} \tag{20.88}$$

$$\sigma_1 = S_x \qquad \sigma_2 = S_y \qquad \sigma_3 = \sigma_4 = 0 \tag{20.89}$$

where $\mathbf{S} = \mathbf{i}S_x + \mathbf{j}S_y + \mathbf{k}(0)$ is a vector that lies along the line of intersection of the stream surface and the physical plane. Equation 20.88 applies on all of the stream surfaces, since the same values for the σ_i satisfy equation 20.87 for all values of $\mathbf{N}$. Consequently, the set of values for the σ_i specified by equation 20.88 applies along the envelope of the stream surfaces, which is the pseudo-pathline [see Section 20–5(c)], and the compatibility equation corresponding to equation 20.88 applies along the pseudo-pathline. The set of σ_i defined by equation 20.89, however, depends on the value of $\mathbf{N}$, since for each value of $\mathbf{N}$ corresponding to a particular stream surface, a different value for $\mathbf{S}$ is obtained. Consequently, the corresponding compatibility equation is applicable only in that stream surface. Thus, an infinite number of compatibility equations are obtained for the set of σ_i corresponding to equation 20.89.

Substituting equations 20.88 and 20.89 into equation 20.58 yields the following two compatibility equations that are valid on the stream surfaces.

$$(up_x + vp_y + p_t) - a^2(u\rho_x + v\rho_y + \rho_t) = 0 \tag{20.90}$$

$$\rho S_x(uu_x + vu_y + u_t) + \rho S_y(uv_x + vv_y + v_t) + S_x p_x + S_y p_y = 0 \tag{20.91}$$

Equations 20.90 and 20.91 are differential operators within the stream surface. There are only two independent directions of differentiation within a surface in three-dimensional space. Consequently, equations 20.90 and 20.91, which are written in terms of partial derivatives with respect to the *three* coordinates x, y, and t, may be written in terms of partial derivatives with respect to any *two* independent directions within the stream surface. Furthermore, equation 20.90 may be written in terms of *total* derivatives in the direction of the pseudo-pathline.

Consider the general function $f(x,y,t)$. The total derivative of f is given by

$$df = f_x\,dx + f_y\,dy + f_t\,dt \tag{20.92}$$

Equation 20.92 may be written as

$$df = \nabla f \cdot d\mathbf{s} \tag{20.93}$$

where $d\mathbf{s}$ is the differential vector distance

$$d\mathbf{s} = \mathbf{i}\,dx + \mathbf{j}\,dy + \mathbf{k}\,dt \tag{20.94}$$

Along a pseudo-pathline, $d\mathbf{s}$ is given by equation 20.76. Consequently, along a

*The largest matrix, in the main matrix, that has a determinant that does not equal zero, is a 2×2 matrix.

pseudo-pathline, equation 20.93 becomes

$$df = \nabla f \cdot \hat{\mathbf{V}}\, dt \tag{20.95}$$

which may be written as

$$f_t = \frac{df}{dt} = \nabla f \cdot \hat{\mathbf{V}} = uf_x + vf_y + f_t \tag{20.96}$$

where t denotes the time of travel of a fluid particle along the pseudo-pathline, and f_t denotes the directional derivative of f along the pseudo-pathline.

The terms inside of the parentheses in equation 20.90 have the same form as equation 20.96. Consequently, those terms may be written as directional derivatives along the pseudo-pathline. Accordingly, equation 20.96 becomes

$$p_t - a^2\rho_t = 0 \qquad (\textit{along the pathline}) \tag{20.97}$$

where $p_t = dp/dt = (up_x + vp_y + p_t)$, etc., and t denotes the time of travel of a fluid particle along the pseudo-pathline. Equation 20.91 cannot be written as a directional derivative along the pseudo-pathline since, by definition, $\mathbf{S}$ is a vector in the stream surface that is not parallel to the pseudo-velocity vector $\hat{\mathbf{V}}$.

Consider next the wave surfaces specified by equation 20.80. To determine σ_i on a wave surface, substitute equation 20.80 into equation 20.67, where the positive root is chosen arbitrarily, and the physical component of $\mathbf{N}$ has been replaced by $\mathbf{n}$. We obtain

$$\begin{vmatrix} \rho a & 0 & \rho n_x & 0 \\ 0 & \rho a & \rho n_y & 0 \\ n_x & n_y & 0 & a \\ 0 & 0 & a & -a^3 \end{vmatrix} \begin{vmatrix} \sigma_1 \\ \sigma_2 \\ \sigma_3 \\ \sigma_4 \end{vmatrix} = 0 \tag{20.98}$$

The rank of the coefficient matrix of equation 20.98 is three*; consequently, only one independent solution exists for the σ_i. Letting $\sigma_4 = -1$ yields the following solution for the σ_i.

$$\sigma_1 = an_x \qquad \sigma_2 = an_y \qquad \sigma_3 = -a^2 \qquad \sigma_4 = 1 \tag{20.99}$$

where $\mathbf{n}$ is the unit vector in the physical plane.

The compatibility equation applicable on the wave surface is obtained by substituting equation 20.99 into the general compatibility equation, equation 20.58. Thus,

$$\rho a n_x (uu_x + vu_y + u_t) + \rho a n_y (uv_x + vv_y + v_t)$$
$$+ (an_x - u)p_x + (an_y - v)p_y - p_t - \rho a^2 (u_x + v_y) = 0 \tag{20.100}$$

Equation 20.100 represents a differential operator within the wave surface. There are only two independent directions of differentiation within a surface in three-dimensional space. Consequently, equation 20.100, which is written in terms of partial derivatives with respect to the *three* coordinates x, y, and t, may be written

*The largest matrix, in the main matrix, that has a determinant which does not equal zero, is a 3×3 matrix.

in terms of partial derivatives with respect to any *two* independent directions within the wave surface. Those two independent directions may be chosen as the direction of the bicharacteristic (i.e., the tangent to a ray of the Mach conoid) and the normal to the bicharacteristic within the wave surface.

Equation 20.93 expresses the total derivative of a general function $f(x,y,t)$, where, along a bicharacteristic ray, $d\mathbf{s}$ is given by equation 20.85. Consequently, equation 20.100 may be written as

$$f_t = \frac{df}{dt} = \nabla f \cdot \mathbf{l} = (u - an_x) f_x + (v - an_y) f_y + f_t \tag{20.101}$$

where t denotes the time of travel of a fluid particle along the pseudo-pathline that is the axis of the Mach cone, and f_t denotes the directional derivative of f along a bicharacteristic ray.

The following term may be added to and subtracted from equation 20.100.

$$\pm \rho a^2 \left[n_x^2 u_x + n_y^2 v_y + n_x n_y (u_y + v_x) \right] \tag{20.102}$$

The result is

$$\begin{aligned} &\rho a n_x \left[(u - an_x) u_x + (v - an_y) u_y + u_t \right] \\ &\quad + \rho a n_y \left[(u - an_x) v_x + (v - an_y) v_y + v_t \right] \\ &\quad - \left[(u - an_x) p_x + (v - an_y) p_y + p_t \right] \\ &\quad + \rho a^2 \left[(n_x^2 - 1) u_x + (n_y^2 - 1) v_y + n_x n_y (u_y + v_x) \right] = 0 \end{aligned} \tag{20.103}$$

By comparing the terms inside of the brackets of the first three terms of equation 20.103 with the directional derivative defined by equation 20.101, equation 20.103 may be rewritten as follows.

$$\rho a n_x u_t + \rho a n_y v_t - p_t + \rho a^2 \left[(n_x^2 - 1) u_x + (n_y^2 - 1) v_y + n_x n_y (u_y + v_x) \right] = 0 \tag{20.104}$$

where $u_t = du/dt = \nabla u \cdot \mathbf{l}$, etc., and t denotes the time of travel of a fluid particle along the pseudo-pathline that is the axis of the Mach cone. The terms inside of the brackets in equation 20.104 are the derivatives normal to the bicharacteristic direction written in terms of partial derivatives with respect to the three coordinates x, y, and t. Those derivatives are termed the *cross-derivatives*.

Two independent compatibility equations are obtained on each stream surface (i.e., equations 20.91 and 20.97), and one independent compatibility equation is obtained on each wave surface (i.e., equation 20.104). At each point, there are an infinite number of characteristic surfaces. The number of compatibility equations that are independent, however, cannot exceed the number of independent governing equations. It is necessary, therefore, to determine which of the possible combinations of compatibility equations are independent. According to Rusanov,[2] one of the several possible sets of independent compatibility equations comprises equation 20.97 along pathlines, and equation 20.104 along three wave surfaces. That set of compatibility equations is appropriate to the numerical algorithms presented in Sections 20–7 and 20–8. They are presented in Table 20.2.

Table 20.2 Characteristic and Compatibility Equations for Unsteady Two-Dimensional Isentropic Flow

Characteristic equations		
$\frac{dx}{dt}=\mathrm{u} \quad \frac{dy}{dt}=\mathrm{v} \quad \frac{dt}{dt}=1$	(*pathline*)	(20.74)
$(dx-u\,dt)^2+(dy-v\,dt)^2=a^2dt^2$	(*Mach conoid*)	(20.83)
Compatibility equations		
$p_t-a^2\rho_t=0$	(*along a pathline*)	(20.97)
$\rho a n_x u_t+\rho a n_y v_t-p_t$ $+\rho a^2[(n_x^2-1)u_x+(n_y^2-1)v_y+n_x n_y(u_y+v_x)]=0$	(*along a bicharacteristic*)	(20.104)

Note: n_x and n_y are the components of the physical unit normal **n** in the x and y directions, respectively. The subscript t denotes directional derivatives in a characteristic direction.

20–6 GENERAL CONSIDERATIONS CONCERNING NUMERICAL INTEGRATION NETWORKS

The characteristic and compatibility equations are derived in Section 20–4 for steady three-dimensional isentropic supersonic flow and in Section 20–5 for unsteady two-dimensional isentropic flow. Before discussing specific finite difference networks for integrating those equations numerically, some general remarks concerning the location of the solution point, the accuracy, and the stability of the numerical analysis are appropriate.

As discussed in Sections 12–5(b) and 19–6(a), the numerical integration network or grid may be based on either a *direct marching method* or an *inverse marching method*. In the direct marching method, the location of the solution point is determined by extending forward the generators of the numerical integration network from known base points. In the inverse marching method, the location of the solution point is prespecified in some manner, and the generators of the numerical integration network are projected rearward to intersect a prior solution surface. The flow properties at the base points are then determined by interpolation in the initial-value surface. Direct marching methods are, in general, more accurate and require less computation time since they require fewer interpolations for the flow properties at the base points. Inverse marching methods are easier to program, and the results are easier to interpret because the solution may be advanced in parallel solution planes.

Numerical integration networks have been devised by following either the characteristic surfaces or the bicharacteristic curves. Accordingly, they are called *characteristic surface networks* and *bicharacteristic curve networks*, respectively. Characteristic surface networks result in simpler finite difference grids, but the bicharacteristic curve networks are usually more accurate because of the more rigorous treatment of the differential domain of dependence. Several characteristic surface networks are discussed in Section 20–7, and several bicharacteristic curve networks are discussed in Section 20–8. Those networks, together with the general considerations discussed in this section, are applicable to both steady three-dimensional supersonic flow and unsteady two-dimensional flow.

For both types of networks, the concepts of the *domain of dependence of the differential equations* and the *domain of dependence of the finite difference equations*

are important. The domain of dependence of the differential equations is the region in the initial-value surface enclosed by the intersection of the Mach conoid emanating from the solution point and the initial-value surface, as illustrated in Fig. 20.21. The domain of dependence of the finite difference equations is the area enclosed within the polygon formed by connecting the outermost points of the finite difference network in the initial-value surface, as illustrated in Fig. 20.21. The latter area is also called the *convex hull* of the finite difference network.

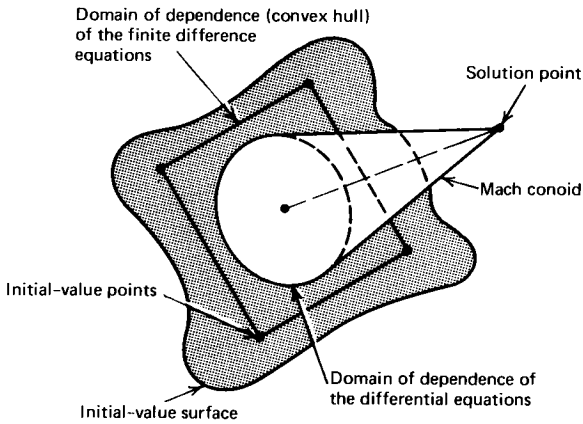

Figure 20.21 Domain of dependence of the differential equations and domain of dependence (convex hull) of the finite difference equations.

The accuracy of the numerical integration method is of prime importance. There are two aspects of the accuracy that must be considered. The *absolute accuracy* of the method refers to the closeness with which the numerically computed solution agrees with the exact solution. The *order of accuracy* of the method refers to the rate at which the error decreases with a reduction in the integration step size. It is difficult to establish the absolute accuracy of a numerical integration method, because it is not possible, except in a few cases, to compare the results obtained from the numerical integration method with those obtained from an exact solution. For flows with three independent variables, there are few exact solutions. The desired order of accuracy may be obtained by employing consistent approximations throughout the application of the finite difference equations. In general, the absolute accuracy increases as the order of accuracy increases. Both first-order methods (in which the accumulated error is directly proportional to the integration step size) and second-order methods (in which the accumulated error is proportional to the square of the step size) have been developed for the method of characteristics in three independent variables. Section 17–6(a) presents a more comprehensive discussion of the considerations of accuracy and of order of accuracy.

First-order accuracy algorithms may be developed by simply replacing the differential operators by forward difference operators, and determining the coefficients of the differential operators and the cross-derivatives (i.e., the derivatives normal to the bicharacteristic direction) in the initial-value surface. That procedure corresponds to the *Euler integration method* for ordinary differential equations [see Appendix A-6(c)].

To obtain a second-order accuracy algorithm, the average values of the coefficients and the cross-derivatives must be employed along the generators of the numerical integration network. That procedure corresponds to the *modified Euler predictor-corrector method* [see Appendix A-6(e)]. The determination of the average values for the coefficients is straightforward. A first-order accuracy method is employed to obtain predicted values of the properties at the solution point. Then, the values of the coefficients may be computed at the solution point and averaged with the values of the coefficients at the base points. The determination of the average values for the cross-derivatives is, however, considerably more difficult. Two approaches for determining the average values for the cross-derivatives have been employed. The first approach determines the cross-derivatives at the solution point and averages those values with the values of the cross-derivatives at the base points in the initial-value surface. The second approach explicitly eliminates the cross-derivatives at the solution point from the finite difference equations by a judicious combination of the finite difference equations. Those two approaches for achieving second-order accuracy are discussed in the following two paragraphs.

Second-order accuracy may be obtained by first constructing an entire solution surface with a first-order accuracy algorithm, and then calculating the cross-derivatives at the solution points by fitting bivariate interpolating polynomials to the flow properties in the solution surface and differentiating those polynomials. The numerical algorithm is then repeated at each solution point on the entire solution surface employing average values of the cross-derivatives along the generators of the numerical integration network. Consequently, the method is a *global iteration procedure*. The global iteration substantially increases the program complexity and the computation time. This method has the additional and more fundamental disadvantage that the cross-derivatives at the solution point are determined from adjacent points in the solution surface, and the latter points lie outside of the domain of dependence of the solution point. From another viewpoint, the adjacent points in the solution surface are determined from points in the initial-value surface outside of the convex hull of the solution point itself. Effectively, then, the convex hull of the solution point is enlarged to include all of the points in the initial-value surface that are employed in the calculation of the adjacent points to the solution point. Consequently, there may be considerable smearing of the numerical solution that does not occur in the exact solution.

Butler[8] devised a bicharacteristic curve network in which the cross-derivatives at the solution point are explicitly eliminated from the difference equations, thereby achieving a method that gives second-order accuracy without employing data at points adjacent to the solution point [see Section 20–8(e)]. Consequently, the method is a *local iteration procedure*. Butler's method is the only explicit numerical integration method that obtains second-order accuracy without violating the domain of dependence of the solution point.

Numerical integration algorithms must also be examined for stability. Richtmyer and Morton[9] discuss the stability criteria applicable to systems of hyperbolic partial differential equations. Courant, Friedrichs, and Lewy[10] (CFL) have shown that a necessary condition for the stability of a numerical method of integration for linear hyperbolic partial differential equations with constant coefficients is that the domain of dependence of the differential equations, which comprises the area enclosed by the intersection of the Mach conoid through the solution point and the initial-value surface, must be contained within the *convex hull* of the difference algorithm; that is the area within the polygon formed by connecting the outermost points of the difference network in the initial-value surface. Figure 20.21 illustrates

the domain of dependence of the differential equations and the convex hull of the finite difference algorithm.

The von Neumann stability condition[9] is a stronger stability criterion that requires that the eigenvalues of the amplification matrix of the numerical algorithm be less than $1+0(\Delta t)$ in absolute value, where the term $0(\Delta t)$ denotes terms of the order of the integration step size. The amplification matrix may be loosely described as the matrix operator that, when applied to the initial-value data, yields the solution values at the point under consideration. The operations specified by the amplification matrix must include all of the numerical procedures applied to the initial data to obtain the solution values, including interpolations, smoothing, and the application of the finite difference forms of the governing equations. Ransom[3] applied the von Neumann stability condition to steady three-dimensional isentropic supersonic flow, and Delaney[7] applied the von Neumann stability condition to unsteady two-dimensional isentropic flow.

Both the CFL stability criterion and the von Neumann stability condition are strictly applicable only for linear difference equations. For nonlinear difference equations, the usual approach is to require that the CFL stability criterion be satisfied and to apply the von Neumann condition locally to the linearized difference equations. Experience supports the soundness of such an approach.[3,5,7]

Redundancy methods have been proposed where more than the minimum number of independent compatibility equations are employed. The solution may be obtained either by averaging the results obtained with multiple sets of compatibility equations or by solving for the dependent variables in a least squares sense.

In the construction of finite difference networks in three variables, characteristic surfaces are approximated by characteristic planes, characteristic conoids are approximated by characteristic cones, and bicharacteristic curves are approximated by the line of tangency between the characteristic planes and the characteristic cones, that is, bicharacteristic lines.

20–7 CHARACTERISTIC SURFACE NETWORKS

As mentioned in Section 20–6, numerical integration networks may be constructed by following characteristic surfaces and by following bicharacteristic lines. In this section, four *characteristic surface networks* are described.

20–7(a) Hexahedral Characteristic Surface Network

Thornhill[11] proposed a direct marching method called the *hexahedral characteristic surface network*, illustrated in Fig. 20.22. That network was called the *tetrahedral characteristic surface network* by Fowell.[12] In that network, the initial-value points 1, 2, and 3 are known, and lines 12, 23, and 13 are drawn between those points. The solution point, point 5, is located at the mutual intersection of the characteristic wave surfaces passing through those lines. Bicharacteristic lines 56, 57, and 58 are the lines of tangency between the characteristic cone and the characteristic planes. The particle path 45 (i.e., a streamline in steady three-dimensional flow and a pathline in unsteady two-dimensional flow) is projected rearward from point 5 to intersect the initial-value surface, which is the plane passing through points 1, 2, and 3. The flow properties at points 6, 7, and 8 are determined by linear interpolation along lines 12, 23, and 13, respectively, and the flow properties at point 4 are found by bivariate interpolation (see Appendix A-2) in the initial-value surface. As illustrated in Fig. 20.22, the CFL stability criterion is satisfied. Consequently, the numerical integration algorithm is stable.

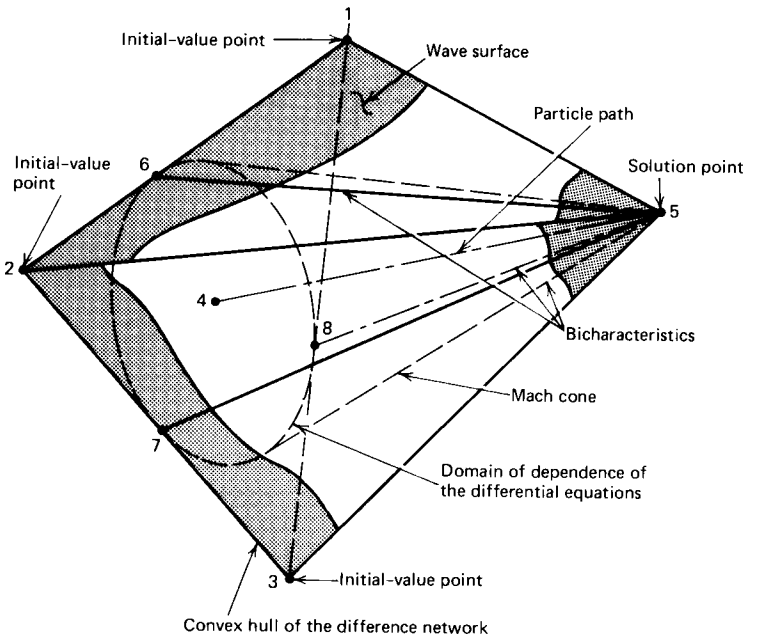

Figure 20.22 Hexahedral characteristic surface network.

Four characteristic lines are determined for the hexahedral characteristic surface network; three bicharacteristic lines and the particle path. It is shown in Section 20–4 that for a steady three-dimensional isentropic supersonic flow, there is one compatibility equation valid along each bicharacteristic, and two compatibility equations valid along the streamline. Consequently, a total of five compatibility equations are available for determining the values of the five flow properties u, v, w, p, and ρ at point 5. For unsteady two-dimensional isentropic flow, discussed in Section 20–5, one compatibility equation applies along each bicharacteristic line and along the particle path. Hence, a total of four compatibility equations are available for determining the values of the four flow properties u, v, p, and ρ at point 5. The cross-derivatives are determined in the initial-value surface. Consequently, the method is a first-order accuracy method.

The hexahedral characteristic surface network was employed by Tsung[13] to determine the steady three-dimensional isentropic supersonic flow past a conical boattail and a delta wing at angle of attack. Reed[14] applied the method to the steady three-dimensional isentropic supersonic flow in nozzles.

The major disadvantages of the hexahedral characteristic surface network are the following.

1. Interpolation is required for obtaining the flow properties at the base points.
2. It is difficult to determine the cross-derivatives at the solution point, and they are needed if second-order accuracy is to be obtained.
3. Interpolation or extrapolation is required in the direction of marching if the solution is to be advanced on parallel planes.

20–7(b) Network of Intersections of Reference Planes with Characteristic Surfaces

Ferrari[15] and Moeckel[16] employed a direct marching method based on the intersections of two characteristic wave surfaces with two reference coordinate planes, as

illustrated in Fig. 20.23. The solution point, point 8, lies at the intersection of the two characteristic wave surfaces and a reference coordinate plane. Points 1, 2, 5, and 6 are initial-value points in the prior solution surface, and points 3 and 7 are located by projecting the stream surface through line 48 rearward to intersect the prior solution surface. Point 4 is a previous solution point in the solution plane being constructed. The curves formed by these intersections are generally not bicharacteristics, and have been called bicharacteristics by Moretti,[17] near or secondary characteristics by Sauer,[18] and semicharacteristics by Katskova and Chushkin.[19] The wave surface compatibility equations are applied along lines 58, 68, and 48, and the stream surface compatibility equations are applied along line 78. The cross-derivatives are determined in the initial-value surface.

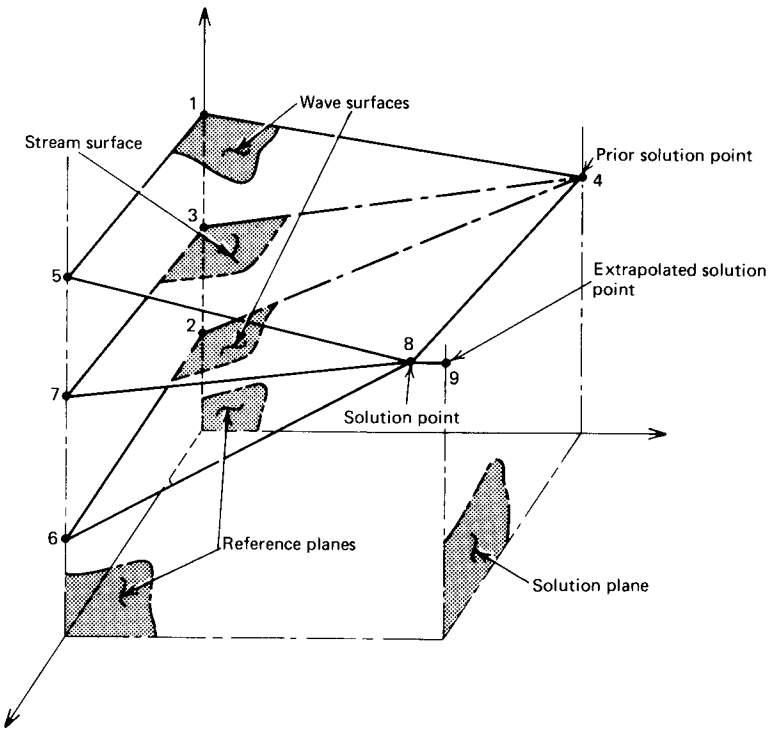

Figure 20.23 Network of intersections of reference planes with characteristic surfaces.

The disadvantages of this method are as follows.

1. Point 4 is outside of the domain of dependence of point 8. Thus, some smearing of the solution occurs.
2. Interpolation is required to obtain the flow properties at the initial-value points 3 and 7.
3. Interpolation or extrapolation is required for maintaining the solution points on parallel planes.
4. To initiate the calculations, the initial conditions are required at the first point 4 on the solution plane. Consequently, an iterative procedure is required for achieving closure of the solution between the first and last reference planes.
5. When large cross flows are present, the differential domain of dependence may fall outside of the convex hull of the difference network, since the network lines

are not, in general, bicharacteristics. In that case, the CFL stability criterion is not satisfied.

6. It is difficult to determine the cross-derivatives at the solution point, and they are needed for obtaining second-order accuracy.

20–7(c) Prismatic Characteristic Surface Network

Based on the work of Titt[20] and Coburn and Dolph,[21] Holt[22] proposed the *prismatic characteristic surface network* illustrated in Fig. 20.24. It is formed by the intersection of two characteristic wave surfaces emanating from two lines in the initial-data surface. The subject network is similar to that based on the intersections of reference planes with characteristic surfaces presented in Section 20–7(b). The only difference is that the end planes are meridional planes through the characteristic cone, defined by two bicharacteristics and the particle path. Accordingly, lines 58 and 68 are bicharacteristics. Fowell[12] called this network the prismatic characteristic surface network.

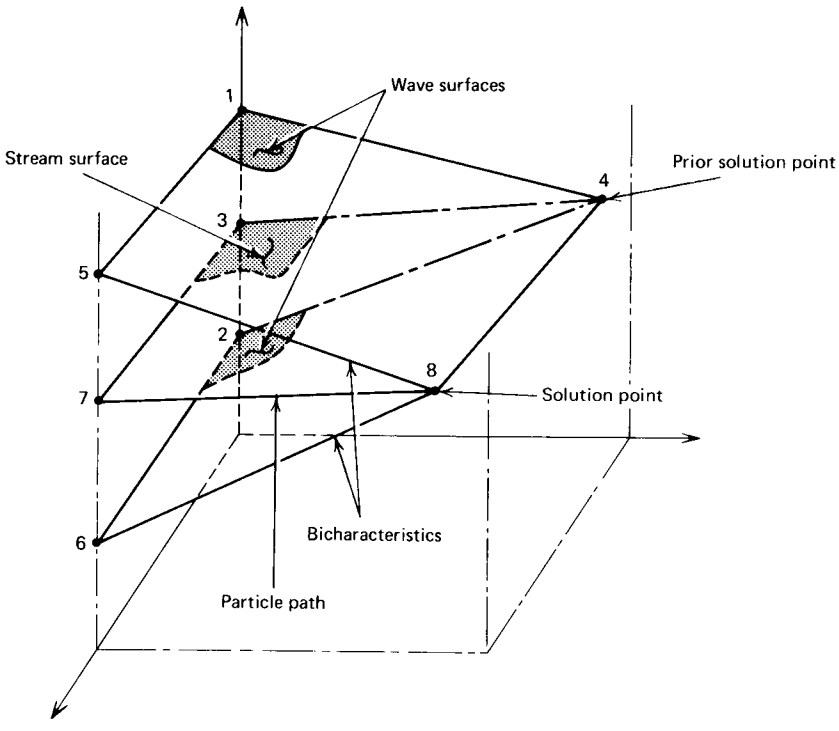

Figure 20.24 Prismatic characteristic surface network.

The prismatic characteristic surface network suffers from the same disadvantages listed in Section 20–7(b) for the network of intersections of reference planes with characteristic surfaces, except for item 5. Apparently, no attempts have been made to apply the subject network.

20–7(d) Near Characteristics Network

A network employing the intersections of characteristic surfaces with a single reference plane, called the *method of near characteristics*, was proposed by Sauer.[18]

The intersections of the wave surfaces and the stream surfaces with the single reference plane are called *near characteristics*. In general, near characteristics are not bicharacteristics or particle paths. An inverse marching method, illustrated in Fig. 20.25, is employed in which the near characteristics are projected rearward from a prespecified solution point, point 4, to intersect the initial-value surface. Flow properties at the base points 1, 2, and 3 are determined by linear interpolation along the intersection of the reference plane with the initial-value surface.

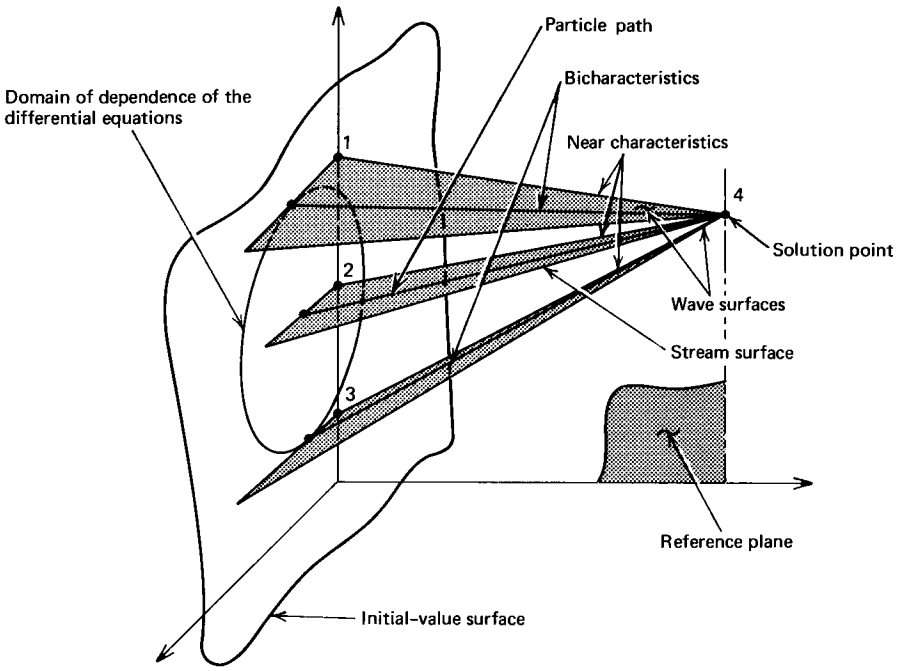

Figure 20.25 Near characteristics network.

The method of near characteristics may also be derived by analogy to the method of characteristics in two independent variables. In applying the near characteristics method, all of the terms in the governing equations that contain derivatives in the direction normal to the reference plane are moved to the right-hand sides of the equations. The momentum equation in the direction normal to the reference plane is not employed at this time. Consequently, the left-hand sides of the remaining governing partial differential equations contain only p, ρ, the velocity components in the directions that specify the reference plane, and their derivatives with respect to the two coordinates defining the reference plane.

If the right-hand sides of those equations are considered as known, that set of equations depends only on the two coordinates defining the reference plane. The characteristic and compatibility equations corresponding to those pseudo-two-dimensional equations are determined by the methods applicable to flows with two independent variables. The corresponding characteristic curves are called *near characteristics*. The compatibility equations applicable along those near characteristics are sufficient for determining all of the flow properties at the solution point, except the velocity component in the direction normal to the reference plane.

The remaining velocity component may be determined from the momentum component equation in the direction normal to the reference plane, which is not employed in determining the near characteristics. A finite difference equation containing the remaining velocity component is obtained by taking the projection of the remaining momentum component equation along the near characteristic particle path. The numerical integration network is then constructed by replacing all of the differentials by forward differences and solving for the flow properties at the solution point.

The main advantage of the method of near characteristics is its simplicity. Only three near characteristics are employed instead of the four required in the other methods. Furthermore, the interpolations for the flow properties at the initial-value points are simple linear interpolations. The solution is obtained at specified points in the system of reference planes. The method has been successfully applied to steady three-dimensional supersonic flows by Moretti,[17] Katskova and Chushkin,[19] Chushkin,[24] and Rakich.[23] The method was applied to unsteady two-dimensional isentropic flow by Cline[25] to determine the boundary conditions for unsteady nozzle flows. The method is particularly well suited to flow about bodies of revolution where meridional planes through the body axis may be taken as the reference planes. It is not apparent that the method of near characteristics can be applied with equal success to more arbitrary flows involving three independent variables.

The major advantages of the method of near characteristics are its similarity to the two-dimensional method of characteristics, and its relative simplicity compared to other three-dimensional methods.

The method of near characteristics has the following major disadvantages.

1. The near characteristics are in general outside of the domain of dependence of the solution point, and smearing of the solution occurs.
2. When strong cross flows are present, the above condition becomes worse.
3. It is difficult to determine the cross-derivatives at the solution point for obtaining second-order accuracy.

Of all of the characteristic surface network methods discussed in this section, the method of near characteristics is the most straightforward to apply.

20–8 BICHARACTERISTIC CURVE NETWORKS

The numerical integration networks discussed in Section 20–7 determine the location of the solution point at the intersections of characteristic surfaces and reference planes. In this section, several numerical integration networks are discussed that locate the solution point at the intersection of bicharacteristic curves.

20–8(a) Hexahedral Bicharacteristic Curve Network

Thornhill[11] proposed the *hexahedral bicharacteristic curve network*, called the tetrahedral bicharacteristic line method by Fowell[12]; the network is illustrated in Fig. 20.26. The solution point, point 5, is located at the mutual intersection of the three characteristic cones having their vertices at points 1, 2, and 3 in the initial-value surface. Lines 15, 25, and 35 are straight-line approximations of the bicharacteristic curves through those points. Point 4 is located at the intersection of the rearward projection of the particle path through point 5 with the initial-value plane. The flow

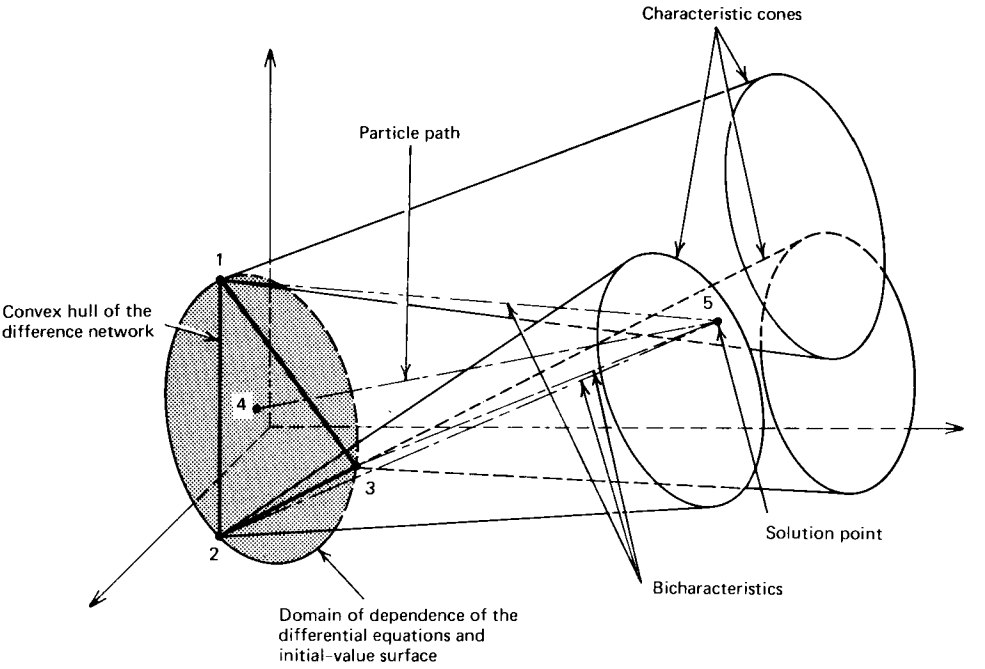

Figure 20.26 Hexahedral bicharacteristic curve network.

properties at point 4 are determined by bivariate interpolation (see Appendix A–2) in the initial-value plane.

The advantage of the subject network is that the bicharacteristic curves through the base points 1, 2, and 3 pass through the solution point, point 5. Consequently, no interpolations are required for determining the flow properties at those points. A disadvantage is the complex calculation required for obtaining the point of intersection of the three conoids. A more serious disadvantage, however, is that the network violates the CFL stability criterion because the differential domain of dependence of the solution point extends outside of the convex hull of the finite difference algorithm, as seen in Fig. 20.26. Fowell[12] applied the network to the analysis of the steady three-dimensional flow over wing-body configurations, but he did not discover the instability of the method because he made only a few calculations by hand. Later numerical work by Sauerwein[26] demonstrated that the method is unstable, and consequently, unsuitable for finite difference calculations.

20–8(b) Modified Hexahedral Bicharacteristic Curve Network

To satisfy the CFL stability criterion, Sauerwein[26] modified the hexahedral bicharacteristic curve network, as illustrated in Fig. 20.27. In the *modified hexahedral bicharacteristic curve network*, the initial-value points 1, 2, and 3 are connected by straight lines, and a circle is inscribed in the resultant triangle. The points where the circle is tangent to the triangle, points 6, 7, and 8, are employed as the base points for constructing the hexahedral bicharacteristic curve network discussed in Section 20–8(a). The flow properties at points 6, 7, and 8 are determined by linear interpolation along lines 12, 23, and 13, respectively. The particle path 45 is projected rearward from point 5 to intersect the initial-value surface, and the flow

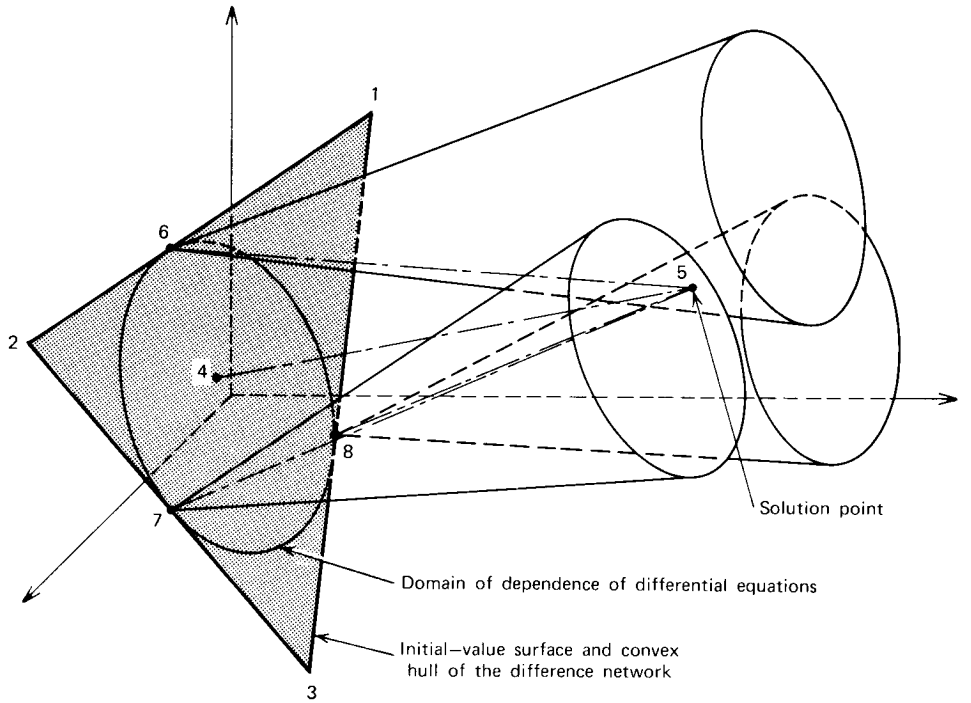

Figure 20.27 Modified hexahedral bicharacteristic curve network.

properties at point 4 are determined by bivariate interpolation in that surface.

Sauerwein[26] demonstrated by computation that the modified network is numerically stable. Otherwise, the modified hexahedral bicharacteristic curve network closely resembles the hexahedral characteristic surface network and, except for its stability, it shares the same advantages and disadvantages.

20–8(c) Inverse Tetrahedral Bicharacteristic Curve Network

Strom[27] proposed the inverse marching method illustrated in Fig. 20.28 where the solution is advanced in a series of parallel solution planes. The location of the solution point, point 6, is determined by projecting the particle path forward from its point of intersection with the initial-value plane, point 5. Four equally spaced bicharacteristic lines are then projected rearward from point 6 to intersect the initial-value plane at points 1, 2, 3, and 4. The flow properties at the latter points are determined by bivariate interpolating polynomials fitted to point 5 and eight neighboring points. The cross-derivatives are determined in the initial-value plane, but they are neglected in the solution plane. Multiple sets of solutions at point 6 are determined by employing the particle path with three of the bicharacteristics at a time. The resulting solution values are subsequently averaged. Accordingly, the subject method may be classified as a redundancy method. The step size between the solution planes is chosen so that the CFL stability criterion is satisfied.

The subject network has the following obvious advantages.

1. The CFL stability criterion is satisfied.
2. Particle paths are followed as the solution progresses, which is a distinct advantage in analyzing nonequilibrium chemically reacting flows.

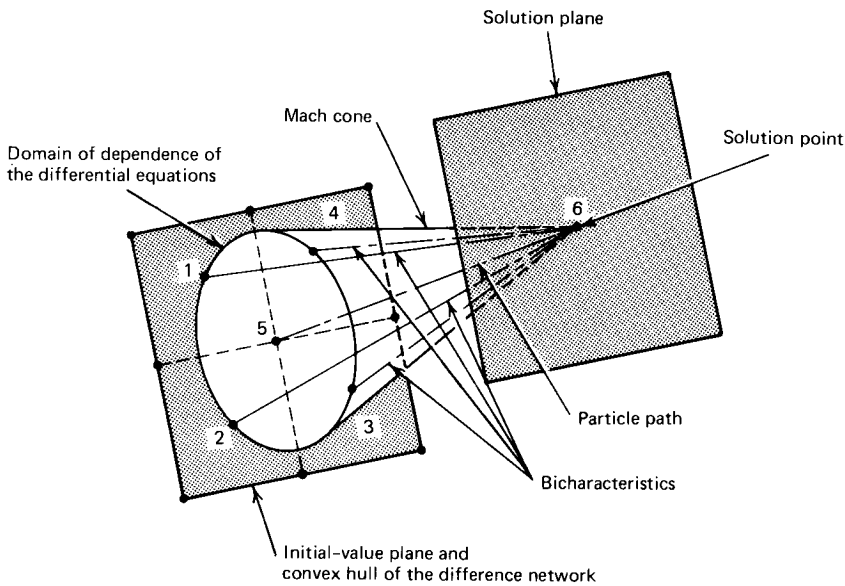

Figure 20.28 Inverse tetrahedral bicharacteristic curve network.

3. The solution is obtained automatically in planes, without further interpolation or extrapolation.
4. The boundary conditions at the solid boundaries, the planes of symmetry, free pressure boundaries, and shock waves are determined in a straightforward manner.

The network suffers from the following disadvantages.

1. Bivariate interpolation is required to determine the flow properties at the base points.
2. The method achieves only first-order accuracy because of the neglect of the cross-derivatives at the solution point.

20–8(d) Inverse Hexahedral Bicharacteristic Curve Network

Cline and Hoffman[28] proposed the inverse marching method illustrated in Fig. 20.29, which is similar to the inverse tetrahedral bicharacteristic curve method discussed in Section 20–8(c) and illustrated in Fig. 20.28. It is Method 1 in Ref. 28. There are two major differences between the subject method and the inverse tetrahedral bicharacteristic curve method proposed by Strom[27]. First, the subject network employs three bicharacteristic lines, oriented 120 deg apart, instead of the four bicharacteristic lines employed by Strom. Second, the subject method achieves second-order accuracy by determining the cross-derivatives in the solution plane by utilizing the global iteration procedure discussed in Section 20–6. The method has been applied successfully to the calculation of steady three-dimensional isentropic supersonic flow in superelliptic nozzles.

The advantages of the network are the same as those attributed to the inverse tetrahedral bicharacteristic curve network discussed in Section 20–8(c), where, in addition, second-order accuracy is obtained.

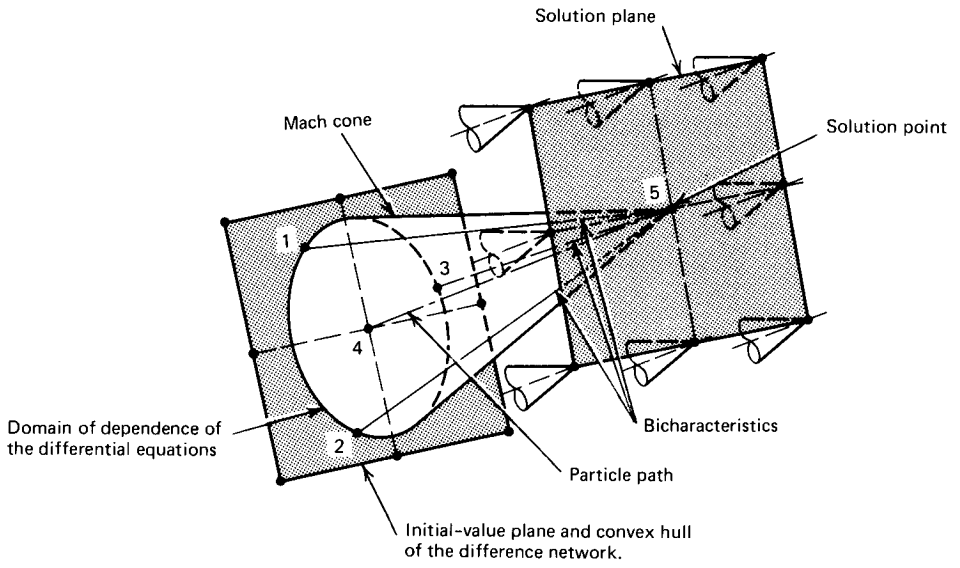

Figure 20.29 Inverse hexahedral bicharacteristic curve network.

The disadvantages of the method are the following.

1. A large number of bivariate interpolations are required in the initial-value surface for determining the flow properties at the base points.
2. Bivariate interpolating polynomials must also be constructed in the solution plane for determining the cross-derivatives in that plane. Those cross derivatives are obtained by differentiating the bivariate interpolating polynomials.
3. The global iteration required to obtain the cross-derivatives in the solution plane and, hence, second-order accuracy, substantially increases the program complexity and the computation time.

20–8(e) Pentahedral Bicharacteristic Curve Network

Butler[8] developed the *pentahedral bicharacteristic curve network* illustrated in Fig. 20.30. The method involves integrating the compatibility equations for the wave surface over the infinite family of bicharacteristic curves passing through a point. In practice, however, the infinite family of bicharacteristics is replaced by four distinct bicharacteristics spaced equally around the Mach conoid. The method obtains second-order accuracy by forming a linear combination of the finite difference forms of the compatibility equations that eliminates explicitly the cross-derivates at the solution point, point 6. The method is not a redundancy method, such as that developed by Strom[27] [see Section 20–8(c)].

Butler introduced the following parameterization of the bicharacteristics, illustrated in Fig. 20.31.

$$d\mathbf{s} = (\mathbf{V} + c\boldsymbol{\alpha}\cos\theta + c\boldsymbol{\beta}\sin\theta)\,dt \qquad (i = 1,2,3) \tag{20.105}$$

where $d\mathbf{s}$ are the rays of a bicharacteristic, t is a parameter specifying the length of a ray, θ is a parametric angle defining a particular bicharacteristic, and $\boldsymbol{\alpha}$ and $\boldsymbol{\beta}$ are unit vectors such that $\mathbf{V}$ (or $\hat{\mathbf{V}}$), $\boldsymbol{\alpha}$ and $\boldsymbol{\beta}$ form an orthogonal set. The parameter c is

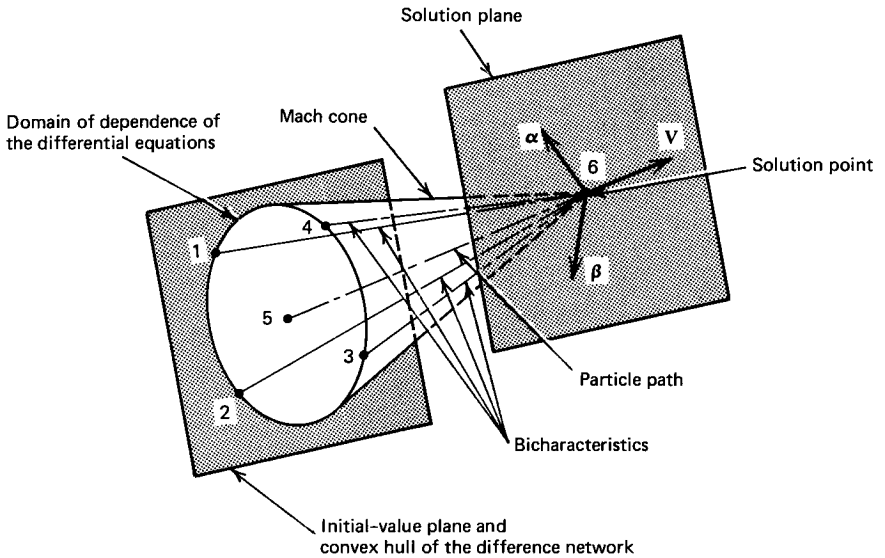

Figure 20.30 Pentahedral bicharacteristic curve network.

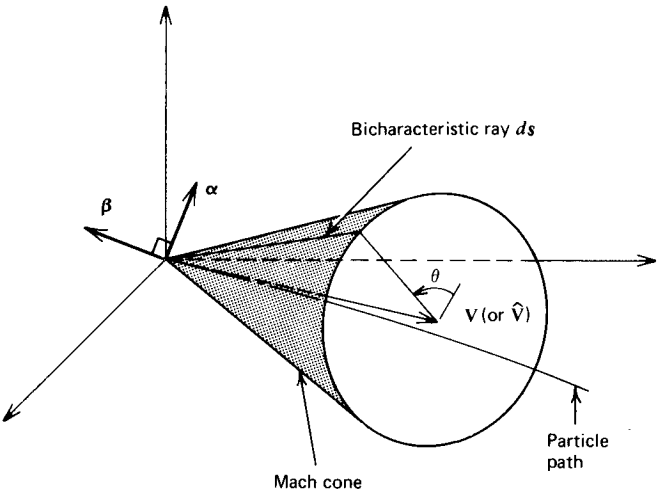

Figure 20.31 Parameterization of the characteristic cone.

the velocity of divergence of the Mach cone (i.e., the rate at which the cone cross-section increases) in the plane normal to the particle path. The bicharacteristic compatibility equations are written in terms of the above parameterization. The compatibility equations valid on the stream surface are unaffected by the bicharacteristic parameterization. Butler also developed a noncharacteristic relation that applies along the particle path by a linear combination of the original partial differential equations.

The four bicharacteristic compatibility equations are then written for $\theta = 0$, $\pi/2$, π, and $3\pi/2$. Those four equations, together with the noncharacteristic equation, are expressed in finite difference form. Three linear combinations of those five equations are formed in which the cross-derivatives at the solution point are *eliminated*. Those three equations and the two compatibility equations valid on the particle path are then solved by the modified Euler predictor-corrector method.

Second-order accuracy is achieved by employing the average values of the coefficients of the compatibility equations.

Elliot,[29] Richardson,[30] and Delaney[7] applied Butler's method to unsteady two-dimensional flows. Ransom[3,4] and Cline[5,6] applied the method to steady three-dimensional supersonic flows. Examples obtained by Ransom[4] and Delaney[7] are presented in Section 20–9. The overall marching algorithm employed by Ransom,[3,4] Cline,[5,6] and Delaney[7] is analogous to that employed by Strom,[27] which is illustrated in Fig. 20.28. By choosing the step size between the solution planes so that the intersection of the characteristic cone with the initial-value surface falls entirely within the convex hull of the difference network, the CFL stability criterion[10] is satisfied. Ransom and Delaney applied the von Neumann stability condition to the overall numerical algorithm and found it also to satisfy that more stringent stability criterion.

The major advantage of the pentahedral bicharacteristic curve network over all of the other networks is that second-order accuracy is obtained without violating the domain of dependence of the solution point.

The major disadvantage of the method is the large number of bivariate interpolations required for determining the flow properties at the base points.

Of all of the methods discussed in Sections 20–7 and 20–8, the pentahedral bicharacteristic curve network proposed by Butler is the only one that achieves second-order accuracy by a local application of the finite difference algorithm at each point of the initial-value surface. All of the other methods achieve only first-order accuracy by a local application of the algorithms. Those methods may, however, achieve second-order accuracy by a global iteration procedure where the cross-derivatives at the solution point are determined by bivariate interpolating polynomials fit in the solution surface. That procedure effectively increases the size of the convex hull of the finite differnece equations and smearing of the solution occurs. The increased complexity and increased computing times required by the global iteration methods are serious disadvantages of those methods.

20–9 APPLICATIONS

The method of characteristics for flows with three independent variables is discussed in the preceding sections. In this section some results obtained by Ransom, Hoffman, and Thompson[4] and Hoffman and Maykut[31] for steady three-dimensional isentropic supersonic flow in nozzles are presented. Some results obtained by Delaney[7,35] for unsteady two-dimensional isentropic flow in turbine cascades are also presented.

20–9(a) Steady Three-Dimensional Isentropic Supersonic Flow In Nozzles

Ransom, Hoffman, and Thompson[4] developed a complete program for the steady three-dimensional isentropic supersonic flow in nozzles based on the pentahedral bicharacteristic curve network proposed by Butler.[8] The global solution for a particular set of initial conditions and boundary conditions is obatined by an algorithm in which the unit processes for interior points, solid boundary points, etc., are applied repetitively. The algorithm consists of integration along a system of streamlines throughout the flow. The specific streamlines that are involved are determined by the network of points that is chosen at the initial-value surface. Those points are chosen so that a uniform spatial distribution is obtained across the flow field and on the boundaries.

The initial-value surface is assumed to be a plane normal to the x direction in a Cartesian coordinate system, and the integration process is applied between a series of planes parallel to the initial-value surface. On the initial-value surface, and each subsequent solution surface, the three thrust components and the three turning moments are determined.

The following boundary conditions apply in supersonic flow problems: solid boundaries, planes of symmetry, constant pressure surfaces, and shock waves. Except for shock waves, the flow boundaries are stream surfaces. The unit process for an interior point is easily modified by replacing one of the compatibility equations for the bicharacteristics with the appropriate boundary condition.

For a solid boundary, the flow streamlines must be tangent to the boundary, and therefore coincide with it. The unit process for an interior point is modified by replacing the compatibility equation for one of the bicharacteristics with the flow tangency condition, equation 20.19. Thus,

$$un_x + vn_y + wn_z = 0 \tag{20.19}$$

where **n** is the unit normal drawn outwardly from the solid surface. The remaining three wave-surface bicharacteristics are oriented so that those corresponding to $\theta = 0$ and π are contained in the tangent plane to the solid surface, and the one corresponding to $\theta = \pi/2$ is located in the interior of the flow field.

It is necessary to make similar modifications to the basic unit process in the case of a constant pressure boundary. For the latter case, the compatibility equation for the fourth bicharacteristic is replaced by the condition that the pressure is known. The latter boundary condition and also the shock wave boundary condition were not developed by Ransom, et al. The plane of symmetry boundary condition is obtained by employing reflection principles to produce image points. The basic unit processes for an interior point and a solid boundary point may then be employed without modification.

The distance between successive solution surfaces must be regulated so that the CFL stability criterion[10] is satisfied at all points of the network. The allowable step size is a function of the local flow parameters and the point spacing, and is given by

$$\Delta x = \frac{u^2}{(cV)}\left[1 - \left(\frac{c}{V}\right)\left(\frac{V^2}{u^2} - 1\right)^{1/2}\right] R_{\min} \tag{20.106}$$

where V is the magnitude of the flow velocity, and $R_{\min}$ is the distance from the point of intersection of the streamline with the initial-value surface and the nearest point on the convex hull of the points utilized in constructing the finite difference network. The paraemter c is the velocity of divergence of the Mach cone in the plane perpendicular to the streamline, and is given by

$$c = \left[\frac{a^2 V^2}{(V^2 - a^2)}\right]^{1/2} \tag{20.107}$$

Figure 20.32 illustrates diagrammatically the overall numerical algorithm. A typical network for the points on the initial-value surface is shown, and the boundary conditions for a solid boundary and a plane of symmetry are illustrated. The algorithm follows streamlines from one solution plane to the next until the desired portion of the flow field has been determined.

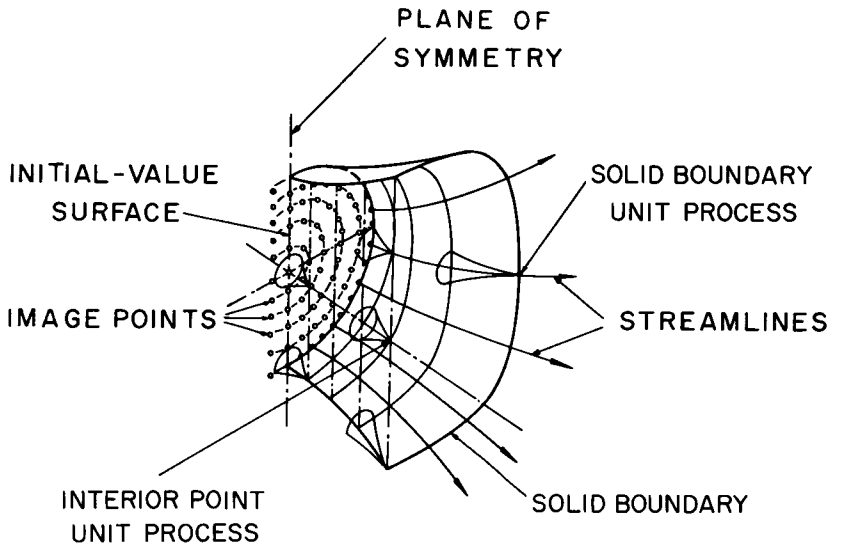

Figure 20.32 Schematic illustration of the overall numerical algorithm.

Figure 20.33 presents an isometric view of the cross-sections and boundary streamlines for one quadrant of a superelliptic nozzle. The term *superelliptic* was used by Ransom, et al., to denote a nozzle having cross-sections given by the general equation

$$\left(\frac{y}{y_o}\right)^{e_1} + \left(\frac{z}{z_o}\right)^{e_2} = 1 \tag{20.108}$$

where y_o and z_o are the y and z coordinate intercepts on the xy and xz coordinate planes, respectively, and e_1 and e_2 are variable exponents. The intercepts y_o and z_o and the exponents e_1 and e_2 are specified as quadratic functions of x and may be different in all four quadrants.

The superelliptic nozzle contour illustrated in Fig. 20.33 is specified by varying the exponents from 2.0 at the inlet to 10.0 at the exit. The cross-sections are, consequently, circular at the inlet and become superelliptic in the diverging section

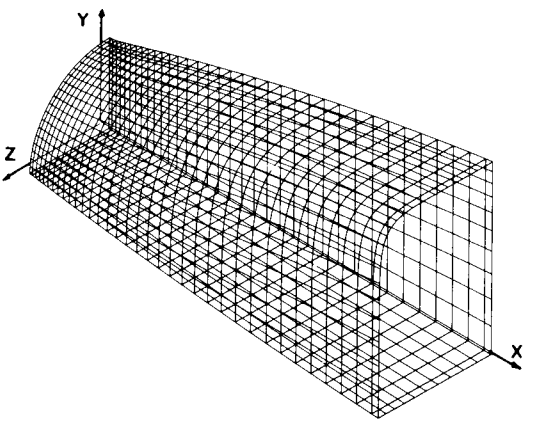

Figure 20.33 Isometric view of a quadrant of the superelliptic nozzle.

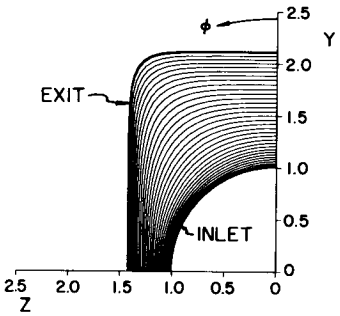

Figure 20.34 Nozzle cross-sections for a quadrant of the superelliptic nozzle.

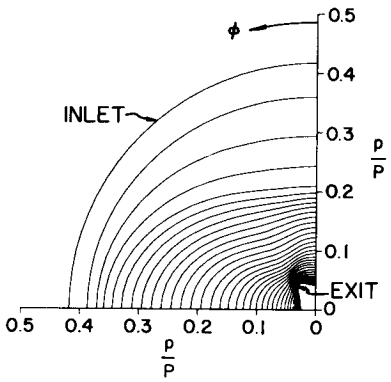

Figure 20.35 Polar pressure plots for a quadrant of the superelliptic nozzle.

of the nozzle. Figure 20.34 presents a plot of the cross-sections for a quadrant of the nozzle, and Fig. 20.35 presents a corresponding polar plot of the wall pressure ratio p/P; the curves apply to the flow of a perfect gas with $\gamma = 1.40$. The initial-value plane is a parallel uniform flow having a Mach number of 1.05.

The polar plots of the wall pressure ratio p/P present the distribution of the wall pressure around the nozzle contour at each cross-section where a calculation is made. The outermost pressure contour corresponds to the innermost cross-section contour. The radial distance to the curve is proportional to the pressure at the wall (normalized by the stagnation pressure) at the corresponding angular location of the wall in the physical plane. The outermost pressure curve is circular because of the assumed uniform pressure distribution on the initial-value surface. The more rapid decrease of the wall pressure in the xy plane than in the xz plane produces a significant circumferential flow component, so that the flow field is a truly three-dimensional flow. Note that the highest pressures in the exit plane are in the corner while the lowest pressures occur at the minor axis intercept. A prediction based on a quasi-three-dimensional flow analysis that neglects cross flows yields exactly the opposite result. The flow field was analyzed by following 121 streamlines, and the solution was obtained on 36 solution planes.

Ransom, et al.,[4] conducted cold flow experiments employing the nozzle configuration illustrated in Fig. 20.33. Figure 20.36 compares the calculated and measured values for the pressure distribution along the major and minor axes of the nozzle cross-section. The predicted and measured pressures for both of the profiles are in good agreement. The point where the two pressure distributions cross is predicted quite accurately.

Another example of steady three-dimensional isentropic flow analyzed by Hoffman and Maykut[37] is the thrust misalignment in a conical propulsive nozzle when the nozzle throat plane is misaligned with respect to the axis of the nozzle divergence. The computer program developed by Ransom, et al.,[4] was utilized in the study. Figure 20.37 illustrates schematically the physical model of the nozzle employed in the study. The conical nozzles had a semiangle denoted by α, and a throat radius of curvature ρ_t equal to one-half the throat radius y_t, that is, $\lambda = \rho_t/y_t = 0.5$. The inlet axis is misaligned by $\theta_i = -1.0$ deg with respect to the axis of the nozzle divergence. The flowing gas is a perfect gas with $\gamma = 1.2$, and in the initial-value plane the Mach number is 1.10. The analysis was performed with 91 streamlines and 34 solution planes.

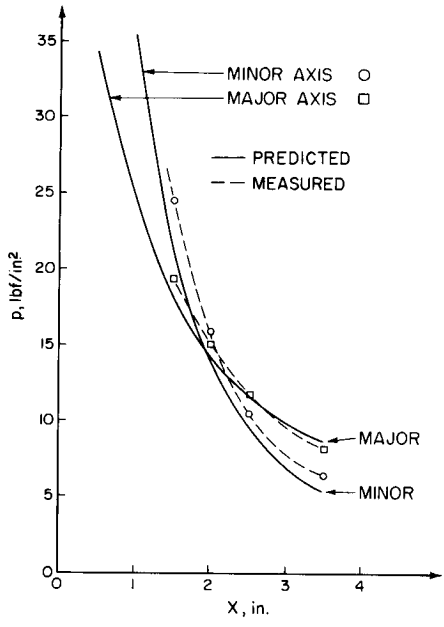

Figure 20.36 A comparision between predicted and measured pressures along the major and minor axes of the superelliptic nozzle.

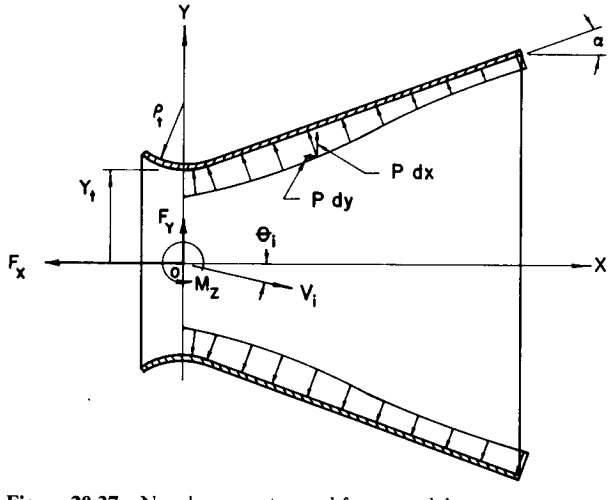

Figure 20.37 Nozzle geometry and force model.

Figure 20.38 presents the calculated values of the side specific impulse I_{F_y} as a function of x/y_t (see Fig. 20.37), with the cone semiangle α as a parameter. Figure 20.39 presents the corresponding results for the specific moment I_{M_z}. The magnitudes of the side force and its moment scale linearly with misalignment angle over the range of θ_i from 0 to -2 deg. The oscillatory nature of the side force and its moment is evident. From the results calculated for a range of cone angle and different inlet geometries, it is possible to select designs that minimize the effects of thrust misalignment.

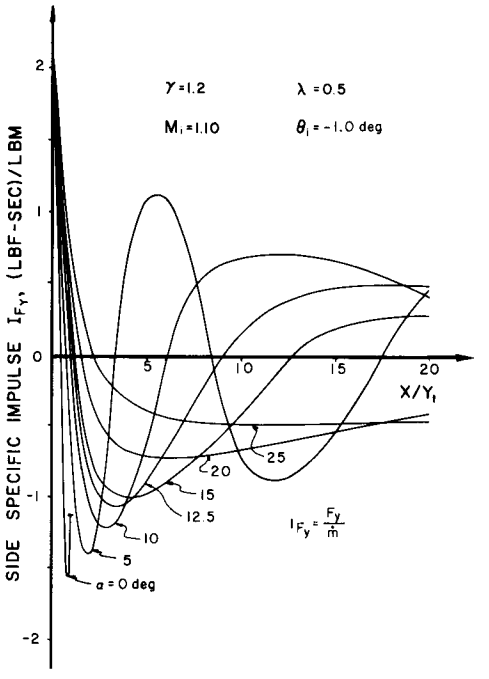

Figure 20.38 Effect of the cone semiangle α on the side specific impulse I_{F_y}

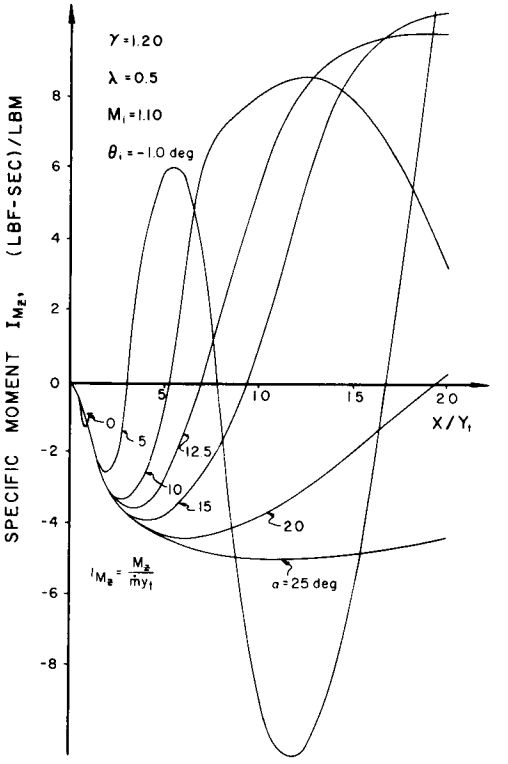

Figure 20.39 Effect of the cone semiangle α on the specific moment I_{M_z}.

20–9(b) Unsteady Two-Dimensional Isentropic Flow in Turbine Cascades[7,35]

The determination of the steady two-dimensional isentropic flow field in the blade passages of either a subsonic axial-flow compressor or an axial-flow turbine is difficult, because the partial differential equations governing subsonic flow are elliptic. Consequently, the solution at every point in the flow field depends on all of the boundary data simultaneously. In the case of an unsteady two-dimensional isentropic flow of an inviscid fluid, however, the governing equations are hyperbolic, and the method of characteristics developed in Section 20–5 may be employed for determining the flow field. Delaney[7,35] developed a complete computer program, based on the pentahedral bicharacteristic curve network proposed by Butler,[8] for calculating the steady two-dimensional isentropic subsonic and transonic flow fields in turbine blade passages, by determining the asymptotic limit at large time of the unsteady flow field having the boundary conditions of the steady flow field.

Figure 20.40 illustrates schematically the turbine blade cascade investigated by Delaney. Figure 20.41 presents the finite difference network for analyzing the flow in the cascade. The grid points are fixed in space, and an inverse integration network is employed. Boundary conditions for the network are: the leading and trailing edge points, the solid boundary points, the upstream and downstream boundary points, and the periodic boundary condition. The unit process for an interior point is modified for a solid boundary point by replacing one of the wave surface bicharacteristic compatibility equations with the flow tangency condition.

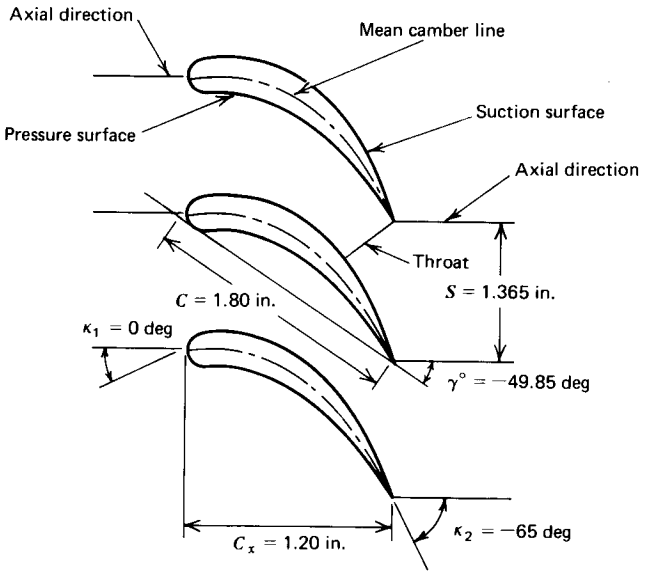

Figure 20.40 Turbine blade cascade nomenclature (taken from Reference 7).

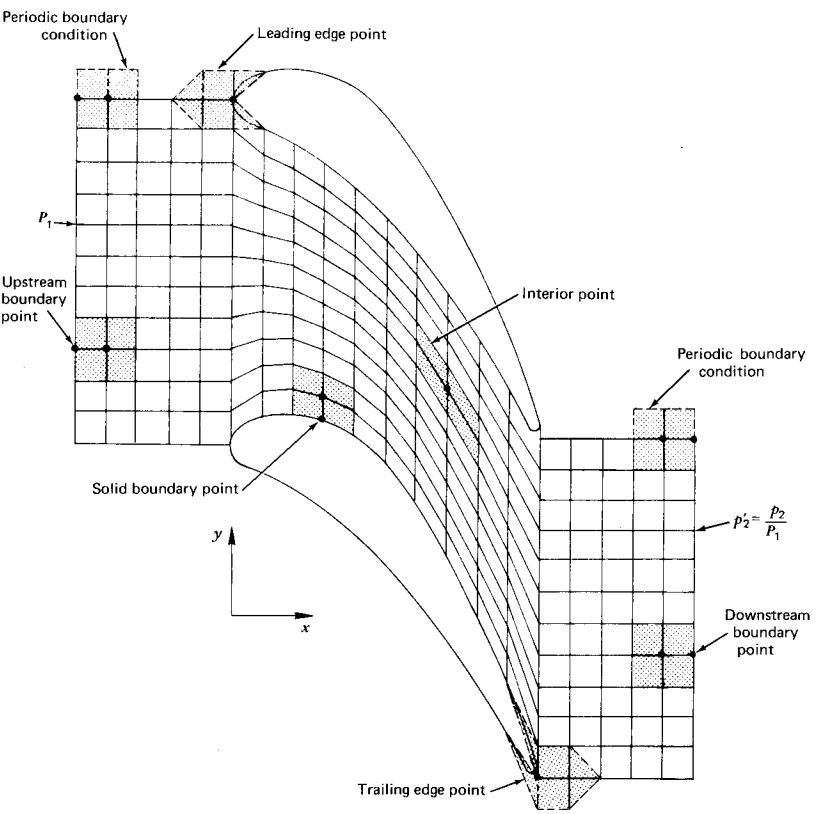

Figure 20.41 Cascade finite difference network (taken from Reference 35).

At the upstream boundary points, the steady-state stagnation pressure and temperature are specified for all time, and the *whirl component* of velocity (i.e., the y component of velocity at the entrance to the cascade) is specified as zero. At the downstream boundary points the steady state static pressure is specified for all time. The leading and trailing edge points are special cases of the solid boundary point. The flow field within each blade passage is identical. Consequently, the periodic boundary condition merely specifies that the flow properties at the top row of points are the same as those at the bottom row of points.

Because the steady state solution is to be determined, any reasonable distribution of the flow properties in the initial-value plane is acceptable. Delaney specified the initial flow properties to be the upstream stagnation properties; that is, $p = P_1$, $\rho = \rho_{o1}$, and $u = v = 0$. The flow is then started by specifying the steady-state static pressure along the downstream boundary. The resulting transient solution is analogous to the physical situation in which a valve is suddenly opened downstream of the cascade.

The global solution for a particular set of steady-state boundary conditions is obtained by the repetitive application of the unit processes for an interior and a boundary point on successive solution planes. The time increment between successive solution planes is regulated so that the CFL stability criterion[10] is satisfied at every point in the network. The allowable step size is given by

$$\Delta t = \frac{R_{\min}}{(|u_i| + a)_{\max}} \tag{20.109}$$

where $R_{\min}$ is the distance from the solution point to the nearest point on the convex hull of the difference network, $u_i = u$ or v, and $(|u_i| + a)_{\max}$ is the maximum value of $(|u_i| + a)$ at all of the points on the convex hull of the finite difference network.

The criterion employed for checking the convergence of the transient solution to the steady state solution is the change in the normalized pressure at all of the grid points as the solution proceeds from one solution plane to the next. When the maximum value of that change is within a specified tolerance, the solution is assumed to have converged.

Delaney presented two cases of steady flow through a turbine cascade: one for subsonic flow throughout and one with regions of transonic flow. The solution grid in both cases comprised 41 uniformly spaced constant *x-lines* with 12 points along each line. The geometric data for the blades are specified in Fig. 20.40. The only difference between the subsonic and transonic flow cases is the value of the static pressure along the downstream boundary, denoted by p_2. For the subsonic flow case, $p_2 = 0.685\ P_1$, while for the transonic flow case, $p_2 = 0.578\ P_1$, where P_1 is the steady-state stagnation pressure along the upstream boundary. In both cases the whirl velocity component along the upstream boundary is zero, so that the velocity along the upstream boundary is in the axial direction. The specific heat ratio of the gas is $\gamma = 1.40$.

Figure 20.42 presents the steady-state velocity vector field. The velocity increases gradually at the passage inlet, increases rapidly through the blade passage up to the throat, then remains approximately uniform at the passage exit. Figure 20.43 presents a plot of the contours of the normalized steady-state static pressure $p' = p/P_1$ for the subsonic flow in the blade passage. The maximum pressure gradient occurs on the suction surface just downstream of the passage inlet, and on the pressure surface just upstream to the passage throat. The pressure is nearly

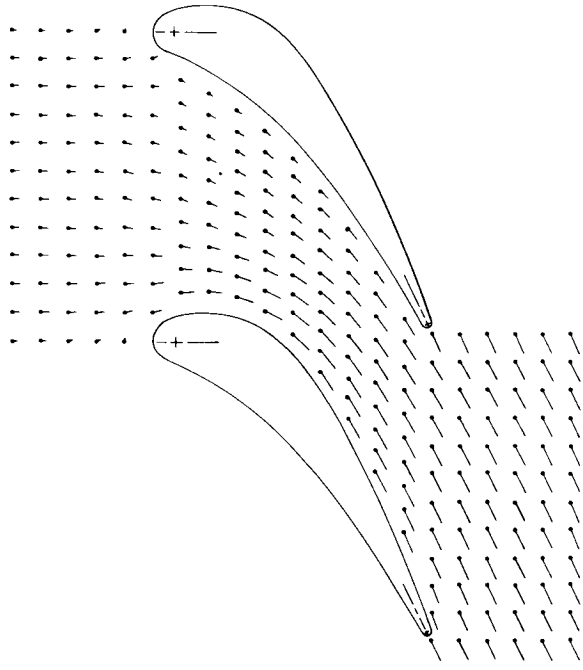

Figure 20.42 Steady-state velocity vector field for the subsonic flow case; $p_2' = 0.685$ (taken from Reference 35).

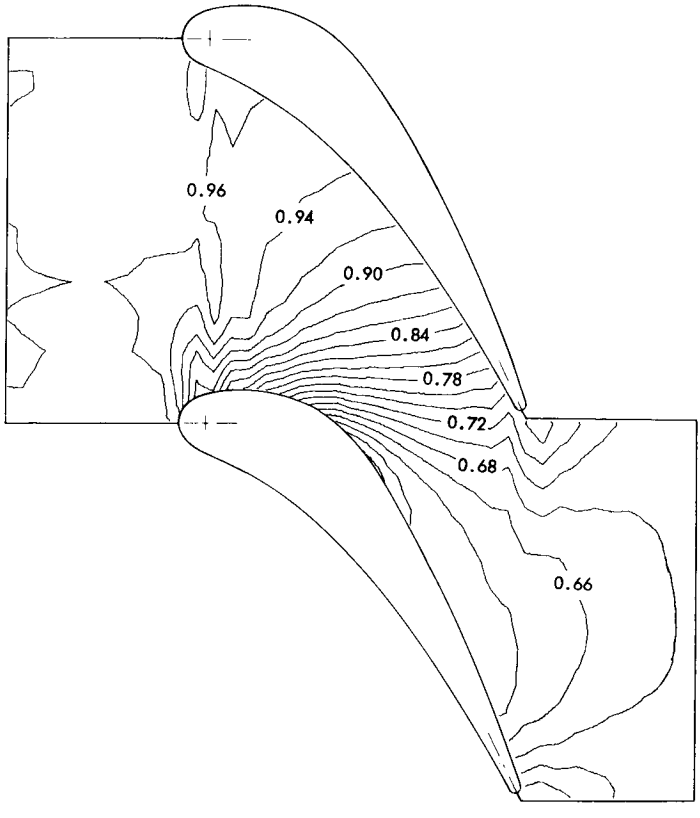

Figure 20.43 Contours of steady-state static pressure p' for the subsonic flow case; $p_2' = 0.685$ (taken from Reference 35).

uniform upstream from the cascade, and the axial pressure gradient is nearly zero at the downstream boundary. For $\gamma = 1.40$, the critical pressure ratio is $(p')^* = 0.528$. It is seen from the values of p' in Fig. 20.43 that the flow is subsonic throughout the blade passage. Figure 20.44 presents curves of constant steady-state Mach number M corresponding to the isobars in Fig. 20.43. Along the upstream boundary, the axial Mach number gradient is nearly zero, but there is a substantial normal Mach number gradient along that boundary. Approximately 1400 time steps were required to obtain the steady state solution.

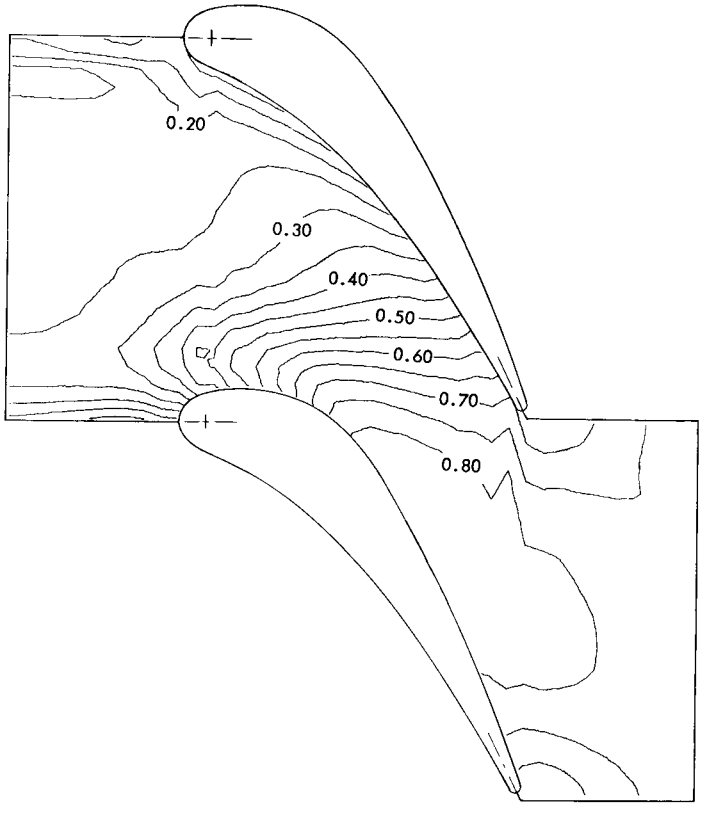

Figure 20.44 Contours of steady-state Mach number M for the subsonic flow case; $p_2' = 0.685$ (taken from Reference 35).

Figure 20.45 presents a comparison of the calculated values of the pressure along the blade surfaces and the measured values determined by Huffman, McClure, Holtmann, and Sinnet.[32] Good agreement between the calculated and measured values is shown.

The transonic flow case presented by Delaney is identical to the subsonic flow case just discussed except that the static pressure along the downstream boundary is $p_2 = 0.578 P_1$. The initial flow field for the transonic case is chosen as the steady-state solution for the preceding subsonic flow case. Figure 20.46 presents the Mach number contours for the transonic flow case. The flow field is almost identical to that presented in Fig. 20.44, except for the small region of supersonic flow located on the suction surface near the trailing edge of the blade. The solution required approximately 1000 time steps.

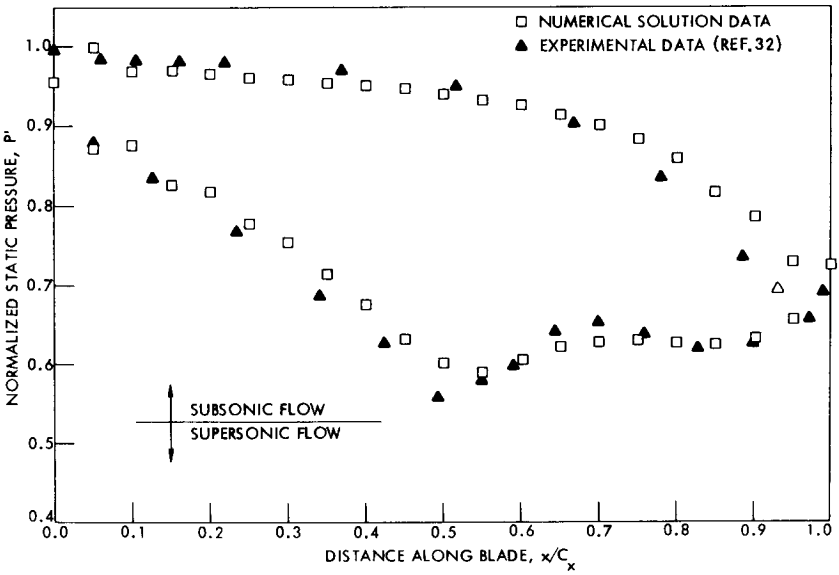

Figure 20.45 Blade surface steady-state static pressure distribution p' for the subsonic flow case; $p_2' = 0.685$ (taken from Reference 35).

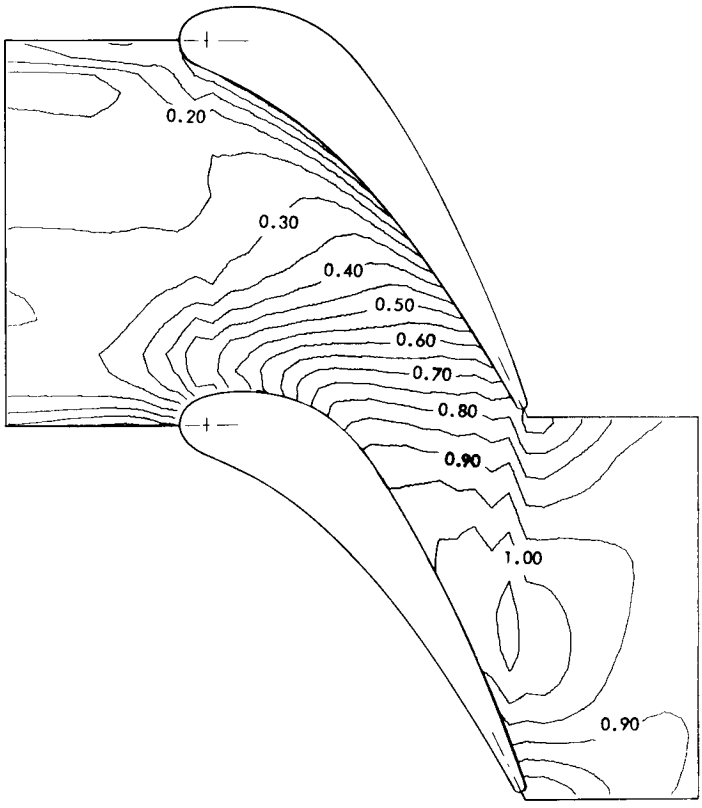

Figure 20.46 Contours of steady-state Mach number M for the transonic flow case; $p_2' = 0.578$ (taken from Reference 35).

The results obtained by Delaney neglected the presence of shock waves. For the transonic flow case illustrated in Fig. 20.46, the effects of any weak shock waves that might be present are probably negligible. If the pressure at the downstream boundary is decreased very much, however, it would be necessary to add a shock-wave tracing capability to the computer program.

The results obtained by Delaney demonstrate the adaptability of the methods developed for analyzing unsteady flow to the problem of obtaining the solution to either a steady subsonic flow problem or a mixed flow problem.

REFERENCES

1. R. Courant and D. Hilbert, *Methods of Mathematical Physics*, Vol. II, Interscience Publishers, New York, 1962.
2. V. V. Rusanov, "The Characteristics of General Equations of Gas Dynamics," *Zhurnal vychislitel 'noi mathematiki mathematicheskoi fiziki*, Vol. 3, No. 3, pp. 508–527, 1963.
3. V. H. Ransom, "A Second-Order Numerical Method of Characteristics for Three-Dimensional Supersonic Flow," Ph. D. Thesis, Purdue University, January 1970.
4. V. H. Ransom, J. D. Hoffman, and H. D. Thompson, "A Second-Order Bicharacteristics Method for Three-Dimensional, Steady Supersonic Flow," *Journal of the American Institute of Aeronautics and Astronautics*, Vol. 10, No. 12, pp. 1573–1581, December 1972.
5. M. C. Cline, "The Analysis of Nonequilibrium, Chemically Reacting, Supersonic Flow in Three Dimensions," Ph. D. Thesis, Purdue University, August 1971.
6. M. C. Cline and J. D. Hoffman, "The Analysis of Nonequilibrium, Chemically Reacting, Supersonic Flow in Three Dimensions Using a Bicharacteristic Method," *Journal of Computational Physics*, Vol. 12, No. 1, pp. 1–23, May 1973.
7. R. A. Delaney, "A Second-Order Method of Characteristics for Two-Dimensional Unsteady Flow with Application to Turbomachinery Cascades," Ph. D. Thesis, Iowa State University, 1974.
8. D. S. Butler, "The Numerical Solution of Hyperbolic Systems of Partial Differential Equations in Three Independent Variables," *Proceedings of the Royal Society of London*, Vol. 255A, pp. 232–252, 1960.
9. R. D. Richmyer, and K. W. Morton, *Difference Methods for Initial Value Problems*, Second Edition, Interscience Publishers, New York, 1967.
10. R. Courant, K. O. Friedrichs, and H. Lewy, "Uber die Partiellen Differenzialgleichungen der Mathematischen Physik," *Mathematische Annalen*, Vol. 100, pp. 32–74, 1928.
11. C. K. Thornhill, "The Numerical Method of Characteristics for Hyperbolic Problems in Three Independent Variables," ARC Reports and Memoranda No. 2615, September 1948.
12. L. R. Fowell, "Flow Field Analysis for Lifting Re-Entry Configurations by the Method of Characteristics," Institute of Aerospace Sciences, Paper No. 61–208–1902, June 1961.
13. C. C. Tsung, "Study of Three-Dimensional Supersonic Flow Problems by a Numerical Method Based on the Method of Characteristics (Specially Adapted for Use on High Speed Electronic Digital Computers)," Ph. D. Thesis, University of Illinois, January 1961.
14. V. L. Reed, "Generalized Three Independent Variable Characteristics Computer Program," Brown Engineering Company, Inc., Huntsville, Alabama, TR R–66–2, Vol. 3, January 1966.
15. C. Ferrari, "Interference Between Wing and Body at Supersonic Speeds- Analysis by the Method of Characteristics," *Journal of Aeronautical Sciences*, Vol. 16, No. 7, pp. 411–434, July 1949.
16. W. E. Moeckel, "Use of Characteristic Surfaces for Unsymmetrical Supersonic Flow Problems," NACA Technical Note No. 1849, March 1949.
17. G. Moretti, "Three-Dimensional Supersonic Flow Computations," *Journal of the American Institute of Aeronautics and Astronautics*, Vol. 1, No. 9, pp. 2192–2193, September 1963.

18. R. Sauer, "Dreidimensionale Probleme der Characteristikentheorie partieller Differential-gleichungen," *Zeitschrift fur angewandte Mathematik und Mechanik*, Vol. 30, pp. 347–356, November-December 1950.
19. O. N. Katskova and P. I. Chushkin, "Three-Dimensional Supersonic Equilibrium Flow of a Gas around Bodies at Angles of Attack," NASA TT F–9790, 1965.
20. E. Titt, "An Initial-Value Problem for all Hyperbolic Partial Differential Equations of Second-Order with Three Independent Variables," *Annals of Mathematics*, Vol. 40, No. 4, pp. 862–891, October 1939.
21. N. Coburn, and C. L. Dolph, "The Method of Characteristics in the Three-Dimensional Stationary Supersonic Flow of a Compressible Gas," Proceedings of the First Symposium on Applied Mathematics, Americal Mathematical Society, 1949.
22. M. Holt, "The Method of Characteristics for Steady Supersonic Rotational Flow in Three Dimensions," *Journal of Fluid Mechanics*, Vol. 1, pp. 409–423, 1956.
23. J. V. Rakich and J. W. Cleary, "Theoretical and Experimental Study of Supersonic Steady Flow around Inclined Bodies of Revolution,"*Journal of the American Institute of Aeronautics and Astronautics*, Vol. 8, No. 3, pp. 511–518, March 1970.
24. P. I. Chushkin, "Numerical Method of Characteristics for Three-Dimensional Supersonic Flows," Chapter 2, *Progress in Aeronautical Sciences*, Vol. 9, Edited by P. Kuchemann, Pergamon Press, New York, 1968.
25. M. C. Cline, "Computation of Steady Nozzle Flow by a Time-Dependent Method," *Journal of the American Institute of Aeronautics and Astronautics*, Vol. 12, No. 4, pp. 419–420, April 1974.
26. H. Sauerwein, "The Calculation of Two- and Three-Dimensional Inviscid Unsteady Flows by the Method of Characteristics," Ph. D. Thesis, Massachusetts Institute of Technology, June 1964.
27. C. R. Strom, "The Method of Characteristics for Three-Dimensional Steady and Unsteady Reacting Gas Flows," Ph. D. Thesis, University of Illinois, January 1965.
28. M. C. Cline and J. D. Hoffman "Comparison of Characteristic Schemes for Three-Dimensional, Steady, Isentropic Flow," *Journal of the American Institute of Aeronautics and Astronautics*, Vol. 10, No. 11, pp. 1452–1458, November 1972.
29. L. A. Elliot, "Shock Fronts in Two-Dimensional Flow," *Proceedings of the Royal Society of London*,Vol. A267, pp. 558–565, 1962.
30. D. J. Richardson, "The Solution of Two-Dimensional Hydrodynamic Equations by the Method of Characteristics," pp. 295–318, *Methods of Computational Physics*, Vol. 3, Edited by B. Alder, Academic Press, New York, 1964.
31. J. D. Hoffman and A. R. Maykut, "Gas Dynamic Gain of Supersonic Thrust Nozzles," *Journal of Spacecraft and Rockets*, Vol. 11, No. 10, pp. 697–704, November 1974.
32. G. D. Huffman, R. B. McClure, R. L. Holtman, and G. T. Sinnet, "Results of a Two-Dimensional Turbine Cascade (AACE II) Test," Detroit Diesel Allison Division, General Motors Corporation, Research Note 71–47, July 1971.
33. A. J. McConnell, *Applications of Tensor Analysis*, Dover Publications, New York, 1957.
34. N. Coburn, *Vector and Tensor Analysis*, Chapters IX to XI, Macmillan, New York, 1955.
35. R. A. Delaney and P. Kavanagh, "Transonic Flow Analysis in Axial-Flow Turbomachinery Cascades by a Time-Dependent Method of Characteristics, "*Journal of Engineering for Power, Transactions of the American Society of Mechanical Engineers,* pp. 356-364, July 1976.

D
tables

Tables D.1a to D.1m present the specific heat, enthalpy, entropy, and equilibrium constant for 13 selected gases in both SI and EE units.

The values of $\overline{m}$ and $\Delta\overline{H}^{\circ}_{f,298}$ presented in Tables D.1a to D.1m are taken from D. R. Stull, H. Prophet, et al., *JANAF Thermochemical Tables*, Second Edition, NSRDS-NBS 37, National Bureau of Standards, June 1971. The values of $\bar{c}^{\circ}_{p}$, $(\overline{H}^{\circ} - \overline{H}^{\circ}_{298})$, $\bar{s}^{\circ}$, and $\log_{10} K_p$ are calculated by the subroutine JANNAF presented in Section 14-3(a) from the c_p versus t curve fits taken from S. Gordon and B. J. McBride, "Computer Program for Calculation of Complex Chemical Equilibrium Compositions, Rocket Performance, Incident and Reflected Shocks, and Chapman–Jouguet Detonations," NASA SP-273, 1971.

Table D.1a Specific Heat, Enthalpy, Entropy, and Equilibrium Constant for Carbon Monoxide CO

$\bar{m}_{CO} = 28.01055$, $\Delta\bar{H}^{\circ}_{f,298} = -110{,}529$ kJ/kmol $= -47{,}520$ Btu/lbmol

T, K	$\bar{c}_p^{\circ}$, kJ/kmol-K	$(\bar{H}^{\circ} - \bar{H}^{\circ}_{298})$, kJ/kmol	$\bar{s}^{\circ}$, kJ/kmol-K	$\log_{10} K_P$	$\bar{s}^{\circ}$, Btu/lbmol-R	$(\bar{H}^{\circ} - \bar{H}^{\circ}_{298})$, Btu/lbmol	$\bar{c}_p^{\circ}$, Btu/lbmol-R	T, R
100	29.791	-5,810	165.431	62.823	39.512	-2,498	7.115	180
200	29.251	-2,862	185.888	33.568	44.399	-1,230	6.986	360
298	29.130	0	197.532	24.030	47.180	0	6.958	537
300	29.131	54	197.713	23.910	47.223	23	6.958	540
400	29.344	2,975	206.115	19.109	49.230	1,279	7.009	720
500	29.804	5,931	212.709	16.235	50.805	2,550	7.118	900
600	30.431	8,942	218.196	14.318	52.115	3,844	7.268	1080
700	31.150	12,020	222.940	12.946	53.248	5,168	7.440	1260
800	31.891	15,172	227.148	11.914	54.253	6,523	7.617	1440
900	32.589	18,397	230.946	11.107	55.160	7,909	7.784	1620
1000	33.182	21,686	234.411	10.459	55.988	9,324	7.925	1800
1100	33.668	25,030	237.597	9.926	56.749	10,761	8.041	1980
1200	34.105	28,419	240.546	9.479	57.453	12,218	8.146	2160
1300	34.499	31,849	243.291	9.099	58.109	13,693	8.240	2340
1400	34.852	35,317	245.861	8.771	58.723	15,184	8.324	2520
1500	35.167	38,818	248.277	8.486	59.300	16,689	8.400	2700
1600	35.449	42,349	250.555	8.234	59.844	18,207	8.467	2880
1700	35.698	45,907	252.712	8.011	60.359	19,737	8.526	3060
1800	35.920	49,488	254.759	7.812	60.848	21,276	8.579	3240
1900	36.116	53,090	256.706	7.632	61.313	22,825	8.626	3420
2000	36.288	56,711	258.563	7.469	61.757	24,381	8.667	3600
2100	36.441	60,347	260.338	7.321	62.181	25,945	8.704	3780
2200	36.575	63,998	262.036	7.186	62.586	27,515	8.736	3960
2300	36.693	67,662	263.664	7.062	62.975	29,090	8.764	4140
2400	36.797	71,336	265.228	6.947	63.349	30,669	8.789	4320
2500	36.889	75,020	266.732	6.841	63.708	32,253	8.811	4500
2600	36.970	78,713	268.181	6.742	64.054	33,841	8.830	4680
2700	37.043	82,414	269.577	6.650	64.387	35,432	8.848	4860
2800	37.109	86,122	270.926	6.564	64.710	37,026	8.863	5040
2900	37.169	89,836	272.229	6.483	65.021	38,623	8.878	5220
3000	37.225	93,556	273.490	6.408	65.322	40,222	8.891	5400
3100	37.277	97,281	274.712	6.337	65.614	41,824	8.903	5580
3200	37.327	101,011	275.896	6.269	65.897	43,428	8.915	5760
3300	37.375	104,746	277.045	6.206	66.171	45,033	8.927	5940
3400	37.422	108,486	278.162	6.146	66.438	46,641	8.938	6120
3500	37.468	112,230	279.247	6.089	66.697	48,251	8.949	6300
3600	37.514	115,979	280.303	6.034	66.949	49,863	8.960	6480
3700	37.561	119,733	281.332	5.983	67.195	51,477	8.971	6660
3800	37.608	123,492	282.334	5.933	67.434	53,093	8.982	6840
3900	37.655	127,255	283.312	5.886	67.668	54,711	8.994	7020
4000	37.702	131,023	284.265	5.841	67.896	56,330	9.005	7200
4100	37.749	134,795	285.197	5.798	68.118	57,952	9.016	7380
4200	37.795	138,572	286.107	5.757	68.336	59,576	9.027	7560
4300	37.841	142,354	286.997	5.717	68.548	61,202	9.038	7740
4400	37.884	146,140	287.868	5.679	68.756	62,830	9.048	7920
4500	37.924	149,931	288.719	5.642	68.959	64,460	9.058	8100
4600	37.961	153,725	289.553	5.607	69.159	66,091	9.067	8280
4700	37.993	157,523	290.370	5.573	69.354	67,724	9.074	8460
4800	38.019	161,324	291.170	5.540	69.545	69,358	9.081	8640
4900	38.037	165,126	291.954	5.508	69.732	70,993	9.085	8820
5000	38.046	168,931	292.723	5.478	69.916	72,628	9.087	9000

Table D.1b Specific Heat, Enthalpy, Entropy, and Equilibrium Constant for Carbon Dioxide CO_2

$\bar{m}_{CO_2} = 44.00995$, $\Delta\bar{H}^\circ_{f,298} = -393{,}522$ kJ/kmol $= -169{,}186$ Btu/lbmol

T, K	$\bar{c}_p^\circ$, kJ/kmol-K	$(\bar{H}^\circ - \bar{H}^\circ_{298})$, kJ/kmol	$\bar{s}^\circ$, kJ/kmol-K	$\log_{10} K_P$	$\bar{s}^\circ$, Btu/lbmol-R	$(\bar{H}^\circ - \bar{H}^\circ_{298})$, Btu/lbmol	$\bar{c}_p^\circ$, Btu/lbmol-R	T, R
100	26.691	-6,386	179.526	205.640	42.879	-2,745	6.375	180
200	32.422	-3,422	199.839	102.923	47.731	-1,471	7.744	360
298	37.173	0	213.697	69.095	51.041	0	8.879	537
300	37.254	69	213.927	68.670	51.096	30	8.898	540
400	41.288	4,002	225.215	51.540	53.792	1,721	9.861	720
500	44.622	8,303	234.798	41.260	56.081	3,570	10.658	900
600	47.357	12,907	243.184	34.404	58.083	5,549	11.311	1080
700	49.593	17,758	250.658	29.506	59.869	7,635	11.845	1260
800	51.430	22,812	257.404	25.830	61.480	9,808	12.284	1440
900	52.968	28,034	263.553	22.969	62.948	12,053	12.651	1620
1000	54.306	33,399	269.204	20.680	64.298	14,359	12.971	1800
1100	55.284	38,879	274.426	18.805	65.546	16,715	13.204	1980
1200	56.162	44,452	279.275	17.242	66.704	19,111	13.414	2160
1300	56.948	50,109	283.802	15.919	67.785	21,543	13.602	2340
1400	57.649	55,839	288.048	14.785	68.799	24,007	13.769	2520
1500	58.272	61,636	292.047	13.801	69.754	26,499	13.918	2700
1600	58.825	67,491	295.826	12.940	70.657	29,016	14.050	2880
1700	59.313	73,399	299.407	12.180	71.512	31,556	14.167	3060
1800	59.743	79,352	302.810	11.503	72.325	34,116	14.269	3240
1900	60.122	85,346	306.050	10.898	73.099	36,693	14.360	3420
2000	60.453	91,375	309.143	10.353	73.838	39,285	14.439	3600
2100	60.744	97,435	312.100	9.860	74.544	41,890	14.508	3780
2200	60.999	103,522	314.931	9.411	75.220	44,507	14.569	3960
2300	61.221	109,634	317.648	9.001	75.869	47,135	14.622	4140
2400	61.417	115,766	320.258	8.625	76.492	49,771	14.669	4320
2500	61.590	121,916	322.769	8.279	77.092	52,415	14.711	4500
2600	61.744	128,083	325.187	7.960	77.670	55,067	14.747	4680
2700	61.881	134,264	327.520	7.663	78.227	57,724	14.780	4860
2800	62.006	140,459	329.773	7.388	78.765	60,387	14.810	5040
2900	62.121	146,665	331.951	7.132	79.285	63,056	14.837	5220
3000	62.229	152,883	334.059	6.892	79.789	65,729	14.863	5400
3100	62.331	159,111	336.101	6.668	80.276	68,406	14.888	5580
3200	62.430	165,349	338.081	6.458	80.749	71,088	14.911	5760
3300	62.528	171,597	340.004	6.260	81.209	73,775	14.935	5940
3400	62.625	177,855	341.872	6.074	81.655	76,465	14.958	6120
3500	62.723	184,122	343.689	5.898	82.089	79,159	14.981	6300
3600	62.822	190,399	345.457	5.731	82.511	81,858	15.005	6480
3700	62.922	196,686	347.180	5.574	82.922	84,561	15.029	6660
3800	63.024	202,984	348.859	5.425	83.324	87,269	15.053	6840
3900	63.127	209,291	350.497	5.283	83.715	89,980	15.078	7020
4000	63.231	215,609	352.097	5.148	84.097	92,697	15.103	7200
4100	63.335	221,937	353.660	5.020	84.470	95,417	15.127	7380
4200	63.438	228,276	355.187	4.898	84.835	98,143	15.152	7560
4300	63.537	234,625	356.681	4.781	85.192	100,872	15.176	7740
4400	63.632	240,983	358.143	4.669	85.541	103,606	15.198	7920
4500	63.721	247,351	359.574	4.562	85.883	106,343	15.219	8100
4600	63.799	253,727	360.975	4.460	86.217	109,085	15.238	8280
4700	63.866	260,111	362.348	4.362	86.545	111,829	15.254	8460
4800	63.918	266,500	363.693	4.268	86.867	114,576	15.267	8640
4900	63.951	272,894	365.011	4.178	87.181	117,325	15.274	8820
5000	63.962	279,289	366.304	4.091	87.490	120,075	15.277	9000

Table D.1c Specific Heat, Enthalpy, Entropy, and Equilibrium Constant for Monatomic Fluorine F

$\overline{m}_F = 18{,}9984, \quad \Delta\overline{H}^\circ_{f,298} = 78{,}910 \text{ kJ/kmol} = 33{,}926 \text{ Btu/lbmol}$

T, K	$\bar{c}_p^\circ$, kJ/kmol-K	$(\overline{H}^\circ - \overline{H}^\circ_{298})$, kJ/kmol	$\bar{s}^\circ$, kJ/kmol-K	$\log_{10} K_P$	$\bar{s}^\circ$, Btu/lbmol-R	$(\overline{H}^\circ - \overline{H}^\circ_{298})$, Btu/lbmol	$\bar{c}_p^\circ$, Btu/lbmol-R	T, R
100	23.291	-4,567	133.411	-37.846	31.865	-1,963	5.563	180
200	23.056	-2,249	149.489	-17.580	35.705	- 967	5.507	360
298	22.754	0	158.640	-10.832	37.891	0	5.435	537
300	22.748	42	158.781	-10.746	37.924	18	5.433	540
400	22.419	2,300	165.280	-7.298	39.476	989	5.355	720
500	22.107	4,526	170.249	-5.213	40.663	1,946	5.280	900
600	21.838	6,723	174.255	-3.814	41.620	2,891	5.216	1080
700	21.626	8,896	177.604	-2.810	42.420	3,825	5.165	1260
800	21.470	11,050	180.481	-2.054	43.107	4,751	5.128	1440
900	21.359	13,192	183.003	-1.463	43.710	5,671	5.101	1620
1000	21.266	15,323	185.249	-.988	44.246	6,588	5.079	1800
1100	21.203	17,445	187.262	-.599	44.727	7,500	5.064	1980
1200	21.148	19,562	189.104	-.274	45.167	8,410	5.051	2160
1300	21.101	21,674	190.795	.002	45.571	9,318	5.040	2340
1400	21.060	23,782	192.357	.240	45.944	10,225	5.030	2520
1500	21.025	25,887	193.809	.446	46.291	11,129	5.022	2700
1600	20.994	27,988	195.165	.627	46.614	12,033	5.014	2880
1700	20.968	30,086	196.437	.787	46.918	12,935	5.008	3060
1800	20.946	32,181	197.635	.929	47.204	13,836	5.003	3240
1900	20.928	34,275	198.767	1.057	47.475	14,736	4.999	3420
2000	20.913	36,367	199.840	1.172	47.731	15,635	4.995	3600
2100	20.901	38,458	200.860	1.277	47.975	16,534	4.992	3780
2200	20.891	40,547	201.832	1.372	48.207	17,432	4.990	3960
2300	20.883	42,636	202.760	1.459	48.429	18,330	4.988	4140
2400	20.876	44,724	203.649	1.539	48.641	19,228	4.986	4320
2500	20.871	46,811	204.501	1.612	48.844	20,125	4.985	4500
2600	20.867	48,898	205.320	1.680	49.040	21,023	4.984	4680
2700	20.863	50,984	206.107	1.743	49.228	21,920	4.983	4860
2800	20.860	53,071	206.866	1.802	49.409	22,817	4.982	5040
2900	20.858	55,157	207.598	1.856	49.584	23,713	4.982	5220
3000	20.856	57,242	208.305	1.907	49.753	24,610	4.981	5400
3100	20.853	59,328	208.989	1.955	49.916	25,507	4.981	5580
3200	20.851	61,413	209.651	2.000	50.074	26,403	4.980	5760
3300	20.848	63,498	210.292	2.042	50.227	27,300	4.980	5940
3400	20.846	65,583	210.915	2.082	50.376	28,196	4.979	6120
3500	20.843	67,667	211.519	2.119	50.520	29,092	4.978	6300
3600	20.839	69,751	212.106	2.155	50.661	29,988	4.977	6480
3700	20.836	71,835	212.677	2.188	50.797	30,884	4.977	6660
3800	20.832	73,918	213.232	2.220	50.930	31,780	4.976	6840
3900	20.828	76,001	213.774	2.250	51.059	32,675	4.975	7020
4000	20.824	78,084	214.301	2.279	51.185	33,571	4.974	7200
4100	20.821	80,166	214.815	2.306	51.308	34,466	4.973	7380
4200	20.817	82,248	215.317	2.332	51.428	35,361	4.972	7560
4300	20.814	84,330	215.806	2.357	51.544	36,256	4.971	7740
4400	20.812	86,411	216.285	2.381	51.659	37,151	4.971	7920
4500	20.811	88,492	216.753	2.403	51.770	38,045	4.971	8100
4600	20.810	90,573	217.210	2.425	51.880	38,940	4.970	8280
4700	20.811	92,654	217.658	2.446	51.987	39,835	4.971	8460
4800	20.815	94,736	218.096	2.466	52.091	40,730	4.971	8640
4900	20.820	96,817	218.525	2.485	52.194	41,625	4.973	8820
5000	20.827	98,900	218.946	2.503	52.294	42,520	4.975	9000

Table D.1d Specific Heat, Enthalpy, Entropy, and Equilibrium Constant for Diatomic Fluorine F_2

$\bar{m}_{F_2} = 38.00$, $\Delta\bar{H}^\circ_{f,298} = 0$ kJ/kmol = 0 Btu/lbmol

T, K	$\bar{c}_p^\circ$, kJ/kmol-K	$(\bar{H}^\circ - \bar{H}^\circ_{298})$, kJ/kmol	$\bar{s}^\circ$, kJ/kmol-K	$\log_{10} K_P$	$\bar{s}^\circ$, Btu/lbmol-R	$(\bar{H}^\circ - \bar{H}^\circ_{298})$, Btu/lbmol	$\bar{c}_p^\circ$, Btu/lbmol-R	T, R
100	26.725	-5,784	171.263	0.000	40.905	-2,487	6.383	180
200	29.291	-2,980	190.602	0.000	45.525	-1,281	6.996	360
298	31.351	0	202.696	0.000	48.413	0	7.488	537
300	31.385	58	202.890	0.000	48.459	25	7.496	540
400	33.048	3,283	212.157	0.000	50.673	1,411	7.893	720
500	34.327	6,655	219.675	0.000	52.468	2,861	8.199	900
600	35.280	10,138	226.022	0.000	53.985	4,358	8.426	1080
700	35.967	13,702	231.515	0.000	55.297	5,891	8.591	1260
800	36.460	17,325	236.352	0.000	56.452	7,448	8.708	1440
900	36.835	20,990	240.669	0.000	57.483	9,024	8.798	1620
1000	37.176	24,691	244.567	0.000	58.414	10,615	8.879	1800
1100	37.407	28,420	248.122	0.000	59.263	12,219	8.935	1980
1200	37.622	32,171	251.386	0.000	60.042	13,831	8.986	2160
1300	37.821	35,944	254.405	0.000	60.764	15,453	9.033	2340
1400	38.006	39,735	257.215	0.000	61.435	17,083	9.078	2520
1500	38.178	43,545	259.843	0.000	62.062	18,721	9.119	2700
1600	38.339	47,371	262.312	0.000	62.652	20,366	9.157	2880
1700	38.489	51,212	264.641	0.000	63.208	22,018	9.193	3060
1800	38.629	55,068	266.845	0.000	63.735	23,675	9.226	3240
1900	38.761	58,937	268.937	0.000	64.235	25,339	9.258	3420
2000	38.885	62,820	270.928	0.000	64.710	27,008	9.288	3600
2100	39.003	66,714	272.829	0.000	65.164	28,682	9.316	3780
2200	39.115	70,620	274.646	0.000	65.598	30,362	9.343	3960
2300	39.223	74,537	276.387	0.000	66.014	32,046	9.368	4140
2400	39.326	78,465	278.058	0.000	66.413	33,734	9.393	4320
2500	39.426	82,402	279.666	0.000	66.797	35,427	9.417	4500
2600	39.523	86,350	281.214	0.000	67.167	37,124	9.440	4680
2700	39.618	90,307	282.707	0.000	67.523	38,825	9.463	4860
2800	39.711	94,273	284.150	0.000	67.868	40,531	9.485	5040
2900	39.803	98,249	285.545	0.000	68.201	42,240	9.507	5220
3000	39.894	102,234	286.896	0.000	68.524	43,953	9.529	5400
3100	39.985	106,228	288.205	0.000	68.837	45,670	9.550	5580
3200	40.076	110,231	289.476	0.000	69.140	47,391	9.572	5760
3300	40.167	114,243	290.711	0.000	69.435	49,116	9.594	5940
3400	40.258	118,264	291.911	0.000	69.722	50,845	9.616	6120
3500	40.350	122,295	293.080	0.000	70.001	52,578	9.637	6300
3600	40.443	126,334	294.218	0.000	70.273	54,315	9.660	6480
3700	40.536	130,383	295.327	0.000	70.538	56,056	9.682	6660
3800	40.629	134,441	296.409	0.000	70.796	57,800	9.704	6840
3900	40.723	138,509	297.466	0.000	71.048	59,549	9.727	7020
4000	40.817	142,586	298.498	0.000	71.295	61,302	9.749	7200
4100	40.911	146,672	299.507	0.000	71.536	63,059	9.772	7380
4200	41.006	150,768	300.494	0.000	71.772	64,820	9.794	7560
4300	41.099	154,874	301.460	0.000	72.002	66,585	9.816	7740
4400	41.192	158,988	302.406	0.000	72.228	68,354	9.839	7920
4500	41.284	163,112	303.333	0.000	72.450	70,127	9.860	8100
4600	41.373	167,245	304.241	0.000	72.667	71,903	9.882	8280
4700	41.461	171,386	305.132	0.000	72.879	73,684	9.903	8460
4800	41.545	175,537	306.005	0.000	73.088	75,468	9.923	8640
4900	41.626	179,695	306.863	0.000	73.293	77,256	9.942	8820
5000	41.703	183,862	307.705	0.000	73.494	79,048	9.961	9000

Table D.1e Specific Heat, Enthalpy, Entropy, and Equilibrium Constant for Hydrogen Fluoride HF

$\bar{m}_{HF} = 20{,}00637, \quad \Delta\bar{H}^{\circ}_{f,298} = -272{,}456 \text{ kJ/kmol} = -117{,}175 \text{ Btu/lbmol}$

T, K	$\bar{c}_p^{\circ}$, kJ/kmol-K	$(\bar{H}^{\circ} - \bar{H}^{\circ}_{298})$, kJ/kmol	$\bar{s}^{\circ}$, kJ/kmol-K	$\log_{10} K_P$	$\bar{s}^{\circ}$, Btu/lbmol-R	$(\bar{H}^{\circ} - \bar{H}^{\circ}_{298})$, Btu/lbmol	$\bar{c}_p^{\circ}$, Btu/lbmol-R	T, R
100	29.020	-5,766	141.891	142.735	33.890	-2,479	6.931	180
200	29.111	-2,859	162.039	71.547	38.702	-1,229	6.953	360
298	29.139	0	173.669	48.116	41.480	0	6.960	537
300	29.140	54	173.849	47.822	41.523	23	6.960	540
400	29.148	2,968	182.233	35.956	43.526	1,276	6.962	720
500	29.170	5,884	188.739	28.831	45.080	2,530	6.967	900
600	29.233	8,804	194.062	24.076	46.351	3,785	6.982	1080
700	29.355	11,732	198.577	20.677	47.429	5,044	7.011	1260
800	29.550	14,677	202.509	18.124	48.368	6,310	7.058	1440
900	29.822	17,645	206.004	16.135	49.203	7,586	7.123	1620
1000	30.169	20,644	209.163	14.543	49.958	8,875	7.206	1800
1100	30.617	23,683	212.060	13.238	50.650	10,182	7.313	1980
1200	31.050	26,767	214.743	12.149	51.290	11,508	7.416	2160
1300	31.468	29,893	217.245	11.227	51.888	12,852	7.516	2340
1400	31.871	33,060	219.592	10.436	52.449	14,213	7.612	2520
1500	32.259	36,267	221.804	9.749	52.977	15,592	7.705	2700
1600	32.631	39,511	223.898	9.148	53.477	16,987	7.794	2880
1700	32.988	42,792	225.887	8.616	53.952	18,398	7.879	3060
1800	33.330	46,108	227.782	8.144	54.405	19,823	7.961	3240
1900	33.655	49,458	229.593	7.720	54.837	21,263	8.038	3420
2000	33.966	52,839	231.327	7.339	55.252	22,717	8.113	3600
2100	34.261	56,250	232.992	6.994	55.649	24,184	8.183	3780
2200	34.542	59,691	234.592	6.679	56.031	25,663	8.250	3960
2300	34.807	63,158	236.133	6.392	56.399	27,154	8.314	4140
2400	35.058	66,652	237.620	6.129	56.755	28,655	8.373	4320
2500	35.295	70,169	239.056	5.886	57.098	30,168	8.430	4500
2600	35.517	73,710	240.445	5.662	57.429	31,690	8.483	4680
2700	35.726	77,272	241.789	5.454	57.750	33,222	8.533	4860
2800	35.922	80,855	243.092	5.261	58.062	34,762	8.580	5040
2900	36.106	84,456	244.356	5.081	58.363	36,310	8.624	5220
3000	36.277	88,076	245.583	4.913	58.656	37,866	8.665	5400
3100	36.437	91,711	246.775	4.756	58.941	39,429	8.703	5580
3200	36.585	95,363	247.934	4.608	59.218	40,999	8.738	5760
3300	36.724	99,028	249.062	4.469	59.487	42,575	8.771	5940
3400	36.853	102,707	250.160	4.339	59.750	44,157	8.802	6120
3500	36.973	106,398	251.230	4.215	60.005	45,744	8.831	6300
3600	37.085	110,101	252.273	4.099	60.254	47,336	8.858	6480
3700	37.189	113,815	253.291	3.989	60.498	48,932	8.883	6660
3800	37.288	117,539	254.284	3.884	60.735	50,533	8.906	6840
3900	37.381	121,272	255.254	3.785	60.966	52,139	8.928	7020
4000	37.469	125,015	256.201	3.690	61.193	53,748	8.949	7200
4100	37.554	128,766	257.128	3.600	61.414	55,360	8.970	7380
4200	37.637	132,526	258.034	3.514	61.630	56,977	8.989	7560
4300	37.718	136,294	258.920	3.433	61.842	58,597	9.009	7740
4400	37.799	140,069	259.788	3.354	62.049	60,220	9.028	7920
4500	37.882	143,853	260.639	3.280	62.252	61,847	9.048	8100
4600	37.966	147,646	261.472	3.208	62.452	63,477	9.068	8280
4700	38.054	151,447	262.290	3.139	62.647	65,111	9.089	8460
4800	38.147	155,257	263.092	3.074	62.838	66,749	9.111	8640
4900	38.246	159,076	263.879	3.010	63.026	68,392	9.135	8820
5000	38.352	162,906	264.653	2.950	63.211	70,038	9.160	9000

Table D.1f Specific Heat, Enthalpy, Entropy, and Equilibrium Constant for Monatomic Hydrogen H

$\bar{m}_H = 1.008, \quad \Delta\bar{H}^\circ_{f,298} = 217{,}986 \text{ kJ/kmol} = 93{,}719 \text{ Btu/lbmol}$

T, K	$\bar{c}_p^\circ$, kJ/kmol-K	$(\bar{H}^\circ - \bar{H}^\circ_{298})$, kJ/kmol	$\bar{s}^\circ$, kJ/kmol-K	$\log_{10} K_P$	$\bar{s}^\circ$, Btu/lbmol-R	$(\bar{H}^\circ - \bar{H}^\circ_{298})$, Btu/lbmol	$\bar{c}_p^\circ$, Btu/lbmol-R	T, R
100	20.786	-4,119	91.897	-110.976	21.949	-1,771	4.965	180
200	20.786	-2,040	106.304	-54.322	25.390	- 877	4.965	360
298	20.786	0	114.604	-35.612	27.373	0	4.965	537
300	20.786	38	114.732	-35.377	27.403	17	4.965	540
400	20.786	2,117	120.712	-25.876	28.832	910	4.965	720
500	20.786	4,196	125.350	-20.159	29.939	1,804	4.965	900
600	20.786	6,274	129.140	-16.336	30.845	2,697	4.965	1080
700	20.786	8,353	132.344	-13.599	31.610	3,591	4.965	1260
800	20.786	10,431	135.120	-11.540	32.273	4,485	4.965	1440
900	20.786	12,510	137.568	-9.934	32.858	5,378	4.965	1620
1000	20.786	14,589	139.758	-8.646	33.381	6,272	4.965	1800
1100	20.786	16,667	141.739	-7.589	33.854	7,166	4.965	1980
1200	20.786	18,746	143.548	-6.707	34.286	8,059	4.965	2160
1300	20.786	20,824	145.211	-5.958	34.683	8,953	4.965	2340
1400	20.786	22,903	146.752	-5.315	35.051	9,847	4.965	2520
1500	20.786	24,981	148.186	-4.757	35.394	10,740	4.965	2700
1600	20.786	27,060	149.527	-4.267	35.714	11,634	4.965	2880
1700	20.786	29,139	150.788	-3.834	36.015	12,528	4.965	3060
1800	20.786	31,217	151.976	-3.448	36.299	13,421	4.965	3240
1900	20.786	33,296	153.099	-3.103	36.567	14,315	4.965	3420
2000	20.786	35,374	154.166	-2.791	36.822	15,208	4.965	3600
2100	20.786	37,453	155.180	-2.509	37.064	16,102	4.965	3780
2200	20.786	39,532	156.147	-2.252	37.295	16,996	4.965	3960
2300	20.786	41,610	157.071	-2.016	37.516	17,889	4.965	4140
2400	20.786	43,689	157.955	-1.801	37.727	18,783	4.965	4320
2500	20.786	45,767	158.804	-1.602	37.930	19,677	4.965	4500
2600	20.786	47,846	159.619	-1.418	38.124	20,570	4.965	4680
2700	20.786	49,924	160.404	-1.248	38.312	21,464	4.965	4860
2800	20.786	52,003	161.160	-1.089	38.492	22,358	4.965	5040
2900	20.786	54,082	161.889	-.942	38.667	23,251	4.965	5220
3000	20.786	56,160	162.594	-.804	38.835	24,145	4.965	5400
3100	20.786	58,239	163.275	-.675	38.998	25,039	4.965	5580
3200	20.786	60,317	163.935	-.554	39.155	25,932	4.965	5760
3300	20.786	62,396	164.575	-.440	39.308	26,826	4.965	5940
3400	20.786	64,475	165.195	-.332	39.456	27,720	4.965	6120
3500	20.786	66,553	165.798	-.231	39.600	28,613	4.965	6300
3600	20.786	68,632	166.383	-.135	39.740	29,507	4.965	6480
3700	20.786	70,710	166.953	-.045	39.876	30,400	4.965	6660
3800	20.786	72,789	167.507	.041	40.008	31,294	4.965	6840
3900	20.786	74,868	168.047	.122	40.137	32,188	4.965	7020
4000	20.786	76,946	168.573	.200	40.263	33,081	4.965	7200
4100	20.786	79,025	169.087	.274	40.386	33,975	4.965	7380
4200	20.786	81,103	169.587	.344	40.505	34,869	4.965	7560
4300	20.786	83,182	170.077	.411	40.622	35,762	4.965	7740
4400	20.786	85,260	170.554	.475	40.736	36,656	4.965	7920
4500	20.786	87,339	171.022	.536	40.848	37,550	4.965	8100
4600	20.786	89,418	171.478	.595	40.957	38,443	4.965	8280
4700	20.786	91,496	171.925	.651	41.064	39,337	4.965	8460
4800	20.786	93,575	172.363	.705	41.168	40,231	4.965	8640
4900	20.786	95,653	172.792	.756	41.271	41,124	4.965	8820
5000	20.786	97,732	173.212	.806	41.371	42,018	4.965	9000

Table D.1g Specific Heat, Enthalpy, Entropy, and Equilibrium Constant for Diatomic Hydrogen H_2

$$\bar{m}_{H_2} = 2.016, \quad \Delta\bar{H}^\circ_{f,298} = 0 \text{ kJ/kmol} = 0 \text{ Btu/lbmol}$$

T, K	$\bar{c}_p^\circ$, kJ/kmol-K	$(\bar{H}^\circ - \bar{H}^\circ_{298})$, kJ/kmol	$\bar{s}^\circ$, kJ/kmol-K	$\log_{10} K_P$	$\bar{s}^\circ$, Btu/lbmol-R	$(\bar{H}^\circ - \bar{H}^\circ_{298})$, Btu/lbmol	$\bar{c}_p^\circ$, Btu/lbmol-R	T, R
100	27.207	-5,587	99.945	0.000	23.871	-2,402	6.498	180
200	28.282	-2,807	119.167	0.000	28.463	-1,207	6.755	360
298	28.859	0	130.580	0.000	31.188	0	6.893	537
300	28.867	53	130.758	0.000	31.231	23	6.895	540
400	29.145	2,956	139.106	0.000	33.225	1,271	6.961	720
500	29.267	5,877	145.625	0.000	34.782	2,527	6.990	900
600	29.345	8,808	150.968	0.000	36.058	3,787	7.009	1080
700	29.456	11,747	155.499	0.000	37.140	5,051	7.035	1260
800	29.639	14,701	159.443	0.000	38.082	6,321	7.079	1440
900	29.899	17,678	162.948	0.000	38.920	7,600	7.141	1620
1000	30.205	20,683	166.114	0.000	39.676	8,892	7.214	1800
1100	30.640	23,725	169.013	0.000	40.368	10,200	7.318	1980
1200	31.069	26,811	171.698	0.000	41.009	11,527	7.421	2160
1300	31.491	29,939	174.201	0.000	41.607	12,871	7.522	2340
1400	31.906	33,108	176.550	0.000	42.168	14,234	7.621	2520
1500	32.312	36,319	178.765	0.000	42.697	15,615	7.718	2700
1600	32.709	39,571	180.864	0.000	43.199	17,013	7.813	2880
1700	33.097	42,861	182.858	0.000	43.675	18,427	7.905	3060
1800	33.474	46,190	184.761	0.000	44.129	19,858	7.995	3240
1900	33.841	49,556	186.580	0.000	44.564	21,305	8.083	3420
2000	34.197	52,958	188.325	0.000	44.981	22,768	8.168	3600
2100	34.541	56,395	190.002	0.000	45.381	24,246	8.250	3780
2200	34.874	59,865	191.617	0.000	45.767	25,738	8.330	3960
2300	35.195	63,369	193.174	0.000	46.139	27,244	8.406	4140
2400	35.504	66,904	194.679	0.000	46.498	28,764	8.480	4320
2500	35.802	70,469	196.134	0.000	46.846	30,297	8.551	4500
2600	36.088	74,064	197.544	0.000	47.183	31,842	8.619	4680
2700	36.362	77,687	198.911	0.000	47.509	33,400	8.685	4860
2800	36.625	81,336	200.238	0.000	47.826	34,969	8.748	5040
2900	36.876	85,011	201.528	0.000	48.134	36,549	8.808	5220
3000	37.117	88,711	202.782	0.000	48.434	38,139	8.865	5400
3100	37.348	92,434	204.003	0.000	48.725	39,740	8.920	5580
3200	37.569	96,180	205.192	0.000	49.009	41,351	8.973	5760
3300	37.780	99,948	206.351	0.000	49.286	42,970	9.024	5940
3400	37.983	103,736	207.482	0.000	49.556	44,599	9.072	6120
3500	38.179	107,544	208.586	0.000	49.820	46,236	9.119	6300
3600	38.367	111,372	209.664	0.000	50.077	47,882	9.164	6480
3700	38.549	115,217	210.718	0.000	50.329	49,535	9.207	6660
3800	38.726	119,081	211.748	0.000	50.575	51,196	9.249	6840
3900	38.898	122,962	212.757	0.000	50.816	52,865	9.291	7020
4000	39.068	126,861	213.744	0.000	51.052	54,541	9.331	7200
4100	39.235	130,776	214.710	0.000	51.283	56,224	9.371	7380
4200	39.402	134,708	215.658	0.000	51.509	57,915	9.411	7560
4300	39.570	138,656	216.587	0.000	51.731	59,612	9.451	7740
4400	39.739	142,622	217.499	0.000	51.949	61,317	9.492	7920
4500	39.912	146,604	218.394	0.000	52.162	63,029	9.533	8100
4600	40.090	150,604	219.273	0.000	52.372	64,749	9.575	8280
4700	40.275	154,623	220.137	0.000	52.579	66,477	9.620	8460
4800	40.468	158,660	220.987	0.000	52.782	68,212	9.666	8640
4900	40.671	162,717	221.823	0.000	52.982	69,957	9.714	8820
5000	40.887	166,794	222.647	0.000	53.178	71,710	9.766	9000

Table D.1h Specific Heat, Enthalpy, Entropy, and Equilibrium Constant for Water H_2O

$\bar{m}_{H_2O} = 18.016$, $\Delta\bar{H}^\circ_{f,298} = -241{,}827$ kJ/kmol $= -103968$ Btu/lbmol

T, K	$\bar{c}_p^\circ$, kJ/kmol-K	$(\bar{H}^\circ - \bar{H}^\circ_{298})$, kJ/kmol	$\bar{s}^\circ$, kJ/kmol-K	$\log_{10} K_P$	$\bar{s}^\circ$, Btu/lbmol-R	$(\bar{H}^\circ - \bar{H}^\circ_{298})$, Btu/lbmol	$\bar{c}_p^\circ$, Btu/lbmol-R	T, R
100	33.240	-6,591	152.401	123.547	36.400	-2,833	7.939	180
200	33.192	-3,273	175.399	60.791	41.893	-1,407	7.928	360
298	33.561	0	188.708	40.047	45.072	0	8.016	537
300	33.572	62	188.916	39.786	45.122	27	8.018	540
400	34.272	3,452	198.663	29.239	47.450	1,484	8.186	720
500	35.202	6,924	206.407	22.885	49.300	2,977	8.408	900
600	36.286	10,498	212.919	18.632	50.855	4,513	8.667	1080
700	37.464	14,184	218.601	15.583	52.212	6,098	8.948	1260
800	38.694	17,992	223.683	13.288	53.426	7,735	9.242	1440
900	39.948	21,924	228.313	11.497	54.532	9,426	9.541	1620
1000	41.215	25,982	232.587	10.061	55.552	11,170	9.844	1800
1100	42.526	30,170	236.577	8.882	56.505	12,971	10.157	1980
1200	43.753	34,484	240.331	7.898	57.402	14,826	10.450	2160
1300	44.901	38,918	243.879	7.063	58.249	16,732	10.725	2340
1400	45.975	43,462	247.246	6.347	59.054	18,686	10.981	2520
1500	46.976	48,110	250.452	5.725	59.820	20,684	11.220	2700
1600	47.910	52,855	253.514	5.179	60.551	22,724	11.443	2880
1700	48.780	57,690	256.445	4.698	61.251	24,803	11.651	3060
1800	49.589	62,609	259.257	4.269	61.922	26,917	11.844	3240
1900	50.341	67,606	261.958	3.885	62.568	29,066	12.024	3420
2000	51.039	72,675	264.558	3.539	63.189	31,245	12.190	3600
2100	51.686	77,812	267.064	3.226	63.787	33,454	12.345	3780
2200	52.286	83,011	269.483	2.941	64.365	35,689	12.488	3960
2300	52.841	88,268	271.819	2.681	64.923	37,949	12.621	4140
2400	53.354	93,578	274.079	2.442	65.463	40,232	12.743	4320
2500	53.828	98,937	276.267	2.223	65.985	42,536	12.857	4500
2600	54.267	104,342	278.387	2.020	66.492	44,860	12.961	4680
2700	54.672	109,789	280.443	1.831	66.983	47,202	13.058	4860
2800	55.046	115,276	282.438	1.657	67.459	49,560	13.147	5040
2900	55.391	120,798	284.375	1.494	67.922	51,934	13.230	5220
3000	55.711	126,353	286.259	1.342	68.372	54,323	13.306	5400
3100	56.006	131,939	288.090	1.200	68.809	56,724	13.377	5580
3200	56.280	137,554	289.873	1.066	69.235	59,138	13.442	5760
3300	56.534	143,194	291.609	.941	69.650	61,563	13.503	5940
3400	56.771	148,860	293.300	.823	70.053	63,999	13.559	6120
3500	56.991	154,548	294.949	.711	70.447	66,445	13.612	6300
3600	57.198	160,258	296.557	.606	70.831	68,899	13.661	6480
3700	57.392	165,987	298.127	.506	71.206	71,363	13.708	6660
3800	57.575	171,736	299.660	.412	71.573	73,834	13.752	6840
3900	57.749	177,502	301.158	.322	71.930	76,313	13.793	7020
4000	57.915	183,285	302.622	.237	72.280	78,800	13.833	7200
4100	58.074	189,085	304.054	.155	72.622	81,293	13.871	7380
4200	58.227	194,900	305.455	.078	72.957	83,793	13.907	7560
4300	58.376	200,730	306.827	.004	73.284	86,300	13.943	7740
4400	58.522	206,575	308.171	-.066	73.605	88,812	13.978	7920
4500	58.665	212,434	309.488	-.134	73.920	91,332	14.012	8100
4600	58.806	218,308	310.779	-.198	74.228	93,857	14.046	8280
4700	58.946	224,195	312.045	-.260	74.531	96,388	14.079	8460
4800	59.086	230,097	313.287	-.320	74.827	98,925	14.112	8640
4900	59.226	236,013	314.507	-.377	75.119	101,469	14.146	8820
5000	59.366	241,942	315.705	-.432	75.405	104,018	14.179	9000

Table D.1i Specific Heat, Enthalpy, Entropy, and Equilibrium Constant for Hydroxyl HO

$\bar{m}_{HO} = 17.0074$, $\Delta\bar{H}^\circ_{f,298} = 39{,}463$ kJ/kmol $= 16{,}966$ Btu/lbmol

T, K	$\bar{c}_p^\circ$, kJ/kmol-K	$(\bar{H}^\circ - \bar{H}^\circ_{298})$, kJ/kmol	$\bar{s}^\circ$, kJ/kmol-K	$\log_{10} K_P$	$\bar{s}^\circ$, Btu/lbmol-R	$(\bar{H}^\circ - \bar{H}^\circ_{298})$, Btu/lbmol	$\bar{c}_p^\circ$, Btu/lbmol-R	T, R
100	31.093	-6,039	150.187	-19.712	35.871	-2,597	7.426	180
200	30.446	-2,964	171.530	-9.476	40.969	-1,274	7.272	360
298	29.977	0	183.594	-6.089	43.851	0	7.160	537
300	29.970	55	183.779	-6.046	43.895	24	7.158	540
400	29.662	3,036	192.355	-4.327	45.943	1,305	7.085	720
500	29.516	5,993	198.955	-3.296	47.520	2,577	7.050	900
600	29.521	8,944	204.335	-2.609	48.805	3,845	7.051	1080
700	29.662	11,902	208.895	-2.120	49.894	5,117	7.085	1260
800	29.918	14,880	212.871	-1.755	50.843	6,397	7.146	1440
900	30.265	17,889	216.414	-1.472	51.690	7,691	7.229	1620
1000	30.675	20,935	219.624	-1.247	52.456	9,001	7.327	1800
1100	31.172	24,028	222.571	-1.064	53.160	10,330	7.445	1980
1200	31.644	27,169	225.304	-.912	53.813	11,681	7.558	2160
1300	32.092	30,356	227.854	-.783	54.422	13,051	7.665	2340
1400	32.517	33,586	230.248	-.674	54.994	14,440	7.766	2520
1500	32.919	36,858	232.506	-.580	55.533	15,847	7.863	2700
1600	33.300	40,170	234.642	-.497	56.043	17,270	7.954	2880
1700	33.660	43,518	236.672	-.425	56.528	18,710	8.039	3060
1800	33.999	46,901	238.606	-.361	56.990	20,164	8.121	3240
1900	34.319	50,317	240.453	-.304	57.431	21,633	8.197	3420
2000	34.620	53,764	242.221	-.253	57.853	23,115	8.269	3600
2100	34.904	57,240	243.917	-.207	58.259	24,609	8.337	3780
2200	35.169	60,744	245.547	-.165	58.648	26,116	8.400	3960
2300	35.419	64,274	247.116	-.127	59.023	27,633	8.460	4140
2400	35.652	67,827	248.628	-.092	59.384	29,161	8.515	4320
2500	35.871	71,404	250.088	-.060	59.732	30,699	8.568	4500
2600	36.075	75,001	251.499	-.031	60.069	32,245	8.616	4680
2700	36.266	78,618	252.864	-.004	60.395	33,800	8.662	4860
2800	36.444	82,254	254.186	.021	60.711	35,363	8.704	5040
2900	36.610	85,907	255.468	.044	61.017	36,934	8.744	5220
3000	36.764	89,575	256.712	.065	61.315	38,511	8.781	5400
3100	36.908	93,259	257.919	.085	61.603	40,095	8.815	5580
3200	37.043	96,957	259.093	.104	61.883	41,684	8.848	5760
3300	37.169	100,667	260.235	.121	62.156	43,280	8.878	5940
3400	37.286	104,390	261.347	.137	62.422	44,880	8.906	6120
3500	37.396	108,124	262.429	.153	62.680	46,486	8.932	6300
3600	37.500	111,869	263.484	.167	62.932	48,096	8.957	6480
3700	37.598	115,624	264.513	.181	63.178	49,710	8.980	6660
3800	37.690	119,389	265.517	.193	63.418	51,329	9.002	6840
3900	37.779	123,162	266.497	.205	63.652	52,951	9.023	7020
4000	37.864	126,944	267.454	.216	63.880	54,577	9.044	7200
4100	37.947	130,735	268.390	.227	64.104	56,207	9.063	7380
4200	38.027	134,533	269.306	.237	64.323	57,840	9.083	7560
4300	38.107	138,340	270.201	.247	64.537	59,476	9.102	7740
4400	38.187	142,155	271.078	.256	64.746	61,117	9.121	7920
4500	38.267	145,978	271.938	.264	64.951	62,760	9.140	8100
4600	38.349	149,808	272.779	.272	65.152	64,407	9.159	8280
4700	38.432	153,647	273.605	.280	65.349	66,057	9.179	8460
4800	38.519	157,495	274.415	.287	65.543	67,712	9.200	8640
4900	38.610	161,351	275.210	.294	65.733	69,370	9.222	8820
5000	38.706	165,217	275.991	.301	65.919	71,032	9.245	9000

Table D.1j Specific Heat, Enthalpy, Entropy, and Equilibrium Constant for Monatomic Nitrogen N

$\bar{m}_N = 14.008, \quad \Delta\bar{H}^\circ_{f,298} = 472{,}646 \text{ kJ/kmol} = 203{,}204 \text{ Btu/lbmol}$

T, K	$\bar{c}_p^\circ$, kJ/kmol-K	$(\bar{H}^\circ - \bar{H}^\circ_{298})$, kJ/kmol	$\bar{s}^\circ$, kJ/kmol-K	$\log_{10} K_P$	$\bar{s}^\circ$, Btu/lbmol-R	$(\bar{H}^\circ - \bar{H}^\circ_{298})$, Btu/lbmol	$\bar{c}_p^\circ$, Btu/lbmol-R	T, R
100	20.797	-4,120	130.475	-243.587	31.163	-1,771	4.967	180
200	20.790	-2,040	144.888	-120.407	34.606	- 877	4.966	360
298	20.786	0	153.188	-79.801	36.588	0	4.965	537
300	20.786	38	153.316	-79.291	36.619	17	4.965	540
400	20.785	2,117	159.296	-58.705	38.047	910	4.965	720
500	20.786	4,196	163.934	-46.338	39.155	1,804	4.965	900
600	20.786	6,274	167.724	-38.082	40.060	2,697	4.965	1080
700	20.786	8,353	170.928	-32.178	40.825	3,591	4.965	1260
800	20.786	10,431	173.704	-27.745	41.488	4,485	4.965	1440
900	20.786	12,510	176.152	-24.294	42.073	5,378	4.965	1620
1000	20.786	14,589	178.342	-21.530	42.596	6,272	4.965	1800
1100	20.792	16,667	180.323	-19.266	43.069	7,166	4.966	1980
1200	20.795	18,747	182.133	-17.378	43.502	8,060	4.967	2160
1300	20.795	20,826	183.797	-15.779	43.899	8,954	4.967	2340
1400	20.793	22,905	185.338	-14.407	44.267	9,848	4.966	2520
1500	20.790	24,985	186.773	-13.218	44.610	10,742	4.966	2700
1600	20.786	27,063	188.114	-12.176	44.930	11,635	4.965	2880
1700	20.782	29,142	189.374	-11.257	45.231	12,529	4.964	3060
1800	20.779	31,220	190.562	-10.439	45.515	13,422	4.963	3240
1900	20.777	33,298	191.685	-9.706	45.783	14,316	4.962	3420
2000	20.776	35,375	192.751	-9.047	46.038	15,209	4.962	3600
2100	20.778	37,453	193.765	-8.450	46.280	16,102	4.963	3780
2200	20.783	39,531	194.731	-7.907	46.511	16,995	4.964	3960
2300	20.790	41,609	195.655	-7.410	46.732	17,889	4.966	4140
2400	20.802	43,689	196.541	-6.955	46.943	18,783	4.968	4320
2500	20.818	45,770	197.390	-6.536	47.146	19,678	4.972	4500
2600	20.838	47,853	198.207	-6.150	47.341	20,573	4.977	4680
2700	20.864	49,938	198.994	-5.791	47.529	21,470	4.983	4860
2800	20.894	52,026	199.753	-5.458	47.710	22,367	4.991	5040
2900	20.931	54,117	200.487	-5.148	47.885	23,266	4.999	5220
3000	20.974	56,212	201.197	-4.859	48.055	24,167	5.010	5400
3100	21.023	58,312	201.886	-4.588	48.220	25,070	5.021	5580
3200	21.080	60,417	202.554	-4.333	48.379	25,975	5.035	5760
3300	21.143	62,528	203.204	-4.094	48.534	26,883	5.050	5940
3400	21.214	64,646	203.836	-3.869	48.685	27,793	5.067	6120
3500	21.292	66,771	204.452	-3.657	48.833	28,707	5.085	6300
3600	21.378	68,904	205.053	-3.457	48.976	29,624	5.106	6480
3700	21.472	71,047	205.640	-3.267	49.116	30,545	5.129	6660
3800	21.575	73,199	206.214	-3.087	49.253	31,470	5.153	6840
3900	21.686	75,362	206.776	-2.916	49.388	32,400	5.180	7020
4000	21.805	77,537	207.326	-2.754	49.519	33,335	5.208	7200
4100	21.933	79,723	207.866	-2.599	49.648	34,275	5.239	7380
4200	22.070	81,924	208.396	-2.452	49.775	35,221	5.271	7560
4300	22.216	84,138	208.917	-2.311	49.899	36,173	5.306	7740
4400	22.371	86,367	209.430	-2.177	50.021	37,132	5.343	7920
4500	22.535	88,612	209.934	-2.049	50.142	38,097	5.382	8100
4600	22.708	90,875	210.432	-1.926	50.261	39,070	5.424	8280
4700	22.890	93,154	210.922	-1.808	50.378	40,050	5.467	8460
4800	23.082	95,453	211.406	-1.695	50.493	41,038	5.513	8640
4900	23.282	97,771	211.884	-1.587	50.608	42,035	5.561	8820
5000	23.491	100,110	212.356	-1.482	50.720	43,040	5.611	9000

Table D.1k Specific Heat, Enthalpy, Entropy, and Equilibrium Constant for Diatomic Nitrogen N_2

$\bar{m}_{N_2} = 28.01348$, $\Delta\bar{H}^\circ_{f,298} = 0$ kJ/kmol $= 0$ Btu/lbmol

T, K	$\bar{c}_p^\circ$, kJ/kmol-K	$(\bar{H}^\circ - \bar{H}^\circ_{298})$, kJ/kmol	$\bar{s}^\circ$, kJ/kmol-K	$\log_{10} K_P$	$\bar{s}^\circ$, Btu/lbmol-R	$(\bar{H}^\circ - \bar{H}^\circ_{298})$, Btu/lbmol	$\bar{c}_p^\circ$, Btu/lbmol-R	T, R
100	29.737	-5,811	159.401	0.000	38.072	-2,498	7.103	180
200	29.273	-2,863	179.852	0.000	42.957	-1,231	6.992	360
298	29.122	0	191.502	0.000	45.740	0	6.956	537
300	29.122	54	191.683	0.000	45.783	23	6.956	540
400	29.243	2,970	200.071	0.000	47.786	1,277	6.985	720
500	29.588	5,910	206.630	0.000	49.353	2,541	7.067	900
600	30.104	8,893	212.068	0.000	50.652	3,824	7.190	1080
700	30.737	11,935	216.755	0.000	51.771	5,131	7.341	1260
800	31.424	15,043	220.904	0.000	52.762	6,467	7.506	1440
900	32.101	18,219	224.645	0.000	53.655	7,833	7.667	1620
1000	32.698	21,460	228.059	0.000	54.471	9,226	7.810	1800
1100	33.208	24,756	231.199	0.000	55.221	10,643	7.932	1980
1200	33.670	28,100	234.109	0.000	55.916	12,081	8.042	2160
1300	34.087	31,488	236.821	0.000	56.564	13,538	8.142	2340
1400	34.463	34,916	239.361	0.000	57.170	15,012	8.231	2520
1500	34.800	38,380	241.750	0.000	57.741	16,501	8.312	2700
1600	35.103	41,875	244.006	0.000	58.280	18,003	8.384	2880
1700	35.373	45,399	246.142	0.000	58.790	19,518	8.449	3060
1800	35.614	48,949	248.171	0.000	59.275	21,044	8.506	3240
1900	35.828	52,521	250.103	0.000	59.736	22,580	8.557	3420
2000	36.018	56,113	251.945	0.000	60.176	24,125	8.603	3600
2100	36.186	59,724	253.707	0.000	60.597	25,677	8.643	3780
2200	36.335	63,350	255.394	0.000	61.000	27,236	8.678	3960
2300	36.467	66,990	257.012	0.000	61.386	28,801	8.710	4140
2400	36.584	70,643	258.566	0.000	61.757	30,371	8.738	4320
2500	36.687	74,307	260.062	0.000	62.115	31,947	8.763	4500
2600	36.780	77,980	261.503	0.000	62.459	33,526	8.785	4680
2700	36.862	81,662	262.892	0.000	62.791	35,109	8.804	4860
2800	36.937	85,352	264.234	0.000	63.111	36,695	8.822	5040
2900	37.004	89,049	265.532	0.000	63.421	38,285	8.838	5220
3000	37.066	92,753	266.787	0.000	63.721	39,877	8.853	5400
3100	37.124	96,462	268.003	0.000	64.012	41,472	8.867	5580
3200	37.178	100,178	269.183	0.000	64.293	43,069	8.880	5760
3300	37.230	103,898	270.328	0.000	64.567	44,669	8.892	5940
3400	37.280	107,623	271.440	0.000	64.832	46,270	8.904	6120
3500	37.329	111,354	272.521	0.000	65.091	47,874	8.916	6300
3600	37.377	115,089	273.574	0.000	65.342	49,480	8.927	6480
3700	37.425	118,829	274.598	0.000	65.587	51,088	8.939	6660
3800	37.473	122,574	275.597	0.000	65.825	52,698	8.950	6840
3900	37.521	126,324	276.571	0.000	66.058	54,310	8.962	7020
4000	37.569	130,078	277.522	0.000	66.285	55,924	8.973	7200
4100	37.617	133,838	278.450	0.000	66.507	57,541	8.985	7380
4200	37.664	137,602	279.357	0.000	66.723	59,159	8.996	7560
4300	37.711	141,371	280.244	0.000	66.935	60,779	9.007	7740
4400	37.756	145,144	281.111	0.000	67.142	62,402	9.018	7920
4500	37.799	148,922	281.960	0.000	67.345	64,026	9.028	8100
4600	37.839	152,704	282.791	0.000	67.544	65,652	9.038	8280
4700	37.876	156,489	283.606	0.000	67.738	67,279	9.046	8460
4800	37.907	160,279	284.403	0.000	67.929	68,908	9.054	8640
4900	37.932	164,071	285.185	0.000	68.115	70,539	9.060	8820
5000	37.950	167,865	285.952	0.000	68.298	72,170	9.064	9000

Table D.11 Specific Heat, Enthalpy, Entropy, and Equilibrium Constant for Monatomic Oxygen O

$\bar{m}_O = 16.000$, $\Delta\bar{H}^\circ_{f,298} = 249{,}195$ kJ/kmol $= 107{,}136$ Btu/lbmol

T, K	$\bar{c}_p^\circ$, kJ/kmol-K	$(\bar{H}^\circ - \bar{H}^\circ_{298})$, kJ/kmol	$\bar{s}^\circ$, kJ/kmol-K	$\log_{10} K_P$	$\bar{s}^\circ$, Btu/lbmol-R	$(\bar{H}^\circ - \bar{H}^\circ_{298})$, Btu/lbmol	$\bar{c}_p^\circ$, Btu/lbmol-R	T, R
100	23.324	-4,464	136.194	-126.750	32.529	-1,919	5.571	180
200	22.477	-2,176	152.084	-61.995	36.325	- 936	5.369	360
298	21.898	0	160.944	-40.606	38.441	0	5.230	537
300	21.890	41	161.079	-40.337	38.473	17	5.228	540
400	21.500	2,209	167.319	-29.475	39.963	950	5.135	720
500	21.256	4,345	172.088	-22.941	41.103	1,868	5.077	900
600	21.113	6,463	175.950	-18.575	42.025	2,779	5.043	1080
700	21.032	8,570	179.197	-15.450	42.801	3,684	5.024	1260
800	20.986	10,671	182.003	-13.102	43.471	4,588	5.012	1440
900	20.951	12,768	184.472	-11.273	44.060	5,489	5.004	1620
1000	20.915	14,861	186.678	-9.808	44.587	6,389	4.995	1800
1100	20.897	16,952	188.671	-8.607	45.063	7,288	4.991	1980
1200	20.881	19,041	190.488	-7.605	45.497	8,186	4.987	2160
1300	20.867	21,128	192.159	-6.756	45.896	9,084	4.984	2340
1400	20.854	23,214	193.705	-6.028	46.266	9,980	4.981	2520
1500	20.843	25,299	195.143	-5.396	46.609	10,877	4.978	2700
1600	20.834	27,383	196.488	-4.842	46.930	11,773	4.976	2880
1700	20.827	29,466	197.751	-4.353	47.232	12,668	4.974	3060
1800	20.822	31,548	198.941	-3.918	47.516	13,564	4.973	3240
1900	20.819	33,631	200.067	-3.529	47.785	14,459	4.973	3420
2000	20.819	35,712	201.135	-3.178	48.040	15,354	4.972	3600
2100	20.821	37,794	202.151	-2.860	48.283	16,249	4.973	3780
2200	20.825	39,877	203.119	-2.571	48.514	17,144	4.974	3960
2300	20.831	41,959	204.045	-2.307	48.735	18,040	4.975	4140
2400	20.840	44,043	204.932	-2.065	48.947	18,935	4.977	4320
2500	20.851	46,127	205.783	-1.842	49.150	19,832	4.980	4500
2600	20.865	48,213	206.601	-1.636	49.346	20,728	4.983	4680
2700	20.881	50,300	207.389	-1.446	49.534	21,626	4.987	4860
2800	20.899	52,389	208.148	-1.269	49.715	22,524	4.992	5040
2900	20.920	54,480	208.882	-1.103	49.891	23,423	4.997	5220
3000	20.944	56,574	209.592	-.949	50.060	24,323	5.002	5400
3100	20.969	58,669	210.279	-.805	50.224	25,224	5.008	5580
3200	20.997	60,768	210.945	-.670	50.383	26,126	5.015	5760
3300	21.028	62,869	211.592	-.543	50.538	27,029	5.022	5940
3400	21.060	64,973	212.220	-.423	50.688	27,934	5.030	6120
3500	21.095	67,081	212.831	-.310	50.834	28,840	5.038	6300
3600	21.132	69,192	213.426	-.204	50.976	29,748	5.047	6480
3700	21.171	71,307	214.005	-.103	51.114	30,657	5.057	6660
3800	21.212	73,426	214.570	-.007	51.249	31,568	5.066	6840
3900	21.254	75,550	215.122	.083	51.381	32,481	5.076	7020
4000	21.299	77,677	215.661	.170	51.510	33,396	5.087	7200
4100	21.344	79,810	216.187	.252	51.635	34,312	5.098	7380
4200	21.392	81,946	216.702	.330	51.758	35,231	5.109	7560
4300	21.440	84,088	217.206	.404	51.879	36,152	5.121	7740
4400	21.490	86,234	217.699	.475	51.997	37,075	5.133	7920
4500	21.541	88,386	218.183	.543	52.112	38,000	5.145	8100
4600	21.593	90,543	218.657	.608	52.225	38,927	5.157	8280
4700	21.645	92,705	219.122	.671	52.336	39,856	5.170	8460
4800	21.698	94,872	219.578	.730	52.445	40,788	5.183	8640
4900	21.752	97,044	220.026	.788	52.552	41,722	5.195	8820
5000	21.805	99,222	220.466	.843	52.657	42,659	5.208	9000

Table D.1m Specific Heat, Enthalpy, Entropy, and Equilibrium Constant for Diatomic Oxygen O_2

$\bar{m}_{O_2} = 32.000, \quad \Delta\bar{H}^\circ_{f,298} = 0 \text{ kJ/kmol} = 0 \text{ Btu/lbmol}$

T, K	$\bar{c}_p^\circ$, kJ/kmol-K	$(\bar{H}^\circ - \bar{H}^\circ_{298})$, kJ/kmol	$\bar{s}^\circ$, kJ/kmol-K	$\log_{10} K_P$	$\bar{s}^\circ$, Btu/lbmol-R	$(\bar{H}^\circ - \bar{H}^\circ_{298})$, Btu/lbmol	$\bar{c}_p^\circ$, Btu/lbmol-R	T, R
100	29.115	-5,755	173.329	0.000	41.399	-2,474	6.954	180
200	28.946	-2,857	193.418	0.000	46.197	-1,228	6.914	360
298	29.354	0	205.037	0.000	48.972	0	7.011	537
300	29.366	54	205.218	0.000	49.016	23	7.014	540
400	30.144	3,028	213.767	0.000	51.057	1,302	7.200	720
500	31.093	6,089	220.593	0.000	52.688	2,618	7.426	900
600	32.069	9,247	226.349	0.000	54.062	3,976	7.660	1080
700	32.972	12,500	231.362	0.000	55.260	5,374	7.875	1260
800	33.744	15,837	235.816	0.000	56.324	6,809	8.060	1440
900	34.370	19,244	239.828	0.000	57.282	8,274	8.209	1620
1000	34.878	22,707	243.477	0.000	58.153	9,762	8.330	1800
1100	35.235	26,213	246.818	0.000	58.951	11,270	8.416	1980
1200	35.576	29,754	249.898	0.000	59.687	12,792	8.497	2160
1300	35.902	33,328	252.759	0.000	60.370	14,329	8.575	2340
1400	36.214	36,934	255.431	0.000	61.009	15,879	8.650	2520
1500	36.513	40,570	257.940	0.000	61.608	17,442	8.721	2700
1600	36.800	44,236	260.305	0.000	62.173	19,018	8.789	2880
1700	37.075	47,930	262.545	0.000	62.708	20,606	8.855	3060
1800	37.340	51,650	264.671	0.000	63.216	22,206	8.919	3240
1900	37.596	55,397	266.697	0.000	63.700	23,817	8.980	3420
2000	37.843	59,169	268.632	0.000	64.162	25,439	9.039	3600
2100	38.082	62,966	270.484	0.000	64.604	27,071	9.096	3780
2200	38.313	66,786	272.261	0.000	65.028	28,713	9.151	3960
2300	38.537	70,628	273.969	0.000	65.436	30,365	9.204	4140
2400	38.755	74,493	275.614	0.000	65.829	32,027	9.257	4320
2500	38.967	78,379	277.200	0.000	66.208	33,697	9.307	4500
2600	39.173	82,286	278.733	0.000	66.574	35,377	9.356	4680
2700	39.374	86,213	280.215	0.000	66.928	37,066	9.404	4860
2800	39.571	90,161	281.650	0.000	67.271	38,763	9.451	5040
2900	39.762	94,127	283.042	0.000	67.603	40,468	9.497	5220
3000	39.949	98,113	284.393	0.000	67.926	42,182	9.542	5400
3100	40.131	102,117	285.706	0.000	68.240	43,903	9.585	5580
3200	40.309	106,139	286.983	0.000	68.545	45,632	9.628	5760
3300	40.482	110,178	288.226	0.000	68.842	47,369	9.669	5940
3400	40.651	114,235	289.437	0.000	69.131	49,113	9.709	6120
3500	40.815	118,308	290.618	0.000	69.413	50,864	9.748	6300
3600	40.974	122,398	291.770	0.000	69.688	52,622	9.787	6480
3700	41.128	126,503	292.895	0.000	69.957	54,387	9.823	6660
3800	41.277	130,623	293.994	0.000	70.219	56,159	9.859	6840
3900	41.420	134,758	295.068	0.000	70.476	57,937	9.893	7020
4000	41.557	138,907	296.118	0.000	70.727	59,720	9.926	7200
4100	41.687	143,070	297.146	0.000	70.972	61,510	9.957	7380
4200	41.810	147,244	298.152	0.000	71.212	63,305	9.986	7560
4300	41.925	151,431	299.137	0.000	71.448	65,105	10.014	7740
4400	42.032	155,629	300.102	0.000	71.678	66,910	10.039	7920
4500	42.130	159,837	301.048	0.000	71.904	68,719	10.063	8100
4600	42.218	164,055	301.975	0.000	72.125	70,532	10.083	8280
4700	42.295	168,281	302.884	0.000	72.342	72,349	10.102	8460
4800	42.360	172,513	303.775	0.000	72.555	74,169	10.118	8640
4900	42.413	176,752	304.649	0.000	72.764	75,991	10.130	8820
5000	42.452	180,996	305.506	0.000	72.969	77,815	10.140	9000

index

conversion factors*

	To convert from	to	multiply by
Length	foot (ft)	meter (m)	0.3048†
	meter (m)	foot (ft)	3.28084
	inch (in.)	meter (m)	0.0254†
	meter (m)	inch (in.)	39.3701
	mile (mi)	meter (m)	$1.609344 \cdot 10^{3}$†
	meter (m)	mile (mi)	$0.621371 \cdot 10^{-3}$
Mass	pound (lbm)	kilogram (kg)	0.45359237†
	kilogram (kg)	pound (lbm)	2.20462
Force	pound (lbf)	newton (N)	4.4482216152605†
	newton (N)	pound (lbf)	0.224809
Temperature	rankine (R)	kelvin (K)	5/9
	kelvin (K)	rankine (R)	1.8
Area	ft^2	m^2	0.09290304†
	m^2	ft^2	10.7639
	$in.^2$	m^2	$6.4516 \cdot 10^{-4}$†
	m^2	$in.^2$	1550.00
Volume	ft^3	m^3	0.028316846592†
	m^3	ft^3	35.3147
	$in.^3$	m^3	$1.6387064 \cdot 10^{-5}$†
	m^3	$in.^3$	$6.10237 \cdot 10^{4}$
Velocity	ft/sec	m/s	0.3048*
	m/s	ft/sec	3.28084
	mi/hr	m/s	0.44704*
	m/s	mi/hr	2.23694
Density	lbm/ft^3	kg/m^3	16.018463
	kg/m^3	lbm/ft^3	0.0624280
Specific volume	ft^3/lbm	m^3/kg	0.0624280
	m^3/kg	ft^3/lbm	16.018463
Pressure	$lbf/in.^2$	N/m^2	6894.7572
	N/m^2	$lbf/in.^2$	$1.45038 \cdot 10^{-4}$
	lbf/ft^2	N/m^2	47.880258
	N/m^2	lbf/ft^2	0.0208854
	atmosphere (atm)	N/m^2	$1.01325 \cdot 10^{5}$
	atmosphere (atm)	$lbf/in.^2$	14.696
	bar	N/m^2	$1.0 \cdot 10^{5}$†
	N/m^2	pascal (Pa)	1.0†

conversion factors* (*cont.*)

	To convert from	to	multiply by
Torque	ft-lbf	m-N	1.35582
	m-N	ft-lbf	0.737562
Energy	Btu	ft-lbf	778.16†
	joule (J)	N-m	1.0†
	calorie (cal)	joule (J)	4.184†
	Btu	joule (J)	1055.04
	joule (J)	Btu	$9.47831 \cdot 10^{-4}$
	ft-lbf	joule (J)	1.3558179
	joule (J)	ft-lbf	0.737562
	Btu/lbm	J/kg	2325.965
	J/kg	Btu/lbm	$4.29929 \cdot 10^{-4}$
	ft-lbf/lbm	J/kg	2.98907
	J/kg	ft-lbf/lbm	0.334552
Power	horsepower (hp)	ft-lbf/sec	550.0†
	watt (W)	J/s	1.0†
	horsepower (hp)	watt (W)	745.700
	watt (W)	horsepower (hp)	$1.34102 \cdot 10^{-3}$
Specific heats, gas constants	Btu/lbm-R	J/kg-K	4186.8
	J/kg-K	Btu/lbm-R	$2.3885 \cdot 10^{-4}$
	ft-lbf/lbm-R	J/kg-K	5.38038
	J/kg-K	ft-lbf/lbm-R	0.185860
Viscosity	lbf-sec/ft^2	N-s/m^2	47.8803
	N-s/m^2	lbf-sec/ft^2	0.0208854
	lbm/ft-sec	kg/m-s	1.48816
	kg/m-s	lbm/ft-sec	0.671971
	Stoke	m^2/s	0.0001†
	Poise	N-s/m^2	0.1†
Mass flux	lbm/sec-ft^2	kg/s-m^2	4.88099
	kg/s-m^2	lbm/sec-ft^2	0.204876
Specific impulse	lbf-sec/lbm	N-s/kg	9.806650
	N-s/kg	lbf-sec/lbm	0.101972

* The conversion factors presented in this table were taken from E. A. Mechtly, "The International System of Units," NASA SP-7012, Second Revision, 1973.

† A dagger (†) following a number denotes that it is an exact definition.